Nuclear Science
NEA/NSC/WPFC/DOC(2015)9
www.oecd-nea.org

Structural Materials for Innovative Nuclear Systems (SMINS-3)

Workshop Proceedings
Idaho National Laboratory
Idaho Falls, United States
7-10 October 2013

OECD
BETTER POLICIES FOR BETTER LIVES

NEA
NUCLEAR ENERGY AGENCY

Nuclear Science **NEA/NSC/WPFC/DOC(2015)9**

Structural Materials for Innovative Nuclear Systems (SMINS-3)

Worshop Proceedings
Idaho National Laboratory, Idaho Falls, United States
7-10 October 2013

NUCLEAR ENERGY AGENCY
ORGANISATION FOR ECONOMIC CO-OPERATION AND DEVELOPMENT

ORGANISATION FOR ECONOMIC CO-OPERATION AND DEVELOPMENT

The OECD is a unique forum where the governments of 34 democracies work together to address the economic, social and environmental challenges of globalisation. The OECD is also at the forefront of efforts to understand and to help governments respond to new developments and concerns, such as corporate governance, the information economy and the challenges of an ageing population. The Organisation provides a setting where governments can compare policy experiences, seek answers to common problems, identify good practice and work to co-ordinate domestic and international policies.

The OECD member countries are: Australia, Austria, Belgium, Canada, Chile, the Czech Republic, Denmark, Estonia, Finland, France, Germany, Greece, Hungary, Iceland, Ireland, Israel, Italy, Japan, Luxembourg, Mexico, the Netherlands, New Zealand, Norway, Poland, Portugal, the Republic of Korea, the Slovak Republic, Slovenia, Spain, Sweden, Switzerland, Turkey, the United Kingdom and the United States. The European Commission takes part in the work of the OECD. OECD Publishing disseminates widely the results of the Organisation's statistics gathering and research on economic, social and environmental issues, as well as the conventions, guidelines and standards agreed by its members.

NUCLEAR ENERGY AGENCY

The OECD Nuclear Energy Agency (NEA) was established on 1 February 1958. Current NEA membership consists of 31 OECD member countries: Australia, Austria, Belgium, Canada, the Czech Republic, Denmark, Finland, France, Germany, Greece, Hungary, Iceland, Ireland, Italy, Japan, Luxembourg, Mexico, the Netherlands, Norway, Poland, Portugal, the Republic of Korea, the Russian Federation, the Slovak Republic, Slovenia, Spain, Sweden, Switzerland, Turkey, the United Kingdom and the United States. The European Commission also takes part in the work of the Agency.

The mission of the NEA is:

- to assist its member countries in maintaining and further developing, through international co-operation, the scientific, technological and legal bases required for a safe, environmentally friendly and economical use of nuclear energy for peaceful purposes, as well as
- to provide authoritative assessments and to forge common understandings on key issues, as input to government decisions on nuclear energy policy and to broader OECD policy analyses in areas such as energy and sustainable development.

Specific areas of competence of the NEA include the safety and regulation of nuclear activities, radioactive waste management, radiological protection, nuclear science, economic and technical analyses of the nuclear fuel cycle, nuclear law and liability, and public information.

The NEA Data Bank provides nuclear data and computer program services for participating countries. In these and related tasks, the NEA works in close collaboration with the International Atomic Energy Agency in Vienna, with which it has a Co-operation Agreement, as well as with other international organisations in the nuclear field.

Foreword

The development of innovative nuclear systems such as Gen IV reactors or critical and subcritical transmutation systems requires a good knowledge of the properties of the materials used for designing these reactors. A common feature in developing nuclear systems is the widely recognised need for experimental programmes to select and characterise structural materials. Structural materials research, both at national and international level, can significantly contribute to the future deployment of new systems.

Since 2007, the OECD Nuclear Energy Agency Nuclear Science Committee organises a series of workshop on Structural Materials for Innovative Nuclear Systems (SMINS) to stimulate an exchange of information on current materials research programmes for innovative nuclear systems with a view to identifying and developing potential synergies.

The third workshop was held on 7-10 October 2013 in Idaho Falls (United States) and organised through the collaboration of the Working Party on Scientific Issues of the Fuel Cycle (WPFC) and the Working Party on Multi-Scale Modelling of Fuels and Structural Materials for Nuclear Systems (WPMM) in co-operation with the European Community (EC) and the International Atomic Energy Agency (IAEA). A total of 74 abstracts were received for either an oral and poster presentation.

These proceedings include the papers presented at the workshop. The opinions expressed are those of the authors only, and do not necessarily reflect the views of the NEA, any national authority or any other international organisation.

Acknowledgements

The OECD Nuclear Energy Agency (NEA) is grateful to the Idaho National Laboratory for helping with the organisation of the Workshop despite the US Government shutdown. The Agency also extends its gratitude to the European Commission (EC) and the International Atomic Energy Agency (IAEA) for their co-operation.

Table of contents

Executive summary

Since 2007, the OECD Nuclear Energy Agency has been organising a series of workshops on Structural Materials for Innovative Nuclear Systems. The third meeting was held on 7-9 October 2013 in Idaho Falls (United States). The main objectives of this workshop are to stimulate an exchange of information on current materials R&D programmes for different innovative nuclear systems. The main topics of the workshop covered **fundamental studies, modelling and experiments** on innovative structural materials including cladding materials for the range of **advanced nuclear systems** such as thermal/fast systems, sub-critical systems, as well as fusion systems.

During the workshop, the following topics were discussed:

- Fundamental studies.
- Metallic materials.
- Ceramic materials.
- Novel materials pathways.
- Ion vs neutron irradiation.

Fundamental studies focused on the identification of mechanisms driving the response of materials under the conditions expected in innovative nuclear systems. These mechanisms may have acted at the atomic or higher scale with the application of multiscale approaches, together with related problems of scale-bridging or numerical methods, were of special interest. Moreover, irradiation experiments and subsequent characterisation of materials with analytical techniques were included in the session if aimed at better understanding the acting mechanisms or drawing physics-based correlations. **Metal alloys, ceramic and ceramic composites** included in- and out-of-core applications which took into account the scope of: data availability and gaps (considering also licensing issues); experimental and modelling needs for specific components or degradation modes; the link between R&D, standardisation and experimental protocols; coolant effects and mechanical properties. Code development and implementation plans were also discussed. Application of SiC composites to LWR systems was of interest as an advanced concept. **Novel materials pathways** considered routes to fabricate materials and components for innovative nuclear systems. The "**ions vs. neutron irradiation**"topic focused on specific irradiation comparisons including mechanical properties and microstructural effects caused by ion or neutron irradiation. Comparative irradiation studies on a common material were also welcome. *Fuel-cladding interaction was not covered in this edition of the workshop*.

The workshop received 74 abstracts, and was scheduled with 5 invited talks, 27 oral presentations and 2 poster sessions (42 posters) from 75 registered participants. However, it was necessary to reorganise the programme at extremely short notice to take into account the effects of the unexpected US government shutdown and the constraints this imposed on the workshop. In total, 38 participants from 12 countries and 2 international organisations attended, and the final number of presentations amounted to 51 (22 oral presentations and 29 posters).

The re-scheduled workshop opened with the welcome address by S. Cornet on behalf of the OECD Nuclear Energy Agency followed by technical sessions:

Session I: Overview on programmes and metal alloys.
Session II: Metal alloys.
Session III: Novel pathways.
Session IV: Ceramic composites, ions vs. neutrons and general.

Session I: Overview on programmes

International perspectives from several current programmes were presented: *Céline Cabet (CEA, France)* described the vision for sustainable nuclear energy that was defined in the European SET-plan, which envisaged a roadmap for SFR then LFR and GFR development in the longer term. Within Europe, the national R&D efforts are to be coordinated within the European Energy Research Alliance Joint Programme for Nuclear Materials (JPNM); the function of the new MatISSE project is to bring the EERA JPNM forwards to integration. The key work packages address: the development of a European R&D roadmap and strategic research agenda; irradiation hardening and creep in F/M alloys; ceramic matrix composites and MAX phase for refractories; ODS alloys; design, selection and qualification of materials for ESNII; and dissemination and communication. *Victor Inozemtsev (IAEA)* described the IAEA tools for programme implementation, which are co-ordinated research programmes (CRP) in addition to technical meetings (TM) and Expert Reviews. Recent examples of CRPs include fuel modelling; accelerator simulation and theoretical modelling of radiation effects (SMoRE); an ODS irradation effects benchmarking exercise; calculation of primary radiation damage, and also accident tolerant fuels and in-core structural materials for water-cooled reactors. *Lyndon Edwards (ANSTO, Australia)* gave an overview of the programmes on the Australian research reactor, which was designed for materials irradiation, isotopes and neutrons and is currently the most modern research reactor in the world. The key materials research themes are: radiation damage and multi-scale modelling to inform experiment design and surveillance programmes; advanced waste forms, such as synroc; PIE, with a focus on micromechanical testing, weld-modelling and synchrotron X-ray studies.

Session II: Metal alloys

Concetta Fazio (KIT, Germany) described the *GETMAT* project, whose objectives has been to procure and test ODS steels for clad and structural components and address their compatibility with environments, including irradiation effects, as well as to perform PIE on F/M steels and to expand understanding on Fe and Fe-Cr alloys. Key recommendations included the need for better understanding of fracture mechanisms to address low toughness (scatter and anisotropy) including a comparative study of ODS and F/M steels, and compatibility with liquid metal environments. *Pär Olsson (KTH, Sweden)* (for L. Malerba, *SCK•CEN, Belgium*) presented new data on nano-structure evolution and mechanical properties in neutron-irradiated Fe-Cr alloys, studied by SANS, APT, PAS and TEM after irradiations at ~300°C; a contribution to the hardening mechanisms was proposed from Cr segregation to dislocation loops. *Céline Cabet (CEA, France)* discussed 9Cr steels for SFR applications and the challenge for welded joints in the design code. These include creep and the influence of thermal ageing and fatigue on subsequent creep rates where new mechanistic models are needed for reliable prediction, particularly at low stress, and also corrosion in liquid sodium. *Concetta Fazio (KIT, Germany)* reviewed materials for Pb-cooled nuclear systems; corrosion mitigation requires control of oxygen in the coolant. Oxidation affects structural integrity and heat transfer; cracking of the oxide scale can also lead to creep rupture. Control of oxygen content at high temperatures may be difficult, but in this situation a coating of an Al-containing Fe-Cr alloy can improve oxidation resistance. *Jim Cole (INL, United States,* for Todd Allen) described the ATR user facility for neutron irradiations, which is open to all nations via a

peer reviewed proposal route and provides access to a range of PIE facilities. A US university lead proposer is generally needed (INL can act as a matchmaker), but not necessarily for rapid-turnaround projects that utilise archive materials or do not require extensive PIE. *Alberto Saez (CIEMAT, Spain)* reported SCC CERT testing at 400°C to 500°C of 316L stainless steel in SCWR environments, in which the composition profile of the double oxide layer was found to be affected by temperature; prior cold work increased SCC susceptibility. *Victor Ignatiev* (Kurchatov Institute, Russian Federation) described studies of Ni-Mo and Ni-W alloys for fuel circuit materials in MSR concepts that would use fluoride-based fuel salts at temperatures of 600-800°C; the key issues include irradiation embrittlement and fission products such as Tellurium, which is shown to cause SCC at 700°C. *Changhuie Jang (KAIST, Republic of Korea)* reported studies of the tensile and creep properties of Ni-based alloys (Alloy 617 and Haynes 230) in high temperature steam at 900°C; carbide redistribution with long-term increase strength but reduces ductility, while surface oxides act as crack initiation sites. *Joel Simpson (INL, United States)* described creep-fatigue degradation in Ni-alloy (Alloy 617) for VHTR applications, tested at 950°C, concluding that separation of creep and fatigue interactions in true creep-fatigue test is problematic. *Julian Benz (INL, United States)* presented work on fatigue and creep crack propagation in Alloy 617 for intermediate heat exchanger and steam generator applications. Crack growth rates, studied at 650°C to 800°C in He, are affected by oxide formation, carburisation and decarburisation, of which carburisation is most detrimental; impure He environments accelerate crack growth due to a lack of oxidation protection. *Dan Shepherd (NNL, United Kingdom)* reported a TRL (technology readiness level) assessment of cladding alloys for advanced nuclear fuels, with a focus on fuels for Gen III and Gen IV systems; the assessment may be used to target research. TRL levels were low for ceramics compared to metals, with cladding TRLs also lower than fuels, indicating that clad development may be a limiting factor.

Session III: Novel pathways

David Gandy (EPRI, United States) described developments in powder metallurgy and HIP, focused on the vision for structural and pressure retaining applications for which large castings and forgings are needed for nuclear as well as for fossil-fuel super critical water plant. Examples include 316L stainless steel and carbon steels, with developments towards approval for components that can be inside the RPV. It was noted that higher fabrication costs may be compensated lower lifetime costs due to better ability to inspect; the more homogeneous structure improves inspection compared to castings and forgings. Power processing also enhances chemistry control and provides an alternate supply route for large components. *Indrajit Charit (Idaho University, United States*) presented a study of spark plasma sintered (SPS) nano structured ferritic ODS steels, utilising lanthanides instead of Yttria for slower diffusion. SPS can be advantageous as oxide particles and nano-clusters form before grain growth can occur. *Akira Kohyama (Muroran Institute of Technology, Japan)* described development work to scale up production of SiC-SiC composites within the INSPIRE & SCARLET programmes, which have been influenced by the recent increased requirements for accident tolerance in Gen III reactors, replacing Zr alloys and establishing the technology basis for fuel assembly fabrication. Irradiation programmes at the Halden reactor are planned. The issues discussed included joining (brazing and treaded joints have been demonstrated) and confidence in gas tightness to address fission product release.

Session IV: Ceramic composites, ions vs neutrons and general

Pär Olsson (KTH, Sweden) described Kinetic MonteCarlo modelling studies of FeCrAl steels, in which there is an optimum composition range to obtain corrosion resistance without 475°C embrittlement with thermal aging due to the effects of Al on the spinodal decomposition rate and its segregation to the surface. *Ji-Yeon Park (KAIST, Republic of Korea)*

described SiC-SiC fibre composites for accident tolerant fuels, and also for VHTR control rod and GFR fuel clad applications, with a fabrication concept of monolithic SiC, composite inner layer and external monolithic SiC; data for mechanical strength tests, corrosion in LWR environments and joining were presented. *Pär Olsson (KTH, Sweden,* for Lorenzo Malerba, SCK-CEN, Belgium) presented atom probe tomography studies of Fe-12Cr in a comparative study of neutron and ion irradiation at 300°C: neutrons form clusters and alpha', but ions form only clusters; the sizes and composition of clusters also differ. The different response can be understood by the high flux of ion irradiation; it was concluded that it was important for ion-irradiations to be supported by underlying physics, and used to focussed experiments on aspects of irradiation damage, not as a direct substitute for neutrons.

NEA welcome address

S. Cornet

OECD Nuclear Energy Agency (NEA)

On behalf of the OECD Nuclear Energy Agency, it is a great pleasure to welcome you to the third international workshop on Structural Materials for Innovative Nuclear Systems.

First of all, I would like to express my thanks to the workshop chairs, Todd Allen and James Marrow as well as all INL staff and the members of both the scientific and organising committees for all their efforts to help preparing this workshop. I would also like to thank the European Commission (EC) and the International Atomic Energy Agency (IAEA) for their cooperation in the organisation of this workshop.

With the emergence of different innovative reactor systems, such as Generation IV reactors, the field of structural materials remains very active. The extreme conditions attributed to operating these new systems such as very high temperature, high burnups, long service life and compatibility with different coolants require the development of materials capable of supporting these conditions.

In this context, the NEA Nuclear Science Committee has already organised two workshops, in 2007 (in Germany) and 2010 (in Republic of Korea), on structural materials for innovative nuclear systems.

The first workshop of 2007 led to the creation of new activities at the NEA in the field of material science. The Working Party of Multi-scale Modelling of Fuels and Structural Materials for Nuclear Systems was established to deal with the scientific and engineering aspects of fuel and structural materials, aiming at establishing multi-scale models and simulations such as validated predictive tools for the design, fuel fabrication and performance of nuclear systems. This working party includes five different expert groups. The WPFC Expert Group on Innovative Structural Materials was also created to conduct joint and comparative studies to support the development, selection and characterisation of innovative structural materials that can be implemented in advanced nuclear fuel cycles, under extreme conditions. The Expert Group has produced a status report on Structural Materials for Innovative Nuclear Systems published in November 2013. These expert groups are still actively participating to the understanding and advances regarding the use of innovative materials.

The Nuclear Science Committee considers the development of structural materials for nuclear application of great importance and therefore fully supports the organisation of this workshop. The objectives of this meeting are to exchange current knowledge on structural materials research issues and ongoing programmes for different types of reactors concepts. This year, we received about 70 papers to be presented either by oral or poster session covering scientific issues of fundamental studies, metal, ceramics, novel materials pathways, and ion versus neutron irradiation. Invited lectures on key issues such as perspectives on materials choices for advanced nuclear systems, code qualification and material date needs, use of user facilities for the development of innovative materials, perspectives on modelling materials far from equilibrium will be presented over the next few days. A discussion on ion versus neutron irradiation will

take place following three short presentations on the subject. A summary session will close the workshop and aims at covering critical experiments, modelling needs and round robin opportunities.

I hope that this workshop will be fruitful and useful for scientists to get a general overview of current research activities in the field of structural materials and will allow more opportunities to establish further international collaborations.

I wish you a very nice stay in Idaho Falls.

Session I

Overview on programmes

Chair: J. Marrow

The new EC FP7 MatISSE project: materials' innovations for a safe and sustainable nuclear in Europe

C. Cabet* **and A. Michaux**
CEA DEN/DANS/DMN, 91191 Gif-sur-Yvette, France

C. Fazio
KIT, Germany

L. Malerba
SMM/SMA/NMS, SCK CEN, Boeretang 200, 2400 Mol, Belgium

M.-F. Maday
ENEA UTT-AT, CR Casaccia, Via Anguillarese 301, 00123 S.M. di Galeria, Rome, Italy

M. Serrano
CIEMAT, Spain

and K.-F. Nilsson
JRC, European Commission

Abstract

The European Energy Research Alliance (EERA), set-up under the European SET-Plan, has launched an initiative for a Joint Programme on Nuclear Materials (JPNM). The JNMP aims to establish key priorities in the area of advanced nuclear materials, identify funding opportunities and harmonise this scientific & technical domain at the European level by maximising complementarities and synergies with the major actors of the field. The JPNM partners submitted the MatISSE proposal which was accepted by the European Commission. The MatISSE project has the ambition to prepare the building of a European integrated research programme on materials innovation for a safe and sustainable nuclear. Emphasis is on advanced nuclear systems in particular sodium-cooled fast reactor (SFR), lead-cooled fast reactor (LFR) and gas-cooled fast reactor (GFR). The aim of the selected scientific and technical work is to make progress in the fields of conventional materials, advanced materials and predictive capabilities for fuel elements and structural components.

Concept and objective of the MatISSE EU project

The MatISSE project aims to build a European integrated research programme on materials innovation for a safe and sustainable nuclear.

With the European Strategic Energy Technology Plan (SET-Plan), the EU aims to foster clean, efficient and low-carbon energy technologies to face up to the energy and environmental challenges of today with binding targets for 2020, in particular on greenhouse gas emission, and with a longer term vision of a low carbon energy society by the 2050 horizon [1]. Several energy technologies have been proposed to achieve this goal, nuclear technology being among them. To achieve these goals, the SET-Plan objectives for nuclear development are addressed by the Sustainable Nuclear Energy Technology Platform (SNETP) which through the promotion of research, encourage the development

and demonstration of sustainable and economic nuclear fission technologies as part of the low carbon energy mix. The SNETP has identified three pillars in its Strategic Research and Innovative Agenda (SRIA) [2]:

- light water reactors with a focus on safety and competitiveness through long-term operation;
- innovative reactors based on fast neutron spectrum and closed fuel cycle, to make more efficient use of uranium resources, generate less long-lived radioactive wastes, and reduce proliferation risks, while developing highly favourable safety characteristics;
- expansion of fission energy use beyond electricity production.

As far as the sustainability target is concerned, the SNETP has defined its strategy and technological pathway for three technologies:

- the sodium fast reactor (SFR) as a first track aligned with Europe's prior experience;
- two alternative fast neutron reactor technologies to be explored on a longer timescale: the lead cooled fast reactor (LFR) and the gas cooled fast reactor (GFR).

The SNETP pilots the European Sustainable Nuclear Industrial Initiative (ESNII), dedicated to demonstrate the sustainability of nuclear energy through the deployment of advanced fission systems [3]. ESNII aims to design and construct prototype/demonstration reactors:

- a prototype SFR ASTRID;
- a LFR Pilot Plant MYRRHA, then a LFR Demonstrator ALFRED;
- an Experimental GFR ALLEGRO.

Advanced fission systems are challenging for materials as they seek for breakthroughs in sustainability and economics (while keeping high safety standards) that result in extreme operating conditions. Many components have to withstand severe conditions: high temperature and mechanical loading, prolonged operation under irradiation, corrosive environments. The viability and potential for innovation of those reactor concepts will crucially depend on the demonstration that the materials for fuel elements and structures can withstand the operating conditions in the longer term. Safe and long-term use of fuel and structural elements relies on the search for innovative materials and the development of robust and predictive evaluation methods in support to their qualification. A superior safety justification is expected which calls for deep understanding and reliable simulation of the behaviour of materials and components under nominal and transient operating conditions. These issues are essentially cross-cutting in terms of relevant materials, of theoretical and experimental work, and of involved research teams, facilities and expertise.

In terms of materials, the building of prototypes and the deployment of advanced systems call for priority issues to be investigated:

- qualification of materials for codification and licensing of structural elements of prototype and demonstration reactors;
- lifetime assessment of components for long-term operation;
- development of materials of superior performance, especially fuel cladding for LFR, SFR and GFR;
- qualification of fuel materials for codification and licensing.

In this context, and in line with the SET-Plan goals, a number of research associations belonging to the European Energy Research Alliance (EERA) have launched a Joint Programme on Nuclear Materials to determine key priority topics and funding

opportunities [4]. The purpose is to support the development of a sustainable nuclear energy in an efficient way. Safety, which draws particular attention since March 2011, has been prominent in the strategy as well. The Joint Programme aims at:

i) developing a common view on strategic needs and a path forward for nuclear materials innovation;

ii) promoting joint prioritisation of research activities;

iii) sharing knowledge, best practices and infrastructures; iv) supporting synergies of European and national efforts; v) identifying a viable business model.

The EERA JPNM addresses cross-cutting scientific and technological high quality research which will benefit all reactors of the three SNETP pillars, with a main focus on the fast neutron systems.

The analysis performed since 2009 by the JPNM has led to the definition of cross-cutting research themes of interest regarding innovative material development and screening; experimental characterisation; fabrication issues including welding, joining, and coating technologies; and pre-normative research.

Common research targets have been agreed in four sub-programmes (SP):

- SP1 – Support to ESNII.
- SP2 – Oxide dispersed strengthened (ODS) steels.
- SP3 – Ceramic composites and refractory alloys.
- SP4 – Modelling: correlation, simulation and experimental validation.

The MatISSE proposal was built to bring forward the EERA JPNM on the way to integration. Innovative materials research for nuclear energy has been going on in several European laboratories and organisations, supported by national programmes, EC funding and other frameworks, such as private-public collaborations. It is intended to reach a common strategic approach and to better align these activities. The MatISSE proposal has been shaped to mirror the JPNM structure and addresses five main objectives. Figure 1 shows the project organisation used for the breakdown into Work Packages. The objectives are related both to the JPNM overall coordination and to targeted technical tasks supporting the above mentioned SPs. As far as the scientific activities are concerned, MatISSE will be consistent with the JPNM requirements by seeking excellence and delivering high quality results in a timely manner both in the experimental and modelling areas. The following sections describe the objectives of the technical tasks (work packages 2 to 5).

Figure 1: MatISSE main objectives and work package breakdown structure

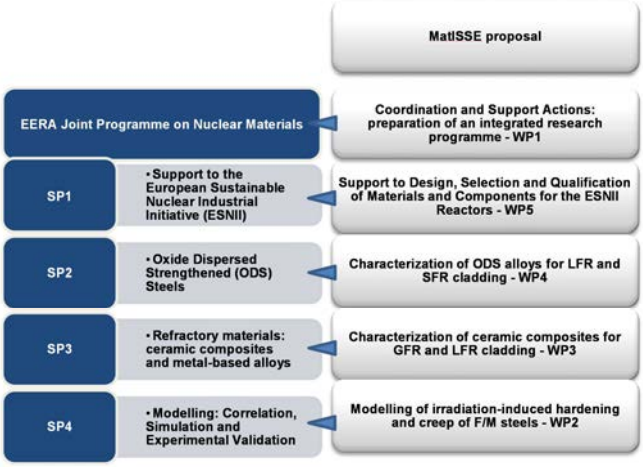

WP2 – Modelling of irradiation-induced hardening and creep in F/M alloys

In FP7/PERFORM60 (Prediction of the Effects of Radiation FOr Pressure Vessel and in-core Materials using multi-scale Modelling – 60 years foreseen plant lifetime) specific attention has been devoted to studying and modelling the effect of C atoms on the nanostructural evolution under irradiation of ferritic alloys, leading to the development of physically reliable computer models that actually simulate an irradiation process up to ~1 dpa in terms of point-defect clusters accumulation. Eventually, a model for the FeC system has been released and progress has been also made in understanding partially the effects of Cu, Ni and Mn on the nanostructure evolution under irradiation of Fe alloys, finding that both these elements, especially Mn, segregate on dislocation loops. In FP7 GETMAT (Gen IV and Transmutation Materials) [5] the focus of modelling has been on Fe-Cr alloys. Advanced modelling techniques have clearly shown that in these alloys, Cr atoms segregate on dislocation loops, thereby making these significantly stronger obstacles for dislocations. Moreover, it has been found that the interaction of screw dislocations with solute-decorated loops having collinear Burgers vector leads to the formation of helical turns that have strength up to 10 times higher than Orowan obstacles. These mechanisms fairly accurately explain the trends for radiation strengthening observed in Fe-Cr alloys with different Cr content. The main result of an extensive experimental programme on commercially pure Fe-Cr model alloys, irradiated with neutrons and ions and subsequently characterised using different microstructural probing techniques, led to the conclusion that in these alloys, and most likely in steels as well, the main cause of radiation strengthening are barely visible dislocation loops decorated with Cr, as well as Ni, Si and P. These features bear a clear resemblance with the so-called late blooming phases that represent currently a concern for the lifetime of pressure vessels in LWRs. There seems to be, therefore, a common mechanism at the origin of the hardening and embrittlement of ferritic-bainitic and ferritic-martensitic steels.

The mechanisms of formation of these hardening features and their kinetics will be further investigated, with a view to develop relevant nanostructure evolution models and to provide, as ultimate objective, support to the elaboration of physically-informed correlations for hardening and embrittlement in this class of steels, as functions of dose, but also dose-rate and temperature.

For what concerns irradiation creep, a wide range of possible mechanisms for its onset have been proposed in the past, such as stress-induced preferential absorption (SIPA) or nucleation (SIPN), anisotropic diffusion, dislocation climb&glide (deriving relevant dislocation mobility laws), slip bands, or others. Relatively simple and semi-empirical models have been historically developed to try to quantify their relative importance, as compared to experiments. Experimentally, however, it is difficult to discriminate between the role of one or another mechanism leading to dimensional changes. So, in the past only very tentative and debated conclusions could be drawn as regards the mechanism to be considered dominant for the different materials examined. Modern atomistic and dislocation simulation techniques (not available 20 years ago, when the creep models were reviewed or proposed) will valuably contribute to screen the plausibility of one or another mechanism, thereby allowing a quantification of their importance and of the parameters that govern them. The results of the investigations will also be used to guide the design of ad hoc *in-situ* ion irradiation experiments, to be performed in the future.

It should be noted that modelling activities have a cross-cutting nature to fuel and structure elements and are also of high interest for the networking with the fusion community, as similar materials and problems are studied in that context, with similar, though not coincident, tools.

WP 3 – Characterisation of ceramic composites for GFRs and LFRs

Advanced refractory materials are necessary for the fuel cladding of a GFR, which is designed to operate at temperatures exceeding current heat-resistant alloy capabilities. To

meet this ambitious goal, the first choice for refractory fuel cladding are silicon carbide fibre-reinforced silicon carbide matrix composites (SiCf/SiC), which are thermally stable and retain their strength and toughness up to very high temperatures (approx. 1 600°C). Assembled with nuclear grade constituents (i.e. 3rd generation SiC fibres, a PyC interphase and a β-SiC matrix infiltrated by chemical vapour infiltration), these materials have the essential pre-requisite of neutronic compatibility with a fast neutron spectrum and should meet the requirements in terms of irradiation and oxidation resistance in the reactor environment.

Nuclear grade SiCf/SiC composites have been developed within the fusion materials programmes in Europe and worldwide for the DEMO "blanket" concept. So far, these composites have been fabricated and investigated as simple flat panels or plates, optimising microstructure to achieve state-of-the-art thermo-mechanical properties. However, the reference geometry for GFR fuel cladding is more complex, the primary option being a fine wall tube. Breakthrough in design and manufacturing route has enabled to achieve leak-tightness by incorporating a refractory metallic liner between two structural SiCf/SiC layers, the so-called sandwich concept. Since manufacturing technologies and parameters primarily affect the material microstructure, prototyping and proof-testing in representative geometry are required. The sandwich concept will be the reference composite for the characterisation activity. The objective is to characterise the fundamental properties of the as-fabricated clad system, considering the mandatory safety requirements of high strength, full leak-tightness, high heat exchange capability and corrosion/erosion resistance to helium coolant. The expected pathways arising from this work are to establish a sound experimental framework (testing methods and evaluation tools) in order to characterise composite cladding materials in the shape of tubes and to produce reliable data to validate component feasibility and performances. This is necessary for the subsequent qualification phase addressing time-dependent component performances.

This will provide the necessary background for further improving the material processing.

To accomplish these objectives in a 4-year timeframe, the work will integrate the technical expertise and scientific knowledge of partners, qualified in the relevant fields. The experimental activities will benefit from the availability of the necessary small-scale facilities and large-scale integrated infrastructures at the participating associations, and their willingness to share them.

The potential of ceramic composites as corrosive/erosive resistant structural materials is also considered for application in heavy liquid metals (HLM: Pb, LBE) such as pump impellers of MYRRHA and LFRs. Materials that are envisaged for this particular application belong to an emerging family of refractory materials known as MAX phases. MAX phases are ternary carbides and nitride compounds with quite unusual, for ceramics, damage tolerance, and an ability to deform plastically even at room temperature when processed so as to achieve an optimal microstructure. Generally speaking, MAX phases exhibit machinability similar to that of graphite, and they are fair thermal conductors with satisfactory thermal shock resistance. Preliminary studies on specific phases from the MAX family have shown oxidation and liquid metal corrosion (dissolution) resistance to HLM as well as appreciable radiation tolerance. However, MAX phases are still characterised by mediocre fracture toughness (< 16 MPa.m1/2) that must be improved before these materials can be used as reliable structural materials in a nuclear system environment. In this respect, MAX phase-based cermets, i.e. composites made of MAX phases embedded in a matrix of the appropriate metal binder, are proposed as a novel material concept. Some research has been included in MatISSE, where a systematic study will focus on the identification of promising MAX phase/metallic matrix combinations. The best candidates will be down-selected against the material property requirements of the MYRRHA pump impeller component, especially in terms of erosion resistance in contact with the fast-flowing liquid LBE.

WP4 – Characterisation of ODS alloys for LFR and SFR cladding

The first core of ESNII systems such as ASTRID and MYRRHA will use austenitic steel cladding for which engineers can rely on former experience. High-Cr F/M steels exhibit superior swelling resistance which should allow for higher burn-up and increase safety margins. However, their strength is limited for higher temperatures (typically above 650°C). ODS alloy versions of ferritic steels, reinforced by a distribution of nano-oxides (or nano-clusters, NC), show higher creep strength and maintain the swelling resistance, making them good candidates for the cladding of advanced fast reactors. Therefore, ODS ferritic and F/M steels are envisioned as reference cladding for high burn-up fuel in fast reactors. The final choice between the 9Cr (Ferritic/Martensitic) and 14Cr (Ferritic) ODS alloys for cladding is still open. Ferritic ODS alloys are preferred due to theirs better environmental compatibility and mechanical properties, while F/M alloys show a more isotropic microstructure and better thermal stability.

The experience gained within the FP7 GETMAT [5] and MATTER [6] projects on the characterisation of plates and/or bars contributes to the knowledge and pre-design of ODS alloys to be used as cladding for fast neutron reactors. FP7 MATTER investigates the formation of NC during the fabrication procedure. Within GETMAT, comprehensive mechanical characterisations at high temperature in terms of tensile, creep and low cycle fatigue (LCF) tests of different ODS alloys have been carried out, but only a basic microstructure characterisation is performed. Besides, these two projects do not comprise any ODS tube while this geometry is the one relevant for the application.

Open points that have been identified as a result of the past and on-going activities on ODS for cladding are:

- formation of NC and their stability under high temperature and neutron/ion irradiation to maintain the properties of ODS alloys during operation;
- fracture and deformation mechanisms: the role of NC on hardening;
- anisotropy: the fabrication of thin-walled cladding tubes is usually made by a succession of cold deformation steps with intermediate heat treatments to avoid cracking. Due to this fabrication process, a deformation-induced anisotropic microstructure may build on with weaker strength and creep properties in the hoop direction than in the axial one.

Within MatISSE a deeper microstructural examination of ferritic and F/M ODS steels (e.g. GETMAT ODS steels) using complementary techniques is included, to study the role of the ODS microstructure on the deformation behaviour and to assess the stability of the microstructure at high temperature and under ion irradiation. Additionally, this microstructure scenario could be used to feed the on-going and future modelling activities and gives valuable information for the target microstructure of tubes.

A huge asset to the European materials community will be the procurement, testing and characterisation of ODS tubes. Past experiences (mainly in France and other non-EU countries) on the fabrication of ODS cladding tubes have shown that it is possible to reduce the anisotropy of the tubes by taking advantage of the austenite to ferrite phase transformation. This is achieved through intermediate heat treatments of 9Cr ODS alloys, and recrystallisation of Fe-12Cr and Fe-14Cr ODS tubes. A clear step forward in the development of ODS tubes for cladding within MatISSE is that ODS cladding tubes of two compositions, Fe-9Cr and Fe-14Cr, will be distributed and characterised, which will give new input to select the best ODS cladding candidate. The anisotropy and its effect on the mechanical behaviour will be assessed by microstructural examinations and high temperature testing under uniaxial and biaxial loading conditions.

To identify design margins of ODS cladding tubes, taking into account transient conditions, a basic characterisation of ODS tubes creep under off-normal conditions at high temperature will be carried out. Burst tests and compatibility of surface modified ODS alloys are also included.

WP5 – Support to design, selection, and qualification of materials and components for the ESNII reactors

The demonstrators and prototype reactors to be designed and constructed in the coming decades will rely on materials that exist commercially today. Analysis of the expected operating conditions as well as the experience gained from past operation of sodium-cooled systems and lead-alloy facilities have identified two material groups of high interest: F/M steels and austenitic steels; nickel based alloys are also considered. Those steels are largely used in the conventional energy generation and the nuclear industry. But ESNII systems require qualification of these materials under more severe conditions – mechanical loading, temperature, irradiation and environment – and for longer design lifetime. Down-selection will be based on performances under normal operation and safety relevant conditions. Pre-normative research for codification and standardisation will then be essential to support the design and licensing of ESNII systems. Moreover, the environmental resistance in corrosive coolants must be investigated and mitigation strategies are already foreseen. Another environment-related process is the interaction between the fuel, oxide fuel and the cladding alloy.

Work Package 5 of MatISSE is composed of four activities that constitute only a small part of the work required to support the design as well as construction of the ESNII prototypes.

Creep-fatigue is one of the most important degradation mechanisms for structural alloys which requires special attention in the design, in particular for F/M steels that are subjected to cyclic softening. The work will complement the study on design rules performed in MATTER [6] and two aspects will be addressed: modelling of the physical mechanisms that lead to cyclic softening and propagation of creep-fatigue cracks. The physics based models will help in improving design rules and is a tool for extrapolation from accelerated test to operational conditions. Crack propagation is not considered in basic Design Rules but components in fast reactors are primarily subjected to thermal loads with large stress gradients and it is therefore crack propagation rather than crack initiation that will control the life of a component.

Functional coatings and surface modifications, primarily for fuel cladding materials but also for structural components such as steam generators, can increase the operating temperature and increase safety margins for corrosion and wear resistance of future nuclear systems, cooled with Pb alloys. It has been shown that reservoir layers containing Al may improve significantly the corrosion resistance in liquid lead alloys. So far optimisation of coating composition has been limited to Al content and Al/Cr ratio (GETMAT project [5]). Adding minor amounts of reactive elements (e.g. Y, Ce, Hf, Zr), can further improve high-temperature performance and stability under irradiation. The Task on “Functional coatings and modified surface layers” is to evaluate of the compatibility of some specific and specially designed coatings for liquid lead and to assess corrosion and mechanical properties of the coated or surface alloyed materials in contact with Pb alloys and the stability under irradiation of FeCrAl-RE alloy coatings.

The fuel cladding will be exposed to high irradiation doses in advanced nuclear reactors. For all reactor concepts, the higher burn-up in combination with minor actinide fuels means that fuel-cladding interaction needs to be addressed to ensure integrity of the fuels pins also in accident scenarios, the fuel itself and the cladding being the first barriers against the release of the radionuclides. The cladding interacts with the fuel through both mechanical and chemical interaction and therefore the integrity and safety assessment of the fuel pin (fuel and cladding) must be seen as one component. The fuel pin integrity has been given much more attention after the Fukushima accident and stricter requirements to demonstrate safety performance is expected also for advanced fission systems. Assessment of the fuel pin requires collaboration between experts of fuel and of structural materials. This integration between the structural materials and fuel communities will be initiated by some preparatory studies that will be performed to assess methods for pin

analysis and to map the existing databases. Fuel pins have been irradiated in previous European programmes for nuclear fuels. Some of these fuel pins will be examined for characterisation and better understanding of fuel-cladding interaction. This experience can be very useful for future studies on the most relevant fuel pins.

Various mechanical tests performed in liquid lead and lead-bismuth eutectics have revealed that properties of F/M steels may be degraded for specific combinations of environmental, mechanical and material parameters. Particularly it was shown that dissolved oxygen concentration, pre-exposure temperature and silicon content in F/M steels may have an effect. However, these observations are still disembodied and the list of the parameters influencing appearance and degree of degradation is extensive but not complete. Therefore qualification of F/M steels, Grade 91 steel particularly, for LFR application is hampered due to existing uncertainties and lack of understanding of underlying mechanisms. Work is therefore proposed in the task "Investigation of environment assisted degradation of material properties in liquid lead alloys" to investigate the mechanisms of environmentally assisted material degradation in liquid lead alloys and to develop a mitigation approach to support design of MYRRHA and LFRs. The research will concentrate on the following effects: low cycle fatigue, fatigue crack growth rate, thermal creep propagation of cracks under constant load conditions. The damaged zones of the selected specimens will be thoroughly characterised by advanced microstructural analysis methods. Results will be used for assessing the effect of environment assisted degradation on the reactor performance and for developing mitigation approaches.

Conclusion

The MatISSE project has the ambition to prepare the building of a European integrated research programme on materials innovation for a safe and sustainable nuclear. European R&D organisations with a variety of expertises, competences and testing facilities have been given the mandate by their governments to contribute to R&D&I efforts on advances in materials for energy. Under the auspices of the European Energy Research Alliance (EERA) initiative, these partners have set-up a Joint Programme on Nuclear Materials (JPNM) with the objective of better coordinating national initiatives, EC funded programmes and, possibly, other private-public or transnational collaborations. One of MatISSE's main objectives is to effectively support the JPNM evolution. Moreover, MatISSE will comprise targeted R&D activities in thematic areas considered as priorities by the JPNM partners:

- to model irradiation-induced hardening and creep in ferritic/martensitic (F/M) alloys;
- to assess the potential of ceramic composites as advanced fuel cladding for GFR and novel structural materials for LFR;
- to contribute to the pre-designing of oxide dispersion strengthened (ODS) steels to be used as cladding for fast neutron reactors;
- to support the design, selection and qualification of commercially available materials to be used for the fast neutron prototypes and demonstrators in terms of creep-fatigue of F/M and austenitic steels; functional coatings and modified surface layers; fuel-cladding interaction; investigation of environment assisted degradation of steels in liquid lead alloys.

The project also includes dissemination and training activities as well as coordination and support actions to accompany the JPNM evolution toward efficient Joint Programming among the Member States, the European Commission and the main European research stakeholders.

Acknowledgements

The European Commission is greatly acknowledged for its financial support through the programme FP7-EURATOM-FISSION (MatISSE Grant agreement no: 604862).

References

[1] SET-Plan (2010), "The European Strategic Energy Technology Plan", doi: 10.2833/14565, Publications Office of the European Union.

[2] SNETP (2013), "SNETP – Strategic Research and Innovation Agenda", ISBN 978-2-919313-04-4, Editors: SRIA Editorial Board and SNETP Secretariat.

[3] SNETP (2010), "The European Sustainable Nuclear Industry Initiative – Concept Paper", Editors: ESNII Task Force and SNETP Secretariat.

[4] EERA, http://www.eera-set.eu/.

[5] GETMAT, "Gen IV and transmutation materials", EC programme FP7-EURATOM-FISSION, project no: 212175.

[6] MATTER, "MATerials TEsting and Rules", EC programme FP7-EURATOM-FISSION, project no: 269706.

IAEA co-ordinated research projects (CRP) supporting development of structural materials for innovative nuclear systems

Victor Inozemtsev and Andrey Zeman
IAEA, Vienna

Abstract

CRPs are the most durable and systematic IAEA programme implementation tool. Their objectives are defined on the basis of requests from the Member States, so they reflect real national needs and priorities. While during many years engineering activities were mainly focused on evolutionary development of existing nuclear power technologies, the last time more and more Member States are involved into innovation programmes targeting better operational parameters, optimised nuclear fuel cycles, and less radioactive wastes. Such innovative nuclear power technologies require new advanced radiation resistant materials, able to reliably operate in earlier non-experienced conditions. Particularly challenging parameters are characteristic for fuel cladding and other structural materials of fuel assemblies that undergo a combination of extreme radiation, chemical and mechanical loads. Development of these materials require considerable efforts, time and money, that brings about a need for international collaboration where the IAEA plays a considerable role.

From 1993 to 2013 the IAEA has implemented a series of three CRPs on fuel modelling (FUMEX), and the joint NEA-IAEA International Fuel Performance Experimental (IFPE) Database of well-reviewed irradiation test results has been created, which aim to verify computer codes developed in different countries for analysis and prediction of fuel behaviour. Nevertheless that semi-empirical approach does not allow penetration into the unknown area of super high doses that requires experimental and theoretical simulations. Hence the IAEA initiated CRPs on accelerator simulation and theoretical modelling of radiation effects (SMoRE, 2008-2013) and on ODSS benchmarking (started in 2011). The presentation provides information about organisation and available results of these recently finished and on-going CRPs, as well as about plans for the near future.

Session II

Metal alloys

Part 1
Chair: D. Gandy

Part 2
Chairs: C. Fazio and R. Wright

Part 1
Chair: D. Gandy

Generation IV and transmutation materials (GETMAT) project: First assessment of selected results

Concetta Fazio*[a], Marta Serrano[b], Alessandro Gessi[c], Jean Henry[d], Lorenzo Malerba[e]

[*a] *formerly,* Karlsruhe Institute of Technology, Program NUKLEAR, Germany;
[*a] *at present,* European Commission, DG JRC – ITU, Materials Research unit, Germany
[b]Centro de Investigaciones Energéticas, Medioambientales y Tecnológicas, Spain
[c]Agenzia nazionale per le nuove tecnologie l'energia e lo sviluppo economico sostenibile, Italy
[d]Commissariat à l'énergie atomique et aux énergies alternatives, France
[e]Studiecentrum voor Kernenergie – Centre d'Étude de l'Énergie Nucléaire, Belgium

Abstract

The Generation IV and Transmutation Material (GETMAT) project has been initiated within the 7th EURATOM framework programme with the objective to support the development of innovative reactor designs. Emphasis has been put on the investigation, both in the theoretical and experimental domains, of selected material properties that are cross-cutting among the various Generation IV and Transmutation systems. The selection of the properties to be investigated has been performed by identifying relevant conditions of key components as cores and primary systems. Moreover, taking into account the envisaged conditions of these components it turned out that innovative materials might be a better choice with respect to conventional nuclear grade steels. Therefore, ODS alloys and 9-12 Cr Ferritic/Martensitic (F/M) steels have been selected as reference for the GETMAT project. The R&D activities have been focused on basic characterisation of ODS alloys produced ad hoc for the project and on an extensive PIE programme of F/M steels irradiated in previous programmes. Finally, first principle modelling studies to explain irradiation hardening and embrittlement of F/M alloys were an additional important task. The objective of this manuscript is to make a first assessment of the results obtained within GETMAT.

Introduction

The key elements at the origin of the GETMAT project have been identified through a thorough analysis performed on innovative reactors that are of relevance within the European Framework [1]. In particular, reactor systems developed for advanced nuclear fuel cycles as well as advanced LWR were considered. Advanced nuclear fuel cycles include technological approaches that allow an optimised use of resources and a safe and optimised radioactive waste management. Nuclear reactors that are able to respond to these objectives are those with a fast neutron spectrum. Two categories of fast neutron reactors have been gaining attention in Europe, i.e. the sub-critical accelerator driven system (ADS) and the fast reactors (FR) [2]. Moreover, supercritical light water reactors (SCWR), considered as technological advancement of current LWR technology, were included in the analysis. A number of innovative reactor designs [4-7] together with their related materials and technological issues have been taken into account. The analysis was conducted in order to identify key reactor components for which advancement in

the area of nuclear materials resulted to be crucial for the envisaged innovative design solutions. In general, all innovative reactor concepts foresee operational temperatures which are higher with respect to the temperature ranges of LWR (the current technology) [8]. However, core components and primary systems will show the highest temperatures and dose rates having therefore the most challenging materials requirements, demanding selection and qualification. For these reasons, the focus of the GETMAT project has been on these components. Moreover, at present, candidate materials for core components and primary systems of almost all reactor concepts considered in Europe are the austenitic and 9-12Cr Ferritic/Martensitic (F/M) steels. However, limits of these two classes of steels can be identified. These limits impose design constraints that might not fit with the original objectives declared for an enhanced sustainability and for innovation. Exemplary of these limits and their consequences especially for the fast neutron systems is the selection of the fuel clad materials. The austenitic steel option imposes an upper fuel burn-up limit due to irradiation swelling and embrittlement phenomena that occur in this class of steel for high irradiation doses (as discussed in past FR development programmes) [9]. The limitation of the fuel burn-up might considerably impact strategies related to sustainability as e.g. the optimisation of use of resources. Limits can be as well identified for the 9-12Cr F/M steels as clad material. Indeed, the temperature window of these steels in an irradiation environment might be limited in the lower range to temperatures above 350°C and in the upper range to temperature below 550°C. The lower limit is due to irradiation hardening and embrittlement phenomena that can occur below 350°C (as discussed e.g. in [10-11]) and the upper limit is due to poor thermal creep and stress-to-rupture resistance of these steels above 550°C (as discussed e.g. in [12]). These temperature limits might impact the realisation of innovative design solutions as well as efficiency and economic viability of the reactor systems.

Therefore, within GETMAT the possibility to use oxide dispersed strengthened (ODS) alloys with a ferritic (F) or ferritic/martensitic (F/M) steel matrix has been proposed as an alternative option to the conventional steels. The focus on ODS alloys was based on data reported in the scientific literature, where it is discussed that these alloys show improved irradiation swelling and improved thermal-creep resistance in the high temperature range [13]. The envisaged applications of ODS alloys were the fuel cladding for all considered reactor systems, i.e. ADS, FR and SCWR, and some structural components as e.g. core support plate. Within this context, properties of the ODS alloys that are of relevance for the given applications (and for all reactor systems) have been investigated. The preliminary assessment of the ODS alloys as materials for nuclear application, has been rounded up with an investigation of possible techniques able to join/weld these materials. Moreover, specific tasks related to environmental effects (corrosion and potential mechanical properties degradation) and options for mitigation of these effects through e.g. the development of corrosion protection barrier have been addressed as well. The environmental effects have been analysed for molten lead, helium with controlled impurities and supercritical water.

The development, optimisation and qualification of ODS alloys for nuclear application is considered a long-term activity, due to the fact that knowledge and relevant data on these materials for the nuclear applications are quite scarce. Therefore, selected needs for short- and medium-term applications (e.g. prototype and demonstration systems [2]) were included in the GETMAT programme. For these systems, conventional steels as 9-12Cr F/M and the austenitic steels AISI 316L, 15Cr-15Ni/Ti are candidate materials for both core components and primary systems. The GETMAT contribution to the design and construction of the ESNII systems occurred through dedicated post irradiation examinations (PIE) of these candidate materials exposed to different irradiation fields and in presence of relevant environments (heavy liquid metals HLM, i.e. Pb and Pb-Bi eutectic; sodium; and gas atmosphere). Moreover, a new irradiation campaign in a fast neutron spectrum and HLM environment and the related PIE has been as well included.

A further topic considered as cross-cutting for all innovative reactor systems is the physical understanding of materials behaviour in terms of microstructure and mechanical properties evolution under irradiation, temperature and stress fields. The physical understanding of material behaviour foresees the prediction of basic mechanisms, from atomic to the microscopic level, which determine materials response to applied thermal and mechanical loads, while being exposed to neutron irradiation. Since the multiscale modelling and experimental validation of nuclear materials is a quite wide area, modelling and experimental activities included in the GETMAT project have been focused on Fe and Fe-Cr alloys (representative of F/M steels) and key aspects included in the investigation were thermo-chemical data (phase diagram of Fe-Cr) and irradiation hardening and embrittlement of these alloys. The theoretical activities were supported by dedicated irradiation experiments (in both ion and neutron fields).

Detailed description of the GETMAT experimental programme can be found in the references [14-15]. In the following sections the results obtained in the above areas will be discussed with emphasis on the high temperature characterisation of the ODS alloy; compatibility of the ODS alloys with coolants; post irradiation examination performed on conventional steels, modelling and model experiments of Fe and Fe-Cr alloys.

ODS alloys procurement and their high temperature characterisation

The ODS alloys have been delivered by CEA (14Cr-ODS) and the Japanese KOBELCO (12Cr-ODS and 9Cr-ODS). The average compositions of the three ODS alloys are given in Table 1. The three ODS alloys haven been produced via powder metallurgy (PM) process which included mechanical alloying (MA), consolidation by hot extrusion, and final thermo-mechanical treatments. Details on the ODS manufacturing process are reported in the references [16-18]. The final quality of the ODS alloy obtained via PM is dependent from several parameters as e.g. mechanical alloying atmosphere, time and velocity, consolidation temperature, and final heat treatments, governing the reproducibility of heats and fabrication costs.

Table 1: Chemical composition of the ODS alloys expressed in wt%

ODS alloy	C	Cr	Mo	W	Ti	Si	Mn	Y2O3
9Cr-KOBELCO	0.096	8.9	0.76	-	n.a.	n.a.	n.a.	0.33-0.38 (calculated)
12Cr- KOBELCO	0.01~0.05	11.6-12.4	-	1.8-2.2	0.24-0.28	≤0.20	≤0.20	0.21-0.25
14Cr- CEA	n.a.	13.98	-	1.03	0.39	0.32	0.29	0.3 (Y = 0.22)

The microstructural analysis performed with transmission electron microscopy showed that the 14Cr-ODS was constituted of small elongated grains (cigar shape) along the extrusion direction (longitudinal direction of the bar) and fine equiaxed grains in the transvers direction of the bar. Moreover, titanium oxides and Cr-rich precipitates of $M_{23}C_6$ type have been identified where the $(Fe, Cr, W)_{23}C_6$ carbides are mainly present at the grains boundaries. A detailed microstructural investigation of the 14Cr-ODS can be found in Reference 19. The 12Cr-ODS plate showed a quite different microstructure, with a bimodal grain size distribution: small grains size < 1 m heavily deformed and some elongated grains size up to 200 m. The biggest grains do not have a preferential orientation, while the smallest grains seem to have a preferential orientation along <110> in the rolling direction. Both the 12Cr-ODS and the 9Cr-ODS show elongated pores along the extrusion direction.

Tensile tests have been performed from room temperature up to 850°C on the three alloys by different laboratories involved in the GETMAT project (detailed description of the tensile test results can be found e.g. in [20,21]. In Figure 1, the yield strengths as measured in the involved laboratories are reported. These results are consistent among them and as can be seen from the figure, the GETMAT 14Cr-ODS and 12Cr-ODS alloys have a lower strength than the 14YWT and 12YWT produced by ORNL. Moreover,

between 400°C and 500°C the yield strength degradation with temperature is steeper with respect to the yield strengths measured below 400°C. As far as the measured elongation is concerned, a peak of ductility at about 600ºC has been observed as well. Similar behaviours on ODS steels have been reported in other works and have been ascribed to changes of the gliding mechanism of the dislocation and changes of the deformation mechanism from intraganular to intergranular at higher temperatures [22]; moreover as described in Reference 22, it can be deduced that the strain hardening mechanism is weakly thermally activated up to 400°C and above 500°C the higher softening can be due to damage processes occurring at grain boundaries.

Figure 1: Yield Strength vs. temperature measured on the GETMAT ODS alloys

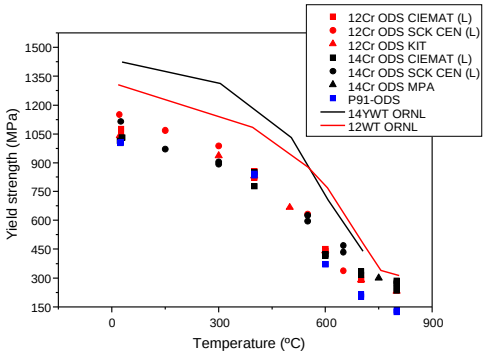

Impact properties of all the ODS alloys have been obtained by testing small KSLT specimens. In general the ductile to brittle transition temperature (DBTT) and the absorbed energy are strongly dependent from the orientation of the notch with respect to the extrusion direction of the tested specimen, confirming the relationship between microstructural and mechanical properties anisotropies. Even if a large scatter on data of absorbed energy has been seen, the general trend observed on the upper shelf energy was that the longitudinal direction showed higher mean values with respect to the transvers direction. Moreover, in the low temperature range the observed fracture mechanism was cleavage like and in the high temperature range it was comparable to a typical ductile fracture; however, in the transition temperature range the samples exhibited delamination like fracture mechanism. A more detailed investigation and explanation of this behaviour is given in Reference 21.

Impact and fracture toughness resistance of the materials are usually not considered for the design of high temperature structural components. However, these data are of relevance from the safety point of view. Therefore, for reactor components as e.g. the core support plate the impact of materials toughness in all relevant temperature and operation regimes should be taken into account for safety considerations. In this framework, it appears that the GETMAT ODS alloys might not be suitable for structural components as e.g. the core support plate.

Creep and low cycle fatigue (LCF) tests have been as well performed on the GETMAT ODS alloys. The creep curves for the GETMAT 14Cr-ODS steel are characterised by very slow secondary creep and sudden rupture at very low deformation with little evidence of tertiary creep. Similar observations have also been reported for other ferritic ODS steels [23]. Even if a large scatter of creep data (on all tested ODS alloys) has been observed, in general a higher time to rupture could be observed with respect to conventional F and F/M steel tested in similar conditions. LCF tests have been carried out at 650ºC and 750ºC with and without hold-time. The LCF results have shown that the alloy is cyclically very stable with practically no hardening/softening. Moreover, an increase in the test temperature has little influence on the fatigue ductility exponent. For a given total strain level, the fatigue life of the alloy is reduced with increasing temperature. Creep fatigue tests (with 10 min hold-time) show smaller number of cycles to crack initiation and there is nearly no difference between results of tests carried out under inert and air environment.

Materials compatibility with coolants

The compatibility assessment of the GETMAT ODS alloys with coolants had a wide scope. However, herein the discussion has been focused on corrosion tests in heavy liquid metal (mainly molten Pb) and in He atmosphere in both cases with controlled impurities; on the impact of molten Pb on mechanical properties and on corrosion protection barriers.

As described in Reference 24, corrosion of materials in molten Pb is driven by the temperature and the flow velocity of the liquid metal, the exposure time, the steel composition, and the non-metallic impurities dissolved in the liquid metal. Corrosion tests on all GETMAT ODS alloys have been performed in a temperature range between 500°C and 750°C in flowing and stagnant conditions and with controlled oxygen potential in the liquid metal. The post corrosion examination have shown that in stagnant and flowing conditions the ODS alloys exposed to oxygen controlled molten Pb are oxidised at their surface. Moreover, in the lower temperature range, with increasing Cr content the oxide layer thickness decreases. Up to about 600°C in general the oxide layer is a multiple layer composed (from the outer surface towards the bulk) by magnetite, Fe-Cr spinel oxide and an oxygen diffusion zone. This behaviour is comparable to the one of F/M steels exposed to similar conditions [24]. However, for some testing conditions the oxide appearance and thickness on the ODS alloys seemed to be affected. For instance, at temperature above 650°C the external magnetite layer tended to disappear; moreover grain dimensions and stress state of the surface seemed to impact the thickness of the oxide layer.

Corrosion tests on the 14Cr-ODS alloy in flowing He have been performed in the temperature range from 750 to 900°C and in oxidising conditions by controlling impurities in He as O_2, H_2, CH_4 and CO. The exposure time was up to 1 000 h. The ODS alloy showed in general a weight increase over time which had a parabolic growth trend. Deviations from this trend were ascribed to a partial spall-off of the oxide layer which might have occurred during the testing or during the sample preparation. The elemental analysis showed that the oxide layer contained mainly Cr with Mn and traces of Ti and Si [25]. In Figure 2, the cross section of the 14Cr-ODS steel tested at three different temperatures is shown.

Figure 2: 1 000 hours exposure of 14 Cr-ODS in He with oxidising impurities. All three samples showed oxide layer at their surface.

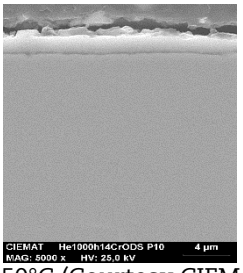

at 750°C (Courtesy CIEMAT)

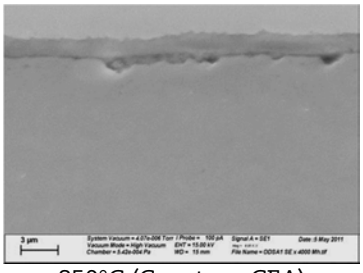

850°C (Courtesy CEA)

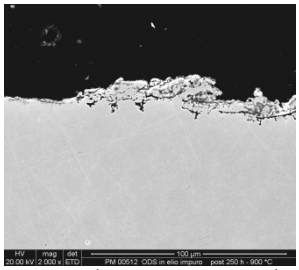

900°C (Courtesy ENEA)

The mechanical properties tests in molten Pb, have been focused on creep-to-rupture and fretting.

In Figure 3, the role of HLM on the *creep properties* of the 9Cr-ODS alloy is shown. The tests have been performed in air and in liquid lead under non-controlled oxygen atmosphere at 600°C. From the data shown, it can be seen that molten Pb tends to reduce the rupture time of the specimens. On the other hand, it was observed that if a compact oxide layer growth on the steel surface the same trend cannot be observed. A possible reason could be the formation of a thick, porous and brittle oxide layer that is formed when the oxygen content in the liquid metal is not controlled. This layer breaks during the tests and allow an intimate contact between the liquid and solid metal, leading to a liquid metal embrittlement mechanisms.

Figure 3: Comparison of 9Cr-ODS creep properties in Pb without oxygen control and air (Courtesy of M. Serrano, CIEMAT)

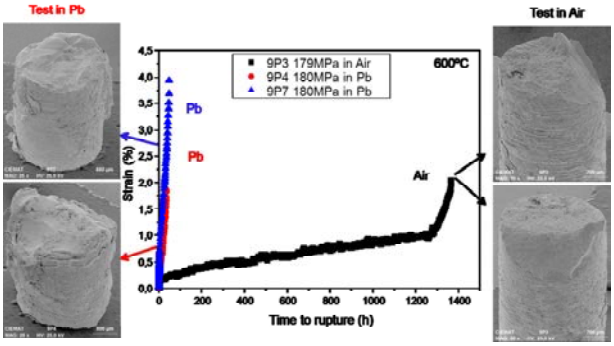

Fretting experiments with the main goal to simulate the interaction between the spacer grid and the fuel cladding or HX tubes were performed on austenitic, F/M steels and steels with a protective corrosion layer obtained with the GESA treatment [26]. Hereafter the results as reported in References 27 and 28 are briefly summarised. As shown by these tests, fretting influences the corrosion behaviour in molten Pb of the tested steels. Protective oxide scales and corrosion barriers are gradually removed by the fretting action. As a result, liquid Pb reaches the bare steel surface and severe corrosion can take place as well as, as discussed before, mechanical properties degradation. In general it has been observed that higher corrosion susceptibility in a given domain results in higher fretting damage. For instance, for austenitic steels dissolution enhanced fretting has been observed, for F/M steels oxidation enhanced fretting was the driving mechanism and for surface aluminised steels, which have a better corrosion resistance with respect to the oxidised steels showed the highest fretting wear resistance.

Further results showed that fretting seems to be a self-mitigating process, characterised by a progressive reduction of the wear rate with increasing time/number of cycles; and a temperature increase, due to its influence on the corrosion processes occurring in liquid lead, enhances fretting wear.

Even if the experimental campaign conducted within GETMAT had a qualitatively nature, it can be assessed that an uncontrolled fretting process can cause severe damage and eventually component failures even after relative short time. Thus, a detailed characterisation of the fretting process and of the possible mitigation methods is advised. Finally, due to the whole variety of possible fretting conditions regarding load, amplitude, frequency, temperature and components geometries, it is suggested that a wider experimental campaign is conducted in order to be able to perform a quantitative assessment on fretting wear in Pb environment.

The contribution on *corrosion protection barrier* was focused on the identification of optimal Al-Cr concentration in Fe-Cr-Al protective layers. As shown in the previous paragraphs and confirmed by literature data e.g. [24], the compatibility of Pb with structural steels, in terms of corrosion and mechanical resistance, causes considerable concern. To mitigate the effects of HLM on the materials, Fe-Cr-Al alloys are proposed as promising corrosion protection layer on the steel surface. In Reference 24, a detailed description of the protection methods are given with relevant references. The contribution of GETMAT to this corrosion protection system was to perform a systematic study concerning the corrosion behaviour of Fe-Cr-Al-based model alloys during their exposure to oxygen-containing (10–6 wt%) lead in the temperature range 400-600°C in order to identify optimal Al and Cr concentration. The experiments, described in details in Reference 29, have shown that chromium and aluminium contents of 12.5-17 wt% and 6-7.5 wt%, respectively, are necessary to obtain a thin, stable and protective alumina scales on Fe-Cr-Al-based alloys in oxidising Pb at 400, 500 and 600°C. In this temperature range, the alumina stability domain shifts with lower temperatures to higher chromium and aluminium concentrations.

Post irradiation examination (PIE)

The objective of the PIE programme was to enlarge the database concerning the effect of irradiation on the relevant properties (i.e. needed for the design, such as dimensional and mechanical properties) of conventional materials selected for core/target components of future GEN IV reactors and ADS. The materials investigated were 9Cr steels such as T91 (9Cr1MoVNb), EM10 (9Cr1Mo) and austenitic steels. The data were generated as part of PIE performed after irradiation campaigns conducted in various radiation environments (more details are given in References 14 and 15). Moreover, the activity included both the design and implementation of a new irradiation campaign called LEXURII [30], followed by the corresponding PIE).

9Cr martensitic steels are known for the excellent radiation resistance (i.e. negligible void swelling, little hardening and moderate degradation of impact properties) when *irradiated in a fast spectrum* at temperatures above approximately 380-400°C up to doses of at least 100 dpa [31]. However, significantly higher irradiation damages (up to about 150 or higher) for the end-of-life neutron exposure of in-core components such as the hexagonal duct is envisaged in the case of future GEN IV reactors. Moreover, it has been argued that the excellent swelling resistance of FM steels is mainly due to a long incubation period (transient regime) and that FM steels should eventually swell at a steady state swelling rate which could be as high as 0.2%/dpa [32]. Therefore, a comprehensive PIE programme was conducted using a hexagonal duct made of 9Cr-1Mo steel (EM10 grade) irradiated in the Phénix reactor up to a maximum dose of 155 dpa (Boitix9 experiment). Tensile and impact specimens were machined at different locations along the duct, corresponding to irradiation temperatures ranging from about 385°C to 530°C and doses in the range 43-155 dpa. Mechanical tests confirmed the very good radiation resistance of EM10 steel for these specific irradiation conditions. Indeed, irradiation induced hardening for all tested specimens, including after irradiation to 155 dpa, was found to be relatively small. Likewise, a moderate degradation of impact properties after irradiation was observed.

As in other metallic alloys, the irradiation temperature has a drastic impact on the evolution of the mechanical properties. For instance at 325°C, in addition to formation of α precipitates, irradiation induced the formation of a high density of small dislocation loops, possibly decorated with solute atoms, which are the main source of the high hardening observed after irradiation (see also section on modelling). In the temperature range of interest for the Boitix 9 wrapper, the dislocation microstructure was found by TEM investigations to be very different and consistent with the measured hardening: at 398°C (112 dpa), a low density of large dislocation loops was observed, while at 439°C (155 dpa), hardly any loop could be detected and the dislocation density was found to be similar to that measured prior irradiation.

In addition to the effect of irradiation on mechanical properties, dimensional stability has been investigated via macroscopic density measurement, which showed that void swelling was very small. This conclusion was confirmed by TEM investigations of the void microstructures (Figure 2). This low void volume fraction and the fact that voids were found to be heterogeneously distributed within the matrix are indications that EM10 steel was still in the incubation stage of void swelling even after irradiation to 155 dpa, which demonstrates the very high swelling resistance of this type of steel.

FM steels were also irradiated with high energy protons and spallation neutrons at the solid spallation target SINQ (PSI) at temperatures in the range [150-350°C]. The purpose was to support the development of materials for the structures of spallation targets and core components of ADS. Investigated FM steels irradiated at the highest doses and helium contents displayed very high hardening and a fully brittle, predominantly intergranular fracture mode. This behaviour, which is not observed for FM steels irradiated in fission conditions at the same temperature and to similar damage dose, is the result of i) matrix hardening due to the formation of small dislocation loops and a very high density of tiny

helium bubbles (~ 3.10^{16} cm^{-3} according to TEM measurements) and ii) strong decrease of grain boundary cohesion due to the presence of helium (as confirmed by ab initio calculations). Likewise, measurements of impact properties after irradiation of FM steels in the SINQ target show a degree of embrittlement significantly greater than that expected after irradiation in fission conditions.

As several advanced nuclear systems will use a HLM (liquid Lead or Lead Bismuth Eutectic) as coolant, the issue of possible combined effects due to irradiation and HLM is of great importance and little has been addressed in the past. This issue was therefore the focus of several tasks within the GETMAT project, via the PIE of ASTIR [33], LEXURII [30] and MEGAPIE [34]. The steels T91 and AISI 316L have been irradiated and/or tested in Lead Bismuth Eutectic (LBE). The ASTIR and LEXUR II PIE have made evident that Liquid Metal Embrittlement (LME) of irradiated T91 is enhanced with respect to non-irradiated conditions [31]. First, the effects of test temperature and strain rate on LME were studied in the case of non-irradiated specimens and it was found that the reduction of the total elongation has a non-monotonic dependence on both parameters: LME occurs only in a particular range of temperature and strain rate. For a strain rate of about 5.10^{-5} s^{-1}, the minimum of the ductility trough occurs at about 350°C. Moreover, a strong LME effect was observed for irradiated specimens tested in LBE. When tested in LBE, multiple cracks initiation occurred at the surface followed by brittle propagation. The average reduction of total elongation due to LME (about 63% reduction compared to tests in Ar atmosphere) was proportionally larger than the average reduction measured in the case of non-irradiated samples. While for non-irradiated specimens, pre-exposure to the liquid metal was found to be a necessary condition of LME occurrence, this was not the case for irradiated specimens. Thus irradiation was found to enhance the LME sensitivity of T91. This conclusion was also supported by the results of PIE performed on T91 specimens irradiated in contact with LBE to about 6 dpa at 350°C (LEXUR II experiment). Also in this case, a drastic reduction of total elongation was observed for irradiated specimens tested in LBE at 350°C compared to values measured in inert atmosphere.

By contrast, for all investigated testing conditions, including tests on specimens irradiated to 2.6 and 6 dpa (as part of ASTIR and LEXURII experiments), austenitic stainless steels (316L and 15-15 Ti grades) did not show any evidence of LME due to LBE.

The PIE of the MEGAPIE target has been a unique opportunity to investigate the behaviour of a real component whose structural materials had been irradiated in contact with flowing LBE and subjected to cyclic thermal/mechanical loadings [34]. It must be emphasised that target dismantling and sample preparation represented an important amount of work successfully carried out by PSI in its hot laboratories [35].

Figure 4: Void microstructure in EM10 steel irradiated to 155 dpa at 439°C (Courtesy J. Henry, CEA)

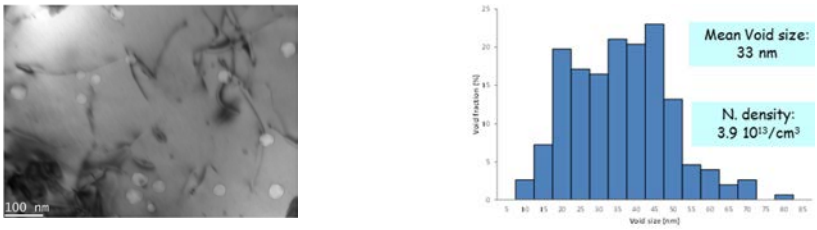

a) TEM micrograph

b) void size distribution. The void volume fraction was measured to be 0.1%

First results have shown that the T91 hemispherical beam entrance window showed significant hardening at room temperature, however the total elongation of the sample with highest dose was found to be still above 10%, indicating a fully ductile behaviour. These results were in line with available data for T91 irradiated in spallation conditions in the same temperature range (close to 300°C) [36]. Moreover, no severe LBE corrosion nor

erosion phenomena were observed on the T91 and 316L components. These findings are consistent with the results of the investigations performed on coupons irradiated in contact with stagnant LBE (LEXURII PIE) which did not reveal any corrosion damage. However, SEM and EPMA investigations performed by PSI and CEA have revealed the presence of a deep crack in the Lower Liquid Metal Container made of T91 steel, located close to the Electron Beam (EB) weld line. Such a deep crack was not present before irradiation, but was perhaps nucleated during welding. Cyclic mechanical loading (due to proton beam trips) may have induced rapid crack propagation, since it has been shown that fatigue crack propagation is accelerated in LBE as compared to crack growth rates in inert environment.

Modelling and model experiments on irradiated Fe and Fe-Cr alloys

The objective here was to understand which nanostructural features are the main cause of radiation, hardening and embrittlement of Fe-Cr alloys and to develop a physical model capable of rationalising the experimental data available on this issue. To achieve this, physical models have been developed to describe the behaviour of Fe-Cr alloys when subjected to thermal ageing and irradiation. Fe-Cr alloys were chosen as model materials for high-chromium ferritic/martensitic steels. The processes of interest were nanostructural and microchemical changes that occur under irradiation or ageing and the corresponding changes in mechanical properties, mainly hardening, which in turn causes embrittlement.

Fundamental properties of Fe and Fe-Cr alloys have been modelled through the development and application of advanced cohesive models, capable of describing the thermodynamic properties and the properties of point-defects (vacancies, self-interstitials) in these materials, as well as extended-defects (dislocations, grain boundaries), possibly including magnetic properties. The development of these cohesive models, then applied for atomistic calculations, required extensive density functional theory (DFT), or first principle (ab initio), calculations. The results obtained can be summarised as follows:

It has been shown that magnetism influences especially the mixing enthalpy of Fe-Cr leading to a modified phase diagram as compared to the standard one. These effects, however, are suitable to be described also by classical potentials that do not explicitly include spins [37]. The strong vibrational entropy of Fe-Cr plays an instrumental role for the shape of the Fe-Cr phase diagram, by lowering the temperature at which the misicibility gap closes. Non-configurational entropy should therefore be included in models that describe thermodynamics from an atomistic standpoint.

The study of the interaction with point defects with all possible solute atoms in iron by DFT [38] revealed that the elements that are found experimentally to form aggregates and to segregate at dislocations or grain boundaries (namely Cr, but also Ni, Mn, Si, P, and Cu) are found to migrate together with point defects, both vacancies and, in a few cases, interstitials interstitials [39]. This proves to be a very effective physical mechanism to explain the mentioned experimental evidence.

The improved interatomic potential developed within the project [37] has been validated and used in studies of dislocation behaviour, defect diffusion, solute-defect interactions, etc. In particular, Metropolis Monte Carlo studies revealed how Cr is expected to re-distribute at steady-state under thermal ageing and, as a tendency, under irradiation. For example, it has been shown that Cr has a tendency to segregate at grain boundaries, while it would tend to stay away from free surfaces, especially voids [38-41]. Figure 5 illustrates graphically these and other results of these studies [40-43].

Radiation effects in Fe and Fe-Cr alloys have been modelled through microchemical and nanostructure evolution models, as well as (radiation) hardening models using as input the results of applying ab initio and/or empirical cohesive models. The former category includes several types of kinetic Monte Carlo (KMC) models, each of them with its advantages and limitations, as well as cluster dynamics (or rate theory) models. The

latter consists basically of the coupling of molecular dynamics (MD) with dislocation dynamics (DD): it is the first time that this coupling [44] is successfully applied to rationalise quantitatively the results of mechanical tests, starting from fully physical considerations [45]. Key results in this area are summarised as follows:

Figure 5: Graphical summary of how Cr atoms tend to redistribute under ageing at steady-state due to thermodynamics driving forces. Results are broadly in agreement with experiments (Courtesy L. Malerba).

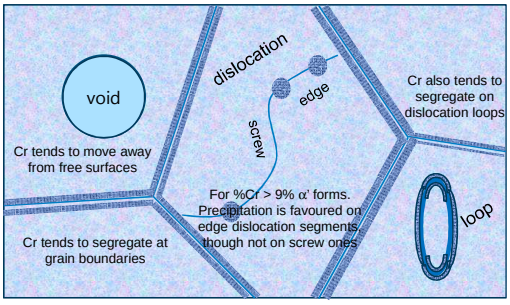

The Atomistic KMC (AKMC) techniques have reached maturity as methodology for the simulation of thermal ageing processes (phase separation, segregation, etc.) driven by diffusion of solute atoms, although some specific difficulties still exist with the diffusion of interstitial species like carbon. The importance of including (semi-empirically) magnetic and vibrational effects emerges from both DFT calculations and experimental studies, and should be considered as one of the main improvements to be introduced in the technique in the long run.

For AKMC simulations of irradiation processes, important progresses have been made to include multiple vacancies and single-interstitials: the effect of Cr on point defect diffusion properties is explicitly accounted for and simulations of resistivity recovery experiments including effect of Cr and C have been successfully performed. Also the calculations of the Lij phenomenological coefficients (Onsager matrix), for use in radiation-induced segregation models, has been performed and processes such as phase separation and segregation can be now successfully simulated starting from fully physical considerations [46-47]. However, the modelling of SIA clusters in an AKMC framework remains challenging. More generally, the correct inclusion in the model of extended defects that imply an intense strain field, such as dislocations and grain boundaries, remains challenging.

The Object KMC (OKMC) and Cluster Dynamics (or Rate Theory) models have been developed and a direct comparison with experiments has been made to validate them. The key difficulty is the determination of parameters for concentrated alloys. Several methods and models have been developed which showed good agreement with experimental trends however with some limitations. The former, on the other hand, allows precipitation to be described and in the long run should be able to treat also the other defects, in a similar way to the "grey-alloy" model, providing also more local information, but for the moment these features are not included in the code.

An extensive MD simulations [48] have been performed in order to assess the friction stress due to solution strengthening in Fe-Cr alloys of different concentrations, as well as to evaluate the critical stress for unpinning of both edge and screw dislocations at defects, including Cr-decorated loops and Cr-rich precipitates, which are assumed to be the main cause of irradiation hardening in Fe-Cr alloys. The studies have been performed for different defect and box sizes, different temperatures and also different strain rates. They have clearly shown that dislocation loops decorated by Cr atoms (and/or other solute atoms), as a consequence of segregation, are stronger obstacles than undecorated loops and are, therefore, candidates to be the main origin of radiation hardening in these (and other) Fe alloys [49].

The MD results of strength of irradiation defects (loops, Cr decorated loops, Cr precipitates, etc.) have been incorporated into a DD model, allowing simulations of radiation strengthening in Fe-Cr alloys as a function of Cr content: it is the first time that a fully physical model manages to account in a quantitative way for the radiation-hardening measured experimentally. Key is the recognition that screw dislocations that interact with loops having collinear Burgers vector may form helical turns, thereby producing hardening effects 10 times larger than the Orowan mechanism. The main sources of hardening are the Cr-NiSiP clusters, if assumed to be small loops with solute atoms segregated on them [45].

In support to the theoretical part experiments were conducted in which selected reference materials (the materials considered were alloys containing nominally 2.5, 5, 9 and 12%Cr) were characterised after neutron and ion irradiation, from the nanostructural, microchemical and mechanical point of view, using a combination of experimental techniques. The activities has produced two main sets of experimental results namely i) characterisation of neutron irradiated Fe-Cr alloys (the neutron irradiation occurred at 300°C for an irradiation damage of 0.06, 0.6 and 1.5 dpa), and ii) characterisation of ion irradiated Fe-Cr alloys (the ion irradiation occurred at 100, 300 and 420°C for an irradiation damage of 1 and 5 dpa).

In both cases the goal was to combine different characterisation techniques in order to get a complete picture of the nanostructural and microchemical changes occurred in the alloys as functions of Cr content and irradiation dose, as well as, partly, temperature. The results for the neutron irradiation are:

Positron annihilation spectroscopy (PAS) [50] and small-angle neutron scattering reveals that [51]: (i) mainly single vacancies are present in FeCr alloys compared to pure Fe: very little vacancy clustering occurs when Cr is present (data for 0.06 dpa); (ii) higher amount of vacancies is observed at higher dose, but nonetheless the presence of Cr reduces the amount of vacancies drastically; (iii) the irradiation-induced clusters detected are Cr-rich ’-phase particles for Fe-12%Cr, while in the other alloys they must contain impurity elements, such as C, Ni, P or Si; (iv) there is a pronounced fluence dependence of the concentration and size of ’-phase particles below 0.6 dpa and a saturation-like behaviour beyond this dose and (v) for lower Cr levels, pronounced fluence dependence below 0.6 dpa was also found.

From Atom Probe Tomography (APT) analysis [52] it could be observed that (i) clusters were only present in the supersaturated alloys (Fe-9%Cr and Fe-12%Cr), (ii) CrSiPNi enriched clusters were observed in all alloys with the same number density: they are suspected to be small loops on which solute atoms segregated; (iii) segregation of Si, P and Cr atoms on dislocation lines and grain boundaries was observed and (iv) zones free of clusters were found around the GBs, suggesting that solute segregation should be the mechanism leading to the formation of the CrSiPNi clusters.

Finally the TEM analysis [53] has shown that dislocation loops are in-homogeneously distributed for 5, 9 and 12% Cr being preferentially located close to grain boundaries and dislocation lines; they are, however, homogeneously distributed for 2.5%Cr. The effect of Cr content on loop distribution might be indirect: it is known that 2.5%Cr alloy is ferritic and has C in the matrix, while the other alloys are F/M and C have segregated at grain boundaries. C in the matrix would act as trap for dislocation loops that, otherwise, would be free to migrate to sinks (dislocations and grain boundaries).

The results obtained from the analysis of ion irradiated Fe-Cr alloys are hereafter summarised:

PAS (coincidence doppler broadening and positron annihilation lifetime spectroscopy) analysis made evident that: (i) vacancy-type defects were produced by the ion irradiation. The amount and size decrease when %Cr increases and also, when the irradiation T increases. Larger voids and more vacancies were observed at the lower dose.

The APT results can be summarised as follows: (i) NiSiPCr rich clusters where observed after ion irradiation (Cr is the main element); No precipitates are observed in this case, differently from neutron irradiation. The X-ray magnetic circular dichroism (XMCD) confirmed a redistribution of Cr atoms, which can be an indication of Cr clustering.

The TEM analysis showed a homogeneous distribution of interstitial dislocation loops are at all conditions as well as denuded zones close to grain boundaries in Fe 12%Cr. Moreover, at 1 dpa there is no significant effect of Cr content (from 9 to 12%) on size or density of defects. Differences are expected in the proportion of ½ 111 loops to 100 loops while at 5 dpa a higher density in 9%Cr, while larger size in 12%Cr are observed.

The differences in structural evolution observed on Fe-Cr alloys when irradiated with ion and with neutrons can be ascribed to the different damage rate applied. Indeed the ion damage rate was in the order of $1 \cdot 10^{-4}$ dpa/s while the neutron damage rate was about $2 \cdot 10^{-7}$ dpa/s.

Summary of achievements and perspectives

The GETMAT project addressed a wide range of scientific and technological items in the materials field considered cross-cutting for more than one innovative reactor systems. The focus was on materials for core components and primary systems. For these parts of the reactor, the identification of materials with promising performance towards high temperature, radiation damage and environmental damage is of high relevance. Within GETMAT the possibility to manufacture and characterise ODS alloys with F or F/M steel matrix for these applications has been investigated. However, experimental activities have been performed also on conventional steels, since it is expected that for the near to medium term development of innovative reactors, these steels will be used. Moreover, theoretical interpretation and modelling of radiation hardening and embrittlement of Fe-Cr alloys with supporting experiments have been a further essential part The results presented in the previous sections allow a preliminary assessment and the identification of future needs.

The project has made it evident that in Europe the manufacturing of large batches of ODS alloys, with F and F/M steel matrix, via the powder metallurgical route needs additional R&D to understand and control chemical and physical processes occurring during the various manufacturing steps, with the aim to enhance the homogeneity and quality of the alloys, as well as to address and solve if possible the problem of the mechanical anisotropy while reducing the costs for production.

The trends of the mechanical properties measured on the GETMAT ODS alloys in the high temperature range are comparable to the behaviour of similar alloys as reported in the open literature. The tensile test results obtained in a temperature range up to about 800°C showed that the GETMAT ODS alloys have an isotropic yield and ultimate tensile strength behaviour, which are higher with respect to the conventional steel. However, it has been also observed that the total elongation in the longitudinal direction is higher with respect to the transverse direction and a steeper softening of the alloys occurring above 500°C has been also observed and attributed to damage mostly occurring at grain boundaries by loading the samples during the tests.

Through the fracture toughness test results the anisotropic behaviour of the GETMAT ODS alloys have been confirmed. Moreover, in general the longitudinal direction showed a higher resistance to crack propagation with respect to the transversal direction; however the obtained toughness data are lower with respect to the conventional steels tested in similar conditions. This last finding was discussed in terms of appropriateness of ODS steels for thick components as e.g. the core support plate of a GFR. It has been argued that for thick components with high loading conditions the materials with this toughness behaviour might not be suitable.

The last high temperature mechanical property here discussed is the creep behaviour. The recorded data have made it evident that the creep resistance of ODS steels is higher with respect to conventional steels. However, the recorded creep curve showed an almost negligible creep rupture strain and almost absence of tertiary creep state.

For what concerns the corrosion behaviour of the GETMAT ODS alloys in molten Pb and He (the chemistry of both environments has been controlled in order to set oxidising conditions), this seems to be comparable to the behaviour of conventional F or F/M steel. Therefore, it can be assumed that similar corrosion mitigation methods as developed for the conventional steels might be applied also for the ODS alloys, i.e. controlling the chemistry of the coolant and/or apply corrosion protection methods on the surface of the ODS alloy.

The post irradiation examination has been focused on 9% Cr F/M steel. It has been confirmed that even at irradiation doses as high as 155 dpa obtained in a fission neutron field and with temperatures above 400°C, the 9% Cr steel EM10 shows excellent mechanical and dimensional stability. On the contrary, in the proton-neutron irradiation field for lower irradiation damage and temperatures 9% Cr steel as T91 showed important hardening and embrittlement. A further important result obtained in this framework is that the neutron irradiation enhances the environmental assisted degradation of the mechanical properties of T91 steel when in contact with molten Pb-Bi eutectic. In similar conditions, the same has been not observed in austenitic steels.

As for the application of ODS as cladding material several items remains to be clarified. These items include the manufacturing process, the composition and specification, the “unconventional” mechanical behaviour including the anisotropy, the mechanical properties evolution under irradiation, etc.

Moreover, for what concerns the application of conventional steels for the building of innovative components as e.g. the neutron spallation target for an ADS preliminary results from MEGAPIE have confirmed some expectation of the T91 behaviour, further results from the PIE of MEGAPIE will be used to confirm preliminary lifetime prediction of the T91 as window of the neutron spallation target. More alarming seems to be the presence of a deep crack close to the electron beam weld line which might have been nucleated during welding and propagated during operation. This needs to be further analysed and recommendations which take into account quality control during fabrication (and welding) of components need to be formulated for safe operation.

Finally, the findings in the modelling and experimental domain of GETMAT have given an essential contribution to the physical understanding of thermal ageing and radiation hardening and embrittlement of Fe-Cr alloys. An important step forward in this domain has been achieved by combining theoretical and experimental results, which has proven to be an effective approach.

Acknowledgements

The authors wish to thank all partners involved in the GETMAT consortium and the European Commission for supporting the project Generation IV and Transmutation Materials (GETMAT) Grant Agreement No. FP7-212175.

The authors wish to thank all participants and associated involved in the EERA JPNM for their contribution to future R&D perspectives.

References

[1] SNETP – SRIA (2013), “Strategic Research and Innovation Agenda”.

[2] “The European Sustainable Nuclear Industrial Initiative. A contribution to the EU Low Carbon Energy Policy: Demonstration Programme for Fast Neutron Reactors”, Concept Paper, October 2010.

[3] Knebel, J.U. (2011), "The EUROTRANS Project: Partitioning and transmutation research in Europe", Proccedings of the Technology and Components of Accelerator-driven Systems Workshop, OECD Nuclear Energy Agency, June 2011.

[4] Alemberti, A. et al. (2013), Progress in Nuclear Energy, December 2013.

[5] Fiorini, G.L., A. Vasile (2011), Nuclear Engineering and Design, Volume 241, Issue 9, September 2011, Pages 3461–3469.

[6] Stainsby, R. (2012), "The Gas-Cooled Fast Reactor: History, Core design and Main Systems", Proceedings, IAEA Education and Training Seminar/Workshop on Fast Reactor Science and Technology Centro Atómico Bariloche, Argentina, October 1-5, 2012.

[7] High Performance Light Water Reactor: Design and Analyses, Front Cover, Editor Thomas Schulenberg, KIT Scientific Publishing, 2012.

[8] Zinkle, S. (2007), "Synergies between fusion and innovative fission systems for structural materials R&D", Proceedings of the Workshop on Structural Materials for Innovative Nuclear Systems (SMINS), OECD/NEA 2007.

[9] Dubuisson, P., D. Gilbon (1991), "Behaviour and microstructure of stainless steels irradiated in the French fast breeder reactors", 2, Japan-France Materials Science Seminar Paris (FR), 22-25 Apr 1991.

[10] Alamo, A. (2002), "Irradiation effects in martensitic steels under neutron and proton mixed spectrum spire contract N°FIKW – CT – 2000 – 00058 final scientific and technical report".

[11] Alamo, A., J.L. Bertin, V.K. Shamardin, P. Wident (2007), Journal of Nuclear Materials, 367–370, pages 54-59

[12] Cheon, J.S. et al. (2009), Journal of Nuclear Materials 392, pages 324-330.

[13] Dubuisson, P., Y. de Carlan, V. Garat, M. Blat, Journal of Nuclear Materials, 428 (2012) 6-12.

[14] Fazio, C. et al., Nuclear Engineering and Design 241 (2011) 3514-3520.

[15] Fazio, C. et al., Journal of Nuclear Materials 392 (2009) 316-323.

[16] De Carlan, Y., "Basic characterisation of 14Cr1WYTi Ferritic ODS", GETMAT Deliverable D1.2a and D1.2b.

[17] Müller, G., "Supply and characterisation of 12Cr ODS", GETMAT Deliverable D13a and D13b.

[18] Heinzel, A. et al, "Production and Characterisation of 9CrMoVNb ODS steel", GETMAT Deliverable D1.3a.

[19] Olivier, P. et al. (2012), Journal of Nuclear Materials 428 (2012) 40–46.

[20] García-Junceda, A. et al. (2012), Materials Science and Engineering: A Volume 556, 30 October 2012, Pages 696–703.

[21] Serrano, M. et al. (2102), Journal of Nuclear Materials 428 (2012) 103–109.

[22] Praud, M. et al. (2012), Journal of Nuclear Materials 428 (2012) 90–97.

[23] Steckmeyer, A. et al. (2012), Journal of Nuclear Materials 426 (2012) 182.

[24] Handbook on Lead-bismuth Eutectic Alloy and Lead Properties, Materials Compatibility, Thermal-hydraulics and Technologies; Edition 2007 OECD/NEA.

[25] Cabet, C. et al., "Corrosion in Gas" GETMAT Deliverable D2.2.

[26] Müller, G. et al, "Materials for innovative Lead Alloy cooled Nuclear Systems – overview", this proceedings.

[27] Del Giacco, M. et al., Journal of Nuclear Materials, In Press, Corrected Proof, Available online 10 July 2013.

[28] Del Giacco, M. et al., Journal of Nuclear Materials, 423 (2012) 79-86.

[29] Weisenburger, A. et al., Journal of Nuclear Materials, 437 (2013) 282-292.

[30] Stergar, E. et al., Journal of Nuclear Materials, In Press, Corrected Proof, Available online 23 November 2013.

[31] Séran, J.L. et al., Journal of Nuclear Materials 212–215 (1994) 588–593.

[32] Garner, F.A. et al., Journal of Nuclear Materials, 276 (2000) 123–142.

[33] Van den Bosch, J. et al. Journal of Nuclear Materials, 398 (2010) 68-72.

[34] Fazio, C. et al., Nuclear Engineering and Design, 238 (2008) 1471-1495.

[35] Wohlmuther, M., Journal of Nuclear Materials, 431 (2012) 10-15.

[36] Dai, Y., Journal of Nuclear Materials 356 (2006) 308–320.

[37] Bonny, G. et al., Journal of Phase Equilibria and Diffusion 31 (2010) 439-444.

[38] Olsson, P., T.P.C. Klaver, C. Domain, Physical Review B 81 (2010) 054102.

[39] Messina, L., P. Olsson, M. Nastar, private communication.

[40] Zhurkin, E.E., J. Kuriplach, T. Ossowski, A. Kiejna, M. Hou, Proc. Multiscale Materials Modelling Conf., Freiburg (2010).

[41] Terentyev, D., X. He, E. Zhurkin, A. Bakaev, Journal of Nuclear Materials 408 (2011) 161.

[42] Zhurkin, E.E., M. Hou, J. Kuriplach, T. Ossowski, A. Kiejna, Nucl. Instr. & Meth. in Phys. Res. B, 269 (2011) 1679.

[43] Zhurkin, E.E., D. Terentyev, M. Hou, L. Malerba, G. Bonny, Journal of Nuclear Materials, 417 (2011) 1082.

[44] Monnet, G., Y.N. Osetsky, D.J. Bacon, Philosophical Magazine 90 (2010) 1001.

[45] Monnet, G., D. Terentyev, private communication.

[46] Castin, N., L. Malerba, Journal of Chemical Physics 132 (2010) 074507.

[47] Martinez, E., O. Senninger, C-C. Fu, F. Soisson, Physical Review B **86**, 224109 (2012).

[48] Tereyentev, D. et al., Acta Materialia 61 (2013) 1444–1453.

[49] Terentyev, D. and A Bakaev 2013 *J. Phys.: Condens. Matter* **25** 265702.

[50] Lambrecht, M. et al., Acta Materialia 59 (2011) 6547–6555.

[51] Heintze, C., A. Ulbricht, F. Bergner, H. Eckerlebe, Journal of Physics: Conference Series **247** (2010) 012035.

[52] Kuksenkoet, V. al., Journal of Nuclear Materials 432 (2013) 160–165.

[53] Matijasevic, V. et al., Journal of Nuclear Materials 377 (2008) 147–154.

Nanostructure evolution under irradiation and correlation with mechanical property changes in neutron irradiated Fe-Cr alloys

Mercedes Hernández Mayoral[a], Frank Bergner[b], Milan Konstantinovic[c], Viacheslav Kuksenko[d], Marlies Lambrecht[c], Boris Minov[c], Cristelle Pareige[d], Philippe Pareige[d], Takeshi Toyama[c,e], Andreas Ulbricht[b], Lorenzo Malerba[*c]

[a]CIEMAT, Division of Structural Materials, Spain
[b]Helmholtz Zentrum Dresden-Rossendorf, Institute of Safety Research, Germany
[c]SCK CEN, Structural Materials Modelling and Microstructure, Institute of Nuclear Materials Science, Belgium
[d]Groupe de Physique des Matériaux UMR-CNRS 6634, Équipe de Recherche Technologique, Université de Rouen, France
[e]Institute for Materials Research, Tohoku University, Japan
*Presenting author

Abstract

High-chromium ferritic/martensitic (F/M) steels are candidate structural materials for several components in most Gen IV reactor concepts because they are less prone to swelling than austenitic steels, while exhibiting better thermal properties. The operating temperature window for these materials is dictated, on the low side, by the reduced ductility associated with radiation strengthening; on the high side, thermal creep strength is the limiting factor. Here we focus the attention on the low temperature limit, i.e. we investigate radiation strengthening and embrittlement in F/M alloys. The latter is known to be influenced by the Cr content. For this reason, Fe-Cr alloys are often used as model materials, in the attempt of understanding the role of Cr.

The present work summarises the results of an extensive nanostructural and mechanical characterisation programme on Fe-Cr alloys neutron-irradiated at 300°C up to doses in excess of 1 dpa, performed in the framework of the FP7/GETMAT project. Three types of nanostructural features have been produced by irradiation in these alloys, which are responsible to different extents for the measured radiation strengthening. It is shown how the Cr content influences directly and indirectly the nanostructure evolution, providing for the first time a possible physical explanation for the dependence of radiation-strengthening and also embrittlement on this variable.

Materials for innovative lead alloy cooled nuclear systems: Overview

Georg Müller,* Alfons Weisenburger, Renate Fetzer, Annette Heinzel and Adrian Jianu

Karlsruhe Institute of Technology, Institute for Pulsed power and Microwave Technology, Germany

Abstract

One of the most challenging issues for all future innovative nuclear systems including Gen IV reactors are materials. The selection of the structural materials determines the design which has to consider the properties and the availability of the materials. Beside general requirements for material properties that are common for all fast reactor types specific issues arise from coolant compatibility. The high solubility of steel alloying elements in liquid Pb-alloys at reactor relevant temperatures is clearly detrimental. Therefore, all steels that are considered as structural materials have to be protected by dissolution barriers. The most common barriers for steels under consideration are oxide scales that form in situ during operation. However, increasing the temperature above 500°C will result either in dissolution attack or in enhanced oxidation. For higher temperatures additional barriers like alumina forming surface alloys are discussed and investigated. Mechanical loads like creep stress and fretting will act on the steels. These mechanical loads will interact with the coolant and can increase the negative effects.

For a LFR (Lead Fast Reactor) Demonstrator and MYHRRA (ADS) austenitic steels (316L) are selected for most in core components. The 15-15Ti is the choice for the fuel cladding of MYHRRA and a Pb cooled demonstrator. For an industrial LFR (Lead Fast Reactor) the ferritic martensitic steel T91 was selected as fuel clad material due to its improved irradiation resistance. T91 is in both designs the material to be used for the heat exchanger. Surface alloying with alumina forming alloys is considered to assure material functionality at higher temperatures and is therefore selected for fuel cladding of the ELFR and the heat exchanger tubes. This presentation will give an overview on the selected materials for innovative Pb alloy cooled nuclear systems considering, beside pure compatibility, the influence of mechanical interaction like creep and fretting.

Introduction

Climate change, peak oil and the growing dependency on states outside EU cannot be answered only employing renewable energy sources like wind and solar. Especially the base load electricity production cannot be guaranteed only considering such kind of electricity production methods. Nuclear energy using Fast Gen IV reactors can fulfill the requirements concerning CO_2 free, base load capability and sustainability. One of the most promising coolants, especially due to its high thermal inertia and thus its long grace times in case of accidents, is the heavy liquid metal (HLM) lead (Pb). For several years worldwide researches have been investigating this coolant and its impact on the reactor design and especially on the materials to be selected. In several EU funded projects, design, safety and some technological aspects of lead (Pb) cooled fast reactors were investigated; e.g. the LEADER [1] project aimed to design a prototypical demonstrator ALFRED and to continue with several design related aspects of the ELFR reactor. The demonstrator ALFRED should be available in the short and medium terms and therefore material selection is, beside safety aspects, also triggered by the actual availability and the status of licencing. As a

demonstrator, the criteria for material selection are somewhat different to a commercial type like the ELFR. Material selection for ELFR considers all aspects relevant to ALFRED including the targeted burn-up and the expected total dpa related damage in particular the fuel pins. In the past, compatibility of structural materials [steels like 316L, T91 and 15-15Ti (1.4970)] that can be employed for Pb cooled fast nuclear reactors were investigated in several EU projects such as EUROTRANS [2-4] and also in other projects worldwide[5-6]. The solubility of steel alloying elements like Ni, Fe, Cr is the reason for the reduced corrosion resistance in contact with Pb. In-situ oxidation is the acknowledged measure to protect steels in Pb up to certain temperatures that are material dependent. Based on experiments and the derived temperature limits, the average core outlet temperatures of ALFRED and the ELFR are set to 480°C. The most challenging conditions with respect to temperature are at the fuel assembly and the heat exchangers. For both, thin protective oxide scales with negligible reduction in heat transfer are the additionally requested material and compatibility properties. This presentation will give an overview on the selected materials for innovative Pb alloy cooled nuclear systems considering, beside pure compatibility, the influence of mechanical interaction like creep and fretting.

Material for core components

Material selection is focused on the actual European lead cooled fast reactor designs investigated at the time, ALFRED the demonstrator and the ELFR as the targeted industrial facility. The operating temperatures of the different reactor components are identical for both of the discussed nuclear reactors, ALFRED and the ELFR (Table 1). Therefore, most of the materials selected to manufacture components like reactor and inner vessel and refuelling equipment are identical for both concepts. One major difference between ALFRED and the ELFR is the expected maximum irradiation damage of the fuel assemblies. The ALFRED design foresees 100 dpa, which allows the use of the 15-15Ti stabilised austenitic steel also employed in the French Phénix reactor [8]. This steel is already licensed for application in nuclear reactors, which is an additional important aspect for material selection for ALFRED. The fuel assembly of the ELFR needs to withstand a maximum radiation damage of 200 dpa that is too high for the best available 15-15Ti stabilised steel [9]. The class of steels that can tolerate such high radiation damage are ferritic/martensitic (f/m) steels, like T91 or specific ODS types.

Table 1: Materials and conditions for the different reactor components of ALFRED and ELFR

Components	Material	Min./Max Temp. Normal Operation (°C)	Max. Lead velocity (m/s)	Max. Radiation damage (dpa/y)	Max. Radiation damage (dpa)
Reactor Vessel	AISI316L	380÷430	0.1	$< 10^{-5}$	0.0002
Inner Vessel	AISI316L	380÷480	0.2	0.1	2.1
Steam Generator	T91/AISI316L	380÷480	0.6	$< 10^{-5}$	0.0001
Primary Pumps	MAXTHAL (Ti_3SiC_2) Coated T91 or SS (Aluminized, Ta)	380÷480	10	$< 10^{-5}$	0.0001
FA Clad FA Structures	15-15Ti / T91 Aluminized	380÷550 380÷530	1 2	- -	100/200 100/200
Dummy Assemblies	T91	380÷480	0.01	-	100/200
Refueling Equipment	AISI316L	380÷480	0.2	0.02	0.3
DHR Heat Exchanger	T91	380÷430	0.2	$< 10^{-5}$	0.0001

Besides improved irradiation stability, the heat conductivity of the f/m steels is almost a factor of two higher compared to austenitic steels like 316L and 15-15Ti stabilised [10]. Therefore, T91 is also discussed as structural material for heat exchangers and steam generator (SG) components. The thermally most loaded components like fuel claddings and steam generators or heat exchangers, where coolant temperatures of 550°C can be reached, with cladding wall temperatures even 20K higher, might require surface

aluminised steels to be operated. For most components, except the pump impeller, the maximum Pb velocity of 2m/s does not require specific attention [11]. Due to the high local velocities that will occur at the pump impeller and the lack of corresponding experimental investigations, material selection for this component cannot be done at the time. Several alternatives like SiSiC, Maxthal or coatings (Ta) are under consideration.

Material compatibility with lead alloys

Compatibility of materials with Pb is mainly determined by the temperature dependant solubility of the alloying elements in the liquid Pb. Ni, Mn, Al and Si have substantial solubility of up to some wt% at 550°C [4]. The main elements of steel, Fe and Cr, are less soluble but still some 10^{-5} wt% cannot be neglected. Alloys like W, Mo and Ta and most ceramics are practically insoluble. Therefore Ni containing metals like austenitic steels suffer more from dissolution attack than Ni free f/m steels like T91. To mitigate dissolution any direct contact between the steel and the liquid Pb should be avoided. The most appropriate method is in-situ oxidation by dissolved oxygen [12]. The oxygen concentration range is determined by the operating temperature range of the reactor. The lower operating temperature of 380°C, to consider some safety margin 325°C (melting tempearture of Pb), defines the upper limit of 10^{-4} wt% oxygen to avoid PbO formation and any related coolant channel blockage. The highest achievable temperature in normal operation conditions (550°C fuel clad) determines the lower limit of dissolved oxygen of 10^{-7} wt% required to prevent or at least mitigate dissolution attack. Such formed oxide scales act as diffusion barrier and can prevent the dissolution. However, especially in case of f/m steels the growth rate of oxide scales can, particularly for longer exposure times, result in severe reduction of the heat conductivity.

f/m Steel T91

The operating temperature range for the f/m steel T91 is described in Table 1 between 380 and 550°C. The upper limit is not designed but material driven and might be increased if adequate solutions are available. The f/m steel T91 does not contain Ni. Therefore, the susceptibility for dissolution attack is reduced compared to the austenitic steels. For the entire foreseen range of temperatures no dissolution attack of T91 steel is expected also for long exposure times if oxygen concentration is kept under control at nominal values [3]. The formation of oxide scales, which is the prevailing mechanism for Ni free f/m steels, is basically independent of whether the medium in contact is pure Pb or LBE. The oxidation potential as the driving force and the diffusion constants in the steel, both determining the oxidation behaviour, are anyway similar for both coolants. Above 480°C typically three layered oxide scales that grow significantly with time are formed (Figure 1a). On average, 30 µm thick scales grow after 6 700 h. Assuming parabolic growth, oxide scales of about 40 µm thickness are formed after 15 000 h. At 550°C oxidation is accelerated and the scatter of the measured data becomes significant (Figure 1b). The average thickness of the spinel scale increases up to almost 60 µm after 15 000 h assuming parabolic oxidation. The large scatter makes long-term prediction difficult.

For long-term prediction selected data are obtained from tests with exposure times of ≥ 2 000 h to allow reasonable extrapolation to the life time in a reactor and to avoid data from the initial process of scale formation (incubation time). Furthermore the materials should have relevant compositions (e.g. Cr content ≥ 9wt%). An important point is the conduction of the experiment. The conditions should be kept constant during the test, to obtain reliable data for an extrapolation to longer time periods. The general behaviour of ferritic/martensitic steels during exposure to LBE for ≥ 2 000 h is summarised in Figure 2 and has two clearly defined regions, in the upper region protective oxide scales are formed and in the lower LBE attack on steel takes place. The border between both regions is the line drawn from the first data point at 300°C/10^{-8} wt% oxygen to 450°C/10^{-8} wt% and then with increasing oxygen concentration up to 550°C/10^{-4} wt%. The diagram shows that the

conditions of compatibility between steel and LBE exist inside a large range of temperatures up to 550°C and oxygen concentrations down to 10^{-8} wt%. Above 550°C there is a large risk of scale failure and dissolution attack onto the steel. Comparison with the situation for tests with more than 4 000 h duration, shows that probability of long time failure in the region with protective scale formation is small. This gives a hint that extrapolation of results obtained after 3 000-4 000 h is a reliable procedure. When failure occurs, it happens mainly before 4 000 h are reached. It should be noted that exposure times of only two protected steels reached 10 000 h and one 15 000 h in the temperature range 450-550°C.

Figure 1: Oxidation of f/m steel T91 in Pb alloy at different temperatures

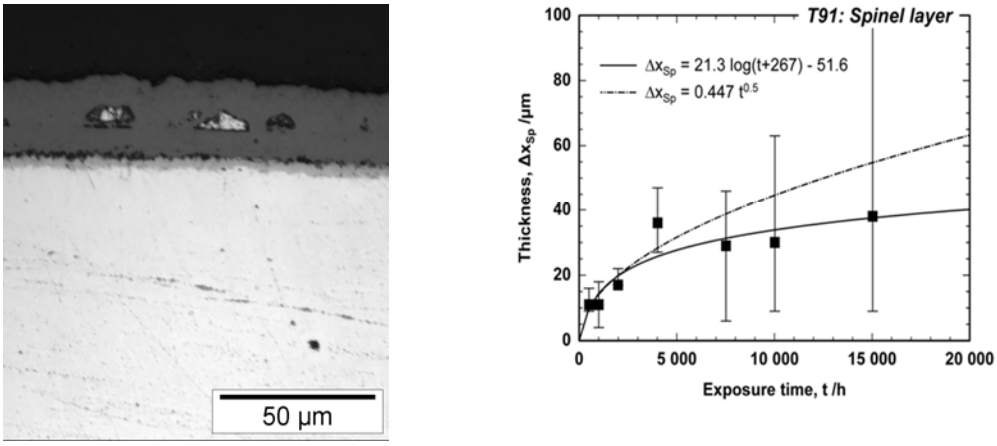

a) Oxide scale formed in PbBi at 480°C b) Oxidation as function of time at 550°C

Figure 2: Fe-Cr steels after exposure to LBE/Pb for ≥ 2 000 h at temperatures ranging from 400-650°C

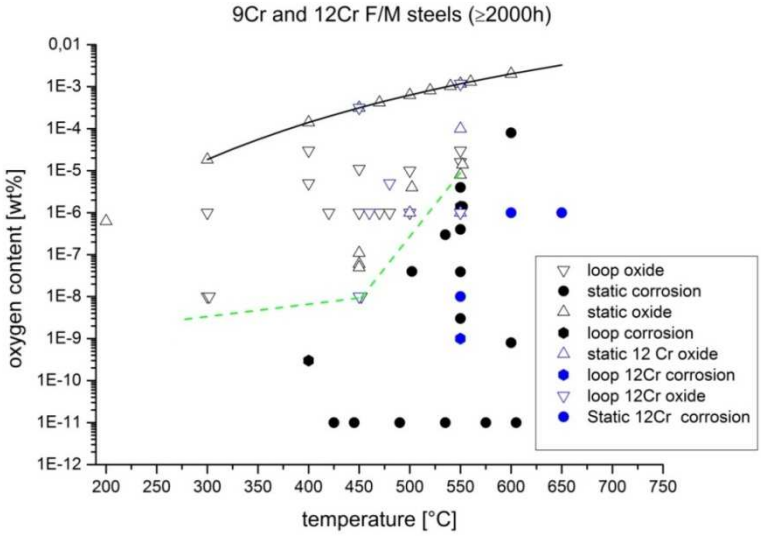

The oxide scales formed on ferritic/martensitic provide good protection against dissolution attack of liquid LBE and Pb, but attention has to be given to the thickness of the scales because of their low thermal conductivity. This concerns mainly the surfaces of the tube walls of fuel pins and heat exchangers that are exposed to high heat fluxes. Therefore, several examinations deal with the growth of oxide scales on these steels and with parameters that control the oxide thickness in the liquid metal environment. Based on numerous experiments on T91 steel in LBE containing 10^{-6} wt% of oxygen in the temperature range of 420-550°C and knowing the wide spread of especially long-term

oxidation data, the following relation for oxide scale growth as function of time and temperature can be given:

$$\delta_S(t,T) = (-0.987 + 2.54 \cdot 10^{-3} T) = [420°C < T < 550°C]$$

$\delta_S(t,T)$ = oxide scale thickness [µm]
t = time [h]
T = temperature [°C]

As an example after 15 000h one obtains an oxide scale thickness of 9.77 µm at 420°C and 50.2 µm at 550°C. After a possible life time of 3 years, the scale would be 66.5 µm at 550°C. High heat fluxes will cause an increase of the temperature gradient across the oxide scale with time because of the growing scale thickness. The consequence is a higher temperature on the metal surface of the tubes, which leads to higher oxidation rates. This function and the resulting oxide thicknesses should not be considered as absolute and final, but gives a rough impression in which range of thickness oxide scales might grow. Besides the lack of precise and reliable data for the long term, the observed oxidation becomes an issue regarding heat removal through fuel claddings and SG and HX tubes. Temperature increase of cladding tubes due to the reduced heat conductivity of the oxide scale and the reduced efficiency of the SG and HX must be considered during design or answered by a different solution like aluminizing of the steel. Besides, the oxygen supply technology also has to consider this effect.

Austenitic steels – 316L, 15-15Ti (1.4970)

The operating temperature range for the austenitic steel 316L is, as depicted in Table 1, between 380 and 480°C. The 15-15Ti to be employed as fuel assembly material can reach temperatures up to 550°C or even higher due to reduced heat transfer properties by the formation and growth of oxide scales. The current upper limits are due to limitations by the material compatibility and might be altered if suitable solutions are availabe. In previous national and international projects Ni containing austenitic steels were mainly tested in Pb-Bi eutectic (LBE) [3]. Due to the higher solubility of alloying elements in LBE than in Pb, a direct transfer of the attained knowledge is not straightforward. The general mechanism, the dissolution of Ni accompanied by penetration of Pb into the steel matrix, is identical for both coolants. However, the rate of dissolution and the resulting temperature and oxygen concentration limits might differ. Below 430°C, the maximum temperature of the reactor vessel, even in LBE no dissolution attack was observed as long as the oxygen content is high enough for the formation of oxide scales. In Pb a better behaviour of the steels can be expected. However, if the oxygen concentration drops to low values even at this temperature dissolution attack will become an issue. Tests with 316L steel showed that at 450°C in LBE with low oxygen content dissolution attack already starts after 2 000 h (Figure 3b) [3]. In LBE, at a temperature of 500°C, dissolution attack is observed after about 10 000 h. In Pb at the same conditions regarding temperature and oxygen content oxide scales still protect the steel (Figure 3a). The usability of the steel 316L up to the selected upper temperature limit of 480°C at "normal" operating conditions seems feasible if the oxygen is controlled within the given limits.

The 15-15 Ti stabilised steel (1.4970), foreseen as fuel cladding material, has to be stable up to 550°C or even 570°C. In LBE this temperature is clearly above the operating range for this steel [3,13]. Local deep dissolution attack starting with leaching of Ni and later Cr will not allow the use of the 15-15Ti in LBE at such elevated temperatures. However, in Pb this steel showed in experiments at same temperature and oxygen activity the formation of protective oxide scales at least in the first 3 000 h of exposure [14-15]. Based on the experience with extrapolation of corrosion data from short to long-term experiments, it is unlikely or at least uncertain whether this steel can be operated in Pb at 550°C for longer times. One difficulty that arised during the experimental work is the so-called incubation time for the dissolution attack. At 500°C e.g at 10^{-8} wt% oxygen a typical oxide scale develops during exposure for 2 000 h (Figure 4a). However, after

5 000 h dissolution attack was observed. A possible mechanism is the enrichment of the high soluble elements like Ni and Mn beneath the outer oxide sale (Figure 4b). These enriched phases are located in the spinel layer and can reach almost the interface with the outwards growing magnetite scale. The magnetite scale is rarely a dense and compact layer and quite frequently penetrated by the liquid metal. Therefore, the Ni and Mn enriched phases might act during prolonged exposure as a starting point for the dissolution attack if they reach the original metal surface and come in interaction with the liquid metal. Therefore all short term tests (< 5 000 h exposure) must be carefully analysed for any sign of local enrichment that can possibly predict the onset or starting of a dissolution attack in future exposure times.

Figure 3: Austenitic steel 316L after exposure to Pb alloy at different temperatures

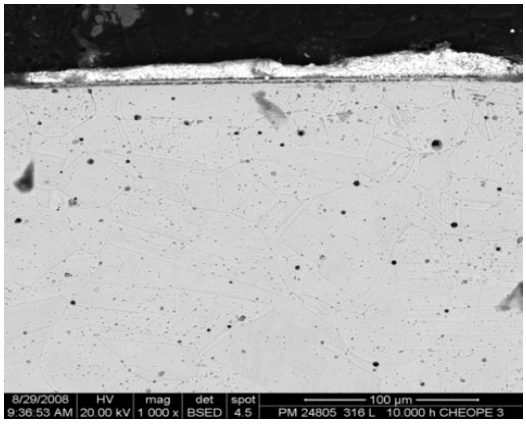

a) exposure in Pb (10^{-6} wt% oxygen) at 550°C for 10 000h

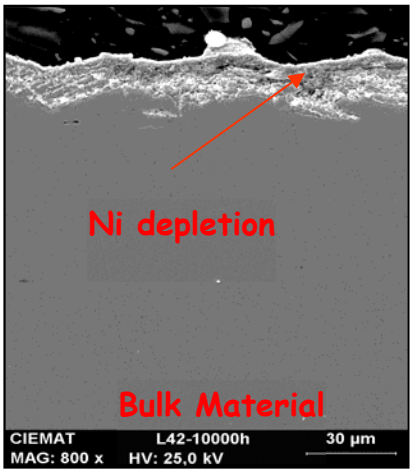

b) exposure in LBE (10^{-8} wt% oxygen) at 450°C for 2 000h

Figure 4: Short time oxidation of austenitic steel in PbBi – Incubation time?

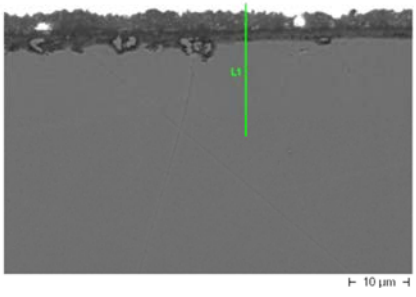

a) SEM cross section of 15-15 Ti stabilised steel after 2 000h exposure at 480°C

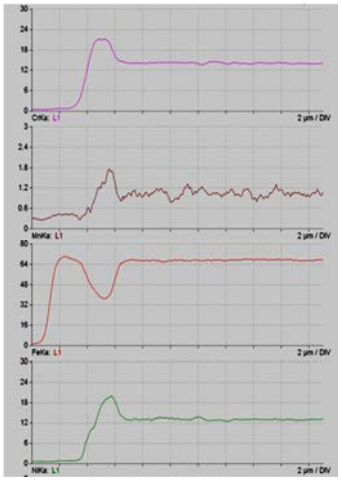

b) EDX line scan at line depicted in Figure a

Like for the f/m steels results of most reliable tests having a minimum duration of 2 000 h were compiled in Figure 5. As seen in the Fe-Cr steels, the diagram divides in two parts, separated by the line from 400°C/10^{-8}wt% to 500°C/10^{-5} wt% up to 540°C/10^{-3} wt%. It should, however, be noted that above 500°C the risk of dissolution attack by leaching out of Ni is high. At 550°C all the specimens fail even in LBE saturated in oxygen.

Figure 5: Austenitic steels after exposure to LBE/Pb for ≥ 2 000h at temperatures ranging from 400-650°C.

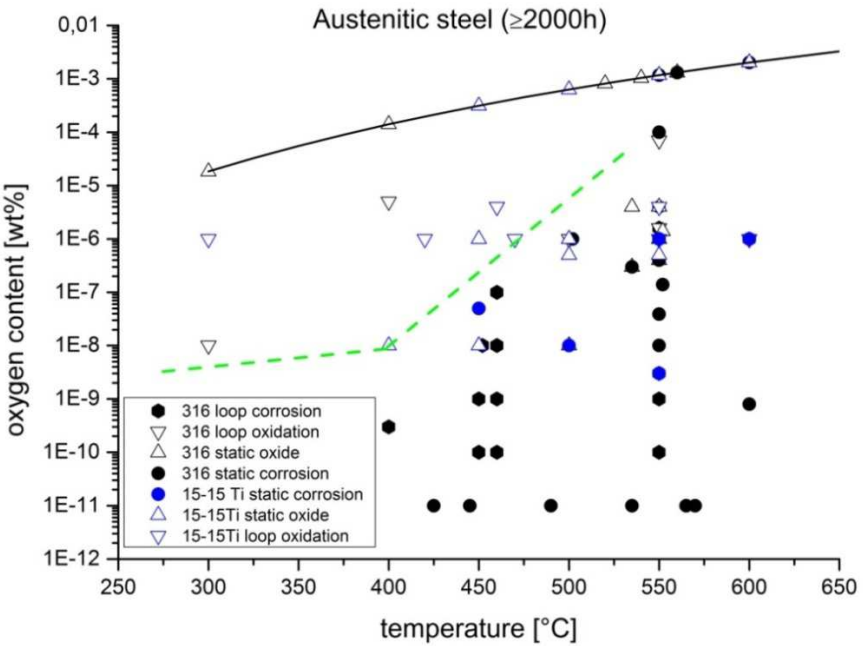

Alternative materials

For the impeller of the pump the temperature range is between 380 and 480°C. Regarding solely corrosion, both classes of steels, 316 type and T91 type, can be used. However, the expected local velocities of up to 10m/s or even higher might be problematic for the use of the materials described above. Localised high velocity flow pattern can severely damage steels as observed in corrosion experiments at IPPE and CIEMAT [3]. 316L steel was heavily eroded in such flow field at temperature and oxygen conditions that are suitable to form protective oxide scales at nominal flow velocities.

The materials discussed at the time are Maxthal, SiSiC or coatings (Ta).

Maxthal: Tests with Maxthal in Pb up to 750°C revealed its excellent compatibility with the liquid metal. The protective oxide scale, depicted in Figure 6a, is quite thin and composed of TiO_2, SiO_2 and mixed oxides. This material is discussed as pump impeller material and has to withstand high local velocities. So far no experiments were conducted to show either the suitability or non-suitability of this material for the selected application. Experiments are planned and will give answers soon.

SiSiC: SiSiC was also tested in Pb up to 600°C and did not show any incompatibility with the liquid metal. Like for the Maxthal no specific test at high flow velocities was performed so far, but due to the known wear resistance of this material beneficial behaviour is expected.

Ta Coating: Ta as refractory metal has no or only very limited solubility in Pb. Therefore coating of an impeller was discussed as another alternative solution. Basic exposure tests in Pb showed the expected incompatibility of Ta with oxygen containing Pb at higher temperatures. At temperatures above 400°C the oxygen diffuses into the Ta and embrittles the material, the hardness increases of a 2mm Ta foil exposed at 500 and 550°C as shown in Figure 6b. For longer times and higher oxygen contents entire oxidation of Ta sheets (200 µm thick) were observed. The simultaneous use of Ta and oxygen in Pb do not seem to be a suitable option for material protection in a Pb cooled nuclear reactor. Tests with a Ta coated steel impeller pump in oxygen reduced Pb are at

the time under preparation. If successful the same impeller will be tested also in oxygen containing Pb at 480°C to monitor whether the oxygen uptake and thus the embrittlement is significantly slowed down at this lower temperature.

Figure 6: Oxidation of Maxthal and Ta in Pb alloys

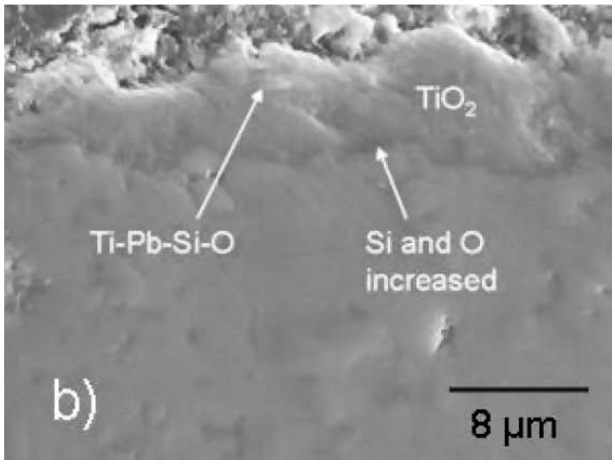

a) Maxthal after exposure to Pb at 750°C – formation of thin protective oxide scales

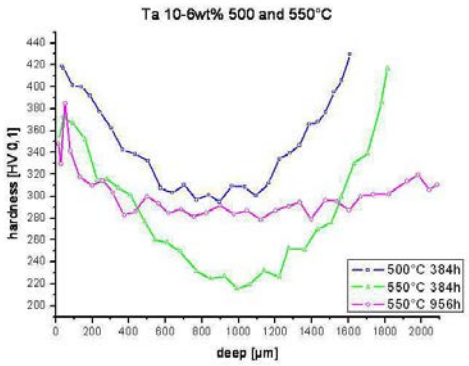

b) Hardness increase by oxygen diffusion of a 2mm Ta foil

Surface protection

Fuel claddings are operated up to 550°C. The use of 15-15Ti stabilised steel for the ALFRED cladding is doubtful or at least critical at this elevated temperature due to expected dissolution. The cladding material of the commercial ELFR, the f/m steel T91, will not suffer from dissolution, but oxidation becomes a severe problem. Therefore, surface protection barriers are required to ensure safe operation of Pb cooled fast reactors at the envisaged temperatures. Dense, stable and slowly growing oxide scales that are formed in-situ are the preferential protection barrier. Alumina, which is employed for protection of stationary gas turbines [16], but at higher temperatures, is one option. Surface aluminizing can be used to enrich a base steel (either 316 or T91 type steel) with aluminum resulting in the potential to form alumina scales during use [17]. One applicable method is the surface alloying of deposited coatings using pulsed electron beams [18]. By that a surface graded material having the target Al concentration in the outer surface region can be manufactured (Figure 7a). Such scales showed their potential to protect steels up to 600°C even in LBE for more than 10 000 h. To ensure the formation of such protective scales over the temperature range of 380 to 550°C an optimised FeCrAl composition was explored experimentally [19]. 12 bulk FeCrAl alloys with different Cr and Al content were manufactured and exposed to Pb at temperatures between 400 and 600°C. After exposure detailed investigation on the nature of the formed oxide scale applying several different techniques like SEM-EDX, XRD, grazing incident XRD and XPS. At 400°C e.g. at the specimen containing 12wt% Cr and 7wt% Al a thin kappa alumina scale was determined (Figure 7b) from the top. The thickness of this scale was evaluated applying SPS to about 35nm. For the entire experimental range the Al content required to from Al-rich oxide scales was determined as a function of Cr content and plotted in so-called oxide map (Figure 8). The Al content is: $C_{Al} = 1.52 - 0.81\ (C_{Cr}) + 0.015\ (C_{Cr})^2$ [wt%].

Figure 7: Surface alloyed FeCrAl layer and bulk

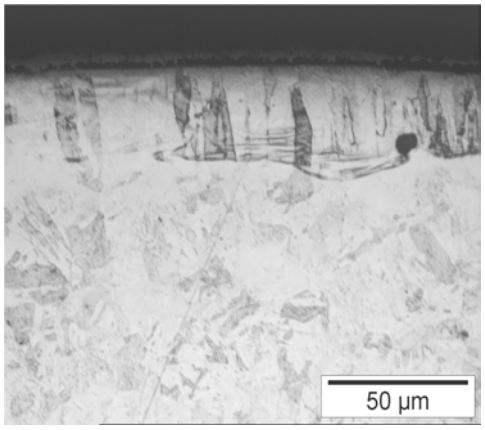

a) Cross Section
of Surface Alloyed Specimen

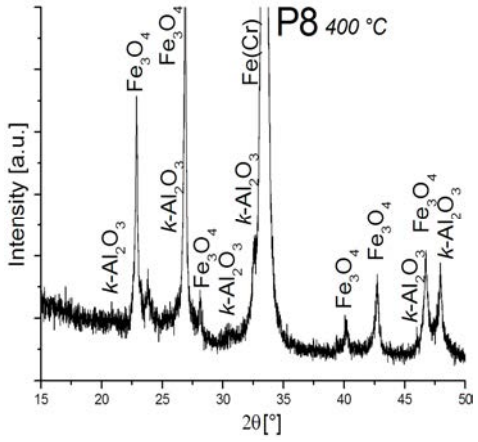

b) XRD (grazing incident) of exposed FeCrAl
at 400°C - kappa Al_2O_3

Figure 8: Oxide map showing the stability region of Al_2O_3 of the FeCrAl alloys

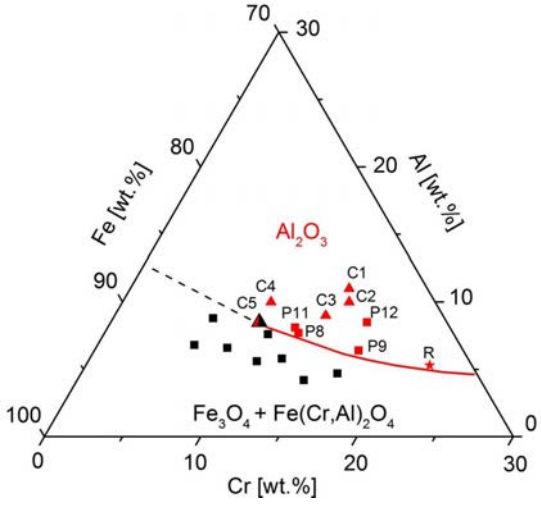

Mechanical property degradation

Besides pure corrosion, mechanical properties like creep strength and wear resistance might be affected by the contact with the liquid metal coolant. It was shown [20-22] that liquid Pb has a deteriorating effect on mechnical properties when in direct contact with the steel. Oxide scales that prevent the direct interaction will, as long as they stay intact, mitigate any effect of the Pb. The creep rupture strength e.g. of f/m steel T91 is reduced remarkably due to the contact with the liquid metal [20]. The influence of the coolant was negligible in case of surface aluminised T91 ("GESA"). There, the thin alumina scale was able to catch the deformations of the steel without cracking. Detailed evaluation allowed to define a threshold stress of about 120 MPa, below which, mainly due to the reduced strain that does not result in oxide scale cracking, the influence of Pb becomes negligible (Figure 6a). 316L type steels in contrast do not show such pronounced effects at all.

Another interesting phenomenon is fretting in Pb, which is a specific type of wear occurring at fuel claddings and heat exchanger tubes. Small amplitudes (< 200 µm) can lead to severe damage. Tests were done at harsh, accelerated conditions to evaluate the possible influence on the life time of the related components [23]. Steel T91 and the

15-15Ti stabilised steel and surface aluminised T91 were explored. Fretting wear can lead to fuel clad penetration at the T91 and 15-15Ti steel of more than 10% of wall thickness depending on the relevant parameters like amplitude load and temperature already after 150 h at a frequency of 10 Hz (Figure 6b). Both steels show in addition a strongly increased wear with increasing temperature. The austenitic steel exhibits at 450°C dissolution attack already after 600 h, which was never observed even for more than 10 000 h at 500°C in Pb. The surface aluminised T91 (GESA-T91) steel has the highest resistance against fretting wear. Post examination based on the construction of fretting maps allowed to predict the parameters that allow safe operation of fuel cladding regarding fretting damage. Loads above 75N and amplitudes below 15 µm combined with surface aluminizing are safe parameters.

Figure 9: Mechanical properties like creep and fretting in Pb alloys

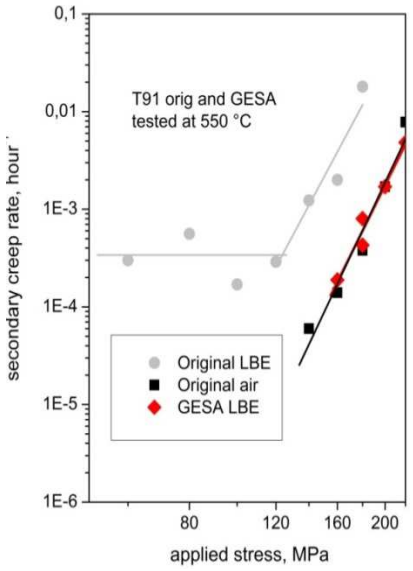

a) Secondary creep rate in LBE and Air

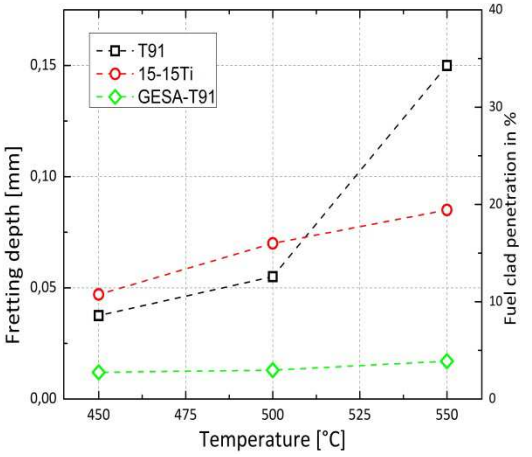

b) Fretting damage as function of temperature

Acknowledgements

The work presented was mainly performed with funding supplied under the EU contract of LEADER FP7-249661 and GETMAT

References

[1 LEADER Lead – cooled European advanced demonstration reactor FP7-249661.

[2] EUROTANS, European Research programme for the transmutation of high active level nuclear waste in an accelerator driven system, FI6W-CT-2004-516520.

[3] Weisenburger, A., C. Schroer, A. Jianu, A. Heinzel, J. Konys, H. Steiner, G. Müller, C. Fazio, A. Gessi, S. Babyan, A. Kobzova, L. Martinelli, K. Ginestar, F. Balbaud.Celerier, F.J. Martin-Munoz, L. Soler Crespo, Journal of Nuclear Materials (2011), Volume 415, Issue 3, 31, 260.

[4] Nuclear Energy Agency (2007), "Handbook on Lead-bismuth Eutectic Alloy and Lead Properties, Materials Compatibility, Thermal-hydraulics and Technologies", OECD/NEA No. 6195, 2007.

[5] Hosemann, P., S. Kabra, E. Stergar, M.J. Cappilo, S.A. Maloy, Journal of Nuclear materials (2010), Volume 403", Issues 1-3.

[6] Kurata, Y., Journal of Nuclear Materials (2011), Volume 415, Issue 3, 31, 254.

[7] Cinotti, L., C.F. Smith, H. Sekimoto, L. Mansani, M. Reale, J. Sienicki, Journal of Nuclear Materials (2011), Volume 415, Issue 3, 31, 245.

[8] International Atomic Energy Agency, Fast Reactor dadatbase – www-pub.iaea.org/books/iaeabooks/7581/fast-reactor-database-2006-update.

[9] Yvon, P., F. Carre, Journal of Nuclear Materials (2009), Volume 385, Issue 2, 217.

[10] Coutsourdis, D., "Materials for Advanced Power Engineering", Part 1 361 KLuwer Academic Publishing Dordrecht 1994.

[11] Alemberti, A., J. Carlsson, E. Malambu, A. Orden, L. Cinotti, D. Struwe, P. Agostini, "European lead- cooled fast reactor", FISA 2009, Prague, 22.

[12] Müller, G., A. Heinzel, G. Schumacher, A. Weisenburger, Journal of Nuclear Materials (2003), Volume 321, Issues 2-3, 256.

[13] Schroer, C., O. Wedemeyer, J. Konys, Nuclear Engineering and Design, Volume 241, (2011), 4913.

[14] Müller, G., G. Schumacher, F. Zimmermann, Journal of Nuclear Materials (2000), Volume 278, Issue 1, 85.

[15] Glasbrenner, H., J. Konys, G. Mueller, A. Rusanov, Journal of Nuclear Materials (2001), Vollume 296, Issues 1-3, 237.

[16] Strauss, D., G. Müller, G. Schumacher, V. Engelko, W. Stamm, D. Clemens, W.J. Quaddakers, "Surface and coatings Technology", 135 (2001) 196–201.

[17] Weisenburger, A., A. Heinzel, G. Müller, H. Muscher, A. Rousanov, Journal of Nuclear Materials (2008), Volume 376, 3, 274.

[18] Engelko, V., B. Yatsenko, G. Mueller, H. Bluhm, "Vacuum 62", (2001) 211.

[19] Weisenburger, A., A. Jianu ⇑, S. Doyle, M. Bruns, R. Fetzer, A. Heinzel, M. DelGiacco, W. An, G. Müller, Journal of Nuclear Materials (2013), Volume 437, pages 282-292.

[20] Jianu, A., G. Müller, A. Weisenburger, A. Heinzel, C. Fazio, V.G. Markov, A.D. Kahtanov , Journal of Nuclear Materials (2009), Volume 394, Issue 1, 102.

[21] Wesienburger, A., A. Jianu, W. An, R. Fetzer, M. Del Giacco, A. Heinzel, G. Müller, V.G. Markov, A.D. Kahtanov, Journal of Nuclear Materials (2012), Volume 431, Issues 1–3, 77.

[22] Van den Bosch, J., R.W. Sapundiev, A. Almazouzi, Journal of Nuclear Materials (2008), Volume 376, Issue 3, 322.

[23] Del Giacco, M., A. Weisenburger, G. Mueller, Journal of Nuclear Materials (2012), Volume 423, Issues 1–3, 79.

Overview of 9Cr steels properties for structural application in sodium fast reactors

Céline Cabet*, Jean-Louis Courouau, France Dalle, Clara Desgranges, Laurent Forest, Laure Martinelli and Maxime Sauzay

CEA, DEN/DANS
CEA Saclay, France

Abstract

A research and development programme has been launched by CEA, EDF and AREVA for the choice and qualification of material for sodium fast reactor (SFR) structural components. The requirements on steam generator (SG) are demanding, with operating temperatures ranging from 240 °C to 530 °C in water/steam and in sodium for an extended design life of several decades. The selection of the SG materials is based on many characteristics: fabrication, welding, thermal properties, mechanical strength at low and high temperature, environmental resistance. 9%Cr steels which are relevant candidate alloys for different designs of SGs have been extensively studied in the past decade. The objective of this paper is to review some advances made at CEA on determining properties of the X10CrMoVNb9-1 steel (hereafter named "grade 91"): welding, modelling of cyclic softening, modelling of long-term creep, compatibility with liquid sodium, corrosion in steam.

Introduction

Sodium fast reactor (SFR) is considered in France as the most mature Generation IV system and the pre-conceptual design of the SFR prototype ASTRID (Advanced Sodium Technological Reactor for Industrial Demonstration) is underway. Material selection and qualification for the major components of ASTRID is a key point for the reactor design and construction. CEA, EDF and AREVA have launched an R&D programme in support of the material validation. Because of their characteristics at high temperature and superior thermal properties (high thermal conductivity, low thermal expansion), 9%Cr steels were contemplated for different designs of steam generators (SG). The operating conditions of SG are demanding with service temperatures ranging from 240°C to 530°C in liquid sodium and water/steam for long design life (several decades). This places high requirements on 9%Cr steels-base metal and welds in terms of long-term behaviour and end-of-life residual properties.

This paper covers some of the latest CEA developments about welding of "grade 91" which is a critical requirement for the construction of large components. It also reviews some of the recent results gained at CEA on the "grade 91" life time assessment in terms of cyclic softening, modelling of long-term creep and compatibility with liquid sodium and steam.

Welding

"grade 91" has wide applications for heat exchanger in the power generation industry, concerning mainly thin structures optimised for creep considerations. As candidate for structural material of SFR SGs, the compromise between achieving good ductility properties and room/high temperature mechanical resistance in welds is needed, granting at a minimum to fulfill requirements of the Order of 12 December 2005 relative to Nuclear Pressure Equipment Arrêté (AESPN). This is why a parametric study was carried out at CEA on welding conditions to improve the welded joint mechanical properties. Many joints have been elaborated by automatic GTAW process with different commercial filler metals (Table 1) and different welding conditions: pulse or continuous welding current, deposition rate (between 0.20 and 1.89 g/cm), post-weld heat treatment temperature (PWHT between 740˚C and 760˚C). The resulting microstructure, impact test and tensile properties were studied.

Table 1: Chemical composition of tested filler materials (mass. %)

Filler metal	C	Si	Mn	P	S	Cr	Mo	Ni	Al	Nb	V	N	Cu
B	0.109	0.22	0.77	0.006	0.002	9.03	0.98	0.46	-	0.059	0.196	0.041	0.03
C	0.09	0.22	0.51	0.005	0.004	8.89	0.91	0.67	0.010	0.08	0.19	0.05	0.03
D	0.08	0.15	1.00	0.006	0.003	9.12	0.89	0.70	-	0.04	0.18	-	0.03

The type of welding current -pulsed or continuous- has little influence on the welded joint microstructure, Ductile-to-Brittle Transition Temperature (DBTT) and ductility. On the other hand the characteristics significantly depend on the deposition rate of filler metal and on the post-weld heat treatment temperature.

- Effect of the deposition rate

Figure 1 shows the impact energy curves for the filler material B, with a PWHT at 760°C and for three different deposition rates. It can be observed that the smaller is the deposition rate per run, the lower is the DBTT. For the lower deposition rate (0.2 g/cm), the welded zone shows a fine fully reaffected grain microstructure, a lower density of precipitates and a lower hardness.

Figure 1: Influence of deposition rate on the weld zone impact energy of "grade 91" (VWT specimens 55×10×10mm³)

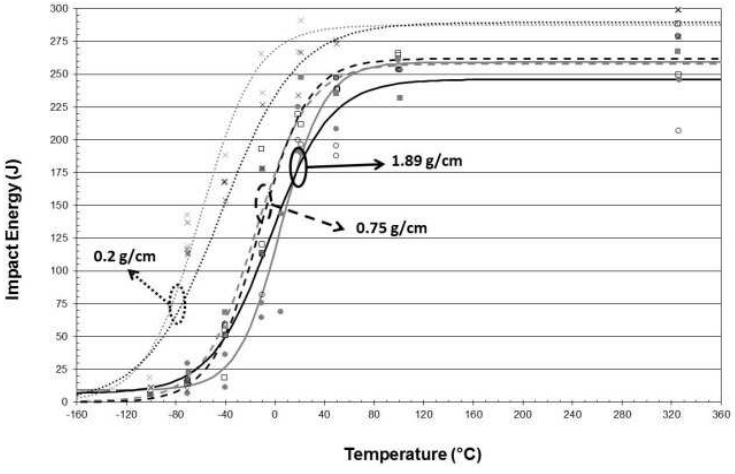

Tensile tests were performed on specimens from the welded zone. While the influence of deposition rate on the tensile strength is insignificant, a decrease in the deposition rate generally causes an increase in the elongation. For instance, filler material B shows an increase in elongation of 7% (PWHT at 740°C) and 12% (PWHT at 760°C) when the deposition rate changes from 1.89 g/cm to 0.2 g/cm.

- Effect of the PWHT

Generally speaking (for filler metal B and C), an increase in the PWHT temperature causes an improvement of elongation after fracture and a diminution of the tensile strength (Rm) at room temperature. The maximum elongation is in decreasing order:

- 25% for product B , PWHT at 760°C, deposition rate 0.75 g/cm;
- 23% for product D, PWHT at 760°C, deposition rate 0.75 g/cm;
- 22% for product C, PWHT at 760°C, deposition rate 0.75 g/cm.

For a PWHT at 740°C, only one tested condition produces Rm below 800 MPa (product D, deposition rate 1.51 g/cm). On the other hand, for a PWHT at 760°C, filler metals B and D exhibit Rm below 800 MPa.

It is concluded that elongation and tensile strength are highly sensitive to the temperature PWHT (740°C-760°C).

Among all tested products and assessed operating conditions, the filler material B with PWHT at 760°C is the most promising with an elongation well higher than 20% and Rm ~580-760 MPa at room temperature.

To complete these mechanical results, it is necessary to check the stability of these properties after ageing treatments. This work is currently in progress on a joint with the identified optimised parameters.

Cyclic softening

The cyclic softening of 9%Cr steels has been extensively studied in the past few years. Alarming results were first obtained on the drop of creep rupture life for pre-cycled specimens with high fatigue damage. Recent data have shown that for more realistic pre-fatigue damage, the creep properties are only moderately impacted. Work is ongoing to quantify the effect of fatigue damage on the creep behaviour. In the meantime, cyclic softening is studied from an experimental and numerical perspective. Recently a micromechanical model has been proposed for predicting both the microstructure evolution and the macroscopic softening of 9%Cr steels [1]. This model based on the self-consistent Kröner homogenisation model [2] is suitable for elastic-plastic constitutive laws. Each martensite block is successively considered as an inclusion within the matrix made of other blocks. The behaviour of the polycrystal is then calculated by an average process over all blocks.

Based on the microstructure evolution as identified through TEM observations [3], two different softening mechanisms are taken into account: the decrease in dislocation densities inside the subgrains and the subgrain size growth. The subgrain size growth is mostly due to the disappearance of low angle boundary dislocations. The final model is mainly based on physical parameters determined from the literature or by microstructural observations and only depends on two adjustable parameters. These two parameters (volume and energy of activation) are fitted from the loading data of the first fatigue loop. The model was applied to 9%Cr steel ''grade 92'' for two different strain rates (Figure 2a). The homogenisation modelling gives good predictions of the cycling softening. It also gives reasonable predictions of the evolution of the subgrain size during cycling with a quick increase at the beginning and then continuous but lower evolution (Figure 2b).

Further work is in progress to take into account other dislocation movements such as climb and to improve the predictions at high temperature. A localisation law adapted from the approach of Molinari et al. [4] will also be implemented to better approximate the viscoplastic behaviour of these steels. With only two fitted parameters, this micromechanical model is an important step forward to predict the real softening of 9%Cr steels in service.

Figure 2: Predictions of the pure fatigue behaviour of "grade 92" for two strain rates

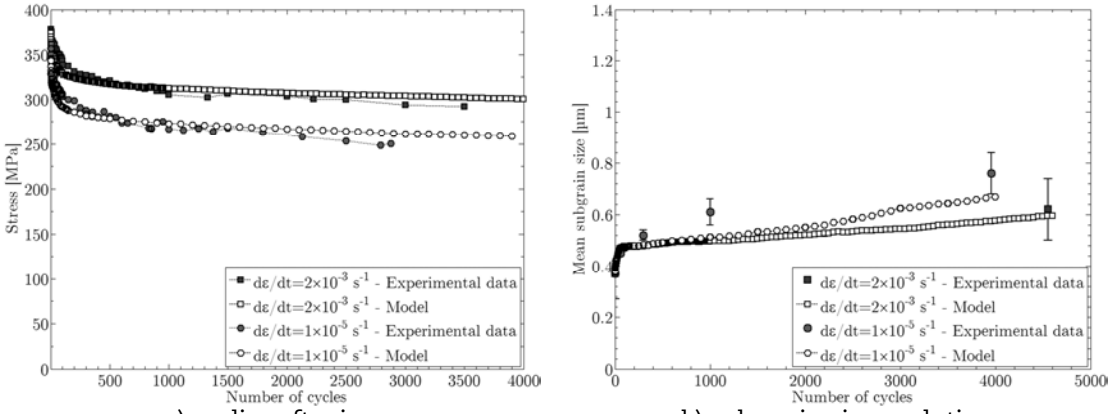

a) cyclic softening b) sub-grain size evolution

Long-term creep damage

Long-term tests have been carried out on 9%Cr steel up to 250 000 h. Observations of failed specimens show that necking is the dominant damage mechanism up to 100 000 h at 600°C and 200 000 h at 500°C [5]. Necking has been simulated taking into account the softening behaviour of martensitic steels; the predicted lifetimes are close to the experimental points (Figure 3a) for:

- a large range of temperatures: 500-700°C,
- a very large range of lifetimes: from one hour to more than 100 000 h,
- all considered martensitic steels whatever the chemical composition and tempering parameters provided the minimum creep strain rates have been measured.

Therefore a master curve is obtained which is in good agreement with experimental data. It should be noticed that even the cross-section evolution during creep tests is well simulated (figure 3b).

Figure 3:
a) Experimental creep lifetimes obtained for various martensitic steels and temperatures (500-700°C) and predicted lifetimes based on necking simulation (upper and lower bounds)
b) Measured and simulated cross-sections for interrupted test on 9%Cr steel at 550°C and 350MPa [6]

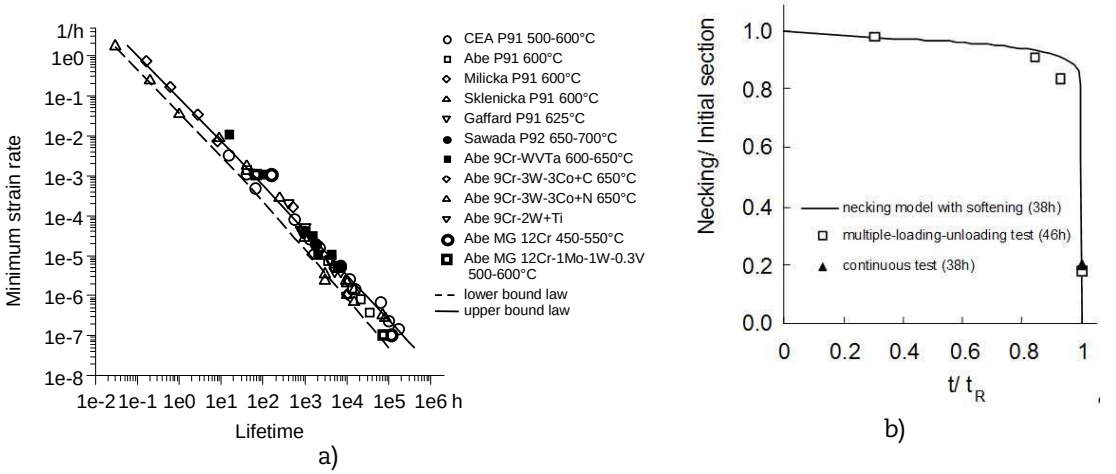

a) b)

For the longest creep tests, intergranular creep cavities are observed (Figure 4a) even if their volume fraction remains very low and do not affect lifetimes up to 100 000 h [6-7].

For longer times, their volume fraction increases and the cavities may affect the lifetime. That is why an additional modelling has been carried out assuming:

- continuous cavity nucleation during creep deformation in agreement with observations;
- cavity growth by vacancy diffusion along grain boundaries which has been shown to be the dominant growth mechanism for martensitic steels in the considered loading conditions.

At 600°C, a change in the stress-time to failure curve is expected. The predicted transition point is about 300 000-400 000 h. This is in good agreement with the only available experimental result at very low stress (70 MPa, 600°C) (Figure 4b).

Figure 4:
a) Intergranular creep cavities in 9%Cr steel tested at 230MPa and 500C for 16 0000 h
b) experimental and predicted lifetime (grey symbols: test data, green line: necking simulation and blue/red curves: intergranular damage simulations) [7]

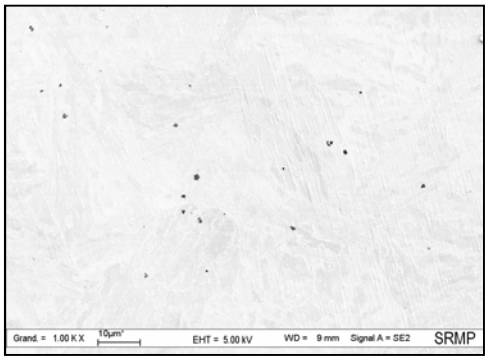

a)

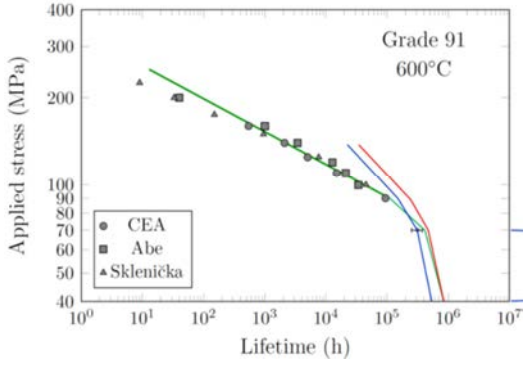

b)

Long-term compatibility with liquid sodium

Few compatibility data are available for 9%Cr steels in sodium at 550°C let alone on the corrosion behaviour on the long run. Therefore, static tests were performed on "grade 91" at 550°C for 1 600 h (test 1) and 5 000 h (test 2) in slightly oxidising and carburising liquid sodium. The oxygen concentration was roughly 10 wppm (µg/g). Samples were extracted every 400 h for test 1 and every 1 000 h for test 2. Characterisation of the corroded specimen morphology includes SEM, XRD, and Glow Discharge-Optical Emission Spectroscopy [8].

Corrosion occurs through oxidation of the sodium-steel interface with the formation of [8-9]:

- a sodium chromite scale ($NaCrO_2$);
- a chromium depleted steel layer where sodium has penetrated (Figure 5a);
- a carburised layer, which is neither hardened nor softened.

The Cr depleted layer exhibits a specific microstructure (martensite tempered laths) and sodium fills the porosity. It is believed that the silicon plays a role in that intergranular attack by promoting the formation of SiO_2 that is then dissolved in sodium through the formation of ($Na_2O.SiO_2$). To our knowledge, this penetration of sodium into the Cr depleted layer has not been documented yet and might play a critical part in the corrosion mechanisms or for other related phenomenon such as liquid metal embrittlement [10]. Further investigations are in progress.

Corrosion kinetics is assessed based on the thickness of each corrosion layer from GD-OES analyses. Both chromium and carbon concentration profiles are used to localise the interfaces between the corrosion layers [8]. This technique appears to be accurate to

evaluate the evolution of the mean thickness over few micrometers even if interfaces are partly inhomogeneous. The thickness of the oxide scale is plotted against time in Figure 5b for both the "grade 91" and the austenitic Stainless Steel 316L(N) (X2CrNiMo17-12-2 controlled nitrogen content) [9]. After 5 000 hours, the oxide scale is 2.5 times thicker than for SS 316L(N), while the Cr depleted layer of "grade 91" steel is 7 times thicker. Thus, "grade 91" appears to be more sensitive to oxidation than austenitic steels andis in agreement with literature data. Both linear and parabolic evolution of the scale thickness fits with the data and results at longer times are needed to discriminate the corrosion law. The rate limiting step of the oxidation mechanism has also to be identified. To complete the experimental database, long-term corrosion tests are ongoing with different oxygen concentration (0 and 200 wppm) at 550°C.

Figure 5: Oxidation of "grade 91" steel in liquid sodium (slightly oxidising and carburising) at 550˚C

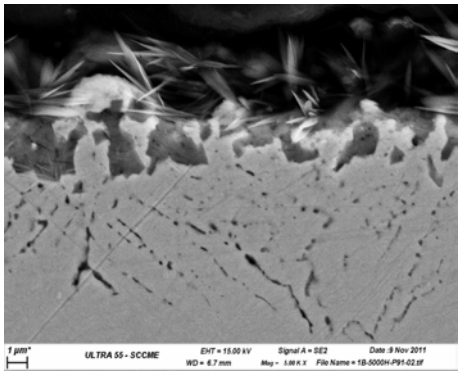

a) specimen exposed for 5 000 h

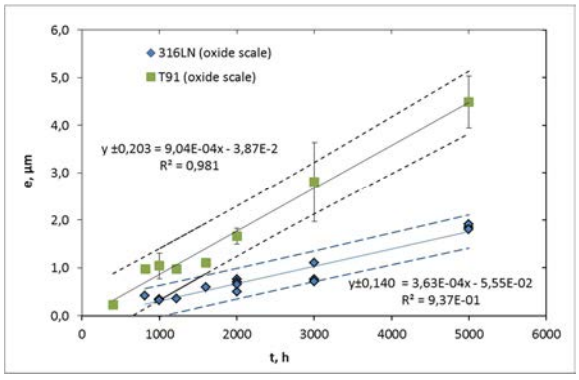

b) evolution of the oxide scale thickness (with 95% confidence hyperboloids) assessed by GD-OES (SS 316LN as reference)

Oxidation in steam

The oxidation of "grade 91" steels in water/steam is an important issue for steam generator applications. The metal loss through oxidation in service must be assessed to design the tube thickness. A dedicated device was developed to perform oxidation experiments in pure water vapour with a circulation loop. The tests were carried out at 550°C and at atmospheric pressure up to 5 000 h. Three sample holders (with two specimens each) were placed in the quartz tube of a furnace and were exposed to pure water vapour with a low flow rate.

Samples were analysed by SEM, Raman spectroscopy and TEM (Figure 6). All samples present the same oxide scale morphology with a three-layer structure consistent with literature data [11]:

- a Fe-Cr spinel layer ($Fe_{3-x}Cr_xO_4$, $0<x<2$) at the metal/oxide interface;
- a magnetite (Fe_3O_4) layer in contact with steam;
- a layer of hematite, formed by oxidation of the magnetite, on top of the magnetite layer.

TEM examinations show that the spinel oxide is composed of a large quantity of small equiaxial grains with an average stoichiometry $Fe_{2.4}Cr_{0.6}O_4$. Near the base metal, Fe-rich and Cr-rich grains are alternatively observed. This observation is in good agreement with the oxidation mechanism proposed to describe the main oxidation process [12]: oxygen is brought to the metal/spinel interface in the molecular form (water molecule). The anionic growth of the internal scale is controlled by the space made available by the metal loss due to formation of the external magnetite scale by cationic flux.

Figure 6: Oxidation of "grade 91" steels in pure steam (holder #3)

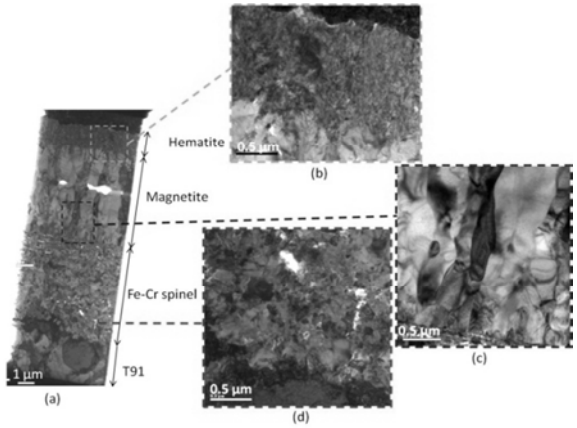

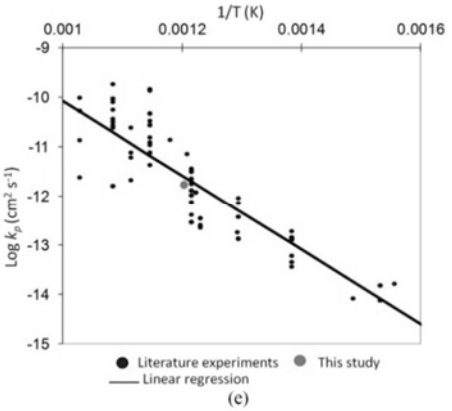

a) TEM picture (48 hours)
b) zoom on the hematite layer
c) zoom on the magnetite layer
d) zoom on the Fe-Cr spinel layer

e) parabolic constants versus temperature

The evolution of the weight gains (from 48 h up to 5 000 h) is shown in Figure 7. The obtained oxidation kinetics is parabolic up to 1 700 h. Figure 7 shows that oxidation rate depends on the sample position in the furnace. In fact, samples from holder #3, which was located downstream of the flow show the higher oxidation rate; and samples from holder #1 placed upstream show the lower oxidation rate. It is believed that the difference in the kinetics with the sample position is linked to the flow rate of water vapour. The reason is not completely understood but it must be linked to the hydrogen production formed during the oxidation of 9%Cr steel by water. The parabolic constant of samples in the downstream position (sample holder #3) is consistent with literature results as observed in Figure 6e.

Figure 7: Oxidation of "grade 91" steel in pure steam: evolution of the mass gain

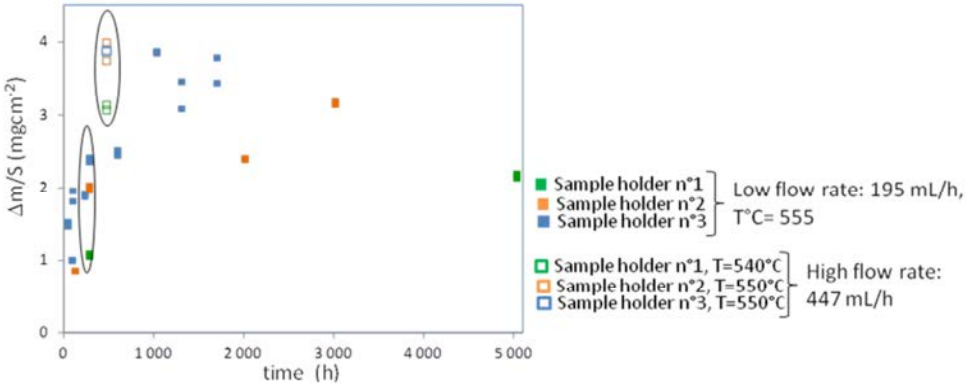

Conclusion

In support of the development of steam generator and circuit for SFR, CEA, EDF and AREVA have extensively studied the properties of 9%Cr steels for several years. Key requirements for "grade 91" steel are the welding of thick components and a design life of 30 years. An overview is given on some recent R&D results obtained at CEA. Development of the welding procedure is ongoing and promising results were obtained through decreasing the quantity of filler metal deposited per run and through improvement of the post-weld heat treatment. For the best conditions and filler metal, suitable impact energy, tensile elongation and Rm were measured and the welded joint meets the standard

requirements with acceptable margin. Cyclic softening during pure fatigue tests has been well predicted by a polycrystalline model. Predictions over longer times should be obtained soon. Creep damage mechanisms have been studied in details showing the influence of necking up to 100 000 h at 600°C and the additional effect of intergranular creep cavitation for longer times. Both mechanisms have been simulated leading to predicted lifetimes in reasonable agreement with experimental data up to a few hundred thousand hours. Corrosion of 9%Cr steel was studied in slightly oxidising and carburising liquid sodium at 550°C. Oxidation was evidenced. The corrosion rate of "grade 91" steel is moderate but higher than the rate for austenitic steels; corrosion kinetics needs to be investigated on longer times. Steam oxidation was investigated in pure steam: over long times, "grade 91" steel form rather thick oxide scales made of spinel, magnetite and hematite. Understanding and modelling of oxidation kinetics is going on.

Acknowledgements

AREVA NP and EDF are greatly acknowledged for their financial support. The authors are grateful to Martine Blat-Yrieix, EDF R&D, Sophie Dubiez-Le Goff, AREVA NP, and Thorsten Marlaud, AREVA NP, for fruitful discussions.

References

[1] Giroux, P.F, F. Dalle, M. Sauzay, C.Caës, B. Fournier, T. Morgeneyer, A.F. Gourgues-Lorenzon (2010), Procedia Engineering, Volume 2, pp. 3984-3993.

[2] Kröner, E. (1961), Acta Metallurgica, Volum 9, pp. 155.

[3] Giordana, M.F., P.F. Giroux, I. Alvarez-Armas, M. Sauzay, A. Armas, T. Kruml (2012), Materials Science and Engineering A, 550, pp. 103-111.

[4] Molinari, A., S. Ahzi, R. Kouddane (1997), Mechanics of Materials, 26, pp. 43-62.

[5] Lim, R., M. Sauzay, A.-F. Gourgues (2011) "Modelling and experimental study of the tertiary creep stage of grade 91 steel", International Journal of Fracture, Volume 169, pp. 213-228.

[6] Lim, R., M. Sauzay, F. Dalle, L. Allais, I. Tournié, P. Bonnaillie, A.-F. Gourgues (2012) "Experimental study and modelling of long-term creep lifetime of modified 9Cr1Mo steels", *Creep 2012*, Kyoto, Japan.

[7] Sauzay, M. (2012), "Déformation et endommagement à haute température des aciers martensitiques revenus. Fatigue, fluage et fatigue-fluage", Techniques de l'ingénieur, M4180, Editions T.I., Paris.

[8] Courouau J.-L., V. Lorentz, M. Tabarant, S. Bosonnet, F. Balbaud-Célérier (2013) "Corrosion by oxidation and carburization in liquid sodium at 550C of austenitic steels for sodium fast reactors", in International Conference on Fast Reactors and Related Fuel Cycles (FR13), March, Paris, France.

[9] Courouau, J.-L. et al (2013) ''Corrosion by oxidation and carburization in liquid sodium at 550C of ferritic martensitic steels for sodium fast reactors'', this conference.

[10] Hemery, S., T. Auger, J.L. Courouau, F. Balbaud-Célérier (2013) ''Effect of oxygen on liquid sodium embrittlement of T91 martensitic steel'', Corrosion Science, doi: http://dx.doi.org/10.1016/j.corsci.

[11] Wright, I.G., R.B. Dooley (2010), International Materials Reviews, 55, 3, pp. 129.

[12] Martinelli, L., F. Balbaud-Célérier, A. Terlain, S. Bosonnet, G. Picard, G. Santarini (2008), Corrision Science, Volume 50, pp. 2537.

Part 2
Chairs: C. Fazio and R. Wright

Stress corrosion cracking and oxidation of austenitic stainless steel 316 L and model alloy in supercritical water reactor

A. Sáez-Maderuelo, D. Gómez-Briceño, G. Diego
CIEMAT, Spain

Abstract

In this work, an austenitic stainless steel type 316 L was tested in deaerated supercritical water at 400°C and 500°C and 25 MPa to determine how variations in water conditions influence its stress corrosion cracking behaviour and to make progress in the understanding of mechanisms involved in SCC processes in this environment. Moreover, the influence of plastic deformation in the resistance of the material to SCC was also studied at both temperatures. In addition to this, previous oxidation experiments at 400°C and 500°C and at 25 MPa were taken into account to gain some insight in this kind of processes. Furthermore, a cold worked model alloy based on the stainless steel 316 L with some variations in the chemical composition in order to simulate the composition of the grain boundary after irradiation was tested at 400°C and 25 MPa in deaerated supercritical water.

Introduction

Generation IV nuclear reactors are the future of nuclear energy. Among all proposed designs, the SCWR is one of the more feasible options due to its more simple design, based on LWR, and the use of standardised materials which are well known. The result is a nuclear reactor with higher efficiency, around 45%, and safer than LWR. In spite of this, corrosion of cladding and structural materials in a not well-known coolant such as SCW is still one of the most important issue to be studied. The current design for the SCWR is a direct cycle system operating at 25 MPa with a inlet coolant temperature that moves from 280ºC to 620°C and an average temperature around 500ºC [1]. In this range, water moves from liquid to the supercritical zone where its behaviour is uncertain although, in general, it is thought to be a mixture between liquid and gas. Specifically, in the range between the critical point (374ºC) and around 450ºC, the properties of water such as density, ionic product and dielectric constant significantly drop [2]. These properties mainly depend on the pressure and increase when pressure increases. Moreover, since these reactors work at high temperature, this variable accelerates the corrosion processes. In fact, corrosion tests in supercritical water (SCW) are being used as an accelerated method to establish the behaviour of highly resistant materials, such as Alloy 690, to corrosion and SCC under LWR conditions, assuming that the mechanisms of corrosion and SCC are the same under the two sets of conditions [3-4] but this is not yet determined therefore it is not easy to interpret results from SCW tests. Austenitic stainless steels are candidate materials to build the SCWR. In many cases, austenitic stainless steels are cold worked to improve their mechanical properties or as result of manufacturing or welding processes. In any case, it has been shown that plastic

deformation in the material accelerates SCC in liquid water [5-6]. For this reason, it is necessary to study the influence of plastic deformation on these alloys in SCW. In this paper the resistance to SCC of austenitic stainless steel 316 L at 400 and 500ºC, 25 MPa in deaerated supercritical water, with and without deformation was studied in order to understand the influence of different variables associated with the process. The SCC tests were performed by means of constant extension rate tensile (CERT) tests. In addition to this, to gain some insight of processes involved, previous oxidation results from a 316 L at 400ºC and 500ºC were taking into account. Futhermore, as a first step to understand the behaviour of these alloys under irradiation conditions in SCW, a cold worked model alloy, based on an austenitic stainless steel 316 L with some changes in its composition that simulates the composition of the grain boundary after irradiation was tested in deaerated SCW at 400ºC and 25 MPa.

Experimental

The austenitic steel 316 type L in as-received condition originated from a rolling plate. This plate was annealed at temperatures between 1 040 and 1 100ºC. Subsequently, the plate was heated at 1 060ºC for 30 minutes and then water quenched (WQ) to avoid carbides precipitation within the grain [7], to homogenise the microstructure and to relax tension from manufacturing process. The microstructure of the material after heat treatment shows an austenitic matrix without carbides in grain boundaries and in the matrix and with a grain size of 45 µm. Moreover, ferrite was observed in the rolling direction. Model alloy was manufactured from a 316 L alloy cast with an alteration in the chemical composition: an increase in Ni and Si content and a reduction in Cr content. After manufacturing process the ingot was heated up to 1 200ºC for 2 h, then it was forged at 1 200°C up to 7-8 mm thickness, annealed at 1 050°C for 30 min., cold rolled and eventually it was annealed at 1050°C. The final thickness of the plates was approximately 10 mm. The chemical compositions of austenitic stainless steel 316 L and model alloy are listed in Table 1. Afterward, samples were machined by Electro Discharge Machining (EDM) from the plate with geometries shown in Figure 1.

Table 1: Chemical composition of the stainless steel 316 L and the model alloy under study (wt%)

	Al	C	Co	Cr	Cu	Fe	Mn	Mo	N	Ni	P	S	Si
316L	–	0.020	0.14	17.39	–	Bal.	1.28	2.20	0.020	11.49	0.032	0.001	0.45
Model	0.031	0.026	–	11.91	0.19	Bal.	0.96	0.381	0.0176	27.90	0.018	0.004	2.63

Figure 1: a) Geometry of the samples for the alloy 316 L. b) Geometry of the samples for the model alloy (all measurements are in mm).

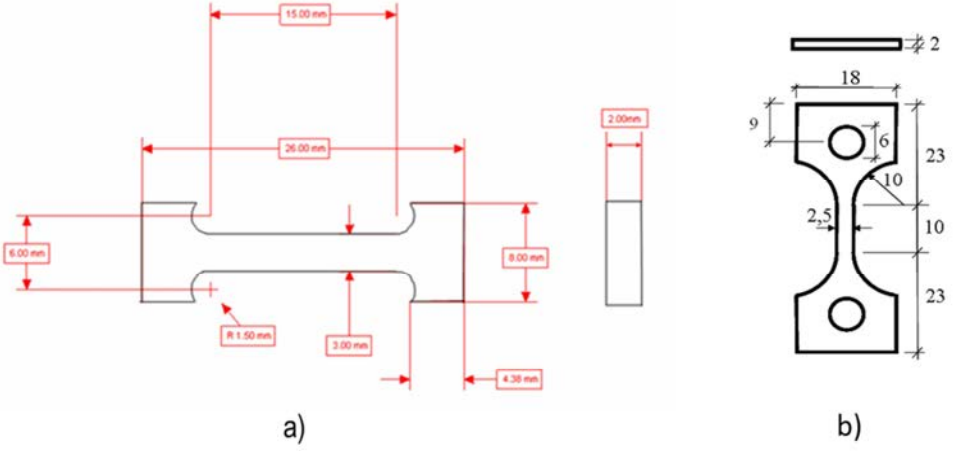

Some samples were strained by tensile at room temperature with a 100 kN MTS servo-hydraulic test machine to a strain rate of 10^{-4} s^{-1} to 20% of elongation for the purpose of studying the effect of strain in the behaviour to SCC of the 316 L and model alloy in supercritical water. The same machine was equipped with a furnace to study the mechanical properties of the material at room temperature, 400ºC and 500ºC. In all cases surfaces of samples were prepared using sandpaper to a grain size of P600. The study of SCC behaviour of 316L steel in supercritical water was carried out by CERT type tests in a circuit designed for this purpose and equipped with an autoclave made of alloy 625 with 4 liter capacity and a charging system that allows testing four samples at a time. Alloy 316 L specimens were tested at 400 and 500°C, at a pressure of 25 MPa in deaerated supercritical water and model alloy specimen was tested at 400ºC and 25 MPa in deaerated supercritical water.

Results and discussion

Austenitic stainless steel

Austenitic stainless steel 316 L was tested to failure in supercritical water at 400°C and up to three different strain percentages: 3, 16 and 35% (failure) at 500°C. The stress-strain curves to failure at both temperatures are shown in Figure 2. Stress-strain curves at 400 and 500ºC in air are included for comparison. At this point, it should be noted that this comparison is possible even though the material was tested in air at a rate faster than the rate of a CERT test (10^{-7} s^{-1}) because face centered cubic (FCC) metals and alloys are not affected (with some exceptions) by changes in the strain rate [8], moreover air is not very aggressive at 400-500ºC. Mechanical parameters and results of surface analysis of 316 L samples after the tests are shown in Table 2.

Figure 2: Stress-strain curves for alloy 316 L tested in supercritical water at 500ºC (a) and 400ºC (b) in deaerated water. (Stress-strain curves at 500ºC and 400ºC in air are included for comparison.)

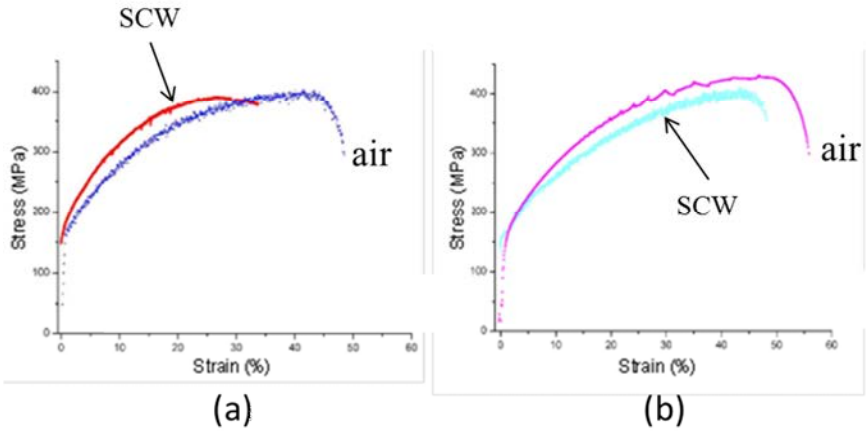

A lower elongation can be observed at both temperatures for samples tested in SCW (Figure 2) due to the effect of the environment. When both elongations are compared it is noticed that the decrease is higher in the sample tested at 500°C where the environment is apparently more aggressive. Moreover, in SCW at 500°C the material shows a higher hardness than in air. However, this effect is not observed in the sample tested in SCW at 400°C. This situation is supported by the crack density since the material has a higher density and a larger size crack at 500 than at 400°C. The higher susceptibility of the material to corrosion processes at 500ºC is evidenced again studying the fracture surfaces, Figure 3. The image obtained by SEM of the fracture surface of the sample tested at 500°C shows a predominantly ductile fracture with small areas of granulated cracks [9]. On the other hand, the fracture surface of the sample tested at 400°C shows only a ductile fracture.

Although the rate used to carry out the CERT test (10^{-7} s^{-1}) is widely used [10,11], considering these results it is possible to ask whether the rate of this order of magnitude is slow enough to demonstrate the susceptibility of the material to SCC or it is too fast and, in cases like the specimen tested at 400°C, masks the possible effect of the environment [12].

Table 2: Results of constant extension rate experiments performed in deaerated supercritical water for the alloy 316 L (<10 ppb O_2).

Material	Test conditions	σ_Y (MPa)	σ_{TS} (MPa)	ε (%)	Strain rate (s^{-1})	Crack density ($n°/mm^2$)	Crack size (μm)	Crack morphology
316 L	500°C/25 MPa/ <10 ppb O_2	223	-	3	10^{-7}	Not observed	-	-
316 L	500°C/25 MPa/ <10 ppb O_2	220	-	16	10^{-7}	Isolated cracks	~ 25	?
316 L	500°C/25 MPa/ <10 ppb O_2	221	391	35	10^{-7}	61	65	?
316 L	400°C/25 MPa/ <10 ppb O_2	260	410	48	10^{-7}	53	36	?

Figure 3: Fracture surfaces of specimens tested at different temperatures in SCW (All surfaces are cleaned.)

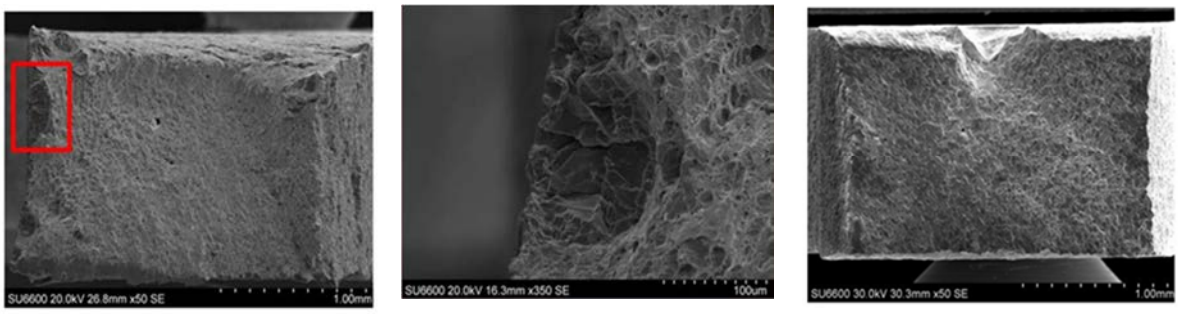

(a) 500°C (b) detail of photo "a" showing SCC (c) 400°C

In addition, study of the SCC by CERT tests is a challenge because of the different trend of the results depending on the criteria used to evaluate them. Teysseyre and Was [10] presented results for several alloys where the material showed different susceptibility to SCC depending on the measurements performed by the authors: density of cracks or crack depth. Stress-strain curves of strained samples tested in SCW at 400 and 500°C are shown in Figure 4. Results of CERT tests for these samples are shown in Table 3.

Figure 4: Stress-strain curves for alloy 316 L strained samples tested in supercritical water in deareated water

(Stress-strain curves in SCW at 400°C and 500°C of samples without strain are included for comparison.)

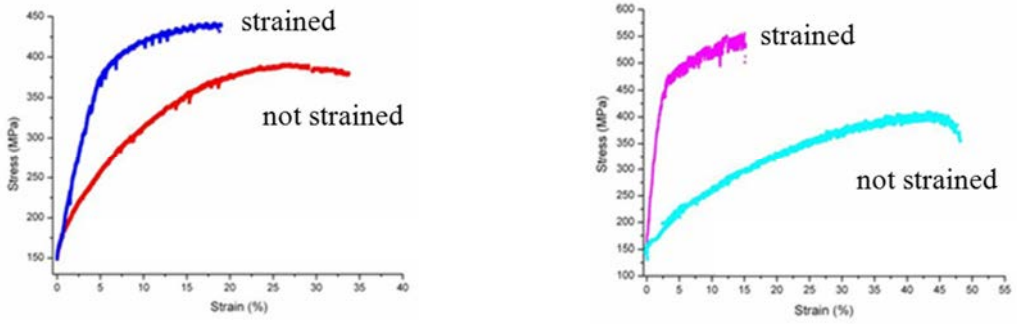

a) at 500°C b) at 400°C

Table 3: Results of constant extension rate experiments performed in deaerated supercritical water for 316 L strained samples.

Material	Test conditions	σ_Y (MPa)	ε (%)	Strain rate (s^{-1})	HV	Crack density ($n°/mm^2$)	Crack size (μm)	Crack morphology
316 L	400ºC/25 MPa/ <10 ppb O_2	473	18	10^{-7}	229	Isolated cracks (+slip bands)	-	?
316 L	500ºC/25 MPa/ <10 ppb O_2	413	17	10^{-7}	220	53	17	?

According to these results, in general, the presence of deformation in the material produces an increase of susceptibility to SCC in SCW of the alloy 316 L, as it happens for the same material under PWR conditions [5]. Again, the sample tested at 500°C is more susceptible of SCC than the one tested at 400°C. Nevertheless, it should be pointed out that the sample tested at 400ºC also shows attacked zones where dislocations emerge, like slip bands. It may be caused by the higher oxidation effect of supercritical water in zones with localised deformation. For this reason, evaluating the crack density in this sample is not easy. In PWR conditions it is accepted that alloy 316 L is susceptible of SCC for hardness around 300 HV [13-15]. However, in supercritical water this material shows cracks for lower hardness values. Currently some authors [15] are taking into account other criteria, such as the maximum applied stress, to evaluate the susceptibility of the material. Comparing stress-strain curves for samples tested in SCW with and without deformation it could be seen again the hardening of sample tested at 500ºC which is higher than the hardening of sample tested at 400ºC. At 500ºC the curve of the sample without strain is closer to the curve of the strained sample. At 400ºC differences between these two curves are more pronounced. Results obtained in this work along with difficulty to evaluate results from a CERT test [10,16] do not establish a clear trend in the behaviour of the material to SCC in SCW, although apparently it may be more susceptible at higher temperature. Before giving an explanation to this behaviour it is important to consider the drop of properties of water into the supercritical zone. Some authors suggest that between 400ºC and 500ºC, around 470ºC where density of water is 100 kg/m^3, the mechanism switches from electrochemical oxidation to chemical oxidation. This change could play an important role in the response of the material to SCC and oxidation in SCW. Previous oxidation tests in SCW performed with the alloy 316 L at 400 and 500ºC and 8 ppm O_2 [1] shows subtle differences between the composition of oxide layers formed at both temperatures like the presence of Ni in the oxide layer formed at 500ºC but not at 400ºC. Another important point that must be considered is the behaviour of the Cr in SCW. Recent articles [17] present Pourbaix diagram for Cr from subcritical to supercritical conditions, specifically to 400°C. Despite the limitations of these diagrams, in test conditions at 400°C and neutral pH, Cr_2O_3 is stable but also depends on the potential of the medium (not known in this study), the oxidation may also be possible. Some authors [18] establish the stability range for Cr_2O_3 at 350°C for an amount of dissolved oxygen between 0 and 400 ppb. The threshold seems to be above 400 ppb at a temperature of 450°C although more studies are necessary to define it clearly. In any case, it is expected that the potential of the reaction Cr^{3+}/Cr^{6+} decreases as temperature increases [19].

Model alloy

The model alloy was previously strained by tensile until 20% of strain and then it was tested in deaerated SCW at 400ºC. Mechanical parameters and results of surface analysis of model alloy sample are shown in Table 4.

Table 4: Results of constant extension rate experiments performed in deaerated supercritical water from prestrained model alloy sample.

Material	Test conditions	σ_Y (MPa)	ε (%)	Strain rate (s^{-1})	HV	Crack density ($n°/mm^2$)	Crack size (μm)	Crack morphology
Model	400°C/25 MPa/ <10 ppb O_2	426	8.7	10^{-7}	256	Isolated cracks (+slip bands)	-	?

It is known that the model alloy is susceptible to SCC under Primary Water Reactor (PWR) conditions [20]. Nevertheless, there is no information about its behaviour in SCW. Although it could be expected a higher susceptibility for the model alloy to SCC in SCW than for the alloy 316 L, according to results obtained in this work there are not big differences between the behaviour of these alloys. Moreover, the evaluation of crack density of the model alloy is not easy due to the existence of attacked zones where dislocations emerge as it was reported for the alloy 316 L strained and tested at 400°C in SCW. On the other hand, comparing results obtained for the model alloy in SCW and results from other authors [20] for the same alloy but obtained under PWR conditions, it could be expected a higher crack density at 400°C than in PWR conditions only because of the effect of temperature. Furthermore, the model alloy was previously deformed up to 20% while the sample tested in water was deformed up to 10%. After CERT test, model alloy in SCW was strained up to around 9% while sample tested in PWR conditions was strained up to 5%. In spite of the most unfavourable conditions, sample tested in SCW do not show clear cracks which are observed in samples tested under PWR conditions (Figure 5). For this reason, the behaviour of the environment seems to be different under both conditions. To gain some insight, more studies are necessary in order to clarify these results where the effect of the environment, which is not well known, seems to play an important role.

Figure 5: Micrographs obtained by scannig electron microscope from model alloy samples previously deformed and tested in liquid water (PWR conditions; a)and in deaerated supercritical water at 400°C (b)

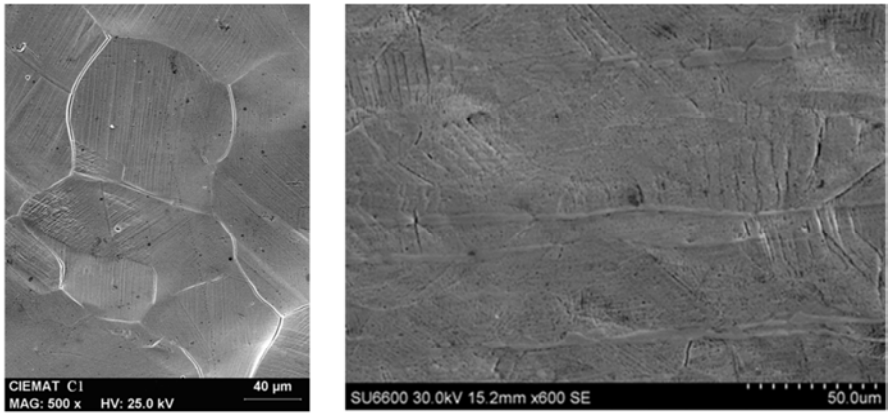

a b

Conclusions

- The stainless steel 316 L has a good behaviour at both temperatures showing a better response at 400°C with a lower crack density on the surface and no signs of corrosion in the fracture surface. Nevertheless, there are several doubts about whether the rate test is appropriate to show the real behaviour of this alloy to SCC in supercritical water at 400°C. Furthermore, the study of the SCC by a CERT test is a challenge because of the different trend of the results depending on the criteria used to evaluate them.

- The presence of deformation in the material increases the susceptibility of the alloy to SCC in supercritical water. Again, the sample tested at 400ºC shows a better response to SCC than the one tested at 500ºC.
- Previous studies of the oxide layers obtained in supercritical water at 8 ppm O_2 show subtle differences between the composition of oxide layers like the presence of Ni only in the oxide layer formed at 500ºC.
- There are not big differences neither between the behaviour of the austenitic stainless steel 316 L and the model alloy previously strained in SCW at 400ºC, in spite of differences in the composition, nor between results from the model alloy tested in PWR conditions and from SCW. For this reason it is suspected that water behaves in a different way in the liquid region and in the supercritical region.

References

[1] Gómez-Briceño, D., F. Blázquez, A. Sáez-Maderuelo (2013), "Oxidation of austenitic and ferritic/martensitic alloys in supercritical water", The Journal of Supercritical Fluids, 78, pp. 103-113.

[2] Watanabe, Y., H. Abe, Y. Daigo, Proceedings of the Int. Symposium on Supercritical Water-Cooled Reactor Design Technology (2000), Tokyo, Japan.

[3] Lian, T., G. Was, T. Allen (2009), "Study of Alloy 690 resistance to SCC initiation in subcritical and supercritical water, in: NRC/Industry Alloys 690/52/152 PWSCC Research Collaboration Meeting, Rockville, August.

[4] (MRP-225) "Testing the Resistance to Stress Corrosion Cracking of Alloy 690 and its Wels Metal in Supercritical Boron/Lithium/H2 solutions" (2007).

[5] Yamazaki, S., Z. Lu, Y. Ito, Y. Takeda, T. Shoji (2008), "The effect of prior deformation on stress corrosion cracking growth rates of Alloy 600 materials in a simulated pressurized water reactor primary water", Corrosion Science, 50, pp. 835–846.

[6] Hou, J., T.Shoji, Z.P.Lu, Q.J.Peng, J.Q.Wang, E.-H. Han, W.Ke (2010), "Residual strain measurement and grain boundary characterisation in the heat-affected zone of a weld joint between Alloy 690TT and Alloy 52", Journal of Nuclear Materials, 397, pp. 109-115.

[7] Wolfe, K. (2012), "Guidelines for selection and use of materials for repairs to BWR internal components", EPRI, 1026603.

[8] Brinkman, C.R. (1999), "Elevated Temperature Mechanical Properties of an Advanced Type 316 Stainless Steel", Oak Ridge National Institute, pp. 10.

[9] Solomon, H.D. (1984), "Transgranular, Granulated and Intergranular Stress Corrosion Cracking in AISI 304 SS", National Association of Corrosion Engineers,40, pp. 493-505.

[10] Teysseyre, S. and G.S. Was (2006), "Stress corrosion cracking of austenitic alloys in supercritical water", Corrosion, 62 [12], pp. 1100-1116.

[11] Muthukumar, N., J.H. Lee, et al. (2011), "SCC behaviour of austenitic and martensitic steels in supercritical pressurized water", Journal of Nuclear Materials, 417 [1-3], pp. 1221-1224.

[12] Novotny, R., P. Hahner, et al. (2011), "Stress corrosion cracking susceptibility of austenitic stainless steels in supercritical water conditions", Journal of Nuclear Materials, 409 [2], pp. 117-123.

[13] Gómez-Briceño, D., M.S. García, J. Lapeña (2009), "SCC Behaviour of Austenitic Stainless Steels in High Temperature Water: Effect of Cold Work, Water Chemistry and Type of Materials". Proceedings 14th Int. Con. Environmental Degradation of Materials In Nuclear Power Systems-Water Reactors, Virginia Beach, Virginia.

[14] Moshier, W.C., C.M. Brown (2000), "Effect of Cold Work and Processing Orientation on Stress Corrosion Cracking Behaviour of Alloy 600", Corrosion, 56, 307–320.

[15] Féron, C., E. Herms, B. Tanguy (2012), "Behaviour of stainless steels in pressurized water reactor primary circuits", Journal of Nuclear Materials, 427, 2012, 364-377.

[16] Ru, X. and R.W. Staehle (2013), "Historical Experience Providing Bases for Predicting Corrosion and Stress Corrosion in Emerging Supercritical Water Nuclear Technology: Part 3-Review", Corrosion, 69 [5], pp. 423-447.

[17] Cook, W.G., and R.P. Olive, "Pourbaix diagrams for chromium, aluminum and titanium extended to high-subcritical and low-supercritical conditions", Corrosion Science, Vol. 58, 2012, pp. 291-298.

[18] Fujiwara, K., K. Watanabe, M. Domae (2007), "Stability of Chromium oxide film formed by metal organic chemical vapor deposition in high temperature water up to supercritical region", NACE, Paper 07411.

[19] Sun, H., X. Wu, E. Han (2009), "Effects of temperature on the oxide film properties of 304 stainless steel in high temperature lithium borate buffer solution", Corrosion Science, 51, pp. 2840-2847.

[20] Karlsen, W., G. Diego, B. Devrient (2010), "Localized deformation as a key precursor to initiation of intergranular stress corrosion cracking of austenitic stainless steels employed in nuclear power plants", Journal of Nuclear Materials, 42, 138-151.

Nickel based alloys compatibility with fuel salts for molten salt reactor with thorium and uranium support

Victor Ignatiev, Alexander Surenkov, Sergey Abalin, Ivan Gnidoy, Alexander Kulakov, Vadim Uglov

NRC KurchatovInstitute, Russian Federation

Abstract

R&D on molten salt reactors (MSR) in Europe are concentrated now on fast/intermediate spectrum concepts which were recognised as long-term alternative to solid fuelled fast reactors due to their attractive features: strong negative feedback coefficients, easy in-service inspection, and simplified fuel cycle. For high-temperature MSR corrosion of the metallic container alloy in primary circuit is the primary concern. Key problem receiving current attention include surface fissures in Ni-based alloys probably arising from fission product tellurium attack. This paper summarises results of corrosion tests conducted recently to study effect of oxidation state in selected fuel salts on tellurium attack and to develop means of controlling tellurium cracking in the special Ni – based alloys recently developed for large power units: molten salt actinide recycler and transmuter (MOSART) and molten salt fast reactor (MSFR). Tellurium corrosion of Ni-based alloys was tested in the temperature range from 730°C up to 800°C in stressed and unloaded conditions with fuel LiF-BeF_2-UF_4 and LiF-BeF_2-ThF_4-UF_4 salt mixtures at different [U(IV)]/[U(III)] ratios from 0.7 up to 500. Following Russian and French Ni-based alloys (in mass%): HN80M-VI (Mo–12, Cr–7.6, Nb-1.5), HN80MTY (Mo–13, Cr–6.8, Al–1.1, Ti-0.9), HN80MTW (Mo–9.4, Cr–7.0, Ti–1.7, W–5.5) and EM-721 (W–25.2, Cr–5.7, Ti–0.17) were used for the study in the corrosion facility. The HN80MTY alloy has shown the best resistance against Te cracking and after test mechanical properties.

Introduction

In this study, main attention has been paid to MOSART and MSFR designs [1,2] with Th–U support fuelled with different compositions of transuranic elements from used LWR fuel. The main attractive features of MOSART and MSFR designs deal with the use of (1) simple configuration of the homogeneous core (no solid moderator or construction materials under high flux irradiation); (2) proliferation resistant multiple recycling of actinides (separation coefficients between TRU and lanthanide groups are high, but within the TRU group are very low); (3) the proven container materials (Ni-based alloys) and system components (pump, heat exchanger etc.) operating in the fuel circuit at temperatures well below 750°C.

The maximum temperature of the fuel salt in MSR primary circuit made of special Ni-base alloy is mainly limited by tellurium intergranular corrosion (IGC) under strain depending on salt Redox potential. Particularly, tellurium, which is a fission product in fuel salt, can embrittle the surface grain boundaries of container materials [3]. For molten salt breeder reactor (MSBR) design with LiF-BeF_2-ThF_4-UF_4 fuel salt the maximum temperature in primary circuit made of Hastelloy-N was limited by 650-700°C. In 2 240 MWt MSBR the fluence of Te on the surface of container material in primary circuit was estimated as $2.9.10^{19}$ at/cm^2 or 6 mg/cm^2 after 30 yrs of reactor operation [3].

The effect of the fuel salt redox potential on the IGC of Ni-based alloys was studied at ORNL [3] under Hastelloy-N alloy specimens testing after 260-hrs exposure at 700°C with the 71.7LiF-16BeF_2-12ThF_4-0.3UF_4 (mole%) fuel containing additives of chromium telluride. It was demonstrated that alloy tellurium cracking, characterised by "K" – a number of cracks per cm multiplied by their average depth in micrometers, depends on fuel salt redox potential, characterised by the ratio of oxidised to reduced forms of uranium [U(IV)]/[U(III)], has a threshold behaviour. It was found for molten salt fluorides mixtures fuelled by uranium that IGC of Ni-based alloys can be avoided by maintaining the system at [U(IV)]/[U(III)] ratios below 60. This can be controlled rather easily now that good analytical methods have been developed. If the UF_3 to UF_4 ratio becomes too low, it can be raised by the addition of some beryllium metal, which, as it dissolves, will rob some of the fluoride ions from the uranium.

Experimental

The purpose of this experiment is to evaluate the cracking tendencies of modified compositions of Ni-based alloys under MOSART and MSFR materials and operating conditions. The most attractive alloys selected [1,2], from the point of chromium corrosion, irradiation embitterment, etc., are included in this experiment, and its purpose is to evaluate the resistance of these materials with fuel salt to IGC over a wide range of the redox potential (from a reduced up to an increased oxidation potential) on the compatibility limits and mechanical loadings.

Current study included 8 cycles, with molten LiF-BeF_2-UF_4 and LiF-BeF_2-ThF_4-UF_4 salt mixtures fuelled by about 2 mole% of UF_4 with additives of Cr_3Te_4 with different [U(IV)]/[U(III)] ratios in the melts: 0.7, 4, 20, 30, 60, 90, 100, 500. Each test included 250-hr exposure of Ni-based alloys specimens at temperatures 730-800°C without and under mechanical loading up to 25 MPa. The Russian and French Ni-based alloys selected for testing have the following compositions (in% mass): HN80M-VI (Mo–12, Cr–7.6, Nb–1.5), HN80MTY (Mo–13, Cr–6.8, Al–1.1, Ti–0.9), HN80MTW (Mo–9.4, Cr–7.0, Ti–1.7, W–5.5) and EM-721 (Cr–5.7, Ti–0.17, W–25.2) [4].

Salt purification

To prepare the fuel salts, metal fluorides are needed with a minimum content of water and impurity of oxides and/or oxyfluorides [5]. They can lead to hard-to-control changes in the chemical composition, the physicochemical properties of the test melt, and the active surface of the electrodes and the samples, with an ultimate adverse effect on experimental results. The anhydrous lithium/beryllium/thorium and uranium fluorides served as batch components for preparating the molten salt mixtures. A ''dry'' technique for production and purification of metal fluorides, their mixtures, and fusion cakes without gaseous HF has been used in our material studies for conversion of UO_2 and ThO_2 to anhydrous tetrafluorides and for the removal of impurity oxide compounds from major solvent constituents [5]. Heating of these mixtures is accompanied by successive reactions of synthesis and decomposition. The total chemical reaction can be described by the equation:

$$MeO_2 + 4NH_4HF_2 \rightarrow MeF_4 + 4NH_4F\uparrow + 2H_2O\uparrow \quad (1)$$

These processes are carried out in air at temperatures up to 400°C and do not require expensive equipment and special measures of safety. Zone melting and filtration of the melts through a nickel filter were used for additional purification of the salt before voltammetry and corrosion studies [5]. Chemical analysis of melt samples after its purification and before corrosion test showed the content of the major impurities (in% mass) as follows: Ni–0.005; Fe–0.024; Cu<0.001; Cr–0.001; oxygen<0.05.

Corrosion facility

The layout of corrosion facility is shown in Figure 1. The facility allows testing the alloy specimens under argon atmosphere in the non-isothermal dynamic conditions with the fuel salt when a temperature of a melt surface is lower than a temperature of near-bottom part (approx. by 40°C). The measurement of the temperature in-depth profile is provided by the thermocouples. The granulated chromium telluride Cr_3Te_4 serves as a tellurium source in the fuel salt. It's located in the specific container ensuring the mixing of melt and delivery of tellurium to specimen's surface. This test section is equipped with electro-chemical probe for measuring the [U(IV)]/[U(III)] ratio [5]. In order to decrease or increase the redox potential of the system, respectively, the metallic beryllium and NiF_2 additions in the fuel salt are used. The sampling to measure concentrations of Fe, Cr, Ni, etc. in salt was carried out at the beginning and at the end of each test.

Figure 1: Corrosion facility layout

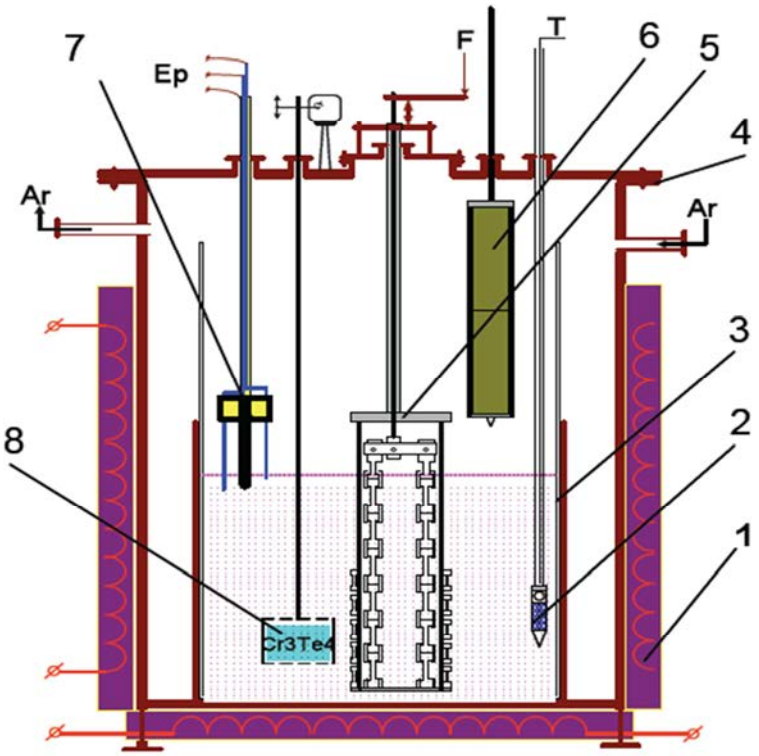

(1) heater
(2) sampler
(3) test section
(4) lid
(5) specimens under stress
(6) metallic Be
(7) device for redox potential measuring
(8) Cr_3Te_4

[U(IV)]/[U(III)] ratio

The voltametric method of measuring the redox potential of the fuel salt is a very important development [5]. The three-electrode device for determinating the [U(IV)]/[U(III)] ratio is shown in Figure 1. The registration of cyclic voltammogram (CV) was performed in a three-electrode mode of polarisation. The molybdenum wire was used as both working and reference electrodes; auxiliary electrode was made of reactor-grade graphite. The relation of concentrations of oxidised/reduced uranium forms [U(IV)]/[U(III)] (CVs of melt recorded in the range of potentials of the uranium recharge were used) was determined by the following equation:

$$[U(IV)]/[U(III)]=\exp[-(E_{0.855p})\cdot(RT/F)] \qquad (2)$$

where $E_{0.855p}$ is a potential of the point on cathodic voltammogram at current $I = 0.855 \times I_p$, I_p – peak current, F – Faraday number, R – universal gas constant, T – fuel salt temperature.

As example CV for the fuel 70LiF-6.9BeF_2-21ThF_4-2.1UF_4 (in mole%) salt with addition Cr_3Te_4 recorded in corrosion test with [U(IV)]/[U(III)] = 20 at T = 735 ^{0}C, ν = 0.1 V s^{-1} is given in Figure 2.

Figure 2: CV of the fuel salt in corrosion test

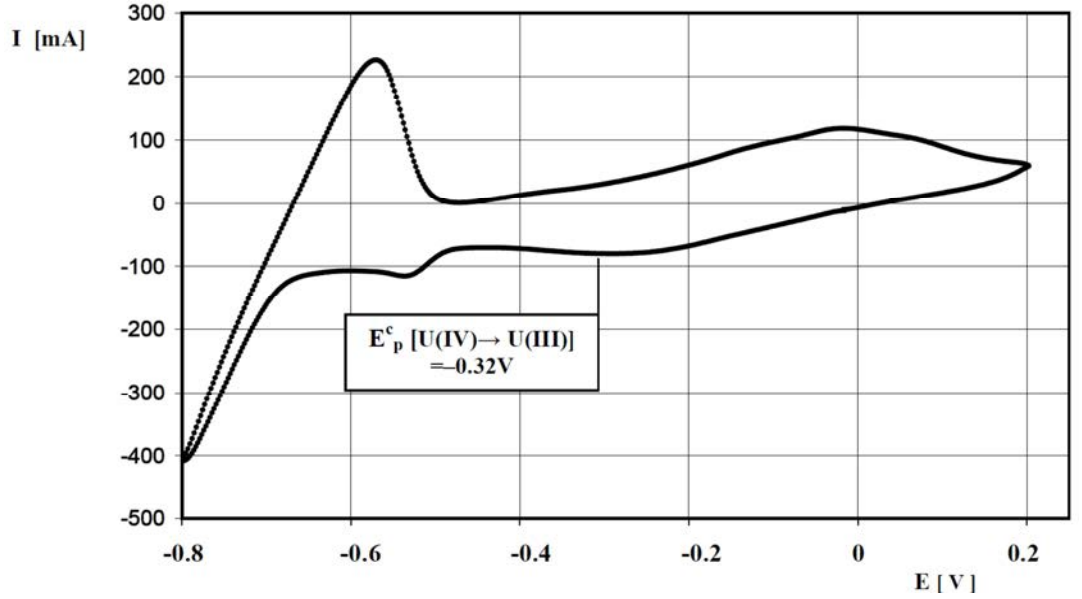

Examination of Ni-based alloys after exposure in the fuel salt

In our tests with fuel salts, the fluence of Te on the surface of material specimens varied from 0.8 to 4 mg/cm^2. This value corresponds to the fluence of Te accumulated on the surface of a container material in primary circuit after 5-20 yrs of operation [1].

Specimens after exposure in the fuel salt were washed off for 60 hrs with aluminum nitrate solutions and then weighed. All specimens were stretched by tensile machine up to rupture at room temperature to expose the surface cracks and look at metallographic analysis. A structure of surface of the material specimens was investigated on prepared metallographic sections by means of NEOPHOT-21 optical microscope. The aim was to identify the films, cracks, deposits of corrosion products and traces of impact of corrosive medium. The analysis of microstructure/strength characteristics for alloys under study after tests is given below.

A tight film has been formed on a surface of all loaded and unloaded alloys specimens during the first test with reducing Li,Be,Th,U/F fuel salt ([U(IV)]/[U(III)] = 0.7). That film cracks and partly peels off under mechanical properties test of specimens. The composition and distribution of elements' content in depth from edge of film to alloy's surface and then in alloy's depth up to ~30 μm were determined by the energy dispersive X-ray (EDX) microanalysis in Helios (FEI, US) dual beam SEM/FIB with attached EDX spectrometer (EDAX, US). Semi-quantitative analysis was performed on the specimens.

After first test all alloys specimens have two layers of interaction of structural alloy with a fuel salt: external of ~20-30 μm thickness and internal surface layer of ~5-8 μm thickness. External layer consists substantially of nickel and uranium at relation approximately from 45 to 50% mass and is respectively similar in content to $U_{12}Ni_{78}$ intermetallide (ε – phase). A fusion process of uranium with nickel occurs, leading to increasing of uranium concentration on specimen's surface; at the same time a loss of nickel occurs in the surface layer. Possibility of such reactions is confirmed by results of electrochemical CV measuring performed on both Mo and Ni working electrodes under first test. The internal surface layer of alloy, where uranium concentration drops to zero,

is depleted in nickel and enriched by chromium and other elements, contained in alloys as dopants. No films or deposits were observed on alloys after the tests in a fuel salt with [U(IV)]/[U(III)] ratios ≥ 4.

Summarising the data available, one should highlight the pattern for "alloy –fuel salt" system behaviour. If oxidation-reduction state of the fuel salt is characterised by the ratio of [U(IV)]/[U(III)] < 1, then potentials of alloy formation of uranium with major alloys components (Ni, Mo and W) are allocated near to basic (zero in tests); that leads to uranium deposition on surface followed by formation of Ni, Mo and W intermetallides. The process is accompanied by formation of intermetallides films on a surface of all alloys. Under next tests with the fuel salt characterised by the [U(IV)]/[U(III)] ratio ≥ 4 the potentials of alloy formation of uranium with major alloy's components are allocated far from a basic potential, and no intermetallides on a surface are formed.

Surface fissuring of all Ni-based alloys under study was not observed in the Li,Be,Th,U/F fuel salt in the three first tests with [U(IV)]/[U(III)] = 0.7, 4 and 20. As seen in Figures 3-5, materials exposure at 750-760°C in the Li,Be,U/F fuel salt with the [U(IV)]/[U(III)] ratio equal 30 and 60 and Li,Be,Th,U/F fuel salt with the [U(IV)]/[U(III)] ratio equal 100 revealed no Te IGC on surface of HN80M-VI, HN80MTY and EM – 721 specimens without and under stress. For these conditions, surface fissuring was found only for HN80MTW specimens without and under stress; the depth of cracks reached 34-38 μm (K = 480-540 pc×μm/cm).

For a [U(IV)]/[U(III)] ratio of 90 in the Li,Be,U/F fuel salt, significant Te IGC was found for E-721 alloy (K = 5 830 pc×μm/cm) only with increase of temperature up to 800°C (see Figure 5c). As seen in Figure 5f, the case with HN80MTY alloy appears much better (K = 530 pc×μm/cm).

Te IGC was found for all tested alloys after 250 hrs exposure in Li,Be,Th,U/F fuel salt with very high [U(IV)]/[U(III)] ratio equal 500 (Figure 5). For main part of tested alloys the intensity of tellurium IGC was lower in unstressed state than in stress condition. In this case for HN80M-VI, HN80MW and EM – 721 specimens dramatic IGC intensity with K = 7000-9 000 pc×μm/cm and the depth of cracks up to 400 μm was observed. The best resistance to IGC at [U(IV)]/[U(III)] = 500 was found for HN80MTY specimens with K = 1 850 pc×μm/cm (four times as low as that of loaded HN80M-VI alloy). The depth of cracks in HN80MTY of 80 μm specimens is significantly lower compared to other alloys.

Data of element structure of telluric inclusions on a surface of the opened crack in a sample of the HN80MTY alloy after tests in fuel salt with [U(IV)]/[U(III)] ratio equal 500 and structure of a crust of deposits of corrosion products on the HN80MTY alloy surface after tests with [U(IV)]/[U(III)] ratio equal 100 are submitted in Figure 6. The measurements by energy-dispersion X-ray spectroscopy method, using an electronic microscope are shown in Figures 6 a and b. Tellurium is found on the surface of an opened cracks to all their depth, and along the grains boundaries (unopened cracks) to the depth up to 80 μm from the specimens surface. In the grains bulk, tellurium is not identified. Tellurium inclusions by the grain boundaries in the depth of specimens have higher concentration of Cr, C, Al and Mo.

After the alloy specimens testing in the Li,Be,Th,U/F melt with [U(IV)]/[U(III)]= 100 on the surface of HN80MTY alloy a loose crust up to 10 μm thick was observed. Te concentration in the crust is up to 3% wt. The crust also contains chromium (up to 20% wt.), molybdenum, carbon and aluminium. Under the crust in the metal and on the grains boundaries tellurium was not revealed (Figures 6c and d). Apparently, tellurium is completely bound into stable compounds on the alloy surface, and its further diffusion on the grains boundaries is blocked.

Figure 3: Microstructure of surface layer for HN80MT-VI (a,b,c) and HN80MTY (d,e,f) specimens after 250 hrs exposure in Li,Be,Th,U/F fuel salt: a,d – without loading at 730-735°C for U(IV)/U(III) = 500; b,e – 25MPa loading at 730-735°C for U(IV)/U(III) = 500; c,f – 20MPa loading at 750°C for U(IV)/U(III) = 100

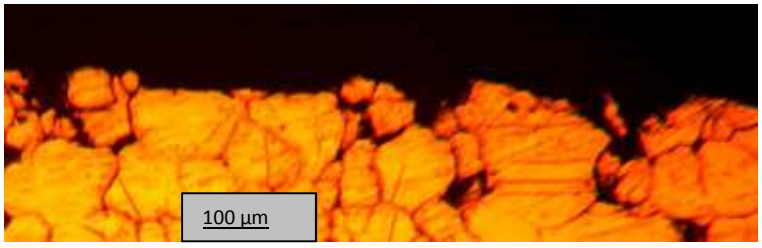

a) K = 3360 pc×µm/cm

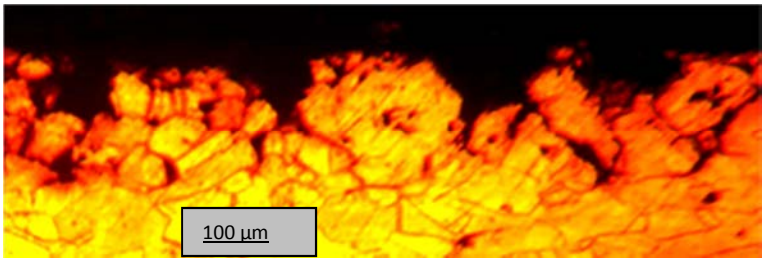

b) K = 8300 pc×µm/cm

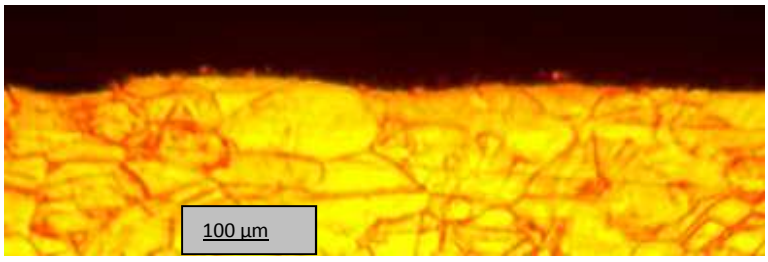

c) no IGC

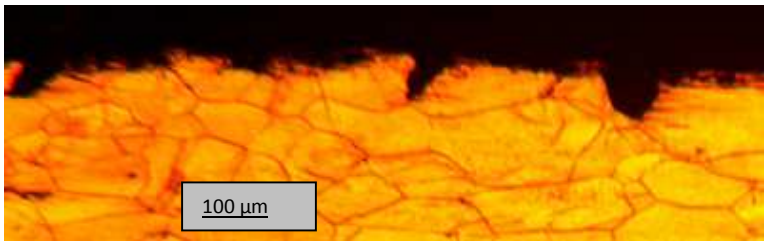

d) K = 1660 pc×µm/cm

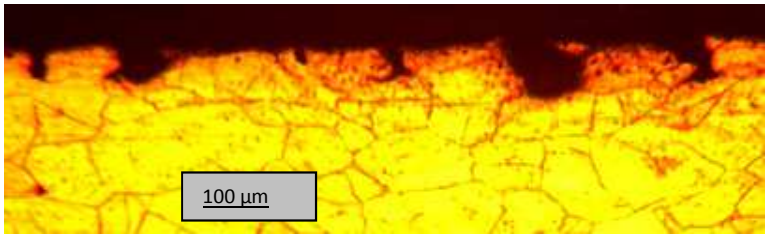

e) K = 1850 pc×µm/cm

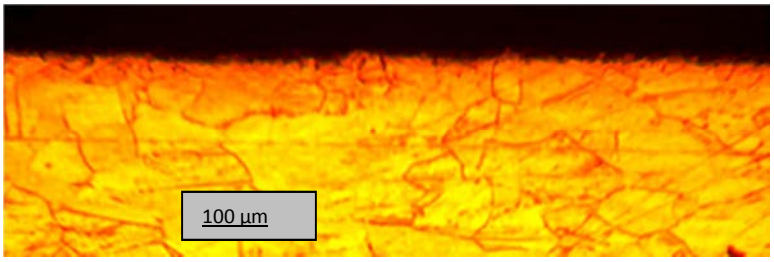

f) no IGC

Figure 4: Microstructure of surface layer for HN80MTW (a,b,c) and EM-721 (d,e,f) specimens after 250 hrs exposure in Li,Be,Th,U/F fuel salt: a,d - without loading at 725-735°C for U(IV)/U(III) = 500; b,e - 25MPa loading at 730-735°C for U(IV)/U(III) = 500; c,f – 20MPa loading at 745-750°C for U(IV)/U(III) = 100

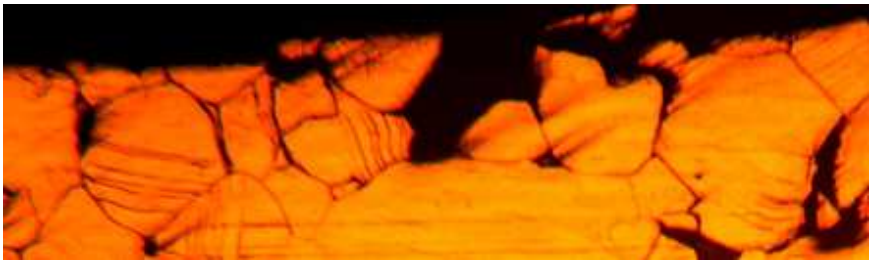

a) K = 7060 pc×μm/cm

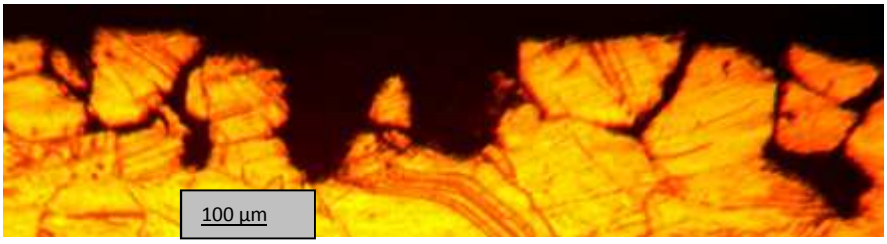

b) K = 8400 pc×μm/cm

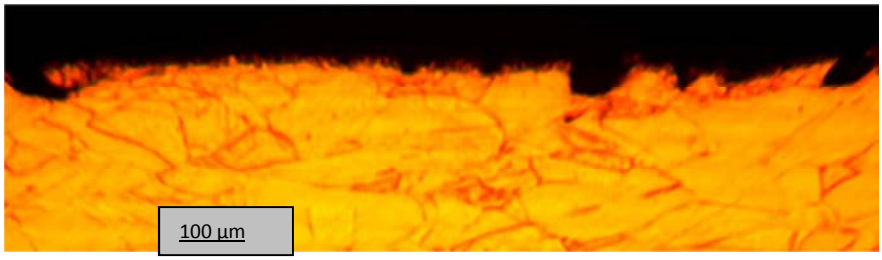

c) K = 540 pc×μm/cm

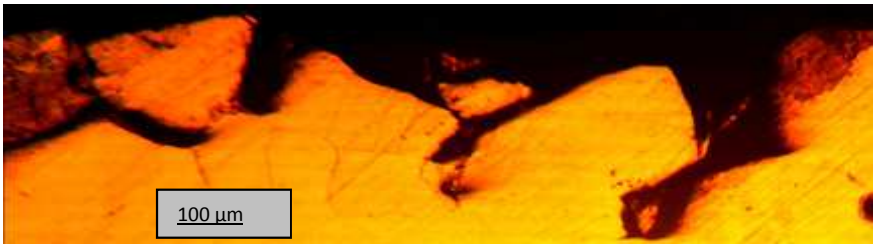

d) K = 6730 pc×μm/cm

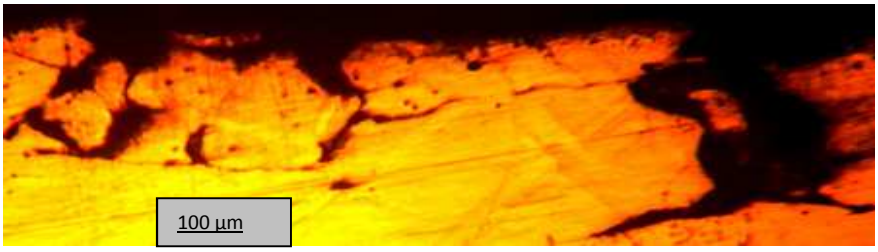

e) K = 9200pc×μm/cm

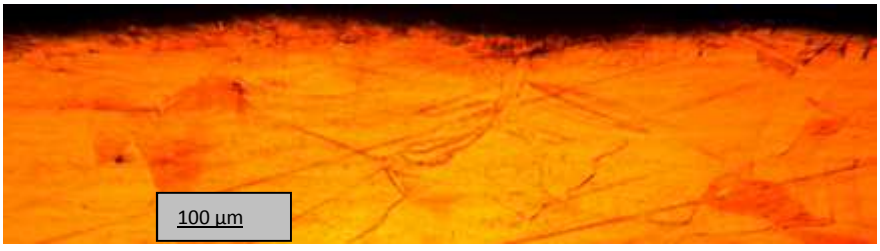

f) no IGC

Figure 5: Microstructure of surface layer for E-721 (a,b,c) and HN80MTY (d,e,f) specimens after 250 hrs exposure in Li,Be,U/F fuel salt: a,d - without loading for U(IV)/U(III) ratios 30 (a,d - at 760°C), 60 (b,e - at 760°C) and 90 (c,f - at 800°C)

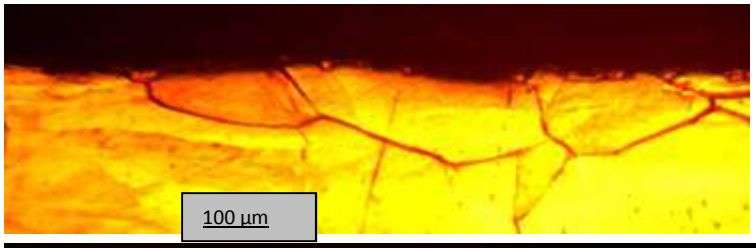

a) no IGC

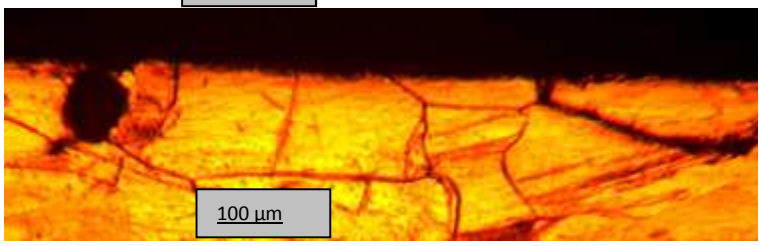

b) K = 3380 pc×µm/cm

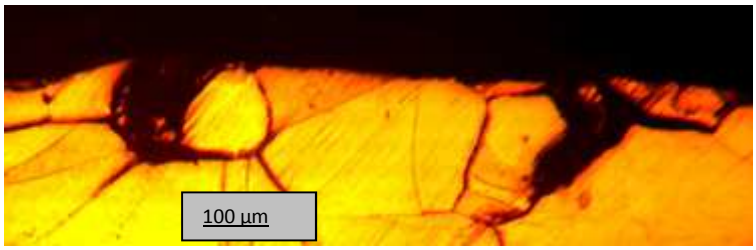

c) K = 5830 pc×µm/cm

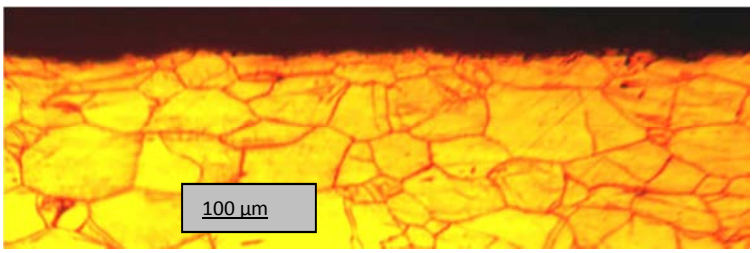

d) no IGC

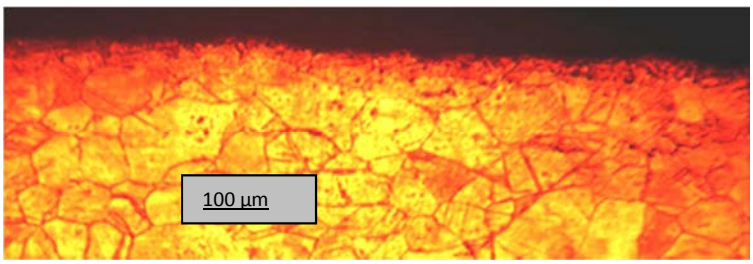

e) no IGC

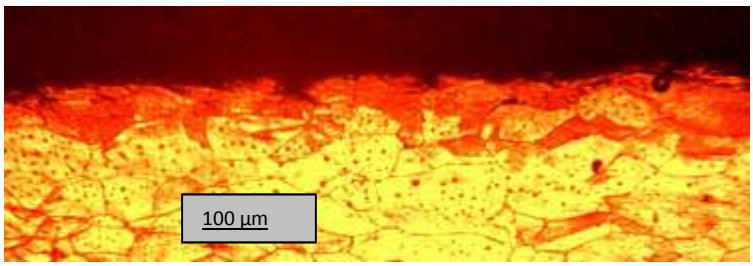

f) K = 530 pc×µm/cm

Figure 6: HN80MTY alloy after corrosion testing in the melt with [U(IV)]/[U(III)] = 500 (a,b) and [U(IV)]/[U(III) = 100 (c,d): a,c – alloy structure and EDMX RSA diagram of scanning elemental composition by points; b,d – elements content in the scanning zone, %wt

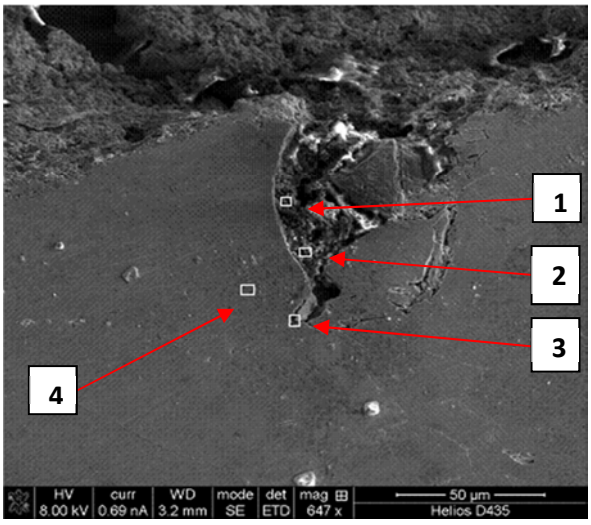

a

Element wt%	1	2	3	4
C	10	10	48	2
Ni	45	47	15	75
Al	1	1	1	1
Si	8	1	-	-
Mo	25	15	17	10
U	1	1	1	-
Te	2	3	1	-
Ti	1	2	1	1
Cr	7	21	16	8

b

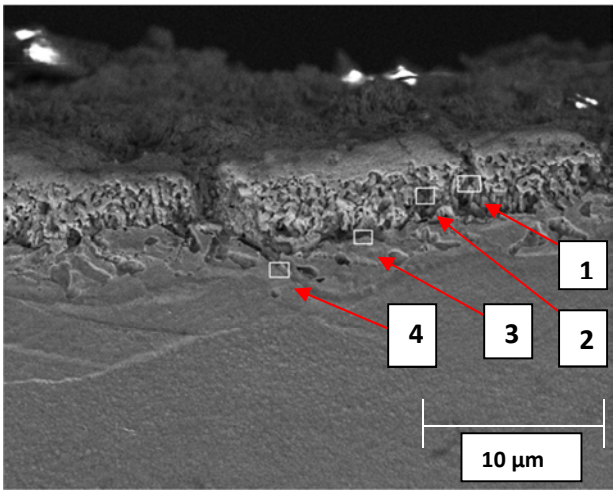

c

Element wt%	1	2	3	4
C	37	26	-	-
Ni	19	25	69	66
Al	2	3	2	1
Si	1	3	-	-
Mo	15	17	11	9
U	1	1	-	-
Te	4	3	-	-
Ti	-	1	-	8
Cr	21	22	18	17

d

After all tests, except one with [U(IV)]/[U(III)] = 500, the strength characteristics of alloys and their structure were changed insignificantly. These changes were apparently stipulated by alloy structure, temperature/time factor and mechanical loads in a greater extent, than impact of a fuel salt containing tellurium additives. All alloys investigated have a good ductility at high strength characteristics. The HN80MTY alloy shows the most stable behaviour under all tests. The mechanical property of this alloy, as compared with other alloys, has a minimal change.

Note, that positive effect of Al addition leading to improving of the HN80MTY alloy resistance to IGC deals with the decrease and change in the character of the carbide phase precipitation along the grain boundaries: carbide phase precipitates, not the continuous way, but falteringly as particles of roundish form, separated by rather big distance from each other.

Conclusion

Current study with molten LiF-BeF_2 salt mixtures containing ThF_4, UF_4 and Cr_3Te_4 additives, included eight cycles with 250-hr exposure time each of Ni-based alloys specimens at 730-800°C under mechanical loading from 0 to 25 MPa, when the [U(IV)]/[U(III)] ratio in the fuel salt varied from 0.7 to 500. The cracking tendencies for most attractive alloys available over a wide range of the salt redox potential as well as specimens' mechanical loading simulating materials and Te fluence conditions of MOSART and MSFR designs were evaluated.

The studies have shown, that the intensity of the Ni-based alloys IGC is controlled by the [U(IV)]/[U(III)] ratio in the fuel salt as well as its temperature. Providing control of the [U(IV)]/[U(III)] ratio, it is possible in such a way to completely eliminate or to minimise Te IGC.

The HN80MTY alloy has the best corrosion and mechanical properties. It does not undergo Te IGC in the molten 75LiF–5BeF_2–20ThF_4 and 73LiF–27BeF_2 salt mixtures fuelled by about 2 mole% of UF_4 with a [U(IV)]/[U(III)] ratio ≤ 100. The alloy has high resistance to tellurium cracking at [U(IV)]/[U(III)] = 500. The alloy can be recommended as the construction material for the MOSART and MSFR primary circuit with selected fuel salts up to a temperature of 750°C.

Further studies concerned surface fissures in Ni-based alloys probably arising from other fission product attack in the MOSART and MSFR primary circuit are required.

References

[1] Ignatiev, V. and O. Feynberg (2011), "Single fluid molten salt actinide recycler and transmuter: fuel cycle and safety related issues", Transactions of the American Nuclear Society, 105, pp. 649-650.

[2] Merle-Lucotte, E. et al. (2011), Launching the thorium cycle with molten salt fast reactor. In: Proceedings of ICAPP *2011*, Nice, France, May, Paper 11190.

[3] McCoy, H. et al. (1978), "ORNL Status of materials development for molten salt reactors", *ORNL-TM-5920*, Oak Ridge, TN, UNITED STATES.

[4] Ignatiev, V. and A. Surenkov (2013), "Alloys compatibility in molten salty fluorides: Kurchatov Institute Experience", Journal of Nuclear Materials, Volume 441, pp. 592-603.

[5] Afonichkin, V., A. Bovet and V. Shishkin (2011), "Salts purification and voltammetric study of electroreduction of U(IV) to U(III) in molten LiF-ThF_4", Journal of Nuclear Materials, Volume 419, pp. 347-352.

Mechanical properties of Ni-base superalloys in high temperature steam environments

Changheui Jang*, Donghoon Kim, Injin Sah, Ho Jung Lee
Korea Advanced Institute of Science and Technology, Republic of Korea

Abstract

The effects of environmental damages on the mechanical properties of Ni-base superalloys, Alloy 617 and Haynes 230, were evaluated for VHTR-HTSE applications. Tensile tests were carried out at room temperature after ageing at 900°C in vacuum, steam, and steam + 20 vol.% H_2 environments up to 3 000 h. Also, creep rupture test were performed in air, steam, and steam + 20 vol.% H_2 environments. The degradations such as oxidation, decarburisation, and redistribution of carbides were studied in view of the interaction of materials with the environment. During the long-term ageing at 900°C in vacuum, secondary phases such as $M_{23}C_6$ and M_6C were precipitated and coarsened, which caused increase in tensile strength and decrease in ductility. For the specimens aged in steam environments, surface and internal oxides acted as preferential sites for crack initiation and consequently, decreased the tensile and creep strength. Also, the formation of decarburisation region resulted in glide plane failure during tensile test and reduction in creep rupture life due to grain boundary migration and recrystallisation. During creep tests, tensile stress caused the crack and void formation in oxide layer. Consequently, fast diffusion of oxidant occurred and environmental damage were accelerated. Among the test conditions, such environmental damage was much severe in steam environments.

1. Introduction

The very-high-temperature gas-cooled reactor (VHTR) combined with high-temperature steam electrolysis (HTSE) could achieve the massive and economical hydrogen production without CO_2 emission [1]. To demonstrate the VHTR-HTSE system, structural integrity of intermediate heat exchanger (IHX), for heat transfer from helium coolant in VHTR to steam in HTSE, should be assured.

Wrought Ni-base superalloys such as Alloy 617 and Haynes 230 are candidate materials for IHX in VHTR-HTSE system utilising good corrosion resistance and mechanical properties at high temperature environments. During operation, these materials will be exposed to high temperature above 850°C, operating pressure about 7MPa, and corrosive condition such as steam environments. The environmental damage caused by such operational exposure would significantly degrade the mechanical properties of IHX materials. However, such studies are not sufficient for the candidate IHX materials, especially in steam environments. Thus, in this study, the effects of long-term exposure on environmental damage and mechanical properties were investigated.

2. Test materials and experimental procedure

Two commercial wrought Ni-base superalloys, Alloy 617 and Haynes 230 were used in this study. The chemical compositions of test materials were analysed by inductively coupled plasma (ICP) method and results are shown in Table 1.

To evaluate the environmental effects on room temperature tensile properties, small size plate type specimen with 0.5 mm in thickness and 5 mm in gauge length were aged in vacuum, steam, and steam + 20 vol.% H_2 conditions at 900°C up to 3 000 h. After the specimens were aged in various environments, tensile test were performed at room temperature with 3×10^{-4}/sec strain rate. The cylindrical specimen with 4 mm in diameter and 16 mm in gauge length was used for creep rupture test. The constant load creep rupture test were carried out in air, steam, and steam + 20 vol.% H_2 environments.

The environmental damages and microstructures were investigated using scanning optical microscope (OM), electron microscope (SEM), electron probe micro analyzer (EPMA), and focused ion beam (FIB) equipped with SEM.

Table 1: Chemical compositions of Alloy 617 and Haynes 230 (wt%)

	Ni	Cr	Fe	C	Si	Mn	Ti	Al	Co	Mo	W
Alloy 617	Bal.	21.6	1.14	0.10	0.50	0.05	0.35	1.50	11.8	8.92	-
Haynes 230	Bal.	21.5	2.94	0.10	0.38	0.46	-	0.29	0.36	1.09	13.08

3. Results and discussions

3.1 Environmental effects on room temperature tensile properties

Figure 1 shows the room temperature tensile strength and elongation after ageing in vacuum, steam, and steam + 20 vol.% H_2 environments. When aged in vacuum condition, tensile strength increased and ductility decreased. However, both strength and ductility decreased when aged in steam and steam + 20 vol.% H_2 environments. Except elongation of Alloy 617, addition of 20 vol.% H_2 additions in steam environment further reduced of tensile strength and ductility for both alloys.

For the as-received specimen, mixture of ductile dimples and brittle facets formed at intra-granular M_6C carbides were present on the fracture surface (Figure 2). After ageing heat treatment in vacuum up to 3 000 h, secondary phases such as $M_{23}C_6$ and M_6C carbides were extensively precipitated and then coarsened in gain boundary and grain, especially for Haynes 230 (Figure 3). Consequently, brittle fracture increased due to inter and intra-granular carbides. The increase in secondary phase such as MC, M_6C, and $M_{23}C_6$ in Ni-base Alloys was known to enhance the strengthening and decrease the ductility [2]. Therefore, the observed increase in tensile strength and decrease in ductility for the specimen aged in vacuum (Figure 1) could be explained by the increase in precipitates during ageing.

Authors reported that environmental damages such as surface oxide layer, internal oxides, and decarburisation were more extensively formed in steam with and without hydrogen environments than in air [3]. Similar results were observed in this study as shown in Figure 4. For Alloy 617, the damage by environments, that is oxidation and decarburisation, was much severe than Haynes 230. On the other hand, the precipitation of carbides was more extensive in the matrix, while the damage by environment was less significant for Haynes 230.

As shown in Figure 5, for Alloy 617, the surface oxide layer was broken in brittle manner, and internal Al_2O_3 oxides provided preferential path for cracking. Consequently, inter-granular cleavage fracture surface were observed until glide plane fracture happened in decarburisation region below. When the grain boundary was fully dissolved, it was reported that the glide plane fracture would be promoted rather than dimple formation [4]. It seems that the contribution of surface and internal oxides to the loss of ductility was greater than that of decarburisation zone to large ductility. As a result, it seems that surface and internal oxide decreased the tensile strength and ductility simultaneously for Alloy 617 aged in steam environments.

Figure 1: Tensile property changes after vacuum ageing and corrosion at 900 °C in steam and steam + 20vol.% H_2 environments up to 3 000 h: (a), (b) Alloy 617 and (c), (d) Haynes 230.

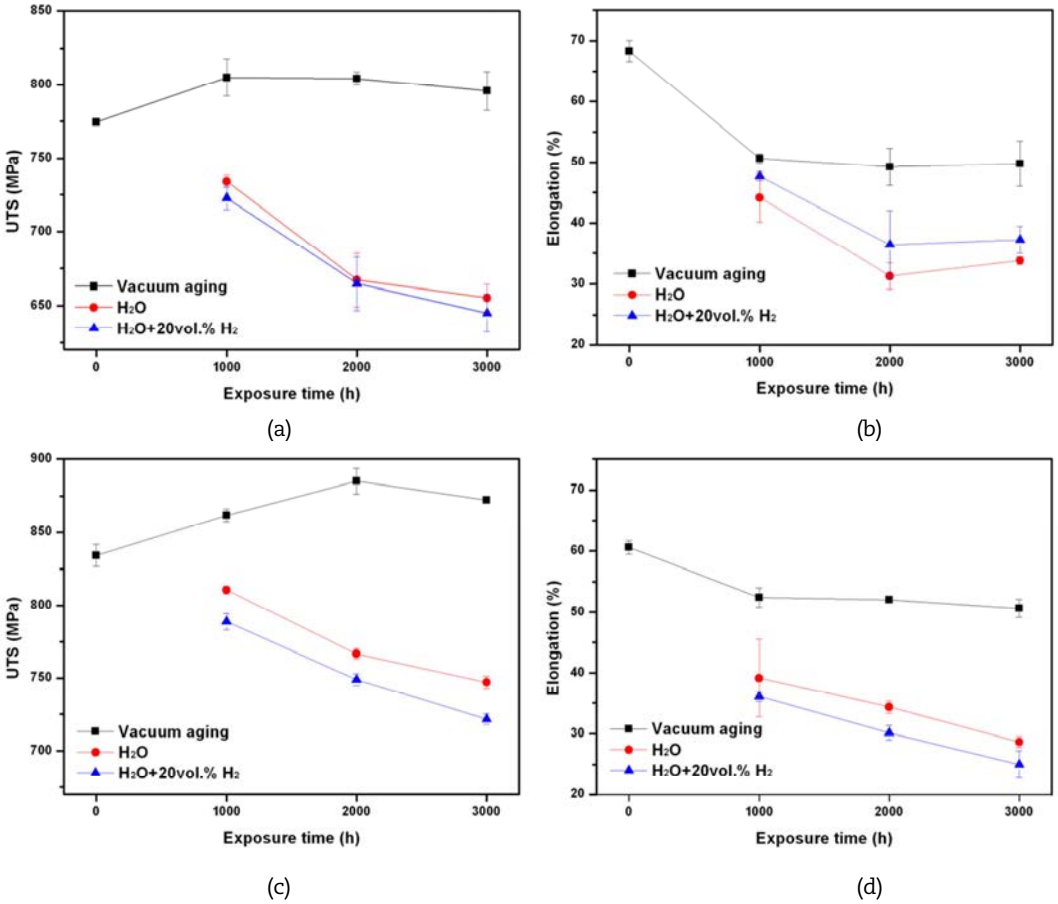

Figure 2: The fracture surfaces of as-received tensile specimen of Alloy 617.

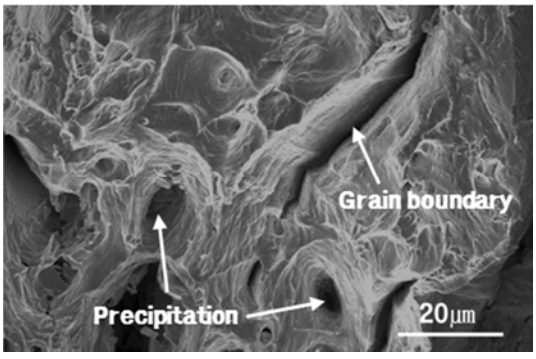

In case of Haynes 230, the size of the broken surface oxide and glide fracture region were smaller than Alloy 617, but partially brittle fracture surface were observed at W-rich M_6C carbide regions. Similar to Alloy 617, the decrease in tensile strength and ductility could be related to the oxidation and decarburisation during ageing in steam environments. In addition, the presence of W-rich carbide below the oxide layer would have contributed further reduction in ductility for longer ageing time (Figure 1).

Figure 3: Microstructures and fracture surfaces of tensile specimen of Alloy 617 aged in vacuum at 900°C after 3 000 h: a) cross-section, and b) tensile fracture surface.

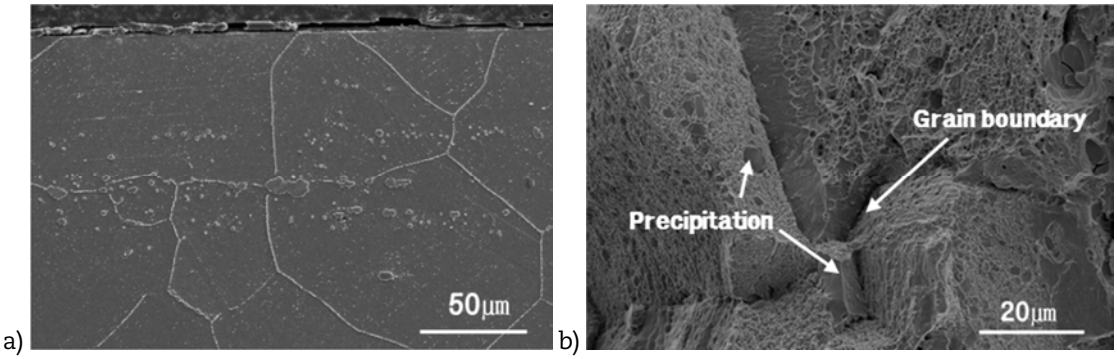

Figure 4: Cross sectional microstructures corroded in steam + 20vol.% H_2 for 3 000 h at 900°C: (a) Alloy 617 and (b) Haynes 230.

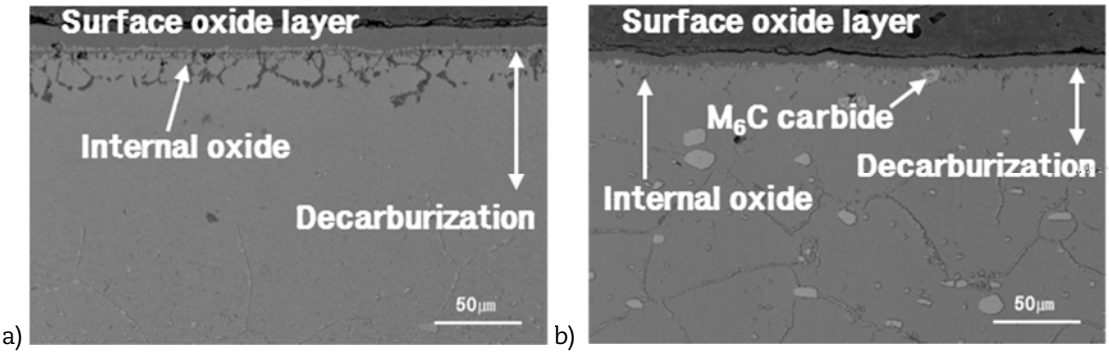

Figure 5: The fracture surfaces of tensile specimens corroded in steam + 20vol.% H_2 for 3 000 h: (a) Alloy 617 and (b) Haynes 230.

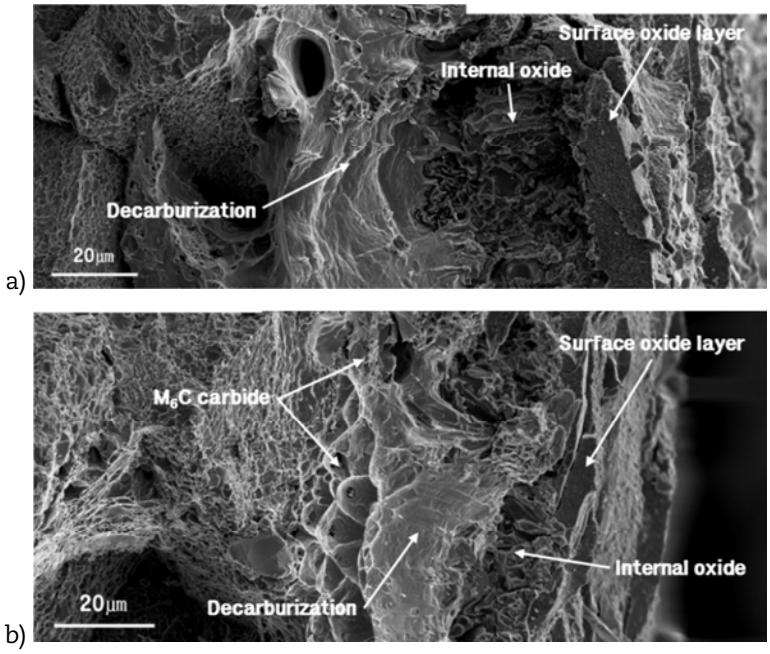

The hydrogen additions in steam environments enhanced the environmental damage such as oxide and decarburisation as reported previously [3]. Consequently, further

degradation of tensile properties was expected for both Alloy 617 and Haynes 230. For Alloy 617, tensile strength was slightly reduced but ductility was higher in steam + 20 vol.% H_2 environments. The larger decarburisation zone would have contributed to higher ductility. However, in case of Haynes 230, both strength and ductility decreased in steam + 20 vol.% H_2 environments. Unlike Alloy 617, decarburisation region of Haynes 230 contained the trans-granular M_6C carbides which disrupted the glide plane fracture and therefore recovery of ductility by larger decarburisation zone was not observed.

3.2 Environmental effects on creep rupture strength

Figure 6 shows the creep rupture life of Alloy 617 and Haynes 230 in various environments. In general, the creep rupture life of both alloys is higher in air than in steam environments. Also, hydrogen additions in steam decreased the creep rupture life for Haynes 230. However, there is no significant effect of hydrogen addition on creep rupture life of Alloy 617.

Figures 7 and 8 show the OM and SEM photos of creep tested specimens showing the carbide redistribution and voids on grain boundary. The creep rupture process was well explained in the literature [5]. First, grain boundary carbides migrated from grain boundaries which are under compressive stress to those that are under tensile stress, which resulted in rearranged grain boundary carbides in perpendicular direction to tensile axis (Figures 7 (a) and 8 (a)). Then, grain boundary migrations occurred at carbide free region and then creep void are initiated. Finally, recrystallisation occurred, which accelerated the creep deformation by breaking up the grains.

These creep deformation mechanisms would be affected by the environmental damage occurred in various environments used in this study. As shown in Figures 7 (b) and 8 (b), oxide layer is broken by tensile load and initiated the surface crack. Then, inter-granular Al_2O_3 provide the preferential sites for surface crack propagation [10]. Eventually, propagation of surface crack would join with internal cracks emanated from the creep voids, resulting in accelerated creep failure. As mentioned previously, the environmental damage was greater in steam environments compared to in air, therefore creep rupture would be accelerated in steam environments (Figure 6).

Figure 6: The creep rupture life in various environments: (a) Alloy 617 and (b) Haynes 230

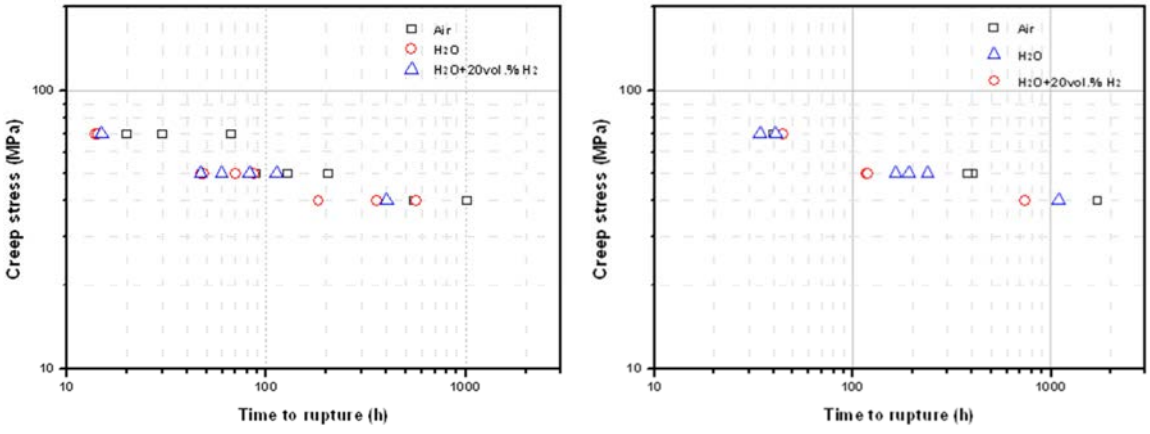

To quantify the environmental damage in various environments, oxide thickness and decarburisation depth were measured and plotted (Figure 9). In general, surface oxide thickness and decarburisation depth were larger in the creep tested specimens compared to isothermal tested specimens. Also, larger oxide layer size and decarburisation depth in steam environments were in good agreement with the shorter creep rupture life of Alloy 617 in such environments. The same relationship was also observed for Haynes 230.

As shown in Figure 10, void and surface cracks were formed in surface oxide layer under loading condition. According to the Kofstad [6], porosity of micochannel formed in oxide layer would permit the inward transport of oxidants. Therefore the fast transport of oxidant through microchannel increased the oxide growth rate in steam environments. Also, gas phase mass transport through void could occur by dissociative transport of H_2O across voids in wet oxygen conditions such as H_2O containing environments and therefore oxide growth rate was faster steam environments as previously reported [3,7,8].

Figure 7: Microstructures of ruptured Alloy 617 under 40MPa at 900°C in steam environment: (a) carbide redistribution, (b) environmental surface damage and cracks

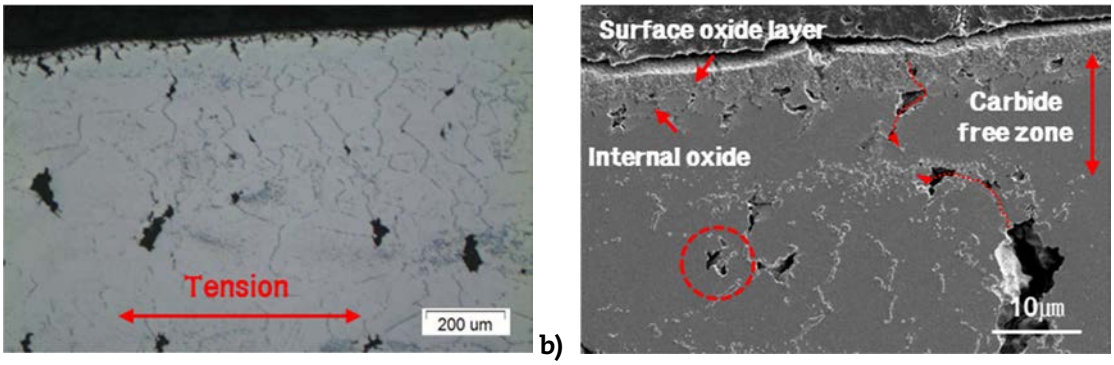

a) b)

Figure 8: Microstructures of ruptured Haynes 230 under 40MPa at 900°C in steam + 20vol.% H_2 environment: (a) carbide redistribution, (b) environmental surface damage and cracks

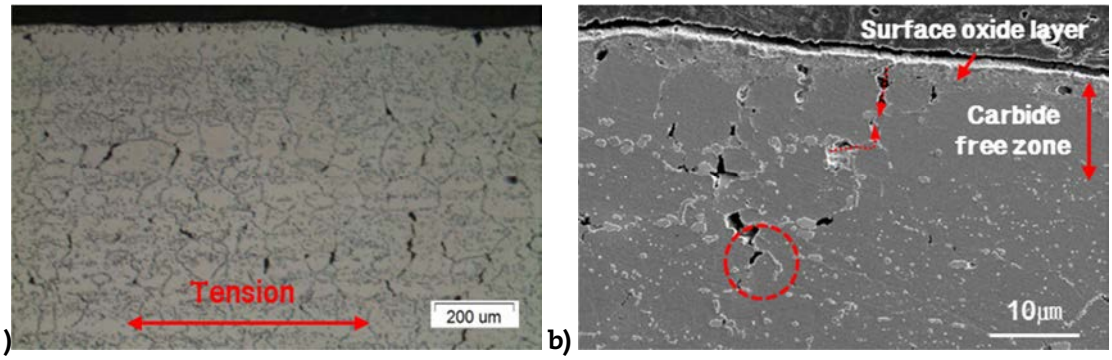

a) b)

Figure 9: Quantifications of (a) surface oxide layer thickness and (b) decarburisation depth after isothermal corrosion test and creep rupture test for Alloy 617

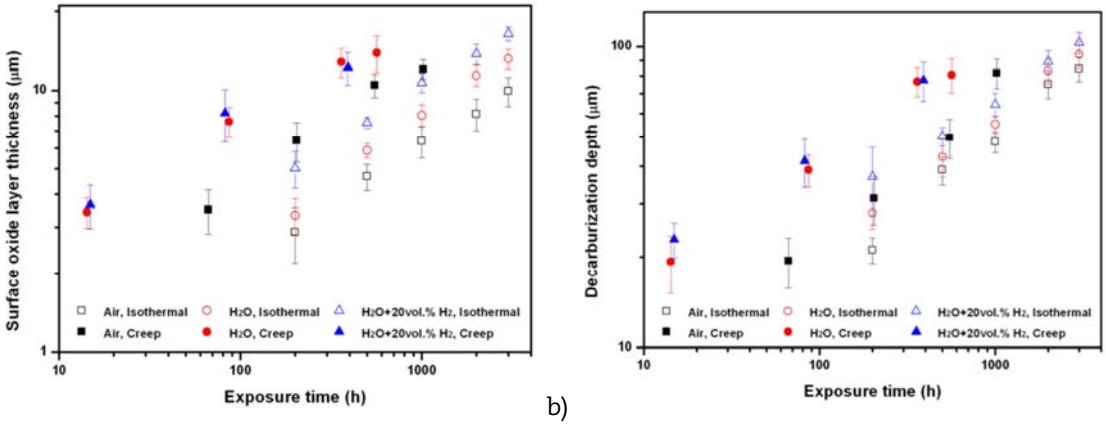

a) b)

Figure 10: Ion-milled cross sectional SEM images of Alloy 617 tested in steam environments: (a) isothermal condition for 500 h and (b) under 50 MPa loading condition

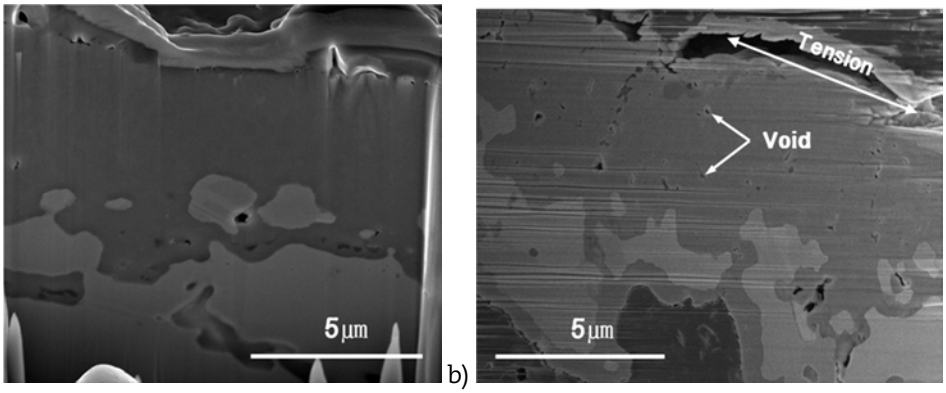

The larger decarburisation depth would also accelerate the creep rupture as grain boundary carbide was known to suppress the grain boundary migration. As in the case of oxide thickness, decarburisation depth was greater under tensile loading and in steam environments (Figure 9). Beneath the surface oxide layer, Cr concentrations were depleted due to Cr-rich surface oxide formations and consequently, Cr-rich $M_{23}C_6$ carbides were dissolved. Therefore, decarburisation depth would be proportional to the thickness of surface oxide layer. Also as previously reported [3], fine grained oxide layer were formed in steam environments (or low PO_2 condition), then substantial inward diffusion of water vapour would occur through increased grain boundary [9]. Thus, decarburisation was accelerated in steam environments, which in turn decreased the creep resistance.

4. Conclusions

The effects of environmental degradations on mechanical properties were investigated for Alloy 617 and Hynes 230. Based on the experiments and analysis, the following conclusions were drawn.

Long-term ageing at 900°C in vacuum caused the precipitation and coarsening of secondary phase such as $M_{23}C_6$ and M_6C, which caused increase in tensile strength and decrease in ductility. However, for the specimens aged in steam environments, surface and internal oxide as well as decarburisation region were formed along with secondary phases. The contribution of surface and internal oxides to the loss of ductility was greater than that of decarburisation zone to large ductility. As a result, tensile strength and ductility decreased simultaneously for specimens aged in steam environments.

In general, the creep rupture life of Alloy 617 and Haynes 230 was higher in air than in steam environments. Also, hydrogen additions in steam decreased the creep rupture life for Haynes 230. However, there is no significant effect of hydrogen addition on creep rupture life of Alloy 617. For both alloys, larger oxide layer size and decarburisation depth in steam environments were in good agreement with the shorter creep rupture life in such environments. Also, the surface oxide thickness and decarburisation depth were larger in the creep tested specimens compared to isothermal tested specimens,

Acknowledgements

This study was supported by the MSIP/NRF (Nuclear R&D Program 2011-0007979 and 2012-0005935) of Korea. Part of the funding was provided by the BK-Plus Program of the MSIP of Education of Korea. Two of the authors are also supported by the Global Ph. D Fellowship Program supported by MSIP/NRF.

References

[1] Carre, F. et al. (2009), "VHTR-Ongoing International Projects", GIF Symposium, pp. 93-102.

[2] Kirchhofer, H. et al. (1984), "Precipitation Behaviour of Ni-Cr-22Fe-18Mo (Hatelloy-X) and Ni-Cr-22Co-12Mo (Inconel 617) after Isothermal Ageing", Nucl. Tech., 66, pp. 139-148.

[3] Kim, D. et al. (2013), "Corrosion characteristics of Ni-base superalloys in high temperature steam with and without hydrogen, Journal of Nuclear Materials, Volume 441 pp. 612-622.

[4] Ohnami, M. (1988), "Plasticity and High Temperature Strength of Materials", *Elsevier Applied Science Publishers LTD, England*.

[5] Kihara, S. et al. (1980), "Morphological Changes of Carbides during Creep and Their Effects on the Creep Properties of Inconel 617 at 1 000°C", Metallurgical and Materials Transactions *A,* 11 pp. 1019-1031.

[6] Kofstad, P. (1985), "On the Formation of Porosity and Microchannels in Growing Scales", Oxidation of Metals, 24 pp. 265-276.

[7] Ikeda, Y. et al., (1978), "Microcrack generation and its healing in the oxide scale formed on Fe–Cr alloys", Oxidation of Metals, 12 pp. 487–502.

[8] Surman, P.L. et al. (1969), "Gas phase transport in the oxidation of Fe and steel", Corrosion Science, Volume 9 pp. 771–777.

[9] Zurek, J. et al., (2008), "Growth and Adherence of Chromia Based Surface Scales on Ni-base Alloys in High- and Low-pO2 Gases", Materials of Science and Engineering: *A,* 477, pp. 259-270.

[10] Jang, C. et al., (2008), "Oxidation Behaviour of an Alloy 617 in Very High-Temperature Air and Helium Environments," International Journal of Pressure Vessels and Piping, 85/6 pp. 368-377.

Novel experiments to characterise creep-fatigue degradation in VHTR alloys

J.A. Simpson, J.K. Wright, R.N. Wright
Idaho National Laboratory, United States

Abstract

It is well known in energy systems that the creep lifetime of high temperature alloys is significantly degraded when a cyclic load is superimposed on components operating in the creep regime. A test method has been developed in an attempt to characterise creep-fatigue behaviour of alloys at high temperature. The test imposes a hold time during the tensile phase of a fully reversed strain-controlled low cycle fatigue test. Stress relaxation occurs during the strain-controlled hold period. This type of fatigue stress relaxation test tends to emphasise the fatigue portion of the total damage and does not necessarily represent the behaviour of a component in-service well. Several different approaches to laboratory testing of creep-fatigue at 950°C have been investigated for Alloy 617, the primary candidate for application in VHTR heat exchangers. The potential for mode switching in a cyclic test from strain control to load control, to allow specimen extension by creep, has been investigated to further emphasise the creep damage. In addition, tests with a lower strain rate during loading have been conducted to examine the influence of creep damage occurring during loading. Very short constant strain hold time tests have also been conducted to examine the influence of the rapid stress relaxation that occurs at the beginning of strain holds.

Introduction

Creep-fatigue deformation is a combination of creep damage and fatigue damage and is expected to be the primary damage mode for a very-high-temperature reactor (VHTR) intermediate heat exchanger (IHX). Transients during start up and shut down produce cyclic loadings, while the stresses relax during steady power operation inducing creep damage. Material that experiences creep-fatigue deformation fails more quickly than material experiencing only creep or fatigue. Therefore, creep-fatigue testing is critical to incorporating a material in the ASME Code for design of nuclear systems. Furthermore, it is important to understand the individual contributions of creep damage and fatigue damage to creep-fatigue failure modes. A variety of experiments have been designed to discern the relative contributions of creep and fatigue to creep-fatigue behaviour at 950°C, the maximum temperature of interest for the VHTR application.

Alloy 617 is the leading candidate for the VHTR IHX and testing is ongoing to generate data so it can be incorporated into the ASME Boiler and Pressure Vessel Code, Section III, Subsection NH for elevated temperature nuclear system design. [1] Creep-fatigue testing (strain-controlled fatigue with a hold time at the peak tensile strain) has been performed in a laboratory setting to reproduce the expected damage mode, as well as continuous low cycle fatigue (LCF) testing (i.e., no hold time) to provide a baseline for the creep-fatigue behaviour [2-5]. This creep-fatigue testing is henceforth referred to as fatigue stress relaxation (FSR) testing since the amount of "creep" deformation that is calculated is a result of stress relaxation rather than conventional tensile creep deformation.

Alternative testing using a load-controlled tensile hold has been developed for ferritic-martensitic steel [6]. This type of test has been called a true creep-fatigue test since the creep portion of the deformation occurs in a manner that is similar to a uniaxial creep test. Load-control testing also offers the potential to provide test conditions that are creep dominated, whereas FSR tests are fatigue dominated because stress relaxation is very rapid in Alloy 617 at high temperatures. These two types of creep-fatigue tests are compared in Figure 1.

Figure 1: Schematic diagrams comparing control mode and specimen response for two types of creep-fatigue testing

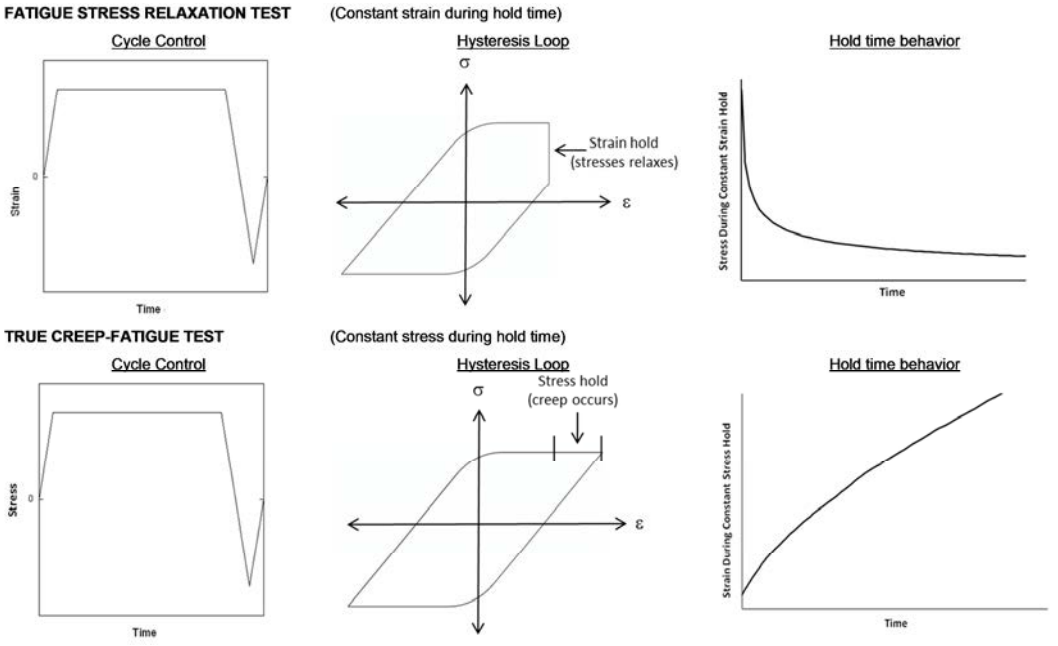

An alternative to the conventional FSR test was designed to study the influence of the loading cycle at slow loading conditions more representative of in-service component loading. At the high temperatures that are being investigated for Alloy 617, it cannot be assumed that creep deformation occurs only during the hold time and not during loading. Decoupling of the creep from the plasticity components during loading is important for constitutive modelling. Furthermore, it is known that Alloy 617 is strain rate sensitive at elevated temperatures and thus the stresses achieved during cycling are lower at lower strain rates, thereby influencing the amount of creep damage during each cycle.

Finally, tests with only a 2 s hold time were performed. Since stress relaxation occurs very rapidly during the hold, these tests help illuminate the impact of the stress relaxation by minimising the time for this to occur and comparing results to the LCF results.

Experimental procedure

All testing was conducted at 950°C with fully reversed cyclic loading.

Load-control tests

Two tests were executed entirely in load control using a loading rate of 1120 N/s, and a target load of ±1767N, corresponding to about 40 MPa. One test had a 30-second tension load hold and one had a 30 minute hold. The stress histories for these two tests are shown in the first column of the first two rows of Figure 2. Both of these tests were conducted in two steps as the total strain experienced by the specimen was greater than

the strain range of the extensometer. Tests were suspended, the extensometer was reset, and the tests were restarted and run to a total strain of nearly 40%, rather than to failure.

Figure 2: Stress and strain histories and stress-strain hysteresis loops from a mid-life cycle for the three tests performed in load control

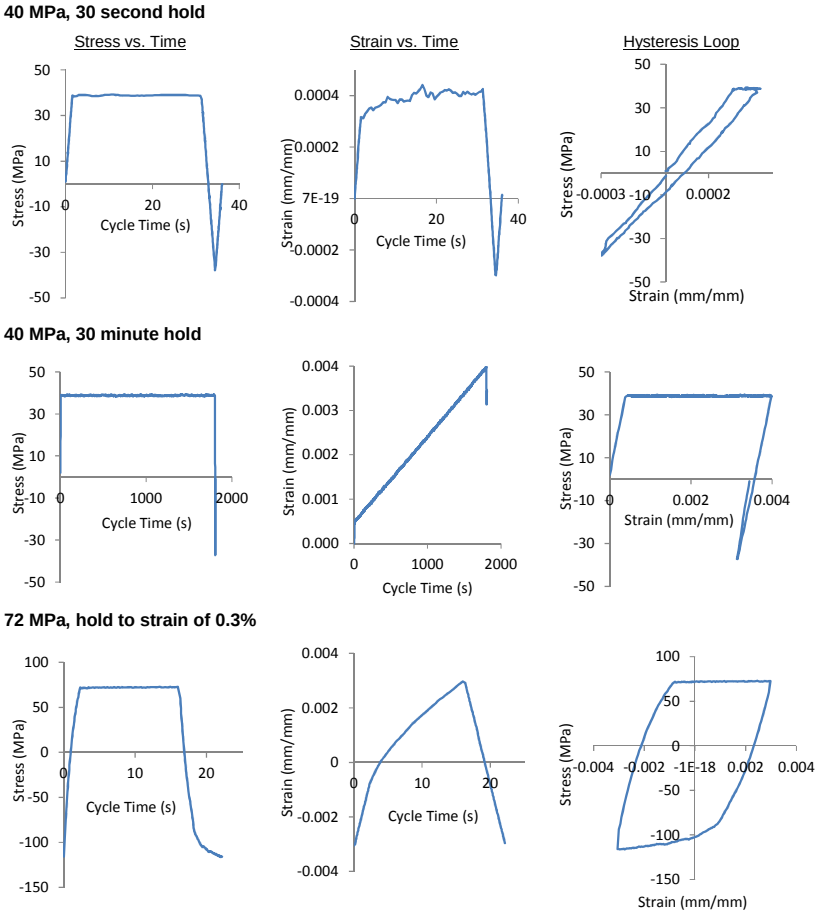

An additional test was designed to demonstrate true creep-fatigue with a stress during the hold of approximately 72 MPa. The specimen was held until a target tensile strain of 0.3% was achieved, rather than holding for a given time as described above. The procedure alternated between strain-control and load-control modes to achieve this result. The cycle started in strain control, applying a tensile strain at a rate of 10^{-3} /s until a load was reached corresponding to the target stress. At that point the specimen was allowed to creep in load control to the target tensile strain value, at which point the cycle was completed in strain control by imposing a compressive strain of -0.3% and then reversing to tension until the target stress is reached again. The stress and strain histories for this test are shown in the third row of plots of Figure 2. Cycling continued until the specimen cracked. Once cracking occurred the tension load criteria could no longer be met and the test effectively became a LCF test with a strain range of ±0.3% strain.

Strain rate variations

A low strain rate FSR test was conducted such that its total cycle time was equal to that of the typical test conditions. The typical strain rate is 10^{-3} /s and for a hold time of 600 s, the total cycle time is 606 s. By using a combination of a strain rate of 10^{-4} /s and a hold time of 546 s, the total cycle time is maintained at 606 s. In addition, a test was run at a strain rate of 10^{-5} /s with a hold time of 600 s. For this strain rate, it was not possible to

have the same total cycle time and maintain significant hold times. In all cases the total strain range was 0.3%. The strain histories of the slower strain rate tests are compared to that of a standard 600 s hold time test in Figure 3.

Figure 3: Strain histories of tests run at different strain rates, illustrating (a) a constant total cycle time and (b) a constant hold time.

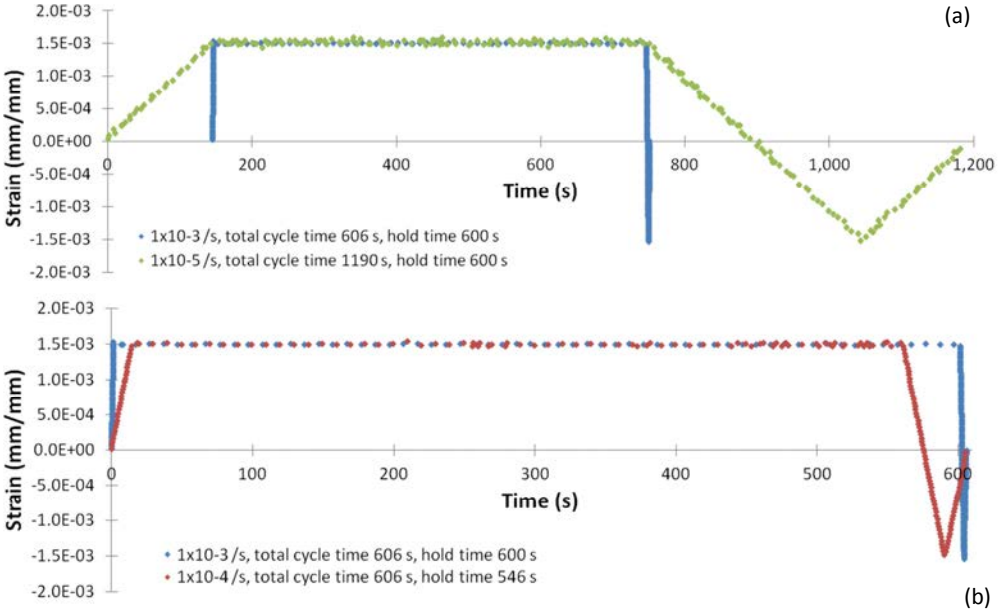

Short hold tests

FSR tests were conducted to 0.3% and 1.0% total strain with a 2 sec constant strain hold time at peak tensile strain. The strain rate was the nominal 10^{-3} /s value used in the baseline LCF and FSR tests.

Results

Load-control tests

The stress-strain hysteresis loops, stress control history and strain response history for both types of load-control tests are presented in Figure 2. The first two rows of plots in Figure 2 are from the constant hold time tests. For the 30 s hold test, most of the strain occurs during loading, while for the 30-minute test, most of the strain occurs via creep during the hold. The hysteresis loops do not resemble the schematic loops of typical creep-fatigue tests shown in Figure 1. Specimens accumulate strain as the tests progress, rather than alternating between controlled strain limits, as is the case for both FSR testing and for the true creep-fatigue test discussed below. The strain accumulation as a function of cycle is shown in Figure 4 for the 30 s hold test. The figure strongly resembles a curve from a traditional creep test for Alloy 617. The rapid strain rate at the end of the test indicates failure was imminent, i.e. even significant additional creep strain would only result in a few additional cycles, and final cycle can be used as an approximation of cycles to failure.

The last row of plots in Figure 2 is from the true creep-fatigue test. The strain accumulates quickly during the tensile hold and most of the inelastic strain accumulated each cycle occurs during the hold. The stress history is not linear during loading because that portion of the test is done in strain control (the strain history is linear in this region). The hysteresis loop shown in Figure 2 resembles the schematic of the true creep-fatigue test shown in Figure 1, although the proportion of strain accumulated during the hold is larger.

Figure 4: Accumulated strain as a function of cycle for load-controlled creep-fatigue test of Alloy 617 at 950°C with 30 second hold time at 40MPa

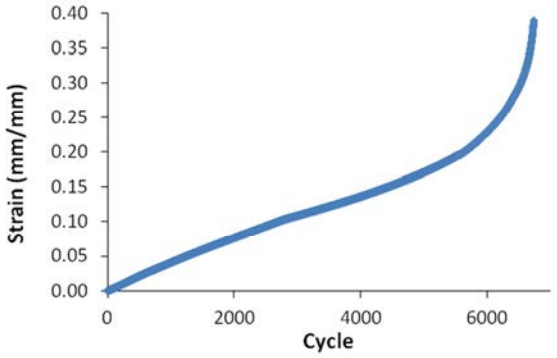

Test conditions and results from the load-controlled creep-fatigue tests are listed in Table 1. The sum of the hold time is calculated as the hold time at a mid-cycle multiplied by the cycles to failure. This value can be compared to the creep rupture time, determined for a 950°C creep test at the tensile hold stress, using a Larson-Miller plot (creep stress vs. the Larson-Miller Parameter which is a function of both time to rupture and test temperature) for a large database of Alloy 617 creep tests. In all cases the sum of the hold time is less than the creep rupture time, illustrating the influence of fatigue damage.

Similarly, the maximum cycle (or cycles to failure) of the creep-fatigue test can be compared to the fatigue life for a 950°C LCF test with the same total strain range, estimated from a total strain range, $\Delta\varepsilon_T$, vs. cycles to failure plot of a database of fatigue tests. A $\%\Delta\varepsilon_T$ of 0.07 appears to be below the fatigue endurance limit, estimated as about 0.15% from the database. Note the database does not go below this level, and it is not known if Alloy 617 actually has an endurance limit at this temperature. In any case, the lifetime is much greater than 10^6 cycles. For both of the time-hold tests, the maximum cycle is much less than the fatigue life, indicating a large influence of creep damage in these tests. The cycles to failure for the strain-hold test is about the same as the fatigue life estimate under similar conditions.

Table 1: Comparison of load-controlled creep-fatigue test lives to creep and fatigue life for similar conditions. Estimates are calculated from stress-strain behaviour of a mid-life cycle

hold type	σ_{hold} (MPa)	$\%\varepsilon_T$	$\%\varepsilon_{in}$[1]	t_{hold} (s)	sum t_{hold} (h)	creep $t_{rupture}$[2] (h)	cycles[3]	fatigue life[4] (cycles)
time	40	0.07	0.0085	30	58	242	7 000	NA[5]
time	40	0.40	0.343	1 800	35	242	70	2 939
strain	72	0.60	0.446	14[6]	6	9	1 560	1 328

1. Inelastic strain – width of hysteresis loop at zero stress.
2. Creep rupture time estimated from Larson-Miller plot for Alloy 617.
3. Cycles to failure for strain hold test, cycle at end of test for time hold tests, a reasonable proximity to failure as strain was increasing rapidly with each cycle at end of test.
4. Fatigue life estimated from 950°C fatigue data for Alloy 617.
5. Total strain appears to below the fatigue endurance limit.
6. Hold time varies significantly with cycle.

Strain rate variations

Figure 5 shows hysteresis loops from a midlife cycle for tests run at strain rates spanning two orders of magnitude. The number of cycles to failure observed for the test run at 10^{-4}/s was within the scatter of the creep-fatigue tests with the faster strain rate of 10^{-3}/s and a hold time of 600 s, as shown in Figure 6.

Figure 5: Hysteresis loops from a midlife cycle for tests run at three different strain rates

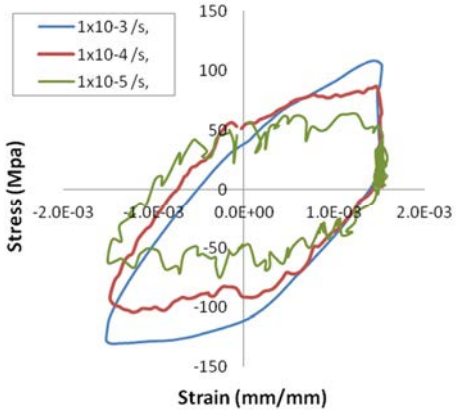

Figure 6: Plot of the cycles to failure as a function of hold time for Alloy 617 in fatigue and creep-fatigue at 950°C for total strain ranges of 0.3 and 1.0%

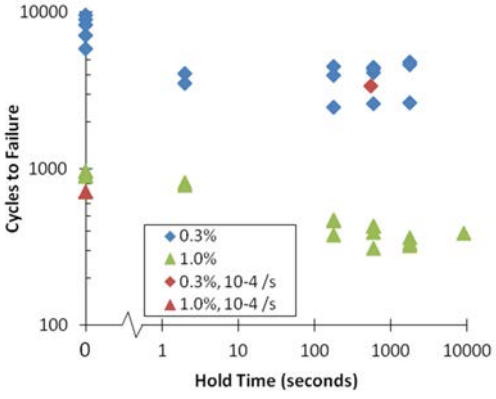

Short hold tests

The data from the FSR tests with 2 second hold times are included in Figure 6. The number of cycles to failure was similar to the longer hold time tests (600 sec and 1 800 sec) at the lower strain range (0.3% total strain) and significantly less than in pure fatigue. At the 1.0% total strain range, the number of cycles to failure was slightly lower than in fatigue but, in this case, higher than the longer hold time tests.

Rapid stress relaxation occurs in Alloy 617 within 2 seconds and is shown for the midlife 0.3% and 1.0% total strain hysteresis loop in Figure 7. The stress drops over 50 MPa during the 2 second hold, a short time relative to creep deformation. Interestingly, cyclic softening behaviour is similar to pure LCF for a given total strain range.

Figure 7: Stress relaxation curves during 2 second hold at mid-life cycle

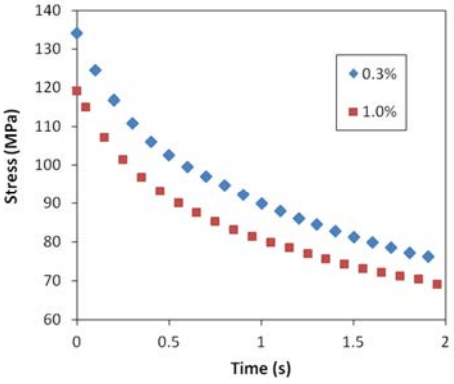

Discussion

Creep-fatigue interaction diagram

In the ASME Boiler and Pressure Vessel Code, Section III, Subsection NH, [1] creep-fatigue life is evaluated by a linear summation of fractions of cyclic damage and creep damage. The creep-fatigue criterion is given by:

$$\underbrace{\sum_j \left(\frac{n}{N_d}\right)_j}_{\text{Cyclic Damage}} + \underbrace{\sum_k \left(\frac{\Delta t}{T_d}\right)_k}_{\text{Creep Damage}} \leq D \qquad (1)$$

where n and N_d are the number of cycles of type j and the allowable number of cycles of the same cycle type, respectively; and Δt and T_d are the actual time at stress level k and the allowable time at that stress level, respectively; D is the allowable combined damage fraction. The cyclic and creep damage terms on the left-hand side of Equation (1) are evaluated in an uncoupled manner, and the interaction of creep and fatigue is accounted for empirically by the D term on the right side of the equation. This can be represented graphically by the creep-fatigue interaction diagram, also known as a damage diagram (d-diagram). The d-diagram proposed in the Draft Alloy 617 Code Case [7] is shown in Figure 8.

Figure 8: Example of a D-diagram for Alloy 617. with intersection coordinates of (0.1, 0.1). Red shading indicates location of experimental data from FSR testing and green shading indicates the predicted range for load-controlled testing

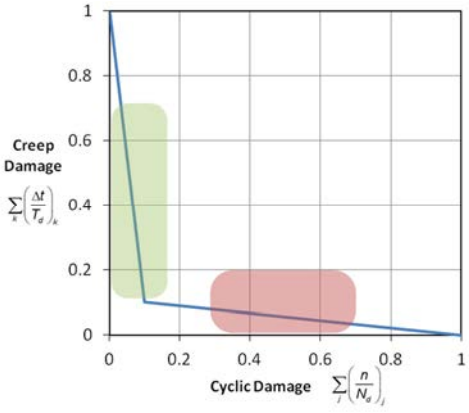

Preliminary analysis of the available Alloy 617 FSR data obtained from tests in air at 950°C supports the fatigue-dominant region of the bilinear creep-fatigue interaction. The data gathered to date for strain ranges of 0.3 to 2.0 and hold times of 0-30 minutes all fall

within the red shading in Figure 8. Efforts to generate creep-fatigue data in the creep-dominant region of the d-diagram using smaller strain ranges and/or longer hold times have been explored and it appears FSR testing cannot populate the creep-significant portion of the d-diagram. The rapid stress relaxation of Alloy 617 observed during the tensile hold limits the amount of creep damage, regardless of test conditions chosen.

It appears a different approach is necessary to fully characterise the creep dominated region of the diagram. Load-controlled creep-fatigue testing enables the rapid accumulation of creep strain during the tensile hold, as the stress is not able to relax, and makes possible experimental conditions that are creep-dominated. Preliminary analysis indicates that data is expected to fall within the green shaded area.

Coffin-manson relationship

The Coffin-Manson fatigue relationship [8-9] illustrates that fatigue cycles to failure is a function of inelastic strain (indicated by the width of the hysteresis loop). The Coffin-Manson plot for Alloy 617 is shown in Figure 9. The blue diamonds and line represent the LCF data and a fit to this data.

It has been previously shown [5,4] that the number of cycles to failure at the 0.3% strain range follow the Coffin-Manson relationship, as shown in Figure 4. This is also the case for the 2 sec hold FSR tests with both 0.3 and 1.0 total strain ranges. However, for the 1.0% total strain FSR tests with longer hold times, the behaviour does not follow the Coffin-Manson fatigue relationship, indicating a greater contribution from creep/stress relaxation. This is similar to the behaviour shown in Figure 6, where the 1.0% 2 s hold FSR test is more similar to the 1.0% LCF tests than to the 1.0% FSR tests with longer hold times.

The 10^{-3} /s strain rate FSR test, as well as some 10^{-3} /s strain-rate LCF tests, fall on the same Coffin-Manson line as the bulk of the LCF tests run at 10^{-3} /s. It appears that the creep/stress-relaxation that occurs during the slower loading rate does not significantly impact the life of the material.

The load-controlled strain hold (true creep-fatigue) test falls on the Coffin-Manson line. Although this test was designed to allow significant creep to occur, both the inelastic strain (as determined by width of the hysteresis loop at mid-cycle) and the cycles to failure are similar to LCF tests with the same total strain range. Both load-controlled time-hold tests fall well below the line.

Figure 9: Coffin-Manson plot showing data from a variety of LCF and creep-fatigue tests

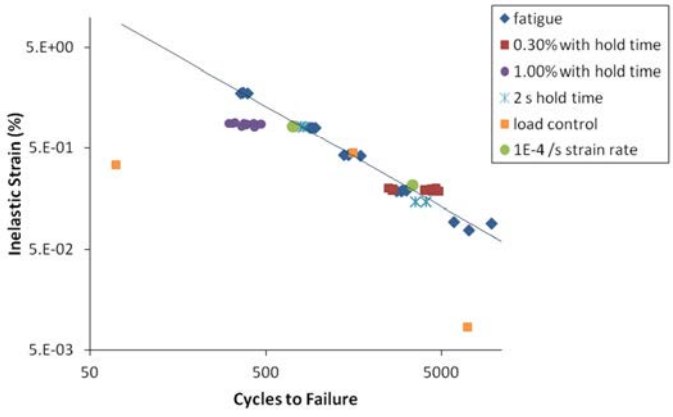

Acknowledgements

The authors gratefully acknowledge L.J. Carroll (INL) and T.-L. Sham (ORNL) for their thoughtful input and discussions regarding development and analysis of novel creep-fatigue tests.

References

[1] ASME, "Boiler and Pressure Vessel Code, Section III, Subsection NH".

[2] Wright, J.K. , L.J. Carroll, J.A. Simpson and R.N. Wright, "Low Cycle Fatigue of Alloy 617 at 850 C and 950 C", Journal of Engineering Materials and Technology, Vol. 135, no. July, pp. 031005-1 - 031003-8, 2013.

[3] Rao, K.B.S., H. Schiffers, H. Schuster and H. Nickel, "Influence of Time and Temperature Dependent Processes on Strain Controlled Low Cycle Fatigue Behaviour of Alloy 617", Metall. Trans. A, vol. 19, no. 2, pp. 359-371, 1988.

[4] Carroll, M.C. and L.J. Carroll, "Developing Dislocation Subgrain Structures and Cyclic Softening During High-Temperatue Creep-Fatigue of a Nickel Alloy", Metallurgical and Materials Transactions A, vol. 44A, no. August, pp. 3592-3607, 2013.

[5] Carroll, L.J., C. Cabet, M. C. Carroll and R. N. Wright, "The development of microstructural damage during high temperature creep of a nickel alloy", International Journal of Fatigue, vol. 47, pp. 115-125, 2013.

[6] Fournier, B., M. Sauzay, C. Caes, M. Noblecourt, A. Bougault and V. P. A. Rabeau, "Creep-fatigue-oxidation interactions in a 9Cr-1Mo martensitic steel. Part I: Effect of tensile holding peried on fatigue lifetime", International Journal of Fatigue, Vol. 30, pp. 649-662, 2008.

[7] Corum, J.M. and J.J. Blass, "Rules for Design of Alloy 617 Nuclear Components to Very High Temperatures", Fatigue, Fracture and Risk, PVP, vol. 215, pp. 147-153, 1991.

[8] Coffin, L.F. and J.F. Travernelli, "The Cyclic Straining and Fatigue of Metals", Trans. TMS-AIME, vol. 215, no. 5, pp. 794-806, 1959.

[9] Manson, S.S. and M.H. Hirschberg, "Fatigue Behaviour in Strain Cycling in the Low and Intermediate Cycle Range", in 10th Sagamore Army materials Research Conference, Raquette Lake, NY, August 13-16, 1963.

Fatigue and creep crack propagation behaviour of Alloy 617 in the annealed and aged conditions

Julian K. Benz and Richard N. Wright
Idaho National Laboratory, United States

Abstract

The crack propagation behaviour of Alloy 617 was studied under various conditions. Elevated temperature fatigue and creep-fatigue crack growth experiments were conducted at 650 and 800°C under constant stress intensity (ΔK) conditions and triangular or trapezoidal waveforms at various frequencies on as-received, aged, and carburised material. Environmental conditions included both laboratory air and characteristic VHTR impure helium. As-received Alloy 617 displayed an increase in the crack growth rate (da/dN) as the frequency was decreased in air which indicated a time-dependent contribution component in fatigue crack propagation. Material aged at 650°C did not display any influence on the fatigue crack growth rates nor the increasing trend of crack growth rate with decreasing frequency even though significant microstructural evolution, including γ' (Ni_3Al) after short times, occurred during ageing. In contrast, carburised Alloy 617 showed an increase in crack growth rates at all frequencies tested compared to the material in the standard annealed condition. Crack growth studies under quasi-constant K (i.e. creep) conditions were also completed at 650°C and a stress intensity of K = 40 MPa$\sqrt{m}$. The results indicate that crack growth is primarily intergranular and increased creep crack growth rates exist in the impure helium environment when compared to the results in laboratory air. Furthermore, the propagation rates (da/dt) continually increased for the duration of the creep crack growth either due to material ageing or evolution of a crack tip creep zone. Finally, fatigue crack propagation tests at 800°C on annealed Alloy 617 indicated that crack propagation rates were higher in air than impure helium at the largest frequencies and lowest stress intensities. The rates in helium, however, eventually surpass the rates in air as the frequency is reduced and the stress intensity is decreased which was not observed at 650°C.

Introduction

Future VHTR deployments based on the NGNP design will require delivery of high temperature heat through heat exchangers up to target temperatures as high as 1 000°C. The intermediate heat exchanger (IHX) is likely the component most critically impacted by increased temperatures. The IHX transfers thermal energy between the primary and secondary heat transport system using helium or derivative gas mixtures to downstream applications such as H_2 production, process heat, and power production (i.e. steam production). The inlet temperature for the IHX will be quite high at 760-950°C and outlet temperatures lower resulting in an extremely large range where changes resulting from ageing and environment will be a concern [1]. Furthermore, structural components in the IHX are assumed to contain flaws from manufacturing or welding that can propagate under loading during normal service and be subject to the synergistic effect of high temperature environmental damage (mainly oxidation) and cyclic thermally induced fatigue stresses, potentially resulting in failure [2,3].

A number of solid solution strengthened nickel- and iron-based alloys have been considered for application in the VHTR program but focus has been mainly on Alloy 617 due to its technical maturity, availability in required product forms, experience base, and high temperature mechanical properties. However, there remains a data and knowledge gap on the crack propagation for this candidate alloy and very few extensive studies have been conducted [4,5]. Furthermore, numerous oxidation based embrittlement mechanisms have been recognised in other nickel base superalloys, especially Alloy 718, which reduces damage tolerance [6-9]. Therefore, research examining the crack propagation behaviour and establishing mechanisms of fracture under combinations of creep, fatigue, and oxidation in these candidate alloys is necessary.

The work here presents some recent results on the crack propagation behaviour of Alloy 617 at a wide range of loading and starting material conditions in which crack lengths were measured using a verified DCPD technique. Testing was also completed in carefully controlled and monitored environmental conditions where limited oxygen was available for oxidation so that comparison could be made to propagation rates in air.

Experimental procedure

Material

The Alloy 617 used in this study was machined from two 1.397 m × 3.505 m (55 in. × 138 in.) of 38 mm (1.5 in.) thick solution annealed plates from a single heat (cast 314626) manufactured by ThyssenKrupp VDM. This heat of material serves as the reference material for the majority of the VHTR related R&D. The ASTM specified chemical composition of Alloy 617 and that of the procured heat are given in Table 2. Strengthening is mainly imparted by solid solution from Co and Mo but also particle strengthening from $M_{23}C_6$, M_6C, Ti(C,N) and other precipitates when in appropriate sizes, distributions, and volume fractions. In addition, the Al and Ti can also form the intermetallic compound γ' over a range of temperatures up to approximately 750°C, which results in precipitation strengthening [10]. Finally, the high Ni, Cr, and Al contents provide the alloy with high resistance to oxidation at elevated temperatures.

Table 2: Chemical composition of Alloy 617 (wt%)

	Ni	Cr	Co	Mo	Fe	Mn	Al	C	Cu	Si	S	Ti	B
Min	44.5	20.0	10.0	8.0	-	-	0.8	0.05	-	-	-	-	-
Max	-	24.0	15.0	10.0	3.0	1.0	1.5	0.15	0.5	1.0	0.015	0.6	0.006
TK314626	54.1	22.2	11.6	8.6	1.6	0.1	1.1	0.05	0.04	0.1	<0.002	0.4	<0.001

Sections of Alloy 617 as-received plate measuring 12”×5”×1.5” were also statically aged in air at 650 ± 1°C for 200, 650, 2 000, and 5 300 hours followed by air cooling. The aged material was subsequently sectioned for metallographic examination or machined for crack growth testing as described in the next section. One machined crack propagation specimen from the as-received plate was also run in a helium corrosion loop capable of simulating various corrosion chemistries. The specimen was carburised at 950°C for 1 028 hours under a flow of helium gas with 197 ppm H_2, 5 ppm CO, and 100 ppm CH_4 impurity concentrations.

Crack propagation testing

The crack growth experiments met the requirements of ASTM E 647-08. Furthermore, the compact specimen design, abbreviated henceforth as C(T) specimen, was used following the requirements in Annex A1 of this standard. The specimen dimensions followed the conventional 0.5T geometry, in that the specimen thickness, B, was one half inch or 12.7 mm and the machined notch length to specimen width ratio, a/W, was nominally 0.4. All specimens were machined from the plate in the L-T orientation, with the crack propagation plane perpendicular to the rolling direction and the direction of applied tension parallel to the long transverse direction of the plate.

Crack propagation tests were conducted on Instron 8 800 servo-electric controlled load frames (Instron, Norwood, MA). The crack length was measured in situ via a DCPD (direct current potential drop) technique using averageing of 2 pairs of voltage leads and reversing current polarity. The DCPD system was controlled by an INL (Idaho National Laboratory, Idaho Falls, ID) developed Labview computer program. A closed form empirical Weibull fit equation developed by GE (General Electric, Schenectady, NY) was used to calculate the crack length from the DCPD voltage measurements. Validation tests of the DCPD crack growth measurement system showed that the actual crack length is underestimated by approximately 3% consistently across the range of crack length tested. The underestimation of crack length does slightly increase the nominal applied stress and stress intensity due to the applied loads being calculated from the DCPD crack length. However, the crack growth rates calculated from regressions of crack length versus time should have had minimal error since the error in crack did not change with the physical crack length in the specimen. The stress intensities reported here were the target values during testing.

Fatigue and creep-fatigue crack propagation tests were conducted in both laboratory air and impure helium environments at 650 and 800°C on material in the as-received, aged, and carburised conditions. The impure helium environment simulated prototypical VHTR conditions (i.e. helium with nominally 10 ppm of H_2O, 55 ppm CO, and 350 ppm H_2 at the inlet) in a ceramic retort assembly. Variation in the actual gas impurity levels are maintained within a range of less than 5% compared to the set point for the duration of the test as measured using a calibrated gas chromatograph and solid state cermet hygrometer. Various combinations of frequency and stress intensity, controlled via the Labview program, were imposed during a test allowing for multiple test steps on each specimen. A triangular waveform with frequencies from 0.01 to 0.5 Hz was used for fatigue crack propagation and a trapezoidal waveform with 10 second loading-unloading ramps and 10, 60, or 300 second holds at maximum load for creep-fatigue. A load ratio, $R = \frac{K_{min}}{K_{max}} = \frac{\sigma_{min}}{\sigma_{max}} = \frac{P_{min}}{P_{max}}$, of 0.05 was used in all fatigue and creep-fatigue tests. The software communicated with the load frame so that constant stress intensity, ΔK or K_{max}, was maintained during each test step by using the updated crack length. With control over the stress intensity, linear crack growths were obtained based on the Paris Law for Stage II crack growth rates:

$$\frac{da}{dN} \propto A(\Delta K)^m \quad (1)$$

where a is the crack length, N is the number of loading cycles, and A and m are empirical constants determined during the test. Finally, quasi static loading creep crack propagation tests were completed on as-received material. The actual applied loads during these tests decreased at a rate of approximately 0.4 to 0.5 N/h for tests lasting 1 000 hours and longer, hence the term “quasi static”. A stress intensity was used simply to define the starting load of the quasi static loading step since the linear elastic fracture mechanics parameter K is invalid during creep (i.e. inelastic) fracture.

Results and discussion

As-received and aged microstructure

The microstructure of the as-received Alloy 617 plate is shown in Figure 10. Although significant inhomogeneity exists in the microstructure, the average grain size measured by the linear intercept method is 150 µm. The as-received microstructure is also characterised by carbide banding and stringers parallel to the rolling direction. The bands range from approximately 100-300 µm wide. Within the carbide banded regions, the carbides form on what appears to be a prior grain structure, that is finer and independent of the present grain boundary structure (i.e. carbide structure traverses the current boundaries without any interaction) as shown in Figure 10(a). In the areas of the matrix outside these banded regions, there are few to no secondary particles besides a small number of Ti(C,N) particles.

In addition, TEM investigation of the as-received, solution annealed Alloy 617 plate found no evidence of γ' precipitates in the FCC γ matrix. The material had a low density of dislocations, as shown in Figure 10b) and did not exhibit a dislocation cell or subgrain structure.

The Alloy 617 plate shows an evolution of microstructure after ageing for relatively short period of 200 hours at 650°C. This observation is consistent with the TTT diagram for Alloy 617 which shows that $M_{23}C_6$, M_6C, and γ' will start to precipitate in as little as two hours at this temperature [11,12]. Comparing the as-

Figure 10: As-received (annealed) microstructure of Alloy 617

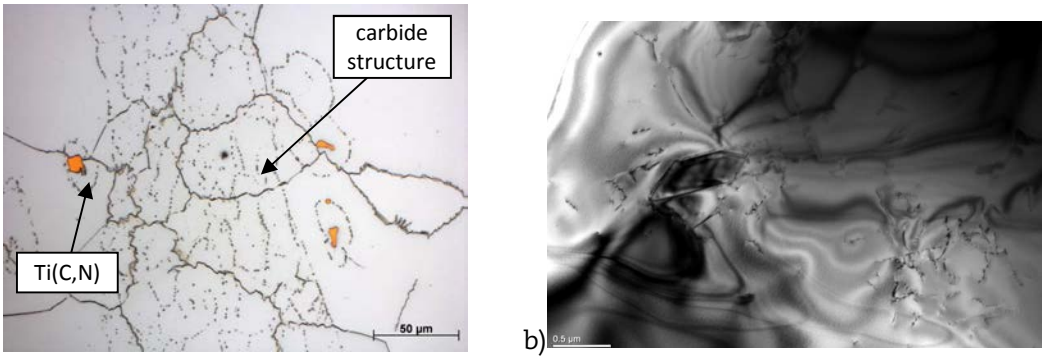

received microstructure to that of aged material, the aged microstructure indicates carbide precipitation after 200 hours. There is still banding present, but the new carbide precipitation has slightly obscured the previous areas with banding or stringers. After 5 300 hours at 650°C, the microstructure does not show a large evolution compared to that of the plate aged for 200 hours, except for further carbide precipitation. Figure 11a shows an optical micrograph of the 5 300-hour aged material indicating carbide precipitation occurred in the regions previously free from carbides. Furthermore, the carbides in the aged material at all ageing times appear to partly retain the cell structure visible in the as-received material in the banded regions. There is no indication of carbide redistribution or precipitation directly on the grain boundaries in the static aged material. TEM investigation confirmed that spherical γ' precipitates are present after static ageing at 650°C. Figure 11(b) shows a dark field image of material aged for 5 300 hours highlighting the γ'. Precipitation of γ' occurs with 2-3 hours of ageing and additional ageing at 650°C results in an increasing particle volume fraction. A slight spherical to cuboidal shape change evolution is apparent after particle coarsening. Selected area diffraction is consistent with the precipitates having the $L1_2$ lattice structure, indicative of the ordered FCC γ' phase, as illustrated by a <111> zone axis SAD pattern in the inset of Figure 11(b).

Fatigue and creep-fatigue crack growth

The fatigue and creep-fatigue crack growth rates for the as-received material in air at 650°C are shown in Figure 12. The relationship of change in crack length, a, with number of fatigue cycles, N, (i.e. da/dN) was linear at all frequencies and stress intensities under constant K_{max} control. In Figure 12, the creep crack propagation rates for the cycles with holds at maximum load were also included. Since these hold time conditions were not continuous waveform cycles like the majority of data on the plot, a frequency was computed for these values by taking the inverse of the sum of the times for loading to maximum load, holding at maximum, and unloading (e.g. for the 60 second hold condition, $f = (10s + 60s + 10s)^{-1}$. The frequencies are 0.0333, 0.0125, and 3.125e-3 Hz for the 10, 60, and 300 second holds, respectively. The as-received Alloy 617 exhibits time dependent fatigue crack propagation as indicated by the increase in crack increment per cycle with decreasing frequency. Power law regressions are fit to the frequency range where da/dN visibly increased with decreasing frequency for each K_{max}.

Figure 11: Microstructure of Alloy 617 aged for 5 300 hours at 650°C

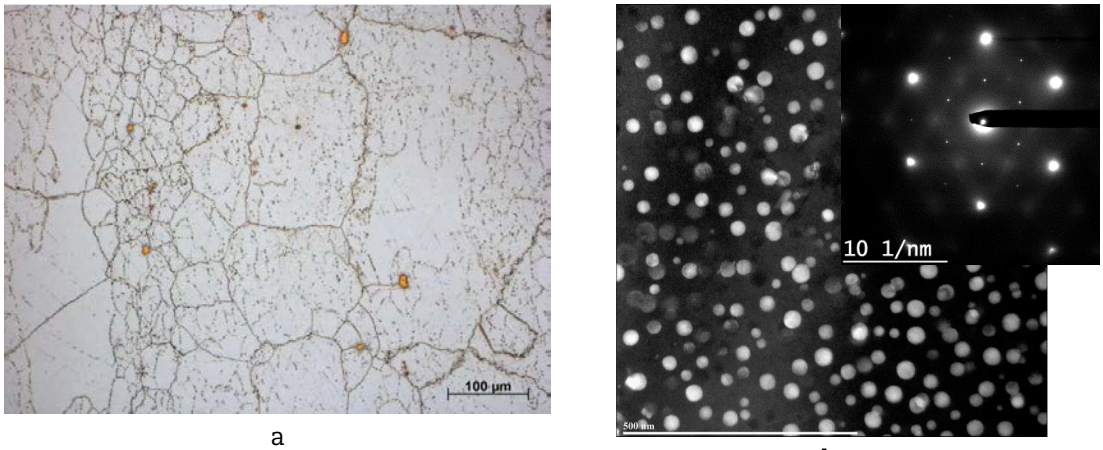

a b

Figure 12: Fatigue crack propagation rate vs. frequency of as-received material in air at 650°C

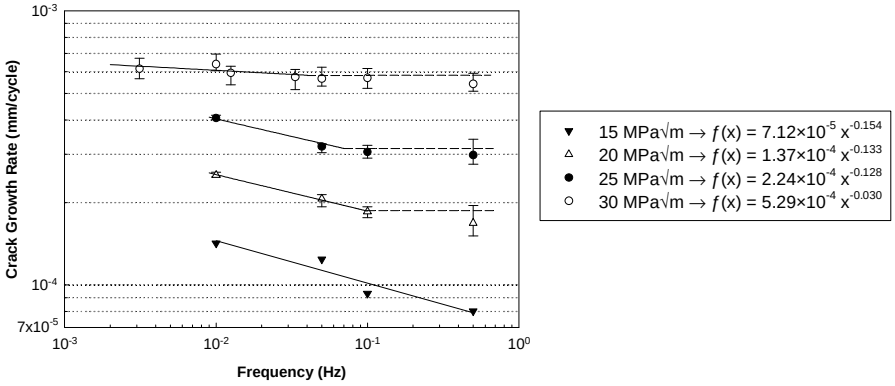

Two important characteristics relating the time dependent fatigue crack propagation to stress intensity change should be noted. The first is that the transition from cycle dependent, or fully time independent (i.e. a horizontal dashed line on da/dN vs. f plot), to time dependent crack propagation occurs at lower frequency as the stress intensity is increased. Furthermore, the results at K_{max} = 15 MPa√m indicate that time dependent crack growth occurred at all frequencies tested up to 0.5 Hz. The second significant finding is that the power law exponent, or slope of the regression on a log-log scale, decreases in the time dependent region as the stress intensity is increased. Both of these findings indicate a time dependent environmental crack tip degradation mechanism, most likely crack tip oxidation. At the lowest stress intensities evaluated, the crack growth rates are low and environmental enhancement of crack propagation occurs at all frequencies evaluated. However, as stress intensity is increased, the time dependent environmental degradation mechanism is given less time operate and thus contributes less to the overall crack propagation. This gives rise to the transition to the transition between time-independent and dependent regions which occurs at approximately 0.1, 0.07, 0.04 Hz for 20, 25, and 30 MPa√m, respectively. At the highest stress intensity evaluated, the time dependence is very low as indicated by the stress exponent of -0.03, which is considerably less than the exponents at the lower stress intensities. Even though considerable time dependent fracture is found to occur in air due to environmental degradation, no deviation from traditional transgranular fracture is observed on the fracture surface during SEM inspection as shown in the lower part of Figure 13. The transition to fully intergranular brittle fracture is not observed to occur until the quasi static loading region which is shown in the upper half of Figure 13.

Figure 13: Transition from transgranular to intergranular fracture from specimen tested in air at 650°C

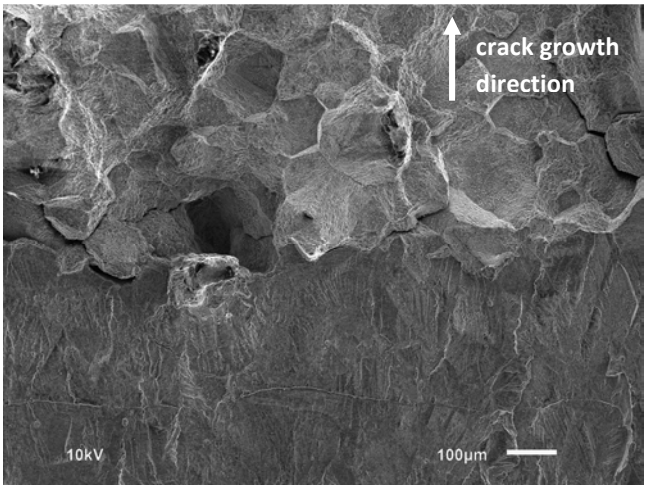

The impact of Alloy 617 starting material condition on crack propagation rates is shown in Figure 14 which includes both aged and carburised material. The as-received crack growth rates are also included in each plot for comparison purposes. Again, both the aged and carburised material show an increase in the crack growth rate in mm/cycle as the frequency is decreased illustrated by Figure 14a. Furthermore, ageing time at 650°C, 200 vs. 5 300 hours, does not indicate any impact on this trend. The environmental degradation mechanism discussed previously appears to have the same effect regardless of any materials differences in the aged and carburised material. However, the data at K_{max} = 30 MPa√m shown in Figure 14b indicates a significant increase in the crack propagation rates of the carburised material compared to the as-received and aged material. The carburisation process also multiplies the time dependent factor shown by the increase in slope below the time independent frequency range of 0.1-0.5 Hz when compared to the remaining data. Finally, Figure 14b indicates that there are possibly small differences in fatigue and creep-fatigue crack growth rates at 30 MPa√m for short versus long ageing times. Only the material aged for 5 300 hours show a small decease in the crack growth rates, especially at frequencies in the 0.1 to 0.5 Hz. However, the error bars on the mean crack growth rate for the as-received material generally envelope all of the rates for the aged material, which makes any conclusions difficult to make without more testing and analysis. Changes in the crack growth rates with ageing time were not expected under fatigue loading. Within a given material system, the crack growth per cycle is generally insensitive to the initial strength levels. However, it is surprising that the creep- fatigue crack growth rates do not show more difference between the as-received and aged material. Although the γ' precipitates do impede dislocation motion during large scale tensile formation such as creep, either by forcing dislocations to bow and/or climb around particles, the small scale yielding around the crack tip during the hold of the creep-fatigue crack propagation cycle does not appear to be affected. Previous work on Alloy 617 and Haynes 230 has indicated that hold times cycles are not necessarily a superposition of the fatigue and creep crack growth rates [13], which appears to be supported by the negligible difference in aged and as-received material crack propagation rates for hold time cycles. However, more investigation is needed to explain this under creep-fatigue crack growth conditions.

Figure 14: Crack propagation rates in air at 20 and 30 MPa√m and 650°C comparing the as-received, aged, and carburised material conditions

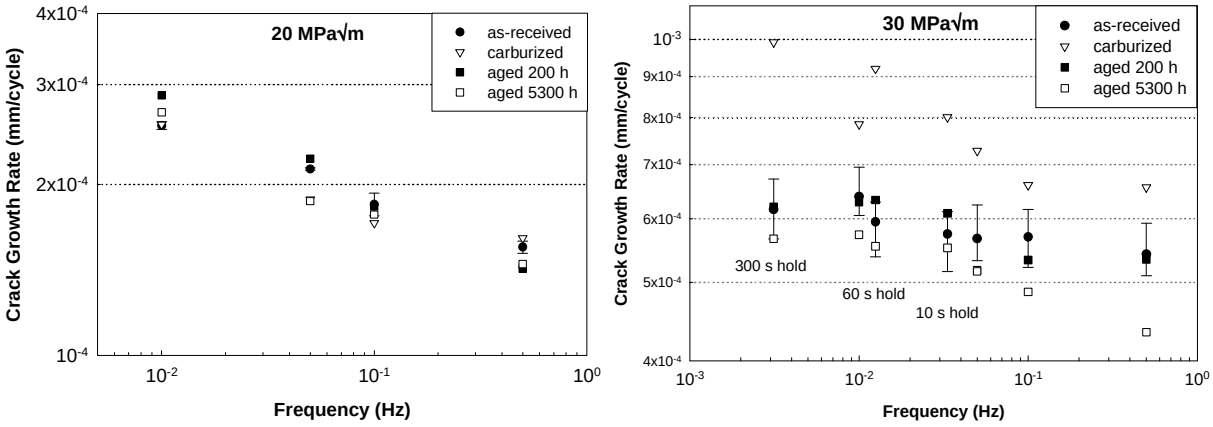

a b

The effect of environment on fatigue crack growth rates at 650°C is shown in Figure 15a. The results shown were all obtained at a stress intensity on 30 MPa√m and indicate that the crack growth rates in the prototypical VHTR impure helium environment are lower than those in air. Although oxygen is available in the impure helium environment from the H_2O vapour and CO gas, the oxygen concentration in air is obviously much higher and thus indicates the environmental enhancement of crack propagation is sensitive to oxygen partial pressure. This result is in concord with numerous studies of fatigue fracture in other nickel alloys [14,15]. The results of the carburised specimen are included in Figure 15a to highlight that the effect of corrosion in a carburising environment is more detrimental to the crack growth rates than increases in oxygen partial pressure. Fatigue crack propagation tests comparing the two environments were also completed at 800°C as shown in Figure 16. At an applied stress intensity of 10 MPa√m as shown in Figure 16a, the crack growth rates are lower in the impure helium environment when compared to air, similar to the results at 650°C. It should be noted that significant time dependent crack growth behaviour is apparent in impure helium in contrast to 650°C, whereas the rates in air indicate fully time independent propagation. Furthermore, the fatigue and hold time fatigue crack propagation eventually surpass those in air when the frequency is decreased sufficiently at 20 MPa√m as shown in Figure 16b. Due to kinetic considerations of oxidation and diffusion of oxygen near the crack tip damage zone, environmental degradation in the damage zone and enhancement of crack growth rates may only present itself at the higher temperature. Furthermore, formation of a protective oxide which prevents further oxygen ingress near the crack tip likely does not occur in the impure helium environment where there is not excess oxygen available.

Quasi static creep crack growth

Crack growth studies under quasi-static loading (i.e. creep) conditions were also completed at 650°C and a stress intensity of K = 40 MPa√m. These results are shown in Figure 15b. This plot shows an increase in creep graph growth rates in the characteristic VHTR impure helium environment compared to the air environment. This is likely due to the same degradation mechanism discussed in the previous section at very low fatigue frequency cycles. The fracture surface in Figure 17 indicates the crack propagation is primarily intergranular as shown by the faceted surface in both (a) air and (b) impure helium. Furthermore, significant secondary intergranular cracking perpendicular to the fracture plane is observed on the fracture surface in both air and impure helium. No dissimilarities were observed in the SEM examination which could explain the higher crack propagation rates in impure helium. Another feature to note in Figure 15b is the

increase in crack growth rate with time, which may be due to ageing of the material. Since the fracture surface is primarily intergranular under these conditions, ageing of the material could potential change the nature of the grain boundaries via mechanisms such as precipitation of brittle secondary phases on and adjacent to the grain boundaries giving rise to accelerated crack propagation. Also, environmental degradation mechanisms such as long range grain boundary oxidation and embrittlement could eventually cause accelerated brittle fracture of oxidised surfaces if oxygen is given enough time to migrate down fast diffusion paths (i.e. grain boundaries). A more likely explanation, however, is that the ageing of the material is changing the resistance of the material and thus affecting the voltage measurement through the specimen over long periods of time. Given that the crack growth measurement is based on the voltage measured in the DC potential drop system, increasing inaccuracies in the crack length may have arisen during testing. Also, soon after the load is applied, a small creep zone forms at the crack tip and then grows with time, eventually invalidating K as the crack tip parameter as noted before. This evolution of the crack tip creep zone would also offer an explanation as to the increase in crack growth rate with time.

Figure 15: Fatigue and creep-fatigue crack growth rates at 30 MPa√m and quasi static loading crack length vs. time at 650°C in different environments

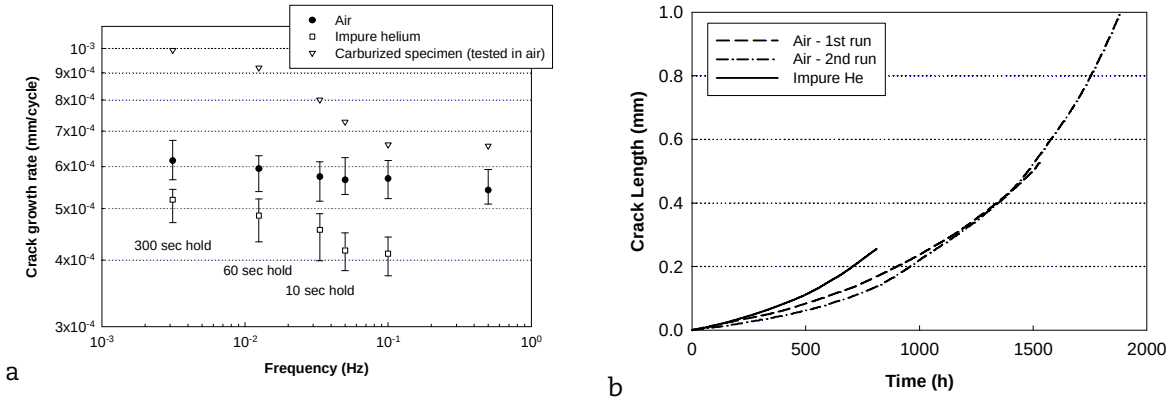

Figure 16: Fatigue crack propagation rates in air and impure helium at 10 and 20 MPa√m and 800°C

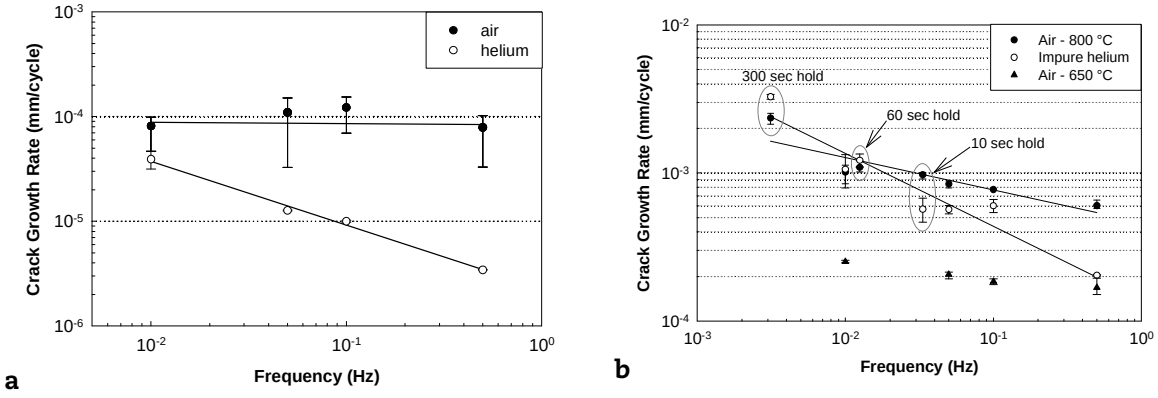

Figure 17: Intergranular fracture surfaces from tests completed in a) air and b) impure helium at 650°C

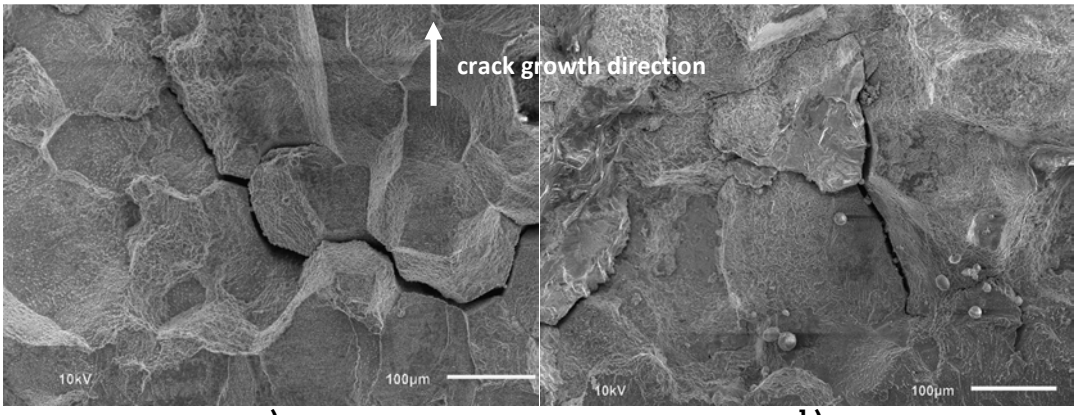

Conclusions

The fatigue, creep-fatigue, and quasi static loading (i.e. creep) crack propagation rates were studied extensively under varying conditions, including changes to starting material condition, environment, fatigue frequency and hold time, and temperature. The main results can be summarised as follows:

- The fatigue crack propagation at 650°C in air indicates time-dependent crack growth behaviour at all stress intensities evaluated due to environmental crack tip interactions, most likely oxidation, although fracture is primarily transgranular. The transition from time dependent to independent behaviour occurs at lower frequency as the stress intensity is increased.
- The higher concentration of oxygen in air results in increased crack growth rates when compared to the rates in prototypical VHTR impure helium at 650°C. However, material carburisation was found to be most detrimental to fracture resistance in Alloy 617, whereas specimen ageing demonstrated little effect on crack propagation rates.
- As frequency is decreased substantially at 800°C, the crack propagation rates in impure helium eventually surpass those in air which is not observed at the fatigue or creep-fatigue conditions tested at lower temperatures. Furthermore, the creep crack propagation rate under quasi static loading in impure helium is higher than in air at 650°C. A possible explanation is that a protective oxide which prevents further ingress of oxygen near the crack tip damage zone does not form in the impure helium environment, allowing for increased environmental degradation when compared to air. Kinetic considerations in regard to the environmental/material interaction could explain the observation of this mechanism at 800°C but not lower temperatures during fatigue type loading.

Acknowledgements

This work is supported by the U.S. Department of Energy, under DOE Idaho Operations Office Contract DE-AC07-05ID14517. Accordingly, the U.S. Government retains a nonexclusive, royalty-free license to publish or reproduce the published form of this contribution, or allow others to do so, for U.S. Government purposes. The authors would also like to thank Tom Lillo for the TEM analysis and Randy Lloyd for assistance with the crack propagation systems.

References

[1] Corwin, W.R. (2006), "US Generation IV reactor integrated materials technology program", *Nucl. Eng. Technol.,* 38[7], pp. 591-618.

[2] Smith, H.H., P. Shahinian, M.R. Achter (1969), "Fatigue Crack Growth Rates in Type 316 Stainless Steel at Elevated Temperature as Function of Oxygen Pressure", *Trans. Metall. Soc. AIME,* 245[5], pp. 947-953.

[3] McMahon, C., L. Coffin (1970), "Mechanisms of damage and fracture in high-temperature, low-cycle fatigue of a cast nickel-based superalloy", *Metall. Trans.,* 1[12], pp. 3443-3450.

[4] Rödig, M., R. Kienzler, H. Nickel, F. Schubert (1988), "Fatigue and creep crack growth in methane reformer tubes at temperatures above 700°C", *Nucl. Eng. Des.,* 108[3], pp. 467-476.

[5] Hsu, S.-S. (1993), "Time-dependent crack growth in a heat-resistant alloy Inconel 617", *J. Nucl. Sci. Technol.,* 30[4], pp. 302-313.

[6] Floreen, S., R. Kane (1979), "An investigation of creep-fatigue environment interaction in a Ni-base superalloy", *Fatigue Fract. Eng. Mater. Struct.,* 2[4], pp. 401-412.

[7] Pedron, J., A. Pineau (1982), "The effect of microstructure and environment on the crack growth behaviour of Inconel 718 alloy at 650 C under fatigue, creep and combined loading", Materials Science and Engineering, 56[2], pp. 143-156.

[8] Andrieu, E., R. Molins, H. Ghonem, A. Pineau (1992), "Intergranular crack tip oxidation mechanism in a nickel-based superalloy", Materials Science and Engineering *A,* 154[1], pp. 21-28.

[9] Bache, M., W. Evans, M. Hardy (1999), "The effects of environment and loading waveform on fatigue crack growth in Inconel 718", International Journal of Fatigue, 21, pp. S69-S77.

[10] Mankins, W.L., J.C. Hosier, T.H. Bassford (1974), "Microstructure and Phase-stability of Inconel Alloy 617", *Metall. Trans.,* 5[12], pp. 2579-2590.

[11] Kirchhofer, H., F. Schubert, H. Nickel (1984), "Precipitation behaviour of Ni-Cr-22 Fe-18 Mo (Hastelloy-X) and Ni-Cr-22 Co-12 Mo (Inconel-617) after isothermal ageing", *Nucl. Technol.,* 66, pp. 139-148.

[12] Wu, Q., H. Song, R.W. Swindeman, J.P. Shingledecker, V.K. Vasudevan (2008), "Microstructure of long-term aged IN617 Ni-base superalloy", Metallurgical and Materials Transactions *A,* 39[11], pp. 2569-2585.

[13] Ma, L., S.K. Roy, M. H. Hasan, J. Pal, S. Chatterjee (2011), "Time-Dependent Fatigue Crack Propagation Behaviour of Two Solid-Solution-Strengthened Ni-Based Superalloys-INCONEL 617 and HAYNES 230", Metallurgical and Materials Transactions *A,* 43A, pp. 491-504.

[14] Sadananda, K., P. Shahinian (1980), "The effect of environment on the creep crack growth behaviour several structural alloys", Materials Science and Engineering, 43[2], pp. 159-168.

[15] Molins, R., G. Hochstetter, J. C. Chassaigne, E. Andrieu (1997), "Oxidation effects on the fatigue crack growth behaviour of alloy 718 at high temperature", Acta Metallurgica, 45[2], pp. 663-674.

Technology readiness level (TRL) assessment of cladding alloys for advanced nuclear fuels

Daniel Shepherd
UK National Nuclear Laboratory (NNL), United Kingdom

Abstract

Reliable fuel claddings are essential for the safe, sustainable and economic operation of nuclear stations. This paper presents a worldwide TRL assessment of advanced claddings for Gen III and IV reactors following an extensive literature review. Claddings include austenitic, ferritic/martensitic (F/M), reduced activation (RA) and oxide dispersion strengthened (ODS) steels as well as advanced iron-based alloys (Kanthal alloys). Also assessed are alloys of zirconium, nickel (including Hastelloy®), titanium, chromium, vanadium and refractory metals (Nb, Mo, Ta and W). Comparison is made with Cf/C and SiCf/SiC composites, MAX phase ceramics, cermets and TRISO fuel particle coatings. The results show in general that the higher the maximum operating temperature of the cladding, the lower the TRL. Advanced claddings were found to have lower TRLs than the corresponding fuel materials, and therefore may be the limiting factor in the deployment of advanced fuels and even possibly the entire reactor in the case of Gen IV.

Introduction

Reliable fuel claddings are essential for achieving the safe, sustainable and economic operation of nuclear stations. Therefore, this paper presents a worldwide assessment of the technology readiness levels (TRLs) of cladding alloys for advanced nuclear fuels. The paper is aimed at highlighting the potential benefits of the various advanced fuel cladding alloys and their current status with regards to commercialisation. This assessment can be used to compare the different alloys and their ceramic competitors.

The assessment has considered both "evolutionary" claddings (i.e. improvements to existing commercial claddings) as well as radically different "revolutionary" claddings. The nuclear reactor systems that could deploy these advanced claddings include current Generation III light and heavy water reactors (LWRs and HWRs) in addition to the potentially revolutionary Gen IV systems which are aimed at generating nuclear energy in a significantly more sustainable and secure manner [1].

The goals of these systems can only be fully realised with the deployment of advanced fuel and cladding technology. Indeed for the Gen IV systems, the deployment of the entire reactor design is dependent on the development and qualification of advanced fuels and cladding technology in order to underpin its safe and efficient operation [1].

Method

Down-selection of advanced cladding materials

In order to conduct TRL assessments, it was first necessary to down-select candidate advanced fuel cladding alloys and ceramics for deployment in Gen III and IV systems. In

addition to those claddings most commonly suggested for deployment in these reactors, some materials currently of interest as fusion structural materials have also been down-selected, which have yet to be widely considered as cladding. This is because there has been a trend in recent years for advanced structural materials developed for fusion research programmes to be subsequently considered as cladding materials for fission systems, especially for Gen IV, but also for Gen III systems. In a similar vein, there has been a trend for some Gen IV cladding technologies to be postulated for application in Gen III reactors.

These down-selections were made by applying knowledge regarding the relevant systems. Fuel particle coatings and potential pipe-work/vessel materials for a Molten Salt Reactor (MSR) are considered alongside the more traditional cladding types, as they also function as a primary barrier to release of fuel material and fission products.

The down-selections are summarised below in order of approximate maximum operating temperature from low to high. This a useful measure of benefit as higher reactor temperatures allow for more thermodynamically efficient electricity generation. Higher temperatures also give the potential for direct heat use in a larger variety of chemical process applications (extraction of hydrogen gas from water is a particular goal of proposed Gen IV reactors with the highest operating temperatures [1]).

- **zirconium alloys**
  - standard
  - surface treated
  - advanced
- **steels**
  - ferritic/martensitic (F/M)
  - reduced activation (RA) F/M
  - surface treated F/M
  - standard austenitic
  - advanced austenitic
  - oxide dispersion strengthened (ODS) F/M
- **semi-refractory alloys**
  - advanced iron (Fe)
  - titanium (Ti) and titanium aluminide (Ti/Al) intermetallics
  - nickel (Ni)
  - hastelloys® (for MSR pipework)
  - vanadium (V)
  - chromium (Cr)
- **refractory alloy liners**
  - niobium (Nb), tantalum (Ta), molybdenum (Mo), tungsten (W)
- **ceramic-based**
  - MAX phase
  - cermets
  - SiCf/SiC
  - Cf/C
  - SiC TRISO fuel particle coatings
  - ZrC TRISO fuel particle coatings

Technology readiness levels (TRLs)

The TRL system is a means of measuring technology maturity, with a degree of standardisation, which allows for comparison between different technologies. Originally defined by Mankins (1995) of NASA [2], TRLs have become adopted by many industries around the world. As the technology matures from the lower TRLs to the higher TRLs, it

moves from a scientific idea through to a fully developed application that has demonstrated its usefulness by being deployed in the real world in an operational situation. Figure 1 illustrates where the development of technologies at different TRLs may be conducted to advance their TRL in a typical national technology supply chain.

Figure 1: TRLs and the national technology supply chain

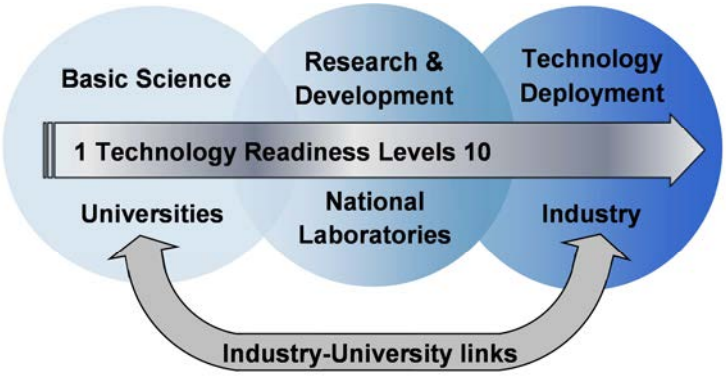

It should be emphasised that the NASA TRLs were defined for systems for individual space missions (often electronic) and the terminology is not always suitable for nuclear industry applications. Hayes and Porter (2007) of INL (Idaho National Laboratory) [3] reported an adaptation of the TRL system for application to fast reactor fuel.

There is some apparent inconsistency between the NASA and the INL definitions (which both have TRLs 1 to 9). For example, INL TRL 1 seems to correspond more closely with NASA TRL 2, due to INL not including basic principles research at the bottom of the scale. Furthermore at the top of the scale, INL TRL 9 could feasibly correspond to an assumed NASA TRL 10, if their definitions were extrapolated to operation of many actual systems as opposed to single missions. Therefore overall, the INL scale appears to be shifted down by one TRL with respect to NASA's.

For the cladding TRL assessments in this paper, a combined approach has been used that includes elements of both the NASA and the INL definitions. Some additional simplification and generalisation was also employed to allow a flexible approach to what is in reality a highly complex situation. Consistency has been maintained with the NASA scale, with TRL 1 still corresponding to basic principles research. In addition, aspects of the more precise INL approach have been incorporated including their guidelines regarding out-of-reactor/in-reactor testing, lead assemblies and core reloads. A TRL 10 has also been defined based on the INL TRL 9 to consider long-term operation of many actual systems. The TRL definitions used for this paper are presented in Table 1 using a "traffic light" colour coding that is employed throughout.

Assessing the TRL of the cladding material down-selections

For each down-selection, a literature search was performed seeking papers in peer-reviewed journals and reports produced by international nuclear organisations (IAEA, OECD/NEA, WNA) as well as the work of national nuclear institutions. Further information was sought where appropriate through attending various conferences and by contact with partners in the international nuclear community. Using this information, it was then possible to use the TRL definitions in Table 1 to assess the TRL of the down-selections.

The ascribed TRLs represent an international best case scenario for each technology with the TRL being representative of its most developed form in the country or countries that have progressed it to the greatest extent. These international TRLs do not necessarily equate to the TRL applicable to individual countries. The assessment also considered TRLs with respect to the reactor type/s for which the cladding is most developed. A lower TRL would apply to the use of the same cladding in a different reactor type.

Table 1: TRL definitions for nuclear fuels and claddings

TRL	Definition and description
10	Widespread, reliable and long-term operation of many actual systems e.g. long-term use of a fuel within a commercial reactor fleet/fleets with many thousands of hours of operating experience and data
9	Successful operation of actual system e.g. assemblies have performed successfully under irradiation in reload quantities (demonstrated by surveillance programme)
8	Actual system constructed and commissioned e.g. assemblies fabricated in reload quantities, may include irradiation with only limited success
7	Prototype successfully demonstrated e.g. lead use assemblies have performed successfully in a prototype or commercial reactor (demonstrated by PIE and/or in-core monitoring)
6	Prototype construction (much more representative than the basic system) e.g. lead use assemblies have been fabricated, and potentially irradiated in a prototype or commercial reactor but with only limited success
5	Basic system successfully demonstrated e.g. test rods have been irradiated and performed successfully in a test reactor (demonstrated by in-reactor instrumentation and/or post irradiation examination (PIE) and/or post irradiation mechanical testing)
4	Integration of components into a basic system e.g. representative assembly sections have been manufactured and subjected to out-of-reactor tests and/or test reactor irradiation trials of individual rods have been conducted with only limited success
3	Basic components fabricated and successfully demonstrated e.g. fuel and/or cladding components have been manufactured and tested out-of-reactor and/or irradiated as a component only
2	Practical applications suggested and concepts formulated e.g. fuel, cladding and/or fuel assembly designs have been established
1	Research identifies the basic principles that underlie the technology e.g. promising materials and/or geometry have been identified

Table source: This table represents an amalgamation of those presented in [2] and [3]

Limitations of TRL assessments

It should be emphasised that a TRL assessment is at best a crude measure of a complex and ever changing international technological situation. Interpretation and use of the definitions in a TRL assessment is inevitably somewhat subjective and challenging to apply consistently.

TRL assessment also gives no indication of the amount of time/effort/cost required to increase a technology's TRL. For example, if two technologies are currently at the same TRL, then there is no guarantee that these will continue to be developed successfully at the same rate. Indeed a technology currently with a lower TRL may reach deployment sooner than another technology which currently has a higher TRL due to increased R&D effort, fewer feasibility issues etc. Importantly, there is no guarantee that any technology will ever reach the highest TRL as it may ultimately be found to be unfeasible during further development.

In spite of these limitations, a TRL assessment may still prove useful as a guide for further study. It should be noted that TRL values are potentially more useful for comparisons between technologies than they are when considered individually as absolute values. TRLs themselves give no indication of the relative benefits of the different technologies if they were fully deployed, though this weakness can be overcome by plotting TRLs against appropriate measures of benefit.

Results

The full details of the TRL assessment of each cladding material down-selection are given in an NNL report produced for the UK Department of Energy and Climate (DECC) [4]. Details include a full description of each material and its benefits, a full written justification for each ascribed TRL, and the most important literature references (typically

4-8 per technology). A summary of the assessments from the full report is given in this paper using the same "traffic light" colour coding as Table 1.

Table 2 gives the ascribed international best case TRLs for the down-selected cladding materials alongside a brief justification and a key reference. Figure 2 then plots these international best case TRLs against their approximate maximum operating temperature from low to high.

Table 2: International best case TRL assessments for advanced claddings

Advanced cladding categories *In order of approximate maximum operating temperature (low to high)*		**Best case TRL**	**TRL Justification and Key Reference**
Zirconium	Standard alloys	10	Used in PWR, BWR and HWR stations worldwide for many years [5].
	Surface treated	3	Some development in Republic of Korea, United States and Russia [6].
	Advanced alloys	8	New products from United States, France, Russia and Japan nearing market [5].
Steels	F/M	7	Successful cladding in a number of prototype SFRs [7].
	RA F/M	3	Extensive development by fusion programme. Qualification in its infancy for fission reactors [8].
	F/M surface treated	3	Development and testing being driven by LFR programmes [9].
	Standard austenitic	8	Past standard LWR clad material that would require updating to modern standards to use once more [10].
	Avanced austenitic	8	Moderate success in large SFRs (BN600 in Russia, Superphenix in France) [7].
	ODS F/M	4	Moderately successful tests of Russian and Japanese rodlet claddings in a basic SFR [7].
Semi-refractory alloys	Advanced Fe	3	Fe-Cr-Al Kanthal alloys being tested for LWR cladding application [10].
	Ti and Ti/Al intermetallic	1	Some development of Ti [11] and Ti/Al [12] for fusion programmes. Yet to be widely considered for fission.
	Ni	7	Tested successfully in UK and US fast reactors in 1970s-1990s [13].
	Hastelloys	5	Pipework in US Molten Salt Reactor Experiment (MSRE) in 1960s with reasonable success [1].
	V	4	Tested as liner in UK fast reactor in 1950s-1960s with limited success [14]. Extensive development of new alloys by fusion programme [15].
	Cr	2	Currently only a few fuel concepts. Very limited irradiation data [16].
Refractory alloy liners	Nb, Ta, Mo & W	4	Tested in fast reactors in 1950s-1980s with limited success (US space reactor programme) [17].
Ceramic-based	MAX phase	2	Capability first discovered in the 1990s. Now a few concepts and first irradiation trials are underway [18].
	Cermets	2	Currently only a few fuel concepts for various reactors [19].
	SiCf/SiC	3	Leading candidate for GFR application and now considered for LWR, SFR and LFR. Extensive development by fusion programme [20].
	Cf/C	2	Some consideration for fission applications. Extensive development by fusion programme [21].
	SiC particle coatings	8	SiC coatings performed successfully in attempted commercial HTRs in Germany and United States. Current programmes in China and Japan [22].
	ZrC particle coatings	6	Needed for VHTR. Irradiation programmes underway in HTR prototypes with some success [22].

Figure 2: Advanced clad TRLs vs. approximate maximum operating temperature

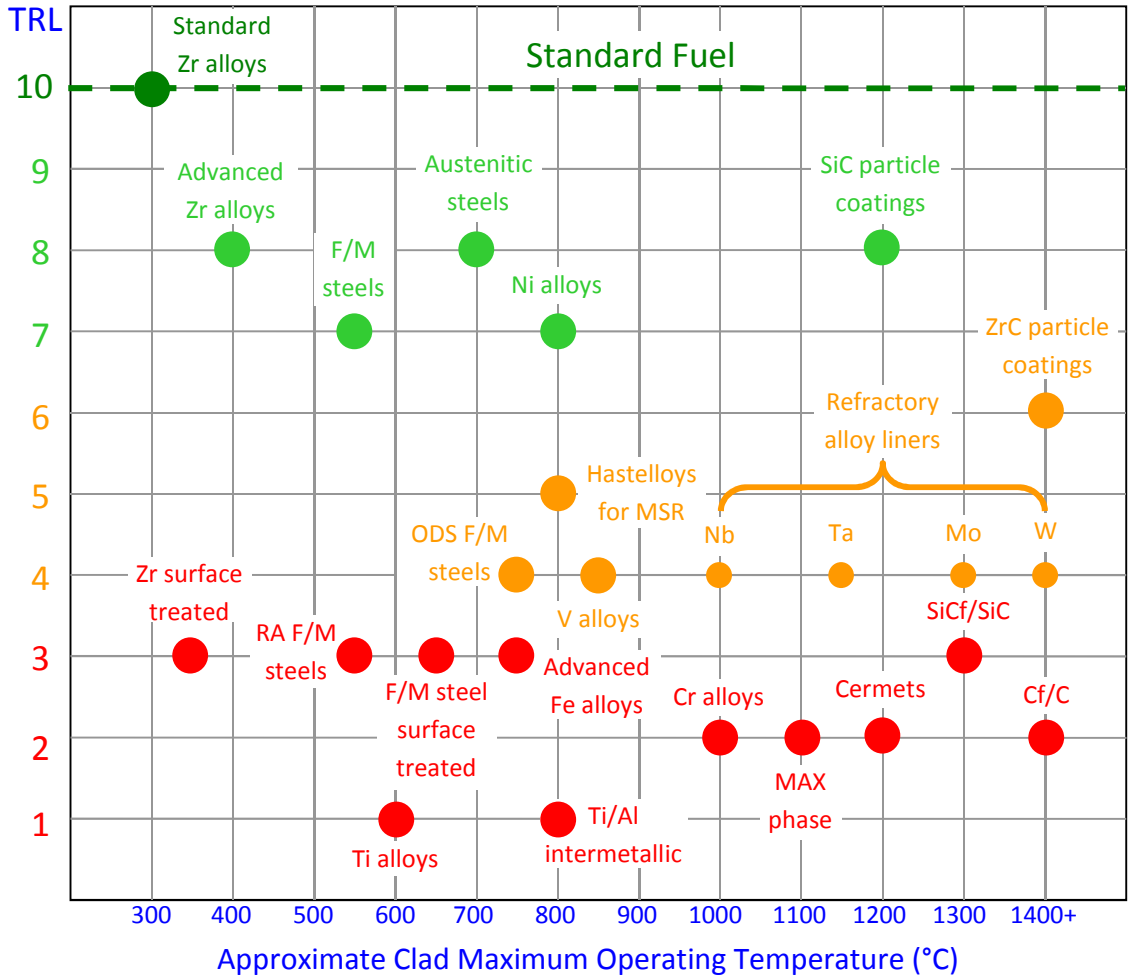

Finally, Table 3 shows which reactor types the cladding materials are relevant to and gives TRLs with respect to each. The reactor types considered are Gen III reactors (LWRs and HWRs) and the six Gen IV systems as listed below [1]:

- **SFR**, **LFR** & **GFR** - sodium, lead & gas-cooled fast reactor respectively.
- **HTR/VHTR** – high- and very-high-temperature reactor.
- **SCWR** - supercritical water reactor.
- **MSR** - molten salt reactor.

Discussion

It can be seen from Table 2 and Figure 2 that in general as the maximum operating temperature of the potential cladding materials increases, the TRL decreases. Therefore Zr alloys have the highest level of technology readiness followed by steels. Refractory and semi-refractory alloys with the exception of nickel alloys have low technology readiness as do ceramic cladding tubes. This was in line with pre-assessment expectations given the revolutionary nature of the materials with the highest potential operating temperatures.

Table 3: TRLs of advanced clads vs. reactor systems

In order of approximate maximum operating temperature (low to high)	**Generation**	**III**	**IV**					
	Reactor	**LWR/ HWR**	**SFR**	**SCWR**	**LFR**	**MSR**	**GFR**	**HTR/ VHTR**
Advanced clad categories	**Outlet temperature**	~325°C (PWR)	550°C	510 – 625°C	480 – 800°C	700 – 800°C	850°C	650 – 1 000°C
Zirconium	Standard alloys	10				Grey indicates that the material is not relevant to the reactor type		
	Surface treated	3		2				
	Advanced alloys	8		3				
Steels	F/M		7		4			
	RA F/M		3	3	3			
	F/M surface treated			2	3			
	Standard austenitic	8 (former standard)	6	3	4		3	
	Advanced austenitic	6	8	3	4		3	
	ODS F/M		4	2	3		3	
Semi-refractory alloys	Advanced Fe	3	2	2	2	2		
	Ti and Ti/Al intermetallic	1	1	1	1			
	Ni		7	3			3	
	Hastelloys					5		
	V		4		2		3	
	Cr	2	2	2	2		2	
Refractory alloy liners	Nb, Ta, Mo & W		4		3		3	
Ceramic-based	MAX phase	2	2	2	2		2	
	Cermets		2		2		2	
	SiCf/SiC	3	3	2	3		3	
	Cf/C	1	1	1	1		2	
	SiC particle coatings						3	8
	ZrC particle coatings						2	6

Notable exceptions to this trend are the SiC and ZrC TRISO fuel particle coatings which have attained reasonably high TRLs in HTR/VHTR programmes. It might be anticipated therefore that these non-traditional cladding forms will be deployed significantly in advance of traditional tube-shaped claddings for such high temperatures. Table 3 shows the diverse and complex relationship between cladding TRLs and reactor types. However, the same general inverse relationship between TRL and operating temperature applies with the same notable exception of HTR/VHTR. It is also evident that the TRLs for individual cladding technologies are higher for just one or two reactor types and much lower for the others. Indeed, for four out of the six proposed Gen IV reactor types the cladding TRL is no higher than 5 at best.

Conclusions

A significant level of further development of advanced claddings will be required before commercial use is possible. Many have TRLs within the usual development range of national laboratories and universities (TRL 7 and below), which suggests that these organisations will need to play a crucial role in bringing them to industry readiness. When compared with a similar TRL assessment of advanced fuels [4], it was found that the corresponding claddings often had a lower TRL. Therefore cladding development may be the limiting factor in the development of new fuel designs, and crucially this may in turn limit the deployment of advanced reactor systems. Therefore, further international development of cladding technology needs to be pursued urgently as an integral part of future advanced reactor and nuclear fuel cycle development programmes.

Acknowledgements

This work has been funded by the UK Department of Energy and Climate Change (DECC) under an "Initial UK National Nuclear R&D Programme". The author would also like to thank the following for their assistance:

- **NNL** – Walter Weaver, Glyn Rossiter, Dr. Glyn Marsh, Ian Palmer, Matthew Fountain, Andy Nickson, Dr. Emma Johnston, Alex Brooke, Dan Mathers, Paul Glenville, Robbie Gregg, Mike Thomas, Kevin Hesketh, Dr. Richard Stainsby, Carol Bullen, Paul Smith and Keith Miller.
- **Others** – Dr. Megan Cooper and Rob Arnold of DECC, Prof. Tim Abram, Aiden Peakman, Joel Turner, Matthew Gill, Dr. Maria-Luisa Gentile of Manchester University; Maxime Zabiego, Marion Le Flem, Christian Poette of CEA; Lars Hallstadius and Ed Lahoda of Westinghouse; Prof. James Marrow and Prof. Steve Roberts of Oxford University.

References

[1] US DOE and GIF (2002), "A Technology Roadmap for Generation IV Nuclear Energy Systems", GIF-002-00.

[2] Mankins, J.C., NASA (1995), "Technology Readiness Levels", NASA White Paper, 6 April.

[3] Hayes, S.L. and D.L. Porter, INL (2007) "SFR Fuel Performance and Approach to Qualification", Presentation to DOE/NRC Seminar Series on Sodium Fast Reactors, 27-28 November.

[4] Shepherd, D. et al., NNL (2013) "Technology Readiness Level assessment of advanced fuels, cladding and associated manufacturing technology", NNL (13) 12502.

[5] Lemaignan, C., CEA (2012), "Zirconium Alloys: Properties and Characteristics", Comprehensive Nuclear Materials, Elsevier, ISBN 978-0-08-056033-5, R.J.M. Konings (Editor), Volume 2.07, pp. 217-232.

[6] Ivanova, S.V. et al., MEPhI and partners (2010), "Methods to Increase Operation Properties of Zirconium Components for New Generation LWR Active Cores", LWR Fuel Performance Conference, 26-29th September 2010, Orlando Florida, United States, Proceeedings, Paper 120, pp. 587-593.

[7] IAEA (2012), "Structural Materials for Liquid Metal Cooled Fast Reactor Fuel Assemblies – Operational Behaviour", IAEA Nuclear Energy Series, No. NF-T-4.3, ISBN 978-92-0-131610-3.

[8] Jones, R.H. et al., PNNL and INL (1999), "Low activation materials", Journal of Nuclear Materials, 271 and 272, pp. 518-525.

[9] Takaya, S. et al., JAEA and partners (2012), "Al-containing ODS steels with improved corrosion resistance to liquid lead-bismuth", Journal of Nuclear Materials, 428, pp. 125-130.

[10] Terrani, K.A. et al., ORNL (2013), "Advanced Oxidation-Resistant Iron Alloys as LWR Fuel Cladding", Enlarged Halden Programme Group Meeting, 10-15 March 2013, Gol, Norway, Proceedings, HPR-378-1, pp. 215-221.

[11] Bilobrov, I. and V. Trachevsky, NASU (2011), "Approach to modify the properties of titanium alloys for use in the nuclear industry", Journal of Nuclear Materials, 415, pp. 222-225.

[12] Hishinuma, A., JAERI (1996), "Radiation damage of TiAl intermetallic alloys", Journal of Nuclear Materials, 239, pp. 267-272.

[13] Rowcliffe, A.F. et al., ORNL (2009), "Perspectives on radiation effects in nickel-base alloys for applications in advanced reactors", Journal of Nuclear Materials, 392, pp. 341-352.

[14] Sinclair, V.M., UKAEA (1961), "Canning materials for D.F.R. fuel elements", UKAEA TRG Memorandum 178.

[15] Chen, J.M. et al. (2011), Southwestern Institute of Physics Chengdu China and partners, "Overview of the vanadium alloy researches for fusion reactors", Journal of Nuclear Materials, 417, pp. 289-294.

[16] Le Flem, M. et al., CEA (2011), "Advanced Materials for Fuel Cladding in Sodium Fast Reactors: From Metals to Ceramics", Presentation to 3rd MATGEN Summer School, 19-23rd September 2011, Lerici Italy.

[17] Cox, C.M. et al., Hanford Engineering Development Laboratory (1984), "Fuel Systems for Compact Space Reactors", HEDL-SA-3065-FP.

[18] Hoffman, E.N. et al., SRNL and partners (2012), "MAX phase carbides and nitrides: Properties for future nuclear power plant in-core applications and neutron transmutation analysis", Nuclear Engineering and Design, 244, pp. 17-24.

[19] Le Flem, M. et al., CEA (2008), "Microstructure and thermal conductivity of Mo-TiC cermets processed by hot isostatic pressing", Journal of Nuclear Materials, 380, pp. 85-92.

[20] Snead, L.L. et al., ORNL (2013), "An Overview of SiC-Based Fuel and Cladding Technologies in Support of Accident Tolerant Fuel Development", Enlarged Halden Programme Group Meeting, 10-15 March 2013, Gol (Norway), Proceedings, HPR-378-1, pp. 203-213.

[21] Venugopalan, R. et al., BARC (2010), "Neutron irradiation studies on low density pan fibre based carbon/carbon composites", Journal of Nuclear Materials, 404, pp. 19-24.

[22] IAEA (2010), "High Temperature Gas Cooled Reactor Fuels and Materials", IAEA-TECDOC-1645.

Section III

Novel pathways

Chair: J.-Y. Park

PM-HIP research for structural and pressuring retaining applications within the electric power industry

David W. Gandy, FASM
Electric Power Research Institute, United States

Abstract

For more than 60 years now, the nuclear power industry has relied on structural and pressure retaining materials generated via established manufacturing practices such as casting, plate rolling-and-welding, forging, drawing, and/or extrusion. During the past three years, EPRI has been leading the development and introduction of another established process, powder metallurgy and hot Isostatic pressing (PM/HIP), for pressure retaining applications in electric power industry. The research includes assessment of two primary alloys: 316L stainless steel and Grade 91 creep-strength enhanced ferritic steels, for introduction into the ASME Boiler and Pressure Vessel Code. Continuing DOE and EPRI research on other structural/pressure retaining alloys such as Alloy 690, SA 508 Class 1, Alloy 625, hard-facing materials, and others are also underway. This research will have a tremendous impact as we move forward over the next few decades on the selection of new alloys and components for advanced light water reactors and small modular reactors. Furthermore, fabrication of high alloy materials/components may require the use of new manufacturing processes to achieve acceptable properties for higher temperature applications such as those in Generation IV applications. Current research by EPRI and DOE will be reviewed and emphasis will be targeted at advanced applications where PM/HIP may be applied in the future.

Introduction

Powder metallurgy (PM) technology integrated with advanced modelling/design capabilities, and state-of-the-art hot isostatic processing (HIP) technology, can have a significant impact on the energy industry's goal of increased efficiency, a reduction of emissions, and lower installation and operating costs. The manufacturing of large and complex components with PM/HIP technology can provide an alternative method to current processes such as forging, plate rolled and welded, and casting. Benefits of making near net shapes (NNS) via PM-HIP includes precise chemistry control on any stainless steel or nickel/cobalt alloy, increased material utilisation, elimination of welding, and improvement in inspectability.

This paper is separated into four parts: 1) initial feasibility assessment – valve body design and production, 2) manufacture of valve bodies from 316L SS and Grade 91 Steel, 3) DOE Nuclear Energy Enabling Technology (NEET) Project, 4) Vision for the Future. The first part highlights a 2010 feasibility assessment performed by EPRI to assess PM-HIP as a potential technology for the pressure retaining components (nuclear and fossil). The second part highlights the manufacture, testing, and subsequent ASME Code Case development for two alloys: 316L SS and Grade 91 steel. Part III reviews an ongoing DOE project under the NEET initiative that focuses on design, processing, manufacturing, and validation studies to assess PM-HIP as a viable method for the production of very large near-net shaped components that incorporate erosion/corrosion resistant surfaces for

nuclear applications. The final section of the paper provides a clear, concise vision regarding what developments are required to enable the PM-HIP process to be fully integrated into use for nuclear energy applications.

Background

PM technology would minimise or eliminate many of the current issues associated with microstructural and mechanical property uniformity, welding difficulties, heat treatment problems, and inspectability in large components. It would also provide an ideal path for manufacturing, addressing a short-term need for domestic fabrication of complex components. In addition, the PM technology would increase material utilisation (hence reducing energy utilisation on a per component basis), reduce machining operations, and *significantly reduce* manufacturing and delivery times. PM technology could allow the use of new alloy systems with high temperature strength, creep resistance, and corrosion/erosion resistance that will enable power generation systems to operate at higher temperatures and pressures and for longer periods of time, which will measurably increase plant efficiency and availability. Once accepted, PM technology would provide addition longer-term transformation opportunities by custom tailoring alloy compositions or manufacturing bi-metallic components for specific applications.

Considerable research has been completed over the last decade to characterise PM/HIP for potential use in nuclear applications. Specifically, Rolls Royce has produced a number of research papers surrounding the development of data for 316L stainless steel to be used in nuclear components as reported in References 1-5. Their research has shown that 316L SS components (thick section tees, large valves, valve seat inserts, and thin-walled toroids, etc.) can be effectively produced with the PM/HIP process resulting in high quality components with superior mechanical and microstructural properties. Rolls Royce has also explored the use of Inconel 600 and 690 powders for component manufacture as described in Reference 6.

Carpenter Technology, in addition to supplying gas atomised powder for many PM/HIP applications, has evaluated consolidated PM components for properties, corrosion resistance, etc. manufactured from stainless steels, borated stainless steels, duplex stainless steels and various high temperature alloys. In all cases the PM materials met or exceeded the capabilities of cast or cast and wrought materials. Examples are illustrated in References 7-12.

Research has also been undertaken by the VTT Technical Research Centre of Finland and Helsinki University [13,14]. Their research includes manufacture and assessment of duplex stainless steels for paper machine roll applications, nitrogen containing austenitic stainless steels for wear applications, 316LN austenitic stainless steels for light water reactor applications, and investigation of ODS alloys.

ASTM currently recognises two standards for producing HIP alloy (ASTM A989) and stainless steel (ASTM A988) flanges, fittings, valves, and parts both for high temperature service applications [15,16].

Other documents will also be of considerable interest to the reader. The first document is an EPRI report [17] that summarises much of the research identified in this paper. References 18-21 provide additional background on the EPRI research conducted to date. The second is an introduction to PM-HIP assembled by the European Powder Metallurgy Association – EMPA [22]. References 17 and 22 are excellent resources for the reader who wants to learn more details about the PM-HIP process.

What is powder metallurgy?

Powder metallurgy is a forming and fabrication technique that consists of multiple stages which include: 1) component design, 2) manufacturing of a metallic powder normally by

gas atomisation, 3) loading of the powder into a can or container, 4) degassing and sealing the can with the contained powder, and 5) consolidation (HIP) by applying high temperature and pressure. HIP is a solid state diffusion process that produces fully dense microstructures with no porosity.

Component design

Component design includes creation of a 3-D model for the component. With this model, a can or container that replicates the final component can be produced to contain the powder (more on this subject below). It is also important to point out that component design includes alloy design. With the PM/HIP process, the manufacturer is able to target a specific composition wherein they may control specific elements such as boron, carbon, or various tramp elements.

Powder atomisation

Powders are routinely manufactured today through a process known as gas atomisation. In this process, a material is induction melted at a high temperature and forced through an orifice (nozzle) at moderately high pressures (Figure 1). A gas is introduced into the molten metal stream just as it leaves the nozzle, creating significant turbulence as the entrained gas expands (from heating). At this point the gas exits into a large collection volume outside of the orifice. The collection volume is filled with gas to promote further turbulence of the molten metal. Gravity or cyclonic separation is used to separate the resulting spherical powder particles of varying sizes and air or gas. The resulting powders are then screened to remove oversized particles and blended to produce a uniform powder size distribution for the intended use. It is important to point out that powder atomisation produces considerably higher quality powders than those produced through powder milling operations. As such, oxidation issues associated with earlier PM/HIP processes are significantly reduced and in many cases eliminated entirely.

Canning or container

The third step in the PM/HIP process is the manufacture of a can (container) which is used to contain the atomised powder during processing. The can is manufactured to a size slightly greater than the component using the 3-D component design drawings established at the beginning of the process. Metallic containers, usually made from thin gauge carbon steel which are welded together, are most often used for the production of large components.

Powder consolidation, vacuum processing, and hot isostatic processing

After the mold or container is completed, the powder is packed into the mold/container and brought to temperature under a high vacuum to consolidate and densify the powder. This process involves simultaneous application of high isostatic pressure and heat ranging from 500 to 1 200°C (900 to 2 200°F) to compress and consolidate the powder within the mold. The process is normally conducted under an inert gas atmosphere and pressures can range from 7 000 psi to 45 000 psi, with 15 000 psi being the most common.

Why consider PM-HIP for large nuclear components?

Large power generation components are commonly fabricated by conventional “tried-and-true” metallurgical processing methods including: casting, rolling, drawing, forging, extrusion, welding, and heat treatment. These processes have been used to fabricate components all the way back until the early part of the 20th century. As materials processing practices have improved over the years, higher quality components have also resulted such as superclean forged rotor and disc steels, directionally solidified and single crystal blade alloys, controlled residual element alloys, creep-strength enhanced ferritic piping/headers, improved component surfacing techniques, etc. One area that has seen remarkable improvements in processing technology is powder metallurgy where component quality, availability, and size have increased dramatically within the past 25 years.

Powder production facilities currently exist to manufacture large quantities of powder for high-quality alloy steels, stainless steels and nickel base alloy parts. Hot Isostatic Processing (HIP) facilities are also available to manufacture large near-net shaped components, which have been demonstrated to a limited extent for specialised aerospace, oil exploration, tools, and other niche applications. High quality components showing good structural uniformity, no segregation, superior mechanical properties, and ease of inspectability have been produced from a number of stainless steels and nickel base alloys.

Large PM produced components have not been utilised in the power generation industry to date primarily due to three technical barriers:

- Materials and processes utilised to manufacture pressure retention or high-temperature power plant components are generally subject to, in the United States, the ASME boiler and pressure vessel code. Until recently, ASME would not allow the use PM produced components for pressure retaining applications (more on this subject in later sections of this paper).
- The sizes and shapes for near-net shaped components have only recently reached a point for consideration and have not been tailored for the compositions/alloys that are of most interest to the industry.
- For iron-based steels alloy systems, the PM/HIP production route is generally more expensive than traditional forging and casting routes. However, for stainless steels and nickel-based alloys, where raw material costs are much higher, PM/HIP appears to be a cost effective solution.

These barriers are slowly being overcome with focused research and effort by EPRI, DOE, PM-HIP vendors, equipment manufacturers, and through support by utilities. EPRI, in conjunction with Carpenter Technology Corporation, has set out to explore how and where PM technologies might be brought to the power industry. PM technologies exhibit several attributes that make them attractive to the power industry. These include:

- Elimination of inspectability issues and concerns.
- Enables manufacture of large, complex components using near-net shape technologies.
- Enables new alloys systems & targeted chemistries.
- Enhances weldability.
- Alternate supply route for long-lead time components.
- Elimination of re-work or repair of large cast components.

Each of these are explored more fully in the following paragraphs.

Inspectability

Inspection of large cast components including pump housings, valve bodies, elbows, flanges, sweepolets, steam chests, turbine casing shells, nozzles, canister plugs, etc. is challenging due to the non-homogenous microstructure within castings. Castings can contain voids, pockets, segregation of tramp elements, inclusions, hot tears, secondary phases, non-metallic particles, among others. These irregularities in the microstructure make inspection of cast components difficult. The use of PM to produce alloys and components results in a very uniform, homogenous microstructure that is considered very inspectable in terms of both detection and sizing.

Near-net shaped (NSS) components

One of the highly desirable attributes of producing components via PM/HIP processing methods is the ability to produce components in a near-net shaped condition which required only minimal machining and clean-up. Cast components are commonly fabricated in an “oversized” condition to allow for irregularities that may occur along the length of the component. Components produced with PM/HIP can be produced very near final shape, resulting in reduced component weight, reduced machining, and ultimately

saving dollars in the overall production of the component. Production by NNS technologies also reduces energy and processing waste during the fabrication process.

New alloy systems and chemistries

Another attribute of PM/HIP processing methods is the ability to alter (or design) the chemistry of a specific component on a component-by-component basis. No longer will a melter/fabricator have to produce a large (several ton) heat of material to fabricate an individual component. Fabricators will now be able to produce individual components (or heats of material) using a specified chemistry. Furthermore, PM/HIP technologies now enable the production of new alloy system. For example, if one wants to control a particular element such as boron or carbon or a residual element such as sulfur or phosphorous, PM/HIP allows for specific control of one or more of these elements.

Enhanced weldability

Cast components are often difficult to weld due to the irregularities in microstructure of the component. Even within one specific alloy system (or materials specification), the weldability of a cast component can vary greatly. The homogeneity of PM/HIP produced alloys eliminate the weldability concerns almost entirely. Once a particular chemistry has been selected, it can readily be reproduced over and over with minimal differences in weldability.

Alternate supply route for long-lead time components

As we enter the era of new plant building within advanced nuclear and fossil generation, long lead-times are commonly encountered since only a limited number of manufacturers are available to produce components for the power industry. Introduction of PM/HIP technologies within the ASME BPV Code will allow utilities to gain improved access to components providing an alternate supply route for components. Manufacturing times will be significantly decreased and overall costs will be reduced.

Elimination of rework or repair of large cast components

One additional attribute of PM/HIP technology that cannot be overlooked is its ability to produce homogeneous microstructures which substantially reduces the number of repairs required in castings. In discussions with various valve manufacturers, it is not uncommon for large cast components to require between 10-50 percent repairs to eliminate casting defects depending on the casting house used. This represents considerable rework and overall lifecycle cost to the manufacturer, which is often not taken account of in the purchase of the casting. Such findings also bring into question the integrity of cast components which leads to overdesign in many cases. PM/HIP can eliminate the need for this rework.

As can be seen from the many potential advantages/attributes described above, PM technologies are ripe for the power industry to consider. The feasibility study and the subsequent work described herein were initiated with this consideration in mind.

Part I: Initial feasibility assessment – valve body design and production

The initial feasibility assessment involved the production of a 316L stainless steel valve body. A general valve body design of a 12-inch diameter valve was provided to Carpenter Technology Corp. for the production of the demonstration valve. A sectional drawing of the valve body is provided in Figure 1.

Upon completion of the container (or can design), the powder was introduced into the container and the component was HIPed. The resulting component is provided in Figure 2. The valve body was provided in the annealed condition and weighed 780 kg (1 716 lbs). Upon receipt of the valve body from Carpenter Technology Corp., EPRI provided the component to its inspection team for characterisation.

Figure 1: Sectional drawing of a 316L stainless steel valve body used as a demonstration piece in this feasibility assessment (dimensions in mm)

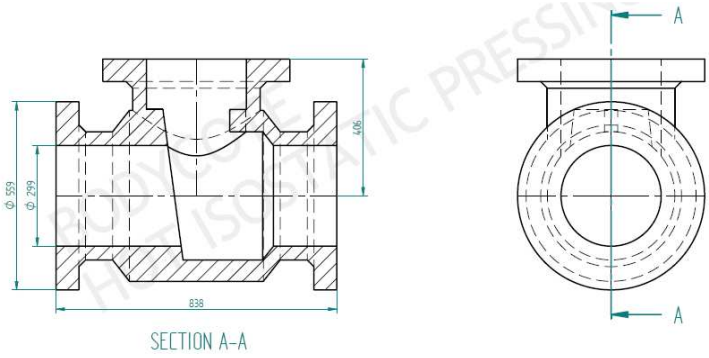

Figure 2: A 780kg (1716 lbs), 316L prototype stainless steel valve body produced during the feasibility assessment. The valve body was sectioned along its center line to reveal its ability to produce a sound, dimensionally stable, component configuration

Inspection

Upon receipt of the PM manufactured valve body, the valve body was photographed and marked for inspection validation. The inspection assessment involved both manual and automated ultrasonic techniques aimed at detection and sizing of various flaws embedded into one of the outboard flanges. Both longitudinal and shear wave assessment techniques were employed using a 1.5 MHz transducer. A total of 6 flaws were inserted into the flange using electro-discharge machining (EDM) techniques. A composite of the embedded flaws is provided in Figure 3. Figure 4 pictorially shows the operators performing manual and automated inspection of the valve body.

Figure 3: Inspection flaws installed at various locations around the diameter of the one flange from the valve body

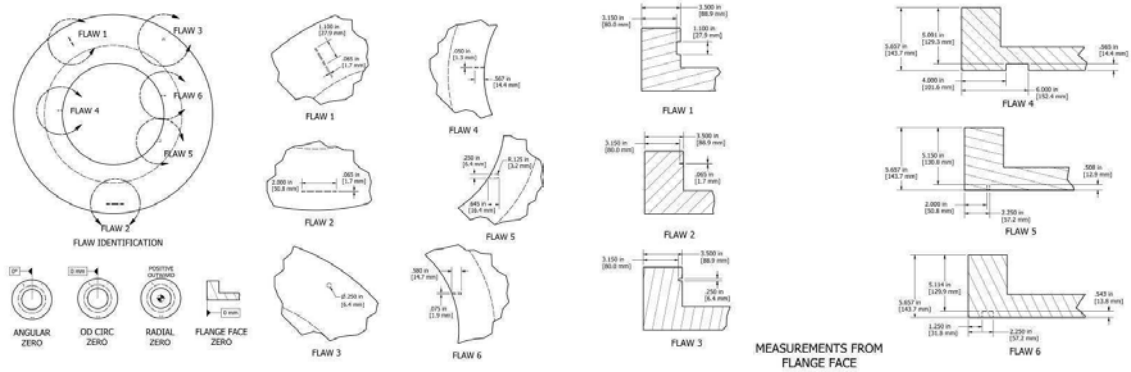

The results of the inspection testing determined that the valve body was highly inspectable and presented no inspection challenges to the ultrasonic inspection process. Similar studies using these standard non-destructive evaluation (NDE) techniques on cast 316 stainless steel have shown the material to be un-inspectable.

Figure 4: Photographs showing manual and automated inspection of the valve body in process

Weldability

Another factor that was considered paramount for consideration of components manufactured from PM/HIP is weldability. No welding was completed on the actual valve body manufactured in this feasibility assessment; however, several test coupons (3 in all) were produced using PM/HIP to the 316L stainless steel specification. Three 12-inch diameter, 1 foot long 316L SS coupons were manufactured and then sectioned for weldability tests. Autogenous and multiple pass welds were applied to the surface of the coupon slices. The PM/HIP plates provided comparable welding characteristics to that of a typical forged stainless steel component.

Valve body assessment – Mechanical and metallographic characterisation

Mechanical testing and metallographic characterisation were performed upon completion of the inspection characterisation performed by EPRI's NDE Center. The testing began with sectioning of the valve body along its center line (Figure 3). The sectioned valve body provides some perspective on the ability of the process to produce intricate shapes and configurations. It should be noted that no finish machining was performed on the part and that the external and internal shapes and surface finish were obtained from the PM/HIP process. Additional sectioning was performed to remove one of the flanges for mechanical testing and metallographic characterisation.

Metallographic characterisation

Characterisation of the microstructure was performed along three different directions to ascertain the uniformity in structure along all directions as shown in Figure 5. The homogeneity of the structure within these three directions is shown in Figures 5a through 5c at a magnification of 200X. Note that little difference exists in the three different views along each of the three directions. The microstructure was predominately austenitic with some isolated carbides observed throughout the matrix. The grain size of the specimens was also recorded for each orientation. An ASTM grain size of 6-7 was measured for each which is consistent with that of a solution heat treated stainless steel alloy.

Figure 5: Photomicrographs of the valve body microstructure along three different directions

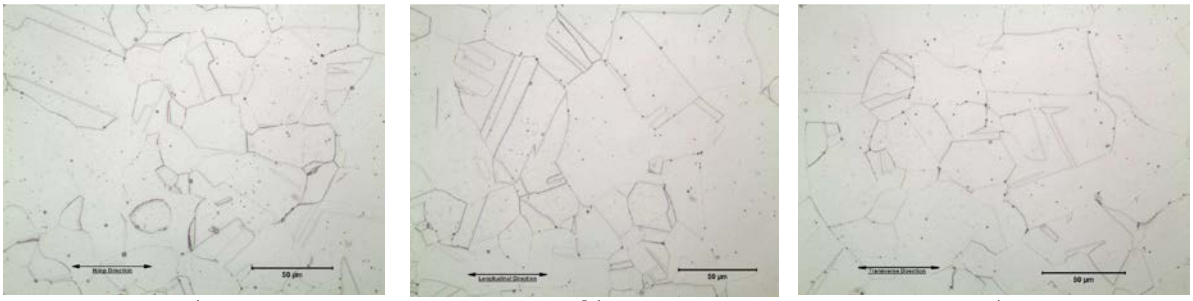

a) b) c)

Chemical composition

The chemical composition was also measured and compared with the 316L ASTM chemistry for the alloy as shown in Table 1. Note that no attempt was made to develop a special, controlled chemistry as widely available atomised powders produced by Carpenter Technologies were utilised to produce the valve body demonstration piece. All of the analysed elements were well within the specification.

Table 1. Chemical composition for the 316L stainless steel valve body

Chemical composition analysis results - (wt%)		
Element	**Valve body**	**316L specification**
Carbon	0.019	0.030 max
Manganese	0.99	2.00 max
Phosphorus	0.006	0.045 max
Sulfur	0.005	0.030 max
Silicon	0.73	0.75 max
Nickel	12.10	10.00 – 14.00
Chromium	17.25	16.00 – 18.00
Molybdenum	2.52	2.00 – 3.00

Mechanical testing

Mechanical testing performed for the valve body included room temperature tensile tests, elevated temperature tensile tests at 316°C (600°F), and Charpy impact toughness tests. The tensile test results are provided in Tables 2 and 3. Note that tests were performed along the longitudinal and transverse directions of the valve body flange.

Table 2: Room temperature tensile test results for the 316L stainless steel valve body

Room temperature tensile test results				
Sample	**0.2% Offset yield strength (psi)**	**Ultimate tensile strength (psi)**	**Elongation (%)**	**Reduction in area (%)**
A – Long	46 900	90 900	52.3	74.6
B – Long	45 300	90 400	51.4	75.3
C – Long	44 700	90 200	52.3	74.4
A – Trans	49 800	90 800	50.6	74.6
B – Trans	47 100	89 700	53.1	73.9
C – Trans	49 000	90 600	50.4	74.0

Table 3: Elevated temperature, 316°C (600°F), tensile test results for the 316L stainless steel valve bod

Elevated temperature 316°C (600°F) tensile test results				
Sample	**0.2% Offset yield strength(psi)**	**Ultimate tensile strength(psi)**	**Elongation (%)**	**Reduction in area (%)**
A – Trans	30 800	71 900	42.1	72.3
B – Trans	29 200	71 400	39.7	71.7
C – Trans	30 100	71 300	40.7	71.4
A – Long	29 200	71 600	40.5	73.2
B – Long	29 700	71 300	40.9	70.7
C – Long	29 500	71 600	41.8	72.3

Charpy impact tests were initiated for specimens removed from the valve body flange. The initial test results determined the toughness to exceed 195 ft-lbs or the capacity of the machine. No additional testing was conducted.

Part II: Manufacture of valve bodies from 316L SS and Grade 91

During the latter half of 2010, and based on the promising results of the initial feasibility studies, EPRI initiated a more targeted research program to focus on the development of several additional valve bodies of varying materials to support ASME BPVC Code Cases. A variety of valve body configurations were manufactured from two different alloys including: 316L stainless steel (for nuclear applications), Grade 91 (fossil applications).

EPRI and Carpenter elected to team with Tyco Valves to manufacture and test three 316L SS valve bodies. The three valve bodies were manufactured to Tyco's drawings/specifications which allowed them to put the valve bodies through their rigorous testing criteria and production machining process. A photograph of one of the valve bodies is provided in Figure 6. Rolls Royce also provided a Tee section manufactured from PM-HIP to support the Code Case development. Mechanical tests and metallographic characterisation were completed for each valve body/tee section and have been used in the assembly of a Code data package. The chemical composition and room and elevated temperature tensile results for one of the valve bodies are provided in Tables 4 and 5. Charpy impact toughness data, though not presented here, exceeded 122 ft-lbs along three orientations for this alloy.

Figure 6: Three 316L stainless steel valves were manufactured by Carpenter Technology to drawing/specifications provided by Tyco Crosby. The valve body shown on the left is the finished valve body. The photograph on the right shows the valve body after it has been sectioned into halves.

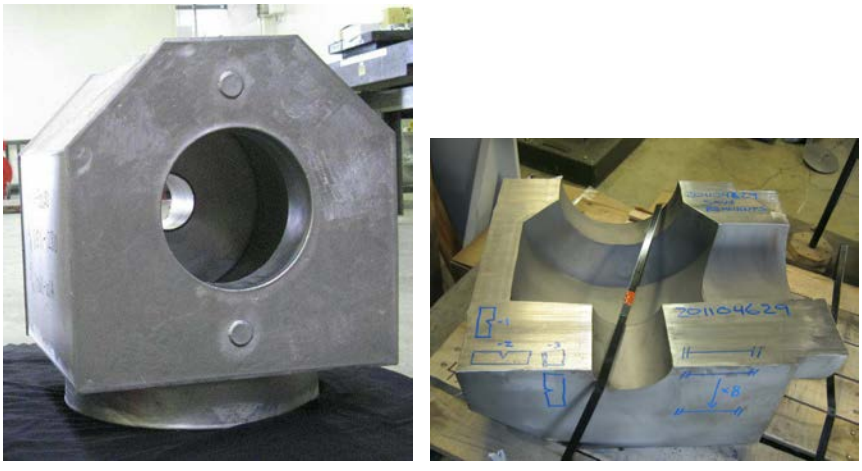

Table 4: Chemical composition of four S31603 (316L) manufactured components

Heat	S31603 (316L) Specification[1]	814520	815111	Y1620B	RR
Size		1892 lbs	1200 lbs	1200 lbs	NS[2]
Product Form		Valve	Valve	Valve	Tee Piece
C	0.030 max	0.013	0.021	0.004	0.022
Mn	2.00 max	0.90	0.95	1.41	1.76
P	0.045 max	0.014	0.009	0.005	0.016
S	0.030 max	0.003	0.004	0.005	0.006
Si	1.00 max	0.70	0.80	0.55	0.32
Ni	10.0-14.0	12.1	13.2	13.3	12.10
Cr	16.0-18.0	17.3	17.3	16.87	17.80
Mo	2.0-3.0	2.55	2.50	2.37	2.50
N	0.10 max				0.090
Others	N/A	O: 0.010	N/A	N/A	O: 0.0140 Cu: 0.020 Co: 0.040

1. Specification = ASTM A988/A988M
2. NS = Not Specified

In parallel, EPRI and Carpenter also initiated production of three Grade 91 valve bodies in conjunction with another major valve manufacturer, GE-Dresser. Teaming with GE-Dresser allowed for component testing and production machining characterisation in a similar manner that would be employed for actual valve production. A photograph of one of the valve bodies is shown in Figure 7. Chemistry data for the three valve bodies is provided in Table 6 and compared directly with the UNS and EPRI specifications for Grade 91 materials.

Table 5: Elevated temperature, tensile test results for one 316L stainless steel valve body manufactured during this project

Temp. (°F)	Temp. (°C)	TS (ksi)	TS (MPa)	YS (ksi)	YS (MPa)	Elong. in 4D (%)	ROA (%)
70	21.1	93.4	644.1	47.4	326.9	50.5	73.5
100	37.8	90.4	623.4	46.1	317.9	54.5	75.0
200	93.3	84.5	582.8	41.7	287.6	46.5	74.5
300	148.9	79.2	546.2	36.6	252.4	46.5	73.0
400	204.4	76.9	530.3	37.3	257.2	45.0	70.5
500	260.0	75.5	520.7	33.6	231.7	45.0	71.5
600	315.6	75.0	517.2	31.1	214.5	44.5	70.5
700	371.1	74.8	515.9	30.8	212.4	41.5	66.5
800	426.7	74.5	513.7	28.5	196.5	44.5	66.0
900	482.2	73.0	503.3	27.8	191.7	44.5	67.5
1 000	537.8	72.6	500.6	26.0	179.3	46.5	66.0

Tensile, yield, elongation and reduction of area plots for the three valve bodies up to 1 300F (704C) are provided in Figures 8-10. The data is plotted against ORNL Report 6303 minimum data. Additionally, creep rupture data was obtained for the three valve bodies and is presented in Figure 11. The data has been plotted against the large industry database on Grade 91 rupture. Two different tempering heat treatments were applied, one at the upper end (1 430°F (777°C)/4.5 hrs of the tempering range and a second near the optimum tempering temperature range (1 375°F (746°C)/4.5 hrs). The lower temperature produced improved long-term rupture properties over the higher temperature tests as one would expect. As of September 2013, both ASME BPVC Code Cases have been approved and should be available for use by January 2014.

Figure 7: Three Grade 91 alloy steel valves (such as the one on the left) were manufactured by Carpenter Technology to drawing/specifications provided by Dresser. The figure on the right shows a Grade 91 valve body that is sectioned into two halves.

Table 6: Chemical composition of K90901 (Grade 91) PM/HIP manufactured components

Heat	Grade 91 Specification		Y1549B		Y1550B		Y1551B	
	UNS K90901 [1]	EPRI [2]	Cert	Ind. Analysis	Cert	Ind. Analysis	Cert	Ind. Analysis
C[A,2]	0.08-0.12		0.09	0.11	0.08	0.10	0.09	0.11
Mn	0.30-0.60		0.44	0.46	0.44	0.46	0.42	0.45
P	0.020 max.		0.002	0.002	0.006	0.01	0.003	0.008
S	0.010 max.		0.009	0.007	0.008	0.007	0.008	0.007
Si	0.20-0.50		0.20	0.30	0.24	0.36	0.22	0.33
Cr[B,2]	8.0-9.5		8.88	8.99	8.42	8.81	8.12	8.46
Mo	0.85-1.05		0.93	0.92	0.88	0.88	0.96	0.90
V	0.18-0.25		0.25	0.25	0.25	0.25	0.22	0.23
Cb	0.06-0.10		0.08	0.08	0.08	0.08	0.07	0.08
Ni	0.40 max	0.20 max	0.08	0.08	0.08	0.08	0.09	0.08
N[A]	0.030-0.070	0.035-0.070	0.04	0.0428	0.04	0.0397	0.04	0.0416
Al	0.040 max.	0.020 max.	<0.01	<0.002	<0.01	<0.002	<0.01	<0.002
Ti		0.010 max.	<0.01	0.002	<0.01	<0.002	<0.01	<0.002
Cu[,2]		0.25 max.		0.03		0.03		0.03
N/Al Ratio		4.0 min.		>21.4		>19.85		>20.8
Calculated A_1 (ORNL Equation),°C			815.3	814.5	814.6	815.5	813.5	813.4
Calculated A_1 (ORNL Equation), °F			1 499.5	1498.0	1498.4	1499.8	1496.3	1496.1
Calculated A_1 (OSU Equation),°C			809.9	806.5	817.1	810.5	819.7	818.0
Calculated A_1 (OSU Equation), °F			1 489.8	1483.7	1502.7	1490.9	1507.5	1504.4

A. Carbon + Nitrogen > 0.12
B. For tubing, the minimum Cr level should be 8.5% for additional corrosion resistance.
1. Specification = ASTM A989/A989M-07
2. *Guidelines and Specifications for High-Reliability Fossil Power Plants: Best Practice Guideline for Manufacturing and Construction of Grade 91 Steel Components*. EPRI, Palo Alto, CA: 2011. 1023199.

Figure 8: Elevated temperature, tensile test results for 3 Grade 91 valve bodies manufactured in this project

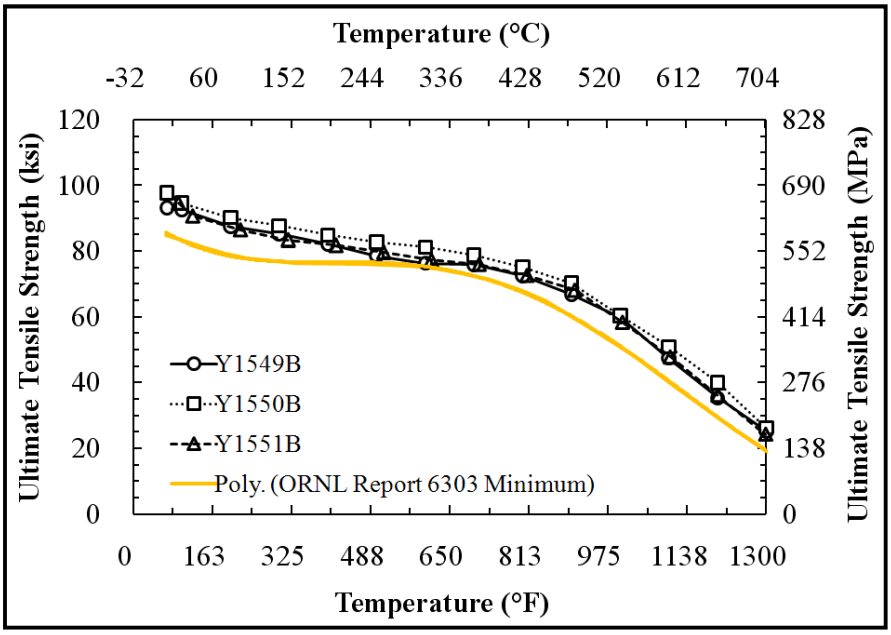

Figure 9: Elevated temperature, yield strength test results for three Grade 91 valve bodies manufactured during this project

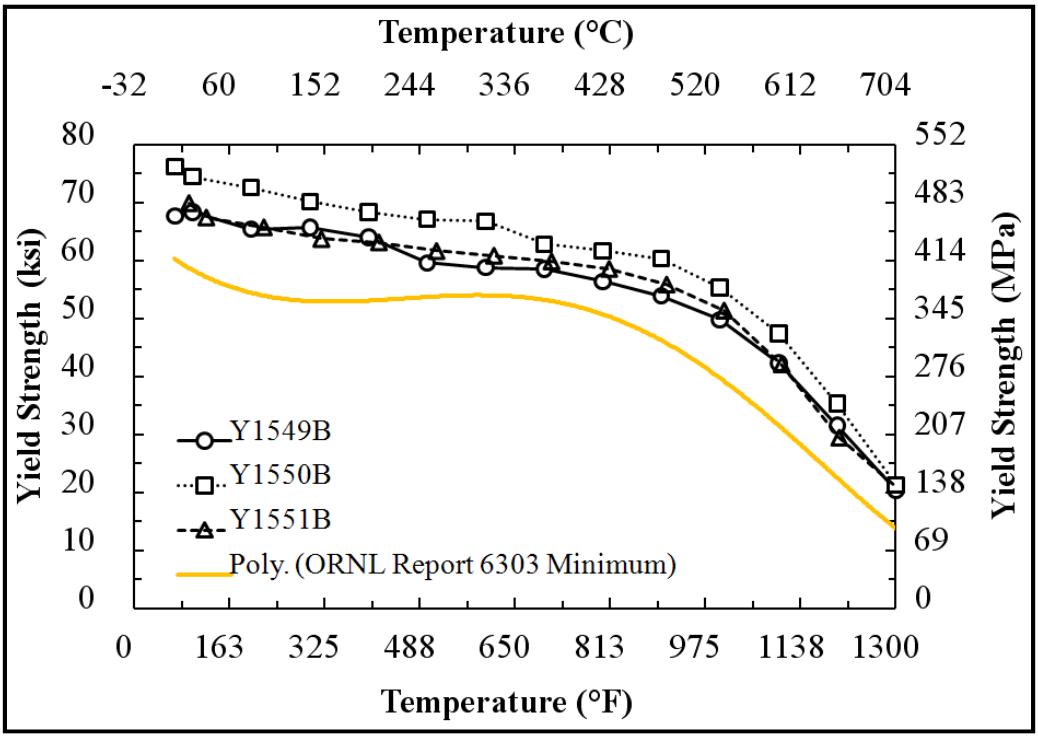

Figure 10: Elevated temperature, elongation and reduction of area test results for three Grade 91 valve bodies manufactured during this project

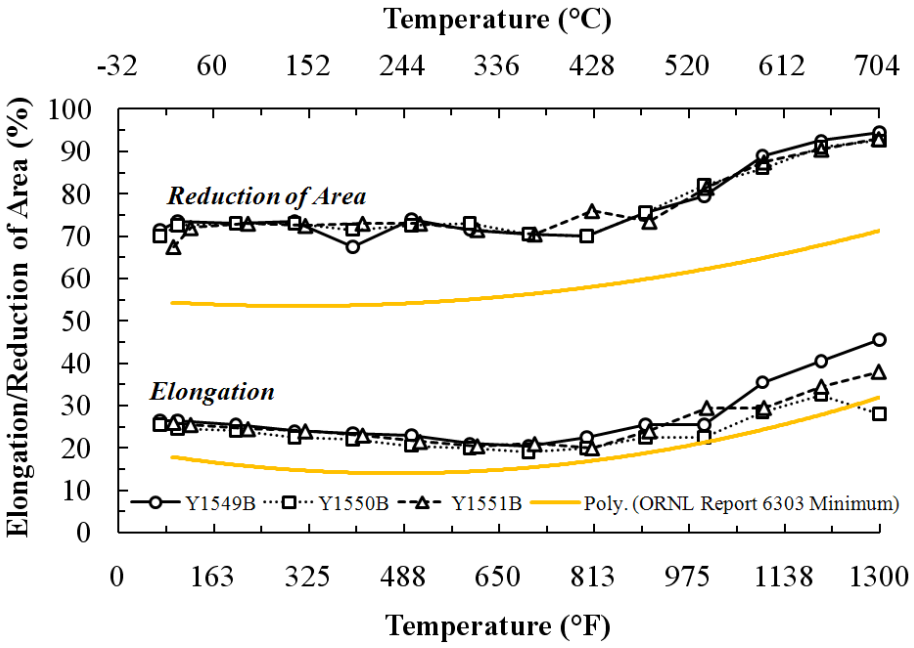

Figure 11: LMP Comparison of heat treatments between tempering at 1 430°F (777°C)/4.5h (Heats Y1549B and Y1551B) and tempering at 1 375°F (746°C)/4.5h (Heat Y1550B)

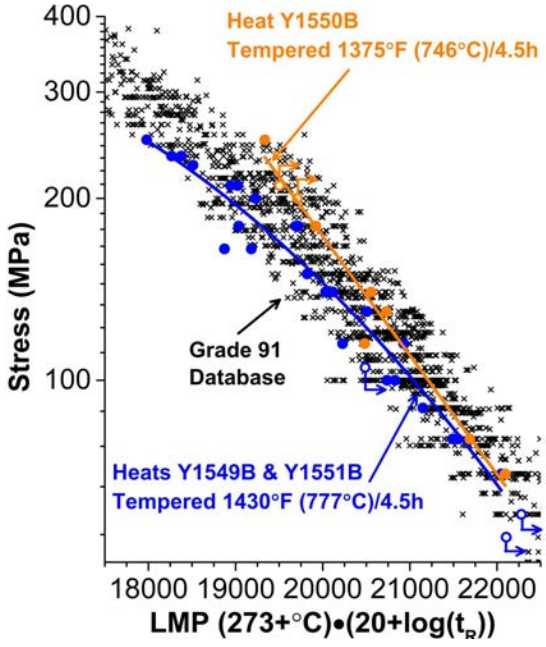

Part III: DOE nuclear energy enabling technology (NEET) project

The research described above provided an excellent platform to launch a project with DOE aimed at developing and demonstrating near-net shaped components for ALWR and SMR nuclear applications. Specifically the project, DE-NE0000544, was initiated (beginning

October 2012) to conduct the necessary design, processing, manufacturing, and validation studies to assess PM-HIP as a method to produce very large NNS components with erosion/corrosion resistant surfaces for use in nuclear and other electrical power generation equipment. The project is focusing on three different families of alloys: low alloy pressure vessel steels, austenitic stainless steels, and nickel-based vessel internals alloys. Key investigators include: EPRI, Carpenter Technology, GE-Hitachi, and Ohio State University. The following provides a brief outline of the project.

- Modelling of NNS component alloy and mold/can design.
- Test coupon development, demonstration, and screening for surfacing applications.
- Low alloy steel PM/HIP component development.
- Nickel-based alloy (Alloy X-750)PM/HIP component development.
- Austentic stainless steel PM/HIP development.
- Mechanical and metallographic characterisation.
- Corrosion testing of test coupons.

During the first year of the project, the team has been focusing on Tasks 1-3 and 6.

Task 1 is currently focused toward development of a can (container) for manufacture of a BWR-2 N-4 Feedwater Nozzle. The nozzle diameter is 36 inches with a 16-inch bore and a total weight approaching 2 500 lbs once completed. Modelling and can design have been initiated by Carpenter with the anticipation that the nozzle will be manufactured during the fall 2013. Production of the large nozzle will demonstrate capabilities to produce very large ferritic RPV materials with good properties (more on this subject below under Task 3).

Under Task 2, down-selection of three hard-facing alloys for application to the inlet mixer has been made and hard-facing alloys NOREM 02, Tristelle 5183, and EPRI H' (a test alloy) have been applied (via PM/HIP) to test blocks (under Task 2). Additional testing will be completed prior to actual application of either of these alloys to the 316L SS diffuser and tail pipe (scheduled for year 2 of the project).

Task 3 of the DOE project is looking to produce the large low alloy steel nozzle described in Task 1 via the PM-HIP process. To accomplish this, three thick section 8.5"×8.5"×25" coupons have been produced (via PM-HIP) to the chemistry specification of SA508 Grade 3, Class 1 material. A CERT for an actual RPV heat of material was obtained and used for guidance. Three separate PM heats (Table 7) were produced by Carpenter during the first quarter to:

- Meet a chemistry close to the CERT material chemistry resulting in a hardenability (carbon equivalent) of approximately CE=0.60.
- Heat chemistries were produced with CE's of 0.55, 0.62, and 0.69. The chemistries represent a low, medium, and a high hardenability ranges for the SA508 steel.

The three powder chemistries were processed via HIP at 2050F and 15 ksi pressure. The resulting coupons were sectioned, heat treated (normalised and tempered), and metallography and mechanical testing evaluation were performed.

A total of nine test plates 8"×2.5"×1.5" have been heat treated under various conditions to establish the appropriate tempering conditions for the three powders (heats). The entire batch was first austenitised (2 050°F for 4 hours and gas quenched) and then normalised (1 650°F for 10 hours and gas quenched). Tempering conditions include 1 175°F, 1 200°F, and 1 225°F for 4, 10, and 20 hours each (a total of nine conditions). Mechanical properties obtained include tensile, hardness, and toughness and were compared with CERT and SA508 Grade 3, Class 1 properties. The results will be used to steer the investigators toward the right chemistry and HT for production of the low alloy steel nozzle and RPV curved plate section which is scheduled for late fall.

Table 7: Projected chemistries for 3 low alloy steel PM-HIP heats

Element	New SA508, Class 1 Grade 3 (Today's Spec)	Actual SA508 Class 1 Grade 3 Heat in New Reactor*	Low Hardenability-- Heat #1 (160116)	Medium Hardenability -- Heat #2 (160114)	High Hardenability -- Heat #3 (160115)
Al	0.025 max	0.018	0.02	0.02	0.02
B	0.003 max	NA	NA	NA	NA
Ca	0.015 max	NA	NA	NA	NA
Cr	0.25 max	0.12	0.09	0.13	0.19
Cu	0.20 max	0.03	0.03	0.02	0.03
Mn	1.20-1.50	1.45	1.26	1.46	1.48
Mo	0.45-0.60	0.50	0.48	0.50	0.55
Nb (Cb)	0.01 max	NA	NA	NA	NA
Ni	0.40-1.00	0.85	0.84	0.84	0.85
P	0.025 max	0.006	0.014	0.011	0.12
Si	0.40 max	0.18	0.18	0.16	0.18
Ti	0.015 max	NA	NA	NA	NA
V	0.05 max	<0.003	0.01	0.01	0.01
C	0.25 max	0.18	0.17	0.20	0.24
S	0.025 max	<0.001	0.006	0.03	0.008
O	NA	NA			
N	NA	NA			
Target Hardenability			0.55	0.62	0.69
CE = C + Mn/6 + Si/24 + Ni/40 + Cr/5 + Mo/4					

Test results from the nine test plates suggest that PM-HIP is capable of producing acceptable tensile, hardness, and toughness properties. Key results are summarised below:

- Ultimate tensile values ranged from 85-110 ksi across all three heats of material for each of three tempering conditions. Note: The SA508 specification calls for the alloy to meet 80-105 ksi. Only one tempering condition produced tensile values above the 105 ksi maximum value, whereas all others met the 80-105 ksi specification.
- Yield strength values ranged from 67-92 ksi across all three heats of material for each of the tempering conditions. Note: The SA508 specification calls for 50 ksi minimum.
- Excellent ductility was demonstrated across all three heats of material across all tempering conditions employed in this study with elongation values ranging from 22-30% and reduction in area ranging from 67-77%. These values easily exceeded the 18% (min) elongation and 38% (min) reduction in area from the SA 508 specification.
- All toughness tests performed exceed the minimum ASME specification requirements at +40°F (30 ft-lbs) by at least 2X. In most cases tested, test values exceeded the minimum by 4X or more.
- The low hardenability (CE) test coupons (HT 160116) produced better Charpy impact toughness results when compared to the medium and high hardenability coupons.
- At the +40°F reference test temperature, HT 160116 tempered at 1 200°F produced toughness values exceeding 133 ft-lbs for both the 10 and 20 hour tempering times. These results easily exceeded the ASME specification by 4-5X.

Again, the test plate results are to be used to provide critical processing information and data for manufacture of the nozzle and arc RPV section later in 2013.

Task 4 of the project will target the manufacture of a high strength nickel based alloy such as X-750 used for a BWR jet pump beam assembly, while Task 5 plans to target an inlet mixer assembly. Both components require critical tolerances and considerable machining, which make them ideal for use in the current EPRI-DOE project. Mechanical and corrosion testing are to be performed in Tasks 6 and 7 respectively to validate properties of the PM-HIP produced NNS components.

Part IV: Vision for the future

As described in the first three sections of this report, considerable R&D has already been performed (or is underway) to bring PM-HIP to the power industry for pressure retaining applications. Additional research remains however to fully integrate PM-HIP technology into commercial nuclear applications. This section seeks to identify specific alloys of interest to the nuclear power industry, various components/applications where PM-HIP might be employed, identify PM-HIP equipment and ancillary needs, and describe the DOE R&D Roadmap initiatives on Advanced Manufacturing. Most importantly, it describes the *Vision and Requirements* to fully bring PM-HIP to the power industry as a viable technology for the manufacture of large, NNS components (including RPV nozzles and ring sections).

Alloys of interest to the Electric Power Industry

The common alloys of interest from a PM-HIP perspective are listed below. Development is underway for several of these alloys either through the current DOE project (described above), EPRI research, or through major OEMs such as Rolls Royce, GEH, Areva. This list provides a reasonable view of the alloys which will require further development before being used in a nuclear plant however.

- ???
- 304L and 316L SS
- IN625 and IN 690
- SA508 Class 1, Grade 3
- Grade 91
- Hard-facing materials – cobalt free
- Corrosion resistant cladding
- HTGR applications – IN282 and IN740
- Si-carbide materials
- Oxide dispersion strengthened (ODS) alloys

Applications/Components

Two of the key attributes (as described earlier in the report) of PM-HIP for the nuclear power industry are improved inspectability and the ability to produce a component as near net-shaped (NNS) component. Replacement of castings for certain applications with PM-HIP components will dramatically improve the inspectability. Fabrication of complex parts via PM-HIP can eliminate significant machining time and labour. A number of key components/applications were discussed in the section on "Why Consider PM-HIP for Large Nuclear Components". A somewhat more comprehensive list of applications/components is provided below to spur thought:

Reactor Pressure Vessel and Outside the RPV

- Valve bodies, valve seats & stems.
- Pump housings.
- Turbine blade leading edges.
- Reactor pressure vessels & nozzles.
- Nozzle-to-safe-ends.
- Small modular reactor vessels.
- Turbine rotors, discs, and casings.
- Functionally graded alloys.
- Elimination of dissimilar metal welds.

RPV Internals

- Control rod drive tubes.
- Fuel channels from sic.
- Tube sheets.
- Corrosion resistant claddings.
- Fuel support bowls/castings.
- Jet pump beams.
- Shroud supports.
- Chimney partitions.
- Inlet mixer assemblies.

Equipment and ancillary needs

The third area where additional effort is required is focused toward capacity and equipment size. Several powder production facilities exist around the world for production of atomised powders; however, if industry begins to build a large number of

nuclear facilities, the powder production capacity will be easily exceeded. New powder production facilities will be required to meet new demand. A few of the key atomised powder producers include:

- Bohler Edelstahl.
- Carpenter Powder Products.
- Erasteel.
- Metso.
- Sandvik Powdermet AB.
- Kennametal.

Additionally, there are a limited number of HIP units currently available to industry. Those known to the author are provided in Table 8. As can be seen, the maximum HIP unit size is limited to 81 in × 164 in (2 m×4.2 m); thus production of larger components (RPV sections, nozzles, rotors, support plates, etc) is severely restricted at present. Production of larger components will require larger HIP units on the order of 12-15 ft (3.6-4.6 m) in diameter. As the nuclear industry begins to further embrace PM-HIP and understand its capabilities, larger units are certain to follow.

Table 8: Large Commercial HIP units in the world

Company	HIP unit size (diameter × length in inches)	Country
Kinzaku Giken	81×164	Japan
BodyCote	71×130	Sweden
BodyCote	58×146	Sweden
BodyCote	66×100	United States
BodyCote	49×98	United Kingdom
ATI	51×115	United States
Alcoa Howmet	59×80	United States
Alcoa Howmet	42×97	United States
Kittyhawk	47×79	United States
Avure (MegaHIP)	124×197 (proposed)	Proposed

DOE advanced manufacturing methods (AMM) for nuclear energy roadmap

The DOE Advanced Manufacturing Methods for Nuclear Energy Roadmap defines six key enabling manufacturing technologies for nuclear energy including: 1) Factory and field fabrication, 2) Life cycle engineering, 3) Welding and additive manufacturing, 4) Concrete and rebar innovations, 5), Coatings and cladding, and 6) Heavy section manufacturing. under the heavy section manufacturing area, PM-HIP is highlighted as the key production technology that DOE will focus on to reestablish the U.S. manufacturing capability toward production of large nuclear components. The technology is described as a "transformational technology" that would enable the U.S. to meet virtually all of the heavy section manufacturing demands for SMRs and ALWRs, while providing an avenue for the U.S. to once again compete internationally in heavy section manufacture. The transformation will move the industry away from conventional forging, casting, and rolled-and-welded technologies to focus on the PM-HIP process.

Specific priorities identified within the heavy section manufacturing portion of the Roadmap include:

- Development and approval of a technical position that allows welds in vessels outside of the beltline region. The EPRI utilities requirements document will need to be amended to accept this position.
- Develop/Demonstrate Nozzle manufacturing capabilities.
- Develop/Demonstrate PM-HIP for large plate (Ring Sections) manufacturing capabilities.
- Manufacture vessel internals via nickel-based alloys.
- Install/Commission a 15 foot diameter HIP Unit.

EPRI and DOE are currently working on all of these priorities within the current NEET project (described in Part III of this paper), with the exception of the fifth item. The current schedule calls for each of the first four items to be completed by the end of 2015. Successful development and demonstration around the first four priorities will provide industry with the background, knowledge, and data to successfully focus on the last priority.

The last priority will require industry partnership with DOE and EPRI to facilitate installation and commissioning of a large HIP unit. It is believed the installation of PM-HIP capabilities within the United States could be established for $75-$100M, which is several orders of magnitude (3-5% of total) less than re-establishing heavy section forging capabilities ($2B range). An increase in powder capacity would easily be absorbed by industry if the demand was there for powder. The real costs would be in the design and commissioning a new HIP vessel (estimated at $50-60M).

Summary

The PM-HIP technique is targeted at components currently manufactured using various casting, rolled-and-welded, and forging methods employed by industry. Attributes of the PM-HIP process that make it attractive to the power industry include:

- Elimination of inspectability issues and concerns.
- Enables manufacture of large, complex components using near-net shape technologies.
- Enables new alloys systems & targeted chemistries.
- Enhances weldability.
- Alternate supply route for long-lead time components.
- Elimination of re-work or repair of large cast components.

The research described in this paper has reviewed the development of two ASME Boiler and Pressure Vessel PM-HIP Code Cases, one for Grade 91 and one for Type 316L stainless steel, along with the supporting data packages required by ASME for each. The research has demonstrated the capability of PM-HIP to produce large, near-net shaped, complex components with superior hardness, tensile, creep, and toughness properties for use in the power industry.

The paper has also highlighted DOE/EPRI research now entering its second year of a 3-year project which was initiated to conduct the necessary design, processing, manufacturing, and validation studies to assess PM-HIP as a method to produce large NNS components with erosion/corrosion resistant surfaces for use in nuclear power generation equipment. The research is focusing on three different families of alloys: low alloy pressure vessel steels, austenitic stainless steels, and nickel-based vessel internals.

Lastly, a clear, concise vision of what developments are required to enable the PM-HIP process to be fully integrated into use for nuclear energy applications within the United States is identified.

Acknowledgements

The author would like to recognise L. Lherbier and D. Novotnak of Carpenter Technology who have worked hand and hand with EPRI to bring PM-HIP technologies to the power industry. I would also like to recognise J. Siefert, J. Shingledecker, D. Purdy, and G. Frederick of EPRI who have contributed greatly to the PM-HIP program. And lastly, I would like to thank B. Burdett, J. Sulley, Ian Hookman, and Jiles Alcock at Rolls-Royce for their efforts and support in assembly of a 316L stainless steel data package for submittal to ASME BPVC.

References

[1] Burdett, W.B., P. Hurrell, A. Gilleland, “Hot Isostatic Pressing of Type 316L Powder for Pressure Retaining Components”, ASME PVP-2004, July 25-29, 2004, San Diego, CA, MK-04-031.

[2] Burdett, W.B. and C.T. Watson, "Hot Isostatic Pressing of Type 316L Powder for Pressure Retaining Components", ASME PVP-2005, July 17-21, 2005, Denver Colorado, PVP 2005-71711, p. 7.

[3] Sulley, J.L. and I.D. Hookham, "Justification and Manufacturing Quality Assurance for the Use of Hot Isostatically Pressed, Reactor Coolant System Components in PWR Plants", Proceedings of ICAPP'08, Anaheim, CA, June 8-12, 2008, Paper 8110, pp. 8-20.

[4] Hookman, B. Burdett, K. Bridger, J.L. Sulley, "Hot Isostatically Pressed (HIPed) Thick-Walled Component for a Pressurized Water Reactor (PWR) Application", Proceedings of ICAPP'09, Tokyo, Japan, May 10-14, 2009, Paper 9389, p. 7.

[5] Sulley, J.L., I.D Hookham, B. Burdett, and K. Bridger, "Introduction of Hot Isostatically Pressed Reactor Coolant System Components in PWR Plants", Proceedings of the 18th International Conference on Nuclear Engineering, ICONE 18, Xi'an China, May 17-21, 2010, ICONE 18-30253.

[6] Jelfs, T. and B. Burdett, "Hot Isostatic Pressing of Inconel 600 and 690 Powders for Pressure Retaining Components", ASME PVP 2011, July 17-21, 2011 Baltimore Maryland, PVP2011-57194.

[7] Lherbier, L.W., J.F.Radavich, "An Evaluation of PM Waspaloy" Proceeding of 11th International Symposium on Advanced Superalloys – Production and Application", May 21-25, 2007, Shanghai, China.

[8] Lherbier, L.W., D.J.Novotnak, "Effect of Thermal History on the Properties and Microstructure of Large Hip'ed PM Superalloy Billet", Proceedings of 11th International Symposium on Superalloys, September 14-18, 2008, Champion, Pennsylvania.

[9] Eklund, A., et al, "Corrosion Properties of PM Hip'ed Stainless Steel", 15th Nordic Corrosion Congress, May 19-21, 2010, Stockholm, Sweden.

[10] Scanlon, J. et al, "Mechanical Properties of PM Hip'ed Stainless Steel – A Comparison to Conventional/Rolled Material, PowderMet 2010 Conference, June 27-30, 2010, Hollywood, Florida.

[11] Bengston, B. et al, "Mechanical Properties of PM Hip'ed Stainless Steels", Stainless Steel World Conference, October 5-7, 2010, Houston, Texas.

[12] Novotnak, D.J., L.W.Lherbier, D.W.Gandy, "Manufacturing Large Complex PM Hip Shapes", Euro PM 2011 Conference, October 9-12, 2011, Barcelona, Spai

[13] Tahtinen, S., "In-Vessel Materials Studies at VTT," VTT Industrial Systems, Association Euratom-Tekes, Annual Seminar, Paasitorni, Helsinki, May 30-31, 2005.

[14] Pertti and H. Hanninen, personal communication, July 4, 2011.

[15] ASTM Standard A988/A 988M-07, Standard Specification for Hot Isostatically-Pressed Stainless Steel Flanges, Fittings, Valves, and Parts for High Temperature Service.

[16] ASTM Standard A989/A 989M-07, Standard Specification for Hot Isostatically-Pressed Alloy Steel Flanges, Fittings, Valves, and Parts for High Temperature Service.

[17] Gandy, D. et al, "Program on Technology Innovation: Manufacture of Large Nuclear and Fossil Components Using Powder Metallurgy and Hot Isostatic Processing Technologies", EPRI Report 1025491, May 2012.

[18] Gandy, D., J. Shingledecker, L. Lherbier, "The Manufacture of Large, Complex Power Plant Components Using Powder Metallurgy and HIP Technologies – A Feasibility Study", EPRI Advanced Materials Conference, Santa Fe, New Mexico, October 2010.

[19] Gandy, D., J. Shingledecker, L. Lherbier, and D. Novotnak, "Powder Metallurgy for Producing Nuclear and Fossil Components", CSC11 Corrosion Solutions 8th International Conference, Lake Louise, Alberta Canada, October 2011.

[20] Gandy, D., J. Shingledecker, and J. Siefert, "Overcoming the Barriers for PM/HIP Technology in Large Nuclear and Fossil Components", ASM Advanced Materials & Processing Magazine, January 2012.

[21] Gandy, D., J. Shingledecker, L. Lherbier, and D. Novotak, "Powder Metallurgy Methods for Producing Components", Stainless Steel World, November 2011.

[22] Introduction to PM HIP Technology, European Powder Metallurgy Association, 2012, www.empa.com.

Processing of a novel nanostructured ferritic steel via spark plasma sintering and investigation of its mechanical and microstructural characteristics

Somayeh Pasebani,[a,d] Indrajit Charit,[a,d] Yaqiao Wu,[b,d] Jatuporn Burns,[b,d] Kerry N. Allahar,[b,d] Darryl P. Butt[b,d] and James I. Cole[c,d]

[a] University of Idaho, Moscow, ID 83844-3024, United States
[b] Boise State University, Boise, ID 83427, United States
[c] Idaho National Laboratory, Idaho Falls, ID 83401, United States
[d] Center for Advanced Energy Studies, Idaho Falls, ID 83401, United States

Abstract

Nanostructured ferritic steels (NFSs) with 12-14 wt% Cr have attracted widespread interest for potential high temperature structural and fuel cladding applications in advanced nuclear reactors. They have excellent high temperature mechanical properties and high resistance to radiation-induced damage. The properties of the NFSs depend on the composition that mainly consists of Cr, Ti, W or Mo, and Y_2O_3 as alloying constituents. In this study, a novel nanostructured ferritic steel (Fe-14Cr-1Ti-0.3Mo-0.5La_2O_3, wt%) termed as 14LMT was developed via high energy ball milling and spark plasma sintering. Vickers microhardness values were measured. Microstructural studies of the developed NFSs were performed by EBSD and TEM, which revealed a bimodal grain size distribution. A significant number density of nano-precipitates was observed in the microstructure. The diameter of the precipitates varied between 2-70 nm and the morphology from the spherical to faceted shape. The Cr-La-Ti-O-enriched nanoclusters were identified by APT studies.

Introduction

Nanostructured ferritic steels (NFSs) have attracted considerable interest for potential use in fuel cladding and other structural applications. These steels possess enhanced microstructural stability, high creep strength and excellent radiation damage tolerance [1,2]. The unique properties of NFSs such as 14YWT derive from the presence of an ultrahigh number density of Y-Ti-O-rich nanoclusters. These nanoclusters are formed due to the mechanical alloying (MA) of Fe-Cr-Ti powders with yttria (Y_2O_3) followed by hot consolidation route [3,4]. The most commonly used rare earth (RE) oxide in the ferritic ODS or NFSs is Y_2O_3. In the present study, an alternative RE oxide, lanthana (La_2O_3) was added to the NFS composition instead of the traditionally used Y_2O_3. Lanthana is stable at high temperatures, insoluble in solid iron at all temperatures and has a high affinity for oxygen. Based on the density function theory calculations by Reed et al. [5], La_2O_3 clusters should have the same general structure as the corresponding yttrium species; however, the bond distances are generally greater. Furthermore, La_2O_3 is more abundant (25-38 wt%) in one of the main US rare earth ores (bastnasite) compared with Y_2O_3 (only about 0.2 wt%). There is no study in the literature on dispersing La_2O_3 to the bulk ferritic matrix to the best of our knowledge. Interestingly, Mueller et al. [6] investigated the oxide dispersion strengthening effect of La_2O_3, Y_2O_3 and ZrO_2 in Mo and found that La_2O_3 doping produced the highest ultimate tensile strength (UTS) and significantly higher creep-

rupture properties compared to the other dopant oxides. Thus, an alloy with the nominal composition of Fe-14Cr-1Ti-0.3Mo-0.5La_2O_3 (wt%), termed 14LMT, has been developed using MA of the constituent powders. A detailed study on the microstructural characteristics of the as-milled 14LMT powder as a function of various MA parameters was carried out by Pasebani et al. [7].

Generally, NFSs are produced via the mechanical alloying followed by the hot consolidation process such as the hot isostatic pressing (HIP) and/or hot extrusion. In this study, such traditional consolidation methods of producing NFSs were replaced by a relatively new technique called spark plasma sintering (SPS). Compared to the hot pressing and HIP, the SPS technique allows sintering at lower temperatures and shorter dwell times. In SPS, the powder mix is placed in a graphite die before being pressed and a DC pulsed voltage is applied to the compact. In the case of electrically conductive materials, the heating is mainly due to the Joule effect. Although the occurrence of the electrical discharge (plasma discharge) is widely mentioned in the literature, its existence has not been conclusively proved. Several other phenomena, such as local melting, surface and volume diffusion and the evaporation of oxide layers, enhance the formation of necks between the powder particles leading to final densification [8].

Heintze et al. [9,10] consolidated the ODS Fe-9Cr model alloys, Fe-9Cr, Fe-9Cr-0.3Y_2O_3 and Fe-9Cr-0.6Y_2O_3 (wt%), using SPS and studied the mechanical properties as well as microstructural characteristics of the alloys. The hardness values for the Fe-9Cr ODS alloys containing 0.3 wt% and 0.6 wt% Y_2O_3 were in the range of 216-322 HV depending on the milling time and initial powder size. Recently, Allahar et al. [11] used SPS to consolidate the Fe-16Cr-3Al (wt%) powder with sequential additions of Y_2O_3 and Ti powders to produce Fe-16Cr-3Al-0.5Y_2O_3 (wt%) and Fe-16Cr-3Al-0.5Y_2O_3-1Ti (wt%) alloys, respectively. The hardness values of the alloys increased to 320-400 and 480 HV after adding 0.5Y_2O_3 and 0.5Y_2O_3-1Ti to the Fe-16Cr-3Al matrix, respectively. The microstructure of the consolidated ODS alloys contained both ultrafine and coarse grains attributed to the occurrence of recrystallisation during SPS at 1 000°C. The TEM and APT studies revealed Y-O and Y-Ti-O-enriched nanoclusters with Y:O:Ti ratio of 3:10:8 and M:O (metal to oxygen) ratio close to 1:1, which were similar to those obtained in NFSs sintered by other hot consolidation methods.

A preliminary investigation [12] on the MAed 14LMT powder revealed nanoclusters in the nanocrystalline ferritic matrix. Subsequently, a detailed study on the MAed 14LMT powder was carried out as a function of MA parameters [7], and the formation of Cr-Ti-La-O-enriched nanoclusters during MA was identified. The present study focuses on the consolidation of the MAed 14LMT powder via SPS. Further, it elucidates the effects of SPS parameters such as temperature, dwell time, heating rate, applied pressure and current, on the density, microstructure and mechanical properties of the 14LMT alloy.

Experimental

The starting constituent powders including Fe (99.9 wt% Fe, average particle size of 40 µm), Cr (99.8 wt%, average particle size of 5 µm), Ti (99.7 wt% Ti, average particle size of 26 µm), La_2O_3 (99.99 wt% La_2O_3, average particle size of 40 nm) and Mo (99.9 wt% Mo, average particle size of 1-2 µm) were mixed together in the nominal proportion of Fe-14Cr-1Ti-0.3Mo-0.5La_2O_3 (wt%). High energy ball milling was performed in an air-cooled SPEX 8000M shaker mill for 10 h using steel balls (8 mm in diameter) as the milling media and the ball to powder ratio (BPR) of 10:1 (here 100 g steel balls were used for milling of 10 g powder mixture in each milling batch).

A Dr. Sinter Lab SPS-515S machine (SPS Syntex Inc., Kanagawa, Japan) available at the Center for Advanced Energy Studies (CAES) was used to consolidate the as-milled powder. A Tri-Gemini cylindrical graphite die with an inner diameter of 12.7 mm and an outer diameter of 38 mm was used. The inner surface of the die was covered with a graphite foil with a thickness of 0.25 mm to facilitate sample removal. In order to inhibit the diffusion of carbon from the graphite foil, a thin niobium foil was placed between the

powder and the graphite foils. The die was wrapped in a layer (4 mm thickness) of graphite felt to minimise heat loss by thermal radiation.

The as-milled powder was sintered under vacuum (7×10^{-3} Torr) at different temperatures (850-1 100°C) for various dwell times (0, 2, 20 and 45 min) using the pulse pattern 12-2 (the cycle consisted of 12 ms current passage followed by no current for 2 ms), a heating rate of 100°C/min, and a pressure of 80 MPa. The dwell time of "0 min" implies that the powder was essentially heated and cooled without any isothermal holding. The applied pressure and the heating rate were also varied between 40-110 MPa and 50-200°C/min, respectively, at a constant temperature of 950°C and a dwell time of 7 min. To investigate the effect of pulsed current, the average electric current was decreased from 275 A (in normal condition) to 150 A by placing a non-conductive ceramic disk between the punch and the powder.

The density of the sintered specimens was measured by Archimedes' method. At least six measurements were made for each specimen. The final relative density was determined as the ratio between the measured and the theoretical density (~7.7 g/cm^3). The Vickers microhardness tests were performed with a Leco LM100 microhardness tester at a 1 000 g-f (9.81 N) with a dwell time of 15 s.

Microstructural characteristics of the sintered specimens were examined using a LEO Supra 35 VP FESEM at an accelerating voltage of 15-20 kV. Some specimens were also prepared for electron back-scatter diffraction (EBSD) characterisation by grinding on 120 to 1 200 grit SiC papers, followed by a final polish in a Buehler Vibromet-2 vibratory polisher using 0.05 µm alumina slurry for 6 to 24 h. The EBSD analysis was performed on a JEOL JSM-6610LV scanning electron microscope (SEM) equipped with an EDAX/TSL Hikari EBSD system. The SEM was operated at an accelerating voltage of 20 kV. The automated scan was performed with a 0.1 µm step size on a total area of 50×50 µm^2. The EBSD data were analysed using the TSL Orientation Imaging Microscopy (OIM™) Data Collection version 5.31 software. After SPS, disks of 3 mm in diameter were mechanically thinned, and electropolished in CH_3OH-HNO_3 (80:20 by vol.%) electrolyte at -40°C using a Fischione Model 110 Twin-Jet Electropolisher. Transmission electron microscopy (TEM) studies along with the energy dispersive spectroscopy (EDS) were performed using a FEI Tecnai TF30-FEG STEM operated at 300 kV.

A focused ion beam (FIB) was used to prepare specimens for the atom probe tomography (APT) studies. The FIB effort was carried out using a Quanta 3D FEG instrument with a Ga-ion source. The APT analysis carried out using an Imago LEAP 4000X HR operating in voltage mode at the specimen temperature of 50–60 K and 20% of the standing voltage pulse fraction. The atom maps were reconstructed using CAMECA IVAS 3.6 software. The method followed here for the cluster analysis was described by Miller et al. [13] and Williams et al. (2013) [14].

Results and discussion

Effects of SPS temperature and time on densification and mechanical properties

The sintering experiments were performed in the temperature range of 850-1 100°C for dwell times of 0 and 2 min at a constant heating rate of 100°C/min and an applied pressure of 80 MPa. The measured density values are plotted as a function of sintering temperatures for the dwell times of 0 (i.e., no dwelling) and 2 min, and designated as plot-1 and plot-2, respectively, in Figure 1. The relative density values in the plot-1 of Figure 1 increased with increasing SPS temperatures from 850 to 1 100°C, with significant increase from 89.5% at 900°C to 97% at 950°C and only a slight increase at temperatures above 950°C. The relative density of 98.5% was achieved at 1 100°C. Similarly, the relative density values in plot-2 of Figure 1 increased with increasing dwell time from 0 to 2 min at temperatures below 950°C and did not show significant difference with increasing dwell time from 0 to 2 min at temperatures above 950°C.

Figure 1: The variation of relative density and microhardness as a function of SPS temperature

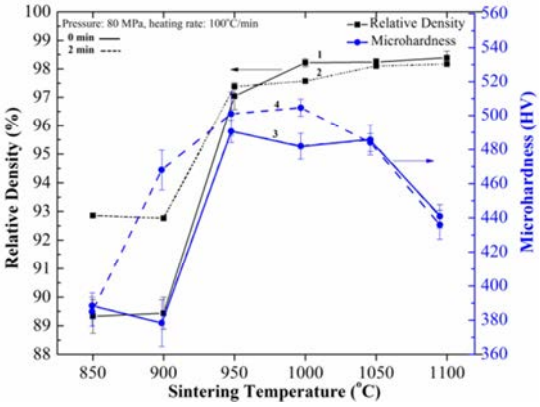

The microhardness values for dwell times of 0 and 2 min are presented in the plot-3 and plot-4 of Figure 1, respectively. The microhardness values shown in plot-3 of Figure 1 progressively increased from 388.5 HV at 850°C to 490.6 HV at 950°C and remained unchanged up to 1 050°C and decreased down to 441 HV at 1 100°C. The microhardness values shown in plot-4 of Figure 1 were consistently higher for the dwell time of 2 min than the dwell time of 0 min at SPS temperatures below 1 000°C. The relative density and microhardness data for 2 min dwell time (Figure 1 – plot 2 and 4) clarified three distinct stages of the sintering process as a function of SPS temperature (850-1 100°C). In the temperature range of 850-900°C, significant hardening occurred without much improvement in densification; at 900-1 000°C both densification and hardening occurred; and above 1 000°C the extent of densification did not change much at all but microhardness was found to be less. It can be argued that at temperatures higher than 1 000°C the microhardness values dropped because of the microstructural evolution possibly due to coarsening of grains and oxide precipitates.

Figure 2: Influence of sintering time on (a) the relative density and (b) microhardness, at SPS temperatures at 850, 950 and 1 050°C

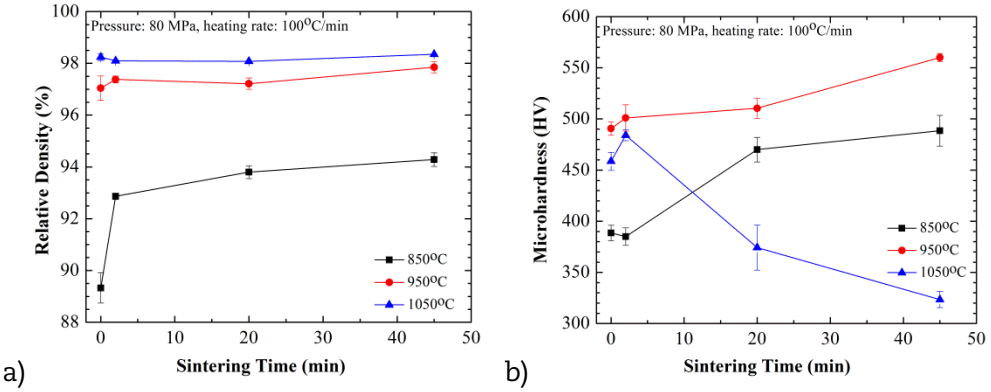

In order to understand the effect of SPS temperature and time, three temperatures (850, 950 and 1 050°C) were selected from Figure 1 and the dwell time was varied between 0 and 45 min at those three temperatures. The density and microhardness were measured and presented in Figure 2a and b, respectively. The relative density of the SPSed specimens increased with increasing SPS temperatures between 850-1 050°C at all dwell times. The microhardness values of the 14LMT alloys SPSed at 850 and 950°C increased consistently with increasing dwell time from 0 to 45 min. However, the microhardness showed a decrease at 1 050°C after 2 min. The microhardness values were 488.5, 591 and 323.5 HV, after SPS at 850, 950 and 1 050°C for 45 min, respectively.

Effect of SPS temperatures and times on the microstructural evolution

SEM and EBSD studies

The SEM micrographs along with corresponding EBSD maps as insets from various 14LMT alloy specimens SPSed at different temperatures for a dwell time of 45 min are shown in Figures 3a-c. A bimodal grain size distribution (nano grains and coarse grains) was observed in all the micrographs and the volume fraction of the coarse grains increased with higher SPS temperatures. Some remained porosity is observed as black regions in the back scattered SEM and EBSD micrographs shown in Figures 3a-c. The area fraction of porosity in the 14LMT alloy SPSed significantly decreased with increasing sintering temperature from 850°C to 950°C. The area fraction of porosity was estimated to be 5.1%, 2.1% and 1.0% at SPS temperature of 850, 950 and 1 050°C, respectively. Grain coarsening occurred with increasing SPS temperature up to 1 050°C as shown in Figure 3c.

Figure 3: SEM and EBSD micrographs of the specimens SPSed for 45 min at (a) 850°C, (b) 950°C, (c) 1 050°C (Note that the inset EBSD microgarphs have a marker scale of 10 µm in length)

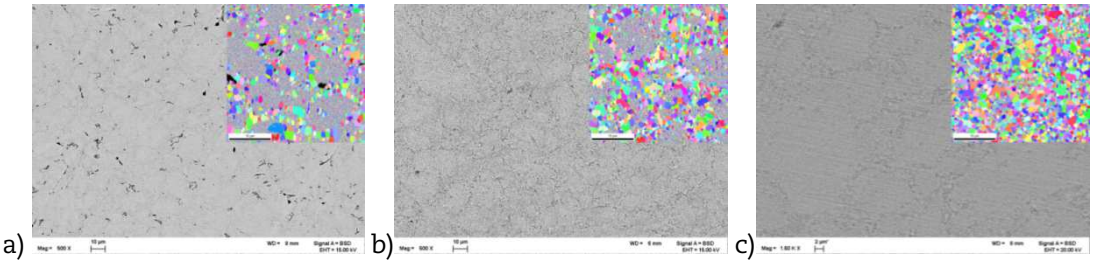

TEM studies

The TEM study was focused on the 14LMT alloy SPSed at 950°C for 45 min. In Figure 4a, an example of the bimodal grain size distribution showed that the ultrafine grains were surrounded by nanograins, and a high number density of the nano-precipitates in both types of grains. A high density of dislocations and nano-precipitates interacting in a grain interior with an average diameter of 1 µm has been shown in Figure 4b. In the vicinity of this micron-sized grain there were nanograins, and dislocation densities in the fine ferrite grains were higher than in the coarse grains as shown in Figure 4c. It has been noticed that in the micron-sized grains the precipitates were larger and/or located at the grain boundaries where as in the nanograins, precipitates were smaller and located inside the grains. A high angle annular dark field (HAADF) STEM micrograph of the sintered 14LMT alloy is shown in Figure 4d.

Nano-precipitates with different Z-contrast could be distinguished from the bcc ferritic matrix as the contrast of these precipitates was due to a difference in their chemical compositions as compared to that of the matrix. Several EDS analyses on a large area located in the matrix revealed a chemical composition of Fe-1.4Ti-15.19Cr-0.23Mo-0.55La (wt%) that was close to the nominal composition. Larger and smaller precipitates were observed along the grain boundaries and in the grain interiors, respectively. Two different types of the precipitates were observed in the HAADF micrograph; the nano precipitates with a darker contrast, spherical morphology and average size varying from 20 to 50 nm (mostly located at the grain boundaries), and the nano-precipitates with a brighter contrast, faceted morphology and average size varying from 2 to 30 nm (mostly located in the grain interior).

Figure 4: TEM micrographs of the specimen SPSed at 950°C for 45 min
a) Bright field micrograph of micron-sized and nanograins
b) a larger grain with high dislocation and precipitate density
c) nanograined region of the microstructure
d) STEM-HAADF image showing the distribution of the nano-precipitates

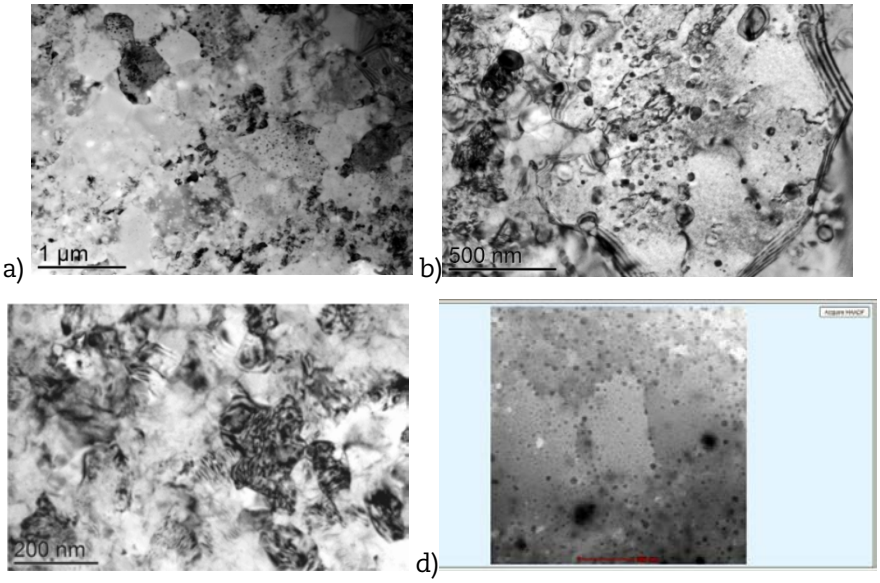

APT studies

Figure 5 illustrates the location of different species (CrO, O, Mo, Ti, TiO, La and LaO) in the APT reconstruction maps of the 14LMT alloy SPSed at 950°C for 45 min. The region sampled in the APT experiment corresponds to the TEM BF image presented prior to the APT maps in Figure 5. A uniform clustering of CrO, TiO, La and O is clearly evident in the APT maps. This was also confirmed by the TEM BF and HAADF micrographs taken from the tip prior to the APT experiment. Such nanoclusters were also noted in the MAed powder as discussed elsewhere [7]. The number density of CrO-TiO-La-enriched nanoclusters in 14LMT alloy SPSed at 950°C for 45 min was estimated to be 1.2×10^{24} m^{-3} with the average Guinier radius of 1.5±0.3 nm. The average cluster composition 8.9 at.% Cr, 17.8 at.% Ti and 5.9 at.% La, 35.6 at.% O along with Fe as the balance. Based on the matrix-corrected cluster composition, the ratio of Cr:Ti:La:O was found to be 4:3:1:5.

Figure 5: A bright field TEM image of an 14LMT (950°C and 45 min) APT specimen prior to analysis (on the top left) and 3-D APT reconstruction maps obtained from the same tip

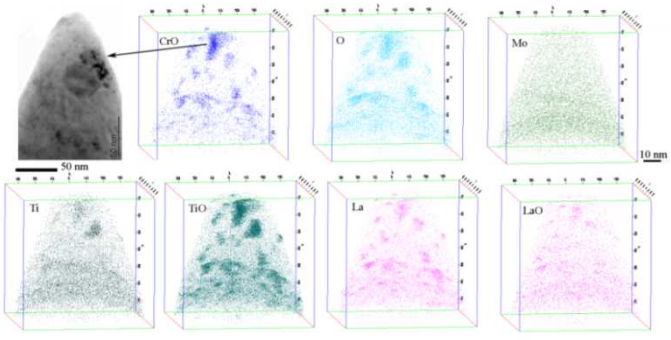

The number density of CrO-TiO-La-enriched nanoclusters in 14LMT alloy SPSed at 950°C for 45 min was estimated to be 1.2×10^{24} m^{-3} with the average Guinier radius of 1.5±0.3 nm. The average cluster composition 8.9Cr-17.8Ti-5.9La-35.6O (at%) along with Fe

as the balance. Based on the matrix-corrected cluster composition, the ratio of Cr:Ti:La:O was found to be 4:3:1:5. Miller et al. [15] a high number density (2×10^{24} m^{-3}) of ultrafine Ti-Y-O-enriched particles with an average Guinier radius of 1.2±0.4 nm in the MA957 ODS alloy. The composition of these particles was estimated by the envelope method to be Fe-(32.9±5.3)Ti-(15.4±7.3)Y-(39.9±6.9)O-(1.7±1.7)Cr-(0.02±0.2)Mo (at%). To study the effect of SPS temperatures on the nanocluster size, distribution and chemical composition, similar APT analysis (not shown here) was carried out on the 14LMT alloy SPSed at 1 050°C for 45 min. Clustering of CrO, TiO and La was clearly observed. The number density of CrO-TiO-La-enriched nanoclusters in the sample consolidated at 1 050°C was estimated to be 0.66×10^{24} m^{-3} with the average Guinier radius of 1.8±0.4 nm. With increasing SPS temperature from 950 to 1 050°C, the number density of nanoclusters decreased whereas the Guinier radius increased. However, the change is found to be minimal. For the oxide precipitates, the concentration ratio of Cr:Ti:La:O was calculated to be about 2:2:4:1 based on the matrix-corrected composition.

Effect of heating rate, applied pressure and pulsed electric current

The relative density and microhardness values for the 14LMT specimens SPSed with various heating rates, applied pressures and pulsed electric currents is summarised in Table 1. The SPS temperature and dwell time was kept at 950°C and 7 min, respectively. The relative density values increased slightly with increasing heating rates from 50 to 200°C/min, which is likely due to a large thermal gradient existing with higher heating rates.

Table 1: Relative density and microhardness for various heating rates, applied pressures and pulsed electric currents (the SPS temperature and dwell time were 950°C and 7 min)

SPS parameter		Relative density (%)	Microhardness (HV)
Heating rate (°C/min)	50	97.75±0.06	513.5±5.3
	100	97.87±0.04	492.7±7.8
	150	98.27±0.06	505.4±10.8
	200	98.40±0.02	482.0±6.4
Applied pressure (MPa)	40	90.76±0.04	300.3±13.3
	60	97.06±0.08	462.2±12.2
	80	97.87±0.04	492.7±7.8
	90	98.11±0.08	533.0±6.5
	110	98.30±.08	549.0±9.5
Pulsed electric current (A)	150	96.18±0.08	447.4±23.1
	275	97.87±0.04	492.7±7.8

The microhardness values slightly decreased with increasing heating rate from 50 to 200°C/min except an increase from 100 to 150°C/min. This higher microhardness values at a lower heating rate might have been caused by a greater oxygen pickup during heating or larger number density of the nano-precipitates and subgrains because of longer provided time for diffusion-based processes such as grain boundary diffusion or surface diffusion. Li et al. [16] have shown that the use of a high heating rate ensures oxide-free, well-sintered clean interfaces between powder particles in contrast to oxide-enveloped, poorly-sintered interfaces achieved with a slow heating rate. However, investigations on the effect of heating rate on densification in the SPSed products have shown conflicting results. For example, the heating rate (between 50 to 700°C/min) had no effects on the density of alumina (non-conductive) and $MoSi_2$ (with a good conductivity) [17,18]. Higher densification has been achieved by increasing the applied pressure from 40 to 110 MPa with a significant rate of increase from 40 to 60 MPa.

The pulsed electric current was decreased from 275 A (in normal condition) to 150 A. The pulse pattern of 12-2 was used in this study. However, the pulse pattern has no or little influence on the grain size and density according to the literature. Although higher density and microhardness were achieved at the higher SPS current, but the difference was not significant. Munir et al. [18] noted that during SPS the current and temperature are dependent variables and their influence cannot be clearly separated. During SPS, the powder is heated by Joule heating by the applied current passing through it. In addition to direct heating role of the DC current, the mass transfer can be enhanced at higher currents due to the increase in concentration of defects and mobility of the defects [18]. Thus, a higher density and hardness could be achieved at higher current levels.

Conclusions

A novel class of NFSs (14LMT alloys) was developed using La_2O_3 as an alternative RE addition via a processing route combining the mechanical alloying and spark plasma sintering techniques [19]. The relative density and hardness increases as a function of temperature and time, but at the sintering temperature of 1 050°C, the hardness decreased presumably due to the coarsening of the grains and some of the oxide precipitates. The optimum hardness and density was obtained at a SPS temperature of 950°C and 45 min. The microstructures of the 14LMT alloys were studied by SEM-EBSD, TEM and APT. The EBSD studies revealed the development of a bimodal grain size distribution via the dynamic recrystallisation process. The particle size and morphology were investigated by TEM and revealed a size range of 2-70 nm. The APT experiments revealed Cr-La-Ti-O based nanoclusters in SPSed 14LMT alloys. The lower heating rates provided higher microhardness values but lower density. Higher density and hardness values were achieved at higher applied pressure and pulsed electrical current. While further work is needed, this study demonstrates that the lanthana addition and SPS could provide novel approaches of alloy design and processing for developing NFSs.

Acknowledgements

This work was supported partly by the Laboratory Directed Research and Development Program of Idaho National Laboratory, Contract DE-AC07-05ID14517, and partly by a grant of the Advanced Test Reactor National Scientific User Facility (ATR NSUF).

References

[1] Odette, G.R., M.L. Alinger, B.D. Wirth (2008), "Recent developments in irradiation-resistant steels", Annu. Rev. Mater. Res., 38, pp. 471-503.

[2] Wu, Y. et al. (2012), "Transmission electron microscopy characterisation of the nanofeatures in nanostructured ferritic alloy MA957", *Acta Materialia*, 60[8], pp. 3456-3468.

[3] Ukai, S., M. Fujiwara (2002), "Perspective of ODS alloys application in nuclear environments", Journa of Nuclear Materials, 307–311, pp. 749-757.

[4] Williams, C.A. et al. (2013), "The formation and evolution of oxide particles in oxide-dispersion-strengthened ferritic steels during processing", Acta Materialia, 61[6], pp. 2219-2235.

[5] Reed, Z.D., M.A. Duncan (2008), "Photodissociation of yttrium and lanthanum oxide cluster cations", Journal of Physical Chemistry, 112, pp. 5354-5362.

[6] Mueller, A.J. et al. (2000) "Evaluation of oxide dispersion strengthened (ODS) molybdenum and molybdenum-rhenium alloys", International Journal of Refractory Metals and Hard Materials, 18, pp. 205-2011.

[7] Pasebani, S. et al. (2013-I), "Mechanial alloying of lanthana-bearing nanostructured ferritic steel", Acta Materialia, 61[15], pp. 5605-5617.

[8] Gendre, M. et al. (2010), "A study of the densification mechanisms during spark plasma sintering of zirconium (oxy-)carbide powders", Acta Materialia, 58[7], pp. 2598-2609.

[9] Heintze, C. et al. (2011), "Microstructure of oxide dispersion strengthened Eurofer and iron–chromium alloys investigated by means of small-angle neutron scattering and transmission electron microscopy", Journal of Nuclear Materials, 2011. **416**(1–2): pp. 35-39.

[10] Heintze, C. et al. (2012), "Nanoscale characterisation of ODS Fe–9%Cr model alloys compacted by spark plasma sintering", Journal of Nuclear Materials, 428, pp. 139-146.

[11] Allahar, K.N. et al. (2013), "Ferritic oxide dispersion strengthened alloys by spark plasma sintering", Journal of Nuclear Materials, 443[1–3], pp. 256-265.

[12] Pasebani, S. et al. (2013-II), "A preliminary study on the development of La_2O_3-bearing nanostructured ferritic steels via high energy ball milling", Journal of Nuclear Materials, 434[1-3], pp. 282-286.

[13] Miller, M.K. (2000), Atom probe tomography, Kluwer Academic/Plenum, New York.

[14] Williams, C.A. et al. (2010), "Nanoscale characterisation of ODS–Eurofer 97 steel: An atom-probe tomography study", Journal of Nuclear Materials, 400[1], pp. 37-45.

[15] Miller, M.K. et al. (2004), "Nanometer scale precipitation in ferritic MA/ODS alloy MA957", Journal of Nuclear Materials, 329–333, pp. 338-341.

[16] Li, X.P. et al. (2013), "The critical role of heating rate in enabling the removal of surface oxide films during spark plasma sintering of Al-based bulk metallic glass powder", Journal of Non-Crystalline Solids, 375, pp. 95-98.

[17] Stanciu, L.A. et al. (2001), "Effects of heating rate on densification and grain growth during field assisted sintering of α-Al_2O_3 and $MoSi_2$ powders", Metallurgical and Materials Transactions A, 32A, pp. 2633-2638.

[18] Munir, Z.A. et al. (2006), "The effect of electric field and pressure on the synthesis and consolidation of materials: A review of the spark plasma sintering method", Journal of Materials Science, Vol. 41, No. 3, pp. 763–777, 2006.

[19] Shen, Z. et al. (2002), "Spark plasma sintering of alumina", Journal of the American Ceramic Society, 85, pp. 1921-1927.

Extra-safe LWR core with SiC/SiC fuel cladding by NITE method

Akira Kohyama and H. Kishimoto
Muroran Institute of Technology, Muroran, Hokkaido, Japan

Abstract

After the East-Japan Earthquake with the Fukushima nuclear plant severe accident, Japanese energy policy clearly declares the urgent need of extra-safe technology for nuclear plant, especially to LWR systems.

As the new direction of the government funded nuclear R & D programmes, Carbon and ceramic based reactor component R & Ds ensuring reactor safe technology have been initiated since 2012. The brief introduction of the program is provided.

The outline of the on-going government funded programmes aiming at the early utilization of SiC/SiC fuel cladding/assembly for LWRs based on NITE –method is introduced.

*The target of those projects is replacement of Zircaloy claddings to SiC/SiC based fuel cladding. The METI fund based projects, such as INSPIRE[*1] by the authors group and the MEXT fund based projects, such as SCARLET[*2] by the authors group have been launched as 5 year termed projects. These projects care for NITE process for making long SiC/SiC fuel pins and connecting technology integration. The recent accomplishment will be presented.*

As the representing results, successful fabrication of SiC/SiC fuel pin with thickness from 0.5 mm to 2 mm and variations of 2D and 3D with layered structure and with woven structure will be presented. The new fabrication method with pre-composite ribbon is also introduced. Those activities are strongly related with large scale production capability of SiC fibres and SiC nano-powders and SiC/SiC fabrication process line establishment including CVD/CVI process facility upgrading. The new CVD/CVI facility at Muroran Institute of Technology is to be used for final SiC surface coating to SiC/SiC fuel cladding.

Notes:
**1: SiC Fuel Cladding/Assembly Research Launching Extra-Safe Technology*
**2: Innovative SiC fuel Pin Research*

Section IV

Ceramics and general

Chairs: V. Inozemtsev and H. Kishimoto

Ab initio based kinetic Monte-Carlo simulations of phase transformations in FeCrAl

Pär Olsson
KTH Royal Institute of Technology, Sweden

Abstract

Corrosion and erosion in lead cooled reactors can be a serious issue due to the high operating temperature and the necessary flow rates. FeCrAl alloys are under consideration as cladding or as coating for stainless steel cladding tubes for lead cooled reactor concepts. The alumina scale that is formed, as Al segregates to the surface and Fe and Cr rich oxides break off, offers a highly protective layer against lead corrosion in a large range of temperatures. However, there are concerns about the phase stability of the alloy under irradiation conditions and of possible induced alpha-prime precipitation. Here a theoretical model of the ternary FeCrAl alloy is presented, based on density functional theory predictions and linked to a kinetic Monte-Carlo simulation framework. The effect of Al on the FeCr miscibility properties are discussed and the coupling of irradiation induced defects with the solutes are treated. Simulations of the micro-structure evolution are tentatively compared to available experiments.

Fabrication and properties of SiC ceramics for the application of LWR fuel cladding

Weon-Ju Kim*, Daejong Kim, Ji Yeon Park, Jeong-Yong Park and Yang-Il Jung
Korea Atomic Energy Research Institute, Republic of Korea

Abstract

Silicon carbide fibre-reinforced silicon carbide matrix (SiC_f/SiC) composites have extensively been studied for fusion and advanced fission energy systems due to their excellent high temperature properties, irradiation tolerance, inherent low activation and other superior physical/chemical properties. Recently, there have also been efforts for applying the SiC_f/SiC composites to fuel claddings for various types of advanced reactors including light water reactors (LWR). For the application of LWR fuel cladding, the kinetics of the SiC corrosion under a LWR condition needs to be clarified to confirm the possibility of a burn-up extension and the cost-benefit effect of the SiC composite cladding. In addition, the development of end-plug joining technology and the matrix microcracking susceptibility would be key challenges for the successful application of SiC composite cladding.

In this study, we have investigated the corrosion behavior of chemically vapor deposited (CVD) SiC under various LWR water simulating conditions. Preliminary results on joining studies using diffusion bonding and laser joining techniques will also be presented. In addition, we present the effect of CVD process parameters on various properties of SiC tubes such as surface roughness, microstructure, stoichiometry, mechanical properties, and so on.

Inhibition of oxidation in nuclear graphite

Philip L. Winston, James W. Sterbentz and William E. Windes
Idaho National Laboratory, United States

Abstract

Graphite is a fundamental material of high-temperature gas-cooled nuclear reactors, providing both structure and neutron moderation. Its high thermal conductivity, chemical inertness, thermal heat capacity, and high thermal structural stability under normal and off-normal conditions contribute to the inherent safety of these reactor designs. One of the primary safety issues for a high-temperature graphite reactor core is the possibility of rapid oxidation of the carbon structure during an off-normal design basis event where an oxidising atmosphere (air ingress) can be introduced to the hot core. Although the current Generation IV high-temperature reactor designs attempt to mitigate any damage caused by a postualed air ingress event, the use of graphite components that inhibit oxidation is a logical step to increase the safety of these reactors. Recent experimental studies of graphite containing between 5.5 and 7 wt% boron carbide (B_4C) indicate that oxidation is dramatically reduced even at prolonged exposures at temperatures up to 900°C. The proposed addition of B_4C to graphite components in the nuclear core would necessarily be enriched in B-11 isotope in order to minimise B-10 neutron absorption and graphite swelling. The enriched boron can be added to the graphite during billet fabrication. Experimental oxidation rate results and potential applications for borated graphite in nuclear reactor components will be discussed.

Introduction

Current Generation IV high-temperature gas-cooled reactors (HTR) are predominately constructed of graphite structural components and graphite fuel elements. The two basic types of HTRs are a prismatic-block or a pebble-bed design. Both design types have an annular active core region enclosed by an inner and outer graphite reflector. The annular region is composed of either prismatic fuel blocks or spherical fuel pebbles where both blocks and pebbles are primarily graphite with embedded low-enriched uranium particles (microspheres). For a nominal core power rating of 350 MW (thermal), the total mass of graphite in these proposed nuclear reactor cores can approach a massive 500 MT of graphite.

The Generation IV designs are cooled with helium gas at temperatures in the range of 550-850°C and at a pressure of 7MPa. In an off-normal event, such as a breach in the primary coolant circuit, the helium gas could escape and the containment building atmosphere could enter the hot core via the primary circuit. To mitigate oxidation damage to the graphite core, the containment building atmosphere is pure nitrogen gas (N2). If the containment building is simultaneously breached, atmospheric oxygen may enter the containment building and the hot reactor core, then the potential for graphite oxidation exists.

In the case of the prismatic reactor design, the fuel block is a hexagonal graphite block with vertically-drilled cylindrical holes for fuel rods and coolant channels. Under normal operating conditions, the fuel rod average can typically reach a normal operating temperature of 1 250°C and heat the surrounding block graphite to 900°C. The coolant channel surface is in direct contact with the cooling helium gas and in an off-normal air

ingress event this surface would be exposed to the oxidising atmosphere. Because gaps exist between the stacked hexagonal blocks, a bypass flow of helium gas is created around and between fuel blocks. Hence, all external prismatic block surfaces could potentially be exposed to oxidising effects of the ingress atmosphere. Since the inner and outer reflector regions are also composed of stacked hexagonal blocks, the bypass flow could also contact the surfaces of these blocks. Therefore, virtually all block surfaces in the prismatic-block core design including core support pedestals could be borated in order to reduce potential of oxidation from an air ingress event.

In the case of the pebble-bed reactor design, the fuel pebbles (~6 cm diameter) are loaded into the annular core region and cooled by the helium gas flow over the pebble. The outer graphite surface of each pebble is in contact with the helium gas. Boration of the outer graphite surface of each pebble would also provide an oxidation-reduction benefit. Similarly, the graphite surfaces of the inner and outer graphite reflectors in contact with the helium gas would likewise need to be borated.

Graphite oxidation characteristics

Graphite can undergo appreciable oxidation at temperatures as low as 400°C in air. In the event of a large break of the helium coolant circulation system, oxygen would be available to convert the solid graphite to gaseous carbon monoxide (CO) and carbon dioxide (CO_2) according to the following exothermic reactions:

$$C + 1/2\ O_2 \rightarrow CO\ (-111\ kJ/mole)$$

$$C + O_2 \rightarrow CO_2\ (-394\ kJ/mole)$$

Heat from these reactions and the reactor core would also allow a portion of the CO_2 to convert to CO:

$$C + CO_2 \rightarrow 2CO\ (172\ kJ/mole)$$

The rate of reaction and the net change in a graphite structure is dependent on the exposed graphite surface area, connected porosity, and degree of graphitisation, as well as the availability of oxygen, reaction temperature, and net absorbed radiation dose [1].

Early Atomic Energy Commission (AEC) tests indicated that irradiation led to in oxidation increases that were multiples of that seen in unirradiated material. Kosiba and Dienes [2,3] noted up to an 18-fold net increase in oxidation at 300°C for material that had previously been irradiated when it was placed in a 610 000 R/hr gamma field. The graphite in these tests was exposed to a fluence of 4×10^{20} neutrons/cm^2, yielding an estimated 2% atom displacement. In this case, the graphite was noted as being "low grade" material. The conclusion was that irradiation displaced atoms, which may be equated with creation of active sites that promoted more rapid oxidation.

Testing of a presumably higher grade of synthetic graphite in England [4] showed that irradiation enhanced oxidation selectively. Examination showed pitting attack at pores and grain boundaries increased by approximately one order of magnitude, as compared to unirradiated material. Pitting was observed on the 0001 face of the crystal, with pit density of 5×10^{10}/cm^2 to 5×10^{11}/cm^2. The pitting was linked to metallic impurities in the graphite. Surface characterisation was done by scanning electron microscopy, with Moire patterns indicating increased presence of interstitial atoms in the irradiated graphite. The irradiation fluence was 2×10^{19} n/cm^2.

Oxidation experimentation by Davidge [5] produced results indicating that oxidation was variable and greatly dependent on oxygen flow.

Several other researchers have shown that the presence of water (as steam) dramatically increases oxidation. As seen below, the reaction with water vapor has a higher enthalpy, and hence, a much higher reaction rate.

$$C + H_2O \rightarrow CO + H_2\ (131\ kJ/mole)$$

$$C + 2H_2O \rightarrow CO_2 + 2H_2 \text{ (-82 kJ/mole)}$$

The hydrogen may also react with the carbon to yield

$$C + 2H \rightarrow CH_4 \text{ (-75 kJ/mole)}$$

$$CO + 2H_2O \rightarrow CO_2 + H_2 \text{ (-214 kJ/mole)}$$

For off-normal HTR air ingress events, moisture in the air could contribute to the oxidation of the reactor core graphite.

Experimental work

The ability of irradiated borated graphite to resist oxidation was observed during post-irradiation examination of graphite components from the Advanced Gas Reactor-1 (AGR-1) experiment. The test was irradiated at the Idaho National Laboratory in the Advanced Test Reactor (ATR). The borated graphite components were exposed to an intense neutron flux over a period of 3 years, or 620 effective full power days. Accumulated fast neutron fluence (>0.18 MeV) on the graphite reached >4.0E+21 n/cm^2.The boron was natural boron containing approximately 19.9 atom percent B-10. The B-10 atoms fissioned in the neutron flux creating energetic helium and lithium nuclei [$n + {}_5{}^{10}B_5 \rightarrow {}_2{}^4He_2 + {}_3{}^7Li_4$] which further displaced graphite atoms and lead to some amount of swelling as in graphite components.

It was in these irradiated graphite components that the degree to which boron can inhibit oxidation was observed.

The AGR-1 experiment was composed of six capsules stacked axially, numbered from 1 to 6, bottom to top as inserted vertically in the reactor. The holders in Capsules 1 and 6 contained 5.5 wt% natural boron carbide (B4C), while holders in Capsules 2-5 contained 7 wt% B_4C. The higher boron content was reduced compact fission power in the ATR core midplane. This material was produced as a special test by GrafTech, Inc. (UCAR Carbon).

The time-averaged, volume-averaged temperature of each experiment capsule containing the irradiated borated graphite components (compact holders) was 1 200°C. The tristructural isotropic (TRISO)-particle fuel compacts placed in the graphite holders isolated the compacts from the steel capsule wall (experiment pressure boundary). The irradiated, borated graphite holders were approximately 101.6 mm (~4 inches) in length with a 50.8 mm (~2 inch) outer diameter. The total graphite holder was approximately 45 g. As fabricated, the holder approximate surface area is 28 000 mm^2 including the 3 vertical holes that contained the compacts. The holders were broken into pieces following removal of the compacts so that they could be transferred by pneumatic capsule (rabbit) from the disassembly cell to the analytical laboratory hot cell where the oxidation and leach processes were performed. The experiment contained 6 holders, one per experiment capsule. Efforts to oxidise the holder graphite to recover mobile fission products led to the observation that the presence of boron greatly inhibits oxidation. Oxidation temperatures ranged from 500 to 900°C in air. When it became apparent that the holders were not being decomposed effectively, a baseline test using 1 g of unirradiated, non-borated graphite was performed. That test indicated that complete ashing occurred in a 48-hour period.

The experiment cross section indicating where the graphite holder component was located is illustrated in Figure 1 below. Figure 2 shows the post irradiation condition of the holder from Capsule 5.

Part of the post-irradiation examination process involved the determination of the distribution of the mobile fission products within each capsule. The graphite holders simulate the graphite in the fuel blocks in the prismatic design. The graphite tends to adsorb a significant fraction of most fission products released from the compacts. The gamma-emitting fission product nuclides are readily measured by gamma spectrometry,

but the beta emitters, in particular strontium-90, can only be detected by reducing the graphite to ash, leaching the ash and doing strontium separation and counting using gas proportional or liquid scintillation detection.

Figure 1: Radial cross section view of AGR-1 experiment

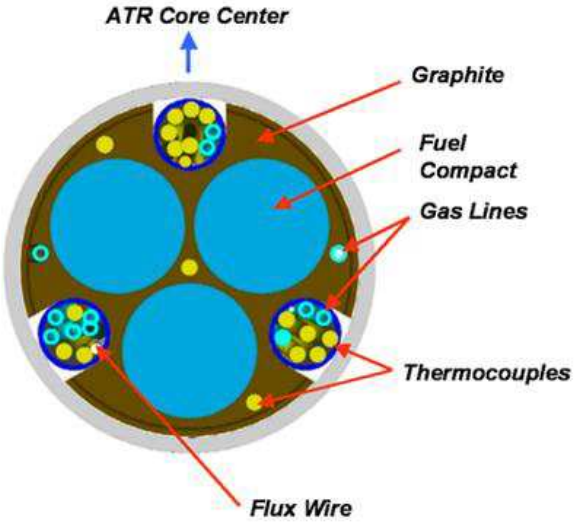

Figure 2: Graphite holder [Capsule 5 post irradiation]

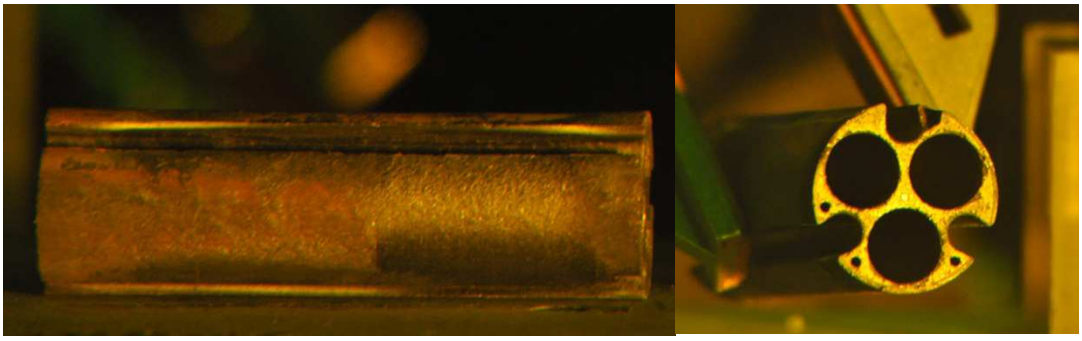

Oxidation test procedure

The holders were transferred pneumatically from the hot fuel examination facility main hot cell, which is an argon atmosphere cell to the MFC-752 Analytical Laboratory air atmosphere hot cells, where wet chemistry analysis preparation can be performed. The process of oxidation and leaching was performed in Hot Cell 5, which is equipped with laboratory glassware for leaching and an air furnace for oxidation. The oxidation and leach activities were performed in shielded cells due to the relatively high activity from fission and activation products in the graphite. The process of direct oxidation was initially undertaken without recognition that the presence of boron in the graphite would affect the oxidation rate. The broken holder pieces were placed in covered (not air-tight) 150 ml quartz beakers. The beakers were placed in a Vulcan muffle furnace, which had been modified with a small fan to promote air circulation through the heated volume. Oxidation was expected to be completed in a matter of hours. Based on previous testing of several nuclear grade graphites, oxidation of greater than 15% of the mass of historical grade H-451 graphite occurred in less than 2 hours at 750°C [6].

The oxidation procedural sequence for the first AGR-1 graphite holder tested (from Capsule 3, the third from the bottom) was as follows: 168 hours at 500°C, reported as

approximately 50% volume reduction by inspection; 40 hours at 750°C with between 10 and 20% change, followed by two cycles at 900°C for 88 hours. These oxidation times far exceeded the expected time for complete conversion. Mass loss was not quantified, because the primary interest was the Sr activity measured in the dissolved ash residue. The final 3 elevated temperature cycles resulted in apparent reaction of the graphite with the silica in the beakers. The boron content in this component was 7%.

Multiple efforts were made on the second oxidation test (Holder 5) to increase availability of oxygen to ensure complete conversion of graphite to ash. This test likewise yielded incomplete ashing. The initial temperature was 750°C, which was maintained for 136 hours, and resulted in a nominal volume reduction of approximately 40% (again by inspection only). The furnace auxiliary blower was set to produce a minimal flow. Following the burn phase the exposed surfaces of the pieces in the beaker were generally white. The second burn continued for 15 hours at 750°C and 24 hours at 900°C. The sample appeared to have melted and one of the two beakers containing the graphite showed some cracking. The third burn was performed at 900°C for 96 hours. By inspection, the graphite in the two beakers was reduced to approximately 15% and 6% of the original volume, respectively. The slow rate of decomposition led to the conclusion that the material did not have sufficient oxygen supply during heating for complete oxidation. Reconfiguration of the beaker lid to allow more airflow and increasing the power to the furnace blower were tried in an effort to improve oxidation rate. The fourth burn was performed for 55 hours at 900°C with the furnace fan at 80% of maximum voltage and the beaker covers removed. The residue at the end of the burn was largely unchanged from previous burn steps. The process is illustrated in Figures 3 through 6 below.

Figure 3 shows two beakers in the furnace containing gray-black and whitish vertical, free-standing pieces that largely retain their initial shape. Figure 4 shows that the material is still able to maintain a vertical shape, while Figure 5 shows the eventual reduction in height and in Figure 6, the attack on the fused silica beaker is visible.

On the assumption that there was a mass transport limitation, the third and fourth holders tested were ground to a nominal 1 mm diameter using a rotary manual grinder. This resulted in minimal change in conversion effectiveness. The particulate agglomerated somewhat, with minimal volume reduction.

Figure 3: Graphite holder pieces following first burn step (136 hrs @ 750°C)

Figure 4: Graphite holder pieces following second burn step (15 hours @ 750°C and 24 hrs @ 900°C)

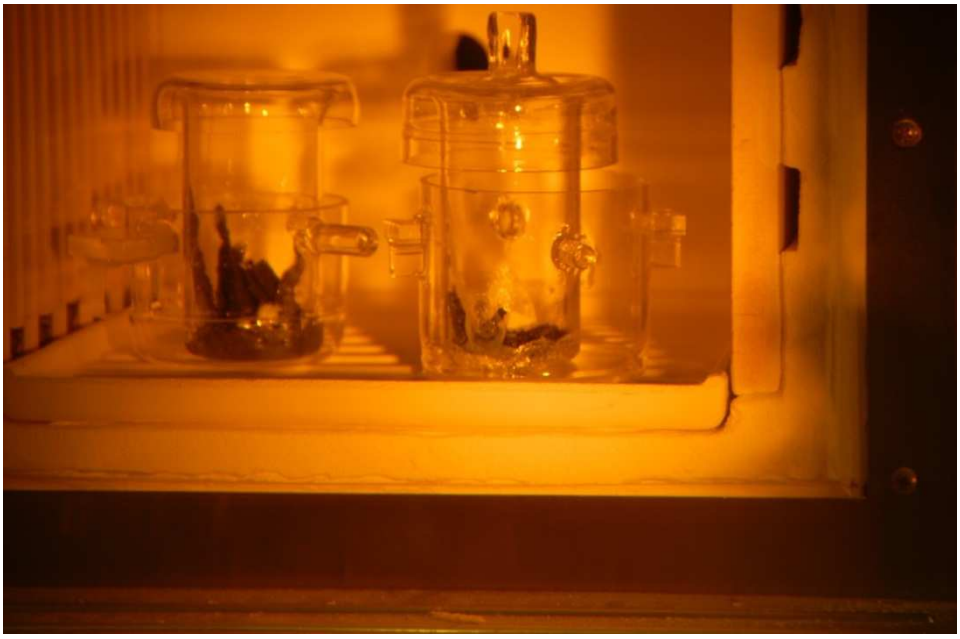

Figure 5: Graphite holder pieces following third burn step (96 hrs @ 900°C)

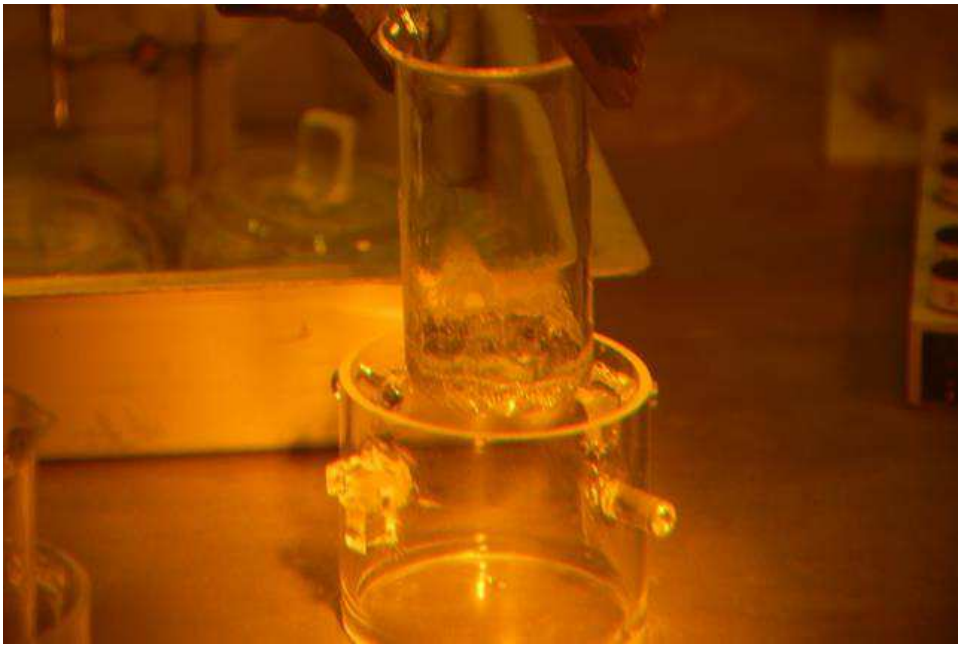

The observed condition after the first two oxidation steps was an apparent glassy surface. Further review of the holder chemistry raised the issue of boron content. A conclusion was reached that the boron-10 was being converted to lithium as a result of neutron irradiation, forming an impermeable glassy lithium carbide surface. Because lithium carbide is water soluble (reacting to form acetylene gas and lithium hydroxide), a process of alternately leaching the material with demineralised water or nitric acid followed by an oxidation cycle. Because it did not generate a gas bubbling reaction, it was concluded that the surface was not Li_4C_2. The material was impervious to insoluble in 4 M HNO_3. It was light and floated on the surface. From these characteristics, it is postulated that LiOH

(MP 450°C) or Li_2CO_3 (MP 723°C) were formed which reacted with the quartz beaker, leaving behind an insoluble borosilicate material. Because the boron used in the holder graphite was natural abundance, only 20% was B-10, meaning that even though the accessible lithium carbide may have dissolved, the remainder was still present as boron-11.

Figure 6: Graphite holder pieces following fourth burn step (55 hrs @ 900°C)

From the discussion of the processes applied, it was apparent that the graphite material was not completely converted to CO or CO_2. To confirm that the system was not oxygen limited, a comparable non-borated graphite sample placed in the same hot-cell furnace was reduced to ash in 8 hours at 750°C. The image following the first burn indicates that the material still has enough structural integrity to remain in its general original upright configuration. Compression testing is required to determine the degree to which boron-containing graphite retains the desired properties following oxidation.

A final technique using sodium-potassium alkali fusion on small samples of the borated holder graphite ground to flour consistency made no definitive improvement on the degree to which the graphite was converted to gas, and the recovery of residual strontium. In this test, the chunks of graphite were ground to a powder using a lab grinder, and 1 g samples were mixed with 6 parts of equimolar $Na_2K_2(CO_3)$ and fused in the furnace at 750°C for 2 hours in a zirconium crucible. The fused salts were dissolved in 8 M nitric acid. The intent was to react the boron carbide with the carbonate salts and separate them from the remaining graphite. The residue was then returned to the furnace for 8 hours, ramping up from 650 to 725°C followed by leaching with nitric acid. Analysis was performed on both the fusion and post-burn leach solutions. Testing on unirradiated material showed effective conversion, with greater than 80% of the graphite being consumed. For the irradiated material, the mass-normalised strontium analysis results were not significantly greater than by the other methods. Gamma ray activity on the resultant filtrate indicated that not all of the graphite was converted to CO or CO_2.

Other examples of oxidation inhibition due to boron in graphite

Since at least 1984, work has been published indicating the oxidation inhibition effects of boron in carbon materials. McKee [7] found that carbon-composites sealed with borate resisted oxidation at 1 200°C. Boron-doped graphite fibre has been tested for oxidation resistance in aerospace applications where the fibre must perform under high temperature conditions at leading edges of airfoils. Howe [8] tested fibres with 3.3 and 4.6% boron and suggests that 1% is the minimum at which oxidation is affected.

Although the borated graphite used in the AGR experiment was prepared as B_4C, similar changes in oxidation inhibition were seen in graphite impregnated with B_2O_3. Savchenko [9] observed a 150°C increase in the oxidation temperature of borated graphite foil. Approximately 2 wt% boron oxide was incorporated into the graphite. Physical properties of flexibility and tensile strength were also enhanced by the inclusion of boron oxide. It is also noted that it is less effective if it is applied as a surface coating rather than impregnating the boron into the graphite.

In some instances, boron acts as a catalyst with regard to oxidation, but it generally inhibits oxidation when present in concentrations beyond a certain percentage. At approximately 4% boron in Saran char, Karra [10] reported an approximate 50% inhibition, while 1.1% boron concentration resulted in a nominal 75% increase in oxidation. Multiple explanations have been offered to explain the inhibition, including boron's effect on increasing graphitisation, as well as the substitution of boron into the graphene structure in place of carbon.

The fact that boron inhibits oxidation in carbon materials has been established. Inclusion of boron in materials for nuclear service has not been widely studied, because of boron's neutronic effects. Because the fuel density of the high temperature reactor is quite low, and the potential neutron absorption by boron, the concerns about neutron economy have generally been presumed to outweigh the positive oxidation effect of boron on carbon. However, natural boron is approximately 20% B-10, which has a thermal neutron absorption cross-section of approximately 0.9 barns (0.0253 eV). The corresponding thermal neutron absorption cross-section for B-11 is 0.0055 barns. Since the B-10 absorption cross section is effectively 164 times greater than B-11, it will be necessary to use boron enriched in the low-absorbing B-11 isotope for application in an HTR for graphite oxidation inhibition. Adding B-11 to block or pebble graphite in an HTR will supplant some carbon atoms, however, the substitution of carbon atoms with B-11 atoms will not create a neutronic reactivity impact to the active core, since the carbon thermal absorption cross section is very small and almost the same as the B-11 cross section. Likewise, the neutron scattering cross section for B-11 is almost identical to that of C-12, which is the main constituent of graphite, hence damage due scattering is expected to be equivalent.

Conclusion

The oxidation tests reported here indicate that presence of 5.5 to 7 wt% boron carbide in graphite inhibits oxidation, even though the neutron capture by boron-10 created more active sites for oxidation reaction. For application to high-temperature gas-cooled reactors, graphite fuel, reflector and support structures could be borated with B_4C enriched in boron-11. Based on our experiments, this inclusion could significantly reduce graphite oxidation (corrosion) during a postulated air ingress event.

Additional tests are required to generate definitive oxidation rate and critical condition values, as well as to determine the changes in structural properties as the oxidation progresses. Compressive strength is a primary structural property of concern. Further testing is needed to determine the effect of inclusion of boron on net compressive strength.

Acknowledgements

The laboratory development and functional test work reported here was performed by Jeffrey Berg and Martin Kearns of the INL MFC Analytical Laboratory.

References

[1] Snead, L, and T. Burchell, Oxidation of High-Quality Graphite for IFE, Laser IFE Workshop, Naval Research Laboratory, February 2001.

[2] Kosiba W.L. and G.J. Dienes, The Effect of Displaced Atoms and Ionizing Radiation on the Oxidation of Graphite, Advances in Catalysis Volume 9, 1957, Pages 398–405 Proceedings of the International Congress on Catalysis.

[3] Kosiba and Dienes USAEC RID-7565 Ppart 1) 1959.

[4] Dawson, I.M. and E.A.C. Follett, "The Observation of Oxidation on Synthetic Graphite Before and After Irradiation", *Proc. R. Soc. Lond.* Vol. 274 No. 1358 386-394, 30 July 1963.

[5] Davidge, P.C.; Tomlimson, M.; Wright, J., 1959-04-01, 4257886, AERE-C/R-1450, Technical Report, Other Information: Orig. Receipt Date: 31-DEC-59, United Kingdom Atomic Energy Authority. Research Group. Atomic Energy Research Establishment, Harwell, Berks, England.

[6] Smith, R., Unpublished research test results, Idaho National Laboratory, 2009.

[7] McKee, D.W., C.L. Spiro and E. Lamby, Effects of Boron Additives on the Oxidation Behavior of Carbons, Carbon Volume 22, p 495, 1984.

[8] Howe, J.Y.*, L.E. Jones Influence of boron on structure and oxidation behavior of graphite fibre, P120 Carbon 42 (2004) 461–467 School of Ceramic Engineering and Materials Science, Alfred University, Alfred, NY 14802, United States. Received 15 August 1999; accepted 15 September 2003.

[9] Savchenko, D.V., A.A. Serdan, V.A. Morozov, G. Van Tendeloo, S.G. Ionov, Improvement of the oxidation stability and the mechanical properties of flexible graphite foil by boron oxide impregnation, New Carbon Materials, 2012, 27(1):12–18.

[10] Karra, M, P.A. Thrower, and L.R. Radovic, "The Role of Substitutional Boron in Carbon: Inhibitor or Catalyst", ACS Fuel Conference 1996, New Orleans.

Other references

Fergus, J.W. and W.L. Worrell, Silicon-carbide/boron-containing coatings for the oxidation protection of graphite. Carbon 33(4):537--543 (1995).

Goodwin, Cameron Slack, Graphite Oxidation and Damage under Irradiation at High Temperatures in an Impure Helium Environment, Authors: Advisors: Al-Sheikhly, Mohamad Department/Program: Nuclear Engineering Type: Dissertation University of Maryland (College Park, Md.) Nuclear engineering graphite Issue Date: 2012.

Moormann, Rainer, Phenomenology of Graphite Burning in Air Ingress Accidents of HTRs Science and Technology of Nuclear Installations Volume 2011, Article ID589747 Forschungszentrum Jülich.

Lang, F.M, M. Brie, and M. deNoblet, Thermal Oxidation Rate of Purified Graphite in Air 1967.

Neutron vs ion irradiation: Differences and similarities in the nanostructural evolution of Fe-Cr alloys irradiated at 300°C

Mercedes Hernández Mayoral[a], Frank Bergner[b], Cornelia Heintze[b], Viacheslav Kuksenko[c], Cristelle Pareige[c], Philippe Pareige[c], Lorenzo Malerba[*d]

[a]CIEMAT, Spain
[b]Helmholtz Zentrum Dresden-Rossendorf, Institute of Safety Research, Germany
[c]Groupe de Physique des Matériaux UMR-CNRS 6634, Équipe de Recherche Technologique, No. 1000, Université de Rouen, France
[d]SCK•CEN, Structural Materials Modelling and Microstructure, Institute of Nuclear Materials Science, Belgium
[*]Presenting author

Abstract

The same four Fe-Cr model alloys have been neutron and ion irradiated at the same temperature (300°C) up to comparable doses and the nanostructural changes have been investigated using different techniques, including TEM and APT for the nanostructure. The neutron irradiated alloys have also undergone extensive mechanical characterisation, while nanoindentation has been applied to the ion irradiated specimens, to evaluate the changes induced by irradiation in their mechanical behaviour. We show that the nanostructural evolution experienced by neutron and ion irradiated alloys is qualitatively and also quantitatively different, most likely as a consequence of the different dose rate, which is orders of magnitude higher with ions than with neutrons. However, qualitatively the trends observed in the dependence of the mechanical properties on Cr content remain similar.

Poster session

The influence of cooling rate from annealing temperature on the microstructure of Haynes 230

Injin Sah, Sunghoon Hong, and Changheui Jang*
Korea Advanced Institute of Science and Technology, Republic of Korea

Abstract

The effects of cooling rate from annealing temperature, which simulated the diffusion bonding process, on the microstructure of Haynes 230 (Ni-22Cr-14W-5Co) were investigated. While the grain boundaries are slightly covered with Cr-rich $M_{23}C_6$ carbides for the diffusion-bonded and quenched condition, precipitates were extensively present on/near the grain boundaries for the furnace-cooled specimens. For the furnace-cooled specimens, lamellar precipitates were extensively formed near the grain boundaries below 1 000°C, with intervals of a few hundred nanometers. Also, grain boundaries were severely serrated for the furnace-cooled specimens. Through electron probe micro analysis and transmission electron microscope, the lamellar precipitates were identified as (Cr,W)-rich $M_{23}C_6$-type lamellar carbides. Despite the differences in microstructure, tensile properties were not much affected by the cooling rate. Creep tests are underway and results will be presented.

1. Introduction

Solid-solution strengthening Ni-base superalloys are key candidate materials for the application of the intermediate heat exchanger (IHX) in a very high temperature gas-cooled reactor (VHTR) [1]. For the manufacturing process of micro-channel type heat exchangers, solid-state diffusion bonding is required [2]. For bonding, high temperature up to annealing temperature is preferred to promote the diffusion of the solute elements across the mating surfaces. However, thermal history during the diffusion bonding process would have influence on the microstructural characteristic not only at the bond-line, but also in the matrix away from the bond-line. In this study, simulated diffusion bonding condition was applied for the as-received alloy, and microstructural features especially near the grain boundaries and their effects on the tensile and creep-rupture properties are discussed.

2. Experimental procedure

A solid-solution strengthened Ni-base superalloy, Haynes 230 (Ni-22Cr-14W-5Co), was used in this study. The heat treatment conditions carried out in this study are summarised in Table 1. To simulate the diffusion bonding procedures, the alloy was exposed to the annealing temperature (1 200°C) for 5 h and then furnace-cooled (HT-A). Further two-step cooling heat treatments (HT-B, C, D, and E) were carried out to investigate the formation of the precipitates. Water quenching was used to keep the microstructure evolved during the cooling process.

Characterisation of the microstructure was performed using scanning electron microscope (SEM), transmission electron microscope (TEM) equipped with energy dispersive X-ray microscope (EDS) and electron backscatter diffraction (EBSD). For the

measurement of the mechanical properties, plate-type specimens were prepared for the tensile (RT and 900°C) and creep-rupture (900°C) properties. Strain rate of the tensile test was 3.33×10^{-4}/s to failure. For the tensile tests at elevated temperature, specimens were heated at the rate of 5°C/min. After the target temperature was reached, the specimens were held for 10 min to homogenise the temperature distribution before the tests.

Table 1: Heat treatment conditions investigated in this study

Designation		Heat treatment condition
HT-A	Holding at 1 200°C for 5 h	1 200-25°C furnace-cooled
HT-B		1 200-1 100°C furnace-cooled + water-quenched
HT-C		1 200-1 000°C furnace-cooled + water-quenched
HT-D		1 200-900°C furnace-cooled + water-quenched
HT-E		1 200-800°C furnace-cooled + water-quenched

3. Results and discussion

3.1 Formation of the discontinuous precipitates

Typical microstructure of the as-received Haynes 230 consists of the equiaxed grains with the average grain size of about 57 μm (Figure 1a). Secondary precipitates such as grain boundary Cr-rich $M_{23}C_6$ and randomly dispersed W-rich M_6C carbides were observed [3-6]. In the microstructure of the furnace-cooled alloys (HT-A), serrated grain boundaries covered with Cr-rich $M_{23}C_6$ carbides and the discontinuous precipitates were present (Figure 1b). While the grain boundaries of the HT-B are slightly covered with $M_{23}C_6$ carbides (Figure 1c), serrated grain boundaries with the formation of precipitates along the initial grain boundary are observed for the HT-C, D, and E (Figures 1d-f). Especially, for the specimen furnace-cooled down to 900°C (HT-D), lamellar morphology typical of discontinuous precipitates [7] extensively occurred near the grain boundaries. Considering that the grain boundary structure of HT-A is similar to that of HT-D, the temperature range for the formation of discontinuous precipitates would be 1 000-900°C during the cooling.

Figure 2 shows the EBSD analysis result for the grain boundaries containing discontinuous precipitates. In Figure 2b, boundaries between 2° and 12° are indicated in green, cyan between 12° and 22°, red between 22° and 32°, pink between 32° and 42°, yellow between 42° and 52°, and white between 52° and 62°. As shown in the figure, grain boundary migration is observed in high angle grain boundaries. As discussed by Williams and Butler [7], the high angle grain boundaries (red and pink color in Figure 2b) appeared in front of the advancing precipitates. To clarify the orientation relationship between the adjacent grains, TEM analysis was performed. According to the SAD (selected area diffraction) pattern analysis, the precipitates have a cube-on-cube orientation with the grain, which is contrary to the direction of thermally activated grain boundary migration. Also, the SAD pattern suggested that the discontinuous precipitates are $M_{23}C_6$ carbides. Additionally, from the EDS analysis, enrichment in Cr content in the precipitate confirmed that the discontinuous precipitates are Cr-rich $M_{23}C_6$ carbides which are typical of the carbides along the initial grain boundaries.

3.2 Mechanical properties

The presence of the discontinuous precipitates observed during the cooling from the simulated diffusion bonding condition is of concern because their deleterious effects on the mechanical properties were reported [4-8]. Especially, Tawancy found the accelerated primary creep rate with limited ductility if the discontinuous precipitates were formed for Haynes 230 during the furnace cooling [4]. Also, under creep-fatigue conditions, inter-granular cracks were only found on high angle grain boundaries with the discontinuous precipitates while not on high angle grain boundaries without the discontinuous precipitates [8].

**Figure 1: SEM micrographs of Haynes 230:
(a) as-received, (b) HT-A, (c) HT-B (quenched at 1 100°C), (d) HT-C (quenched at 1 000°C), (e) HT-D (quenched at 900°C), and (f) HT-E (quenched at 800°C)**

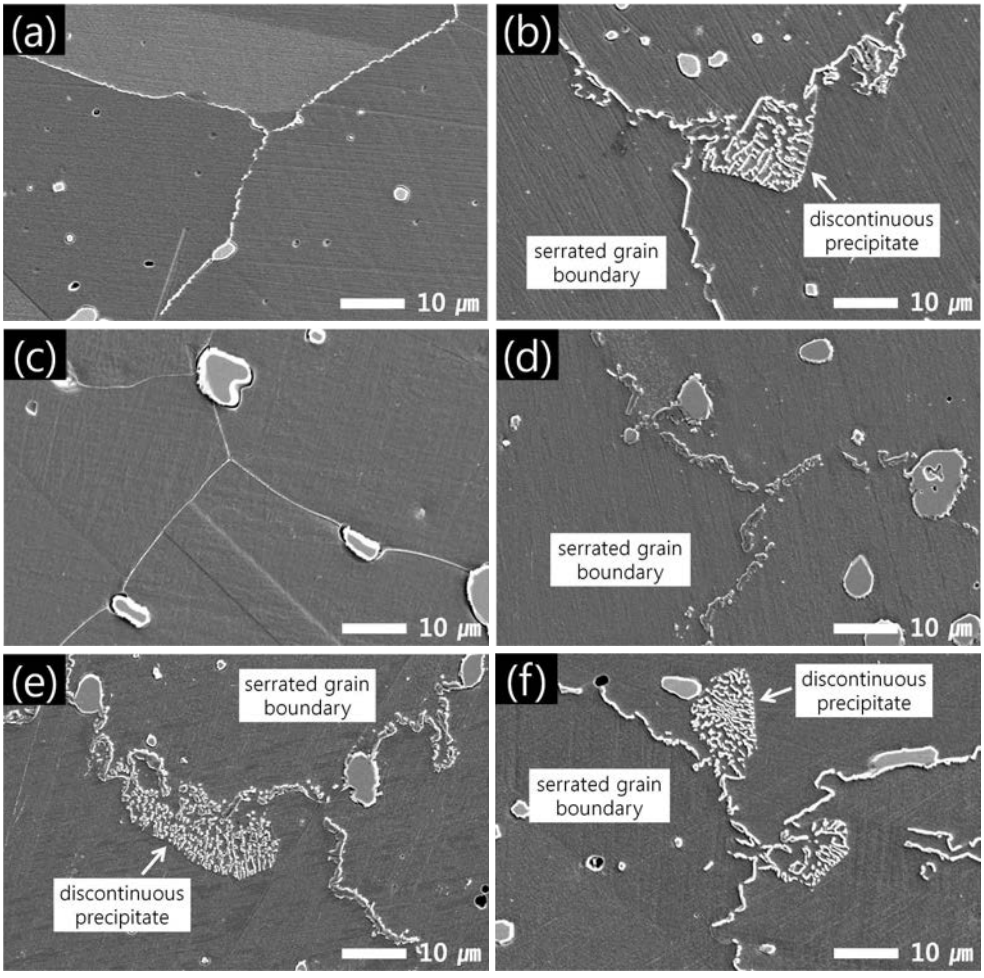

Figure 2: EBSD analysis results for the discontinuous precipitates observed in HT-D

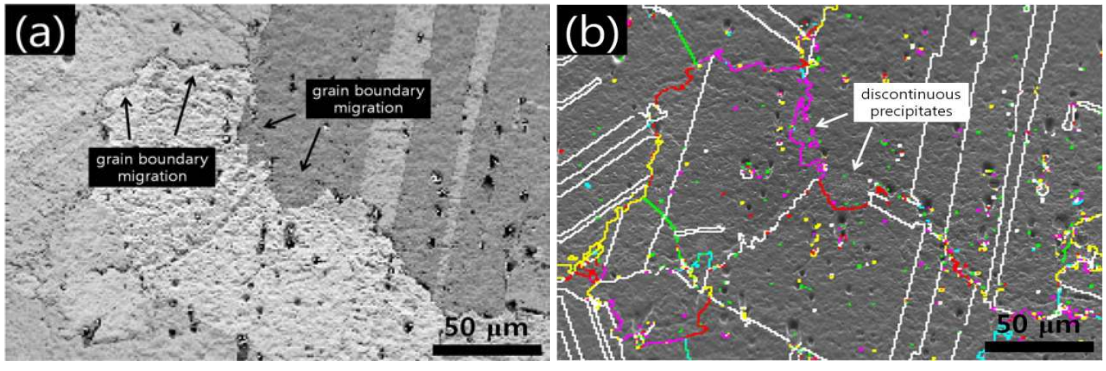

Tensile properties of the as-received and heat-treated (HT-A) specimens at room temperature and 900°C are summarised in Table 2. At room temperature, reduction of the yield strength, ultimate tensile strength, and elongation was generally observed. Reduction of the strength might result from the increased grain size up to about 86 μm; however, the decrease in elongation of the HT-A specimen would have been resulted from the development of the discontinuous precipitates. As the carbides on/near the

grain boundaries are brittle and the bond strength to the adjacent grains are lower, it is thought that the premature failure would occur in the vicinity of the discontinuous precipitates. By the same token, the reduction of the strengths could also be contributed from the microstructural characteristics (i.e., discontinuous precipitates) at the interface of the carbides and the matrix.

Table 2: Tensile properties of the as-received and heat-treated and furnace-cooled (HT-A) Haynes 230 both at RT and 900°C

Material	**As-received**			**HT-A**		
Tensile property	**YS (MPa)**	**UTS (MPa)**	**Elong (%)**	**YS (MPa)**	**UTS (MPa)**	**Elong (%)**
RT	449	851	62.9	397	807	51.5
900°C	222	259	75.3	203	213	77.3

The influence of the discontinuous precipitates on creep-rupture behaviour is shown in Figure 3. At elevated temperature above the equi-cohesive temperature where the strength of the grain boundaries equals to that of the grains, grain boundary is more susceptible for inter-granular cracks [9]. While the discrete grain boundary carbides could effectively impede the grain boundary sliding [4], the discontinuous precipitates at the high angle grain boundary observed in this study are thought to have a detrimental effect on creep deformation due to the lower bond strength with the adjacent grains. Further creep-rupture tests and electron microscopic analysis are in progress to demonstrate the deformation mechanism.

Figure 3: Creep-rupture result of Haynes 230

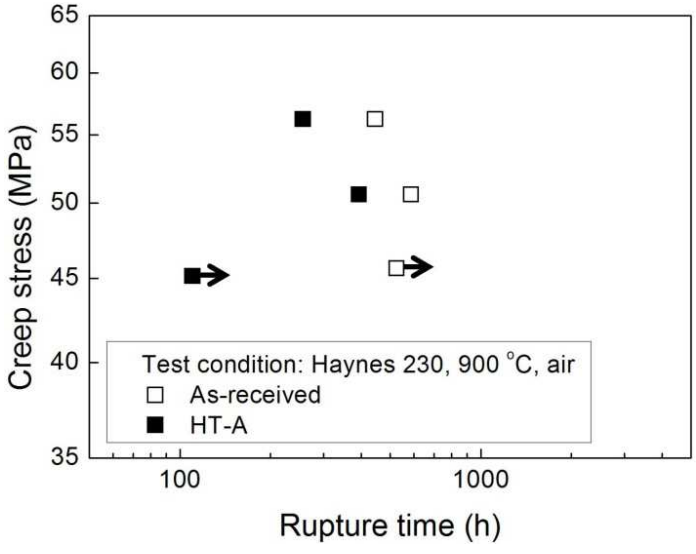

4. Conclusions

The objective of this study was to verify the relationship of the mechanical properties with the microstructure of the heat-treated Haynes 230. Especially, the heat treatment conditions performed in this study simulated the diffusion bonding process. For the furnace-cooled specimens, discontinuous precipitates (Cr-rich $M_{23}C_6$ carbides) induced by the grain boundary migration were observed in the temperature range of 900 and 1 000°C with the discrete carbides formed along the initial grain boundaries. Reduction of the tensile elongation and the creep-rupture life is caused by the presence of the discontinuous precipitates on/near the grain boundaries, which might result in lowering the bond strength with the adjacent grain.

Acknowledgements

This study was supported by the MSIP/NRF (Nuclear R&D Program 2013035153) of Korea. Part of the funding was provided by the BK21-Plus Program of the MSIP of Korea. One of the authors is also supported by the Global Ph. D Fellowship Program supported by MSIP/NRF.

References

[1] Corwin, W.R. (2006), "U.S. Generation IV reactor integrated materials technology program", Nuclear Engineering and Technology, 38[7], pp. 591-618.

[2] Sah, I., D. Kim, H.J. Lee, C. Jang (2013), "The recovery of tensile ductility in diffusion-bonded Ni-base alloys by post-bond heat treatments", Materials & Design, Volume 47, pp. 581-589.

[3] Guanghai Bai, Jinshan Li, Rui Hu, Tiebang Zhang, Hongchao Kou, Hengzhi Fu (2011), "Effect of thermal exposure on the stability of carbides in Ni-Cr-W based superalloy", Materials Science and Engineering: A, Volume 528, Issue 6, 15 March 2011, pp. 2339-2344.

[4] Tawancy, H.M. (1992), "High temperature creep behaviour of an Ni-Cr-W-B alloy", Journal of Materials Science, 27, pp. 6481-6489.

[5] Kim, D., I. Sah, C. Jang (2010), "Effects of high temperature aging in an impure helium environment on low temperature embrittlement of Alloy 617 and Haynes 230", Journal of Nuclear Materials, 405, pp. 9-16.

[6] Kim, D., I. Sah, C. Jang (2011), "Effects of aging in high teperature helium environments on room temperature tensile properties of nickel-base superalloys", Materials Science and Engineering: A, Volume 528, Issue 3, 25 January 2011, pp. 1713-1720.

[7] Williams, D.B., E.P. Butler (1981), "Grain boundary discontinuous precipitation reactions", International Metals Reviews, Vol. 26, No. 3, pp. 153-183.

[8] Chen, X., Z. Yang, M.A. Sokolov, D.L. Erdman III, K Mo, J.F. Stubbins (2013), "Low cycle fatigue and creep-fatigue behaviour of Ni-based alloy 230 at 850°C", Materials Science and Engineering: A, Volume 563, 15 February 2013, pp. 152-162.

[9] Frost, H.J., M.F. Ashby (1982), "Deforamtion mechanism maps: the plasticity and creep of metals and ceramics", Pergamon Press, pp. 53-59.

Assessment of thin-walled cladding tube mechanical properties by segmented expanding Mandrel test

Karl-Fredrik Nilsson
Institute for Energy and Transport, Joint Research Centre, EC, The Netherlands

Abstract

This paper presents the principles of the segmented expanding mandrel test for thin-walled cladding tubes, which can be used as a basic material characterisation test to determine stress-strain curves and ductility or as a test to simulate mechanical pellet-cladding interaction. The paper discusses the strengths and weaknesses of the test method and it illustrates how the test can be used to simulate hydride reorientations in zirconium claddings and quantify how hydride reorientation affects ductility.

Introduction

A number of mechanical tests for thin-walled cladding tubes for nuclear fuel have been proposed such as ring-compression test, ring-tensile test, burst test, four-point bend tests and different mandrel tests [1-3]. The main purpose of a mechanical test is material characterisation, but simulation of representative loadings such as mechanical pellet-cladding interaction could also be a main objective. A material characterisation test should be as simple as possible to analyse and the deformation of the specimen should preferably evolve in a stable manner also under softening or defect growth. A test with axisymmetric displacement controlled loading would be ideal. A test to simulate pellet-cladding interaction should include the key interaction features. In this paper we will explore the segmented expanding cone-mandrel (ECM) test both as a material characterisation test and as a test to simulate the mechanical pellet-clad interaction. We will illustrate the application by investigating the ductility of zirconium alloys with re-oriented hydrides.

Description of the ECM test

The segmented expanded cone-mandrel (ECM) test was proposed in the eighties [4]. Figure 1a shows the principles of our test set-up [5][6] which consists of a cone, segments and the tube specimen. The set of segments is manufactured from a cylindrical body with outer radius equal to the inner radius of the tube to be tested. A conical volume with the same angle as the cone is removed from the central part of the cylinder. The cylinder is then cut into equal sized segments. When the cone is displaced vertically by a specific value,u_z, a corresponding radial displacement, $u_r = \tan(\frac{\theta}{2}) \cdot u_z$, is imposed on the segments and the inner surface of the tube. The segments do not carry any hoop stress and have a very small deformation. The tube will be subjected to a periodic but controlled radial displacement from the segments. At the segment edges more complex stress and strain concentrations occur that depend strongly on the friction between the segments and the cladding tube. As a component test it is desirable that the stress variations induced by the

segments are representative for mechanical fuel-cladding interaction whereas for a material characterisation test one would like to minimise them. Different loadings can be obtained by controlling the number of segments and the friction coefficient. The deformation becomes more axi-symmetric by increasing the number of segments and by reduced friction between the tube and the segments. A tube with segments and cone ready for testing is shown in Figures 1b and 1c after testing with significant deformation. The designed prototype for the experiment consists of a lower cylindrical block, a cone with angle 20° and sets of segments. The segments and cone were made from STAVAX, which is a very hard and wear resistant material. The height and outer diameter of the cylinder from which the segments are made are 9.7 mm and 9.2 mm respectively. The diameter of the cylindrical hole at the bottom is 2.8 mm and at the upper end it is 6.2 mm to fit the cone. The lower block has a hole with a diameter suitable to allow enough travel for the cone to move down into it, whilst still providing a sufficient support for the assembly of segments and tube with pure sliding. The vertical displacement and the reaction force are recorded during loading and the change in diameter is measured by a transverse extensometer. The test can be performed under load or displacement control. The contact surfaces in the examples below were sprayed with teflon to minimise friction.

Figure 1:
a) Schematic illustration of the principles for the cone mandrel test before loading and with 5% and 50% applied strain
b) loaded specimen with extensometer for strain measurement
c) tested tube at large deformation with cone and segments

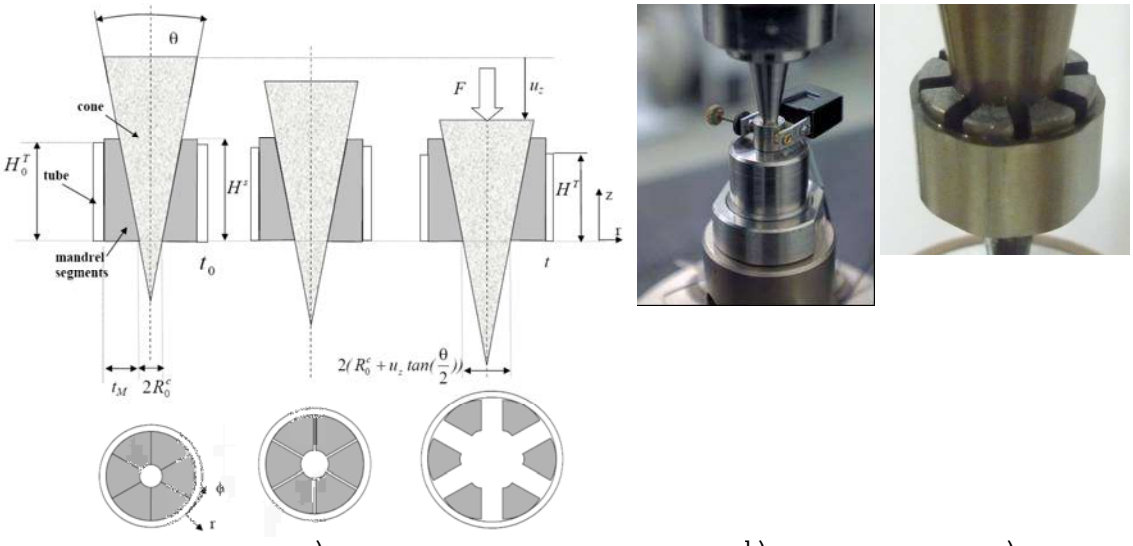

a) b) c)

Basic assessment of the SEM test

Stress-strain curve and axisymmetric model

Figure 2a shows the measured reaction forces versus the normalised radial displacement for six different tests. The first number in the legend (6, 8, 10 or 12) indicates the number of segments and the second number the sequence number of the test. The difference between the curves could stem from variation in the tensile properties between the tested tubes, or from variability of the test method itself. For instance it is obvious that the alignment of the segments between the tests and the friction between the different surfaces may vary between tests. Nevertheless the variation is not very large.

Figure 2: a) Measured reaction force vs. applied radial displacement; computed hoop stress-strain curve using the axi-symmetric analytical model and measured forces and displacement; b) Test 8-4 with different values of the friction coefficient but equal for all contact; c) all test tests with hard cone and friction coefficient = 0.04 d) friction coefficient 0.2 for all surfaces (None) and 0.2 for all but the surface indicated in the figure

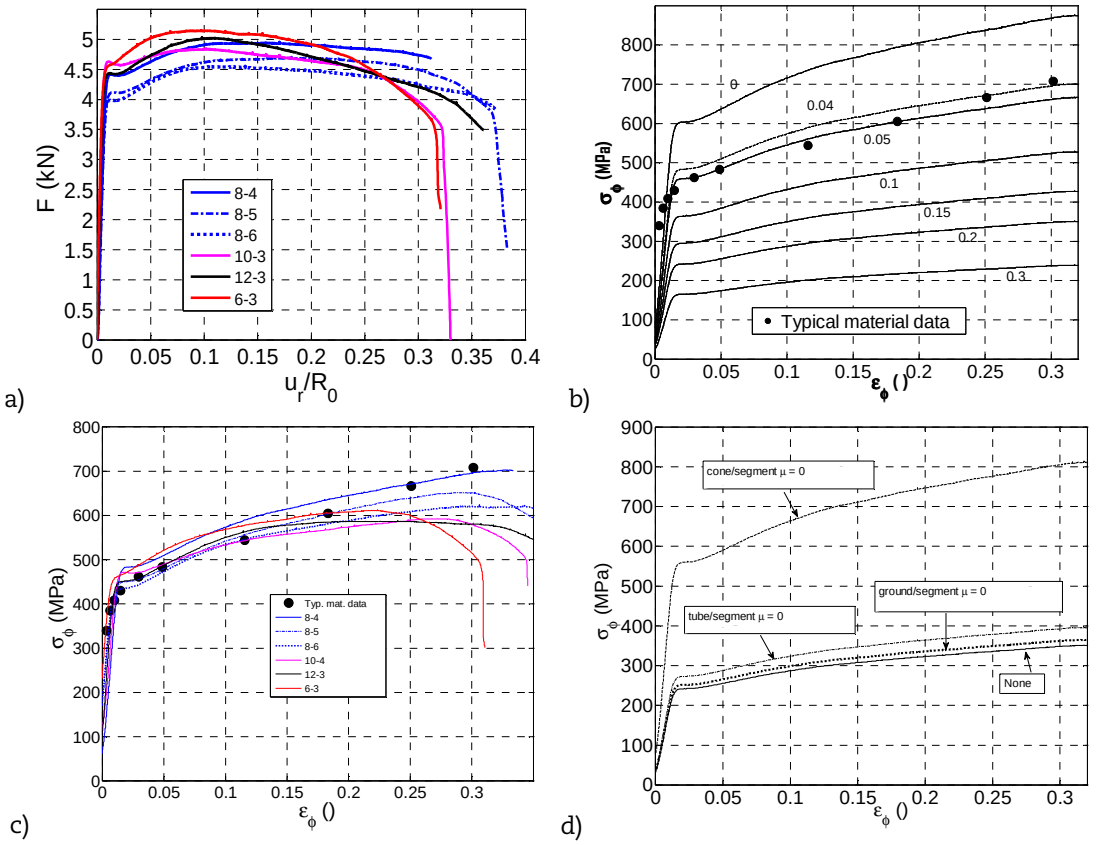

The test can be analysed with a semi-analytical model with the following assumptions: i) the deformation and loading are axisymmetric; ii) the cone and the segments are rigid but the segments do not carry any hoop stresses; iii) the contact model is a simple Coulumb friction; iv) the tube has constant hoop stress and is stress free in the axial direction, the radial stress is much smaller than the hoop stress and set to zero and there are no shear stresses; v) the material possesses orthotropic symmetry and plastic deformation is assumed to follow the Hill classic quadratic yield criterion. The equations are given in [5,6].

Figure 2b shows the computed stress-strain curves from the measured displacement and forces of test 8-4 for seven different values of the friction coefficient (0 to 0.3). The same friction coefficient is assumed between all contact surfaces and the material is assumed to be isotropic. The symbols in Figure 2b represent "typical data" from AREVA. A typical friction coefficient for teflon is 0.04 and we note that the computed curve with this value agrees quite well with the typical curve for this friction coefficient. In Figure 2c, the stress strain curves computed with a friction value of 0.04 are plotted for all six specimens. The curves diverge more at higher loads when localised plastic deformation develops in the opening between segments. Figure 2d shows the computed stress-strain curves from the data from test 8-4 for four different friction cases; one when the friction coefficient is 0.2 for each of the three contact surfaces and in the other cases it is 0.2 for two surfaces and 0 for one. The most important observation is that the friction has by far the largest effect for the cone/segment surface.

Effect of stress concentrations as segment edge

The edges of the expanding segments induce local stress concentrations on the cladding that qualitatively simulate the mechanical interaction between cracked fuel pellets and the cladding tube. This stress concentration decreases with increasing number of segments and gets stronger with increasing friction coefficient between segment and cladding tube. To assess this effect a 2D finite element analysis was performed for a half a segment. Figure 3 shows a typical FE-mesh set-up for the eight segment geometry. A controlled radial displacement is imposed on the inner surface of the segment, symmetry conditions are imposed along the lower boundary for segment and tube, whereas the upper boundary of the segment is traction free. Coulumb friction is assumed between tube and segment. Typical stress-strain curves for zircaloy-2 and STAVAX are used for tube and segment respectively.

Figure 3: Finite element and associated boundary conditions model for the 8-segment mandrel and tube

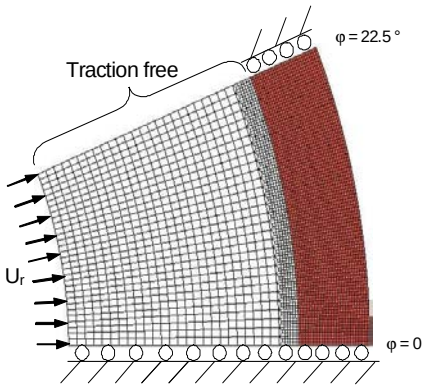

Figure 4: a) Hoop strain distributions along inner surface at 10% applied strain for different values of the friction coefficient with 8 segments; b) picture of undeformed tube and tube after large plastic deformation

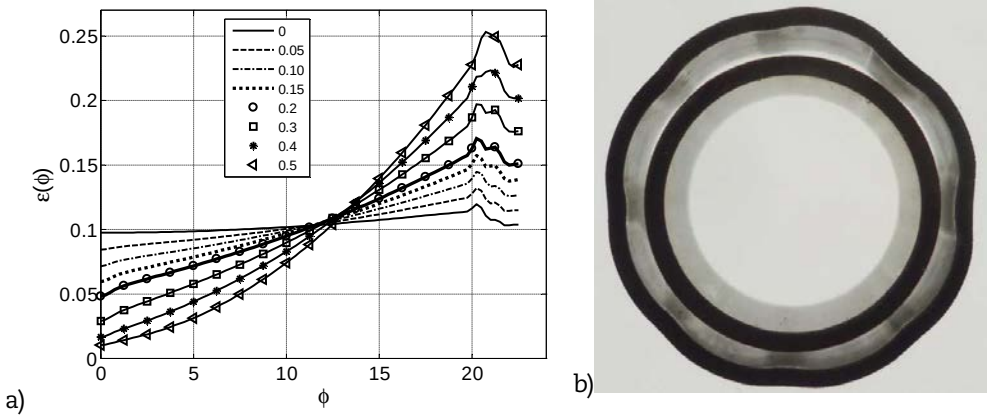

Figure 4a shows the computed hoop strain distributions along the inner surface of the tube at 10% applied strain for friction coefficients ranging from 0 to 0.5. The friction coefficient clearly influences the strain distribution. When the friction coefficient is zero the strain is almost axisymmetric. A friction coefficient of 0.5, which is typical for fresh fuel, gives a strain concentration factor of 2.5 at the inner surface. The deviation from axisymmetry increases with loading. Figure 4b shows an undeformed tube and a deformed tube loaded to 30% strain. The number of segments as well as the friction coefficient has a large impact on the variation in the tube's stress and strain distributions. The computed plastic effective strain distribution in the tube and cone at an applied engineering strain of 26% is plotted in Figures 5a and 5b for the case with 12 segments and zero friction coefficient and 8 segments

and friction coefficient 0.5 respectively. With friction the highest strain in the tube develops in the gap between the segments as clearly seen in Figure 5b. The stretched zones are also clearly seen in Figure 4b. Most of the overall plastic strain takes place in these regions with large deformation and low hardening of the material. This plastic strain localisation is the reason why the computed stress strain curves from the mandrel test as outlined above and illustrated in Figure 2 underestimates the plastic hardening at large strains. This effect increases with higher friction and fewer segments. It can also be noted that there is some plastic deformation at the inner segment corner. This may influence the load distribution since the curvature does not perfectly match the cone.

Figure 5: Computed plastic effective strain in segment and tube at applied radial displacement $\frac{u_r}{R} = 0.26$ a) 12 segments, μ = 0; b) 8 segments, μ = 0.5

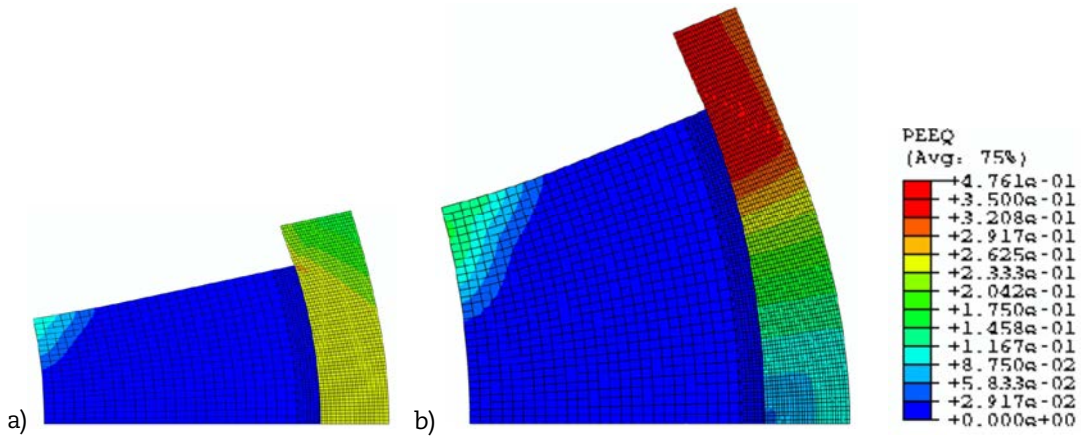

Applications of the SEM test

Hydride reorientation and embrittlement

Ziconium alloy fuel cladding pick up hydrogen from corrosion during reactor operation. When the spent fuel is cooled in water pools the hydrogen precipitates as hydrides with primarily circumferential orientation due to the texture of the cladding tube [7,8]. When the spent fuel is transferred from wet to dry storage the temperature increases to typically 400°C whereby the hydrides dissolve and the internal pressure in the cladding tubes increases to 6-16 MPa. When the cladding tubes are slowly cooled the hydrogen reprecipitates as radial hydrides due to the hoop stress [8]. At 400°C, the typical threshold value for hydride re-orientation is 60-100 MPa [8], which is attained from the internal pressure in the fuel claddings. The hydrides are much more brittle than the matrix material when the temperature is below 300°C. It has been observed that radial hydrides may drastically reduce the ductility of fuel claddings at low temperatures [7,8]. The ductility reduction is believed to be caused by a process where first hydrides fracture (typically at 1% strain) whereby the cladding tube becomes a multi-cracked material. Elasto-plastic fracture mechanics can then be applied to assess the ductility [9].

We used the mandrel test to first induce hydride re-orientation and subsequently to determine the ductility. To this end zircaloy-2 tubes that had been charged with nominal hydrogen content 100, 200 and 300 ppm were used. The re-orientation was achieved applying a constant load F and then heating up the ECM set-up in a furnace to a prescribed temperature, keeping the temperature constant for a specified and then slowly cooling the ECM set-up. Heat-up rate, cooling rate, hold time and number of cycles were varied between the tests.

The maximum temperature was set to slightly above 400°C and the constant load was selected to give a hoop stress of about 100 MPa. A typical load and temperature history is shown in Figure 6. Figure 7 shows micrographs of tested tubes with hydride content of 100,

200 and 300 ppm before and after reorientation. The re-orientation is obvious from the naked eye observation of the micrographs. The hydrides were mapped from micrographs with MATLAB based in-house image processing routines. Each individual hydride exceeding a threshold length was identified with respect to orientation, length and position.

Figure 6: Example of thermal and mechanical loading using SEM test to induce hydride re-orientation

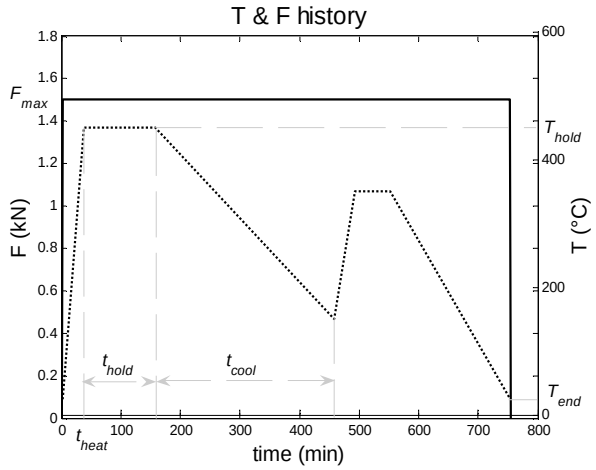

Figure 7: Examples of micrographs of tubes with nominally 100, 200 and 300 ppm hydrogen before and after re-orientation test. $Nrad_{45}^{X}$ and ε_{max} are the measured fraction of radial hydrides and the ductility for the specific specimens. X stands for the magnification of micrographs used for the hydride characterisation.

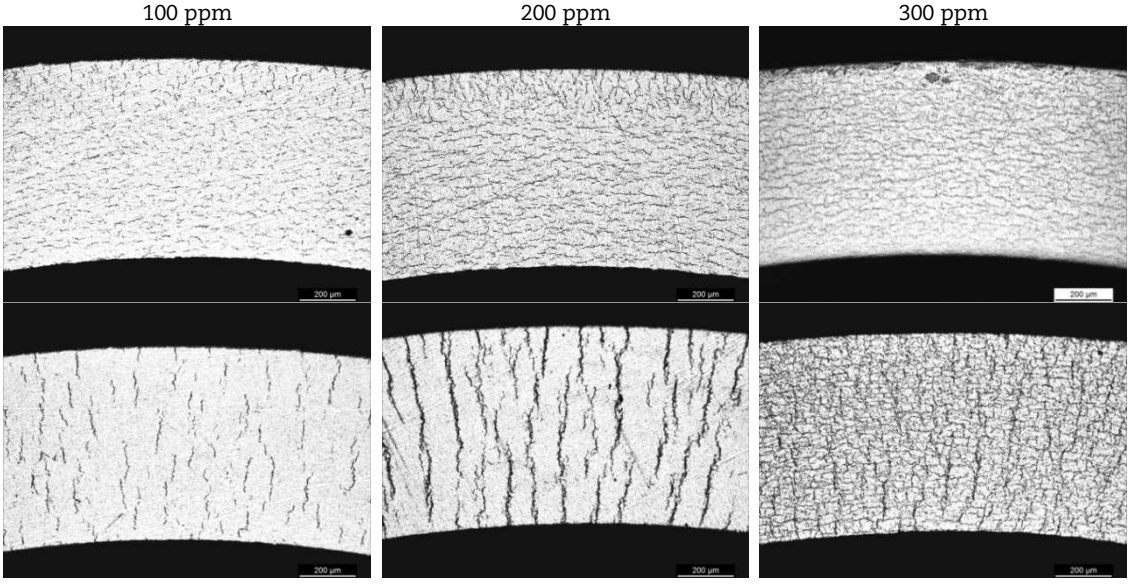

There is no agreed definition on hydride re-orientation. We consider hydrides that have an orientation larger than 45° from the circumferential direction as re-oriented. The re-orientation is then defined by the total length of radial hydrides divided by the length of all hydrides ($Nrad_{45} = \sum a_i(\varphi > 45°)/\sum a_i$) The re-orientation and other hydride parameters are derived from the image processed micrographs.

Tube specimens with different hydrogen content, as-received as well as re-oriented were subsequently tested by the SEM test in displacement controlled mode to measure the ductility. The ductility was defined as the hoop strain at which the specimen failed.

Figure 8 shows the measured ductility versus the content of radial hydride (measured radials hydride fraction multiplied with total hydrogen content). The symbols represent different levels of charged hydrogen. The observations from these tests are in line observations from spent fuel claddings: at these stresses and temperatures hydride re-orientation is likely; radial hydrides induce a significant loss of ductility; a smaller fraction of hydrides will be re-oriented at very high hydride levels resulting in a saturation of hydride embrittlement at high hydrogen levels.

Figure 8: Measured ductility vs. density of radial hydrides

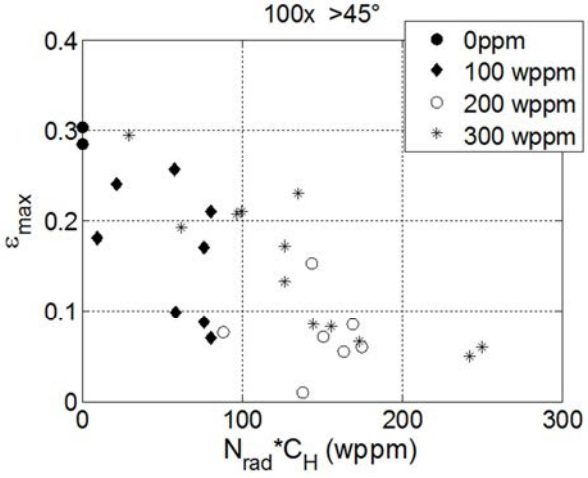

Corrosion loops

The AMALIA laboratory at JRC consists of corrosion loops with instrumented test sections for assessment of environmental assisted degradation. The present loops simulate conditions for boiling water, pressure water and super-critical water reactors and a loop with lead cooled reactors is under design. Conventional mechanical material testing systems produce the load on the specimen by using a moving pull rod, which is disadvantageous for testing in liquid or pressurized environments since pressure boundary feed-throughs cause problems with leakage and friction forces that are difficult to fully control. With bellows-based Pneumatic Loading Apparatus (PLA) it is possible to design test set-ups with no moving parts over the pressure boundary, i.e. a loading unit connected to the control unit via pressure lines and electrical feedback connectors only. Another advantage is that very accurate load control can be achieved. A PLA has therefore been developed by P. Moilanen [10] and implemented into the AMALIA lab for different specimen tests. A SEM loading device has now been designed for AMALIA based on the PLA. The on-line vertical displacement during the test will be recorded (bellows movement) and the change in diameter is measured indirectly by an LVDT displacement gauge. The device can then be used for stress corrosion cracking of cladding tubes under well controlled conditions. Figure 9 outlines the design.

Discussion

A number of proposed tests exists for thin-walled cladding tubes for material characterisation or safety assessment. The methods are complementary as they all have their strengths, drawbacks and limitations. Some strengths of the ECM-tests include: a small amount of material is needed and no specific specimen preparation is required; it is simple to perform; the analysis is simple provided the loading is reasonably axisymmetric; it is easy to combine with defect assessment; it can be performed as load

or displacement controlled; the test can be used both as a material characterisation test and simulation of mechanical fuel-cladding interaction. There are also a number of limitations. The most obvious one is the large influence of the friction between cone and segment and that the friction is difficult to control. Furthermore fraction my change as the surfaces may roughen with repeated tests. This problem can be mitigated by alternative materials for cone and segments that are very hard and have very fine surfaces. Another drawback is that the loading is uniaxial whereas the stress field is typically bi-axial. The test is difficult to perform in a hot cell since it is difficult to align the segments accurately using remote manipulators.

Figure 9: PLA test frame for segmented expanding mandrel

Conclusions

This paper has presented the principles of the segmented expanding mandrel test for thin-walled cladding tubes. As shown the test can be used as a mechanical characterisation test to determine the stress-strain curve in the hoop direction and the ductility. Moreover the expanding segments can simulate mechanical fuel cladding interaction from cracked fuel. The test is also relatively simple to perform in harsh environments using bellow based loading systems.

References

[1] Billone, M.C., Assessment of Current Test methods for Post-LOCA Cladding Behaviour, NUREG/CR-7139, ANL-11/52.

[2] Martin-Rengel, M.A. et al. (2012), Revisiting the method to obtain the mechanical properties of hydrided fuel cladding in the hoop direction, Journal of Nuclear Materials, 429, pp. 276-283.

[3] Yagnik, S.K. et al. (2008), “Round-Robin Testing of Fracture Toutgness Characteristics of Thin-Walled Tubing”, Journal of ASTM International, Vol. 5, Issue 2, pp 205-225.

[4] Nobrega, B.N., King, J.S., Was, G.S., Wisener, S.B. (1985), Improvements in the design and analysis of the segmented expanding mandrel test, Journal of Nuclear Materials, 131, 99-104.

[5] Nilsson, K.-F, O. Martin, C. Chenel-Ramos, J. Mendes (2011), Nuclear Engineering and Design, 241, 445-448.

[6] Nilsson, K.-F. and M. Negyesi (2011), Assessment of fuel cladding integrity by the segmented expanding mmandrel Test (SEM, Transactions SMiRT, 6-11 November 2011, New Dehli, India, Div-I: Paper ID# 65.

[7] Marshall, R.P. and M.R. Louthan (1963), Tensile properties of Zircaloy with Oriented Hydrides, ASM Transactions Quarterly, 56, pp. 693-700.

[8] Chu, H.C., S.K. Wu, R.C. Kuo (2008), Hydride re-orientation in Zircaloy-4 cladding, Journal of Nuclear Materials 373, pp. 319-327.

[9] Nilsson, K.-F., N. Jakšić and V. Vokál (2010), An elasto-plastic fracture mechanics based model for assessment of hydride embrittlement in zircaloy cladding tubes, Journal of Nuclear Materials., 396, pp. 71-85.

[10] Moilanen, P. et al., New applications of pneumatically powered testing equipment for extreme environments, in Baltica IX, Interantional Conference on Life Management and Maintenance for Power Plants, VTT Technology 106, ISBN 978-951-38-8026-2.

Characterisation of precipitates in weldments performed in an ASTM A335 Gr P91 steel by the FCAW process

A.L. Marzocca[a], M.I. Luppo[b] and M. Zalazar[c]

a) Instituto Sabato, Universidad Nacional de San Martín – Comisión Nacional de Energía Atómica, Buenos Aires, Argentina
b) Gerencia Materiales, Comisión Nacional de Energía Atómica, Buenos Aires, Argentina
c) Facultad de Ingeniería, Universidad Nacional del Coahue, Buenos Aires, Argentina

Abstract

In order to increase the thermal efficiency of advanced power generation systems higher operation temperatures and pressures should be used. The P91 steel has excellent mechanical properties from room temperature up to approximately 600°C due to a distribution of a fine-sized Nb and V carbonitrides. In this context, special attention must be put on the welds. The failure of a component may be initiated in a localised and microscopic region of the weldments, either during welding or in service. This is due to the differences in the behaviour of the various regions of the weld because of the heterogeneity in its microstructure.

In the present work the characterisation of precipitates in the fusion zone, heat affected zone and base material was performed on a circumferential weldments by means of transmission electron microscopy. The weldments were obtained using a semi-automatic welding process under gas mixture protection with two different filler materials, one of them traditional and the other containing W.

Introduction

Ferritic-martensitic steels of the 9Cr-1Mo type (T9/P9) and 9Cr-1MoNbV type (T91/P91) have been extensively used in conventional and nuclear power plant components, heat exchangers, piping and tubing, etc., due to an excellent combination of properties such as creep resistance, toughness and resistance to oxidation at high temperatures [1] and they are proposed for structural components for the so-called Generation IV reactors due to their high void swelling resistance [2].

T91 steels are supplied in a normalised and tempered condition. Their microstructure consists of lath martensite containing a high density of dislocations and precipitates: $M_{23}C_6$ and MX [3]. MX precipitates pin the dislocations increasing the creep strength significatively. The stability of $M_{23}C_6$ and MX is critical to the long-term performance of these alloys [4].

As a result of the severe thermal cycle caused by the welding process, the original microstructure is altered and a so-called heat affected zone (HAZ) is formed [5]. Quite often, the failure of a component is initiated in a localised, microscopic region of weldments, either during welding or in service [6]. The temperatures achieved during welding could be related to the calculated equilibrium phase diagram of P91 steel shown in Figure 1, where the different zones corresponding to the weldments are illustrated: the fusion zone (FZ), the coarse-grained zone (CGHAZ), the fine-grained zone (FGHAZ), the intercritical zone (ICHAZ), the subcritical zone (SCHAZ) and the zone of unchanged base material (BM) [5].

Figure 1: Schematic of the sub-zones of the HAZ corresponding to the calculated equilibrium phase diagram of P91-type steel [5].

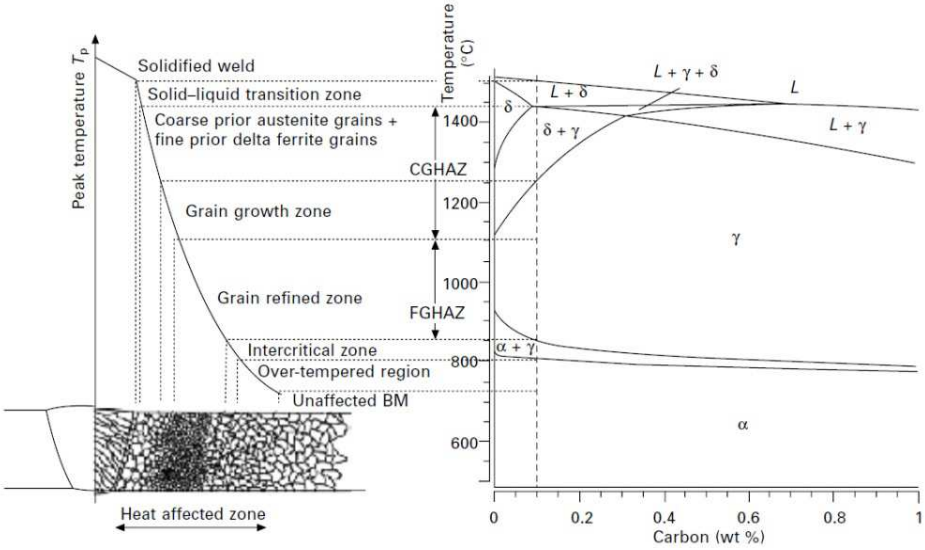

The formation of creep damage by Type IV mechanism is strictly limited to fine grained regions [7]. Type IV cracking is considered as the major "end of life" failure mechanism for ferritic creep-resistant steel weldments in the power generation industry. There are indications that the thermal cycles that are experienced in the FGHZA promote a chromium-rich "modified Z-phase" of the form Cr(V,Nb)N during creep at the expense of MX precipitates [4].

In a previous work [8] the chemical composition of the weld metal, the location of the delta ferrite, the transversal tensile properties of the joint and the microhardness of weldments of a P91 steel were determined. The purpose of the present study was the characterisation of the precipitates present in the FZ, CGHAZ, FGHAZ and BM by means of transmission electron microscopy on carbon extraction replicas.

Experimental procedure

The weldments were performed in a pipe of P91 steel provided by JFE Corporation, Japan, with a wall thickness of 28.5 mm and diameter of 350 mm. The material was received in the standard metallurgical condition (SMC): normalised at 1 050ºC, 10 minutes and tempered at 785ºC, 45 minutes. The chemical composition is shown in Table 1.

Table 1: Chemical composition of the P91 steel (wt%)

C	Mn	Si	Ni	Cr	Mo	Al	Nb	Ti	V
0.107	0.39	0.318	0.173	9.26	0.86	0.004	0.088	0.0017	0.21

The process employed was flux-cored arc welding (FCAW) under 80%Ar/20%CO_2 gas shielding [8]. The filler materials were two rutilic slag wires AWS A5.29/A5.29M:2010 E91T1 and E91T1-G, one traditional (TMo) and the other with the addition of W (TMoW), whose chemical composition are shown in Table 2.

Table 2: Chemical composition of the TMo and TMoW filler materials (FM) in wt%

FM	C	Mn	Si	Ni	Cr	Mo	Nb	Ti	V	W
TMo	0.103	0.94	0.318	0.48	9.92	0.93	0.024	0.046	0.25	
TMoW	0.107	0.81	0.403	0.51	9.64	0.47	0.035	0.037	0.22	1.67

Two samples were obtained with each wire as it is shown in Figure 2: STMo (TMo filler material) and STMoW (TMoW filler material). The preheat and interpass temperatures were 230–260°C. The welding parameters used in this work were: welding voltage 25–26 V, welding current 140–170 A, welding speed 2.5–3.0 mm/s, weld heat imput 1.5 kJ/mm [8]. Five welding passes were needed to fill up the joint.

Figure 2: Macrograph showing a cross section view of the STMo and STMoW samples

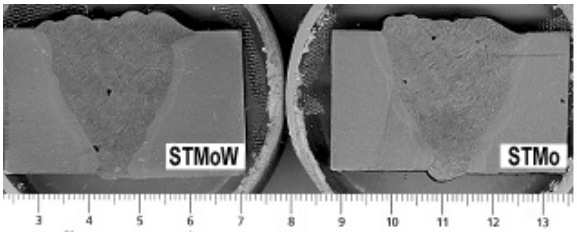

The weldments were slowly cooled in air and subjected to PWHT at 760ºC during 4 hours, with a up and down temperature ramp of 120°C/h [8].

The metallographic preparation was carried out by polishing up to diamond paste down to 1 µm and etching with the Vilella reagent. An Olympus X51 optical microscope was used to identify each sub-zone of the HAZ. The distribution of the precipitates in the matrix was observed by means of a Zeiss Supra 40 scanning electron microscope with field emission gun (FEG-SEM).

The identification of precipitates was carried out in a Phillips CM200 transmission electron microscope (TEM) on carbon replicas extracted from each sub-zone of the STMo (FZ, CGHAZ, FGHAZ, BM) and from the material in the standard metallurgical condition. In the STMoW sample carbon replicas were only extracted from the FZ, since the HAZ and BM of both welds were subjected to the same thermal cycles. TEM is equipped with an EDAX-DX4 system for energy dispersive analysis of X-rays (EDS). Precipitates were identified taking into account a previous study carried out on a similar steel [9] by a combination of selected area diffraction (SAD) patterns and EDS analysis, to avoid ambiguous identification of similar precipitates: $M_{23}C_6$ (space group: 225-Fm-3; lattice parameter, a = 1.066 nm; 58Cr-32.2Fe-8.4Mo-1.4V); MX type I or NbCN (space group: 225-Fm-3; a = 0.44082 nm; 81.5Nb-12.7V-5.8Cr); MX type II or VN (space group: 225-Fm-3; a = 0.41295 nm; 67.1V-11.8Nb-21.1Cr/ 57.1V-21.3Nb-19.9Cr); MX type III or "wings" (core: NbCN, "wings": VN).

Results and discussion

Identification of the HAZ sub-zones by means of optical microscopy

Figure 3a shows an optical micrograph of the different zones in the STMo sample. Figures 3b, c and d show optical micrographs of the FZ, CGHAZ and FGHAZ, respectively. The grain size in each sub-zone was the parameter that was taken into account to confirm that the replicas came effectively from the selected region. The presence of inclusions in the FZ (in Figure 3b, an inclusion is indicated by the arrow) also was the criterium used to distinguish this zone from the CGHAZ sub-zone, since the grain size in the border of both regions is similar.

The FZ has elongated grains with inclusions. The CGHAZ has large grains, generally equiaxed, with a continuous reduction in size from the region adjacent to weld to the FGHAZ sub-zone.

Figure 3: Optical micrographs of the STMo sample

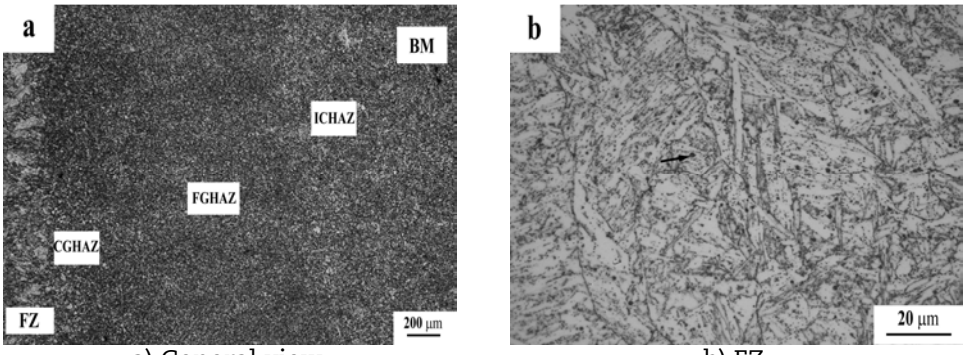

a) General view b) FZ

c) CGHAZ d) FGHAZ

Identification of precipitates in the SMC and BM of weldments

Figures 4a and 4b show the microstructure of the SMC and BM of weldments, respectively.

Figure 4: FEG-SEM micrographs of the SToM sample

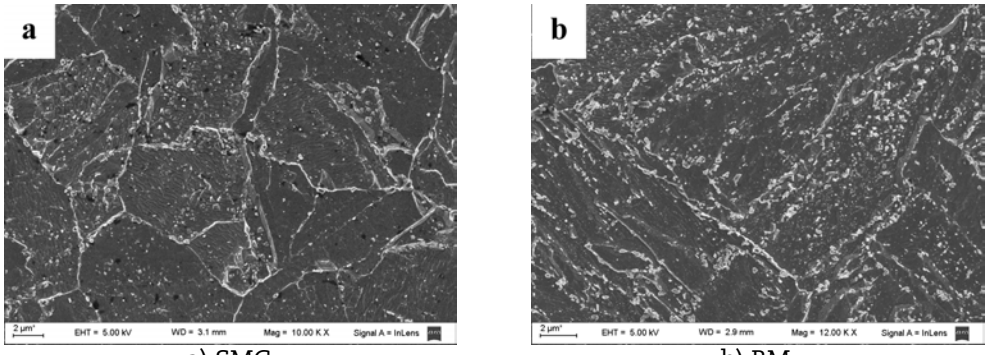

a) SMC b) BM

Figure 5a shows the $M_{23}C_6$ carbides (M = 55.4Cr-32.2Fe-11.5Mo-0.9V) identified in the SMC. In this sample "wings" were observed, as it is shown in Figure 5b. VN isolated precipitates (Figure 5c) or clusters (Figure 5d) were identified. The chemical composition of VN precipitates is 55.3V-22.7Cr-22Nb. The $M_{23}C_6$ are the major observed precipitates followed by the VN.

Precipitates found in the BM of weldments are shown in Figure 6. Figures 6a and 6b show spherical particles identified as NbCN (89.7Nb-6.5V-3.7Cr). VN precipitates are isolated (Figure 6c) or forming clusters (Figure 6d) with a chemical composition of 57.8V-17.9Cr-33.5Nb. $M_{23}C_6$ precipitates with M = 59.7Cr-30Fe-8.4Mo-1,9V and "wings" are shown in Figures 6d and f, respectively.

Figure 5: TEM micrographs from the P91 steel in the SMC

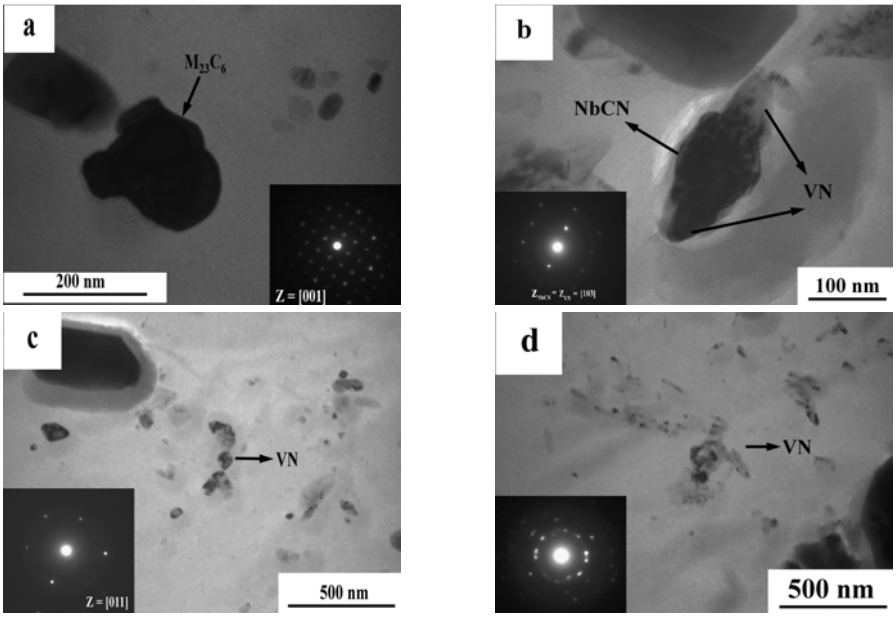

The BM was not affected by any thermal cycle during the weldment process and only received the PWHT, namely a tempering at 760°C for 4 hours. As in the SMC, in the BM the $M_{23}C_6$ carbide was the major observed precipitate, but in contrast with the SMC, the next precipitated phase as for the estimated volume fraction was the NbCN instead of the VN particles.

Identification of precipitates in the FZ of both welded joints

Figure 7a shows a FEG-SEM micrograph of the FZ of the STMoW. Figure 7b shows the inclusion indicated by the arrow in the Figure 7a which is surrounded by precipitates. FEG-SEM micrographs of the STMo are similar.

The FZ of both welded joints has the same type of precipitates (VN and $M_{23}C_6$) and inclusions. In the STMo sample, a cluster of VN precipitates (66.6V-19.3Nb-14.1Cr) and a $M_{23}C_6$ precipitate (with M = 53.4Cr-28.4Fe-12.4Mo-4.3V) are shown in Figure 8a. Figures 8b and 8c show VN (51V-27.1Nb-21.8Cr) and $M_{23}C_6$ (M = 51Cr-23.1Fe-3.7Mo-17.1W-2V) precipitates of the STMoW sample. Inclusions are characteristic of the FZ of both weldments (Figure 8d). Particles precipitated around inclusions are $M_{23}C_6$.

Identification of the precipitates in the HAZ

Figure 9 shows FEG-SEM micrographs of the CGHAZ (Figure 9a) and FGHAZ (Figure 9c) of the STMo sample.

The CGHAZ shows $M_{23}C_6$ precipitates principally at the PAGBs with M = 62.5Cr-28.5Fe-7.8Mo-1.2V. A uniform distribution of fine MX precipitates is shown in Figures 10a, 10c and 10e. The EDS analysis showed that there are three types of solutes distribution in M: 66V-13.9Cr-20.1Nb; 47.6V-16.4Cr-36Nb y 25V-13Cr-62Nb. Despite these differences in the microchemistry, crystallographically all particles correspond to VN as confirmed by their SAD pattern.

$M_{23}C_6$ precipitates of the FGHAZ have M = 61.7Cr-28.9Fe-8.1Mo-1.3V. The MX identified precipitates were VN with M = 71.9V-17.1Cr-11Nb (Figure 10.b), NbCN with M = 89.5Nb-3.5Cr-7V (Figure 10d) and wings (Figure 10f).

Figure 6: TEM micrographs of extraction replicas of the BM

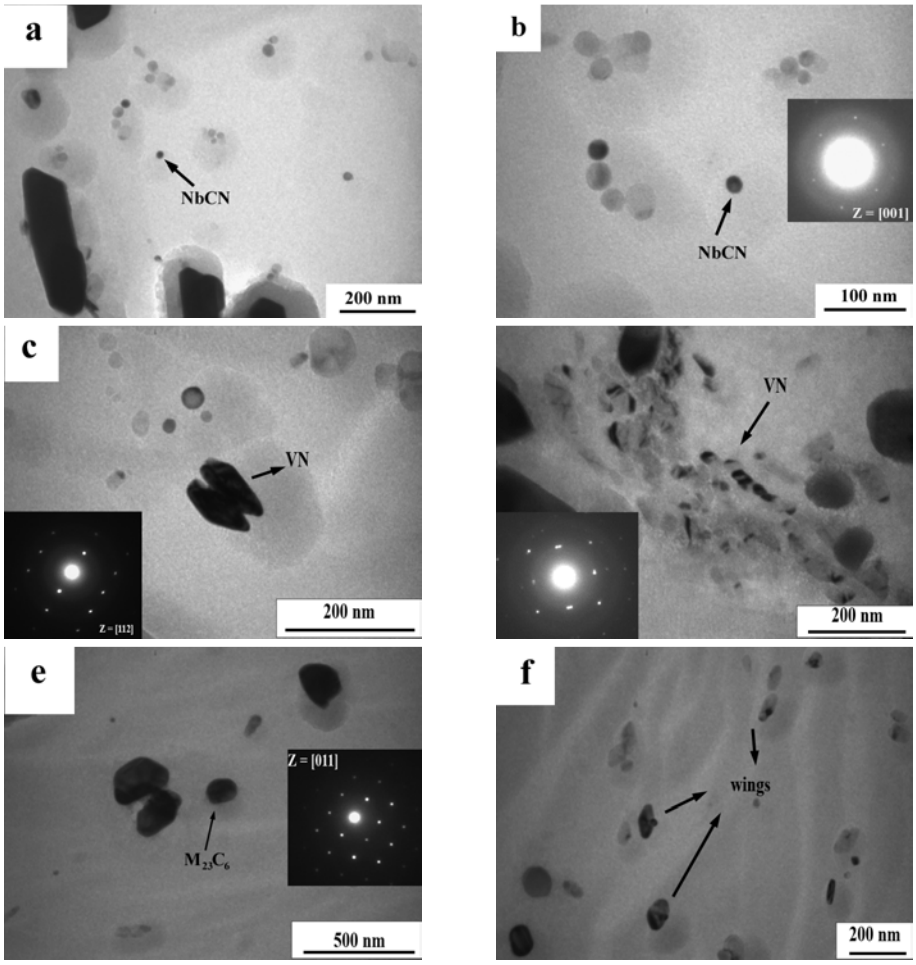

Figure 7: FEG-SEM micrographs of the STMoW in the FZ

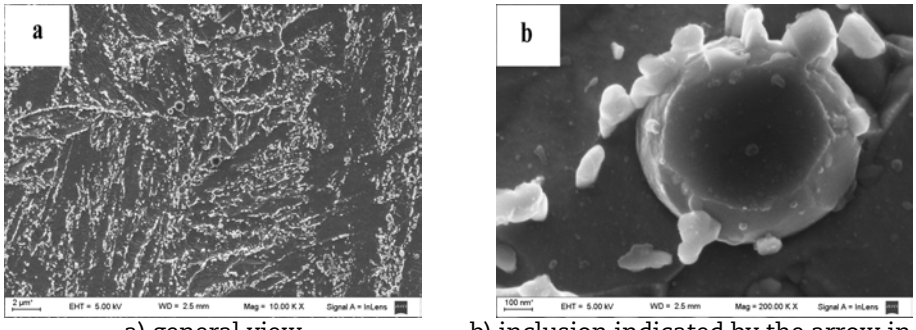

a) general view b) inclusion indicated by the arrow in a)

The microstructure of the CGHAZ sub-zone can be interpreted by means of the phase diagram showed in Figure 1. This region is heated into the higher temperature part of the γ-phase region during welding and the original carbide particles are dissolved, resulting in coarse prior austenite grain [1]. During the PWHT, the reprecipitation of $M_{23}C_6$ and MX takes place, as it is shown in the micrograph of Figures 10a, 10c and 10e.

Figure 8: TEM micrographs of extraction replicas of the FZ of the STMo and STMoW samples

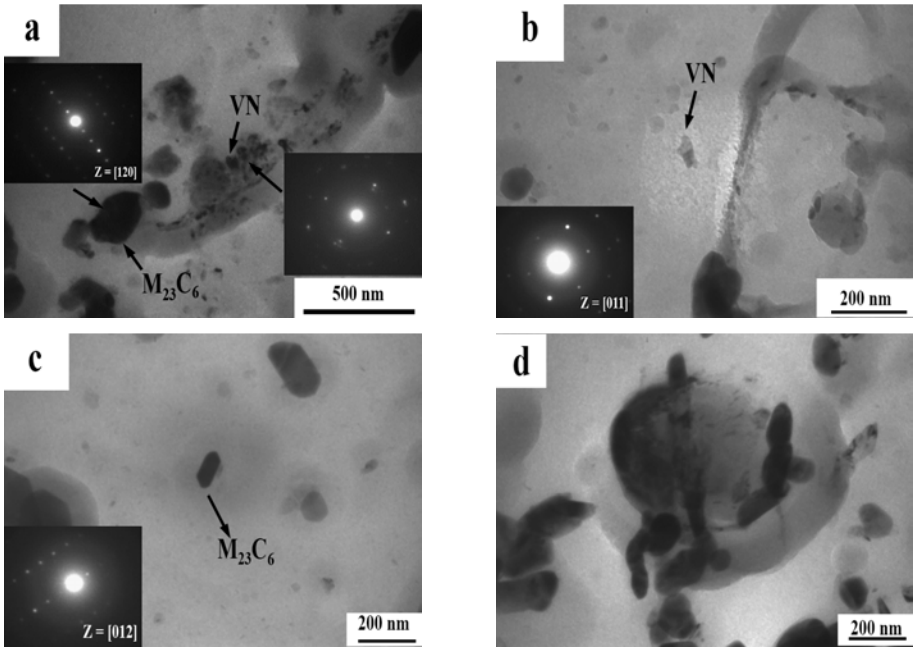

Figure 9: FEG-SEM micrographs of the STMo sample: a) CGHAZ, b) FGHAZ

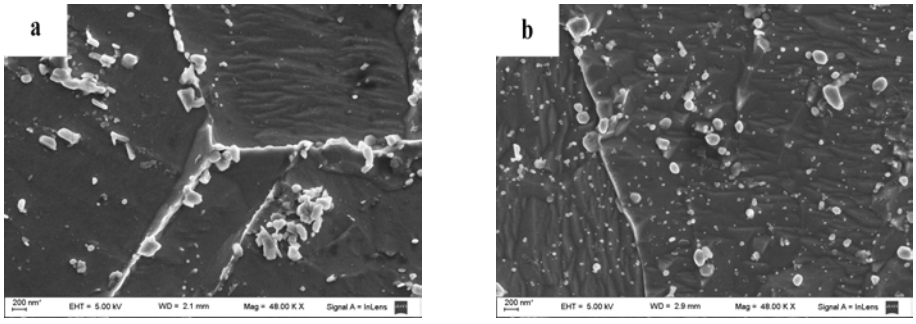

The FGHAZ is heated into the lower temperature part of the γ-phase during welding (Figure 1). The grains are finer than CGHAZ sub-zone because some of the original precipitates are not dissolved and inhibit grain growth [1]. During the PWHT the coarsening of the undissolved precipitates and the precipitation of new particles would take place.

Precipitation strengthening is one of the most effective mechanisms active in ferritic creep-resistant steels [5,7]. Comparing Figures 10d and 10e it is observed that the MX in the CGHAZ are finer that in the FGHAZ sub-zone. The dispersion of fine precipitates stabilises free dislocations and the subgrain structure which increases hardness. This fact would explain why hardness in the CGHAZ is higher that hardness in the FGHAZ as was measured by Ramini et al. [8].

Figure 10: TEM micrographs of carbon replicas extracted from the CGHAZ (a,c,e) and FGHAZ (b,d,f) of the STMo sample

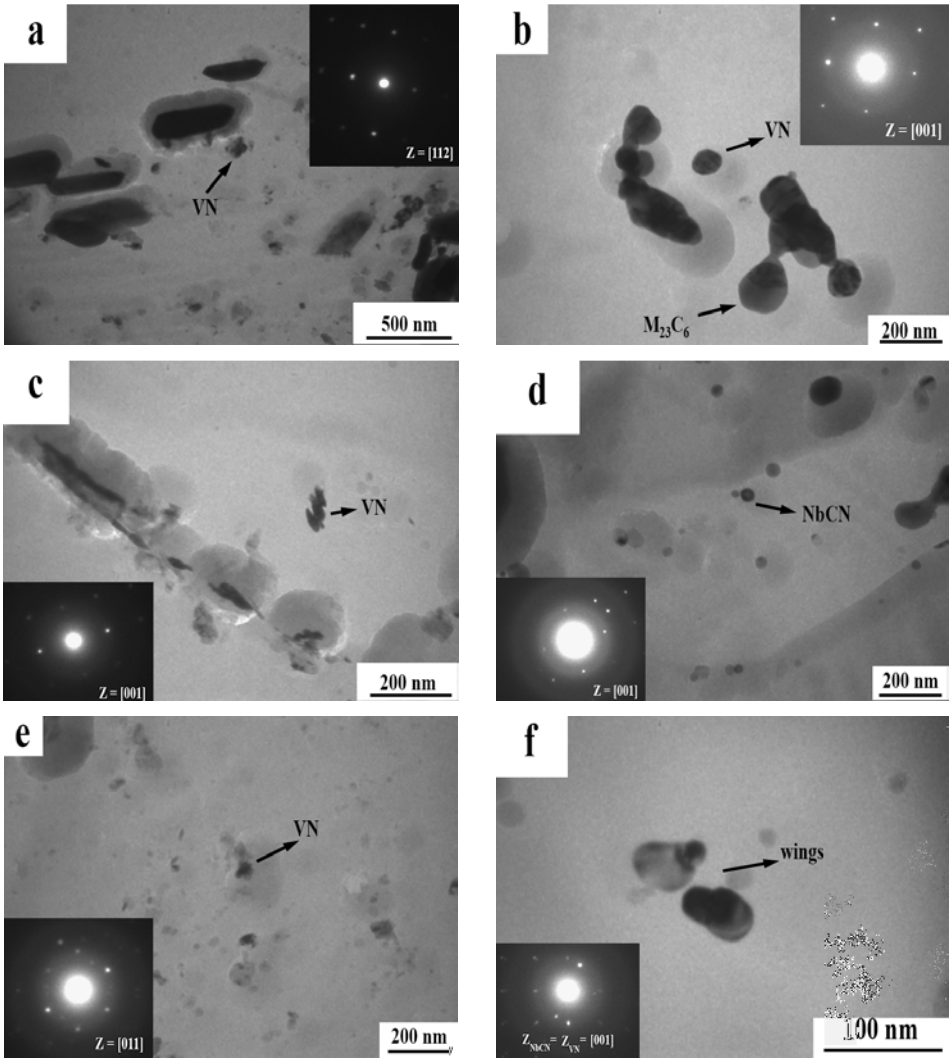

Conclusions

Multilayer welds generate a HAZ with overlapped thermal cycles in the vertical direction and localised modifications in the horizontal direction. In the present study the challenge of isolating the precipitates of different sub-zones of the HAZ (~ 3 mm-thickness) was achieved by means of several characterisation techniques: macrography, optical microscopy, FEG-SEM and TEM. Precipitates present in the standard metallurgical condition and in the FZ (STMo/STMoW), CGHAZ, FGHAZ and BM sub-zones were described. The $M_{23}C_6$ carbide was the major observed precipitate in all zones, with W present in its chemical composition for the FZ of the STMoW sample. The VN precipitates were present in all the studied regions showing a size decrease and a greater dispersion in their chemical composition in the CGHAZ. The NbCN were only present in the BM and FGHAZ. Wings were identified in all zones, except in the CGHAZ and FZ.

Acknowledgements

The authors wish to thank Dr. P. Bruzzoni for his valuable assistance.

References

[1] Klueh, R.L. (2005), "Elevated-temperature ferritic and martensitic steels and their application to future nuclar reactors", International Materials Reviews, 50[5], pp. 287-310.

[2] Natesan, K. et al. (2006), "Preliminary materials selection issues for the next generation nuclear plant reactor pressure vessel", Argonne National Laboratory-Ext-06-45.

[3] Abe, F. (2008), "Precipitate design for creep strengthening of 9%Cr tempered martensitic steel for ultra-supercritical power plants", Science and Technology of Advanced Materials, 9, 013002, pp. 1-15.

[4] Francis, J.A. et al. (2006), "Type IV cracking in ferritic power plant steels", Materials Science and Technology, 22[12], pp. 1387-1395.

[5] Cerjak, H. et al. (2008), "Creep strenth of welded joints of ferritic steels", Creep resistant steels, Edited by F. Abe, T.U. Kern and R. Viswanathan, Woodhead Publishing and Maney Publishing, pp. 472-503.

[6] Vijayalakshmi, M. et al. (1999), "Microstructural zones in the primary solidification structure of weldment of 9Cr-1Mo steel", Metallurgical and Materials Transaction A, Volume 30, Issue 1, pp. 161-174.

[7] Cerjak, H. (2008), "The role of welding in the power generation industry", Proceedings of the International Conference Safety and Reliability of welded components, pp. 17-27.

[8] Ramini, R. et al. (2011), "Characterisation of circumferential welds of 9CrMo advanced steels", XXXVII Congresso Nacional de Soldagem (CONSOLDA 2011), Natal, RN, Brasil.

[9] Zavaleta Gutiérrez, N. et al. (2011), "Evolution of precipitated phases during prolonged tempering in a 9%Cr1%MoVNb ferritic-martensitic steel: Influence on creep performance", Materials Science and Engineering A, 528A[12], pp. 4019-4029.

[10] Klueh, R.L. et al. (2001), "High-chromium ferritic and martensitic steels for nuclear application", JASTM. Nuclear Sci. Technol., 39[8], pp. 865-871.

Development of yield and tensile strength design curves for Alloy 617

Nancy Lybeck*[a] and T.-L. Sham[b]
Idaho National Laboratory[a], United States
Oak Ridge National Laboratory[b], United States

Abstract

The U.S. Department of Energy Very High Temperature Reactor Program is acquiring data in preparation for developing an Alloy 617 Code Case for inclusion in the nuclear section of the American Society of Mechanical Engineers (ASME) Boiler and Pressure Vessel (B&PV) Code. A draft code case was previously developed, but effort was suspended before acceptance by ASME. As part of the draft code case effort, a database was compiled of yield and tensile strength data from tests performed in air. Yield strength and tensile strength at temperature are used to set time-independent allowable stress for construction materials in B&PV Code, Section III, Subsection NH. The yield and tensile strength data used for the draft code case has been augmented with additional data generated by Idaho National Laboratory and Oak Ridge National Laboratory in the United States and CEA in France. The standard ASME Section II procedure for generating yield and tensile strength at temperature is presented, along with alternate methods that accommodate the change in temperature trends seen at high temperatures, resulting in a more consistent design margin over the temperature range of interest.

Introduction

The U.S. Department of Energy (DOE) has selected the high-temperature gas-cooled reactor (HTGR) design for the Next Generation Nuclear Plant (NGNP) Project. The NGNP will demonstrate the use of nuclear power for process heat, hydrogen, and electricity production. The reactor will be graphite moderated with helium as the primary coolant. Due to the high design temperature, the requirements of materials for the intermediate heat exchanger are among the most demanding. Based on the technical maturity, availability in required product forms, experience base, and high-temperature mechanical properties, Alloy 617 is the leading candidate construction material for the NGNP intermediate heat exchanger.

Alloy 617 is not currently qualified for use in American Society of Mechanical Engineers (ASME) Boiler and Pressure Vessel (B&PV) Code Section III, although it is allowed in Section I and Section VIII, Division 1 (non-nuclear service). A draft ASME Code case for incorporating Alloy 617 in Section III was developed in the early 1980s [1], but efforts to gain the approval from the ASME Code committees were discontinued due to a loss in interest by DOE and its contractor.

Minimum yield strength and average tensile strength at temperature are used to set time-independent allowable stress for structural materials in B&PV Code, Section III, Subsection NH. As part of the draft code case effort, a database was compiled of yield and tensile strength data from tests performed in air by Huntington Alloys, Inc. Section II, Part D, Appendix 5, recommends the submittal of tensile strength, yield strength, reduction of area, and elongation at 50°C intervals, from room temperature to 50°C above the maximum intended use temperature for three heats of appropriate product forms and sizes.

A large portion of the research in the U.S. DOE Very High Temperature Reactor (VHTR) Materials Research and Development Program is code qualification of Alloy 617 for successful and long-life application at the high-temperature conditions planned for the NGNP. Idaho National Laboratory (INL) has generated tensile test data for two different product forms at multiple temperatures. Additional data have been acquired from Oak Ridge National Laboratory (ORNL) and the *French* Alternative Energies and Atomic Energy Commission (*CEA*). These data sets have been combined with the original Huntington Alloys data to create a more complete data set for analysis, with 198 data points representing 14 heats and five product forms of Alloy 617, as seen in Table 1. Statistical equivalence of the older and newer data is considered for both yield and tensile strength to assess if the older, and more numerous, data can be leveraged in combination with data from newer heats produced with current mill practices, to set time-independent allowable stresses. The standard ASME Section II procedures for calculating yield strength and tensile strength at temperature are presented, along with alternate methods that accommodate the change in temperature trends seen at high temperatures, resulting in a more consistent design margin over the temperature range of interest.

Table 1: Sources of tensile and yield strength data for analysis

Heat	Product form	Source	Number of data points	Material vendor
VDM	Plate	CEA	17	VDM
XX00A1USL	BAR	Huntington	7	Huntington
XX00A4USL	BAR	Huntington	12	Huntington
XX00A5USL	BAR	Huntington	10	Huntington
XX05A4UK	BAR	Huntington	22	Huntington
XX07A7UK	BAR	Huntington	22	Huntington
XX00A1USL	CR SHEET	Huntington	8	Huntington
XX00A5USL	CR SHEET	Huntington	3	Huntington
XX20A5UK	CR SHEET	Huntington	12	Huntington
XX26A8UK	CR SHEET	Huntington	21	Huntington
XX00A3USL	FORGING	Huntington	4	Huntington
XX00A3USL	PLATE	Huntington	4	Huntington
188155	BAR	INL	30	VDM
314626	Plate	INL	9	VDM
XX01A3US	Plate	ORNL	10	Huntington
XX09A4UK	Plate	ORNL	7	Huntington

Yield strength analysis

The ASME Section II method for determining the yield strength at temperature can be summarised as follows [2]:

- The yield strength data are normalised by dividing by the average room temperature yield strength for the respective heat.
- A best fit trend curve $R_Y(T)$ is generated for the normalised yield strength data as a function of test temperature.
- The minimum yield strength at temperature is defined as $S_y(T) = S_Y R_Y(T)$, where S_Y is the specification minimum yield strength at room temperature.

Additionally, the temperature trend of $S_y(T)$ is required to be either constant or decreasing with increasing temperature.

Yield strength at temperature design curves

Generally, a fifth-order polynomial is used to obtain the trend curve of the normalised strength data per ASME Code practice. Following the approach taken in [3], a better fit to

the normalised yield strength data can be achieved by using a piecewise continuous exponential decay function so that:

$$R_Y(T) = \begin{cases} a_1 + b_1 e^{c_1 T}, T \le T_0 \\ a_2 + b_2 e^{c_2 T}, T > T_0 \end{cases}$$

where T is the temperature in Celsius, and the model parameters a_1, a_2, b_1, b_2, c_1, c_2, and T_0 are estimated from the data. The exponential decaying function enforces the requirement that the strength curve decreases with increasing temperature.

The ASME Section II methodology outlined above was used to generate the yield strength at temperature. The specification minimum yield strength at room temperature for Alloy 617 is 240 MPa. Two curves were generated: one was based on Huntington and ORNL data, which were both generated from older heats manufactured by Huntington, and the other on the combined data set. As seen in Figure 1, the combined data set gives lower values, with a maximum deviation of 3 MPa below 800°C, and 22 MPa above 800°C.

Figure 1: Estimated yield strength at temperature using the ASME method with a piecewise exponential

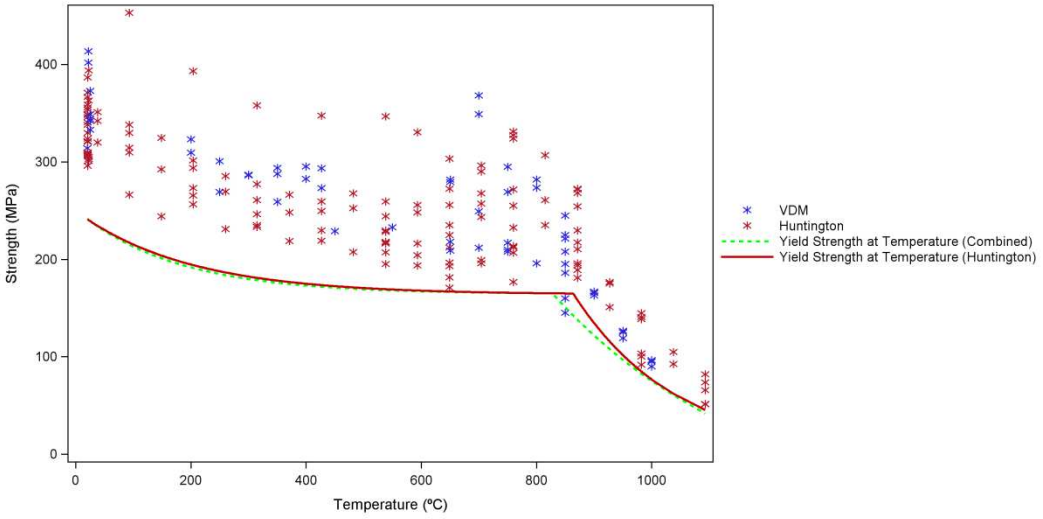

The margin between the yield strength at temperature and the yield strength data decreases noticeably as temperature increases, providing a conservative lower bound at lower temperatures, but running through the data at the highest temperatures.

Based on these results, alternate methods were explored for modeling yield strength that take into account the change in temperature trends seen at high temperatures. The piecewise exponential decay model used above was fit to the raw yield strength data, rather than the normalised data, resulting in a model for yield strength at temperature in the form:

$$S_y(T) = \begin{cases} a_1 + b_1 e^{c_1 T}, T \le T_0 \\ a_2 + b_2 e^{c_2 T}, T > T_0 \end{cases}$$

where T is the temperature in Celsius, and the model parameters a_1, a_2, b_1, b_2, c_1, c_2, and T_0 are estimated from the data.

Figure 2 shows the yield strength data along with the best fit exponential decay model (solid black curve). The horizontal line represents the specification minimum yield strength at room temperature. The ASME method was used with the best fit decay model for the normalised data to generate the minimum yield strength at temperature (solid orange line). Tabulated values in the ASME B&PV Section II for yield strength are shown by the red asterisks. The lower bound of an approximate 95% confidence interval for an

individual prediction (i.e., a prediction bound) was generated based on the decay fit to the raw data (dashed blue line). Finally, the best fit exponential decay model for the raw data was offset by the maximum difference between the best fit line and the 95% prediction bound (dashed green line). The identified parameters from the best least-squares fit to the normalised and raw yield strength data are given in Table 2. For the 95% prediction bound and constant offset curves, the corresponding yield strength at temperature would be the lower of 240MPa and the values from these two curves.

Figure 2: Analysis of Alloy 617 yield strength at temperature

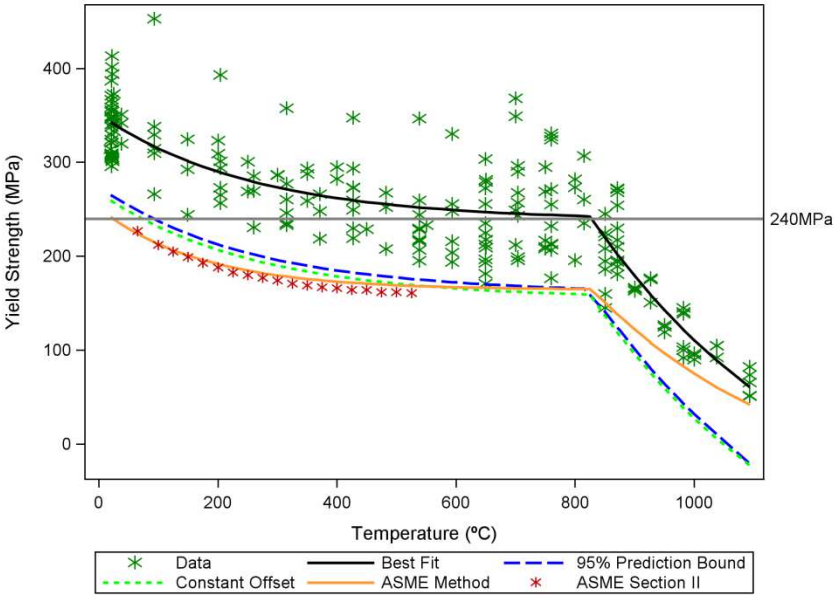

Table 2: Best-fit parameter coefficients for normalised and raw yield strength

Parameter	Normalised data	Raw data
a_1	6.84562963934E-01	2.38153391390E+02
b_1	3.60968416894E-01	1.13078337003E+02
c_1	-5.75159974584E-03	-3.89777152722E-03
T_0	8.27494333565E+02	8.24563909014E+02
a_2	-2.88565545061E-01	-1.33424255707E+02
b_2	9.98257402054E+00	2.87168957389E+03
c_2	-2.80957331723E-03	-2.46522971908E-03

Statistical equivalence of the yield strength data sets

The combined data set consists of 198 sets of tensile data from 14 heats of material in five different product forms, as shown in Table 1. The Huntington data that was used in the suspended draft code case represents approximately two-thirds of the new data set. The Huntington data are very old; a natural question that arises is if the newer heats of Alloy 617 have similar, or even better, tensile properties as the older heats represented by the Huntington data. The ORNL data were also generated from an older heat produced by Huntington; the INL and CEA data were generated from newer heats produced by VDM.

An analysis was performed on the yield strength data to examine the statistical equivalence of the data sets. The data from INL and CEA were combined in one group (labelled VDM), and the Huntington and ORNL data formed the second group (labelled Huntington). The best piecewise exponential model was generated for each data group.

The results are shown in Figure 3, where the solid lines are the best estimate curve and the dashed lines are the 95% confidence bounds for the expected value (mean). The 95% confidence bounds are overlapping for the entire temperature range; there is no evidence to suggest a difference in the two data sets.

Figure 3: Analysis of statistical equivalence of the yield strength data

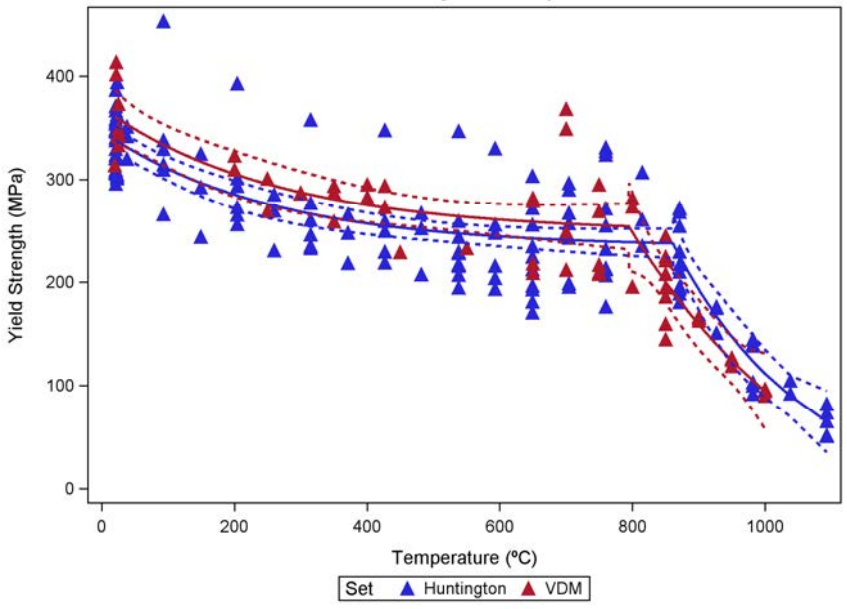

Tensile strength analysis

The ASME method for determining the tensile strength at temperature can be summarised in the following three steps [2]:

- The tensile strength data are normalised by dividing by the average room temperature tensile strength for the associated heat.
- A best fit trend curve $R_T(T)$ is fit to the normalised tensile strength data as a function of test temperature.
- The average tensile strength at temperature is defined as $S_u(T) = 1.1 * S_T R_T(T)$, where S_T is the specification minimum tensile strength at room temperature.

Again, the temperature trend of $S_u(T)$ is required to be either constant or decreasing with increasing temperature.

Tensile strength at temperature design curves

Following the approach taken in [3], a piecewise continuous exponential decay function was selected to fit the normalised yield strength data:

$$R_T(T) = \begin{cases} a_1 + b_1 T, T \leq T_0 \\ a_2 + b_2 e^{c_2 T}, T > T_0 \end{cases}$$

where T is the temperature in Celsius, and the model parameters a_1, a_2, b_1, b_2, c_2, and T_0 are estimated from the data. Parameter estimation was performed using least squares estimation, enforcing continuity at T_0.

The ASME Section II methodology outlined above was used to generate the tensile strength at temperature. Two curves were generated: one was based on the original draft code case data and the ORNL data (labelled Huntington), and the other on the complete

data set. As seen in Figure 4, the additional data cause changes in the tensile strength at temperature curve. For higher temperatures, the resulting curve is more conservative, with a maximum difference of 86 MPa.

Figure 4: Estimated tensile strength at temperature using the ASME method with a piecewise exponential decay model

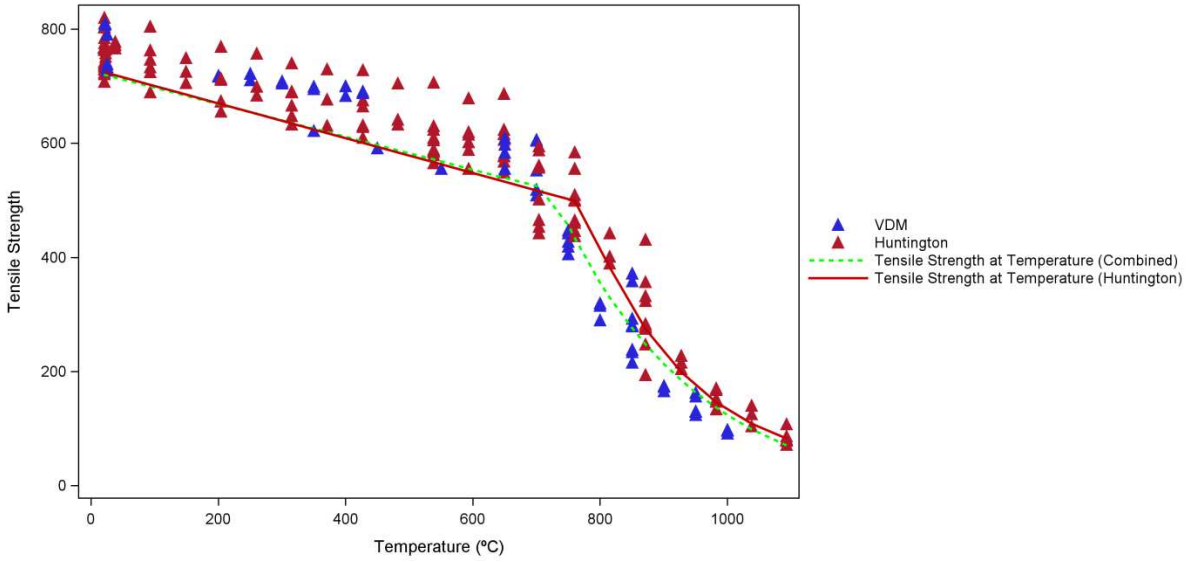

As with the yield strength at temperature curve, the position of the curve relative to the average of the data changes with temperature. Near room temperature, the curve lies slightly below the average value of the data. At higher temperatures, the curve lies above the average value of the data.

Based on these results, the piecewise exponential decay model used above was fitted to the raw tensile strength data, rather than the normalised data, resulting in a model for tensile strength at temperature in the form:

$$S_u(T) = \begin{cases} a_1 + b_1 T, T \leq T_0 \\ a_2 + b_2 e^{c_2 T}, T > T_0 \end{cases}$$

Where T is the temperature in Celsius, and the model parameters a_1, a_2, b_1, b_2, c_2, and T_0 are estimated from the data. Parameter estimation was performed using least squares estimation, enforcing continuity at T_0.

Figure 5 shows the tensile strength data along with the best fit exponential decay model (solid black curve). The horizontal line represents the specification minimum tensile strength at room temperature. The ASME Section II method was used with the best fit decay model for the normalised data to generate the tensile strength at temperature (solid orange line). Tabulated values in the ASME B&PV Section II Part D for tensile strength at temperature are shown by the red asterisks. The lower bound of an approximate 95% confidence interval for the expected value (mean) was generated based on the model fit to the raw data (dashed pink line). Finally, the best fit exponential decay model for the raw data was offset by the maximum difference between the best fit curve and the 95% confidence bound (dashed green line). The identified parameters from the best least-squares fit to the normalised and raw tensile data are given in Table 3. For any of these curves, the corresponding tensile strength at temperature would be the smaller of the curve and 655 MPa.

Figure 5: Analysis of Alloy 617 tensile strength at temperature

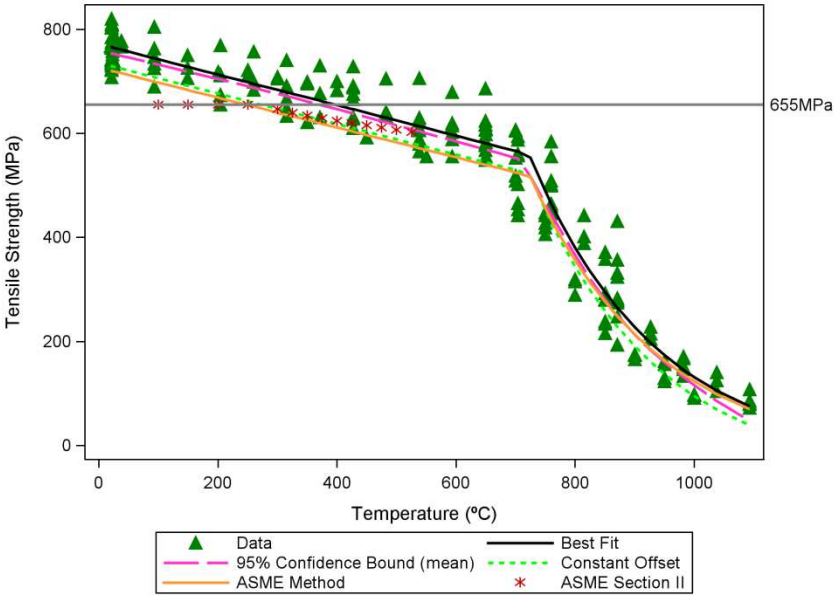

Table 3: Best-fit parameter coefficients for normalised and raw tensile strength

Parameter	Normalised data	Raw data
Y	1.00809519519E+00	7.71748461184E+02
b_1	-3.98933842187E-04	-2.93524772281E-01
T_0	7.24094783303E+02	7.22747336965E+02
a_2	-3.91607682652E-02	-2.84714696511E+01
b_2	2.18506626389E+01	1.74564181628E+04
c_2	-4.64136570776E-03	-4.69127568771E-03

Statistical equivalence of the tensile strength data sets

To analyse statistical equivalence of the data sets, the normalised tensile strength data from INL and CEA were combined in one group (labelled VDM), and the Huntington and ORNL data formed the second group (labelled Huntington). The best least-squares fit exponential decay model was generated for each data group, as seen by the solid lines in Figure 6. The results show that the 95% confidence bounds for the mean (dashed lines) are overlapping for lower temperatures (approximately 0-700°C), but that they are not overlapping for higher temperatures.

Based on these results, linear models were fit to the Huntington and VDM data sets for lower (≤700°C) and higher (>700°C) temperatures. The results shown in Figure 7 are consistent with the previous analysis, with overlapping confidence bounds for lower temperatures, and non-overlapping confidence bounds above 700°C. This indicates there is a difference between the data sets for higher temperatures. Because the additional data sets have lower tensile strength values, the resulting design curves will be more conservative for the joint data set.

Figure 6: Statistical equivalence of the tensile strength data

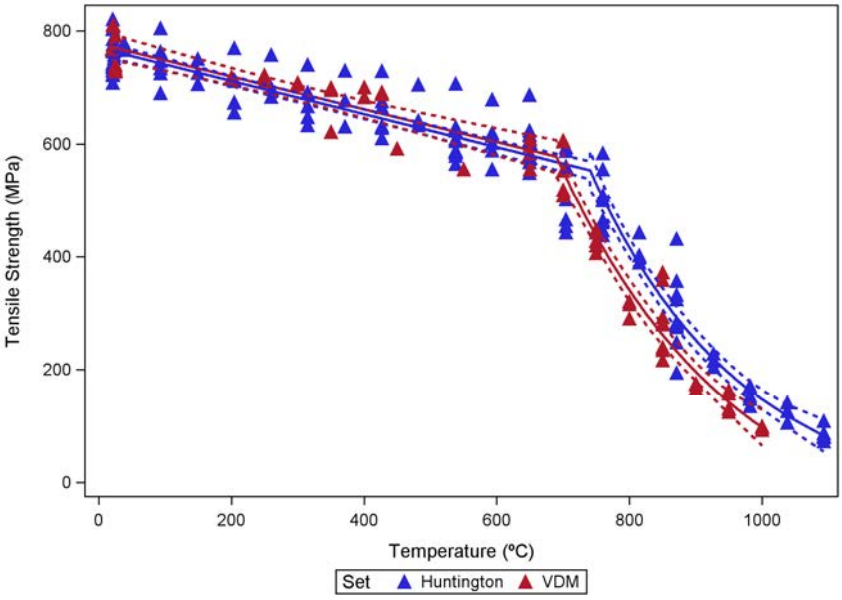

Figure 7: Model fit to tensile strength grouped by temperature and data source

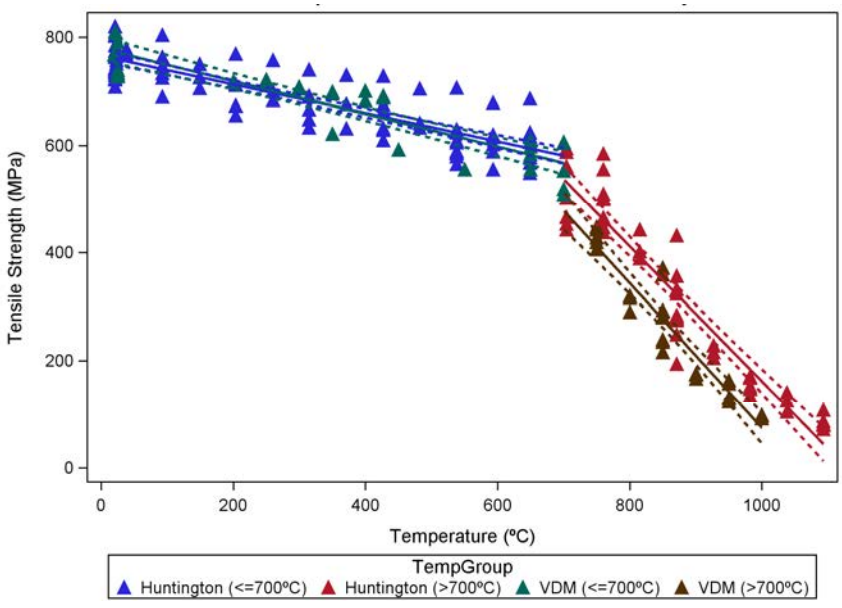

Conclusions

The main objective of this study is to determine whether tensile data determined from recent material heats with current mill practice are statistically equivalent to the historical data generated from heats with older mill practice. It was found that the yield strength data from the newer Alloy 617 heats are consistent with those from the older Huntington heats. However, the tensile strength data from the newer Alloy 617 heats are slightly lower than those from the Huntington heats.

Sham, Eno, and Jensen [3] first noted an inconsistent margin resulting from using the ASME Section II methodologies for yield strength and tensile strength at temperature for the large temperature ranges of interest for Alloy 617. Sham et al. [3] suggested an

alternate method for generating the design curves using the Huntington data set. Kim et al. [4] repeated the analysis using an expanded data set including data collected through world-wide literature surveys, data from manufacturing companies, and KAERI data. In this paper, the alternate methodology was presented with minor modifications for a data set including data from Huntington, CEA, ORNL, and INL.

The SAS procedure NLIN was used to generate all curve fits, as well as the prediction bounds. The 95% prediction bound for yield strength at temperature provides a consistent, meaningful statistical lower bound to summarise the yield strength data, and would be a good candidate for use as yield strength at temperature. The 95% confidence bound for mean tensile strength at temperature provides a consistent, meaningful statistical lower bound for average tensile strength, and would be a good candidate for tensile strength at temperature.

Acknowledgements

This manuscript has been co-authored by Battelle Energy Alliance, LLC under Contract No. DE-AC07-05ID14517, and by UT-Battelle, LLC under Contract No. DE-AC05-00OR22725, with the U.S. Department of Energy. The United States Government retains and the publisher, by accepting the article for publication, acknowledges that the Government of the United States retains a nonexclusive, paid-up, irrevocable, world-wide license to publish or reproduce the published form of this manuscript, or allow others to do so, for United States Government purposes.

The authors would like to acknowledge Richard Wright of Idaho National Laboratory for supporting this work.

References

[1] Corum, J.M. and J.J. Blass (1991), "Rules for Design of Alloy 617 Nuclear Components to Very High Temperatures," Proceedings of 1991 ASME Pressure Vessels and Piping Division Conference, ASME PVP Vol. 215, pp. 147-153.

[2] "An International Code 2010 ASME Boiler & Pressure Vessel Code, 2011a Addenda: Section II Part D Properties (Metric) Materials," ASME, 2011.

[3] Sham, T.-L., D.R. Eno, K.P. Jensen (2008), "Treatment of High Temperature Tensile Data for Alloy 617 and Alloy 230," Proceedings of 2008 ASME Pressure Vessels and Piping Division Conference, PVP2008-61128, Chicago, Illinois.

[4] Kim, W.-G., S.-N. Yin, J.-Y. Park, S.-D. Hong, Y.-W. Kim (2012), "An improved methodology for determining tensile design strengths of Alloy 617," Journal of Mechanical Science and Technology 26(2), PP. 379-387; DOI 10.1007/s12206-011-1024-5.

Microstructural characterisation of a P91 steel normalised and tempered at different temperatures

C. Hurtado-Noreña*[a], C.A. Danón[b], M.I. Luppo[b] and P. Bruzzoni[b]
[a] Consejo Nacional de Investigaciones Científicas y Técnicas (CONICET), Argentina
[b] Gerencia Materiales, CAC-Comisión Nacional de Energía Atómica, Argentina

Abstract

9%Cr-1%Mo martensitic-ferritic steels are used in power plant components with operating temperatures of around 600°C because of their good mechanical properties at high temperature as well as good oxidation resistance. These steels are generally used in the normalised and tempered condition. This treatment results in a structure of tempered lath martensite where the precipitates are distributed along the lath interfaces and within the martensite laths. The characterisation of these precipitates is of fundamental importance because of their relationship with the creep behaviour of these steels in service. In the present work, the different types of precipitates found in these steels have been studied on specimens in different metallurgical conditions. The techniques used in this investigation were X-ray diffraction with synchrotron light, scanning electron microscopy, energy dispersive microanalysis and transmission electron microscopy.

Introduction

9-12% Cr steels were developed in the first half of the past century and have been widely used as high temperature materials in the petrochemical industry and power plants. They are also considered in the nuclear industry as candidate materials for different components in advanced fission reactors and fusion reactors [1]. In comparison with conventional austenitic stainless steels, the 9-12% Cr steels present a lower thermal expansion coefficient, a higher thermal conductivity and a lower swelling under irradiation which make them preferred for high-temperature power applications. The advanced nuclear reactors (i.e. Generation IV nuclear reactors) comprise, among others, the supercritical reactors, which operate at pressure and temperatures above the critical point of water (218 atm and 374°C). The increase of the vapor temperature leads to an increase of the thermal efficiency of the power plant, thus producing more electricity at a lower cost. 9-12% Cr steels are adequate for these conditions due to their high resistance to both thermal fatigue and high-temperature oxidation. The maximal operation temperature will be mainly determined by the creep behaviour and the compatibility of the material with the process fluids.

Members of the 9-12% Cr family are the 9%Cr-1%Mo steels. They are commercially identified as T9 and P9. The 9%Cr-1%Mo steels have been widely used in components power generation plants: steam generators, steam pipes, etc. As members of the 9-12%Cr family they present outstanding properties at service temperature: resistance to creep and high-temperature oxidation, low-thermal expansion coefficient, high-thermal conductivity. The creep resistance is further improved in the case of the so-called modified the 9%Cr-1%Mo steels (T91 and P91) which contain small amounts of Nb and V

as micro alloying elements. The presence of Nb and V favours the formation of submicron MX type carbonitride (M = Nb,V; X = C,N) with particle size lower than 0.1 µm. The presence of these particles improves the creep resistance.

Prior to be put in service, the 9%Cr-1%Mo steels are usually subjected to a normalising and tempering treatment. This treatment produces a microstructure of tempered lath martensite with carbides and/or carbonitrides. The more abundant carbides are the $M_{23}C_6$, which present sizes comprised between 60 nm and 150 nm and are mainly located along the lath boundaries and the prior austenite grain boundaries. In the case of the P91/T91 steels, there is a fine distribution of the Nb-rich and/or V-rich MX precipitates mentioned above. In some cases small amounts of M_2X type precipitates were found within the laths [3]. The microstructure which results from the normalising and tempering treatment is very stable at service temperature and is the main cause of the good mechanical properties mentioned above. The normalising treatment generally comprises an austenisation at temperatures between 1 040 and 1 060°C during 30 minutes, followed by air cooling. The subsequent tempering treatment is carried out at 780°C during 40 minutes and is also followed by air cooling. As mentioned above, the resulting microstructure is very stable at the service temperature of ca. 600°C. However, it can undergo changes in the case of local overheating or prolonged exposure to elevated temperatures. This leads to higher corrosion rates and the degradation of the creep properties [4,5]. 9%Cr-1%Mo steels do not suffer hydrogen embrittlement (HE) at the service conditions. However, at room temperature these steels may experience HE –i.e during plant stops-, especially in welded parts or after storage in corrosive environments.

In a previous work [6] tempering treatments at different temperatures were performed on a P91 steel; the role of these treatments on the interaction of the material with hydrogen was investigated. In the present work, the different types of precipitates which are formed after those thermal treatments are characterised.

Experimental details

An ASTM A213 grade 91 steel was used for the present work. The chemical composition is shown in Table 1.

Table 1: Chemical composition of the P91 Steel in wt%

C	Mn	Si	Cr	Mo	N	V	Cu	Sn	Al	Nb	Ni
0.110	0.360	0.260	8.210	0.900	0.061	0.213	0.150	0.009	0.011	0.085	0.150

This steel contains V and Nb as micro alloying elements, which confer specific characteristics and properties to the material. The ASTM A213 standard establishes the following ranges of concentration for these elements: V 0.18% to 0.25% and Nb 0.06% to 0.10%.

The samples were obtained from a seamless P91 pipe with a wall thickness of 32 mm and an external diameter of 219 mm. The samples were subjected to normalising and tempering treatments; the tempering treatments were performed at different tempering temperatures with the objective of obtaining different microstructural conditions of the material. Prior to the thermal treatments the samples were encapsulated in quartz tubes with argon atmosphere. The different thermal treatments are described in Table 2. The treatment of the as-received (AR) material was performed and reported by the manufacturer of the steel.

Table 2: Thermal treatments performed on the P91 steel. Identification of the resulting metallurgical conditions

Thermal treatment	Identification
As received: Normalised at 1 060°C.Tempered at 780°C, 40 min	**AR**
1 050°C, 30 min; air cooled	AC
AC + tempered 300°C, 1 h	T300
AC + tempered 400°C, 1 h	T400
AC + tempered 500°C, 1 h	T500
AC + tempered 600°C, 1 h	T600

The techniques used for the characterisation of the different metallurgical conditions and the preparation of the corresponding samples were as follows:

X-ray diffraction (XRD): the samples were disks of 35 mm diameter. The surface to be analysed was polished with SiC from #150 grit up to #600 grit; then it was electropolished with a mixture of $HClO_4$ 10 wt% in Butyl Cellosolve.

Scanning electron microscopy with field emission gun (FEG-SEM): conventional metallographical techniques were used, i.e polishing with SiC from from #150 grit up to #600 grit, diamond paste 6 µm and 1 µm, etching with 50%Nital + 50% Villella at room temperature, etching time ca. 40 s.

Transmission electron microscopy (TEM): the samples used in the XRD measurements were etched with Vilella. Then, carbon extraction replicas were obtained. Additionally, thin films were prepared for AC and T300 conditions. For the preparation, discs of 3 mm in diameter were cut, then those were polished with SiC paper of 600 mesh to obtain a final thickness of ~0.1 mm. Disks were electropolished to electron transparency using an automatic Struers Tenupole 5 Jet Electropolisher with a 10% perchloric acid/methanol solution cooled to ≤-35°C. Various dissolution/cleaning solutions were used: ethanol, distilled water.

The XRD measurements were performed at the Brazilian synchrotron light laboratory (LNLS), Campinas, Brazil. The runs were performed using radiation energy of 7 keV which corresponds to a wavelength of 1.7712 Å. On each sample, a general scan in the range $20° \leq 2\theta \leq 130°$ was performed; this was followed by detailed scans in angular regions of interest. The latter angular intervals were selected according to the position of the reflections of the expected phases: retained austenite (γ Fe), and carbides/carbonitrides: MX, M_2X, M_3C, M_7C_3, $M_{23}C_6$.

The extraction replicas were observed in a Phillips CM200 TEM which is equipped with an EDAX-DX4 system for energy dispersive analysis of X-rays (EDS). Selected area electron diffraction (SAD) pattern was used to determine the crystallographic structure of the extracted particles. The lattice parameters used to index the diagrams were those obtained from the synchrotron light XRD measurements or the tabulated in the literature for the different expected compounds.

Results and discussion

As-received condition

The as-received (AR) condition of the P91 steel presents a microstructure of tempered martensite (Figure 1). The prior austenite grain boundaries are decorated by precipitated particles which present a different morphologies and sizes ranging from 100 nm to 500 nm. Smaller particles are observed in the interior of the prior austenite grains.

Figure 1: FEG-SEM micrograph of the P91 steel in the AR condition

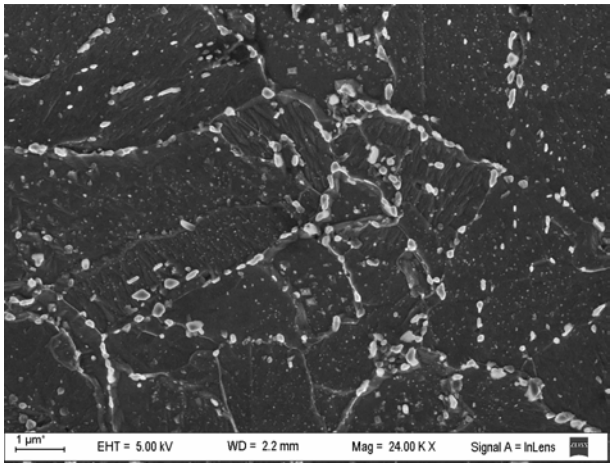

The precipitates that decorate the prior austenite grain boundaries were identified by TEM and the SAD patterns as Cr-rich carbides (Cr = 62, Fe=30, Mo=8) with the $M_{23}C_6$ structure. The smaller precipitates were identified as MX type carbonitrides. The EDS data show that two types of MX carbides are present, Nb-rich (Nb=55.1, V=33.8, Cr=11.1) and V-rich (Nb=20.7, V=58.8, Cr=20.5). Figure 2 is a TEM micrograph showing the $M_{23}C_6$ particles.

Figure 2: TEM micrograph of the P91 steel in the AR condition. $M_{23}C_6$ particles are shown. In the corner, a SAD pattern produced by one of the particles.

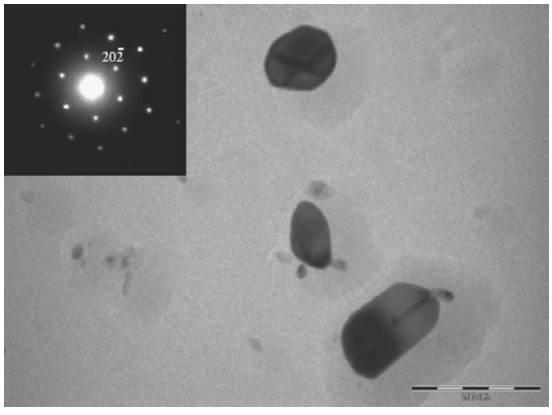

Normalised (AC) condition

Figure 3 shows a FEG-SEM micrograph of the P91 steel in the AC condition. The observed microstructure presents the characteristic features of lath martensite. Packets or groups of elongated regions with similar spatial orientations are observed. The regions have a length of 5 to 30 µm and a width of 0.5 to 5 µm. These regions are separated by boundaries which have a witdth of 100 to 300 nm. Particles, which in most cases present an elongated morphology, are observed within the regions described above. Most of these particles present one or two preferential orientation within each region. These particles were identified by TEM SAD pattern and EDS as M_3C (Fe=85%, Cr=15%). Nb-rich MX particles were found in this sample too. The XRD diffractogramme of this condition showed the presence of retained austenite.

Figure 3: TEM micrograph of the P91 steel in the AC condition

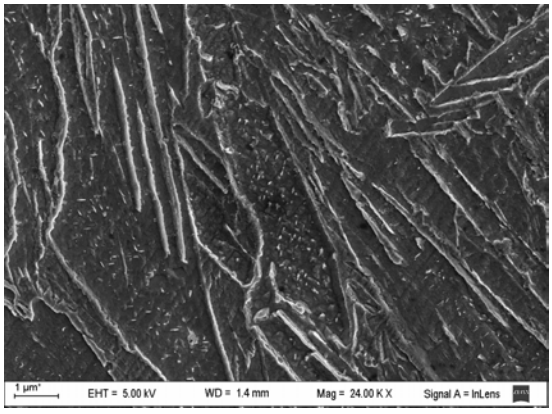

Tempered conditions (T300, T400, T500, T600)

The conditions T300 and T400 present a microstructure which is typical of lath martensite. In Figure 4, which corresponds to the T300 condition, packet and block boundaries are observed. Precipitated particles are present in the interior of the laths. These particles present diverse morphologies and sizes. The spherical and elongated shapes predominate. Three different types of precipitates were identified by TEM in the T300 condition. These are M_3C, M_7C_3 and MX. EDS analysis revealed that M_3C particles are nearly Fe_3C (Fe=85%, Cr=15%), whereas the M_7C_3 particles are enriched in Cr and the MX particles are enriched in Nb. Figure 5a is a TEM micrograph corresponding to the T300 condition. In the upper left corner the SAD pattern of the particle identified as M_7C_3 is shown. An EDS spectrum of an M_7C_3 type precipitate is presented in Figure 5b.

Figure 4: FEG-SEM micrograph of the P91 steel in the T300 condition

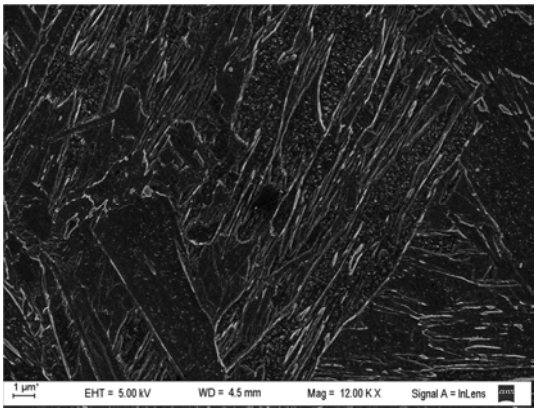

The microstructure of the steel tempered at 400°C presents similar morphologic features as those of the steel tempered at 300°C. In the T400 condition, precipitates of the type Fe_3C, Nb-rich MX and M_2X were identified.

Both in the T300 and T400 conditions, the presence of retained austenite was evidenced by the XRD measurements. Figure 6 shows a diffractogramme corresponding to the T300 condition.

Figure 5:

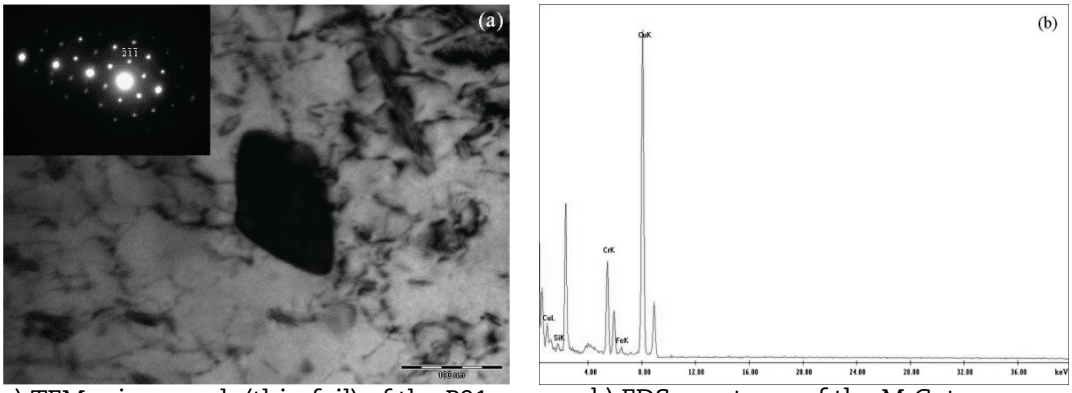

a) TEM micrograph (thin foil) of the P91 steel in the T300 condition.

b) EDS spectrum of the M_7C_3 type precipitate.

Figure 6: General diffractogramme of the P91 steel in the T300 condition. Showing the ferrite and austenite reflections.

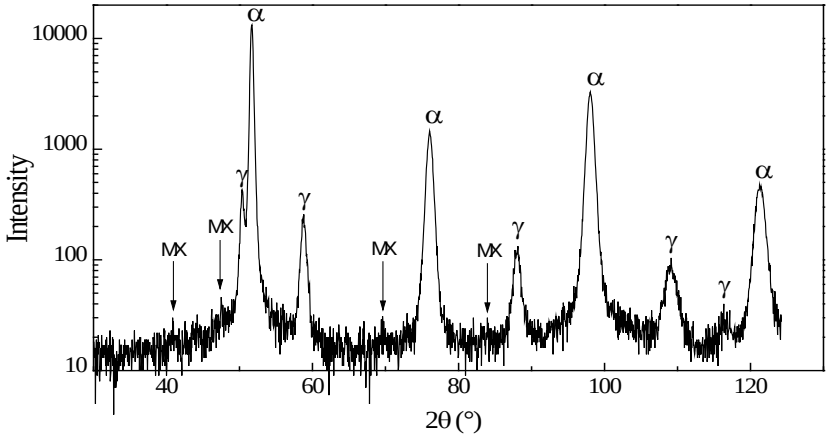

Besides the reflections corresponding to the major phase (ferrite, α) the reflexions of the austenite (γ) phase are clearly observed. The austenite peaks are well defined and of high intensity. Smaller peaks can be observed in the same diffractogramme. They correspond to the minor phase Nb-rich MX. These latter peaks are of very low intensity due to the low volume fraction of the MX phase.

The metallurgical condition T500 presents a microstructure of tempered martensite (Figure 7a). This figure shows that after tempering at 500°C, some characteristic features of the AC condition still persist: prior austenite grains which contain packets of blocks with similar orientation. Beyond this similarity, a great amount of precipitated particles is observed. The former austenite grain boundaries as well as the boundaries of regions within the grain are decorated by precipitates of different morphologies and sizes. In the interior of the latter regions a high amount of fine precipitates, most of them with an elongated shape are observed. The elongated precipitates are oriented along definite directions. Up to three such orientations can be recognised within a single region. These precipitates were identified by TEM and EDS as M_3C (Cr=51.5, Fe=48.5) (Figure 7b).

Figure 7: a) FEG-SEM micrograph of the P91 steel in the T500 condition. b) TEM micrograph showing details of the precipitates found in this condition.

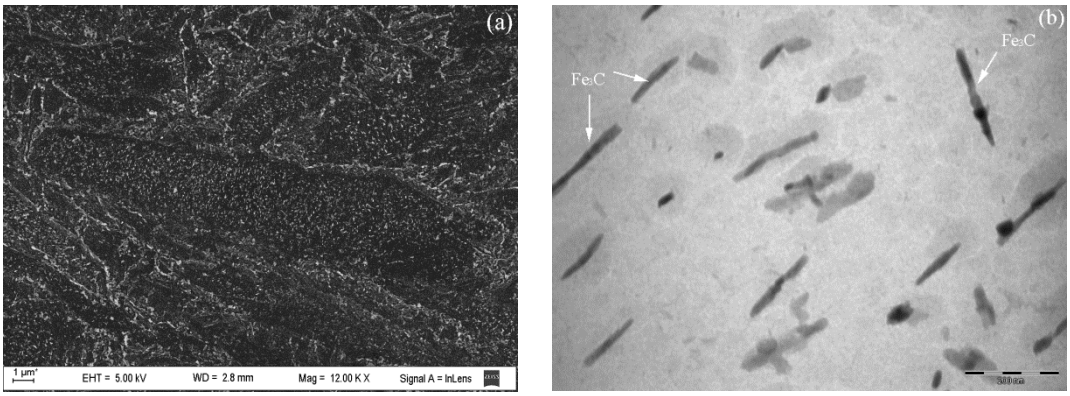

Precipitates of the type M_2X, Nb-rich MX and $M_{23}C_6$ were also identified by TEM in the P91 steel tempered at 500°C. Figure 8 is a TEM micrograph which shows a M_2X type precipitate with its corresponding SAD pattern. The observation of the FEG-SEM images leads to the conclusion that, among all the metallurgical conditions studied in the present work, the T500 condition presents the higher amount of precipitated particles.

Figure 8: TEM micrograph showing a precipitate of the MX type in the T500 condition. In the upper left corner, a SAD pattern of the M_2X type precipitate is shown.

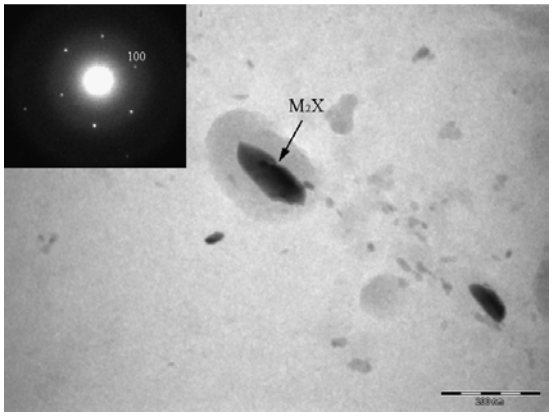

The microstructure of the P91 steel after being tempered at 600°C (T600 condition) contains a great amount of precipitates. Additionally, globular shaped particles with sizes around 200 nm are observed. The amount of precipitates obtained after tempering at 600°C is similar to that of the T500 condition and is notably larger than that of the T300 and T400 conditions. The particles extracted from the T600 condition were identified by TEM as the following compounds: $M_{23}C_6$ carbides, hexagonal M_2X carbonitrides and cubic MX carbonitrides. Some reflections corresponding to the mentioned phases $M_{23}C_6$, M_2X and MX were observed using XRD with synchrotron light. The lattice parameters of these compounds were determined from the X-ray diffraction data, and these parameters were used to index the electron diffraction diagrams obtained by TEM.

The chemical composition of the different precipitated phases in the T600 condition was determined by using energy dispersive X-ray analysis. The results indicate that the $M_{23}C_6$ particles are Cr-rich, with some amounts of Fe and Mo in their composition (Cr=65, Fe=25, Mo=10). The M_2X precipitates are also rich in chromium and contain Mo as a minor component. Concerning the MX precipitates found in the T600 condition, they were classified as Nb-rich and V-rich.

Figure 9: FEG-SEM micrograph of the P91 steel in the T600 condition

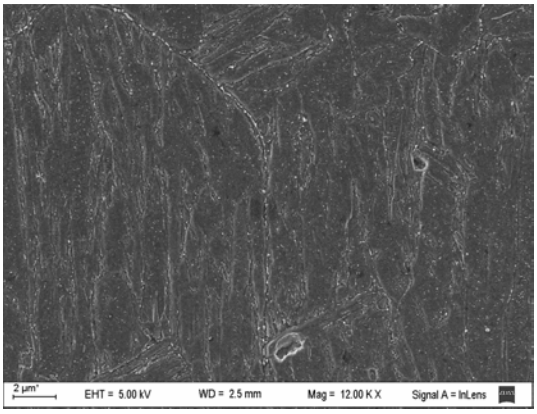

Table 3 presents a summary of the different phases which were identified and characterised by the different techniques in the present investigation.

Table 3: Identified phases in the P91 steel in the different metallurgical conditions. Detected (TEM=1, DRX=2); Not detected (-). (*) Lattice parameters determined from the X-ray diffraction data (nm)

Condition	Phases						
	Fe γ	Fe_3C	M_2X	M_7C_3	MX Nb-rich	MX V-rich	$M_{23}C_6$
AR	-	-	-	-	1	1	1, 2
AC	2	1, 2	-	-	1	-	-
R300	2	1	-	1	1, 2	-	-
R400	2	1	1	-	1, 2	-	-
R500	-	1, 2	1, 2	-	1	-	1, 2
R600	-	-	1, 2	-	1, 2	1	1, 2
(*)	-	-	a=0.2816 c=0.4458	-	a=0.4381	-	a=1.0632

Although the MX type precipitates were detected in all the samples, the nature of these particles, V-rich or Nb-rich, is different between the material tempered at low temperature and the material tempered at high temperature. The size of the MX particles present in the AC, T300 and T400 condition ranges from 100 to 250 nm, their shape is nearly spherical and they are Nb-rich. It must be recalled that niobium carbonitride is very insoluble. In order to completely dissolve NbCN, the austenite phase must be heated at temperatures higher than 1 100°C [1]

These facts suggest that the Nb rich carbonitrides were not completely dissolved during the austenizing treatment at 1 050°C; therefore, some of these particles remain after the normalising treatment (AC) as residual, undissolved carbides. These very stable Nb rich MX particles are not altered by the subsequent tempering treatments, and should be observed in the T300, T400, T500 and T600 conditions. However, the T600 and AR conditions present, besides the Nb-rich precipitates, other MX type precipitates which are enriched in vanadium. These latter precipitates present smaller size than the Nb-rich ones, and they are formed at tempering temperatures of 600°C and above. Zavaleta-Gutiérrez et al. [7]. observed the MX precipitates type I, type II and type III. The type I and type II precipitates correspond respectively to the Nb-rich and the V-rich precipitates found in the present investigation. The type III precipitates have been designated in the literature as “wings”, these particles present a particular morphology in which V-rich rods grows in a Nb-rich spherical core. The type III precipitates were not found in the present work.

The presence of cementite (M_3C, Fe_3C) has been established by TEM techiques in the AC, T300, T400 and T500 conditions. However, this phase could not be detected by X-ray diffraction. This is attributed to the fact that the main reflections of the cementite phase coincide with those of α ferrite, i.e. the major phase of the steel. In the 9%Cr steels, the Fe_3C phase precipitates as a fine dispersion of particles with dendritic morphology at tempering temperatures lower than 350°C [8]. The presence of this phase in the AC condition is attributed to the auto tempering of the martensite during the normalising treatment.

The M_2X type precipitates begin to form at temperatures close to 400°C. In this type of steels, they usually are Cr-rich carbonitrides. These carbonitrides form due to the high Cr concentration and also to the higher diffusivity of this sustitutional element in comparison with the alloying elements Mo, V and Nb [2]. Based on the chemical compositions obtained by EDS, we assign this phase to the compound Cr_2X (X = C,N). This result agrees with the results reported in [9], where it is informed that for 9Cr-1Mo steels subjected to a normalising treatment followed by a tempering treatment at temperature in the range $400°C \leq T \leq 750°C$, the precipitation of coherent M_2X type particles may occur in short tempering times and generally this particles are enriched in Cr.

The $M_{23}C_6$ phase, which is present in the P91 steel after tempering at high temperature, is preceded by the M_2X phase. At tempering temperatures of 500°C and higher, the coarsening of the M_2X precipitates begin. At temperatures near 550°C these precipitates are gradually replaced by Cr-rich $M_{23}C_6$ type precipitates which mainly nucleate at the martensite lath boundaries and in the prior austenite grain boundaries [1]; this behaviour is coincidently observed in the present metallurgical conditions of the P91 steel.

Conclusions

The second phase particles which precipitate in a P91 steel after different normalising and tempering treatments have been characterised by XRD diffraction with synchrotron light, FEG-SEM, TEM and EDS.

The present observations allow us to present the following proposals concerning the sequence of precipitation or dissolution of second phase particles in the P91 steel as a function of the tempering temperature:

- The MX phase particles which are present in the P91 steel after tempering at 300°C or 400°C are Nb-rich; they exhibit a spherical shape and correspond to precipitates which were not completely dissolved during the austenizing stage.
- The V-rich MX type precipitates are found in the P91 steel after tempering at temperatures higher than 600°C. These particles present smaller sizes than the Nb-rich ones. These fine precipitates are those that improve the creep resistance of the P91 steel.
- The M_2X particles are gradually replaced by $M_{23}C_6$ particles as the tempering temperature and time increase.
- The Fe-rich M_3C cementite particles are formed by auto-tempering and persist at tempering temperatures of 500°C or lower.

Acknowledgement

The Brazilian Synchrotron Light Laboratory (LNLS), Campinas, Brazil, allowed some of the authors to use their installations, in particular the XRD1 line, and also contributed with financial support.

References

[1] Klueh, R.L. and D.R. Harries (2001), "High-Chromium Ferritic and Martensitic Steels for Nuclear applications", ASTM.

[2] Jones, W.B., C.R. Hills and D.H. Polonis (1991), "Microstructural evolution of modified 9Cr-1Mo steel", Metallurgical Transactions, 22A, pp. 1049-1058.

[3] Klueh, R.L. (2004), "Elevated-termperature ferritic and martensitic steels and their application to future nuclear reactors", ORNL/TM-2004/176.

[4] Parvathavarthini, N., R.K. Dayal and J.B. Gnanamoorthy (1996), "Effect of microestructure on corrosion behaviour of 9% chromium-1% molybdenum steel", Corrosion Science, 52, pp. 540-551.

[5] Saroja, S., M. Vijayalakshmi and V.S. Raghunathan (1993), "Effect of prolonged exposures of 9Cr-1Mo-0.07C steel to elevated temperatures", Materials Transactions, JIM, 34, pp. 901-906.

[6] Hurtado-Noreña, C. and P. Bruzzoni (2010), "Effect of microstructure on hydrogen diffusion and trapping in a modified 9%Cr–1%Mo steel", Materials Science and Engineering A, 527, pp. 410-416.

[7] Zavaleta-Gutiérrez, N., M.I Luppo and C.A. Danón (2007), "Heterogeneous austenite grain growth in ASTM A213-T91 steel", ISIJ International, 47, pp. 1178-1187.

[8] Kaneko, K., S. Matsumura, A. Sadakata, K. Fujita, W.-J. Moon, S. Ozaki, N. Nishimura and Y. Tomokiyo (2004), "Characterisation of carbides at different boundaries of 9Cr-steel", Materials Science and Engineering A, 374, pp. 82-89.

[9] Vijayalakshmi, M. and B. Raj (2006), "Phase Evolution Diagrams, a new approach to mean metal temperature of ferritic components", Universities Press.

Environmentally assisted cracking and irradiation embrittlement of CF-8 and CF-8M cast austenitic stainless steels in high-purity water

Y. Chen,*[a] B. Alexandreanu,[a] K. Natesan,[a] and A. S. Rao[b]
[a] Argonne National Laboratory, United States
[b] US Nuclear Regulatory Commission, United States

Abstract

Cast austenitic stainless steels (CASS) are used for components with complex geometries in the cooling system of light water reactors (LWRs). Due to both thermal ageing and irradiation embrittlement, the long-term performance of CASS materials is of concern. To assess the impact of thermal ageing and irradiation embrittlement on the cracking behaviour of CASS materials, crack growth rate and fracture toughness JR curve tests were carried out on CF-8 and CF-8M compact-tension specimens in high-purity water with low dissolved oxygen. The as-received and thermally aged CASS specimens were irradiated to 0.08 dpa to investigate the combined effect of thermal ageing and neutron irradiation. The crack growth rates of irradiated CASS materials were compared with previous results on unirradiated specimens. While no elevated cracking susceptibility was observed for the irradiated specimens at this dose level, a slightly better corrosion fatigue performance was found in the CF-8 than in CF-8M materials. Thermal ageing history had little effect on the crack growth behaviour in the test environment. Transgranular cleavage-like cracking was the main fracture mode in the crack growth rate tests, and delta ferrite morphology could be seen in some areas on the fracture surfaces. Compared to thermal ageing, neutron irradiation had a dominant role in the fracture toughness JR curve tests. The loss of toughness due to neutron irradiation was much more significant in the as-received than in the thermally aged CASS specimens. The fracture toughness of CASS specimens was reduced to a similar level after neutron irradiation regardless of their thermal ageing history. This suggests a more rapid development of embrittlement in the as-received than in the thermally aged CASS specimens under neutron irradiation.

Introduction

Cast austenitic stainless steels (CASS) are used extensively in light water reactors (LWRs). The CF grade CASS alloys have compositions similar to that of 300-series austenitic stainless steels (SSs), and are most often used for reactor components with complex shapes, such as pump casings, valve bodies, piping, and elbows in cooling systems, and control rod guide tube spacers in core internals [1]. Similar to wrought SSs, CASS alloys possess excellent corrosion resistance and mechanical properties [2]. A good combination of strength and ductility gives rise to excellent fracture toughness. Stable tearing occurs in CASS materials well above their yield strength before final fracture [3]. In addition to their applications in LWRs, high-performance CASS alloys have also been developed for future nuclear energy systems [4]. As a cost-effective manufacture method, advanced CASS alloys can provide a viable option for the first wall shield modules and the divertor cassette of the International Thermonuclear Experimental Reactor.

The solidification microstructure of CASS alloys consists of both delta ferrite and austenite. The fraction of ferrite phase in a casting is controlled by its chemical composition and thermal history [5,6]. The ferrite-austenite duplex microstructure is

critical for the mechanical properties and corrosion resistance of CASS. Since thermal-mechanical treatments cannot be easily implemented in castings, the strength of CASS mainly relies on the duplex microstructure. Beck et al. [7] showed that the tensile and yield strengths of CASS materials increase with ferrite content at both room and elevated temperatures. The delta ferrite is also crucial for the soundness of steel castings. A minimum fraction of delta ferrite is often required to reduce the tendency of hot cracking in castings. In addition, ferrite phase can also improve the resistance to sensitisation, and therefore reduce the susceptibility to stress corrosion cracking (SCC) [8,9].

While the duplex microstructure is mostly beneficial, delta ferrite can also exert a detrimental effect on the fracture resistance of CASS. Exposed to elevated temperatures between 300 and 500°C, delta ferrite is vulnerable to thermal ageing embrittlement. An increased tensile strength and reduced ductility are commonly observed in CASS alloys after prolonged thermal ageing treatments [10-12]. Consequently, the upper-shelf impact energy is reduced, and the ductile-to-brittle transition temperature shifts higher. The extent of the embrittlement increases with ferrite content and is sensitive to the morphology of delta ferrite [3]. Because of the thermal ageing embrittlement, the long-term performance of CASS materials is of concern at elevated temperatures. Besides the thermal ageing embrittlement, CASS alloys used in nuclear energy systems are also subjected to neutron irradiations. Displacement damage resulting from fast neutron bombardments can also affect the microstructural evolution profoundly. Irradiation hardening and embrittlement may generate further degradation in ferrite phase, leading to an additional loss of fracture toughness. While the thermal ageing embrittlement of CASS materials has been studied extensively, very limited data exist in the open literature for neutron-irradiated CASS at present [13,14]. It is not clear if a combination of irradiation and thermal ageing would reduce the fracture resistance to a lower level than either of the degradation mechanisms can impart alone. A better understanding of the combined effect of thermal ageing and neutron irradiation is crucial for the assessment of long-term performance of CASS components in nuclear energy systems.

Experimental

Two heats of static castings with different Mo contents (CF-8 and CF-8M) were examined in the current study. Table 1 shows their chemical compositions. The ferrite contents of the CF-8 and CF-8M were 23% and 28%, respectively. Both as-received and thermally aged specimens were included in this study. The thermal ageing was carried out at 400°C for 10 000 hr in a previous research program [3]. Figure 1 shows the optical images of the as-received (i.e., unaged) and thermally aged CF-8. A vermicular microstructure resulting from primary ferrite dendrites is clearly visible on the polished sample surfaces. Neither the morphology nor the volume fraction of delta ferrite was affected significantly by the applied thermal ageing treatment. Similar microstructures were also observed in the unaged and aged CF-8M specimens.

Table 1: Chemical compositions of the cast stainless steels

Cast grade	Heat	Composition (wt. %)								
		Mn	Si	P	S	Mo	Cr	Ni	N	C
CF-8	68	0.64	1.07	0.021	0.014	0.31	20.46	8.08	0.062	0.063
CF-8M	75	0.53	0.67	0.022	0.012	2.58	20.86	9.12	0.052	0.065

Figure 1: Optical images of unaged and thermally aged CF-8

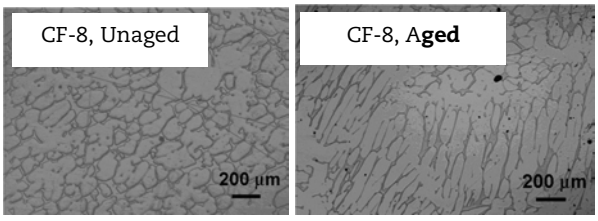

The samples used in this study were 6.5-mm thick compact-tension (i.e., 1/4T-CT) specimens. Figure 2 shows a picture of the CT specimen. The starter notch was about 6 mm. To ensure an in-plane crack growth, side grooves approximately 5% of the sample thickness were machined on both sides of specimen.

Figure 2: 1/4T-CT specimen used in this study.

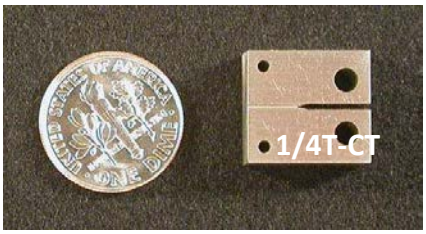

The samples were irradiated in a helium-filled capsule in the Halden reactor. The irradiation temperature was about 315°C. The estimated fast neutron fluence (E > 1 MeV) was about 5.56×10^{19} n/cm^2, corresponding to a displacement damage of 0.08 dpa for SS samples. More details of the irradiation can be found in Reference 15.

The tests were conducted in a 316-SS autoclave in high-purity water containing with less than 10 ppb dissolved-oxygen (DO). The water was circulated at a rate of 20-30 mL/min during the test, and the conductivity was kept below 0.07 μS/cm. The temperature and pressure of the autoclaves were kept at ~320°C and ~1 800 psig, respectively.

Crack extensions were monitored continuously with a direct current potential drop (DCPD) method during the test. Four electrical leads were spot welded on the CT sample. A constant current was passed through the sample, and the potential drop across the crack mouth was measured and related to the crack extension with a calibrated correlation curve. All DCPD measurements in this study were corrected with post-test SEM measurements on the fracture surfaces.

Crack growth rate (CGR) and J-R curve tests were carried out with a servo-hydraulic system in a shielded hot cell. The specimen was first pre-cracked in the test environment at 320°C, and then transitioned to a constant-load SCC test. Corrosion-fatigue CGRs were measured at different stages of the test under cyclic loading. After the test was transitioned to a constant-load test successfully, SCC CGRs were recorded with or without periodical partial unloading (PPU). Since elevated susceptibility to cracking is unlikely at this low dose level, the SCC CGR tests were kept short in the present study. Following the SCC CGR test, a fracture toughness J-R curve test was carried out in the test environment to assess the extent of embrittlement resulting from neutron irradiation and thermal ageing. The CGR test provides a SCC starter crack for the subsequent fracture toughness J-R curve test.

Results

All specimens were pre-cracked with a triangular waveform in the test environment. The two CF-8 specimens (unaged and aged) were pre-cracked at ~17 MPa m$^{1/2}$ and 1 Hz, and the two CF-8M specimens were pre-cracked at ~14 MPa m$^{1/2}$ and 2 Hz. Following the initial precracking period, environmentally enhanced cracking was induced by a series of test steps with gradually increased rise times and load ratios. The measured cyclic CGRs were evaluated against fatigue CGR in air to assess environmental enhancement. Elevated CGRs were observed for all CASS specimens after 0.7-1 mm crack extension. In general, environmental enhancement was more evident in the CF-8M than in CF-8 specimens. No significant difference was observed in corrosion fatigue response between the unaged and aged CASS specimens.

Constant-load CGR tests were conducted with and without periodic partial unloading (PPU) after environmentally assisted cracking was stabilised. For the test periods with

PPU, a hold-time of one or two hours was applied. Moderate CGRs in the range of 10^{-11} m/s were observed between 15-19 MPa $m^{1/2}$ with PPU for all specimens regardless their thermal ageing condition. Without PPU, however, the constant-load CGRs were negligible for the two CF-8 and the unaged CF-8M specimens. A CGR less than 2×10^{-12} m/s were recorded for the thermally aged CF-8M at ~19 MPa $m^{1/2}$. An accurate determination of such a low growth rate would require a much longer test time than possible in the current study. Table 2 shows all SCC CGRs recorded in these tests.

Table 2: SCC CGRs of 0.08-dpa CF-8 and CF-8M in low-DO high-purity water

Sample ID	Material	Ageing condition	K (Mpa $m^{1/2}$)	PPU, hold time (hr)	CGR (m/s)
E-1	CF-8, 23%	Unaged	14.9	2	1.8E-11
			16.8	2	2.7E-11
F-1	CF-8, 23%	10k hr @ 400°C	16.0	2	2.7E-11
I-1	CF-8M, 28%	Unaged	17.9	2	1.9E-11
J-1	CF-8M, 28%	10k hr @ 400°C	15.5	2	1.8E-11
			15.6	1	2.5E-11
			19.0	2	5.5E-11
			18.9	1	6.4E-11
			18.9	w/o PPU	<2.0E-12

All fracture toughness J-R curve tests on the irradiated CASS specimens were carried out in the test environments at ~320°C. The tests were performed with a constant stain rate of 0.43 μm/s. For each test, the values of J-integral were calculated from the load vs. load-line displacement. A J-R curve was then constructed by fitting the calculated J values and corresponding crack lengths to a power law relationship ($J=C^*\Delta a^n$). The J values at the 0.2-mm offset blunting line (J_Q) were reported in Table 3 along with the power-law curve fitting results. Because of the low strength and high fracture toughness of CASS materials, the required crack tip constraint and upper limit of J integral were invalid with the 1/4T-CT specimens used in this study. Thus, the J_Q values obtained in this study cannot be validated for J_{IC} per ASTM E1820.

Table 3: J-R curve test results of 0.08-dpa CF-8 and CF-8M

Sample ID	Material	Ageing condition	J-R results		
			C	n	J_Q (kJ/m²)
E-1	CF-8, 23%	Unaged	359	0.57	183
F-1	CF-8, 23%	10k hr @ 400°C	372	0.62	171
I-1	CF-8M, 28%	Unaged	336	0.66	145
J-1	CF-8M, 28%	10k hr @ 400°C	259	0.64	106

After the J-R tests, the specimens were fractured in air at room temperature. Replicas of the fracture surfaces were produced from the tested sample and examined with a SEM. All fracture surfaces of the irradiated CASS specimens displayed similar fracture morphologies. The fracture surface of the unaged CF-8 specimen is shown in Figure 3 as an example. Transgranular cleavage-like fracture is the dominant morphology in the CGR test region. Vermicular ferrite at dendrite cores are seen at the later stage of the CGR test (as shown in Figure 3c). Beyond the CGR test region, the dominant fracture mode is ductile dimples resulting from microvoid coalescence. No obvious difference can be seen between the thermally aged and unaged CASS specimens.

Figure 3: SEM images of the fracture surface replica of unaged CF-8, (a) along the sample centreline, (b) J-R test region, (c) SCC CGR test region, and (d) precracking region. Crack propagation from bottom to top for all images.

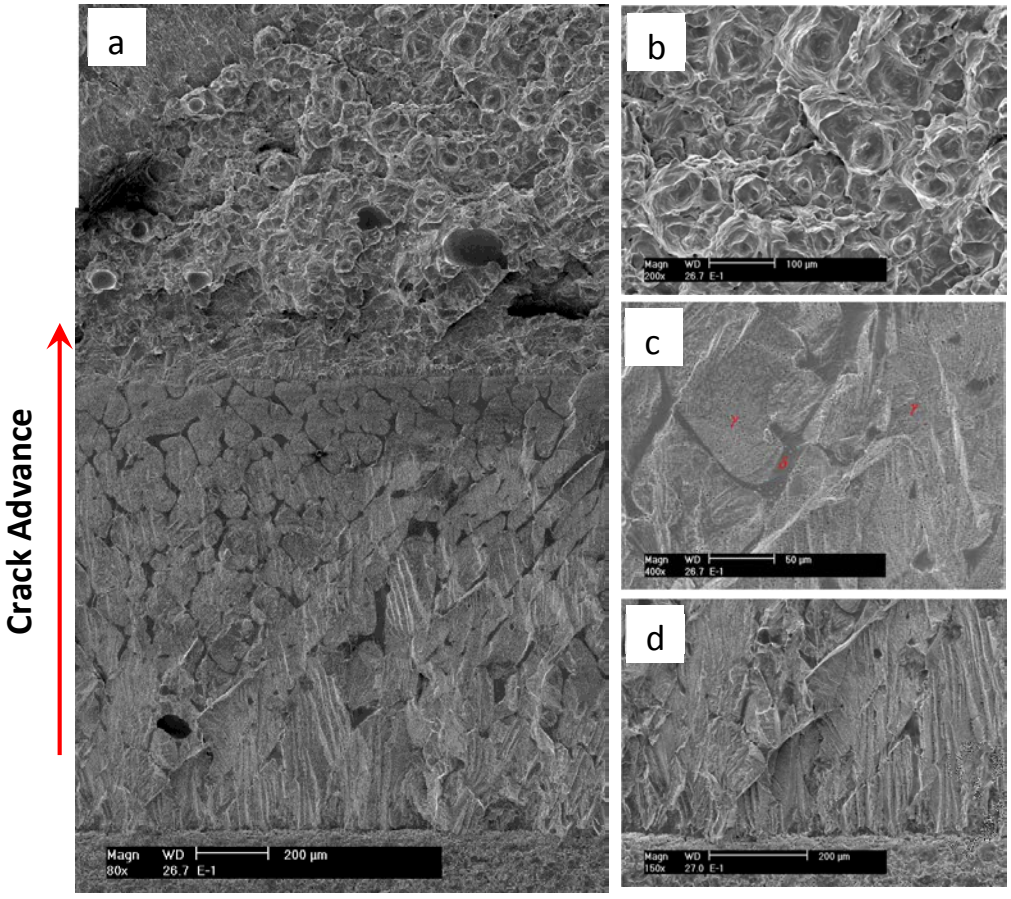

Discussion

Crack growth rates under cyclic loading

To evaluate environmentally enhanced cracking, the obtained cyclic CGR data are fitted to an empirical correlation ($CGR_{env} \propto CGR_{air}^{0.5}$) for each CASS specimen. The best fit curves for each data set of the CASS specimens are compared in Figure 4. The best fit curves of both unaged and thermally aged CF-8 CASS are below those of the CF-8M. Obviously, the CF-8M samples are more susceptible to environmentally assisted cracking compared to the CF-8 under the current test condition. The differences between the unaged and aged specimens in Figure 4 are small. It appears that thermal ageing does not have a significant impact on the cyclic cracking behaviour of CASS at 0.08 dpa.

SCC crack growth rates

Constant-load SCC CGRs obtained in this study are plotted in Figure 5 along with the SCC CGRs reported by Terachi et al. [16] on unirradiated 304 and 316 SSs tested in PWR water. A reference line that bounds the CGR data for unirradiated and sensitised 304 SS in high-DO environment is also included. All the data points of the 0.08-dpa CASS specimens are well below the high-DO reference line, and are comparable to the CGRs of unirradiated cold-worked SSs tested in a similar low-corrosion-potential environment. This good SCC resistance suggests that neutron irradiation, up to 0.08 dpa, does not elevate the cracking susceptibility of CASS significantly.

Figure 4: Best-fit curves of cyclic CGR data at 0.08-dpa dose

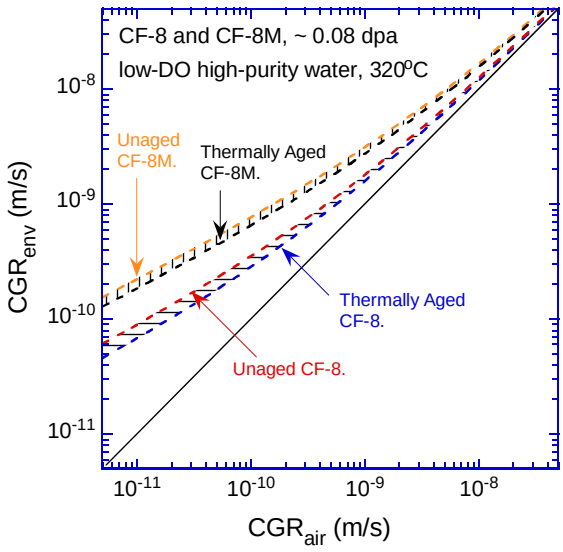

A low susceptibility to SCC is expected for CASS owing to the beneficial effects of ferrite. It has been shown that unirradiated CASS samples are more resistant to SCC than wrought SSs in high-DO water. The superior SCC performance of the duplex microstructure may arise from the deformation behaviour of the ferrite phase. Using a nano-indentation measurement, Wang et al. [17] showed that the hardness of ferrite phase is higher than that of austenite phase in CF-8. Our fractographic examinations also showed little plasticity within the ferrite phase during SCC tests. By delaying the development of plastic deformation in ferrite phase, a slip-dissolution mechanism could be hindered to some extent in a duplex microstructure. This beneficial effect of ferrite could be diminished, in principle, by thermal ageing or irradiation embrittlement. A deteriorated fracture resistance of ferrite grains would accelerate the development of plastic strain in surrounding austenite phase. In fact, elevated SCC CGRs have been observed in a thermally aged CF-8M at ~2.4 dpa [13]. This observation suggests that the beneficial effect of a duplex microstructure may be eliminated or greatly reduced by neutron exposure to a sufficiently high fluence.

The unaged and aged data points shown in Figure 5 are very similar regardless of CASS grades. Thermal ageing does not appear to affect the cracking susceptibility of the CASS specimens in the low-DO high-purity water. This lack of sensitivity to thermal ageing history is consistent with that observed in cyclic CGR tests. The small difference between the CF-8 and CF-8M is statistically insignificant, given the large data scatter and inherent uncertainties in short CGR tests.

Fracture toughness

Figure 6 shows the comparison of the fracture toughness J_Q values of the irradiated (this study) and unirradiated CASS materials (a previous thermal-ageing study [3]). Both irradiated and unirradiated CASS specimens were obtained from the same heats with the same thermally aged conditions. While the irradiated J-R tests were performed on 1/4T-CT specimens at 320°C in high-purity water, the unirradiated tests were carried out on larger samples (1T-CT) at 290°C in air. Figure 6 shows that neutron irradiation, even at 0.08 dpa, has a significant impact on the fracture toughness of CASS. The extent of irradiation embrittlement is greater for unaged than aged specimens. After irradiation, the fracture toughness values of unaged CASS are less than one-third of their original unirradiated values. For thermally aged CASS, a 30% reduction in fracture toughness is observed after irradiation.

Figure 5: Constant-load CGRs of 0.08-dpa CASS in low-DO high-purity water

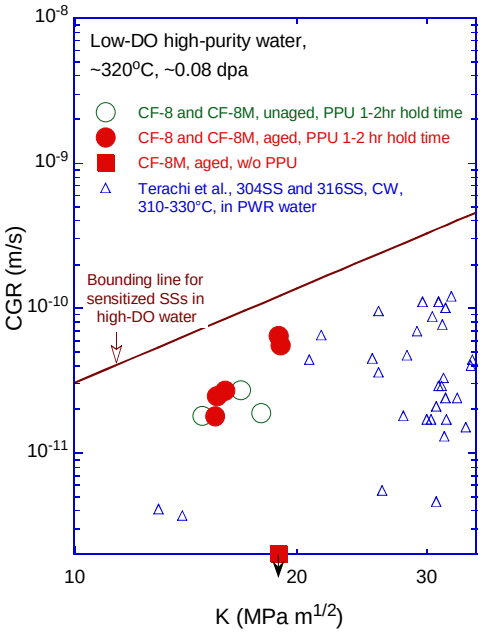

The differences in fracture toughness between unaged and aged specimens were reduced after irradiation. The drastically different fracture toughness values between unaged and thermally aged specimens become somewhat comparable after irradiation. The similar post-irradiation properties suggested a dominant role of neutron irradiation (compared to thermal ageing) in promoting embrittlement in CASS materials. Our results also showed that both corrosion fatigue and SCC of CASS became insensitive to thermal ageing history after irradiation (e.g. Figures 4 and 5). It appeared that the unaged microstructure was deteriorated more rapidly than the thermally aged microstructure under neutron bombardments. Consequently, the cracking behaviour between the aged and unaged specimens became similar after irradiation.

While the irradiation damage seems to be a dominant factor for embrittlement, a combined effect of thermal ageing and irradiation damage does reduce the fracture resistance of CASS further. As shown in Figure 6, the fracture toughness values of thermally aged and irradiated specimens are approximately 30% lower than those of thermally aged specimens. This implies an interaction between thermal ageing and irradiation embrittlement. Thus, the extent of thermal ageing embrittlement of CASS needs to be examined closely under neutron irradiation.

Figure 6: Fracture toughness of CF-8 and CF-8M

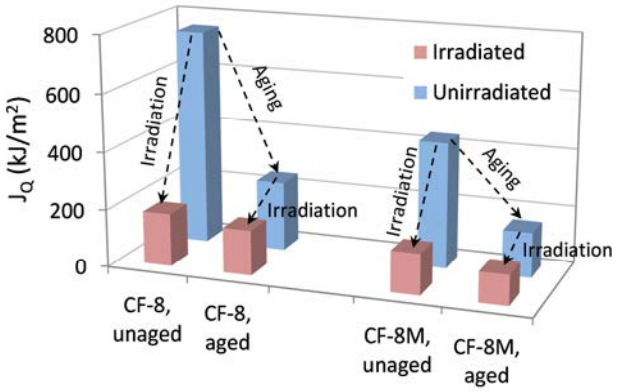

Note: the unirradiated results are obtained from 1T-CT specimens at 290°C in air, and the irradiated results are obtained from 1/4T-CT specimens at 320°C in water.

Summary

Crack growth rate tests have been carried out on the CF-8 and CF-8M specimens with high ferrite contents. The samples were irradiated to 0.08 dpa, and the CGR tests were performed in low-DO high-purity water at 320°C. Environmentally enhanced cracking was observed for all CASS specimens, and cyclic CGRs and constant-load SCC CGRs were obtained. Only moderate SCC CGRs in the range of 10^{-11} m/s were recorded for the CF-8 and CF-8M specimens regardless of their thermal ageing history. In general, the CASS materials showed good resistance to both corrosion fatigue and SCC at 0.08 dpa.

Following the CGR tests, fracture toughness J-R curve tests were performed on the CASS specimens in the test environment. Neutron irradiation had a significant impact on the fracture toughness of CASS. At 0.08 dpa, the fracture toughness values of unaged specimens were about one-third of their initial unirradiated values. An additional 30% reduction in fracture toughness was also observed for thermally aged specimens after irradiation. The combined effect of thermal ageing and irradiation damage can reduce the fracture resistance of CASS to a higher extent than any one of the degradations can achieve alone.

Acknowledgements

The authors would like to thank Drs. O.K. Chopra and W.J. Shack for their contribution to this project. Our special thank go out to Ms. T. M. Karlsen, OECD Halden Reactor Project, Halden, for helping arrange irradiations and sample transfer. Dr. Y. Yang of University of Florida, and Drs. J. Pakarinen and Y. Huang of University of Wisconsin-Madison are acknowledged for their contributions to the experimental effort. This work is sponsored by the Office of Nuclear Regulatory Research, U.S. Nuclear Regulatory Commission, under Job Code N6519; Program Manager: A.S. Rao.

References

[1] U.S. NRC (2006), "Expert Panel Report on Proactive Materials Degradation Assessment," NUREG/CR-6923.

[2] Blair, M., and T.L. Steven (1995), Steel Castings Handbook, Sixth Edition, Steel Founders' Society of America and ASM International.

[3] Chopra, O.K., and A. Sather (1990), "Initial Assessment of the Mechanisms and Significance of Low-Temperature Embrittlement of Cast Stainless Steels in LWR Systems", NUREG/CR-5385, ANL-89/17.

[4] Busby, J.T., P.J. Maziasz, A.F. Rowcliffe, M. Santella, M. Sokolov (2011), "Development of High Performance Cast Stainless Steel For ITER Shield Module Applications", Journal of Nuclear Materials, 417, pp. 866-869.

[5] Aubrey, L.S., P.F. Wieser, W.J. Pollard, and E.A. Schoefer (1982) "Ferrite Measurement and Control in Cast Duplex Stainless Steel," in Stainless Steel Castings, ASTM STP 756, pp. 126-164.

[6] Schaeffler, A.L. (1949), "Constitution Diagram for Stainless Steel Weld Metal", Metal Progress, 56, No 11, pp. 680-680B.

[7] Beck, F.H., E.A. Schoefer, J.W. Flowers, and M.G. Fontana (1965), "New Cast High-Strength Alloy Grades by Structure Control", in Advances in the Technology of Stainless Steels and Related Alloys, ASTM STP 369.

[8] Beck, F.H., J. Juppenlatz, and P.F. Wieser (1976), "Effects of Ferrite and Sensitization on Intergranular and Stress Corrosion Behaviour of Cast Stainless Steels", in Stress Corrosion - New Approaches, H. L. Craig, Jr., ed., ASTM STP 610.

[9] Hughes, N.R., W.L. Clarke, and D.E. Delwiche (1982), "Intergranular Stress-Corrosion Cracking Resistance of Austenitic Stainless Steel Castings", in Stainless Steel Castings, V.G. Behal and A.S. Melilli, eds., ASTM STP 756.

[10] Fisher, R.M., E.J. Dulis, and K.G. Carroll (1953), "Identification of the Precipitate Accompanying 885F Embrittlement in Chromium Steels," Transactions of AIME 197, No. 5, pp. 690–695.

[11] Grobner, P.J. (1973), "The 885 F (475 C) Embrittlement of Ferritic Stainless Steels", Metallurgical and Materials Transactions B, 4, No. 1, pp. 251-260.

[12] Nichol, T.J., A. Datta, and G. Aggen (1980), "Embrittlement of Ferritic Stainless Steels", Metallurgical and Materials Transactions A, 11, No. 4, pp. 573-585.

[13] Chopra, O.K., and W.J. Shack (2008), "Crack Growth Rates and Fracture Toughness of Irradiated Austenitic Stainless Steels in BWR Environments", NUREG/CR-6960, ANL-06/58.

[14] Mills, W.J. (1988), "Fracture Toughness of Irradiated Stainless Steel Alloys", Nuclear Technology, 82, No. 3, pp. 290-303.

[15] Chen, Y., B. Alexandreanu, and K. Natesan (2013), "Crack Growth Rate and Fracture Toughness Tests on Irradiated Cast Stainless Steels", ANL-12/56.

[16] Terachi, T., T. Yamada, T. Miyamoto, K. Arioka (2012), "SCC growth behaviours of austenitic stainless steels in simulated PWR primary water", Journal of Nuclear Materials, 426,pp. 59–70.

[17] Wang, Z., F. Xue, J. Jiang, W. Ti, and W. Yu (2011), "Experimental Evaluation of Temper Ageing Embrittlement of Cast Austenitic Stainless Steel from PWR", Engineering Failure Analysis, 18, P. 403.

Irradiation project of SiC/SiC fuel pin "INSPIRE": Status and future plan

Akira Kohyama and Hirotatsu Kishimoto
OASIS, Muroran Institute of Technology, Japan

Abstract

After the March 11 Disaster in East-Japan, Research and Development towards Ensuring Nuclear Safety Enhancement for LWR becomes a top priority R&D in nuclear energy policy of Japan. The role of high temperature non-metallic materials, such as SiC/SiC, is becoming important for the advanced nuclear reactor systems. SiC fibre reinforced SiC composite has been recognised to be the most attractive option for the future, now, METI fund based project, INSPIRE, has been launched as 5-year termed project at OASIS in Muroran Institute of Technology aiming at early realisation of this system. INSPIRE is the irradiation project of SiC/SiC fuel pins aiming to accumulate material, thermal, irradiation effect data of NITE-SiC/SiC in BWR environment. Nuclear fuel inserted SiC/SiC fuel pins are planned to be installed in the Halden reactor. The project includes preparing the NITE-SiC/SiC tubes, joining of end caps, preparation of rigs to control the irradiation environment to BWR condition and the instruments to measure the condition of rigs and pins in operation. Also, basic neutron irradiation data will be accumulated by SiC/SiC coupon samples currently under irradiation in BR2. The output from this project may present the potentiality of NITE-SiC/SiC fuel cladding with the first stage fuel-cladding interaction.

Introduction

The East-Japan disaster on March 11, 2011 caused significant damages over all the systems in East-Japan, including severe accident of TEPCO Fukushima nuclear plants. The disaster had strong impact on European energy policy and the US energy policy. There is a big divergence within European countries about their responses to the same event. For example, in the United Kingdom, policy makers remained firm on their decision to increase nuclear power generation in the near future. On the contrary, in Germany, the federal government decided to, at least, temporarily shut down old generation nuclear reactors. The Japanese government appears rather close to the UK response while the majority of the Japanese public responded closely to the German [1]. The disaster caused drastic shift of the Japanese energy policies from The "3rd phase basic plan of science and technology of Japan" and "Framework for Nuclear Energy Policy", where nuclear energy was emphasised to be the core energy for the society [2,3]. The "4th phase basic plan of science and technology" was issued on August 2011, where, as the baseline understandings followed the explanations about the present-status of Japan under "the after effects of the crisis" and inevitable needs of drastic changes/improvements of nuclear energy systems were pointed out.

Based on the "Basic Energy Policy" (June, 2010) and the "4th Phase Basic Plan of Science and Technology" (August 2011), the revised version of "Framework of Nuclear Energy Policy for 2012" had been prepared, but was cancelled on 2 October 2012 and ended the long history from 1958. However, the followings were discussed and urgent needs were recognised.

- Restructuring nuclear energy policy towards safety assurance and recovery of public trust.
- Restructuring nuclear energy policy under large drop of energy dependence on nuclear.
- Establishment of "The highest level of nuclear safety".

Figure 1: The history of major SiC composite R&D by Kohyama Group

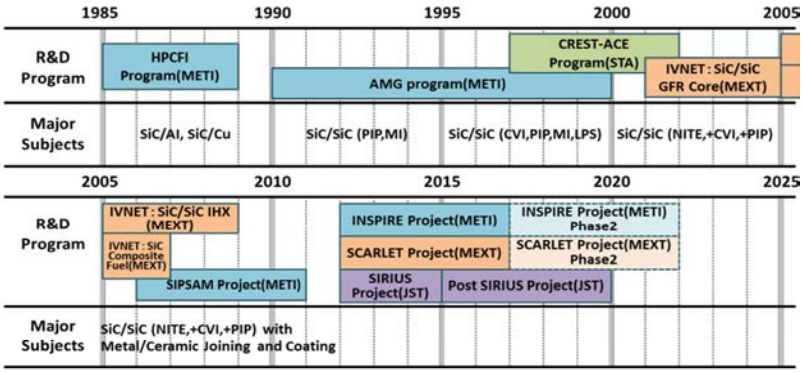

HPCFI : High Performance Composite Materials for Future Industries AMG : Advanced Materials Gas-Generator
CREST-ACE : Core Research for Evolutional Science and Technology –Advanced materials for Conversion of Energy
IVNET : Innovative Nuclear Energy Technology development SIRIUS : SiC Integration Research for Innovative Utilization of Geothermal Energy Source
INSPIRE : Innovative SiC Fuel-Pin Research SIPSAM : Support Industry Program/SiC/SiC for Al Die-Casting Machine by Hot-Chamber Method
SCARLET : SiC Fuel Cladding/Assembly Research Launching Extra-Safe Technology

The Japanese Ministry of Economy, Trade and Industry (METI) initiated a "Research and Development towards Ensuring Nuclear Safety Enhancement" programme, where "Innovative Silicon-carbide Fuel Pin Research" (Project INSPIRE) was approved as a five-year termed project [4]. Also, the Japanese Ministry of Education, Culture, Sports, Science and Technology (MEXT) programme on "Innovative Nuclear Research and Development", has been changed from 2012 to emphasise "Basic Technology Development for Nuclear Safety Innovation", and started late 2012, where "R&D of Basic Fabrication Process Technology of SiC/SiC Fuel Cladding for Extra-Safe Reactor Core" was approved as one of 12 proposals approved. This project called as "SiC Fuel Cladding/Assembly Research, Launching Extra-Safe Technology"; the SCARLET Project [4,5]. This paper is introducing the "INSPIRE" project; its current status and future plan.

Application of SiC and SiC/SiC to nuclear system was intensively done in Japanese FBR programme and followed by fundamental research for LWR engineering. Then Japanese inventions of PAN type carbon fibres and PCS type SiC fibres were becoming strong basis for C/C and SiC/SiC R&D activities for nuclear application in Japan. Those were basic research activities under JAERI (now, JAEA) and Universities/National Institutes. Figure 1 briefly summarises SiC/SiC related activities under Kohyama research group. In this figure, shift from mmC (metal matrix ceramic composite; SiC/Al, C/Al) to CMC (ceramic matrix ceramic composite; C/C, SiC/SiC) can be seen together with continuing efforts in nuclear and aero-space areas including domestic programmes for fission. In addition, nuclear engineering related international activities have been continuously conducted and many radiation effect data has been accumulated [6].

What is "INSPIRE" Project?

The "Research and Development towards Ensuring Nuclear Safety Enhancement" programme funded by Japanese Ministry of Economy, Trade and Industry (METI) has been initiated late 2012 and "Innovative Silicon-carbide Fuel Pin Research" (Project INSPIRE) was approved as a five-year termed project. Under the same programme, Toshiba Corp. has approved a joint project with IBIDEN, Tohoku University and University of Tokyo, where R&D of innovative CVI technology for fabricating fuel pin for LWRs is ongoing. Both projects aim to establish SiC/SiC fuel cladding for advanced LWRs with Nuclear Safety Enhancement.

Figure 2: The current project plan (April 1, 2013)

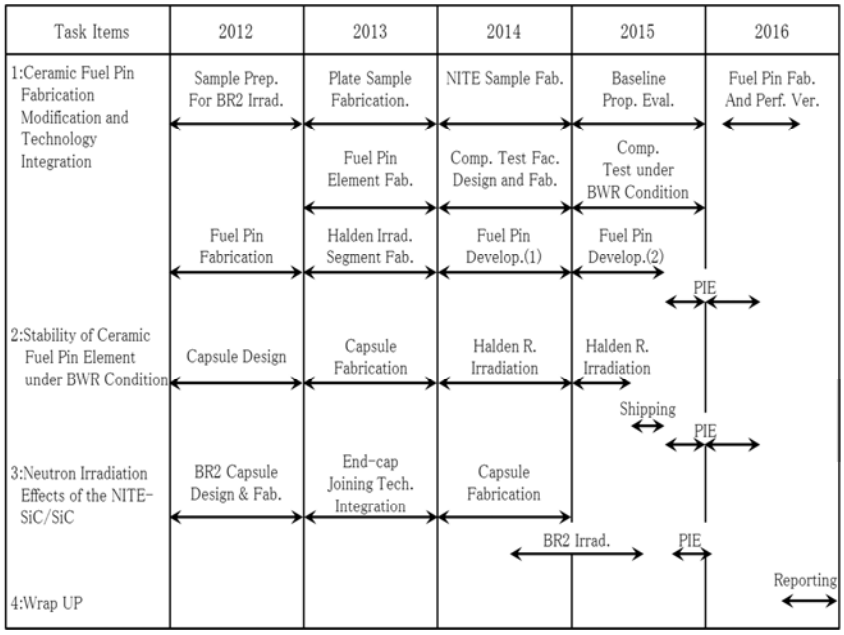

The "INSPIRE" project aims to establish technological basis and to verify the feasibility of the NITE-method based on SiC/SiC fuel pin elements and fuelled with SiC/SiC fuel pin segment to be used as the replacement of Zircaloy fuel pin/assemblies for LWR core component. The goal of the phase 1 (2012–2016), is to prepare to the next step for "Lead Test Rod R&D".

The important performances of NITE-based SiC/SiC fuel cladding to be confirmed are:

1) Compatibility with reactor water and nuclear fuel under PWR condition.
2) FP gas leak tightness.
3) Stability under Halden reactor irradiation.

Those verifications are using the NITE-based SiC/SiC fuel cladding produced by a large-scale production process at OASIS, Muroran Institute of Technology and Muroran Establishment of IEST Co., Ltd [7].

The "INSPIRE" project consists of the three following tasks:

1) Ceramic Fuel Pin Fabrication Modification and Technology Integration
   The goal of the fabrication modification is to establish large scale production process of NITE-based SiC/SiC fuel pin with a final goal of 4-m length. The verification of the performance should be done with the 1-m length fuel pins. The important technology integration includes design and fabrication of end-cap by Zircaloy 2 and welding process establishment with SiC/SiC fuel pin.

2) Stability of Ceramic Fuel Pin Element under BWR Condition
   Irradiation in the Halden reactor will confirm the baseline stability of NITE-based SiC/SiC fuel pin. These tests will be carried out in BWR condition water loop with nuclear fuel capsuled fuel pin elements. The current irradiation plan is to finish reactor irradiation by the end of 2015. Based on the results, including PIEs, the modified NITE process and related products will be provided.

3) Neutron Irradiation Effects of the NITE-SiC/SiC
   To establish engineering database for the design and fabrication of NITE- based SiC/SiC fuel pin, neutron irradiation effect database is essential. This task will provide baseline neutron irradiation effect data from BR2 irradiation and Halden

reactor irradiation. Currently, BR2 irradiation had started and the second irradiation planning is suspended.

Although the "INSPIRE" Project was approved as 5-year termed programme, the budget situation of METI only allows confirming for the Japanese fiscal year 2013 with the large budget reduction more than 30% from the original plan. The Halden reactor irradiation task is currently under approval only for JFY 2013. Also, under this condition, BR2 irradiation task should be suspended for JFY 2013. The current project plan is shown in Figure 2.

What is NITE-Process for "INSPIRE" Project?

Long efforts for improving the original NITE-process to meet large scale industrial production, technology and facility R&D of intermediate process materials, such as green sheets and pre-preg sheets, have been intensively carried out in this decade. The new concept of NITE process with dry sheets for "INSPIRE" project has modified the original aqua-slurry into polymer based SiC nano slurry which is made into flexible dry sheets like green sheets for polymer matrix composite materials. These sheets allow storage, handling to make preforms. Figure 3 shows the current fabrication line of dry sheets for "INSPIRE" project, where 40 cm width green sheets and UD/2D prepreg sheets are made continuously. The facility was installed December 2010 and a recent upgrade was done August 2012 for improving production speed and quality.

Figure 3: Green and prepreg sheets fabrication line

R&D target and current status

The "INSPIRE" project primarily looks for replacing the current Zircaloy cladding for LWRs into NITE-SiC/SiC cladding. Thus, the specification is aimed to satisfy ASTM Standard B 353-91, for LWR application. The "INSPIRE" project aims to produce 10 mm inner diameter, 1 mm wall thickness and 200 mm long claddings with sufficient gas tightness. The followings are the current targeted value for the NITE-SiC/SiC cladding.

Dimensional accuracy

Diameter: ±0.05mm, Straightness: 1/1200, Wall Thickness: ±10%, Roundness: 1/2000 (accomplished under special machining with order made tool: an example is shown in Figure 4)

Figure 4: SiC Cladding with extra-fine machining

The baseline mechanical properties

Axial tensile strength: 300MPa, Hoop Strength: 100MPa$^{(Comp)}$/300MPa$^{(Tens.)}$, Fracture at accident: no straight/crystallographic through thickness fracture (>0.2% Pseudo-plasticity).

Environmental resistance

Out-of-reactor oxidisation test, LOCA simulation test: Better than Zircaloy. Neutron Damage Resistance: 1) Soundness check up to 10 GWd/t exposure at Halden Reactor under BWR water condition. 2) Confirm mechanical property degradation less than 5% at BR2 reactor irradiation.

The current plan of Halden reactor irradiation

The "INSPIRE" project primarily looks to replace the current Zircaloy cladding for LWRs into NITE-SiC/SiC. Due to the unclear budget situation of METI toward JFY 2014, Multi-year contract with Halden Reactor Project is suspended and the single year contract is now under final negotiation.

The conceptual planning and design of the irradiation segment and rods has been finalised at the end of JFY 2012. The following is the brief summary of the conceptual planning and design activity between "INSPIRE" project and Halden Reactor Project.

Test rig to be applied

- The irradiation is to be carried out in a test rig within a pressure flask, cooled by water at BWR thermal-hydraulics and chemical conditions. Some details are shown in Figure 5.
- The rig will accommodate 6 test rods, typically 20 cm long, arranged in two clusters, as shown in Figure 5. The rods will be equipped with cladding elongation detector for measuring on-line the amount of pellet-cladding mechanical interaction (PCMI) and cladding permanent growth due to PCMI and neutron irradiation.

The test rods

- The six rods may contain different variants, such as different cladding.
- The fuel pellets will be fabricated at the IFE establishment at Kjeller, under agreed specifications. The cladding tube and the end plugs will be provided by the "INSPIRE" project, which is also to define, in consultation with Halden Reactor Project. The rod inner pressure is atmospheric pressure under current design. The fuel rod assembly, gas filling and end-plug welding will be realised by IFE following further discussions and under agreed specifications. To meet Halden reactor requirements for inserting those test rods into the reactor, preliminary discussions and test fabrication with TIG welding was done through the "INSPIRE" project.

Based on very preliminary investigation, the first conceptual design of the test rod was basically agreed. Figure 6 indicates components to be jointed. For the operation at Halden reactor site for the final insertion of nuclear fuel and shield welding of end cap by EBW facility of Halden, three types of Zircaloy elements and a SiC/SiC fuel pin element with fine threading both ends will be fabricated. The element (A) is SiC/SiC fuel pin element with fine threading, element (B) is Zircaloy tube with inner threading and elements (C1) and (C2) are Zircaloy end cap. The elements (C1) and (C2) are connected by threading to make 6 rods into 3 segments to be inserted irradiation rig, as shown in Figure 5.

Figure 5: Conceptual drawing of the test rig

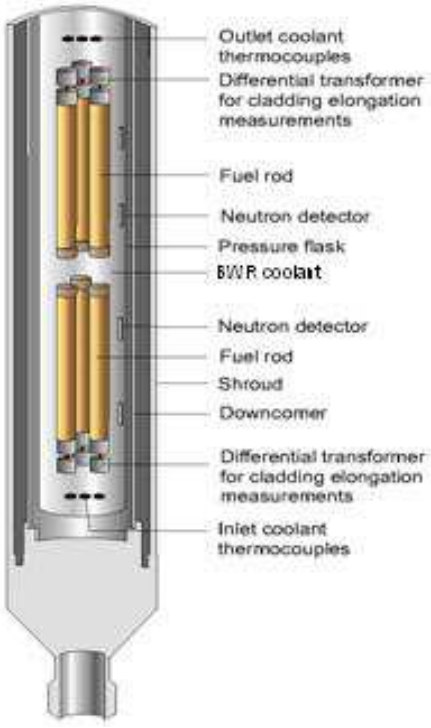

Figure 6: Concept of the test rod

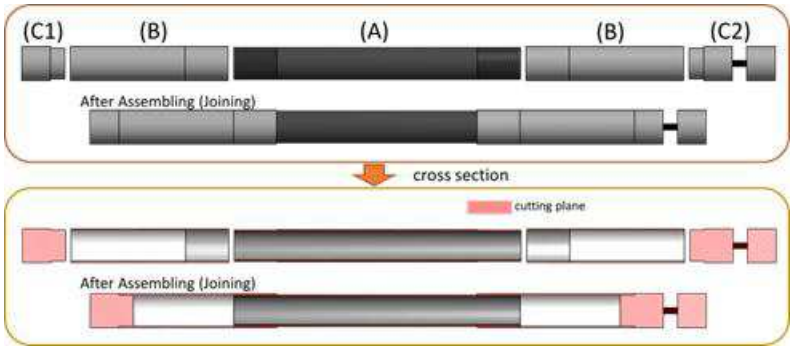

In-reactor operation

It is foreseen that the test will be run at power conditions typical for commercial fuel, i.e. 20-25 kW/m at beginning of irradiation and then gradually decreasing. The PCMI and permanent cladding strain will be assessed continuously during the irradiation.

R&D Roadmap towards Phase-2

Although METI has only approved "Phase-1" proposal, the mid-term planning requires "Phase-2" plan with reliable background and supporting R&D structure. Under the preliminary planning with the "INSPIRE" project members, "Phase-2" roadmap was initiated. As indicated in Figure 7, "Phase-1" is to give feasibility of NITE-SiC/SiC fuel cladding contributing the nuclear reactor safety enhancement within a reasonable timescale and with an economical and technological attractiveness. Phase-1 target is to clearly present the level of the technology "ready to move Lead Test Rod R&D". Neutron irradiation research activities outside this project, such as MEXT programme for reactor experiment under IMR, Tohoku University and US-Japan Programme for Fusion Reactor Materials, should support this project especially for PIE and database establishment. Large budget and industrial support should be required for large scale R&D of fuel cladding to meet power reactor utilisation. This should be satisfied for Phase-1 and Phase-2 activities. The target of Phase-2 is to prepare and complete "Lead Test Rod" experiments, which will lead to the next step, The "Lead Test Assembly". By the end of Phase-2, large-scale production industrial infra-structure should be established.

Figure 7: R&D Roadmap for "INSPIRE"

Phase-1

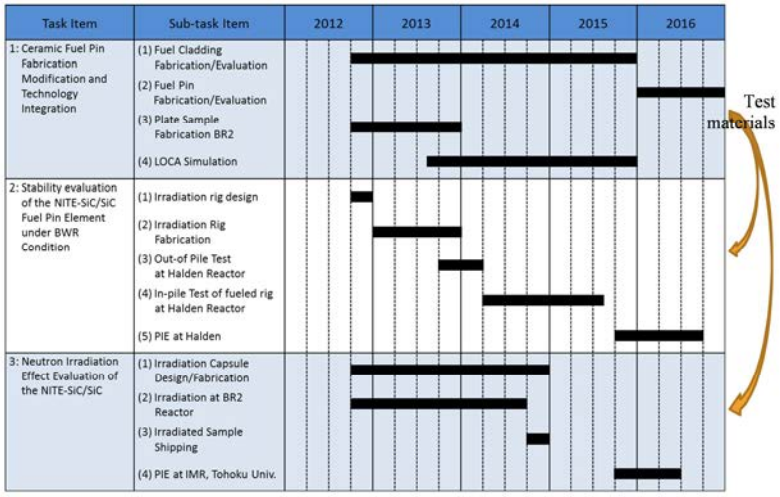

Phase-2

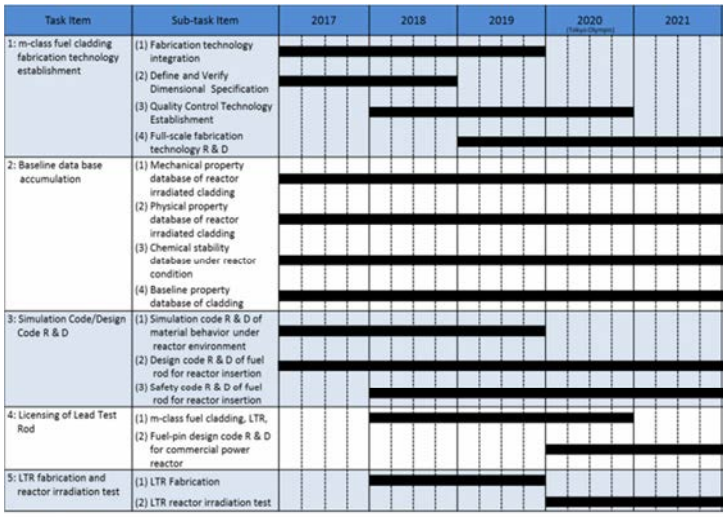

Also, the basic concept for reactor safety and efficiency will be adjusted to fully utilise the attractiveness of advanced SiC/SiC fuel cladding and fuel assembly, as well as channel box.

Conclusions

The new METI funded project, "INSPIRE", where SiC/SiC Fuel cladding R & D for ultra-safe nuclear reactors by new NITE method is introduced and the programme outline, the current status with recent accomplishments and the future plan are briefly introduced.

The goal of the "INSPIRE" project is to provide soundness of the SiC/SiC claddings by the current NITE method before and after reactor irradiation in Halden Reactor and BR2 reactor. The Halden reactor experiment will provide the first PCMI data as high as 10 GWd/t level under BWR condition.

The "INSPIRE" project is to establish the technological basis to produce SiC/SiC cladding to be replaced from the current Zircaloy cladding used in LWRs. The mid-term R&D roadmap is also presented and the importance of Phase-2 activity is emphasised.

The "INSPIRE" project may lead to an early realisation of SiC/SiC fuel pin/assembly into LWRs ensuring reactor safe technology enhancement in a realistic and economical way.

Acknowledgements

The present study is mainly supported by the Ministry of Economy, Trade and Industry (METI) on "Research and Development towards Ensuring Nuclear Safety Enhancement" programme. The authors acknowledge the member of OASIS and of "INSPIRE" project for their contribution and support for this project. The support to OASIS by Muroran Institute of Technology is also greatly appreciated.

References

[1] Wittneben, B.B.F. (2012), "The impact of the Fukushima nuclear accident on European energy policy", J. Environmental Sci. Policy, 15, pp. 1-3.

[2] White Paper on Science and Technology (2009), MEXT, Japan.

[3] Framework for Nuclear Energy Policy (2005), Atomic Energy Commission, Japan.

[4] Kohyama, A. (2013), "INSPIRE Project for R&D of SiC/SiC Fuel Cladding by NITE Method" Proceedings of the 10th Pacific Rim Conference on Ceramic and Glass Technology, American Ceramic Society, in press.

[5] Kishimoto, H. and A. Kohyama (2013), "SiC/SiC Fuel Cladding R&D Project, "SCARLET", Status and Future Plan, in this volume.

[6] Advanced SiC/SiC Ceramic Composites (2002), Editors A. Kohyama, M. Singh, H.T. Lin and Y. Katoh, Ceramics Transactions, Vol.144, American Ceramic Society.

[7] Kohyama, A., Y. Kohno, H. Kishimoto, J. S. Park, and H. C. Jung (2010), "Industrialization of Advanced SiC/SiC Composites and SiC Based Composites; Intensive activities at Muroran Institute of Technology under OASIS", Proceedings of ICC3T. Yamashita et al. (2002), "Rock-Like Oxide Fuels and Their Burning in LWRs", Journal of Nuclear Science and Technology, 39[8], pp. 865-871

Modelling the ductile brittle fracture transition in reactor pressure vessel steels using a cohesive zone model based approach

Pritam Chakraborty * and S. Bulent Biner
Modelling and Simulation Department, Idaho National Laboratory, United States

Abstract

Fracture properties of Reactor Pressure Vessel (RPV) steels show large variations with changes in temperature and irradiation levels. Brittle behaviour is observed at lower temperatures and/or higher irradiation levels whereas ductile mode of failure is predominant at higher temperatures and/or lower irradiation levels. In addition to such temperature and radiation dependent fracture behaviour, significant scatter in fracture toughness has also been observed. As a consequence of such variability in fracture behaviour, accurate estimates of fracture properties of RPV steels are of utmost importance for safe and reliable operation of reactor pressure vessels. A cohesive zone based approach is being pursued in the present study where an attempt is made to obtain a unified law capturing both stable crack growth (ductile fracture) and unstable failure (cleavage fracture). The parameters of the constitutive model are dependent on both temperature and failure probability. The effect of irradiation has not been considered in the present study. The use of such a cohesive zone based approach would allow the modelling of explicit crack growth at both stable and unstable regimes of fracture. Also it would provide the possibility to incorporate more physical lower length scale models to predict DBT. Such a multi-scale approach would significantly improve the predictive capabilities of the model, which is still largely empirical.

Introduction

There has been significant effort to model the different failure mechanisms that are active at different temperature regime in RPV steels. At lower temperatures, unstable failure by cleavage fracture is identified as the dominant failure mechanism. This is characterised by slip induced micro-crack formation at carbides and their extension into macroscopic cracks depending on the local deformation state and microstructure. Physics based models have been proposed in [1-3] to explain these mechanisms of cleavage initiation in steel. However these models do not relate cleavage initiation at a microscopic length scale to the fracture toughness. To develop such a correlation, a model has been proposed in [4], in which it is assumed that cleavage failure happens when crack tip stress (δ_f) exceeds a critical value over 1 or 2 grain diameters. However this model fails to capture the scatter in fracture toughness associated with cleavage failure. Modifications have been made to this model in [5] in which a critical volume ahead of the crack tip has been considered to explain the scatter in fracture toughness due to cleavage failure. A more rigorous statistical model has been proposed by Beremin [6] in which a Weibull distribution [7] is used to relate fracture stress to failure probability at lower and transition temperatures where cleavage fracture is the dominant mechanism. The Weibull parameters are obtained from fracture tests performed at lower temperatures and are assumed to be temperature independent. The temperature dependent variation of fracture toughness is considered by modifying the flow stress of the material. Analytical solutions and FE simulations with hardening plasticity are used to obtain crack-tip stress fields. Though this model has been fairly successful in

capturing the scatter in fracture toughness at and near the lower shelf, it requires the modelling of stable crack growth near the transition regime to provide accurate results. Stable crack growth primarily takes place through void nucleation, growth and coalescence. By incorporating ductile damage models proposed by Rousselier [8] or Gurson [9] to simulate stable crack growth prior to unstable failure, improved predictions can be made. In [10,11], DBT using Charpy specimens have been performed using Rousselier model [8] in conjunction with Beremin model [6] to predict onset of cleavage failure. Modifications have been made to the Beremin model by introducing the effect of plastic strain and history of maximum principal stress to evaluate the critical Weibull stress. Irradiation effects have also been considered in their work. DBT of German low alloy pressure vessel steel using CT-specimens have been analysed in [12] by considering a non-local Rousselier model [13] in conjunction with Beremin model [6]. The non-local model eliminates the mesh-dependency typically observed in local strain-softening models. In addition to the Beremin model, a local stress based model in conjunction with Weibull distribution has also been proposed in [14] as a cleavage initiation indicator. Though these approaches have been able to capture the fracture toughness variability at and near lower shelf, an improved model consisting of both ductile and cleavage mode of crack growth is necessary to predict the entire DBT region accurately. In addition, the model should have the provision to incorporate more physical lower length scale models as in [15].

In the present work, a cohesive zone based model has been proposed to analyse DBT in RPV steel. A unified model has been developed which incorporates both ductile damage and cleavage failure mechanisms through temperature and failure probability dependent parameters. The flow strength of the bulk material is varied to obtain the temperature dependent bulk material behaviour. It is assumed that without cleavage, the cohesive law follows a traction-separation behaviour of ductile-damage as described in [16]. From the known flow-stress evolution at different temperatures separate ductile-damage traction-separation parameters can thus be obtained from a unit cell analysis. However depending on the temperature and failure probability, unloading in the cohesive law due to cleavage can start earlier, and can reduce the fracture toughness of the material. With the use of such a cohesive law, scatter in the fracture toughness with temperature can be successfully obtained. The results from this methodology are compared with experiments and Master Curve reported in [13].

The organisation of the paper is as follows: the unified cohesive law to capture ductile damage is described first, followed by the calibration process using unit cell analysis to obtain the cohesive law parameters of ductile damage without cleavage failure. The calibration procedure to obtain the cleavage dependent cohesive parameters is described next. Two different temperatures are considered and comparisons are made with experiments. The paper is concluded in the last section.

Unified cohesive zone model

For a material undergoing ductile damage, the underlying traction separation law consists of an initial steady state void growth and coalescence, followed by rapid coalescence and complete loss of strength once a critical void volume fraction is reached. The traction-separation law proposed in [16] has been used in the present work to represent ductile damage where the traction is related to the separation by:

$$\sigma = \sigma_0 \begin{cases} 2\left(\dfrac{\delta}{\delta_e}\right) - \left(\dfrac{\delta}{\delta_e}\right)^2, \text{ when } 0 < \delta < \delta_e \\ 1, \text{ when } \delta_e < \delta < \delta_c \\ 2\left(\dfrac{\delta-\delta_c}{\delta_f-\delta_c}\right)^3 - 3\left(\dfrac{\delta-\delta_c}{\delta_f-\delta_c}\right)^2 + 1, \text{ when } \delta_c < \delta < \delta_f \end{cases} \quad (1)$$

where σ_0 is the maximum stress and δ_e, δ_c, δ_f are the separation distances when maximum stress is reached, at onset of damage (unloading) and final failure respectively. The global Load-CMOD is nearly insensitive to the shape of the traction-separation law as reported in [17]. Hence a constant maximum stress (σ_0) during steady void coalescence has been assumed, as can be seen from Equation 1. For the unified cohesive law it is assumed that:

(i) for a given flow stress (at a given temperature), the shape of the traction separation law is fixed by ductile damage;
(ii) depending on temperature and failure probability the maximum stress at unloading (σ_{max}) and failure separation distance (δ_f) varies;
(iii) the separation distance at onset of unloading (δ_c) determines the amount of ductile damage before cleavage failure.

A schematic of the proposed unified traction separation law is shown in Figure 1.

Figure 1: Schematic of unified traction separation law

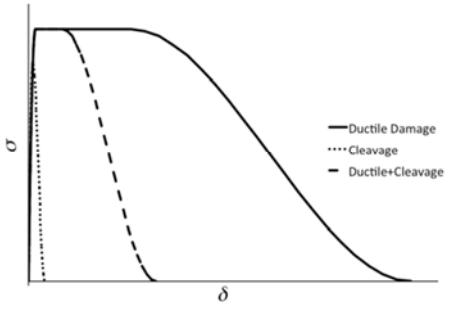

The traction separation law for cleavage failure follows a similar law as shown in Equation 1 but without the hold at σ_0 and is given by:

$$\sigma = \sigma_{\max}\begin{cases} 2\left(\frac{\delta}{\delta_c}\right)-\left(\frac{\delta}{\delta_c}\right)^2, \text{ when } 0<\delta<\delta_c \\ 2\left(\frac{\delta-\delta_c}{\delta_f-\delta_c}\right)^3-3\left(\frac{\delta-\delta_c}{\delta_f-\delta_c}\right)^2+1, \text{ when } \delta_c<\delta<\delta_f \end{cases} \quad (2)$$

where σ_{max} is the maximum stress ($\sigma_{max} < \sigma_0$) and δ_c, δ_f are the separation distances at onset of damage (unloading) and final failure respectively. In order to improve the stability of FE simulation using cohesive zone model, particularly due to cleavage failure, an artificial viscosity term has been added to the basic traction separation law following (Gao, 2004) as:

$$\tilde{\sigma}(\delta) = \sigma(\delta) + \langle sign(\delta_f - \delta)\rangle \xi \frac{d}{dt}\left(\frac{\delta}{\delta_c}\right) \quad (3)$$

where ξ is the viscosity parameter. In [18], an exponential cohesive law [19] with elastic response for bulk material has been used to describe the methodology. In the present work, the formulation has been extended to Equations 1 and 2 with Von Mises plasticity for bulk material. Since the viscosity term adds artificial dissipation to improve convergence behaviour under unstable crack growth, it can affect the global response significantly. A parametric study has been performed to estimate the sensitivity of global force-displacement to viscosity parameter. A 1T-CT specimen with an initial crack length of 26.1 mm is considered. The cohesive parameters considered are δ_c = 0.0001 mm, δ_f = 0.0005 mm and σ_{max} = 1 810 MPa. Five different viscosity parameters are used and the corresponding modified traction-separation behaviour for $d\delta/dt$ = 0.001 mm/s and t = 0.001s is shown in Figure 2(a). The corresponding force-CMOD is shown in Figure 2(b). The simulation did not converge without viscosity (ξ = 0).

As can be observed from the figures, the global load-CMOD and predicted fracture toughness have a strong dependence on the viscosity parameter. A higher value of viscosity parameter though allows larger time steps, over estimates the fracture toughness significantly. Hence a viscosity parameter ξ = 1 has been considered in the present work.

Figure 2: A study of the effect of viscosity

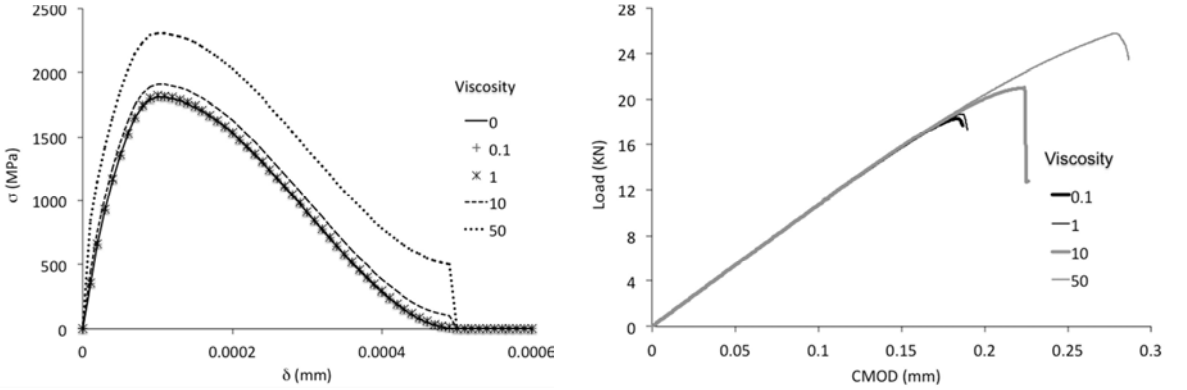

a) Traction-separation law (b) Load-CMOD (crack mouth opening displacement)

Unit cell analysis and evaluation of cohesive zone parameters

The cohesive zone parameters for ductile-damage are obtained from plane strain unit cell analysis with the material behaviour captured using rate dependent Gurson model. Enhancements proposed in [20] incorporating void nucleation and accelerated void coalescence is considered. In the rate dependent Gurson model, the plastic component of rate of deformation tensor is obtained from:

$$\underline{D}^p = \dot{\lambda}\frac{\partial \phi}{\partial \underline{\sigma}} \tag{4}$$

where the flow potential ϕ is represented by:

$$\phi = \frac{\sigma_e^2}{\sigma_m^2} + 2f^* q_1 \cosh\left(\frac{q_2\sigma_h}{2\sigma_m}\right) - 1 - q_3 f^{*2} \tag{5}$$

And the flow rate $\dot{\lambda}$ is obtained from equivalence of plastic power as:

$$\dot{\lambda} = \frac{(1-f)\sigma_m \dot{\varepsilon}_m}{\underline{\sigma} : \partial\phi / \partial\underline{\sigma}} \tag{6}$$

In Equations 4-6, σ_e is the Von Mises stress, σ_h is the hydrostatic stress, σ_m is the stress in the matrix, σ_m is the viscoplastic strain in the matrix, f* is the modified void volume fraction and q_1, q_2, q_3 are parameters. The viscoplastic strain in the matrix is evolved using a power law as:

$$\dot{\varepsilon}_m = \varepsilon_o \left(\frac{\sigma_e}{\sigma_m}\right)^{\frac{1}{m}} \tag{7}$$

where ε_0 is the reference strain rate and m is the flow exponent. The evolution of void is governed by:

$$\dot{f} = \dot{f}_g + \dot{f}_n \tag{8}$$

where void growth rate $\dot{f}_g$ is defined by:

$$\dot{f}_g = (1-f)tr(\underline{D}^p) \tag{9}$$

and a strain controlled void nucleation rate $\dot{f}_n$ is defined by:

$$\dot{f}_n = \frac{f_N}{s_N\sqrt{2\pi}}\exp\left(-\frac{1}{2}\left(\frac{\varepsilon_m-\varepsilon_N}{s_N}\right)^2\right)\dot{\varepsilon}_m \tag{10}$$

where f_N, $_N$ and ε_N are parameters. Accelerated coalescence of void after a critical void volume fraction is modeled using:

$$f^* = \begin{cases} f, \text{ for } f \le f_c \\ f_c + \dfrac{f_u - f_c}{f_f - f_c}, \text{ for } f > f_c \end{cases} \tag{11}$$

where $f_u = 1/q_1$ and f_c and f_f are critical and final void volume fractions respectively.

For the unit cell analysis, a crack tip triaxiality of 3 is assumed and the stress ratio $\beta = \sigma_{11}/\sigma_{22}$ is evaluated from:

$$\beta = \frac{\sqrt{3}H - 1}{\sqrt{3}H + 1} \tag{12}$$

where H is the triaxiality. Two spring elements with constraints are attached at one corner of the unit cell to maintain a fixed stress ratio. A very low strain rate of 0.001/s has been used to simulate quasi-static behaviour.

The room temperature (T = 20°C) data reported in [12,13] has been considered to obtain the Gurson parameters and corresponding traction-separation law for ductile damage. The material parameters are listed below.

(i) Elastic properties [12]	E = 210 GPa, ν = 0.3
(ii) Void parameters [12]:	f_0 = 0.0003, f_c = 0.05, f_f = 0.3
(iii) Void nucleation parameters [20]:	f_N = 0.04, s_N = 0.1, $_N$ = 0.3
(iv) Flow potential parameters [20]	q_1 = 1.5, q_2 = 1, $q_3 = q_1^2$
(v) Viscoplastic parameters	m = 0.005, ε_0 = 0.0001/s

A very low value of m has been considered to simulate rate independent behaviour.

From the unit-cell analysis the $\sigma\varepsilon$ response along the primary loading direction (22) is obtained. The response is fitted with Equation 1 and is shown in Figure 3.

The following parameters for the traction separation law are obtained:

(i) Maximum stress σ_0 = 1 869 MPa
(ii) Normalised separation distances δ_e/h = 0.005, δ_c/h = 0.04, δ_f/h = 0.346.

To use the non-dimensional traction separation law parameters in FE simulations, a cell height h needs to be prescribed. Following [21], h = 0.1 mm has been considered which is based on mean inter particulate distance. Plane strain simulation is performed for a 1T-CT specimen with an initial crack length a_0 = 26.1 mm and width W = 50 mm to verify the cohesive zone parameters for ductile damage. The FE mesh of the CT specimen is shown in Figure 4. A mesh dimension of 0.02 mm X 0.02 mm different from the cell height is considered at the crack tip. The Load-CMOD (crack mouth opening displacement) and J-resistances are compared with [12,13] and are shown in 5(a) and 5(b)

respectively. The J-resistance curve is obtained following ASTM E1152 [22]. As can be observed from the Figures, the correlation with experiments is quite satisfactory.

Figure 3: σ-ε evolution along primary loading direction (22) obtained from unit cell analysis using rate dependent Gurson model and corresponding traction separation law at T = 20°C

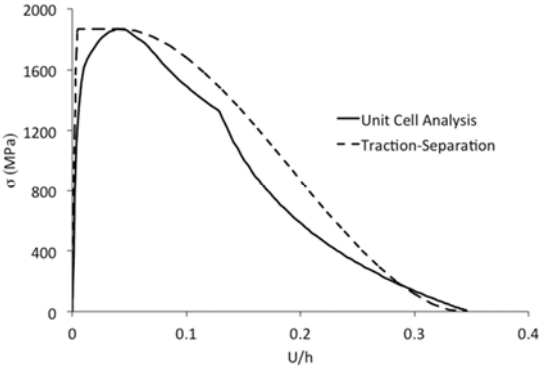

Figure 4: FE mesh of the 1T-CT specimen

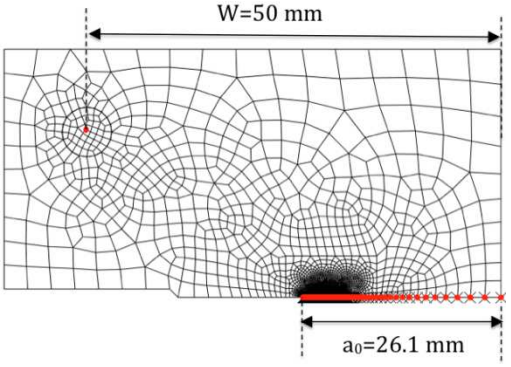

Figure 5: Comparison with experiment at T = 20°C

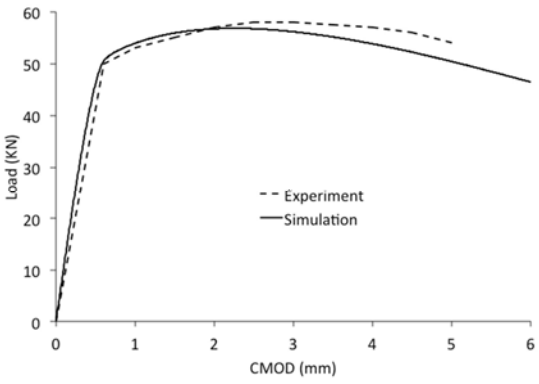

(a) Load-CMOD

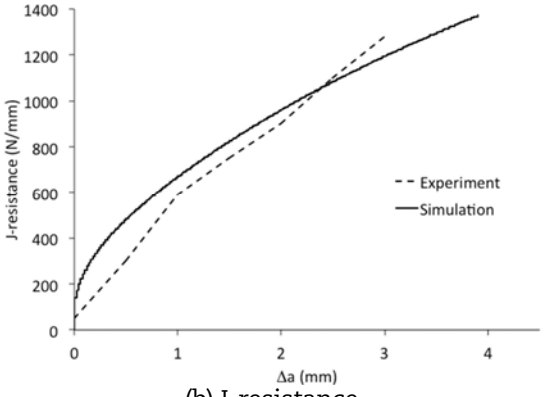

(b) J-resistance

Unified cohesive law parameters and comparison with master curve

To obtain the parameters of the unified cohesive law, the flow and fracture test results at T = -100°C [12,13] are considered for calibration. Unit cell analysis with the rate dependent Gurson model parameters described in previous section but a different flow stress behaviour is used [12,13]. The non-dimensional traction separation law is shown in Figure 6.

Figure 6: σ-ε evolution along primary loading direction [22] obtained from unit cell analysis using rate dependent Gurson model and corresponding traction separation law at T = -100°C

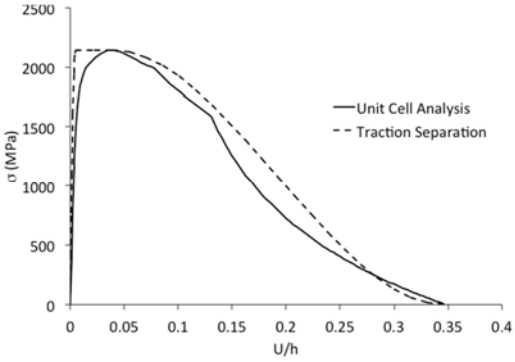

At T = -100°C, failure happens primarily due to cleavage with very little stable crack growth. Hence Equation 2 is used as the traction separation law with maximum stress σ_{max} corresponding to critical Weibull stresses reported in [12,13]. These are 1 840 MPa and 2 069 MPa corresponding to 5% and 95% failure probabilities respectively. The critical separation distance δ_c for 5% and 95% failure probabilities is obtained from the ductile damage traction-separation law using

$$\delta_c : \sigma_0 \left(2\left(\frac{\delta_c}{\delta_e}\right) - \left(\frac{\delta_c}{\delta_e}\right)^2 \right) = \sigma_{\max} \qquad (13)$$

and are 0.00015 and 0.0002 mm respectively. The separation distance at final failure δ is obtained from a sensitivity study and comparison with experimentally obtained fracture toughness [12,13]. The traction separation law and Load-CMOD for 5% and 95% failure probabilities are shown in Figures 7(a) and 7(b) respectively. Comparison of fracture toughness with Master Curve is shown in Figure 8. As can be observed from Figure 8, $\delta_f = 3\delta_c$ provides reasonable estimate of fracture toughness.

Figure 7: Unified cohesive zone model at T = -100°C

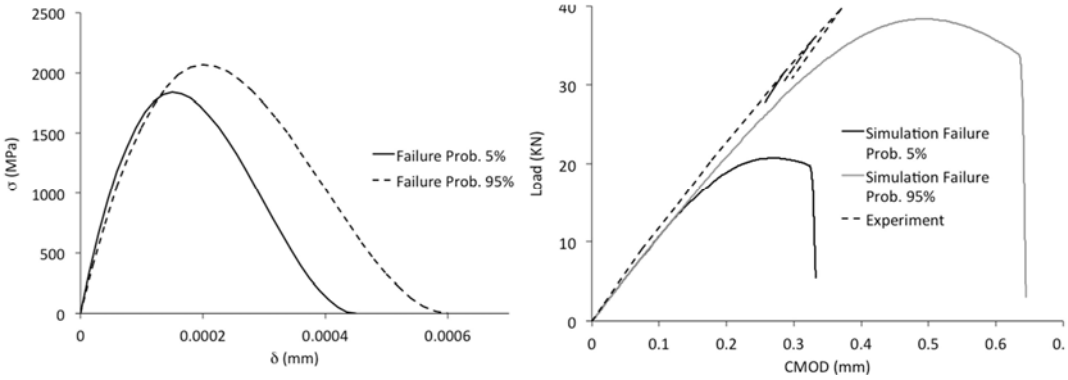

a) Traction separation law b) Load-CMOD

In [10,11] and [12,13], the Weibull parameters calibrated at -100°C are used at other temperatures to predict DBT. For the unified cohesive zone law, a similar assumption is made and the maximum stress σ_{max} is held fixed for respective failure probabilities at all other temperatures. The critical separation distance δ_c is evaluated from corresponding ductile damage traction separation law and separation distance at final failure from $\delta_f = 3\delta_c$. As a test case, T = -20°C is considered in the present work. For the 5% probability case, cohesive law parameters σ_{max} = 1840 MPa, δ_c = 0.00018 mm and $\delta_f = 3\delta_c$ is used. The

predicted fracture toughness is compared with the Master curve and is shown in Figure 8. As can be observed from the comparison, $\delta_f = 3\delta_c$ grossly underestimates the fracture toughness. This is due to higher levels of plastic deformation at higher temperatures for the same maximum failure stress and hence larger value of δ_f needs to be considered. A final separation distance $\delta_f = 0.001$ mm provides reasonably good match as can be seen from Figure 8. For failure probability of 95% at T = -20°C $\sigma_{max} = 2069$ MPa exceeds for σ_0 for ductile damage ($\sigma_0 = 2001$ MPa). Under such situation Eq. 1 is used as the traction separation law. Values of $\delta_c = 0.001$ mm and $\delta_f = 0.0016$ mm provides reasonable match with the Master Curve and is shown Figure 8.

Figure 8: Comparison of fracture toughness between unified cohesive law and master curve

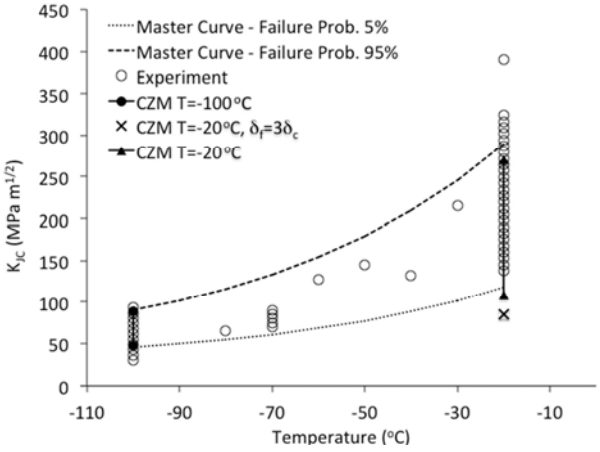

Work is in progress to obtain a correlation for δ_c and δ_f with flow parameters and cohesive zone parameters at T = -100°C.

Conclusions and future work

A unified cohesive zone model has been proposed in the present study to model DBT of RPV steel. In this method both the ductile and cleavage mode of crack growth is modeled as opposed to existing methodologies where stable crack growth through ductile damage is only modeled and initiation of unstable cleavage failure is predicted using a probabilistic model as post-processing after the simulations. The current unified approach avoids the post-processing after the simulations. In the model, it is assumed that the traction separation law follows ductile damage till the onset of unloading due to cleavage. The traction separation parameters for ductile damage for different temperatures were obtained from unit cell analysis. A viscosity term has been added to the traction separation law to improve its stability. The cohesive zone parameters for cleavage failure were calibrated from experiments at T = -100°C. The extensibility of these parameters for other temperatures have been shown by comparing the predictions with experiments at T = -20°C.

An improved correlation between the critical separation distances and temperature needs to be further developed and is in progress. Presently the cohesive law parameters are calibrated from experimentally obtained fracture toughness data, however, more physical lower length scale models can be used to derive the cohesive law parameters.

Acknowledgements

This work was supported by Life Extension of LWRs programme at INL.

References

[1] Knott, J.F. (1977), "Micromechanisms of fracture and the fracture toughness of engineering alloys", Fracture, 1, pp. 61-91.

[2] McMahon, C.J. Jr. and M. Cohen (1965), "Initiation of cleavage in polycrystalline iron", Acta Metallurgica, 13, pp. 591-604.

[3] Smith, E. (1966), "The nucleation and growth of cleavage microcracks in mild steel", in Proceedings of the Conference on the Physical Basis of Yield and Fracture, London, pp. 36-46.

[4] Ritchie, R.O., J.F. Knott, and J.R. Rice (1973), "On the relationship between critical tensile stress and fracture toughness in mild steel", Journal of the Mechanics and Pysics of Solids, 21, pp. 395-410.

[5] Curry, D.A. and J.F. Knott (1979), "Effect of microstructure on cleavage fracture toughness in mild steel", Metal Science, 13, pp. 341-345.

[6] Beremin, F.M. (1983), "A local criterion for cleavage fracture of a nuclear pressure vessel steel", Metallurgical and Materials Transactions A, 14A, pp. 2277-2287.

[7] Weibull, W. (1953), "A statistical distribution function of wide applicability", Journal of Applied Mechanics, 18, pp. 293-297.

[8] Rousselier, G. (1987), "Ductile fracture models and their potential in local approach of fracture", Nuclear Engineering and Design, 105, pp. 97-111.

[9] Gurson, A.L. (1977), "Continuum theory of ductile rupture by void nucleation and growth: Part I – Yield criteria and flow rules for porous ductile media", Transactions of the ASME, Series H, Journal of Engineering Materials and Technology, Volume 99, pp. 2-15

[10] Tanguy, B., J. Besson, R. Piques, and A. Pineau (2005), "Ductile to brittle transition of an A508 steel characterised by Charpy impact test. Part I: experimental results", Engineering Fracture Mechanics, 72, pp. 49-72.

[11] Tanguy, B., J. Besson, R. Piques, and A. Pineau (2005), "Ductile to brittle transition of an A508 steel characterised by Charpy impact test. Part II: modelling of the Charpy transition curve", Engineering Fracture Mechanics, 72, pp. 413-434.

[12] Samal, M.K., M. Seidenfuss, E. Roos, B.K. Dutta, and H.S. Kushwaha (2008), "Experimental and numerical investigation of ductile-to-brittle transition in a pressure vessel steel", Materials Science and Engineering: A, 496, pp. 25-35.

[13] Samal, M.K., M. Seidenfuss, E. Roos, B. K., Dutta, and H. S. Kushwaha (2008), "Finite element formulation of a new nonlocal damage model", Finite Elem. Ana. Des., 44, pp. 358-371.

[14] Margolin, B.Z., V. A. Shvetsova, A. G. Gulenko, and V. I. Kostylev (2006), "Application of a new cleavage fracture criterion for fracture toughness prediction for RPV steels", Fatigue & Fracture of Engineering Materials & Structures, 29, pp. 697-713.

[15] Vincent, L., M. Libert, B. Marini, and C. Rey (2010), "Towards a modelling of RPV steel brittle fracture using crystal plasticity computations on polycrystalline aggregates", Journal of Nuclear Materials, 406, pp. 91-96.

[16] Scheider, I. and W. Brocks (2003), "Simulation of cup-cone fracture using the cohesive model", Engineering Fracture Mechanics, Volume 70, pp. 1943-61.

[17] Tvergaard, V. and J.W. Hutchinson (1992), "The relation between crack growth resitance and fracture process parameters in elastic-plastic solids", Journal of the Mechanics and Physics of Solids, 40, pp. 1377-1397.

[18] Gao, Y.F. and A.F. Bower (2004), “A simple technique for avoiding convergence problems in finite element simulations of crack nucleation and growth on cohesive interfaces”, Modelling and Simulation in Materials Science and Engineering, Vol. 12, pp. 453-463.

[19] Xu, X.P. and A. Needleman (1994), “Numerical simulation of fast crack growth in brittle solids”, Journal of the Mechanics and Physics of Solids, 42, pp. 1397-1434.

[20] Tvergaard, V. and A. Needleman (1984), "Analysis of the cup-cone fracture in a round tensile bar”, Acta Metallurgica, 32(1), pp. 157-169.

[21] Anvari, M., I. Scheider, and C. Thaulow (2006), “Simulation of dynamic ductile crack growth using strain rate and triaxiality-dependent cohesive elements,” Engineering Fracture Mechanics, 73, pp. 2210-2228.

[22] Anderson, T.L. (1994), Fracture Mechanics, 2nd Ed. New York, United States: CRC Press.

SiC/SiC fuel cladding R&D Project "SCARLET": Status and future plan

Hirotatsu Kishimoto*and Akira Kohyama
OASIS, Muroran Institute of Technology, Japan

Abstract

This paper provides the recent progress in SiC/SiC development towards early utilisation for LWRs based on NITE method. After the March 11 Disaster in East-Japan, ensuring safe technology for LWR became a top priority R&D in nuclear energy policy of Japan. Along this line, replacement of Zircaloy claddings with SiC/SiC based fuel cladding is becoming one of the most attractive options and a MEXT fund based project, SCARLET, and a METI fund based project have been launched as 5-year termed projects at Muroran Institute of Technology. These projects care for NITE process for making long SiC/SiC fuel pins and connecting technology integration. The SCARLET project also includes coolant compatibility and irradiation effect evaluations as LWR and LMFBR materials. The outline and the present status of the SCARLET project will be briefly introduced in the present paper.*

Introduction

After the March 11 Disaster in East-Japan ensuring safe technology for the light water reactor (LWR) became a top priority R&D in nuclear energy policy of Japan. The Ministry of Education, Culture, Sports, Science and Technology (MEXT) in Japan is funding for the researches, and a MEXT fund based project named "SCARLET" has been launched at Muroran Institute of Technology. The replacement of Zircaloy claddings with SiC/SiC based fuel cladding is one of the most attractive options to establish the nuclear safety. The "SCARLET" project aims to prepare basic technologies for the mass production of the SiC/SiC claddings.

SiC for nuclear applications have been researched since the 1960s, and its attractive property of SiC were represented until the early 2000s. The dimensional and microstructural stabilities of SiC under the neutron irradiation were an issue for a long time. Early research indicated a trend of swelling of SiC against the irradiation temperature [1,2]. The swelling of SiC decreases with temperature between 200°C and 1 000°C. The phenomenon is caused by the accumulation of point defect damage by the fast neutron. SiC has many polytypes and its character strongly depends on the processes, the trend of swelling of SiC at high temperature has been uncertain until the 2000s. Heavy ion and high temperature neutron irradiation experiments represented dose and temperature dependences of point-defect induced swelling [3], and the void swelling behaviours [4]. These researches showed that SiC has reasonable dimensional and microstructural stabilities against the fast neutron irradiation.

Because of SiC is a ceramics, SiC fibre reinforced SiC matrix (SiC/SiC) composites are planned to be used for the structure of nuclear components. SiC/SiC composites have higher toughness than the monolithic SiC, and show quasi-elongation which is necessary as a structural material. The development of SiC fibres has also a long history [5,6]. The

early SiC fibres which had amorphous structure were used for the fabrication of SiC/SiC composites, and the composites were irradiated in fission reactors [7]. After the experiments, the SiC fibres shrunk and the flexural strength of the SiC/SiC composite was significantly reduced. The prospects of SiC/SiC composites were doubted, but it was finally revealed that the fibre shrinkage by the crystallisation of amorphous phase caused the strength reduction after neutron irradiation. The use of stoichiometric and highly crystallised SiC fibres such as Tyranno-SA and Hi-Nicalon Type-S solved this problem [8]. The SiC/SiC composites reinforced using the crystallised SiC fibres are able to keep the strength after the neutron irradiation [9].

The important natures of SiC as nuclear materials are stoichiometric and crystallised structure. The condition is also applied to the SiC matrix of composites. A chemical vapour infiltration (CVI) method is able to form an excellent stoichiometric SiC matrix [10]. Polymer impregnation and pyrolysis (PIP) and reaction sintering (RS) methods are not good to form the stoichiometric SiC matrix [11,12]. The RS method is able to form a dense matrix, but the CVI and PIP methods cannot form it. To establish SiC/SiC industries, many Japanese government funded programmes have been carried out. A nano-powder infiltration and transient eutectic phase (NITE) method is an excellent fruit of them [13]. The NITE method is an applied liquid phase sintering, and it is able to form dense and stoichiometric SiC matrix. The other important character of the NITE method is that the flexibility of size and shape of components. Its shorter process time is also important because of the lower cost of products. Based on the accumulation of research of SiC/SiC composites and the NITE method, the SCARLET project was launched in 2012. The present paper introduces the outline of the project and new technologies for SiC/SiC cladding fabrication.

What is "SCARLET" Project?

MEXT programme on "Innovative Nuclear Research and Development" approved 11 projects in 2012 among the title "Basic Technology Development for Nuclear Safety Innovation". Three of them are related to materials, and two projects were for ceramic composite developments. The "SCARLET" at Muroran Institute of Technology focuses on the research of basic fabrication process technology of SiC/SiC fuel claddings for both light water and molten sodium cooled reactors. The objective in 5 fiscal years of the "SCARLET" is to establish a solid basis of SiC/SiC cladding/assembly production. Because the objective of the project is to make-a way to the early realisation of the SiC/SiC fuel pin assembly into nuclear power reactor, "SCARLET" includes the following feasibility studies:

a) proof of the reality of SiC/SiC fuel cladding as a replacement of zircalloy fuel in a short term;
b) feasibility demonstration of SiC/SiC fuel cladding sodium cooled fast breeder reactor and gas cooled fast reactor.

Actual activities of the "SCARLET" project are:

1) to establish large scale production basis of SiC/SiC fuel cladding by NITE method;
2) to integrate technologies of making SiC/SiC fuel pins having 1 metre length and assembly of fuel pins;
3) to evaluate properties of SiC/SiC claddings including environmental tolerance evaluation under LWRs and liquid metal cooled fast breeder reactor (LMFBR).

The project is managed by OASIS at Muroran Institute of Technology. The term of the project is 5 fiscal years from 2012 to 2016. Figure 1 shows the tasks and schedule of the "SCARLET" Project. The structure consists of 4 main tasks which were provided to the TFs as follows.

Task 1: SiC/SiC fuel cladding production technology

Task 1 is performed at OASIS in Muroran Institute of Technology. The original NITE method is able to make a good composite, but there were many issues as a mass

productive technique. Because the original NITE method was a hand-made technique, the quality control and rapid/mass production of SiC/SiC products were impossible. OASIS in Muroran Institute of Technology has developed new "Intermediate SiC materials" to solve them. The intermediate SiC materials such as SiC green sheets and SiC/SiC prepreg sheets make the fabrication of composites easier than before [14]. SiC/SiC preforms are fabricated by these intermediate SiC materials, and sintered in high temperature pressurised environments. For the mass production of SiC/SiC claddings, more special techniques need to be invented. A pre-composite ribbon (PCR) is a kind of a prepreg sheet but having a long and narrow shape as same as a "ribbon". The other techniques are filament winding and hot roller press forming (HRPF) methods. The outline of recent NITE process is shown in Figure 2. These new techniques are actually developed, especialy for the making of cladding preforms. The SiC fibres and raw materials of SiC matrix are densely wired and tube-shape formed. After the fabrication and densification process, the SiC/SiC preforms are sintered by a hot isostatic pressing (HIP) method. OASIS is in charge of the development of intermediate SiC processing, applying the new technologies for the production of the SiC/SiC claddings and supply materials to other tasks.

Figure 1: Tasks and schedule of SCARLET Project

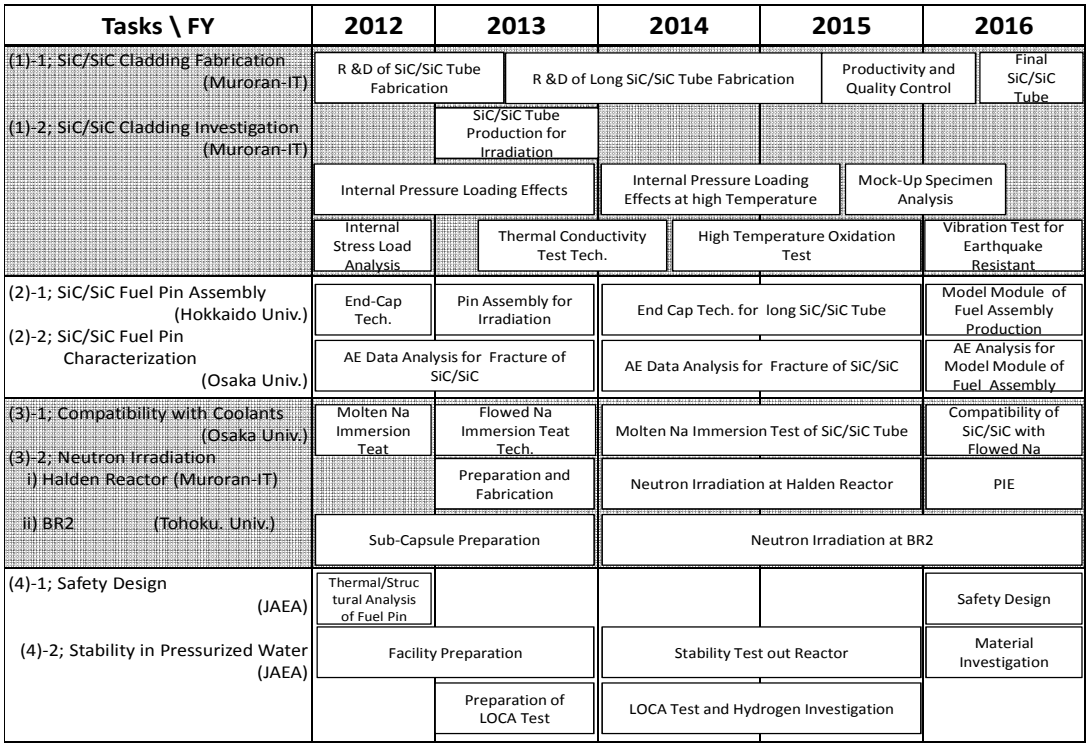

Task 2: Assembly technology

Task 2 is for assembly technique developments of SiC/SiC fuel pin. The responsible organisation of the task is Hokkaido University. The main goal of the task is to develop the end-plug joint technology. This task includes complex objectives. The highest priority subject is to establish basis of end-plug technologies for long NITE SiC/SiC claddings. Another subject is to assemble mock-up fuel pins as specimens for the neutron irradiation experiments in fission reactors. In this task, basic technology of acoustic emission investigation for NITE SiC/SiC fuel pin assemblies is also developed by Osaka University.

Figure 2: Outline of NITE process in SCARLET project

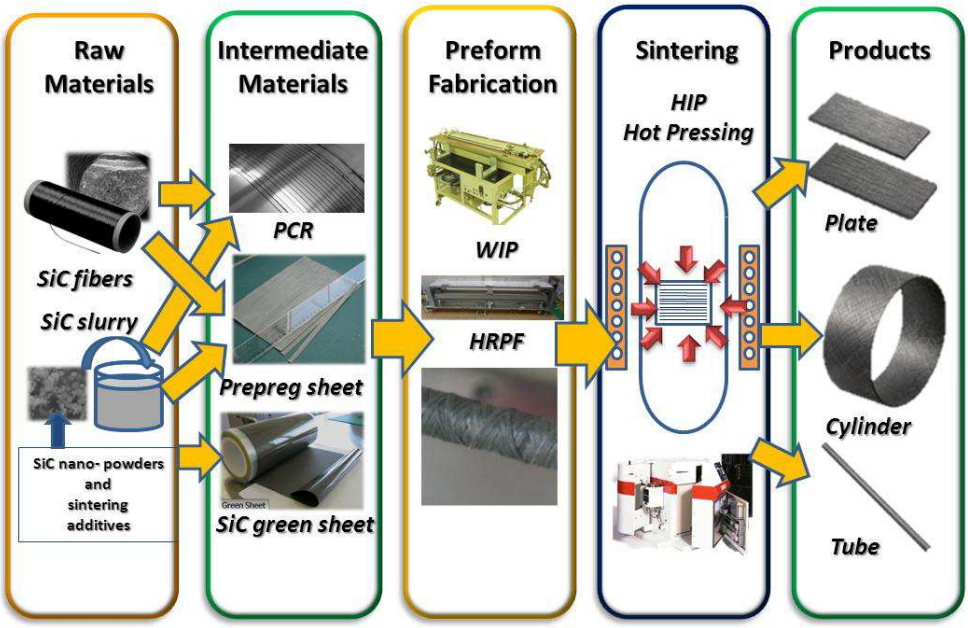

Task 3: Environmental effect evaluation

Task 3 will be performed by two universities, Tohoku University and Osaka University. Tohoku University is in charge of neutron irradiation experiments. The "SCARLET" project is planning to use two fission reactors, Halden reactor in Norway and BR2 in Belgium. In Halden reactor, NITE SiC/SiC tubes without nuclear fuels will be irradiated in a PWR condition. The detail of the experiment will be described later on. Coupon shape NITE SiC/SiC and joint specimens will be irradiated at BR2 to characterise the irradiation effects on materials. The condition will be 290°C in a helium gas environment. The fluence and dose on SiC in BR2 are estimated to be about 1×10^{24} n/m^2 and 0.1 dpa, respectively. Task 3 includes coolant and cladding compatibility investigations. The coolant in this task is mainly molten sodium, and this task inspects the capability of NITE SiC/SiC as claddings in LMFBR. The experiments are performed at Osaka University.

Task 4: Engineering and safety design

Task 4 consists of three subjects: applicability investigation of SiC/SiC as cladding for safety design, stability characterisation in pressurised high temperature water as same as the PWR conditions, LOCA simulation test. JAEA is in charge of task 4.

Project schedule

The term of the project is 5 fiscal years as shown in Figure 1. The project started in November 2012. The former two years were used for the accumulation of basic technologies and the preparation of neutron irradiation experiments. The latter three years will be dedicated to the fabrication of long SiC/SiC tube as a mock-up of cladding. The neutron irradiation experiments at Halden reactor and BR2 are provided in the latter term. The project will be finished in March 2017.

New technologies in "SCARLET" project

The "SCARLET" project develops new technologies to fabricate NITE SiC/SiC claddings. SiC green sheets and SiC/SiC prepreg sheets simplify handling, fabrication, and stabilise the quality of SiC/SiC composites. In the "SACRLET" project, the shape of the products is

limited to be long tubes. Because the green sheets and the prepreg sheets are not for tubes only, special methods and intermediate SiC materials are developed aiming to fabricate tubes with a simple and stable procedure.

Pre-composite ribbons

Normal SiC prepreg sheets need to be cut to be narrow for the winding around tubes. This is not efficient, and cut and paste procedures of SiC prepreg sheets are time consuming. Thus, a new intermediate SiC material named pre-composite ribbon (PCR) is being developed. The PCR is a wire-like intermediate material of SiC fibres and nano-powders. For the making of PCR, the SiC fibres are spread and dipped in the SiC nano-powder slurry, and hardened flat and dried. The PCR is very convenient for the mechanised winding of SiC fibres with appropriate orientation on a cladding. The PCR is able to wind the SiC fibres with SiC nano-powders at the same time resulting in forming a preform of a cladding tube efficiently. The outline of PCR production, a schematic image of automatic PCR winding and well-arranged SiC fibres on SiC/SiC preforms are shown in Figure 3.

Figure 3: PCR and filament winding in SCARLET Project

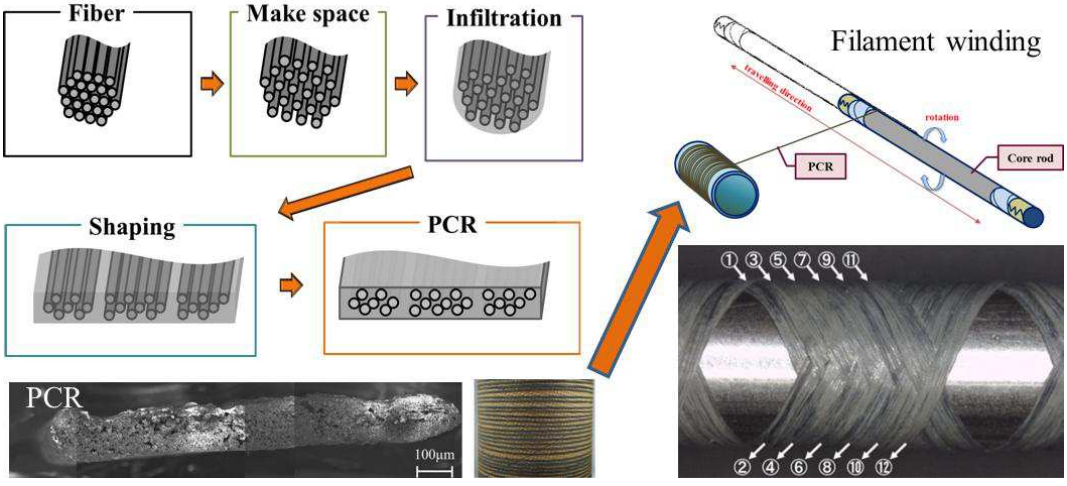

Intermediate densification process

Because NITE is an applied liquid sintering, the last step of the process is sintering at elevated temperature. The volume of a SiC/SiC preform is reduced during the sintering resulting in the disorder of SiC fibre orientation on the products. For the suppression of the fibre disorder, densification processes for SiC/SiC preforms are very important. During the PCR winding on a SiC/SiC preform, the densification process needs to apply to the SiC/SiC preform repeatedly. The densification process suppresses macro pores between fibre bundles, and pushes SiC nano-powders in the SiC bundles. The process reduces the volume change during the sintering process, and results in the suppression of SiC fibre disorder. The densification process is brought about using a warm isostatic pressing (WIP) and a newly developed technique named as hot-roller press forming (HRPF). The WIP is to press the preforms by hydraulic pressure. Because the WIP is performed in a pressure chamber, the removal of pores is progressed efficiently, but its operation is relatively complex. The HRPF is a simpler mechanical method which uses three cylindrical rollers. The cylindrical three rollers press a SiC/SiC preform, and shape the SiC fibres along the circumference. During the fabrication of SiC/SiC cladding preform, the PCR winding and the HRPF are alternately performed. The SiC/SiC preforms are densified using not only the HRPF but the WIP. The schematic image of HRPF concept, images before and after the HRPF treatment are shown in Figure 4.

Figure 4: HRPF method in SCARLET Project

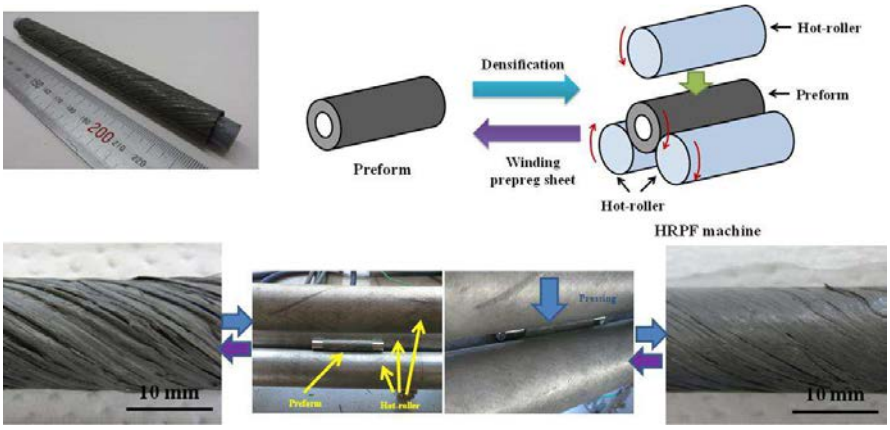

Neutron irradiation experiment plan in "SCARLET" Project

The "SCARLET" project is planning to use fission reactors, both BR2 and Halden reactor. The irradiation of coupon shape materials will be performed at BR2 to investigate irradiation effects for NITE SiC/SiC composite. Additionally, joint specimens aiming to screen the end-cap technique also need to be irradiated because of few irradiation effect data. The irradiation condition will be 290°C in helium gas environment. This environment is convenient to distinguish the irradiation effects because the material modification in reactor coolants includes both irradiation and pressurised water effects. The fluence and dose on SiC in BR2 are estimated to be about 1×10^{24} n/m^2 and 0.1 dpa. At Halden reactor, the irradiation plan is mainly for NITE SiC/SiC tube and mock-up fuel pin without nuclear fuels. Figure 5 shows a schematic image of a rig and rods for the irradiation experiment in Halden reactor. The neutron irradiation will be performed in a rig with PWR environment. 6 rods will be settled in the rig. 3 rods will be the SiC/SiC specimen rods and the other will be zircalloy cladding rods with UO_2 fuel. Each SiC/SiC specimen rod consists of 5 SiC/SiC tube segments without fuels sealed by the end-plugs. The rig will be set in the PWR loop of Halden reactor and the irradiation is planned to be performed in two Halden reactor cycles of 80-100 full power days. The irradiation environment will be at 290°C in 15.5 MPa pressurised water. The fluense and dose for SiC/SiC are roughly estimated to be $3.4\text{-}4.3\times10^{24}$ n/m^2 and 0.3-0.4 dpa, respectively.

Figure 5: Neutron irradation plan at Halden Reactor

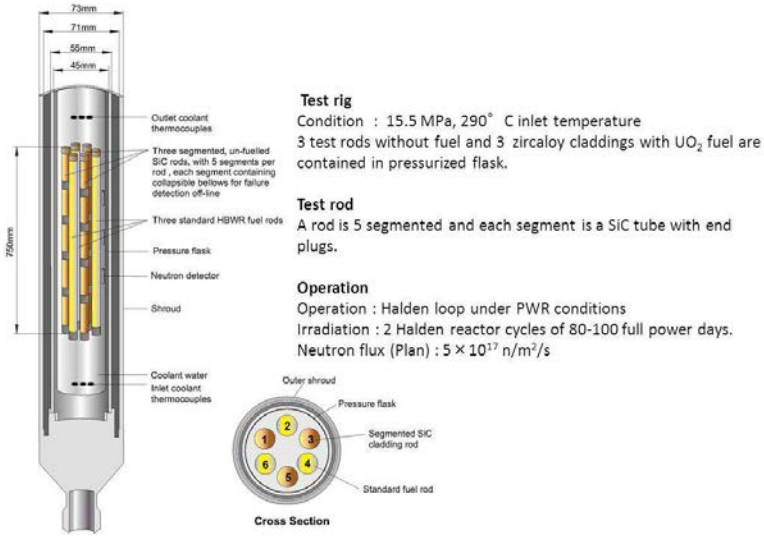

Conclusion

Aiming to replace Zircaloy fuel claddings with SiC/SiC based materials is an option, MEXT, in Japan, is funding a 5-year termed project, SCARLET, launched at Muroran Institute of Technology. This project includes 1 m length SiC/SiC cladding mock-up fabrication, developments of assembly techniques of fuel pins and characterisation including material properties, compatibility with coolants, and neutron irradiation effects in fission reactors. The "SCARLET" project is in progress and based on the new process techniques such as SiC green sheet and SiC prepreg sheet. Additional new technologies for cladding fabrication such as PCR and HRPF are invented and applied for the process. The neutron irradiation experiments are planned using Halden reactor and BR2. The "SCARLET" aims to establish a solid basis of SiC/SiC cladding/assembly production in 5-year activity.

Acknowledgements

The present study is mainly supported by the Ministry of Education, Culture, Sports, Science and Technology of Japan (MEXT) on "Innovative Nuclear Research and Development" programme. The authors acknowledge the member of OASIS and of "SCARLET" project for their contribution and support for this project.

Footnotes

*SiC fuel Cladding/Assembly Research Launching Extra-safe Technology

References

[1] Price, R.J. (1969), "Effects of fast-neutron irradiation on pyrolytic silicon carbide", Journal of Nuclear Materials, 33, pp. 329–377.

[2] Blackstone, R. (1971), "The expansion of silicon carbide by neutron irradiation at high temperature", Journal of Nuclear Materials, 39, pp. 319-322.

[3] Katoh, Y., H. Kishimoto, A. Kohyama (2002), "The influences of irradiation temperature and helium production on the dimensional stability of silicon carbide", Journal of Nuclear Materials, 307–311, pp. 1221–1226.

[4] Snead, L.L., Y. Katoh, S. Connery (2007), "Swelling of SiC at intermediate and high irradiation temperatures", Journal of Nuclear Materials, 367–370, pp. 677–684.

[5] Youngblood, G.E., R.H. Jones, A. Kohyama, L.L. Snead (1998), "Radiation response of SiC-based fibres", Journal of Nuclear Materials, 258-263, pp. 1551-1556.

[6] Yajima, S. et al. (1976), "Development of a silicon carbide fibre with high tensile strength", Nature, 261, pp. 683-685.

[7] Ishikawa, T. et al. (1998), "High-strength alkali-resistant sintered SiC fibre stable to 2200°C", Nature, 391, pp.773-775.

[8] Kishimoto, H., K. Ozawa, S. Kondo and A. Kohyama (2005), "Effects of Dual-Ion Irradiation on the Swelling of SiC/SiC Composites", Mater. Trans., 46, pp. 1923-1927.

[9] Jones, R.H. et al. (2002), "Promise and challenges of SiCf/SiC composites for fusion energy applications", Journal of Nuclear Materials, 307–311, pp. 1057–1072.

[10] Stino, D.P., A. J. Caputo, R. A. Lowden (1986), "Synthesis of Fibre-Reinforced SiC Composites by Chemical Vapor Infiltration", American Ceramic Society, Bulletin, 65, pp. 347-350.

[11] Snead, L.L., R.H. Jones, A. Kohyama and P. Fenici (1996), "Status of Silicon Carbide Composites for Fusion", Journal of Nuclear Materials, 233-237, pp. 26-36.

[12] Kotani, M., A. Kohyama, K. Okamura, K. Inoue (2000), "Fabrication of High Performance SiC/SiC Composite by Polymer Impregnation and Pyrolysis Method", Ceramic Engineering and Science Proceeding, 21, pp. 339-364.

[13] Kohyama, A., H. Kishimoto (2013), "SiC/SiC composite materials for nuclear applications", Nuclear Safety and Simulation, 4, pp. 72-79.

[14] Kohyama, A., J.-S. Park, H.-C. Jung, (2011), "Advanced SiC fibres and SiC/SiC composites toward industrialization", Journal of Nuclear Materials, 417, pp. 340–343.

3D cellular automata finite element (CAFE) modelling and experimental observation of damage in quasi-brittle nuclear materials: Indentation of a SiC-SiC_{fibre} ceramic matrix composite

Luis Saucedo Mora[a], Mahmoud Mostafavi[a,b], Danial Khoshkhou[c], Christina Reinhard[d], Robert Atwood[d], Shuang Zhao[e], Brian Connolly[c] and T. James Marrow[*a,b]

University of Oxford, [a] Department of Materials, [b] Oxford Martin School,
Parks Road, Oxford OX1 3PH, United Kingdom
[c] University of Birmingham, United Kingdom
[d] Diamond Light Source, Harwell Science and Innovation Campus, United Kingdom
[e] National University of Defence Technology, China

Abstract

Cellular automata integrated with finite elements (CAFE) have been used to develop a method to account for the effect of microstructure on quasi-brittle damage development. The microstructure is simulated explicitly by subdividing a finite element into smaller cells. A heterogeneous structure is created from key cells (seeds) using defined characteristics; the influence of the initial finite element mesh is effectively removed during the development of the microstructure. Graded microstructures, textures, particle anisotropy and multiple phases can be readily simulated, such as those in composites and porous materials. A mesh-free framework has been developed to compute the damage development through the microstructure, using cellular automata. With this method, we can study the development of discontinuous cracking and damage coalescence, and its sensitivity to microstructure. Experiments have been carried out to observe the three-dimensional development of damage, using high-resolution synchrotron X-ray computed tomography and digital volume correlation to observe Hertzian indentation of a SiC-SiC fibre composite, quantifying damage by measurement of the displacement fields within the material. The results demonstrate the applicability of the modelling strategy to damage development, and show how model input data may be obtained from small specimen tests, which could be performed at elevated temperatures with irradiated materials.

Introduction

Quasi-brittle materials have heterogeneous structures, typically with brittle constituents. This important class of structural materials includes SiC-SiC_{fibre} ceramic-matrix composites, as well as concrete, nuclear graphite, zirconia toughened alumina, and geological structures like rocks and tectonically faulted formations and also biomedical materials such as bone and bone replacements. Their damage or defect tolerance is much less than engineering metal alloys, but can be quite significant compared to fully brittle materials such as monolithic ceramics. They differ in their length-scales of both their structures and the distributions of damage, and have varying degrees of brittleness.

Quasi-brittle fracture is an emergent characteristic, and this cannot be treated satisfactorily with numerical methods based on macromechanics. Because of their complex

microstructure, the continuum approach can be too simple for these materials, and needs a finer discretisation to obtain satisfactory results. In numerical terms, this means that the computational cost of advanced methods, such as cohesive elements or embedded cracks, is often too high for engineering scale problems. However, including the role of the microstructure is critical to reproduce structural behaviour in these materials.

In this paper we apply the cellular automata finite element (CAFE) method to model Hertzian indentation in a SiC-SiC_{fibre} composite. Such composites are candidate materials for high temperature fuel cladding in several Generation IV nuclear reactor concepts. The influence of the microstructure on the development of the damage and strain fields is significant in these materials, and for this reason the microstructure needs to be introduced into the model. The ultimate goal of this research is to be able to predict the influence on fuel-cladding integrity of the microstructure and the degradation of its properties under normal and extreme conditions, in order to better select materials and optimise the fabrication of fuel components.

The paper is structured as follows: first we describe the mechanical properties and fabrication process of the SiC-SiC composite; after this, the experimental programme and the analysis of the data are explained. From those results we propose a numerical modelling method that can simulate the interaction between the microstructure and the Hertzian indentation, validating this against the experimental results.

Material

The SiC/SiC_{fibre} composite was fabricated in three steps: preparation of SiC fibre performs, deposition of fibre coating and fabrication of SiC/SiC composites. The 3-dimensional 4-directional (3D4d) fibre preforms were woven by Bolong Co. Ltd (China), with a fibre fraction volume of approximately 40 %. The KD-I SiC fibre used, made by the National University of Defence Technology, China [1] has a diameter of 12.5 μm, tensile strength of 1.6-2.0 GPa and a density of 2.4 g cm^{-3}. This is a polymer-derived multiphase fibre consisting of β-SiC crystalline, Si-C-O amorphous and free carbon phases. A pyrolytic carbon (PyC) coating was deposited onto the surface of the fibres to form the fibre/matrix interphase through a CVD (Chemical Vapor Deposition) process. The SiC/SiC_{fibre} composite was fabricated via the PIP (Polymer Infiltration and Pyrolysis) process; the polycarbosilane precursor (PCS) was infiltrated into the preform and heated up to 1100°C in an inert atmosphere, with the infiltration and pyrolysis process repeated for about 10 cycles until weight increase was less than 1%. The final heat treatment was at 1400°C for 1 hour in an inert atmosphere. Table 1 shows the measured mechanical properties of the material [1].

Table 1: Mechanical properties of the SiC/SiC_{fibre} composite [1]

Modulus (GPa)	Hardness (GPa)	Modulus (GPa)	Hardness (GPa)	Flexural Strength (MPa)	Modulus (GPa)
fibre		matrix		composite	
115	14	188	20	514	82

Experimental programme

The three-dimensional microstructure of the composite sample was characterised by X-ray computed tomography, with the development of damage from indentation studied using three-dimensional digital image correlation (digital volume correlation, DVC) [2,3] of the tomography images. The high-resolution synchrotron X-ray computed tomography was performed at the Diamond Light Source, Joint Engineering, Environmental and Processing beam line (I12 – JEEP), using radiographic projections obtained at an X-ray beam energy of 53 keV with a nominal voxel size of 0.9 μm. The exposure time was 2 seconds per radiograph with projections at increments of 0.03 degrees over 180° rotation. The specimen,

a rectangular prism (3×3 mm square, 3 mm high), was indented by a 5 mm radius ZrO_2 ball under displacement control using a loading stage that had been modified to accommodate the indenter.

A reference tomograph was recorded before indentation under a small pre-load (10 N), applied to reduce rigid body movement between successive scans, then a scan was recorded in situ under a maximum applied load of 275 N (indentation depth 43 µm, measured from radiographs); this dropped to 245 N during the tomography scan. A combined Fourier-wavelet ring artefact removal algorithm [4] was used to suppress ring artefacts in the reconstructed tomographs. These arise from instrument features such as defective or inefficient pixels in the scintillator; if not adequately supressed they can significantly increase noise in the DVC analysis as they do not displace with the material.

Vertical slices through the tomography data are shown in Figure 1, before and during indentation. The complexity of the microstructure is clear; large macro-pores, fine micro-pores and oriented bundles of fibres with elongated inter-fibre pores are observed. The damage induced by the indentation occurs over a length scale (~0.5 mm) that is comparable to the length scale of the microstructure.

Figure 1: Vertical slice through the tomographic image of the SiC-SiC$_{fibre}$ sample

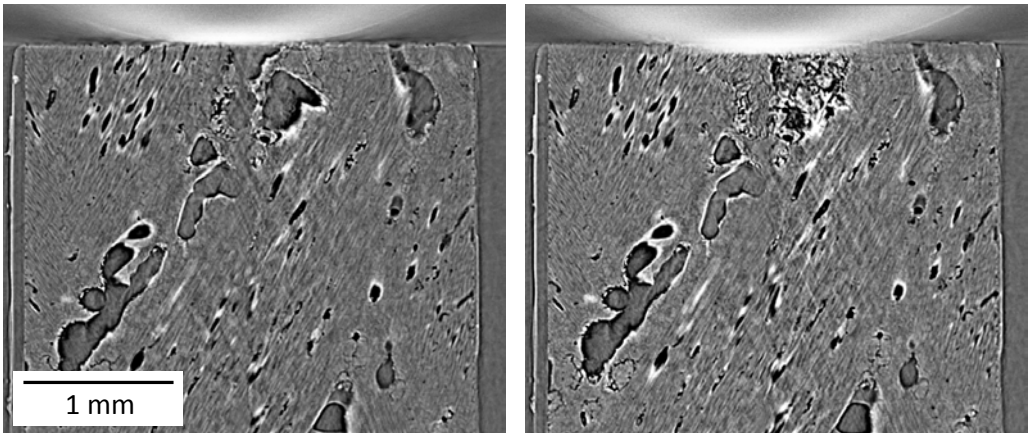

a) before indentation **b) in situ under indentation**

Analysis

The tomographic data of the scanned specimen were analysed using the Avizo Fire software to obtain a statistical description of the porosity, which would be used subsequently to create the CAFE simulation. To reduce noise, 3-D median image filtering was applied to prepare the data sets before segmentation, which was done by contrast thresholding to identify the groups of inter-fibre pores (Figure 2a); each group was assigned a unique label field material, with fifteen groups observed in the analysis volume. The 3-D material statistics collected for each fibre pore including 3-D volume, length, width, orientation and the spatial coordinates of the pore's origin. Binary thresholding was performed to define a bounding volume for each pore group, with centreline trees evaluated for each pore group to obtain the mean radius and tree length. A similar analysis was carried out for the small micro and larger macropores in the matrix.

The DVC analyses were carried out using the Davis StrainMaster 8.1 software [5], correlating the loaded 3D tomographic dataset against the unloaded reference to map the relative displacements. Each dataset, which originally measured 4 016×4 008×2 672 voxels (160 GB as 32 bit data) was cropped to 3 500×3 500×2 000 voxels and converted to 8 bit data (reduced to 24 GB) for the analysis. The vertical (z) rigid body movement (~ 50 µm) between datasets was corrected prior to image correlation by visual matching of image slices in a horizontal *xy* plane close to the indented surface; translations of 32 µm in *x*

and 49 µm in y were similarly applied. These displacements arise from the compliance of the loading jig. The following image correlation parameters were judged to be optimal; 256×256×256 voxel interrogation window, 50% overlap and 1 pass, followed by 64×64×64 interrogation window, 50% overlap and 2 passes. Reducing the final interrogation window size in image correlation increases the displacement map spatial resolution, though excessive noise arises with smaller window size [6]. Overlapping interrogation windows may improve the displacement map spatial resolution in smoothly changing fields, allowing the use of larger interrogation windows to reduce measurement noise. Increasing the number of passes may also reduce noise, with a diminishing effect with increasing passes. Finally, minor (i.e. sub-voxel) rigid body translations and rotations were corrected [7], such that the relative displacements remote from the indentation, i.e. close to the bottom surface of the sample, were zero.

Numerical modelling

To simulate the indentation we used the CAFE method (Cellular Automata integrated with Finite Element) [8] to account for the effect of microstructure on quasi-brittle properties within a finite element simulation. In the CAFE method the microstructure is modelled explicitly by subdividing a finite element into smaller elements called cells. The heterogeneous microstructure is created from key cells, called seeds, from which particle-like regions may be grown with defined characteristics. By this topological approach we obtain sets of cells with variable properties to model the microstructure (rules are enforced during the selection of the seeds to avoid overlap between particles). Graded microstructures, textures and particle anisotropy can be readily simulated in microstructures with multiple phases. The influence of the initial finite element mesh is erased during the development of the microstructure.

A mesh-free framework has been developed to compute the fracture development through the microstructure, using cellular automata to calculate the damage to the microstructure. With this method, we can study the development of discontinuous cracking and fracture, and its sensitivity to microstructure, by using two sets of elements representing the finite element model and the microstructure. The first is used to link the engineering scale problem with the microstructure, obtaining the stress and strain fields of the macromechanical problem. With those, we compute the micro-mechanical fields using the second set of elements, which describes explicitly the microstructure. The material properties of the finite elements are recomputed according to the microstructure damage; hence the redistribution of strain and stress with crack propagation and damage is computed. Factors such as the effects of size on crack path and crack stability are therefore addressed. The fracture path is completely free with respect to the finite element mesh. Consequently, very complex fracture behaviour can be modelled, such as multiple or discontinuous cracks.

Reproduction of the microstructure in the model

A key aspect of the CAFE method is its capability to reproduce the microstructure, and thereby to insert discontinuities into the continuum model. To investigate its application to damage development in a ceramic-matrix composites we need to reproduce numerically the main significant microstructure features that are observed experimentally, which are the inter-fibre pores and also the significant macro pores. The elongated inter-fibre pores were therefore distributed randomly in the simulation of the specimen within the identified bounds of the 15 groups of fibre bundles, with their dimensions, orientation and position defined randomly using parameters from their measured statistical distributions (Figure 2b). The macro and micro-pores were similarly distributed randomly in the matrix (Figure 3). A number of simulations were developed; for consistency with the experiment a simulation was selected that had a large pore close to the indentation point (Figure 4). The model therefore consisted of SiC matrix and SiC fibres within the 15 fibre bundles with mechanical properties given in Table 1, and empty pores.

Simulation of hertzian indentation damage

The CAFE simulation aims to describe the heterogeneous development of damage at the microstructure scale, whilst being consistent with the deformation at the continuum macroscale. To simulate the continuum effects of damage, the material properties of the finite elements are recomputed according to a damage criterion imposed in the FEM. This is done in an iterative loop that relaxes the stresses of the FEM in order to accommodate the displacement of the indenter while ensuring that the critical strength of the material is not exceeded. Once this is achieved, the nodal displacements of the relaxed FEM are used as an input of the mesh-free framework that deals with the microstructure. Again a relaxation is carried out in the microstructure to fit the nodal displacements of the FEM, introducing damage into cells in which a critical strain is exceeded [8]. The procedure is explained in more detail below.

The objective was to investigate whether the general characteristics of the observed damage were developed in the simulation of an indentation, so as a first approximation a simple 2-parameter damage model was used in the FEM simulations. The damage model was initially applied to the FEM as follows: first the FEM was computed without damage and the Von Mises stresses evaluated (the imposed boundary conditions are null displacements at the bottom of the sample and the measured 43 µm z-displacement of the rigid indenter ball into the top surface), second we reduced by an arbitrary factor the Young's modulus of any element in which the Von Mises stress exceeded the critical stress; we then recomputed the same problem with updated Young's moduli. This relaxation was done until all the elements had a Von Misses stress lower than the critical strength; in this analysis a critical stress of 500 MPa was chosen, which is very close to the flexural strength of the composite [1]. The factor by which the modulus of damaged elements was reduced was adjusted to obtain a reaction force close to the experimentally applied force of 275 N; for a modulus reduction factor of 30, the calculated reaction force was 274 N. Once the continuum behaviour of the sample was properly simulated, the nodal displacements of the FE mesh were used as an input of the mesh-free calculation in order to develop the damage in the microstructure. For this, the failure strain of the cells around the inter-fibre pores was chosen to be 0.005 (~ critical stress/Young's modulus); the critical strain for the stronger matrix was arbitrarily chosen to be 0.01. The relaxation from damage in the microstructure was again determined iteratively; at every step we identified cells with a strain coefficient above unity, (i.e. strain/critical strain); we treated these as damaged and recomputed the mesh-free model by reducing the Young's modulus in the same way as previously. This was repeated until all cells had a strain lower than their critical strain. The obtained simulation was one in which all the cells and elements were consistent with the physical model of the material and the global model provided the same response (i.e. the same reaction force) to the same boundary condition (i.e. displacement of the indenter) as its experimental counterpart. The CAFE simulation contained 800 pores (1 105 950 cells and 4 800 nodes, i.e. 6 nodes per pore); its computational cost was 7.5 hours running as a serial code as a single thread, compared to 550 seconds for the continuum FEM simulation (343 nodes and 1 080 tetrahedral elements), both running on a Intel Core i7-3930K, 3.20 GHz machine. Further studies are being carried out to compare the computational cost of the CAFE method with an FEM of equivalent discretisation; the CAFE method is amenable to parallel computing.

The observed compressive strain field in a vertical section under the indentation is shown in Figure 5, compared with the CAFE simulation result for the same section. The experimental data show a region of large displacements under the indentation, with some areas of poor correlation, which are due to the effects of damage; significant changes in the image will prevent DVC from converging (the areas of high deformation around the sample edge are image correlation errors due to the interface). The CAFE simulation predicts a similar sized zone of high strain, with some local strain concentrations due to the macropores. The slight asymmetry in the experimental data

may be due to either to anisotropy of the microstructure or a component of shear loading from misalignment of the loading rig, and will be investigated in future simulations.

Figure 2: Inter-fibre pore distributions within fibre groups: a) experimentally observed structure after segmentation; b) numerical simulation

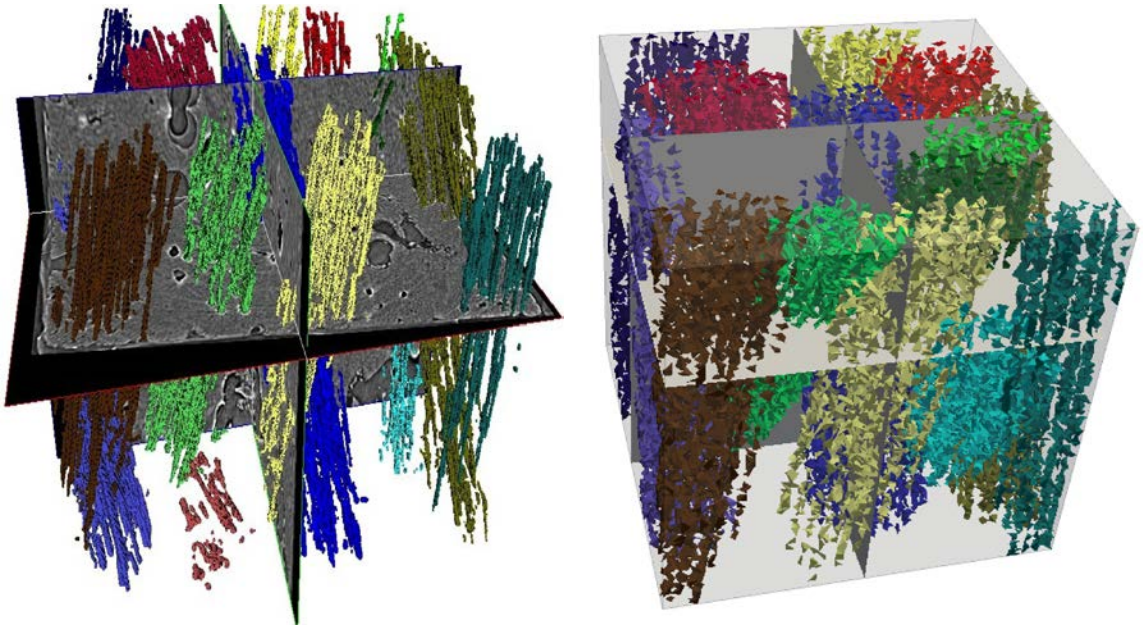

a) **b)**

Figure 3: Macro and micropore distributions in the matrix: a) experimentally observed structure after segmentation; b) numerical simulation

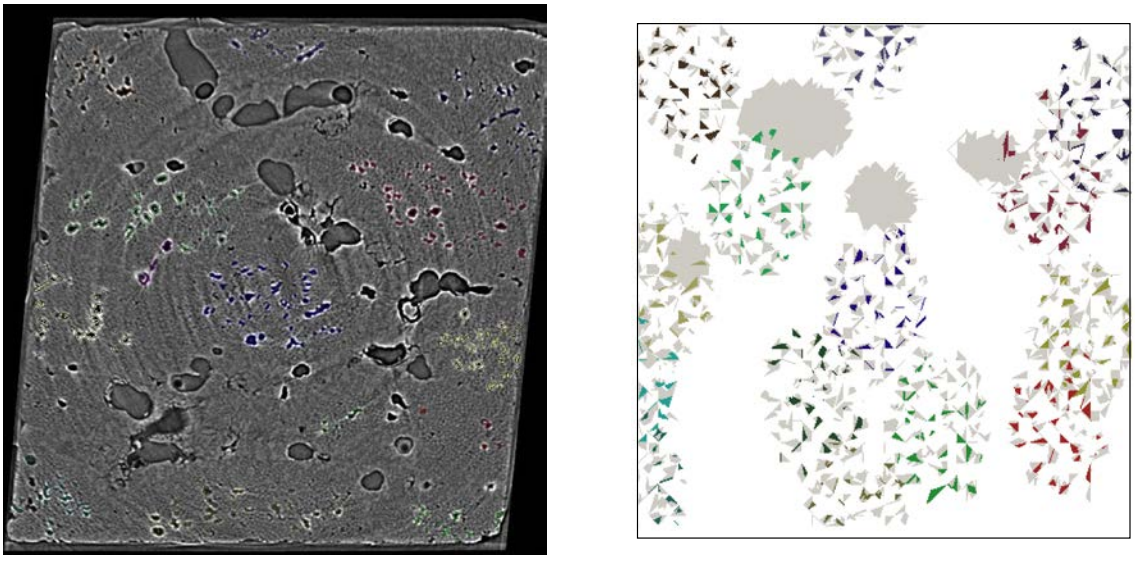

a) **b)**

Figure 4: Overall view of the structure in the numerical simulation: fibres (white), macro-pores (red) and micro-pores (orange) a) cross-section, b) surface view

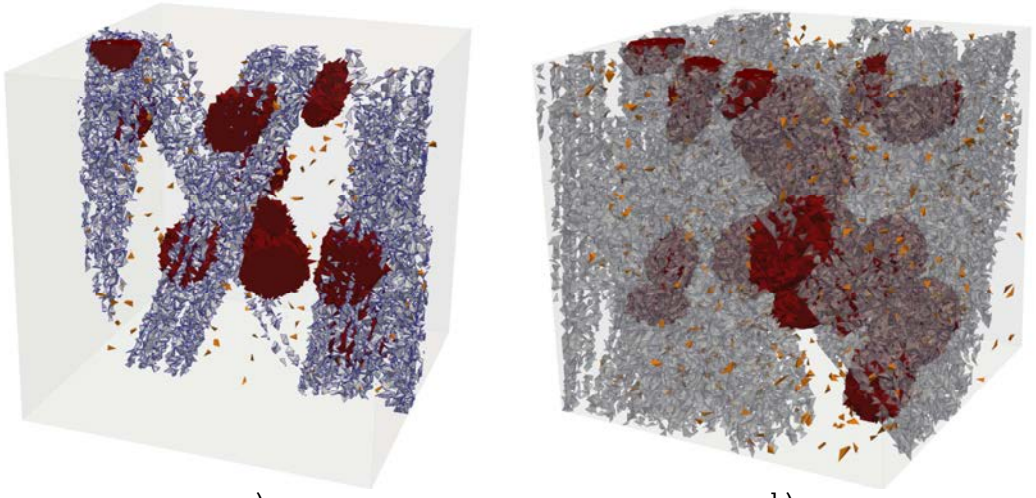

Figure 5: Comparison between experiment and CAFE simulation in a vertical section (3 mm × 2 mm) under the indentation: a) Experimental data with displacement vectors overlaid (white areas have poor correlation), CAFE simulation of displacements showing b) macro-pores and c) inter-fibre pores and macro-pores.

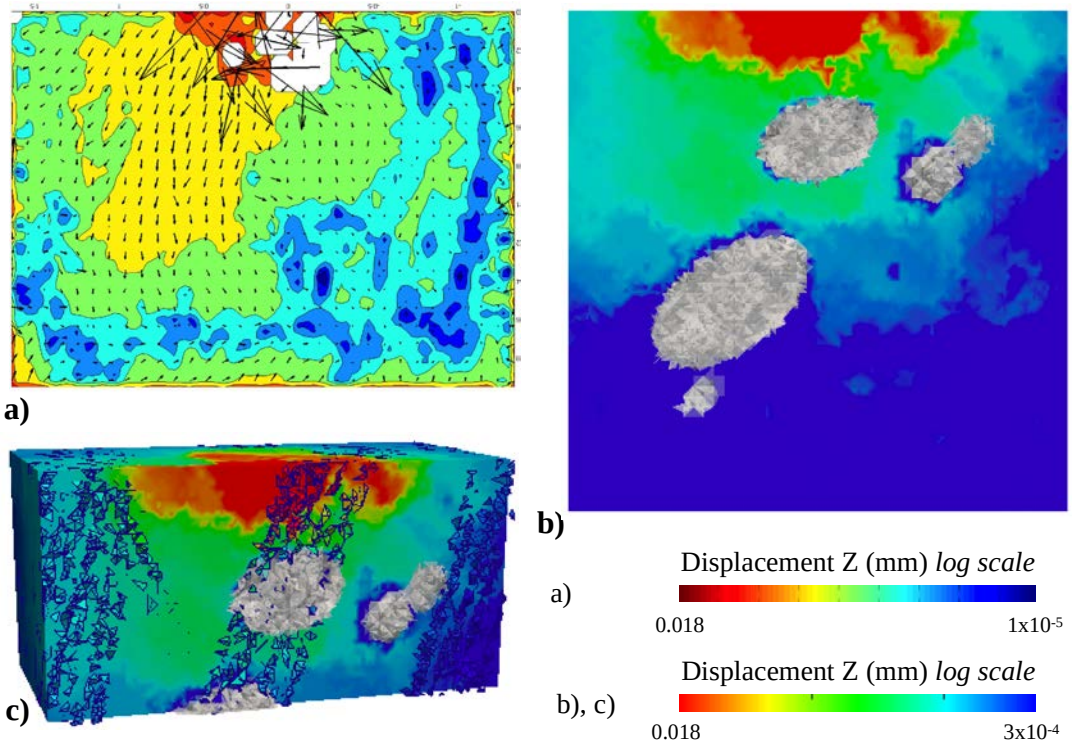

Further comparison is made using the compressive displacements and strains along the *z*-axis under the indentation (i.e. at *x*=1.5 mm and *y*=1.5 mm), which are shown in Figures 6 and 7 together with quarter slices of the CAFE numerical simulation in which the macro-pores are shown and the FEM that describes the continuum. As the CAFE

simulation cells are not necessarily located exactly on the z-axis, the displacement data for all the cells within 1/30 of the side length (i.e. 100 µm) from the z-axis are shown. For the strain data in Figure 7c, due to the variations in the CAFE displacements, only representative strain values from cells on the z-axis are plotted. The agreement between the experiment, CAFE simulation and FEM-damage simulation is generally good, particularly remote from the indentation where the deformation is elastic. The data for a simple elastic FEM simulation for a reaction force of 275 N are also shown; agreement is good only in the elastic region. The variability in the CAFE displacements is due to the local effects of pores on the development of damage; there is a significant influence from the large pore that is beneath the indentation, which is generally consistent with the observed effect of a similar sized pore in the experimental data. The continuum FEM-damage simulation does not capture this behaviour.

The sensitivity of the CAFE simulation to the microstructure components is shown in Figure 8, which shows the effects of including either the inter-fibre pores or macro-pores, compared with a full simulation of both and the continuum FEM simulation with damage (all simulations contain micro-pores in the matrix). In the CAFE simulations, the dark gray colour denotes damaged cells in which the critical strain was reached. Comparing the simulations with and without macro-pores (Figures 9a and 9b), it can be seen that there is increased deformation and damage where a macro-pore is close to a bundle of inter-fibre pores. This is due to the stress concentrating effect of the macro-pores, which is also seen in the absence of fibres (Figure 8c), where larger displacements are observed in the vicinity of the macro-pores. The global pattern of deformation is similar in the CAFE and FEM simulations, but the inclusion of microstructure provides a higher fidelity description of the localisation of damage. This is a necessary ingredient of a model that can capture the effects of microstructure in damage propagation and failure of the composite material.

Figure 6: Comparison between the numerical and experimental vertical compressive displacement: a) FEM simulation with damage, b) CAFE simulation, c) displacements along z-axis

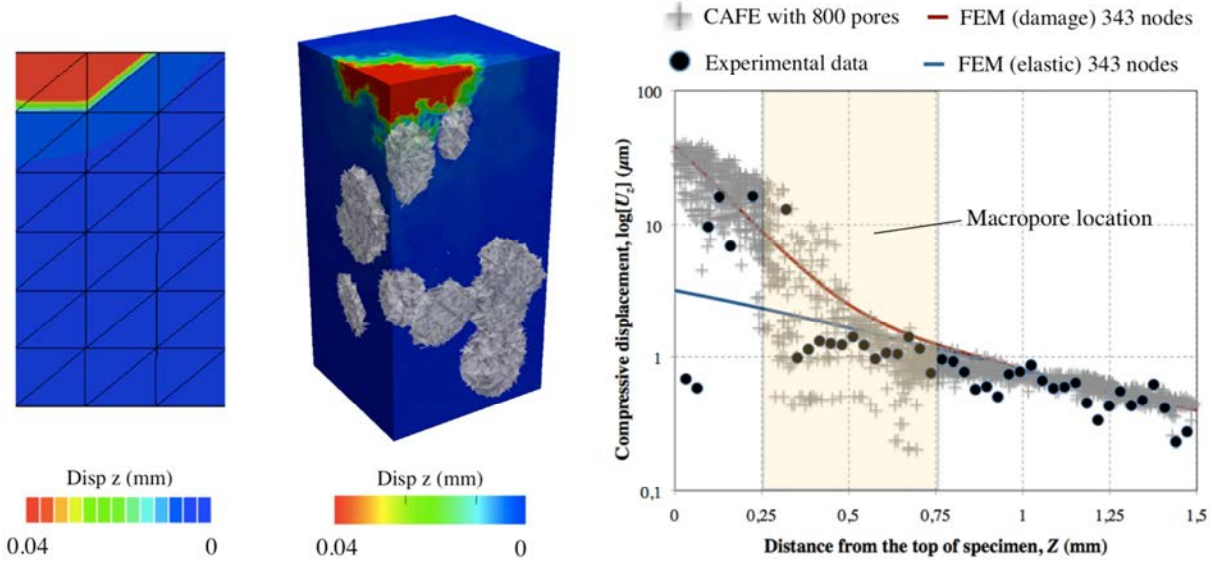

a) b) c)

Figure 7: Comparison between the numerical and experimental vertical compressive strain: a) FEM simulation with damage, b) CAFE simulation, c) strains along z-axis

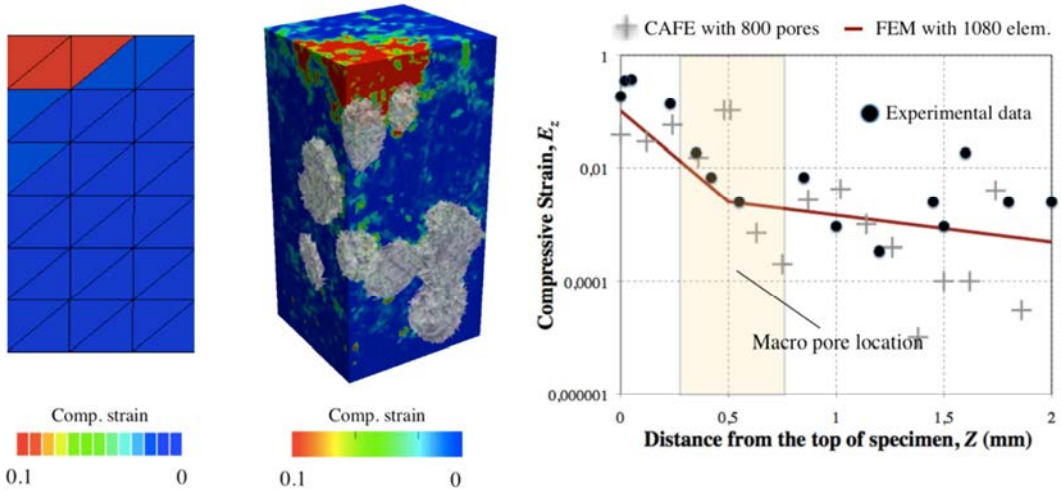

a) b) c)

Figure 8: Influence of the pores and fibres on the compressive displacement field; CAFE simulation

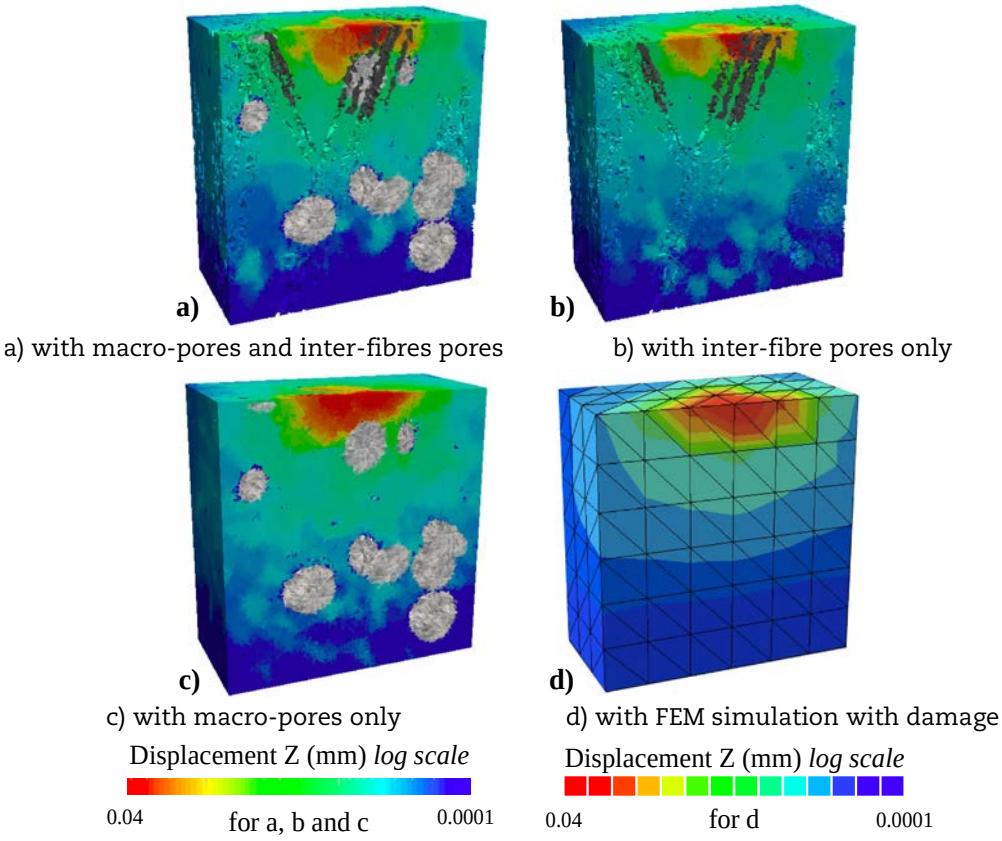

a) with macro-pores and inter-fibres pores

b) with inter-fibre pores only

c) with macro-pores only

d) with FEM simulation with damage

Conclusions

Hertzian indentation in a SiC-SiC_{fibre} composite has been observed using high-resolution computed synchrotron X-ray tomography, with the three-dimensional full field displacements measured by digital volume correlation. Segmentation of the tomographic

data provided the inputs to a "cellular automata with finite element" (CAFE) simulation of damage development; comparison of the model outputs with the measured deformation show the simulation captures the significant features of the distribution of damage.

The CAFE methodology introduces microstructure into a continuum FE model, and successfully reproduces the general features observed in the experimental data. The results demonstrate the applicability of the modelling strategy to damage development; parallelisation of the CAFE computations will increase the efficiency compared to FEM simulations of similar fidelity and discretisation. The aim of this work is to obtain model input data from small specimen tests, such as indentation that can be performed at elevated temperatures with irradiated materials, in order to predict the sensitivity to microstructure of damage development in nuclear materials operating in extreme conditions.

Acknowledgements

This work was carried out with the support of the UK EPSRC project "QUBE: Quasi-Brittle fracture: a 3D experimentally-validated approach" (EP/J019992/1). The authors acknowledge the beam time award at the Joint Engineering, Environmental and Processing (I12) beamline (Experiment EE7730) and the help of Dr. D.M. Collins, Dr. H. Çetinel and Mr. S. Barhli to conduct the experiment. MM and TJM gratefully acknowledge the support of Oxford Martin School and MM acknowledges the support of Linacre College, Oxford through a Junior Research Fellowship. The Manchester X-Ray Imaging Facility (Dr. S.A. McDonald and Professor P.M. Mummery) are thanked for the loan of the loading rig.

References

[1] Zhao, S., X. Zhou, J. Yu, P. Mummery (2013), "Effect of heat treatment on microstructure and mechanical properties of PIP-SiC/SiC composites", Journal of Material Sciences and Engineering, 559, pp. 808-811.

[2] Bay, B.K., T.S. Smith, D.P. Fyhrie and M. Saad, (1999), "Digital volume correlation: Three-dimensional strain mapping using X-ray tomography", Experimental Mechanics, 39, pp. 217-226.

[3] Mostafavi, M., N. Baimpas, E. Tarleton, R.C. Atwood, S.A. McDonald, A.M. Korsunsky, T.J. Marrow, (2013), "Three-dimensional crack observation, quantification and simulation in a quasi-brittle material", Acta Materialia, 61, pp. 6276-6289.

[4] Münch, B., P. Trtik, F. Marone, M. Stampanoni, (2009), "Stripe and ring artifact removal with combined wavelet-Fourier filtering", Optics Express, Volume 17, Issue 10, pp. 8567-8591.

[5] DaVis, User's manual, (2012), Gottingen: LaVision GmbH.

[6] Sutton, M.A., W.J. Wolters, W.H. Peters, W.F. Ranson and S.R. McNeill, (1983), "Determination of displacements using improved digital correlation method", Image and Vision Computing, Volume 1, Issue 3, pp. 133–139.

[7] Mostafavi, M., Y. Vertyagina, C. Reinhard, R. Bradley, X. Jiang, M. Galano and J. Marrow (2013), "3D studies of indentation by combined X-ray tomography and digital volume correlation", Seventh International Conference on Materials Structure & Micromechanics of Fracture (MSMF-7, Brno, Czech Republic).

[8] Saucedo, L. and T.J. Marrow, (2013), "3D cellular automata finite element method to model quasi-brittle fracture", Twelfth Intentional Conference on Engineering Structural Integrity Assessment Conference proceedings, ESIA 2013, Manchester, EMAS publishing.

Noninvasive ultrasonic measurements of temperature distribution and heat fluxes in nuclear systems

Yunlu Jia and Mikhail Skliar
Department of Chemical Engineering, University of Utah, Salt Lake City, United States

Abstract

Measurements of temperature and heat fluxes through structural materials are important in many nuclear systems. One such example is dry storage casks (DSC) that are built to store highly radioactive materials, such as spent nuclear reactor fuel. The temperature inside casks must be maintained within allowable limits of the fuel assemblies and the DSC components because many degradation mechanisms are thermally controlled. In order to obtain direct, real-time measurements of temperature distribution without insertion of sensing elements into harsh environment of storage casks, we are developing noninvasive ultrasound (US) methods for measuring spatial distribution of temperature inside solid materials, such as concrete overpacks, steel casings, thimbles, and rods. The measured temperature distribution can then be used to obtain heat fluxes that provide calorimetric characterisation of the fuel decay, fuel distribution inside the cask, its integrity, and accounting of nuclear materials. The physical basis of the proposed approach is the temperature dependence of the speed of sound in solids. By measuring the time it takes an ultrasound signal to travel a known distance between a transducer and a receiver, the indication about the temperature distribution along the path of the ultrasound propagation may be obtained. However, when temperature along the path of US propagation is non-uniform, the overall time of flight of an ultrasound signal depends on the temperature distribution in a complex and unknown way. To overcome this difficulty, the central idea of our method is to create an US propagation path inside material of interest which incorporates partial ultrasound reflectors (back scatterers) at known locations and use the train of created multiple echoes to estimate the temperature distribution. In this paper, we discuss experimental validation of this approach, the achievable accuracy and spatial resolution of the measured temperature profile, and stress the application of this new method to temperature and heat flux measurements in DSC and other nuclear systems.

Introduction

Process temperature is the primary characteristic that must be monitored in energy conversion processes, such as gasification, nuclear fission and degradation of nuclear waste. In a traditional approach, the measurement of the temperature profile across process containment requires the use of multiple temperature sensors inserted into the structure. The measured temperatures can then be used in process monitoring, assessment of containment integrity and, in nuclear applications, the assessment of radioactive decay and the accountability of nuclear materials. The service and replacement of insertion sensors are difficult and costly in nuclear applications. At the same time, these sensors are often subjected to harsh environment of elevated temperatures, high pressures, continuous radiation, and various physical and chemical stresses, heterogeneities and concentration gradients, all of which tend to shorten their useful service life.

In order to obtain direct, real-time measurements of temperature distribution without insertion of sensing elements into harsh environment of storage casks and other nuclear systems, we are developing noninvasive ultrasound (US) methods for measuring spatial distribution of temperature inside solid materials, such as concrete overpacks, steel casings, thimbles, and rods. This largely non-invasive approach can be used to measure temperature profile in solids and apply the result to estimate the corresponding heat fluxes.

Approach

The physical basis of the proposed approach is the temperature dependence of the speed of sound (SOS) in solids [1-3]. By measuring the time it takes an ultrasound signal to travel a known distance between a transducer and a receiver (the time of flight, TOF), which can be the same device in the pulse-echo mode of operation, the indication about the temperature distribution along the path of the ultrasound propagation may be obtained. In its simplest implementation, consider a sample of a solid material of known thickness L maintained at a uniform temperature. Assuming a pulse-echo method, the measurement of the TOF (return delay) of an ultrasound pulse, created by an ultrasound transducer coupled to one side of the sample and reflected from its distal end, may be used to calculate the speed of sound as:

$$SOS = \frac{2L}{TOF}. \qquad (1)$$

The reflection from the distal end occurs due to a change in ultrasound impedances caused by changes in density and the speed of sound at the boundary of the sample. The dependence of the speed of sound on the temperature, $SOS=f(T)$, obtained experimentally or theoretically, would then allow us to estimate the temperature of the sample. However, when temperature of the sample is non-uniform, the overall time of flight depends on the temperature in a complex and unknown way:

$$TOF = \int_{r_h}^{r_c} f(T(t,r))dr \qquad (2)$$

and does not provide sufficient information to estimate the temperature distribution across the sample, $T(r)$. By adding constraints on the feasible solution, an estimation of a unique temperature distribution based on measurements in the integral form (2) may be possible. Examples of such constraints may include the requirement that $T(r_c) = T_c$ where T_c is an independently measured surface temperature in the proximity of the ultrasound transducer and $T(r)$ is monotonically increasing, as would be the case for a dry containment of spent nuclear fuel of thickness $L= r_c - r_h$ (with $r_h \le r \le r_c$ where r_h and r_c are the coordinates of the hot and cold surfaces of the containment) heated from the inside by radioactive decay, and where T must satisfy the heat conduction model:

$$\rho C \frac{\partial T}{\partial t} = k \frac{1}{r} \frac{\partial}{\partial r}\left(r \frac{\partial}{\partial r}\right) T \qquad (3)$$

where ρ, C, and k are refractory density, heat capacity, and thermal conductivity, respectively.

The central idea of the proposed method to directly measure temperature in solids using ultrasound pulse-echo testing is to create an US propagation path inside the material of interest which incorporates partial ultrasound reflectors (back scatterers) at known spatial locations. A measurement of the temperature distribution begins with US pulse, generated by an ultrasound transducer. This pulse will be partially reflected from each scatterer in the US propagation path through the solid material and return to the receiver as a train of partial echoes. The TOF of the first echo gives an indication on the average temperature in the 1st zone between the transducer and the first internal scatterer. The next return echo will originate from the second scatterer. By subtracting the TOF of the second and the first echoes, the average speed of sound and the corresponding average temperature between scatterers 1 and 2 can be estimated, and so on until the estimate of the temperature distribution throughout the solid material is obtained. With that distribution known, the temperature of the last (distal) segment can be used to determine $T(r_h) = T_h$, the temperature on the inside of the containment.

In the described approach, the sensitive electronic components are kept away from harsh environments and it is only required that the ultrasound propagation path is engineered to provide multiple internal partial reflectors and the US transducer is acoustically coupled to the outside surface of the containment, representing minor modifications to the containment or other nuclear subsystem. The overall system for measuring temperature distribution: (a) the engineered ultrasound propagation path either embedded as an insert or incorporated into the containment to provide partial ultrasound reflections from predetermined locations; (b) an ultrasound transducer and receiver, which can be implemented as single or distinct components; (c) the analog and digital ultrasound instrumentation used to generate the excitation pulse and then acquire and amplify the return echoes, and (d) the signal processing system that determines the time of flight for each echo and then uses this information to calculate the speed of sound in the corresponding segment of the containment. The temperature in each segment is then obtained using SOS vs. temperature correlation found experimentally or from theory.

In the specific implementation of the described approach, we used the envelope cross-correlation [4] between the echo waveforms obtained at different temperatures to determine the difference in the time of flight, ∆TOF, as a function of temperature. This method uses both the phase and the amplitude of the waveforms to find ∆TOF which makes it suitable for use with dissipative material, including concrete overpacks. The typical results obtained with a cementitious sample are illustrated in Figure 1.

Figure 1: The ΔTOF between echo waveforms at different temperatures is calculated by cross-correlation with a reference waveform acquired at 20°C

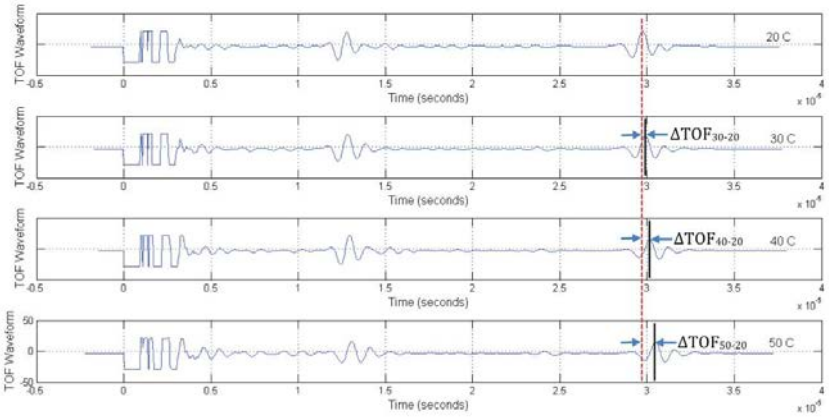

Given the measurements of the time of flight, the speed of sound in each segment between two consecutive backscatterers inside the sample, SOS_i, is calculated at each temperature using the following equation:

$$SOS_i = \frac{2L_i}{(TOF_{refi} - TOF_{refi-1}) + (\Delta TOF_i - \Delta TOF_{i-1})} \quad (4)$$

where L_i are the thickness of each consecutive layer of the sample; TOF_{refi} are the times of fight of reference echoes originating from the three internal interfaces and the distal end of the sample; ΔTOF_i are the differences between time of flights at reference and test temperatures. The overall length of the sample was measured using a micrometer, and the speed of sound at the reference temperature was calculated using equation (1). With known speed of sound at the reference conditions, the thicknesses of each layer Li were calculated at reference conditions using the measurement of TOF_{refi}.

Experimental validation

The experimental validation was carried out with a cementitious sample. A 2" I.D. PVC tubing was using as a mold and the water-cement mixture was poured into a vertically oriented mold. Partial internal ultrasound reflections from known spatial locations inside

the sample are needed to enable direct US measurements of the temperature distribution. It was found that by casting multiple layers of the same composition and allowing for a partial curing before casting the next layer, enough variation in acoustic impedance is introduced to create partial US reflections at the interface.

A 4" cementitious sample which we used during the experiment was created by sequentially casting four layers (each 1" thick) of a stand Type I/II Portland cement mixture into the PVC form and allowing 30 minutes curing time before casting the next layers. Such implementation of the containment with an embedded partial internal ultrasound reflector is particularly appealing since each layer has essentially identical thermal, chemical and mechanical properties. After removing the solidified sample from the form, it was allowed to cure at room temperature until its ultrasound properties have stabilised.

The ultrasound tests of cementitious samples were carried out using panametrics pulser/receiver (model 5072PR) and panametrics transducer (model V302) with a central frequency of 1 MHz, coupled to a sample using ultrasound gel. The data were acquired using Tektronix oscilloscope (model MSO 2024) interfaced to a computer. The data processing of acquired US waveforms was performed using custom Matlab code.

To establish SOS vs. temperature correlation, the sample was placed inside the fabricated heating fixture depicted in Figure 2, which consisted of a thermally insulated steel container and an internal heating blanket (silicon rubber blanket by BriskHeat®) that tightly surrounded the sample. The temperature of the heating blanket was measured by a thermocouple and controlled by a PID controller. The surface temperature of the sample was measured by four thermocouples attached with high-temperature adhesive tape in the middle of each layer of the sample surface. Two additional thermocouples were used to measure the temperature of the top and bottom surfaces of the sample.

Figure 2: The experimental setup

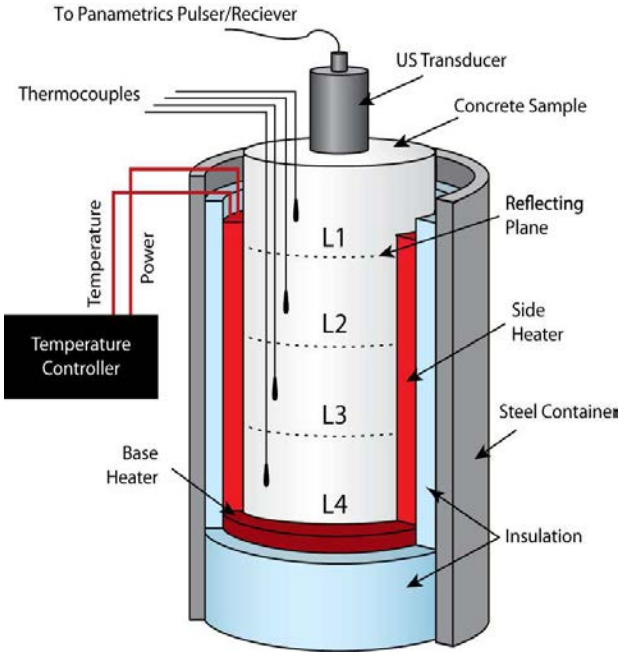

The ultrasound transducer was coupled to the surface of the top layer of the sample. To prevent the damage to the transducer, the top surface of layer 1 extended above the fixture to allow for partial cooling of the sample; in this arrangement, layer 1 is effectively used as a delay. The test temperatures were from 20 to 100°C spanned in 10°C increments. After each temperature change, sufficient time was allowed for thermal equilibration to occur before attempting the time of flight measurements. The sequence of temperatures for which the

SOS measurements were conducted was randomised. The randomisation included all repeat experiments for each temperature. Such randomisation avoids measurement bias from one experiment to the next. In order to calculate the 95% confidence interval, tests at each temperature were repeated at least 6 times in random order.

To test the proposed method for measuring non-uniform temperature distribution, the sample was placed inside the fixture shown in Figure 2 and heated using the base heater only. After the temperature measurements provided by surface thermocouples stabilised at constant values, an ultrasound excitation pulse was applied to the sample and the four return echoes were acquired. Using the envelop cross-correlation method, the TOF of each echo was determined, and the result was used to estimate the apparent speed of sound in each layer needed to produce the observed time of flight for each echo. Based on the calibration data, thus obtained SOS of each layer provided the corresponding temperature of each layer.

Results and discussion

The speed of sound vs. temperature results for all four layers of the sample, obtained using the described procedure, are shown in Figure 3. The obtained SOS on the vertical axis is plotted as a function of the temperature measured by a thermocouple located at the bottom of the model refractory sample. The data for all four layers were used to obtain a linear fit of the speed of sound as a function of temperature. The obtained correlation is plotted with the 95% confidence interval, shown as the shaded area. The comparison of the thermocouple measurements of the surface temperature in the middle of each layer and the apparent temperature of each layer obtained with the proposed method is shown in Figure 4. Both methods show a similar trend in temperature distribution and an excellent agreement in the estimated axial thermal fluxes, which are proportional to $\frac{\partial T}{\partial r}$.

Figure 3: The calibration curves for the SOS as a function of temperature for all four layers of the sample were obtained using envelop cross-correlation data analysis methods. The shown linear fit *SOS=SOS(T)* is based on data for all four layers. The shaded area shows the 95% confidence interval for the obtained linear fit.

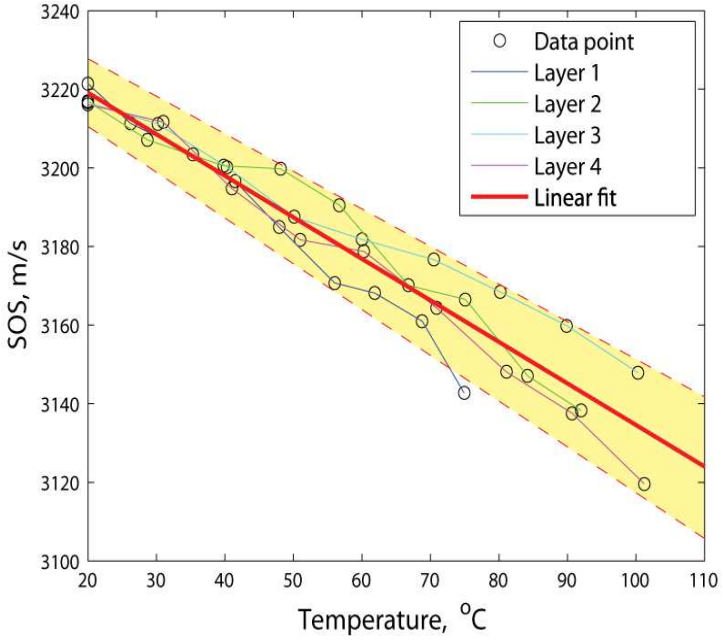

Two factors likely contributed to the observed difference in the measured temperature. First, it is reasonable to expect that the surface temperatures of the sample are indeed lower than the internal temperature measured noninvasively by the ultrasound, explaining some of the observed differences. Second, the thermocouples provide essentially point-wise measurements of temperature, while the ultrasound measurements depend on temperature distribution along the entire sample. The results shown in Figure 4 assume a step-wise constant temperature distribution for each layer. A much more accurate estimate of the temperature distribution will be obtained if a more realistic "sub-grid" parameterization is used. For example, we expect that by requiring that the temperature distribution satisfies the realistic heat transport model (e.g. the conduction model of equation (3) supplemented with the boundary temperature condition at the traducer location) the accuracy of the ultrasound measurements of the temperature distribution and the estimation of the hot boundary temperature will improve.

With the known temperature distribution along the path of the ultrasound propagation, the corresponding heat flux through the solid material can be calculates as $q = -k\frac{\partial T}{\partial r}$.

Figure 4: Comparison of thermocouple and ultrasound measurements of temperature distribution in the sample heated from the bottom

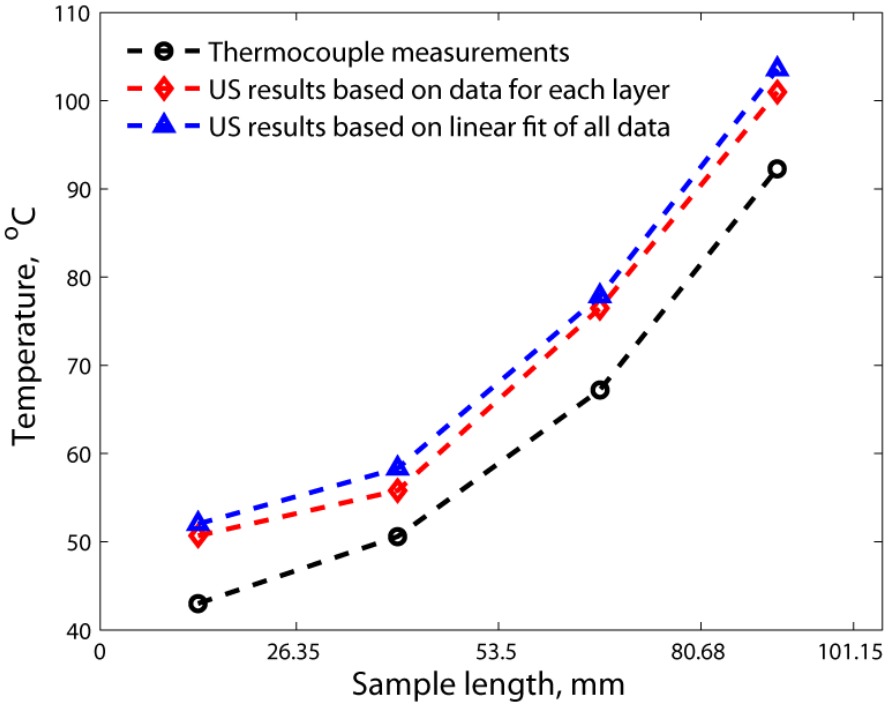

Conclusions

This paper describes novel method for measuring temperature distribution in solid materials and its experimental validation. This method is capable of providing an accurate, in-situ, and real-time measurements of the temperature distributions and heat fluxes in solid components of nuclear and other systems characterised by harsh environments.

Acknowledgements

The authors acknowledge support the U.S. Department of Energy's National Energy Technology Laboratory, under award number DEFG2611FE0006947.

References

[1] Jia, Y., M. Puga, A. Butterfield, D. Christensen, K. Whitty, and M. Skliar (2013), "Ultrasound Measurements of Temperature Profile Across Gasifier Refractories: Method and Initial Validation", Energy and Fuels, 27, pp. 4270–4277.

[2] Mi, X., S. Zhang, J. Zhang and Y. Yang 2003 "Automatic ultrasonic thermometry", Presented at 15th Symposium on Thermophysical Properties, 22-28 June 2003, Colorado, United States.

[3] Kychakoff, G., A. Hollingshead, S. Boyd (2005), "Use of acoustic temperature measurements in the cement manufacturing pyroprocess", Cement Industry Technical Conference, 15-20 May 2005, Kansas City, Missouri, United States, Conference Record, pp. 23-33.

[4] Le, L.H., "An investigation of pulse-timing techniques for broadband ultrasonic velocity determination in cancellous bone: A simulation study," Physics in Medicine and Biology 43:2295-308, 1998.

Atomistic studies of cation transport in tetragonal ZrO_2 during zirconium corrosion

Xian-Ming Bai,* Yongfeng Zhang and Michael R. Tonks
Idaho National Laboratory, United States

*Corresponding author. Email: Xianming.Bai@inl.gov

Abstract

Zirconium alloys are the major fuel cladding materials in current reactors. The water-side corrosion is a significant degradation mechanism of these alloys. During corrosion, the transport of oxidizing species in zirconium dioxide (ZrO_2) determines the corrosion kinetics. Previously, it has been argued that the outward diffusion of cations is important for forming protective oxides. In this work, the migration of Zr defects in tetragonal ZrO_2 is studied with temperature accelerated dynamics and molecular dynamics simulations. The results show that Zr interstitials have anisotropic diffusion and migrate preferentially along the [001] or c direction in tetragonal ZrO_2. The compressive stresses can increase the Zr interstitial migration barrier significantly. The migration of Zr interstitials at a grain boundary is much slower than in a bulk oxide. The implications of these atomistic simulation results in the Zr corrosion are discussed.

1. Introduction

Zirconium (Zr) based alloys are the primary fuel cladding materials used in light-water reactors. Because they directly contact water coolant during the service, the water-side corrosion is the major degradation mechanism of these alloys. Many factors can affect the corrosion process of Zr alloys, such as alloy elements, radiation, alloy microstructures, coolant temperature, and stress [1]. From a microscopic point of view, corrosion involves mass transport through cation and anion defects mediated diffusion. Therefore, understanding how these factors affect the mass transport is important for understanding the macroscopically observed corrosion behaviour.

When a Zr alloy contacts water, a thin layer of zirconium dioxide (ZrO_2) forms on the Zr metal surface [1-3]. Experimental studies have shown that the water-side oxide mainly has a monoclinic phase [3,4] because this phase is thermodynamically stable at the coolant temperature (~ 600 K). At the transition region between the oxide and metal, the oxide has a stress-stabilised tetragonal phase [3,4]. This tetragonal oxide is often believed to serve as a passive layer for corrosion [3]. The further corrosion of the metal or growth of the ZrO_2 takes place via two steps. In the first step, a reaction takes place so that the oxide splits the water into hydrogen and oxygen ions [1-3]. It is believed that this reaction process is fast so that it is not the rate-limiting step [3]. In the second step, the transport of the oxidising species through the oxide layer takes place so that the oxide grows [1-3]. The mass transport can be realised via either inward anion (oxygen ion) or outward cation (zirconium ion) diffusion in ZrO_2. In addition, electron transport from the metal/oxide interface to the water/oxide interface is required for the reaction to continue. The transport of all these oxidizing species is through the ZrO_2 layer formed on the alloy surface. In many previous studies, it was argued that either the oxygen diffusion or

electron transport is the rate-limiting step[2,3,5]. However, the role of the cation diffusion in the oxide receives little attention. Hultquist et al. [6] have conducted experimental studies to investigate the role of cation and anion transport on the corrosion behaviour of a few metals and alloys. They concluded that when the anion transport is dominant, the resulting oxide has many cracks; when the cation transport is prevailing, the formed oxide has many cavities in the metal/oxide interface; if the anion and cation diffusion is balanced, the oxide has a low density of cracks and cavities so that the oxide is "self-repairing" and therefore more protective. This work demonstrates that the cation diffusion may be important for governing the corrosion kinetics.

When a Zr metal becomes an oxide, the molar volume increases by about 56% (i.e. the Pilling-Bedworth ratio is 1.56) [1]. Therefore, near the oxide/metal interface, the oxide is subjected to a strong compressive stress. In our previous study [7], we have shown that a compressive stress increases the anion (oxygen) defect migration barrier significantly while a tensile stress reduces the barrier moderately. It is unclear whether the stress influences the cation migration in a similar way. Some microstructural features such as grain boundaries are typically believed to be the fast mass transport paths. However, in oxides the grain boundary diffusion may be complicated by spatial charge effects. In this study, we use atomistic modeling to investigate how these factors affect the cation transport in tetragonal ZrO_2, an important oxide phase related to Zr corrosion.

2. Methodology

The atomistic modeling methods used in this study are temperature accelerated dynamics (TAD) [8] and molecular dynamics (MD). A rigid-ion interaction potential developed by Schelling et al. [9] is used to describe the interaction between ions in both methods. This potential consists of a Buckingham term and a Coulomb term. It predicts that ZrO_2 has a stable tetragonal phase at low temperatures and a cubic phase at high temperatures. The tetragonal-to-cubic transition temperature is about 1 850 K, lower than the experimental value of 2 573 K [10]. In all the simulations presented here, the temperature is below 1 850 K so that the oxide is in the tetragonal phase. As evaluated in our previous study [7], this potential predicts that the lattice parameters of the tetragonal phase (represented by a pseudo-fluorite unit cell) are a=b = 5.081 Å and c = 5.126 Å at 0 K, in good agreement with experimental values [10].

TAD is used to study the migration paths and barriers of cation defects in different scenarios. TAD employs basin-constrained MD simulations at a high temperature to search for many relevent defect migration paths and uses the nudged elastic band method [11] to calculate the migration barrier of each path. Then TAD applies transition state theory to accept the transition that is most likely to occur at a low temperature of interest. Since TAD does not have any *a priori* assumptions of the defect migration paths, some non-intuitive defect migration mechanisms such as cluster diffusion [12,13] and anisotropic diffusion [14] can be found. In this work, the high temperature is set to 1 800 K and the low temperature is set to 1 000 K. The cutoff distance of the potential is set to 8 Å and the time step is 1 fs.

MD is used to calculate the mean square displacements (MSD) of Zr ions in a defect-containing system. The MSD is related to defect diffusivities through the Einstein relation:

$$\left\langle \left| \vec{r}_i(t) - \vec{r}_i(0) \right|^2 \right\rangle = 6Dt \text{ , } (1)$$

where $\vec{r}_i(0)$ and $\vec{r}_i(t)$ are the initial and final positions of the ith ion at time t, the bracket represents the average over all Zr ions, and D is diffusivity. Therefore, the slope of a MSD vs t plot is proportional to the diffusivity. In this work the simulation time is in the range between 10 and 20 ns, and the temperature is in the range between 1 400 K to 1 700 K. MD is conducted with the LAMMPS simulation package [15]. The time step is 2 fs and the cutoff distance is 11 Å. All the MD simulations are conducted in a NPT ensemble (constant number of atoms, pressure, and temperature).

3. Results

3.1 Anisotropic Zr defect migration mechanisms

In this section the migration mechanisms of Zr point defects (interstitials and vacancies) in tetragonal ZrO_2 are investigated. The space group of tetragonal ZrO_2 is $P4_2/nmc$ [10]. For convenience, the crystal structure is illustrated with a pseudo-fluorite unit cell ($a=b<c$), as shown in Figure 1(a). The oxygen ions have some small displacements from the perfect fluorite structure along certain directions, about 0.035c predicted by this potential, as indicated by the small arrows on the oxygen ions in Figure 1(a). As shown in our previous work [7], such structural distortions induce a strong anisotropy in the oxygen defect migration barriers. Similar effects also occur for Zr defects as shown below.

Figure 1. Migration mechanisms of Zr defects in tetragonal ZrO_2. The tetragonal structure is presented with a pseudo-fluorite structure. (a – b) Migration paths of a Zr interstitial and the energy landscapes along these paths. (c – d) Migration paths of a Zr vacancy and the corresponding energy landscapes. Blue spheres – Zr ions; Green spheres – O ions that have a downward displacement; Dark red spheres – O ions that have an upward displacement; Red spheres – Zr interstitial sites; Small arrows – oxygen displacement directions in tetragonal ZrO_2.

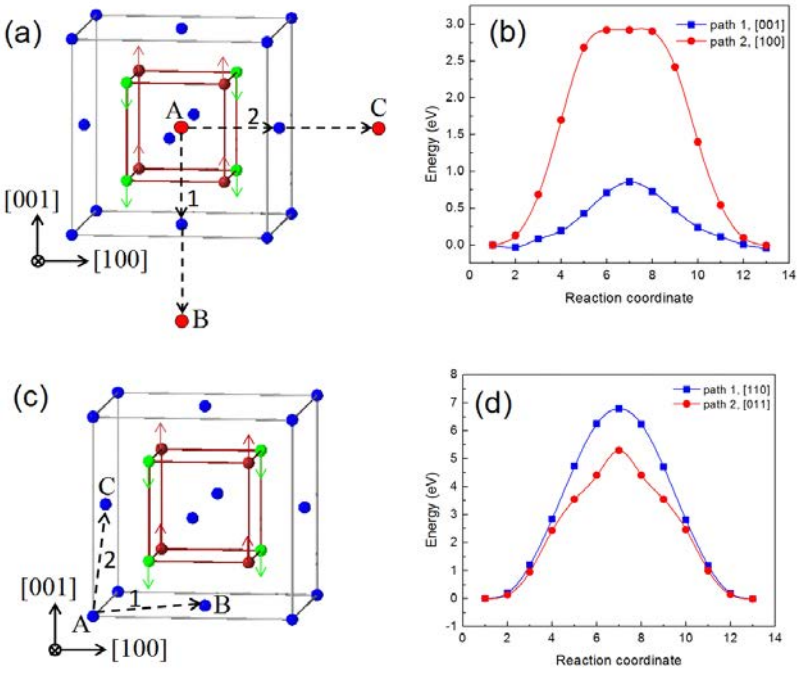

The migration mechanisms of a Zr interstitial are illustrated in Figure 1(a). The favorable interstitial site is an octahedral interstitial site, which is the center of the pseudo-fluorite unit cell [indicated by A in Figure 1(a)]. During the migration, the Zr interstitial displaces a nearby Zr lattice ion and pushes it to a new interstitial site such as B or C in Figure 1(a). In tetragonal ZrO_2, the migration paths 1 and 2 are not equivalent. The energy landscapes of the two migration paths are shown in Figure 1(b). In the path 1, the Zr interstitial migrates along the [001] or c direction with a barrier of about 0.86 eV. In the path 2, the interstitial migrates along the [100] or [010] direction (a or b direction) with a barrier of about 2.92 eV. Therefore, Zr interstitials should migrate preferentially along the [001] direction. This anisotropic diffusion would be pronounced at low temperatures such as the coolant temperature (~600 K) in reactors.

The migration mechanisms of a Zr vacancy are illustrated in Figure 1(c). The Zr vacancy hops to its nearest neighboring sites along <110> directions such as from A to B (path 1) and from A to C (path 2). The energy landscapes of the two migration paths are shown in Figure 1(d). The barriers are high, about 6.8 eV for path 1 and 5.3 eV for path 2. Therefore, Zr vacancies are expected to be immobile at 600 K. In the rest of this paper, only the Zr interstitial migration is investigated. For comparison, the Zr defect migration barriers along different paths in tetragonal ZrO_2 are summarised in Table 1.

Table 1. Anisotropic Zr defect migration barriers in tetragonal ZrO_2. The crystallographic orientations refer to the orientations in the pseudo-fluorite unit cell.

Zr defect migration barriers (eV)	
Zr_I	0.86 ([001], path 1) 2.92 ([100], path 2)
V_{Zr}	6.80 ([110], path 1) 5.30 ([011], path 2)

The anisotropic Zr interstitial migration can be explained by the crystal structure of the tetragonal phase. Figures 2(a) and 2(b) show the projections of the oxygen sublattice along the [001] and [100] directions, respectively. Clearly the projection of oxygen sublattice forms a square for the [001] projection and a parallelogram for the [100] projection. Therefore, a Zr interstitial may have a larger migration volume when it migrates along the [001] direction than along the [100] direction. As a result, it is easier for a Zr interstitial to diffuse along the [001] direction than the [100] direction.

Figure 2. Schematic illustration of the projection of the oxygen sublattice along different orientations. (a) Along the [001] direction. (b) Along the [100] direction. The red and green spheres represent oxygen ions having the different oxygen displacements shown in Figure 1(a).

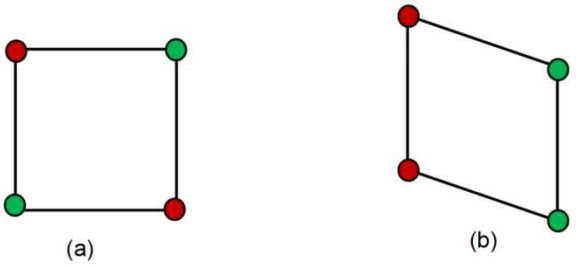

3.2 Strain effects on Zr interstitial migration

As mentioned earlier, the tetragonal ZrO_2 is subjected to large compressive stresses induced by the large volume increase resulting from the metal to oxide transformation during corrosion. In our previous study [7], we have shown that a compressive strain increases the oxygen defect migration barriers significantly. In addition, the tetragonal phase can transform to the cubic phase under a compressive strain so that the anisotropy in the oxygen defect migration vanishes. In this work similar effects are also found for Zr interstitials. In our calculation, a 3% compressive strain is applied to the simulation system isotropically. Under this strain, the tetragonal phase transforms to the cubic phase [7]. Here we use a negative sign to represent the compressive strain. The energy landscapes of the Zr interstitial migration along the [001] and [100] directions under the -3% strain are shown in Figure 3. For comparison, the energy landscapes along the two directions at the zero strain are also shown in this figure and the results are summarised in Table 2. The migration barrier is about 3.03 eV for the [001] direction and 3.33 eV for the [100] direction under the -3% strain. Clearly, the anisotropic Zr interstitial migration behaviour observed at the zero strain almost vanishes because of the tetragonal-to-cubic phase transformation. The migration barrier increases significantly in the [001] direction but only slightly in the [100] direction. Overall, the compressive strains that occur naturally during the corrosion can suppress the Zr transport in the oxide.

Figure 3. The energy landscapes of the anisotropic Zr interstitial migration at 0% and -3% strains.

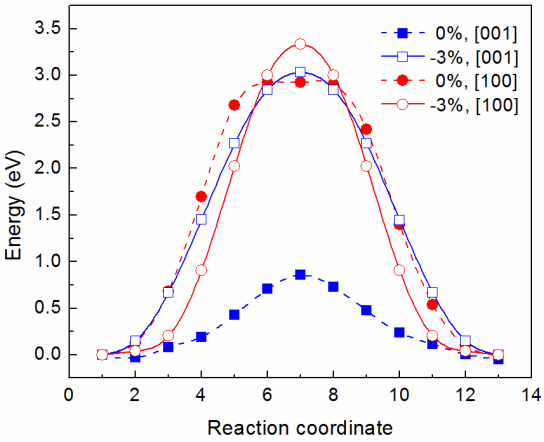

Table 2: Comparison of the Zr interstitial migration barriers along different directions under 0% and -3% strains

Zr interstitial migration barriers (eV)	
0% strain	-3% strain
0.86 ([001]) 2.92 ([100])	3.03 ([001]) 3.33 ([100])

3.3 Grain boundary vs bulk diffusion

Grain boundaries (GBs) are typically assumed as fast mass transport paths. However, in oxides the situation may be more complex due to the space charge effects. To investigate whether Zr interstitials migrate faster along GBs than in bulk, a Σ5[100](0-13) tilt GB with a rotation angle of 50.86° is created in tetragonal ZrO_2. The pristine GB consists of 3 024 ions. To find the minimum-energy GB structure for this GB, the so-called "gamma surface mapping" method is used [16]. After the mapping, the minimum-energy GB structure is obtained, as shown in Figure 4(a). The GB energy of this structure is about 1.15 J/m^2, which is a relatively low-energy GB in oxides.

Figure 4. Comparison of Zr interstitial diffusion in a GB and a bulk in tetragonal ZrO_2.
(a) The pristine minimum-energy GB structure of the Σ5[100](0-13) tilt GB.
The blue spheres represent Zr ions and red spheres represent oxygen ions.
The GB position is indicated by the dashed line.
(b) The comparison of the mean square displacements of a Zr interstitial in the GB and bulk.

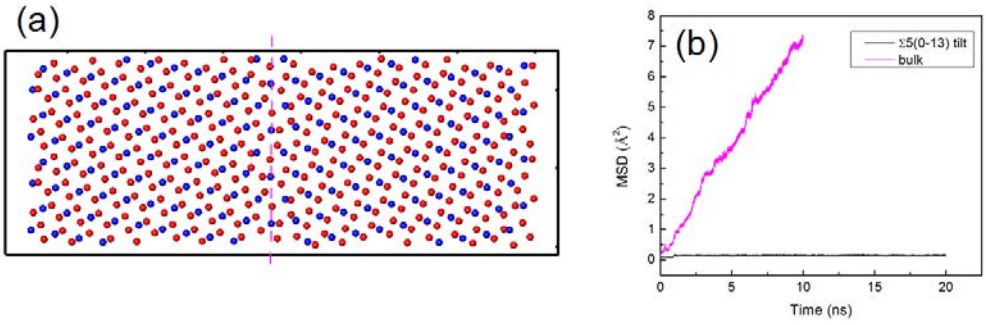

To investigate the Zr interstitial migration at this GB, a Zr interstitial is introduced to the GB. MD simulation is then conducted at 1 700 K for 20 ns in a NPT ensemble. The mean square displacement (MSD) of the Zr ions is calculated. For comparison, the MSD of

the Zr ions in a bulk system that contains a Zr interstitial is also calculated. The results are shown in Figure 4(b). The striking result is that the MSD in the bulk system increases significantly with time while the MSD in the GB does not increase much. This result indicates that the Zr interstitial migrates more slowly in the GB than in the bulk, which is somewhat counter-intuitive. Since the Zr interstitial migrates very slowly in the GB, we are unable to calculate its migration barrier in this GB. But we expect that it is much higher than that in the bulk based on the comparison shown in Figure 4(b).

4. Discussion

As mentioned at the beginning, the cation diffusion during oxide growth may reduce the density of cavities and cracks and lead to more protective oxide [6]. Previous tracer-diffusion experiments showed that the Zr self-diffusion in ZrO_2 is slow and the activation barrier is about 4.5 eV [17,18]. Such a high diffusion barrier may lead to the conclusion that cation transport does not contribute to the Zr corrosion process [3]. However, in tracer-diffusion experiments the cation diffusion is mediated via vacancies. In Zr corrosion, Zr interstitials may form in the metal-rich solid solution near the metal/oxide interface or can be created by irradiation. Currently, the studies of Zr interstitial diffusion are very limited, both experimentally and theoretically. Therefore, this work suggests that future studies may investigate the role of cation diffusion on Zr corrosion, particularly in reactor conditions.

Motta et al. [3,19] showed that the protective oxide consists of a highly oriented tetragonal phase with $(002)_t$-type texture. The orientation relationship between metal, tetragonal, and monoclinic phases in a protective oxide is:

$$(10\text{-}10)_{Zr} \,//\, (002)_t \,//\, (020)_m. \quad (2)$$

On the other hand, such a $(002)_t$ oriented oxide was not found in the non-protective oxide [3,19]. In this work, we show that Zr interstitials migrate preferentially along the [001] direction. If this is true in reality, then the protective oxide (i.e. it requires cation diffusion) should grow mainly along the cation-diffusing [001] direction so that the plane parallel to the oxide/metal interface is $(002)_t$. However, the oxide growth is a complex behaviour and many factors can modify the texture of the oxides. Therefore, more systematic studies are needed to validate our hypothesis.

In this work, we show that Zr interstitials migrate more slowly at the $\Sigma 5$ GB than in the bulk. The previous tracer diffusion experiments showed that the Zr self-diffusion at GBs is about 7 orders of magnitude faster than in bulk at about 1 200 K in yttria-stabilised-zirconia [17,18]. Therefore it seems that our result is counter-intuitive and contradicts the experimental observation. Note that in this work only the defect migration is studied. In tracer-diffusion or self-diffusion experiments, both defect formation and migration energies are involved. Typically GBs have much lower defect formation energies than in bulk and therefore the overall effect could be that GBs can have faster diffusion than in bulk. In addition, the low-energy GB studied in this work may not represent the non-ideal GBs in reality. Therefore, studies of other GBs of different GB characters are needed in the future.

This work uses a simple rigid-ion potential to model the cation migration in tetragonal ZrO_2. We should note that this potential lacks of the charge-transfer capability and it cannot represent the full nature of the oxide. Future density-function-theory-based calculations and well-designed experiments will be valuable for validating some results obtained in this work.

5. Conclusions

In this work, temperature accelerated dynamics and molecular dynamics simulations are performed to examine the cation migration in tetragonal ZrO_2, an important phase appeared during Zr corrosion. The anisotropic crystal structure effects, stress effects, and

GB effects on cation diffusion are investigated and their implications in Zr corrosion are discussed. It is found that the migration of Zr interstitials is highly anisotropic in tetragonal ZrO_2 and the migration is preferentially along the [001] direction. Under compressive stresses, it is found that the migration barrier of Zr interstitials increases significantly and becomes isotropic. The migration of Zr interstitials along a special grain boundary is also studied in this work. The result shows that Zr interstitials migrate more slowly along the GB than in bulk, suggesting that some GBs may not be fast transport paths for cation diffusion, if defects already form such as under irradiation (i.e. defect formation energy is not considered). Although this work provides the results from a purely theoretical point of view, they may serve as hypotheses for designing future experimental studies.

Acknowledgements

This work is supported by the Laboratory Directed Research and Development program (LDRD project # 12-026) at Idaho National Laboratory. This manuscript was authored by a contractor (Battelle Energy Alliance, LLC) of the US Government under the Department of Energy Contract No DE-AC07-05ID14517. Accordingly, the US Government retains and the publisher, by accepting the paper for publication, acknowledges that the US Government retains a nonexclusive, paid-up, irrevocable, world-wide license to publish or reproduce the published form of this manuscript, or allow others to do so, for US Government purposes.

References

[1] Adamson,R., B. Cox, A. Strasser, and P. Rudling (2007), "Corrosion Mechanisms in Zirconium Alloys", in ZIRAT12 Special Topic Report Corrosion Mechanisms in Zirconium Alloys.

[2] Allen, T.R., R.J. M. Konings, and A.T. Motta (2012), "5.03 Corrosion of Zirconium Alloys", in Comprehensive Nuclear Materials, edited by J.M.K. Editor-in-Chief: Rudy (Elsevier, Oxford), pp. 49-68.

[3] Motta, A. (2011), "Waterside corrosion in zirconium alloys", JOM, **63**, pp. 59-63.

[4] Yilmazbayhan, A. et al. (2004), "Structure of zirconium alloy oxides formed in pure water studied with synchrotron radiation and optical microscopy: relation to corrosion rate", Journal of Nuclear Materials, **324**, pp. 6-22.

[5] Cox, B. (2005), "Some thoughts on the mechanisms of in-reactor corrosion of zirconium alloys", Journal of Nuclear Materials, **336**, pp. 331-368.

[6] Hultquist, G. et al. (2001), "Self-Repairing Metal Oxides", Oxidation of Metals, **56**, pp. 313-346.

[7] Bai, X.-M., Y. Zhang, and M.R. Tonks (2013), "Strain effects on oxygen transport in tetragonal ZrO2", Submitted, pp.

[8] Sørensen, M.R., and A.F. Voter (2000), "Temperature-accelerated dynamics for simulation of infrequent events", Journal of Chemical Physics, **112**, pp. 9599-9606.

[9] Schelling, P.K., S.R. Phillpot, and D. Wolf (2001), "Mechanism of the Cubic-to-Tetragonal Phase Transition in Zirconia and Yttria-Stabilised Zirconia by Molecular-Dynamics Simulation", Journal of the American Ceramic Society, **84**, pp. 1609-1619.

[10] Aldebert, P., and J.-P. Traverse (1985), "Structure and Ionic Mobility of Zirconia at High Temperature", Journal of the American Ceramic Society, **68**, pp. 34-40.

[11] Henkelman, G., and H. Jónsson (2000), "Improved tangent estimate in the nudged elastic band method for finding minimum energy paths and saddle points", Journal of Chemical Physics, **113**, pp. 9978-9985.

[12] Bai, X.-M., A. El-Azab, J.G. Yu, and T.R. Allen (2013), "Migration mechanisms of oxygen interstitial clusters in UO2", Journal of Physics: Condensed Matter, Vol. 25, No. 1, 9 January 2013, pp. 015003.

[13] Bai, X.-M., and B.P. Uberuaga (2012), "Multi-timescale investigation of radiation damage near TiO2 rutile grain boundaries", Philosophical Magazine, **92**, pp. 1469-1498.

[14] Uberuaga, B.P., and X.-M. Bai (2011), "Defects in rutile and anatase polymorphs of TiO_2: kinetics and thermodynamics near grain boundaries", Journal of Physics: Condensed Matter, Vol. 23, No. 43, 2 November 2011, pp. 435004.

[15] Plimpton,S. (1995), "Fast Parallel Algorithms for Short-Range Molecular-Dynamics", Journal of Computational Physics, Vol. 117, pp. 1-19.

[16] Hoagland, R.G., and R.J. Kurtz (2002), "The relation between grain-boundary structure and sliding resistance", Philosophical Magazine A, **82**, pp. 1073-1092.

[17] Kilo, M. et al. (2003), "Cation self-diffusion of ^{44}Ca, ^{88}Y, and ^{96}Zr in single-crystalline calcia- and yttria-doped zirconia", Journal of Applied Physics, Vol. 94, Isssue 12, 15 December 2003, pp. 7547-7552.

[18] Drings, H. et al. (2009), "Enhanced 95Zr diffusion in grain boundaries of nano-crystalline ZrO2·9.5 mol% Y2O3", Physica Status Solidi (A), **206**, pp. 54-58.

[19] Motta, A.T. et al. (2008), "Microstructural Characterisation of Oxides Formed on Model Zr Alloys Using Synchrotron Radiation", Journal of ASTM International, **5**, pp. 486.

Surface structure of Cr0.5 Ti0.5N coatings after heavy ions irradiation and annealing

Sergey Kislitsin[1], Igor Gorlachev[1], Vladimir Uglov[2]
[1]Institute of Nuclear Physics, Almaty, Kazakhstan
[2]Belarusian State University, Minsk, Belarus

Abstract

Results of surface structure investigations of TiCrN coating on carbon steel after irradiation by helium, krypton and xenon heavy ions are reported in the present publication. The series of $Cr_{50}Ti_{50}N$ coatings on carbon steel with thickness of 50,..., 300 nm were formed by vacuum arc deposition techniques. Specimens with TiCrN coating on carbon steel were irradiated by low energy $^4He^{+1}$ (22 keV) and $^4He^{+2}$ (40 keV) ions and high energy Xe^{+18} and Kr^{+14} ions with energy of 1.5 MeV/nucleon. Fluence of He ions was 1.0×10^{17} ion·cm^{-2}, fluence of Xe and Kr ions was 5×10^{14}-1.0×10^{15} ion·cm^{-2}, irradiation temperature did not exceed 150°C. Study of surface structure was performed by scanning electron microscopy (SEM) and atomic force microscopy (AFM). Methods of Roentgen diffractometry and Rutherford backscattering was applied for determination of structure and thickness of coating. In case of irradiation with Xe^{+18} and Kr^{+14} ions an investigation of surface morphology and structure was done after successive two hours vacuum annealing of irradiated samples at temperatures 400°C, 500°C and 600°C.

It was shown that after irradiation by Xe and Kr ions on the surface of coating convexities appear, surface density of which correlates with ion flux. In the case of Xe, ions irradiation generated convexities of spherical and elongated shape with dimensions ranging from ten to hundreds nm. In the case of Kr ions, only spherical globules were generated, dimensions of which are 10-30 nm. The most likely explanation of observed surface damage is that: convexities on the surface are generated at ion bombardment of specimens with coating. Convexities are the traces of ions passing through coating and they are due to structural reconstruction at energy release along a trajectory of ions braking. Convexities of elongated shape represent overlapping traces from two passing ions. When the projective range of Xe and Kr ions exceeds coating thickness, damage structures is generated in the substrate and convexities are the traces of undersurface damages. After subsequent two hours vacuum annealing convexities dimensions on the surface became smaller. Overlapping convexities, observed in case of Xe ions bombardment, became separate and confirmed the hypothesis that elongated convexities are the overlapping of traces from two near passing ions. Surface flaking or coating lamination was not observed after irradiation by xenon and krypton at the above mentioned fluencies of irradiation.

Introduction

Development of nuclear power shows increased requirements to used structural materials, technologies of their manufacture and the control of serviceability. Development of new structural materials is an actual challenge for creation of reactors of generations III+ and VI. According to the requirements, reactors of Generation IV should possess high levels of efficiency and safety during a period of active operation of 40-60 years. It is possible to satisfy these requirements by a high degree of burn up of the nuclear fuel, increased

temperatures of the coolant (800°C–1 200°C), that imposes special requirements for structural materials of nuclear installations. These materials should possess high mechanical strength; radiation stability of structure and properties under irradiation; minimal activation ability; stability of geometrical parameters of the units made of them, high resistance to corrosion against fuel materials and the coolant. Development of new structural materials is conducted in several directions, such as, for example, development oxide dispersed strengthened (ODS) ferrite martensite steels, high nickel content alloys of nimonic PE-16 type, austenite steels with special dopants.

Alongside with these directions, development of materials with coatings possessing high physical-mechanical properties, used for protection of the basic material from radiation, thermal and aggressive environment impact is considered as perspective. Ceramic coatings are now being used to increase the resistibility of structural steels for high-temperature reactors to radiation embrittlement and swelling [1,2]. Among them, the special attention of the leading nuclear centers of the United States, Japan, France, Russia and other countries is focused on nitrides of transition metals. They represent the greatest interest for use as protective radiation-resistant materials in nuclear-power installations of generation III + and IV [3,4]. Interest in nitrides of transition metal can be explained by their special physical and mechanical properties, combining both properties of ceramics and metals. Coatings based on nitrides of the transition metals possess the increased hardness, wear-and corrosion resistance, thermal stability [5-7] that allows considering them as perspective protection for structural materials. Nitride coatings are already examined as perspective for covering of surface cladding of generation VI gas-cooled fast reactors (GFR) [8] and it makes actual studying of their radiation resistance. As shown in our investigations, the best results have been found out for multicomponent composite coatings based on the solid solutions of nitrides of several transition metals (Ti-Cr-N, Ti-Zr-N, Ti-Mo-N and others) [9,10]. However stability of the physical-mechanical properties of such coatings under irradiation is insufficiently studied and this impedes their possible use as radiation-resistant protective coating. The objectives of this work are to study changes on the surface structure of titanium-chromium-nitrogen coatings on steel, caused by alpha-particles irradiation simulating the accumulation of helium due to nuclear reactions at neutron irradiation, as well as by irradiation of krypton and xenon ions simulating fission fragments of nuclear fuel.

1. Experimental

Titanium-chromium-nitrogen coatings were deposited on surface of carbon steel (< 0.2 weight % C) substrates by vacuum arc deposition with ion bombardment (VAD). Vacuum arc deposition regimes was as follows: Ti and Cr cathodes, residual nitrogen pressure – $P_N = 10^{-1}$ Pa, bias voltage of 60 V, cathodes current of 100 A, deposition time of 1,…,4 min. The series of TiCrN coatings with approximately equal content of titanium and chromium on carbon steel with a thickness of 50,…, 300 nm were formed. The procedure of coating formation is presented in details in the litterature [5,7]. Specimens were disks with diameter of 15 mm and thickness of ~ 1 mm (Figure 1).

Figure 1: Shape of specimens with TiCrN coating

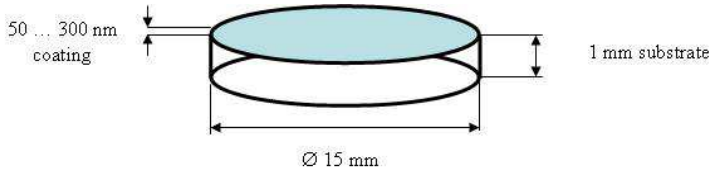

Analysis of coating element content, by using energy dispersive X-ray microanalysis EDXA (Figure 2) shows that the coating composition is a compound of titanium, chromium and nitrogen, with a titanium content of - 52.51 ± 0.07 at.% and a chromium content of - 47.49 ± 0.07 at. %.

Irradiation of specimens with TiCrN coating by alpha-particles was performed on low energy channel of heavy ion cyclotron DC-60 of Astana branch of INP. Specimens were irradiated by $^{4}He^{+1}$ ions irradiation with an energy of 22 keV per charge, i.e. hole ion energy consists E($^{4}He^{+2}$) = 40 keV, irradiation fluence – F = 1×10^{17} ions/cm^2), irradiation temperature did not exceed 150°C.

Figure 2: X-ray spectrum from the coating side

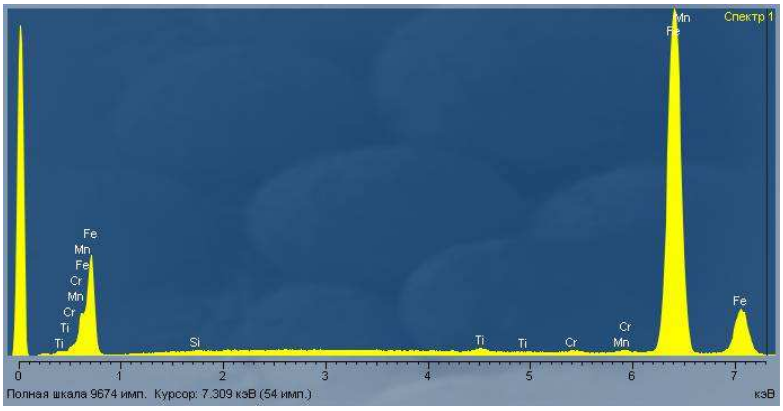

Table 1: Element content obtained by the processing of EDXA spectra

Element	Content at. %	
	Coating	Substraste
Fe	–	99.05 ± 0.22
Si	–	0.37 ± 0.19
Ti	52 ± 0.1	–
Cr	48 ± 0,1	–
Mn	–	0.58 ± 0.02

Irradiation of specimens with TiCrN coating by krypton ions ($^{84}Kr^{+14}$) and xenon ions ($^{132}Xe^{+18}$) with an energy of 1.5 MeV per nucleon was performed on high energy channel of heavy ion cyclotron DC-60. Total ion energy in case of ^{84}Kr was equal to ~ 125 MeV, F = 1×10^{16} ions/cm^2, irradiation temperature did not exceed 150°C. Total ion energy in case of ^{132}Xe was equal to ~ 200 MeV, F = 1×10^{16} ions/cm^2, irradiation temperature did not exceed 150°C.

Structure, thickness and surface morphology of the coatings were studied by X-ray diffractometry (XRD), Rutherford backscattering on protons (RBS) [11], scanning electron microscopy (SEM) and atomic force microscopy (AFM).

2. Experimental results and discussion

2.1 Effect of low-energy alpha-particles irradiation on the structure of TiCrN coating

Structural and phase stability: according to [5], chromium-titanium-nitrogen coatings deposited on the metallic substrate by VAD method at 450°C – 500°C, constitute solid solutions (Ti, Cr) N having an FCC lattice. Formed by condensing of combined plasma streams titanium and chromium in a nitrogen atmosphere, the phase composition of the TiCrN coatings represents a mixture of phases, content of which varies from (Ti, Cr) N + Cr to TiN + (Ti, Cr) N with an increase in the relative atomic concentrations of titanium to chromium. For example, increasing the chromium content leads to the formation in coating of a mixture of phases solid solutions (Ti, Cr) N and Cr, increasing titanium content leads to formation of a mixture of phases solid solutions (Ti, Cr) N and TiN.

The X-ray diffractometry of samples both before and after implantation by low-energy alpha-particles was carried out to identify the structural and phase composition of the coating. Examples of diffractogrammes of TiCrN coating on steel substrate shooting in Bragg-Brentano and grazing geometry before and after alpha-particles implantation are shown in Figure 3. According to the diffractogrammes in Figure 3, it is difficult to judge on the structural-phase state of the coating. The lack of diffraction patterns from coating of unirradiated and irradiated coating surfaces, apparently, is due to its small thickness (50 nm – 100 nm).

Figure 3: Diffractogrammes of TiCrN coating on steel: before helium ions irradiation a) – shooting in Bragg-Brentano geometry b) – grazing beam; c, d - shooting in Bragg-Brentano geometry after helium ion implantation, c) – $^4He^{+1}$, E = 22 keV, F = 1×10^{17} ion/cm^2, d) – $^4He^{+2}$, E = 40 keV, F = 1×10^{17} ion/cm^2

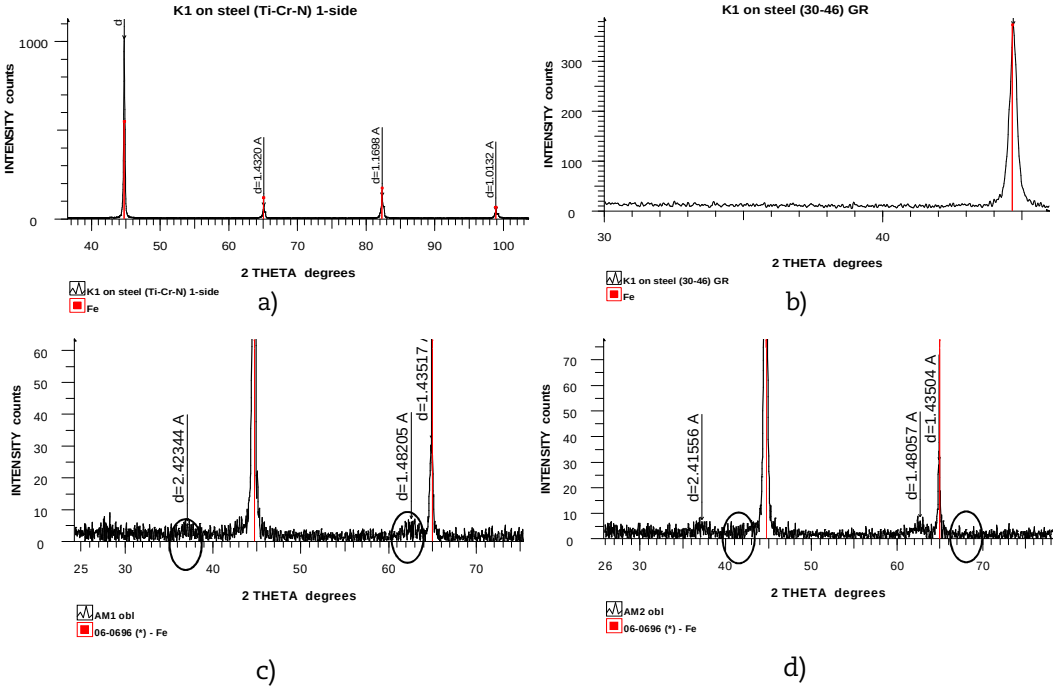

The diffractogramme of unirradiated TiCrN coatings on steel, shooting in Bragg-Brentano and grazing geometry, contains only diffraction pattern from the (110) (200) (211) (220) planes of BCC-lattice of steel (lattice constant a = 2.868 Å) as seen in Figures 3a and 3b, respectively. As can be seen from the Figures 3c and 3d, irradiation by helium ions with energy of 22 keV and 40 keV to a fluence of 1×10^{17} ion/cm^2 did not lead to significant changes in the phase composition – on diffractogrammes, only the diffraction pattern of the BCC lattice steel was clearly observed. Irradiation, however, resulted in changes of the diffraction pattern – significant increased background, reflection peaks from the planes of the BCC steel lattice became wider and on the diffractogrammes of the irradiated samples mild reflections at angles 2Θ equal to 37° and 62° appeared. However, the identification of the phase at which these reflections belong is not possible. The diffractogramme from the steel substrate is similar to the diffractogramme from the coating side of unirradiated sample. This argues in favour of radiation effects of line broadening and of background increase marked on the irradiated coating surface of the samples.

For samples with TiCrN coating of 100 nm thickness on silicon, only reflections from the FCC lattice of silicon were observed on diffractogramme of non-irradiated and irradiated with helium ions samples are observed. On the diffractogramme of the non-irradiated samples with TiCrN coating of 300 nm thickness besides FCC reflexes of silicon,

two weak diffraction lines were observed, as shown in Figure 4. These X-ray peaks can be attributed to modifications of titanium nitride. Procedure of deposition of TiCrN coating on silicon substrate is similar to the deposition of the same coatings on steel substrate. Content of this phase is small and for its identification, a diffractogramme was recorded in the range of 2Θ angles of 34°-44° with smaller step (Figure 4). The diffuse shape of the diffraction peaks and the shift with respect to the standard reflections indicates the low degree of perfection of the crystal lattice and the deviation from stoichiometry. TiN phase reflexes are absent on the diffractogramme of the sample irradiated by helium ions with energy of 40 keV to a fluence of 1×10^{17} ion/cm^2.

Figure 4: Diffractogrammes of CrTiN coating on Si:
a - before helium ions irradiation, shooting in Bragg-Brentano geometry,
b - after implantation by $^4He^{+1}$, E = 22 keV, F = 1×10^{17} ion/cm^2, shooting in Bragg-Brentano geometry

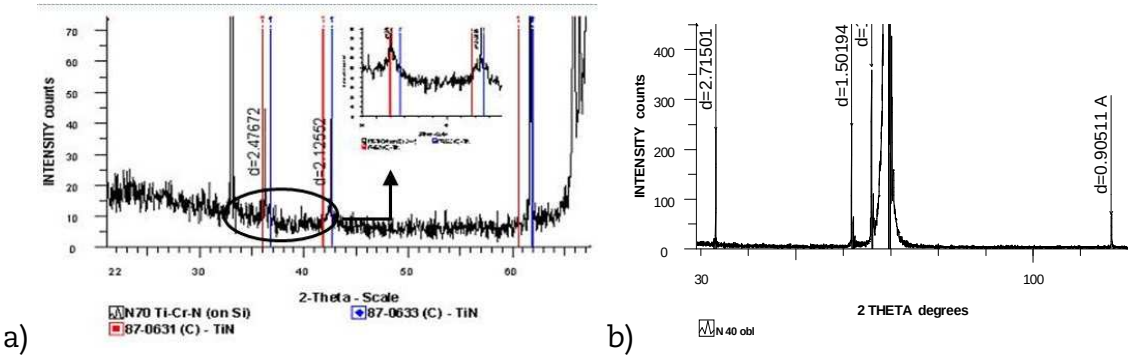

Effect of irradiation with low-energy alpha-particles on the surface morphology of the TiCrN coating: as follows from the AFM and SEM studies, surface structure of TiCrN coating has undergone changes under low energy alpha-particles bombardment. AFM images of the surface structure of the coating TiCrN before irradiation, after irradiation by helium $^4He^{+1}$ with an energy 22 keV and helium ions $^4He^{+2}$ with an energy of 40 keV to the same fluence of 1×10^{17} ion/cm^2 are shown in Figures 5a,b and c respectively.

Figure 5: Surface relief of the TiCrN coating on steel (AFM study): a - before irradiation,
b - after irradiation by helium ions with energy E = 22 keV to fluence of F = 1×10^{17} ions/cm^2,
c - after irradiation by helium ions with energy E = 40 keV to fluence of F = 1×10^{17} ions/cm^2

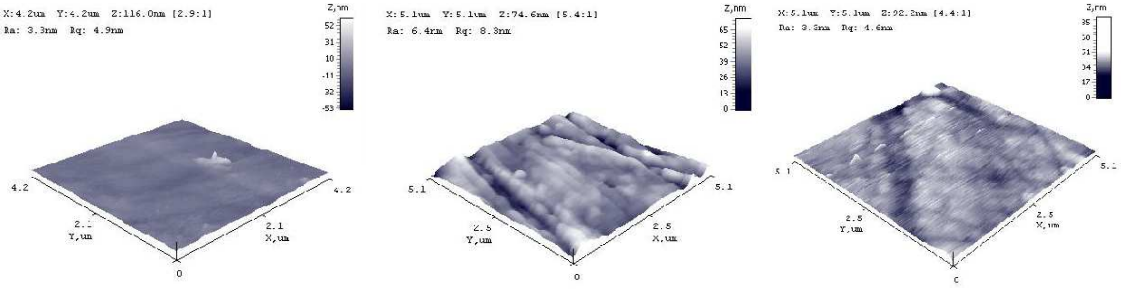

Comparison of the images in Figures 5a, 5b and 5c shows the changes of the surface roughness of TiCN coating on the energy of incident helium ions. For unirradiated TiCrN coating average surface roughness consists ~ 52 nm, surface roughness of irradiated by 22 keV helium ions consists of – 65 nm and surface roughness of irradiated with 40 keV helium ions ~ 85 nm. Moreover, it is evident that the irradiated surface of TiCrN coating became more developed compared with the non-irradiated surface of the sample. This is due to two effects: surface spattering at helium ions bombardment and energy release during braking helium ions in the coating layer. Despite the fact that for alpha-particle the sputtering surface coefficient Ks is small (Ks~0.01 atom/ion as estimated from TRIM

calculation for alpha-particle energy of 40 keV) in comparisong with heavy ions Ar or Kr, the sputtering leads to the formation of a more developed surface. The energy loss at braking helium ions in coating leads to local heating of the surface and thermal rearrangements, which also contributes to the formation of more developed surfaces.

The results of SEM studies of the coating surface structure confirm the results of AFM studies. SEM images with different magnification of the unirradiated and irradiated coating surface and image of stainless steel surface irradiated by $^4He^{+2}$ with an energy of 40 keV to fluence F = 1×10^{17} ions/cm^2, are shown in Figure 6.

Figure 6. SEM images: a – surface of the unirradiated TiCrN coating on carbon steel, b – surface of structural stainless steel 12Cr18Ni10Ti irradiated by $^4He^{+2}$ ions (E = 40 keV, F = 1×10^{17} cm^{-2}), c – surface of the TiCrN coating on carbon steel irradiated by $^4He^{+1}$ ions (E = 20 keV, F = 1×10^{17} cm^{-2}), d – surface of the TiCrN coating on carbon steel irradiated by He^{+2} ions (E = 40 keV, F = 1×10^{17} cm^{-2}).

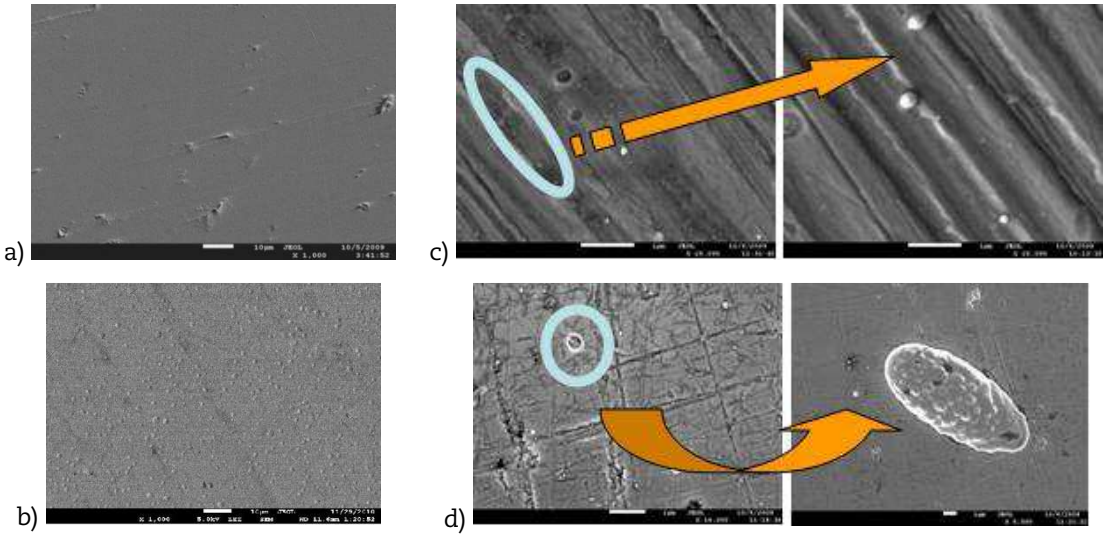

Photographs in Figure 6a, b performed at magnification ×1 000, photographs in Figure 6c and d performed at higher magnifications – ×14 000 - ×20 000.

It can be seen from Figures 6c and d after irradiation by alpha-particles with an energy of 20 keV and 40 keV at the surface of TiCrN coating objects of size of a few nanometers appeared, which seems to be helium-filled bubbles. They are visible at high magnification – right hand photos in Figures 6c and 6d. Note that in the photographs of the irradiation with ions $^4He^{+1}$ surface, separate bubbles located far from each other are observed, while on the surface irradiated by ions of $^4He^{+2}$, more complex structures are observed (compare Figures 6c and 6d). In Figure 6 where the surface structure of the TiCrN coating is shown before irradiation, such “objects” are not observed.

To compare the effects of irradiation on the surface structure in Figure 4b, the image of the surface of stainless structural steel 12Cr18Ni10Ti irradiated by $^4He^{+2}$ ions with an energy of 40 keV to the same fluence F = 1×10^{17} cm^{-2} is shown. On the steel surface, numerous blisters are clearly visible – helium-filled bubbles dimensions of which are of the order of tens of nanometers. The comparison of images of the surface structures of the steel and TiCrN coating led to the conclusion that TiCrN coatings significantly suppress the formation of blisters and flaking.

Results of surface structure studies of irradiated with alpha-particles coatings of TiCrN on silicon substrate are shown in Figure 7. Thickness of coating on silicon was the same as for a carbon steel. As seen in Figures 7 a and b, after irradiation by alpha-particles with energy 40 keV up to fluence F = 1×10^{17} cm^{-2} on the surface of the coating not

only blistering, but also flaking occured– opening of helium bubbles causing delamination of the TiCrN coating.

The reason for such a difference of the surface structure of TiCN coating on steel and on silicon is explained below: projective range of helium ions with energy 40 keV in TiCrN coating consist ~ 200 nm, according to SRIM calculations.

Figure 7: SEM images of TiCrN coating on silicon substrate irradiated with $^{4}He^{+2}$ ions up to fluence F = 1 × 10^{17} cm^{-2}, magnification a) – ×1 000, b) – ×10 000, c) – ×20 000, respectively

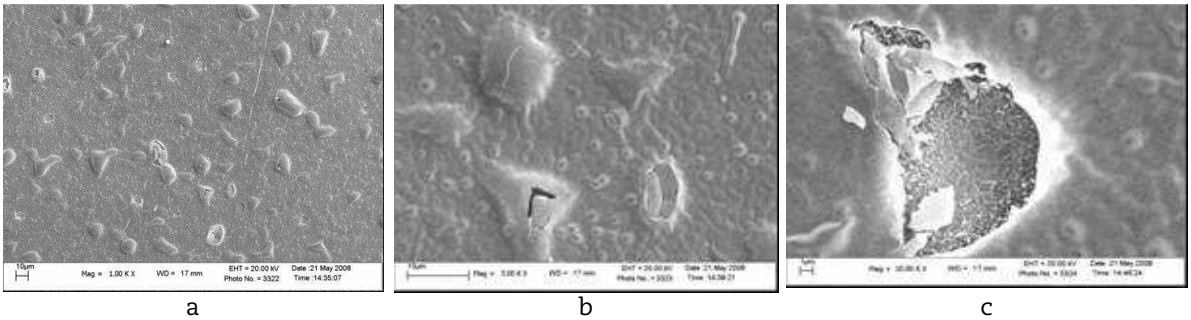

a b c

The projective range of 40 keV alpha-particles both for TiCrN coating on steel and on silicon exceed the thickness of coating or lays in the region of interface substrate – coating. Therefore stopped alpha-particles are lays in the substrate material and visible objects on the surface of coating represents the traces of undersurface helium bubbles formed in the base material.

As silicon undergoes much more voids formation, including the formation of inert gas bubbles, compared to steel, the process of gas swelling in silicon proceeds more intensively than in steel. It leads to the formation of larger gas bubbles and to larger gas pressure in bubbles and therefore opening of helium bubbles on the surface and to flaking and delamination of the TiCrN coating.

Study of unirradiated and irradiated specimens with TiCrN coatings on carbon steel by Rutherford backscattering method on protons give results presented in Figure 8 and in Table 2. In Figures 8a, b and c, RBS spectrums of backscattered protons and their approximation are shown.

Figure 8: RBS spectrums of unirradiated and irradiated by helium ions specimens with TiCrN coating on carbon steel – black curves, results of approximation – red curves; a) – unirradieted sample, b – irradiated by 4He+1 ions, c) – irradiated by $^{4}He^{+2}$ ions.

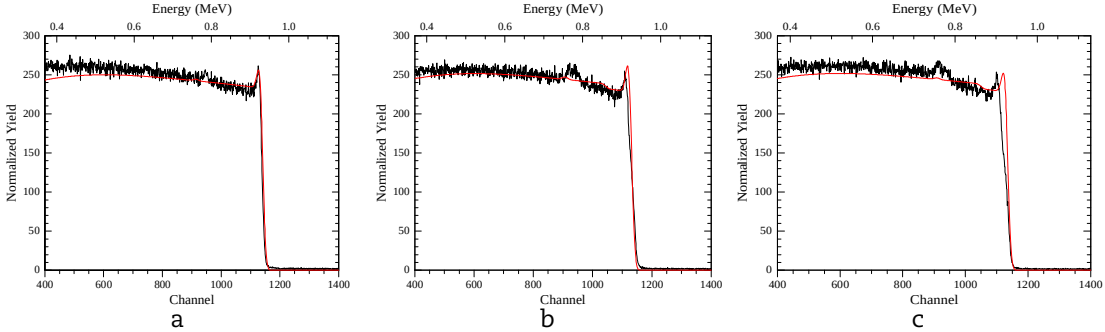

a b c

Approximations from Figures 8a, b was used for calculations of element content along distance from the surface coated by TiCrN (Table 2). Shift and decreasing of the amplitude of the peak corresponding to the irradiated TiCrN coating can be explained by the implantation of helium in the subsurface area, that is resulting in a relative decrease of the content of the main coating components (Ti and Cr) as well as a cracking of carbon

compounds from the vacuum on the sample surface under irradiation. Therefore, the presence and quantity of helium and carbon in subsurface layers (Table 2), were calculated from the condition of the best agreement of the experimental and simulated spectra in the coverage area, keeping in mind the presence of the invisible He and C components in the spectra. Shift and decreasing of the amplitude of peak corresponding to irradiated TiCrN coating can be explained by implantation of helium in the subsurface area, resulting in a relative decrease of the content of main coating components (Ti and Cr) as well as the cracking of carbon compounds from the vacuum on the sample surface under irradiation.

The results of RBS study confirmed our suggestion that the range of alpha-particle with energy of 40 keV exceed the coating thickness and gas bubbles nucleate in substrates.

Table 2: Estimated values of element contents along the distance from surface for unirradiated and irradiated by heliun ions specimens with TiCN coating on carbon steel

Unirradiated specimen with TiCrN coating on carbon steel						
Distance from surface, nm	Content at.%					
	Cr	Ti	N	Fe		
<50	35	35	30	0		
>50	0	0	0	100		
Speciment with TiCrN coating on carbon steel irradiated by ions $^{4}He^{+1}$, E = 22 keV						
Distance from surface, nm	Content at.%					
	Cr	Ti	N	He	C*	Fe
<50	35	35	30	?	?	0
50-300	0	0	0	15	0	85
>300	0	0	0	0	0	100
Speciment with TiCrN coating on carbon steel irradiated by ions $^{4}He^{+2}$, E = 40 keV						
Distance from surface, nm	Content at.%					
	Cr	Ti	N	He	C*	Fe
<50	35	35	30	?	?	0
50-300	0	0	0	15	0	85
>300	0	0	0	0	0	100

- carbon film is appear at the surface during irradiation in vacuum chamber

? content of helium was determined from normalisation requirement

2.2 Effect of high-energy krypton and xenon ions irradiation on the structure of TiCrN coating

Structural and phase stability: studies of the structure of the TiCrN coating with thickness 50 nm-100 nm on a carbon steel by X-ray diffractometry before irradiation by xenon and krypton ions showed that only X-ray reflexes from carbon steel are observed on the diffractogramme and they are similar to the ones shown in Figures 3a and b. At the same time, the RBS method showed that the coating contains Ti and Cr in approximately equal amounts (Table 2).

Studies of the coating structures after irradiation by $^{84}Kr^{+14}$ and $^{132}Xe^{20+}$ with energy 1.5 MeV/nucleon to a fluence of 5×10^{14}-1×10^{15} ion.cm^{-2} by X-ray diffractometry showed that no significant changes in the structure of the coating and the substrate. Only the reflections of BCC lattice of steel with the slight broadening of the diffraction peaks there are in the diffractogrammes. In Figure 9 is shown the diffraction pattern TiCrN coating on steel irradiated by $^{132}Xe^{20+}$ ions to a fluence of 1×10^{15} ions cm^{-2}.

Comparison of diffraction pattern of unirradiated (Figure 3 a) and of irradiated (see Figure 9) the TiCrN coatings on steel shows that the structure changes are insignificant.

Figure 9: Diffractogramme of TiCrN coating on steel irradiated by $^{132}Xe^{20}$ ions with energy 1.5 MeV/nucleon to a fluence of 1×10^{15} cm^{-2}

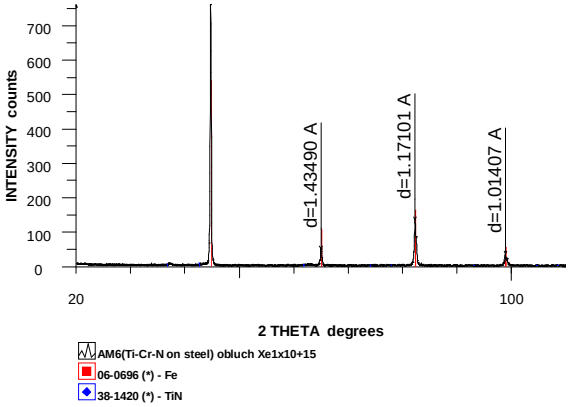

RBS researches also revealed no changes in the structure of coatings after irradiation by $^{84}Kr^{+14}$ and $^{132}Xe^{20}$ with an energy of 1.5 MeV/nucleon. This is due to the fact that the projective range of krypton and xenon ions with energies ~ 125 MeV and ~ 200 MeV, respectively, exceeds almost twice the range of the 1 MeV protons at the analysis of the structure by the RBS method.

Effect of irradiation with high-energy kripton ions and subsequent annealing on the surface morphology of the TiCrN coating: the influence of irradiation with high-energy ions of krypton and xenon revealed in changes of the surface structure of TiCrN coating. The structure of the surface before irradiation and after irradiation was investigated by AFM and SEM.

AFM images of the surface structure of both unirradiated and irradiated by krypton ions samples are shown in Figure 10. As seen in Figure 10a, the surface roughness before irradiation does not exceed 35 nm

Figure 10: The surface structure of the TiCrN coating on steel

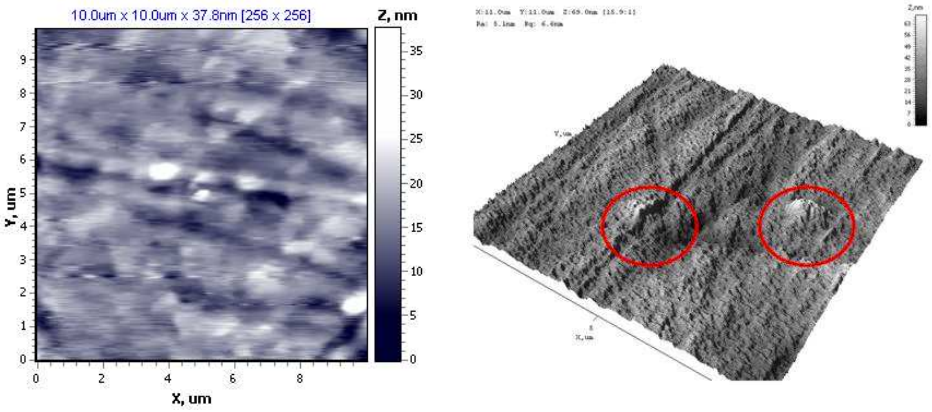

a) before irradiation by krypton ions b) after irradiation by krypton ions

As seen from a comparison of Figures 10a and 10b, the surface structure of the coating before irradiation and after irradiation by krypton is considerably different. It is seen that after irradiation on the background of relatively smooth coating surface (roughness ~ 10-15 nm) the convexities of spherical shape were observed, height of which ~ 50-60 nm and the diameter of the order of tens of nanometers (they displayed by red circles in Figure 10b). These convexities appeared to be traces on the surface from bombarding particles, i.e. ion tracks.

Results of SEM study of coatings surface are presented in Figure 11, showing the structure before (Figure 11a) and after irradiation (Figures 11b and c).

Figure 11: SEM photographs of the surface of TiCrN coating on steel
a - before irradiation, magnification × 70 000;
b, c - after the krypton irradiation, magnification ×40 000 and ×200 000, respectively

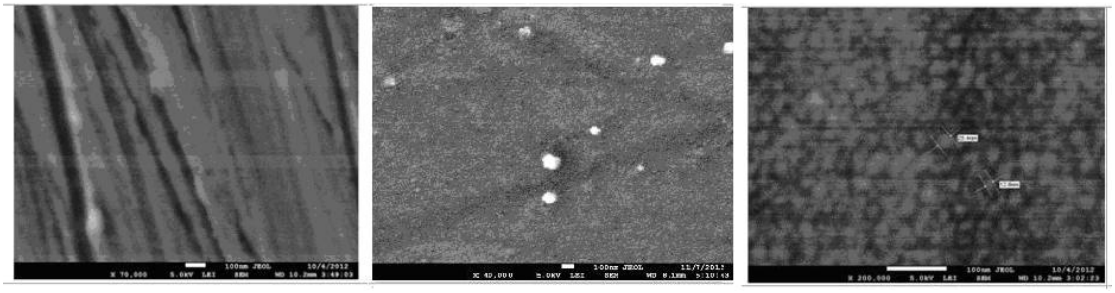

a b c

Comparison of the surface structure in Figures 11a,b and c shows appearance of convexities on the irradiated surface of coating – traces of incident krypton ions moved through coating. This result entirely confirms those obtained with AFM studies. The diameter observed on the surface convexities reaches from 13 nm up to 26 nm. Surface density of convexities correlates with the fluence of bombarding ions and supports the assumption that the convexity is ion tracks.

Samples with coatings irradiated by krypton ions were subjected to successive two-hour vacuum annealing at temperature of 400 ± 5°C, 500 ± 5°C and 600 ± 5°C. SEM images of irradiated coating surface after annealing are presented in Figure 12.

Figure 12: SEM photographs of the surface of TiCrN coating
on steel after post irradiating successive two-hours isochronal annealing:
a) after the krypton irradiation, before annealing, magnification ×200 000;
b) after two-hours annealing at 400 ± 5°C, magnification ×200 000;
c) after next two-hours annealing at 500 ± 5°C, magnification ×170 000

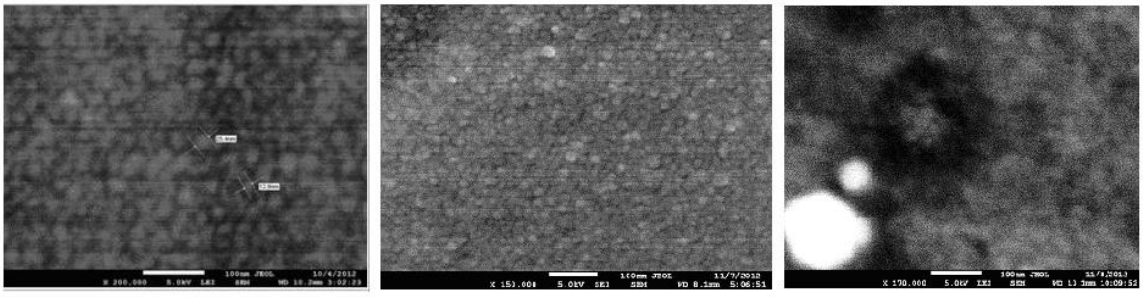

a) b) c)

From Figure 12a, visible evolution of the surface structure, namely, the reduction of the size of convexities formed under irradiation. Annealing at 400°C leads to reduction of the convexities size and the next annealing at 500°C leads to disappearance. In addition, the coating delaminating or opening of the convexities on the surface was not observed after irradiation or after post irradiating annealing in the temperature range 400°C-600°C.

Effect of irradiation with high-energy xenon ions and subsequent annealing on the surface morphology of the TiCrN coating: studies of surface structure, similar to those which were conducted on samples coated with TiCrN irradiated by high-energy krypton ions, were performed on samples irradiated by 200 MeV xenon ions. Results of surface structure studies by AFM are shown in Figure 13.

Figure13: AFM images of the TiCrN coating surface before and after irradiation with high-energy xenon ions
a - before irradiation; b, c - after irradiation by 132Xe20 + with an energy of 1.5 MeV / nucleon, with different resolution

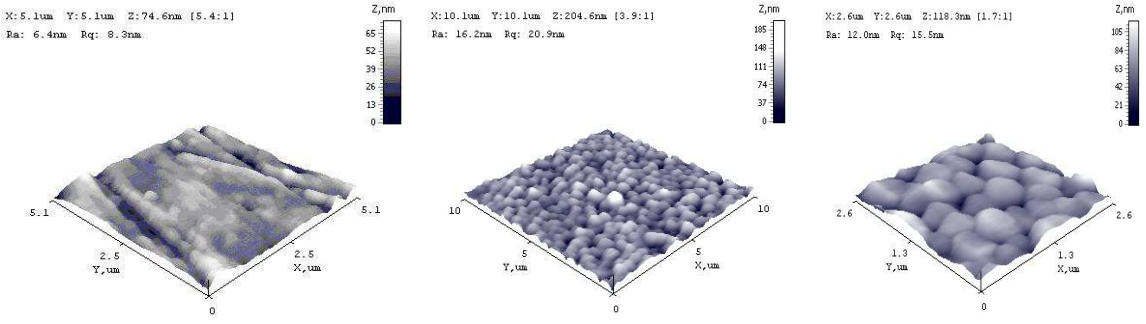

a b c

From comparison of the AFM images of the coating surface relief before and after irradiation by high energy xenon ions (Figures 13a, b and c), it can be seen that the surface roughness increased significantly – from 40 nm for non-irradiated to 170 nm for irradiated. Besides the surface, convexities or globules appeared at the surface (Figures 13b and c), where the density correlates with the fluence of xenon ions. An image at higher magnification (Figure 12c), allows us to estimate the diameter of the globules, order of which is ~ 100-400 nm.

SEM studies results shows that the structure of the TiCrN coating surface irradiated by high energy xenon ions has changed to a greater degree than after irradiation by high-energy krypton ions. Figure 14 shows the SEM images of the coating surface before irradiation and after irradiation by xenon ions performed at different magnification.

Figure 14 Structure of the TiCrN coating surface on carbon steel: a - before irradiation, b, c - after irradiation by $^{132}Xe^{20+}$ with energy of 1 MeV/nucleon to the fluence of 1×10^{15} ion•cm^{-2}, magnification ×27,00 and ×14,000, respectively

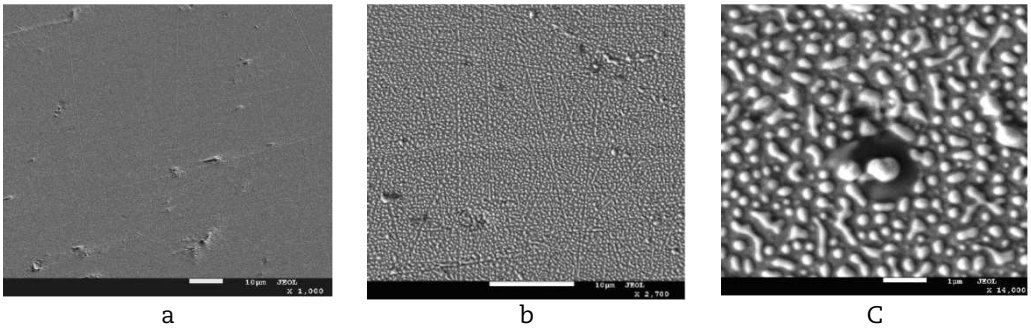

a b C

From comparison of surface images in Figures 14a, b and c, it is seen that the surface coating has significantly changed under irradiation by xenon ions. Globules with a dimension from tens to hundreds of nanometers are observed on the coating surface. As well as after irradiation by high-energy krypton ions, the appearance of the convexities (globules) on the surface after irradiation by high-energy xenon ions can be explained by "swelling" of the surface due to the energy release at passage of bombarding xenon ions through material. SEM study is in agreement with the results of coating surface study by AFM.

Unlike krypton ion irradiation after irradiation by xenon the globules size is much larger and an overlapping is observed of tracks from near incident ions. Overlapping of tracks can be explained by two factors: a larger diameter of tracks on the surface, which is a consequence of the difference in the energy of the incident xenon ions (~ 200 MeV)

and krypton (~125 MeV) and higher energy loss during passing of xenon ions through material. The second reason is the twice higher fluence of xenon ions and, correspondingly, higher density of tracks on surface.

Samples irradiated by xenon ions were subjected by successive two-hour vacuum annealing at temperatures of 400 ± 5°C, 500 ± 5°C and 600 ± 5°C. SEM images of irradiated coating surface after annealing are presented in Figure 15.

From the comparison of the surface images in Figure 15a, b, c and fig.15d, f, g, the dependence of globule ensemble evolution from temperature of successive annealing is noted. The surface structure, i.e. structure of the globules formed under irradiation is transformed in the process of successive annealing. If after two hours annealing at temperature of 400°C structure did not change much then after annealing at 500°C and especially after annealing at 600°C the structure of globules changes significantly.

Figure 15: The surface structure of the TiCrN coating on steel after irradiation by $^{132}Xe^{20+}$ with an energy of 1.5 MeV/nucleon to a fluence of 1×10^{15} ions/cm^2 and subsequent isochronous two hours annealing
a – after irradiation by xenon ions, magnification ×14 000
b c – after annealing at temperature of 400°C, magnification ×10 000 and ×35 000, respectively
d,e,f – after annealing at temperature of 500°C, magnification ×10 000, ×35 000 and ×100 000, respectively

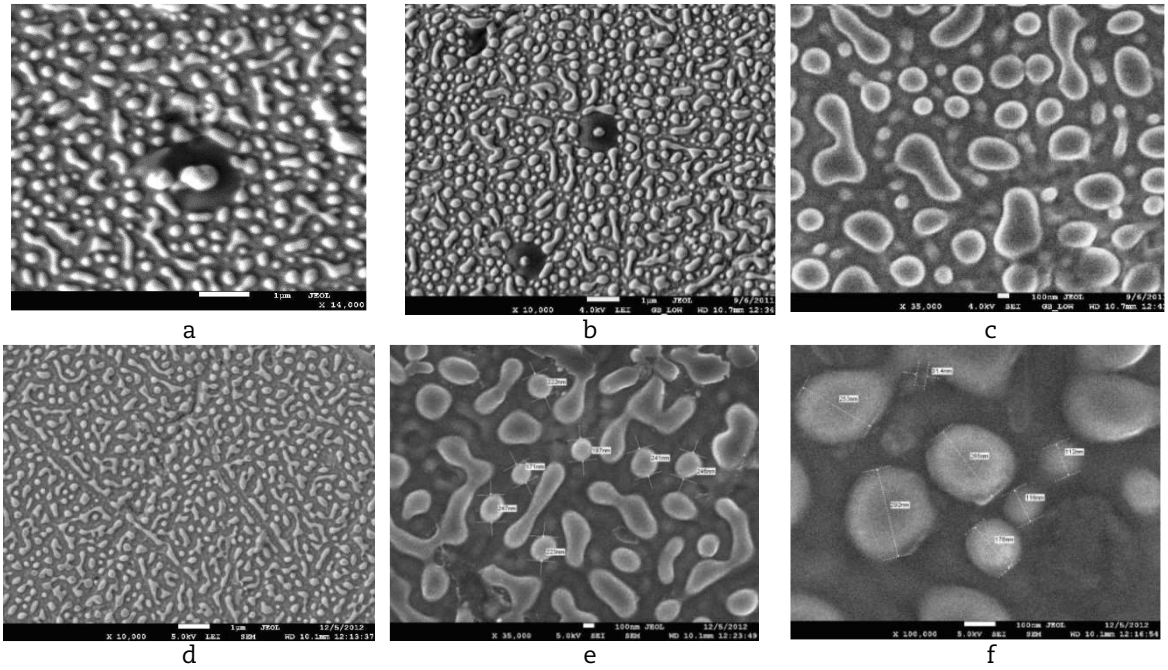

The process of formation and evolution of the globules occurs as follows: globules with dimensions from 100 nm to 400 nm are observed on coating surface immediately after irradiation. Their fine structure is clearly visible in Figure 15b. Globules may have different shapes – spherical or elongated. Globules of spherical type, seem to have formed on the place of incident of the single xenon ions. Globules of more complicated shape, have probably formed in those areas of the surface where overlap heat affected zones at braking of the incident xenon ions. In favour of that globules on the surface are tracks from the incident ions indicate the correlation between the surface density of globules and fluence of bombarding xenon ions. The two-hour annealing at 400°C leads to a clearer separation of the globules, but their size only slightly changes. After subsequent annealing at 500 and 600°C, the transformation of the globules looks more – globule diameter on the surface decreases and the overlapping traces of nearby incident ions of xenon becomes separated.

In our opinion, the observed pattern of formation and transformation of the globule ensemble in case of irradiation by krypton and xenon ions confirms the proposed mechanism of surface radiation damages at bombardment by heavy ions and its evolution during subsequent annealing. Under bombardment by xenon ions on the surface of TiCrN coating globules are formed which are the tracks from passing krypton and xenon ions. They are formed due to structural changes at energy release along the trajectory of ion braking. In fact, these structures are latent tracks along which the structural changes occurred due to local release of energy and globules on the surface – their manifestation. Formation of more complex shapes of globules is explains by overlapping tracks of the incident ions. Thermal annealing leads to structure recovery, i.e. to reducing the size of separate globules on the surface. Globules of more complex shape also transformed – structure recovery during annealing leads to separation of tracks and to decreasing of their size [12].

3. Conclusion

Studies of the effect of irradiation by low-energy alpha particles with an energy E = 40 keV to a fluence of F = 10^{18} cm^{-2}, high-energy ions ^{84}Kr and ^{132}Xe with energy E = 1.5 MeV / nucleon to fluences F = $10^{14} \div 10^{15}$ cm^{-2} on steel with TiCrN coatings of thicknesses (50÷300 nm) showed:

- Irradiation by low energy (20-40 keV) alpha particles leads to the following effects. For TiCrN coating of thickness 50-300 nm, the projective range of 40 keV alpha–particles exceeds thickness of coating and they stop in the substrate, for 20 keV alpha–particles the projective range is in interface substrate – coating region. Implanting of helium generates nucleation of gas bubbles in substrate and the small globules visible on the surface represent indications of gas bubbles nucleated in the substrate. Such indications are connected with surface areas where there are structural inhomogeneities, such as grooves or dimples. TiCrN coating having high mechanical properties suppress blistering and flaking compared to stainless steel. Thicker coating seems to be able to suppress gas swelling in much more degree.
- Irradiation by high-energy (1.5 MeV/nucleon) Kr and Xe ions leads to the following effects. Globules appear on the surface of coating, surface density of which correlates with ion fluence. In the case of Kr ions irradiation, spherical globules from 10 to 30 nm were generated. In case of Xe ions irradiation, globules of spherical and elongated shape from 10 up to hundreds nanometers were formed. A probable explanation surface damage is that, unlike irradiation with alpha-particles in which the globules on the surface are the indications of subsurface gas bubbles, after irradiation with heavy ions Kr and Xe the globules on the surface indicates the passage of single heavy ions but not gas bubbles. Globules on the surface are traces from passing ions resulting in structural transformation at energy release along trajectory of ions braking. Globules of elongated shape represent overlapping traces from two near passing ions. As the projective range of both Xe and Kr ions significantly exceed coating thickness, the structure of damages is generated in substrate and the globules are an indication of undersurface damages. At alpha-particle bombardment the energy release from single helium ion is negligibly small compared to the energy release from single heavy ion and transformation of the structure does not occur, but due to small migration energy, low solubility and high density in straggling region helium atoms are collected into gas bubbles. After a subsequent two hours vacuum annealing, the globules dimensions on the surface decreased. Overlapping globules observed in case of Xe ions bombardment became separated and confirmed that elongated globules are the overlapping traces from two near passing ions. Surface flaking or coating delamination was not observed after irradiation at the above mentioned fluences of irradiation and at subsequent annealing.

The common conclusions that can be drawn from these studies are that: TiCrN coatings of nanometer thickness are able to considerably reduce surface swelling and coating delamination at irradiation by low energy alpha-particles up to a fluence 10^{18} cm^{-2}. At irradiation by high energy heavy ions of inert gas, surface swelling takes place but delamination of coating does not occur.

References

[1] Murty, K.L., I. Charit, Structural Materials For Gen-IV Nuclear Reactors: Challenges And Opportunities, Journal of Nuclear Materials, Vol. 383, 2008, p. 189-195.

[2] Kurata Y., H. Sato, H. Yokota, T. Suzuki (2012), "Development of aluminum powder alloy coating for innovative nuclear system with lead-bismuth // Structural Materials for Innovative Nuclear Systems", Workshop Proceedings, Daejon, Republic Korea, 31 August – 3 September 2010, OECD/NEA, No 6896, p. 177-188.

[3] Ciriello, A., V.V. Rondinella, D. Staicu, J. Somers (2007), Thermophysical characterisation of nitrides inert matrices: Preliminary results on zirconium nitride, Journal of Nuclear Materials, Volume 371, p. 129-133.

[4] Belous, V.A., A.S. Kuprin, V.L. Ovcharenko, E.N. Reshetnjak, M.G. Halomeev, S.K Goltvjanina (2012), " Corrosion resistance of multicomponent arc-vacuum nitrides coating in reactor water", Proceedings of XX International conference on physics of radiation phenomena and radiation material science, Alushta, 10-15 September 2012, KIPT 2012, p. 333-334. (in Russian).

[5] Uglov, V.V., V.M.Anischik, S.V.Zlotski, G.Abadias, S.N.Dub (2005), Stress and mechanical properties of Ti-Cr-N gradient coatings deposited by vacuum arc, Surface & Coatings Technologies, Volume 200, Issue 1-4, pp. 178 – 181.

[6] Ivanovskii, A.L. (1996), Triple carbides and nitrides on the base trasition metals and IIIB- and IVB groups, Chemistry Progress, Vol. 65, No. 6, pp. 499-518 (in Russian).

[7] Uglov, V.V., V.M.Anischik, V.V.Khodasevich, M.M.Danilionak, D.P.Rusalsky, V.A. Ukhov (2007), Thermal stability of nitride coatings formed by ion-plasma deposition, Vacuum, Volume 81, pp. 1345-1347.

[8] Gavarini, S., N.Toulhoat, C.Peaucelle, P.Martin, J. Mende, Y.Pipon, H.Jaffrezic (2007), "Xenon migration behaviour in titanium nitride", Journal of Nuclear Materials, Volume 362, iss.2-3, p. 364-373.

[9] Uglov, V.V., D.P. Rusalski, S.V. Zlotski, A.V. Sevriuk, G. Abadias, S.B. Kislitsin, K.K. Kadyrzhanov, I.D. Gorlachev, S.N. Dub (2010), "Stability of Ti-Zr-N coatings under Xe-ion irradiation", Surface & Coatings Technologies, Volume 204, pp. 2095–2098.

[10] Kislitsin, S., K. Kadyrzhanov, V. Uglov, D. Rusalski, G. Abadias, S. Dub (2012), "Study of heavy ion irradiation on structure of triple titanium nitride base coating", Structural Materials for Innovative Nuclear Systems, Workshop Proceedings, Daejon, Republic Korea, 31 August – 3 September 2010, OECD, NEA No. 6896, p. 87.

[11] Arzumanov, A.A., A.N. Borisenko, I.D. Gorlachev, A.S. Eliseev, K.K. Kadyrzhanov, S.N. Lysukhin, A.V. Platov, A. Sapozhnikov, "Tandem accelerator UKP-2-1 in nuclear-physical investigations", Preprint N 21, Almaty: Institute of nuclear physics, 2002, 35p.

[12] Kislitsin, S.B., I.D.Gorlachev, V.V.Uglov (2013), Surface structure of titanium-chromium-nitrogen coatings irradiated by Kr, Xe and He ions. Abstract of IX International conference "Nuclear and Radiation Physics", Almaty, 24-27 September, 2013, INP 2013, p. 81. (in Russian).

List of participants

Australia

EDWARDS, Lyndon
Head, Institute of Materials Engineering
Australian Nuclear Science and
Technology Organisation
PMB 1, Menai, Sydney
NSW 2234

Tel: +61 0 297 173 652
EM: led@ansto.gov.au

Czech Republic

LIDDELL, Petr
Hlavni 130
Husinec – řež
250 68

Tel: +420 00420266172273
EM: ldd@ujv.cz

France

CABET, Céline
CEA, DEN/Département des matériaux
pour le nucléaire
CEA Saclay – Bat 520
91191 Gif-sur-Yvette

Tel: +33 1 69 08 16 15
EM: celine.cabet@cea.fr

Germany

HOFFMANN, Jan
Herrmann-von-Helmholtz-Platz 1
76344 Eggenstein-Leopoldshafen

Tel: +49 721 6082 3476
EM: j.hoffmann@kit.edu

Japan

KISHIMOTO, Hirotatsu
27-1 Mizumoto-cho,
Muroran, Hokkaido 050-8585

Tel: +81 143 46 5615
EM: hkishi@mmm.muroran-it.ac.jp

KOHYAMA, Akira
OASIS, Muroran Institute of Technology
27-1 Mizumoto-cho, Muroran 050-8585

Tel: +81 143 46 5680
EM: kohyama@mmm.muroran-it.ac.jp

SUZUDO, Tomoaki
JAEA
Shirakata Shirane 2-4, Tokai-mura
Naka-gun, Ibaraki-ken319-1195

Tel: +81 (29) 282 5434
EM: suzudo.tomoaki@jaea.go.jp

Kazakhstan

KISLITSIN, Sergey
Institute of Nuclear Physics
Ibragimov Str 1
050032 Almaty
Tel: ++7 777 386 86 39
EM: skislitsin@inp.kz

Korea (Republic of)

PARK, Ji Yeon
Nuclear Materials Research Division
Korea Atomic Energy Research Institute
Daedeok Daero 1045, Deokjin-dong,
Yuseong-gu
Daejeon 305-353
Tel: +82 42 868 2311
EM: jypark@kaeri.re.kr

SAH, Injin
291 Daehak-ro
Yuseong-gu
Daejeon
Tel: +82 42 3503864
EM: injin@kaist.ac.kr

Russian Federation

IGNATIEV, Victor V.
Head of Laboratory
Inst. of Nuclear Reac
RRC – Kurchatov Institute
Kurchatov sq. 1, 123182 Moscow
Tel: +7 499 196 71 30
EM: ignatev_vv@nrcki.ru

Spain

SAEZ, Alberto
Avenida Complutense, 40
28040 Madrid
Tel: +34 913466606
EM: alberto.saez@ciemat.es

Sweden

MESSINA, Luca
Reactor Physics Department
KTH – Royal Institute of Technology
AlbaNova University Centre
106 91 Stockholm
Tel: +46 855378209
EM: messina@kth.se

OLSSON, Pär
Associate Professor
Reactor Physics Division
KTH – AlbaNova
106 91 Stockholm
Tel: +46 8 55 37 82 08
EM: polsson@kth.se

United Kingdom

MARROW, James
University of Oxford
Department of Materials
Parks Road, Oxford OX1 3PH
Tel: +44 1865 273938
EM: james.marrow@materials.ox.ac.uk

PIMBLOTT, Simon M.
University of Manchester
Dalton Cumbrian Facility
Westlakes Science and Technology Park
Moor Row
Cumbria CA24 3HA
Tel: +44 161 275 1325
EM: simon.pimblott@manchester.ac.uk

SHEPHERD, Daniel
NNL
Sellafield
Seascale
Cumbria CA20 1PG
EM: daniel.shepherd@nnl.co.uk

United States

ALLAHAR, Kerry
995 University Blvd
Idaho Falls, ID 83415
Tel: +1 208 533 8169
EM: kerryallahar@boisestate.edu

BAI, Xianming
2525 Fremont Avenue
PO Box 1625, MS 3835
Idaho Falls, ID 83415
Tel: +1 208 526 2496
EM: xianming.bai@inl.gov

BENZ, Julian
PO Box 1625
MS 2213
Idaho Falls, ID 83415
Tel: +1 208 526 1102
EM: julian.benz@inl.gov

CHAKRABORTY, Pritam
2525 Fremont Ave
Idaho Falls
Idaho
Tel: +1 208 526 1635
EM: pritam.chakraborty@inl.gov

CHARIT, Indrajit
875 Perimeter Drive MS3024
Moscow, ID 83844-3024
Tel: +1 208 885 5964
EM: icharit@uidaho.edu

CHOI, Yong-Joon
INL
PO Box 1625
MS 3835
Idaho Falls, ID 83415
EM: yong-joon.choi@inl.gov

DEEVI, Seetharama
12642 Grendon Drive
Midlothian
VA 23113
Tel: +1 8048691836
EM: seetharama.deevi@fuqua.duke.ed

GANDY, David
Tel: +1 704 595 2695
EM: davgandy@epri.com

HAIDYRAH, Ahmed
Nuclear Engineering
Missouri University of Science & Technology
222 Fulton Hall
Rolla, MO 65409-0170
Tel: +1 573 466 2222
EM: ashdz2@mst.edu

LYBECK, Nancy
Idaho National Laboratory
2525 Fremont Ave.
P.O. Box 1625, MS 3605
Idaho Falls, ID 83415-3605
Tel: +1 208 526 1033
EM: nancy.lybeck@inl.gov

MA, Wen
MIT
144 Albany st. room 2214
Cambridge, MA 02139
Tel: +1 617 324 27 23
EM: sucaba@mit.edu

SIMPSON, Joel
EM: joel.simpson@inl.gov

TOMAR, Vikas
Tel: +1 765 494 3423
EM: tomar@purdue.edu

WHARRY, Janelle
1910 University Drive
Boise, ID 83725-2090
Tel: +1 208 426 5659
EM: janellewharry@boisestate.edu

WINSTON, Philip
2525 Fremont St
Idaho Falls, Idaho
Tel: +1 208 526 3679
EM: philip.winston@inl.gov

WRIGHT, Richard N.
Idaho Falls, ID 83415
Tel: +1 208 526 6127
EM: richard.wright@inl.gov

WU, Yaqiao
995 University Blvd.
Idaho Falls, ID 83401
Tel: +1 208 533 8112
EM: yaqiaowu@boisestate.edu

YOUSSEF, Mostafa
77 Massachusetts Avenue
NW13-202
Cambridge, MA 02139
Tel: +1 617 253 5466
EM: myoussef@mit.edu

International Organisations

European Commission (EC)

FAZIO, Concetta
JRC – ITU
Karlsruhe
Germany
EM: concetta.fazio@ec.europa.eu

International Atomic Energy Agency (IAEA)

INOZEMTSEV, Victor
Nuclear Fuel Cycle and Materials Section
P.O. Box 100
1400 Vienna
Austria
Tel: +43 1 2600 22760
EM: v.inozemtsev@iaea.org

OECD Nuclear Energy Agency (NEA)

CORNET, Stéphanie
Nuclear Fuel Cycle Physicist, Data Bank
12 boulevard des Iles
92130 Issy-les-Moulineaux
France
Tel: +33 (0) 1 45 24 10 82
EM: stephanie.cornet@oecd.org

OECD Nuclear Energy Agency
12, boulevard des Îles
92130 Issy-les-Moulineaux, France
Tel.: +33 (0)1 45 24 10 15